



**OXIDATIVE POTENTIAL AND CANCER RISK OF AMBIENT  
PARTICLES IN AN URBAN COASTAL AREA OF CHINA:  
CHEMICAL CHARACTERIZATION, SOURCE  
APPORTIONMENT, AND RESPIRATORY DEPOSITION**

**LORD FAMIYEH, MSc**

**THESIS SUBMITTED FOR THE DEGREE OF DOCTOR OF  
PHILOSOPHY**

**FACULTY OF CHEMICAL AND ENVIRONMENTAL ENGINEERING**

**UNIVERSITY OF NOTTINGHAM**

**2023**

## **Abstract**

Particulate matter (PM) continues to be a significant contributor to the deterioration of air quality and is known to cause both acute and chronic health effects in exposed populations. The health effects associated with PM depend on their size, chemical composition, and sources. For instance, the chemical composition of PM, including polycyclic aromatic hydrocarbons (PAHs), are recognized for their highly carcinogenic properties. The assessment of health risks associated with PM is increasingly focused on measuring oxidative potential (OP) rather than mass concentration. OP has emerged as a highly promising metric in this regard. The study focuses on two specific aspects: the cancer risk associated with PAHs and the OP induced by the chemical compositions of PM. The study commenced with a comprehensive year-round field campaign for aerosol sampling in Ningbo, a coastal city in China. The field campaign focused on PM with an aerodynamic diameter of  $\leq 2.5 \mu\text{m}$  ( $\text{PM}_{2.5}$ ),  $2.5\text{--}10 \mu\text{m}$  ( $\text{PM}_{10}$ ), and size fractionated PM. The study involved detailed chemical characterization, analysis of source contributions to PAHs lung cancer risk and OP, and modeling the deposition of OP in various regions of the human respiratory tract.

The risk assessment of PAHs documented in the literature has predominantly concentrated on the 16 priority PAHs, inadvertently neglecting other PAHs that possess a high cancer risk. Consequently, there is a risk of underestimating the overall risk level. Additionally, in this study, we utilized the World Health Organization (WHO) and Environmental Protection Agency (EPA) unit risk methods to estimate the Lifetime Excess Cancer Risk (LECR) and address the errors frequently reported in the literature regarding

these methods. The results of the lung cancer risk assessment conducted in this study revealed that the inclusion of highly carcinogenic PAHs, such as 7H-benzo[c]fluorene and various dibenzopyrene derivatives (e.g., dibenzo[a,h]pyrene, dibenzo[a,l]pyrene, and dibenzo[a,e]pyrene), increased the risk of lung cancer by four-fold. This significant increase in LECR suggests that future investigations should consider incorporating more highly carcinogenic PAHs into the risk assessment framework to accurately estimate the lung cancer risk posed by PAHs. The traditional approach for estimating the lung cancer risk associated with PAHs is the use of the component-based potency factor, as adopted by the EPA. In contrast, the WHO approach requires the use of benzo[a]pyrene (BaP) as a marker for the complex mixture. Consequently, employing the WHO unit risk and component-based potency factor approach resulted in significant overestimation of the lung cancer risk. In our study, we utilized the EPA unit risk and component-based potency factor approach to estimate the LECR of 16 and 20 PAHs, resulting in values of  $5.1 \times 10^{-7}$  and  $2.23 \times 10^{-6}$ , respectively. However, when employing the WHO unit risk and component-based potency factor approach, we observed a 14-fold increase in the LECR estimates for the same set of 16 and 20 PAHs ( $7.45 \times 10^{-6}$  and  $32.4 \times 10^{-6}$ , respectively). By adopting the appropriate WHO approach, we estimated the LECR to be  $3.11 \times 10^{-6}$ , which closely aligns with the LECR estimated for the 20 PAHs using the EPA approach. Our findings revealed that incorporating additional PAHs in the component-based potency factor approach enhanced the comparability of EPA estimations with those of the WHO. This, in turn, led to a more precise assessment of the lung cancer risk associated with PAH exposure. Moreover, in our study, we identified five sources associated with PAHs in our study domain. These sources include

natural gas combustion, vehicular exhaust, coal combustion, biomass burning, and the volatilization of urban fuel. Among these sources, our finding indicated that natural gas combustion, coal combustion, and vehicular exhaust emissions make significant contributions to the LECR. Therefore, implementing measures to reduce the levels of PAHs from these three sources would significantly impact the reduction of LECR and improve the overall public health of the population in Ningbo, China.

The investigation of the OP induced by the water- and methanol-soluble fractions of PM<sub>2.5</sub> was conducted using a comprehensive year-round field campaign. Two acellular assays, namely Dithiothreitol (DTT) and Ascorbic acid (AA), were employed in this investigation. This study took into account diurnal and seasonal variations, focusing on identifying the key factors that drive the OP, such as chemical species and sources. The OP induced by water-soluble fractions of PM<sub>2.5</sub> in both DTT and AA assays were higher at nighttime ( $0.39 \pm 0.10 \text{ nmol min}^{-1}\text{m}^{-3}$  and  $0.31 \pm 0.22 \text{ nmol min}^{-1}\text{m}^{-3}$ , respectively) than during the day ( $0.25 \pm 0.13 \text{ nmol min}^{-1}\text{m}^{-3}$  and  $0.23 \pm 0.09 \text{ nmol min}^{-1}\text{m}^{-3}$ , respectively). The OP induced by methanol-soluble fractions were consistently higher during nighttime compared to daytime. The higher OP induced by PM<sub>2.5</sub> during the night can be explained by the fact that aerosols during this time were more photochemically aged, as evidenced by low BaA/Chr and LMW-PAHs ratios. Moreover, the bivariate polar plots revealed a strong association between nighttime OP and marine/sea spray from the Ningbo-Zhoushan port and East China Sea, which is in line with our findings that nighttime aerosols are more acidic compared to daytime aerosols. The elevated aerosol acidity at night contributed to high levels of OP, as it enhanced the dissolution of trace metals in the aerosols. However, we

reached the conclusion that photochemically aged aerosols were the primary contributor to the elevated levels of OP at night, based on the weak-to-moderate correlation found between nighttime OP and trace metals. The OP induced by water- and methanol-soluble fractions of PM<sub>2.5</sub> exhibited seasonal variations. The water-soluble fractions in the DTT assay showed higher OP in winter ( $1.31 \pm 0.49 \text{ nmol min}^{-1} \text{ m}^{-3}$ ), followed by summer ( $1.22 \pm 0.19 \text{ nmol min}^{-1} \text{ m}^{-3}$ ), autumn ( $1.19 \pm 0.26 \text{ nmol min}^{-1} \text{ m}^{-3}$ ), and spring ( $1.00 \pm 0.37 \text{ nmol min}^{-1} \text{ m}^{-3}$ ). The higher OP in winter was attributed to a strong correlation with trace metals, specifically Fe and Cu. During the summer, the AA assay detected higher OP in both the water- and methanol-soluble fractions. This was attributed to the photochemical aging process and the high aerosol acidity levels observed in the summer aerosols. The Positive Matrix Factorization (PMF) model was employed to identify six sources of PM<sub>2.5</sub> in Ningbo. These sources encompass industrial emissions, biomass burning, secondary aerosols, sea spray/marine emissions, vehicular emissions, and road dust. During the field campaign, the three dominant sources contributing to the mass concentration of PM<sub>2.5</sub> were industrial emissions, secondary aerosols, and vehicular emissions. The bivariate polar plots clearly demonstrated that the primary local sources of industrial emissions, which have a significant impact on PM<sub>2.5</sub> pollution in Ningbo, are the industrial facilities situated in the Wangchun industrial zone, as well as the Zhenhai and Beilun industrial parks. The plots indicated that vehicular emissions originated from the freeways and highways that surrounded our study area. In addition, the plots demonstrated that the precursor gases of secondary aerosol - namely SO<sub>2</sub>, NO<sub>2</sub>, and VOCs - originate from local industrial facilities and vehicular traffic. The analysis of air mass trajectories revealed that long-range transport from Inner Mongolia,

the East China Sea, Northern China, and Taiwan contributed to the levels of PM<sub>2.5</sub> in Ningbo. To estimate the contribution of six sources to PM<sub>2.5</sub>-induced OP, this study used Multiple Linear Regression (MLR) analysis. The findings emphasize the variability in source contributions to both PM<sub>2.5</sub> mass concentration and OP, depending on the assay and extraction solvent used for OP measurement. Targeting mass concentration alone, as currently done in PM<sub>2.5</sub> pollution regulation, would not sufficiently reduce health risks. Thus, future regulatory efforts should incorporate both the source contributions of mass concentration and OP to effectively mitigate risks associated with PM<sub>2.5</sub>.

The health risk of six size-fractionated PM (ultrafine:  $\leq 0.49$ ,  $0.49\text{--}0.95$   $\mu\text{m}$ , accumulation:  $0.95\text{--}1.5$ ,  $1.5\text{--}3$   $\mu\text{m}$ , coarse:  $3\text{--}7.2$ ,  $\geq 7.2$   $\mu\text{m}$ ), and PM<sub>2.5</sub> and PM<sub>10</sub> were compared by modeling their OP deposition in the various regions of the human respiratory tract. This began with a comparative OP assessment of water- and methanol-soluble fractions of these particles in DTT and AA assays. The OP induced by water-and-methanol-soluble PM size fractions measured by DTT assay exhibited unimodal size distribution with peak concentration in accumulation particles ( $0.95\text{--}1.5$   $\mu\text{m}$ ). The high OP induced by water-and-methanol-soluble fraction of  $0.95\text{--}1.5$   $\mu\text{m}$  was dominated by industrial emissions and vehicular traffic. In contrast, in AA assay, the OP exhibited trimodal size distribution with the concentration peaked in coarse particles, followed by ultrafine particles, and accumulation particles. The high OP of coarse particles in AA assay was attributed to industrial emissions, vehicular traffic, and marine/sea spray. The OP induced by water- and methanol-soluble fractions of PM<sub>10</sub> was consistently higher than that of PM<sub>2.5</sub> in both DTT and AA assay. The OP induced by PM<sub>10</sub> exhibited a strong correlation with Cu, Fe, WSOC,

and quinones. The high concentration of Cu and Fe in the presence of quinones causes the synergistic effect, thereby elevating the OP levels of PM<sub>10</sub>. The bivariate polar plots revealed vehicular traffic, and road dust are potential sources contributing to the high OP induced by water-and methanol-soluble fractions of PM<sub>10</sub>. In all OP measurements, the DTT assay consistently demonstrated high OP in the water-soluble fractions, indicating its higher responsiveness to a wide range of water-soluble chemical species, including trace metals, high molecular weight (HMW) quinones, and humic-like substances (HULIS). In contrast, the AA assay exhibited higher OP in the methanol-soluble fractions, suggesting its high sensitivity to water-insoluble chemical species that were extracted in methanol. This study has demonstrated, for the first time, that the DTT assay is the most effective method for assessing the OP of water-soluble fractions, while the AA assay is best suited for evaluating the OP of methanol-soluble fractions. The Multiple-path particle dosimetry (MPPD) model was employed to simulate the deposition of OP in the Extrathoracic (ET), Tracheobronchial (TB), and Pulmonary (PL) regions of the respiratory tract. The patterns of OP deposition in the DTT and AA assays showed similarities. Both assays measured similar levels of OP deposition for ultrafine particles. However, the DTT assay demonstrated higher values for accumulation particles, whereas the AA assay exhibited higher levels for coarse particles. These findings hold significant implications for assessing the health risks associated with ambient particles across various size ranges. Moreover, this study investigated for the first time a potential link between OP and the particle deposition dose in various regions of the respiratory tract. The results indicated that this relationship varies depending on the type of assay used. In the case of the DTT assay, a weak correlation was observed. The DTT assay

is sensitive to a broader range of water-soluble chemical species present in particle doses within our study area. Conversely, no correlation was observed in the AA assay, suggesting that the substances causing OP, as detected by AA, may not significantly contribute to the dose of each PM size fraction collected in our study domain. These findings indicated that the particle deposition dose, which depends on the particle concentration in the ambient air and exposure conditions, is not a suitable metric for predicting OP or the potential health risk posed by ambient particles.

**Keywords:** oxidative potential, cancer risk, ambient particles, source apportionment, respiratory deposition



## Papers published

The following papers related to my PhD research have been published.

1. **Lord Famiyeh**, Ke Chen, Jingsha Xu, Yong Sun, Qingjun Guo, Chengjun Wang, Jungang Lv, Yu-Ting Tang, Huan Yu, Collin Snape, Jun He. A review on the analysis methods, source identification, and cancer risk evaluation of atmospheric polycyclic aromatic hydrocarbos. *Sci. Total. Environ.* 2021, 789, 147741.
2. **Lord Famiyeh**; Chunrong Jia; Ke Chen; Yong Sun; Qingjun Guo; Yu-Ting Tang; Dongsheng Ji. Size Distribution and Lung-Deposition of Ambient Particulate Matter Oxidative Potential: A Contrast Between Dithiothreitol and Ascorbic Acid Assays. *Environ Poll.* 2023, 336, 122437.
3. **Lord Famiyeh**; Chunrong Jia; Ke Chen; Yong Sun; Qingjun Guo; Yu-Ting Tang; Dongsheng Ji. Breathing in danger: Unveiling the link between human exposure to outdoor PM<sub>2.5</sub>-bound PAHs and lung cancer risk in an urban residential of China. *Sci. Total. Environ.* 2023, 789, 167762.
4. Ke Chen, Jingsha Xu, **Lord Famiyeh**, Yong Sun, Dongsheng Ji, Honghui Xu, Chengjun Wang, Sarah E. Metcalfe, Raghu Betha, Sailesh N. Behara, Chunrong Jia, Hang Xiao, Jun He. Chemical Constituents, Driving Factors, and Source Apportionment of Oxidative Potential of Ambient Fine Particulate Matter in a Port City in East China. *J. Hazard. Mater.* 2022, 440, 129864.

## Planned publications

The following manuscript are currently being prepared for publication.

1. **Lord Famiyeh**; Chunrong Jia; Ke Chen; Yong Sun; Qingjun Guo; Yu-Ting Tang; Dongsheng Ji. Discovering the Hidden Risks of Fine Particles: Chemicals and Source-Driven Analysis of Oxidative Potential.
2. **Lord Famiyeh**; Chunrong Jia; Ke Chen; Yong Sun; Qingjun Guo; Yu-Ting Tang; Dongsheng Ji. Comparative Analysis of WHO and EPA Methods for Lung Cancer Risk Assessment from Particle-associated Polycyclic Aromatic Hydrocarbons: Incorporating Pulmonary Deposition Dose.
3. **Lord Famiyeh**; Chunrong Jia; Ke Chen; Yong Sun; Qingjun Guo; Yu-Ting Tang; Dongsheng Ji. Strategies for Minimizing the Oxidative Potential of Fine and Coarse Particles in an Urban Coastal Hotspot City in China.

## **Acknowledgements**

I would like to extend my sincere gratitude to all those who have contributed to the success of this research project. First and foremost, I am deeply grateful for the guidance and support of my supervisors, Prof. Jun He, Prof. Qingjun Guo, and Prof. Collin Snape. Their expertise and direction throughout the project were invaluable. I would especially like to acknowledge Prof. Jun He's unwavering support and expertise in aerosol science, as well as Prof. Qingjun Guo's constructive feedback that refined my research. Their consistent provision of constructive criticism and advice greatly influenced the outcome of this study. Furthermore, I would like to express my appreciation to Prof. Jun He for providing continued financial support as a Graduate Research Assistant after my stipend ended in three years.

I would also like to express my sincere gratitude to Dr. Yu-Ting Tang for her invaluable guidance in the field of health risk assessment. She has consistently made herself available to provide support whenever I needed it. Additionally, I want to acknowledge the exceptional assistance provided by the lab technicians, Karey Shan, Jason Wang, Kate Yuan, and Jane Zhang. Their dedication and expertise, particularly in equipment training, significantly propelled the progress of this project. Furthermore, I extend my gratitude to the health and safety officer, Helene Xu, for her diligent efforts. I am immensely thankful for the significant contributions of the Graduate School and the Faculty of Science and Engineering in enhancing my graduate experiences through various training programs. I am also grateful for the financial support received from the Ningbo government. Additionally, I express my appreciation to the UNNC-IGSNRR for granting me the esteemed DTP scholarship, which has afforded me the invaluable opportunity to participate in the joint Ph.D. program.

I would like to sincerely thank my friends, Robert Suya, Dennis Amable, Cephas Attahu, Alex Bawah, and Caleb Kelly, for their valuable insights and unwavering motivation throughout this project. Finally, I extend my deepest appreciation to my wife, Margaret Ndede, and our children. Their unwavering support, encouragement, and love have been a constant source of inspiration and motivation during this remarkable journey.

## Table of Contents

<b>Abstract</b> .....	<b>i</b>
<b>Papers published</b> .....	<b>viii</b>
<b>Planned publications</b> .....	<b>viii</b>
<b>Acknowledgements</b> .....	<b>x</b>
<b>Table of Contents</b> .....	<b>xii</b>
List of Figures .....	xvii
List of Tables.....	xxix
List of symbols and abbreviations.....	xxxv
<b>Chapter 1 Introduction</b> .....	<b>1</b>
1.1. Background .....	1
1.2. Statement of the problem .....	4
1.3. Aims of the study .....	9
1.4. Specific objectives .....	10
1.5. Research methodology .....	11
1.6. Thesis outline .....	13
<b>Chapter 2 Literature Review</b> .....	<b>13</b>
2.1 OP for PM toxicological assessment.....	13
2.2 Acellular assays for OP measurement.....	14
2.2.1 Dithiothreitol (DTT) assay .....	15
2.2.2 Ascorbic acid (AA) assay.....	17
2.3 OP induced by PM chemical compositions .....	18
2.4 Size distribution of PM chemical compositions .....	21
2.5 Occurrence of PM-induced OP in China and outside China.....	22
2.6 Multiple-path particle dosimetry (MPPD) model .....	13
2.7 Respiratory deposition of ambient particles OP .....	16

2.8	Casual link OP and health endpoints .....	17
2.9	Methods for pollution source apportionment.....	19
2.9.1	Receptor modeling .....	19
2.9.2	Molecular biomarkers .....	21
2.9.2.1	Levogluconan .....	21
2.9.2.2	Homohopanes.....	22
2.9.2.3	PAHs .....	23
2.10	Source dispersion characteristics and transport to receptor site.....	25
2.11	Lung cancer risk of particulate-bound PAHs.....	26
2.12	Source contribution to OP induced by PM <sub>2.5</sub> and lung cancer risk of PAHs ...	28
<b>Chapter 3 Materials and Methods.....</b>		<b>30</b>
3.1	Study area.....	30
3.2	Aerosol particle sample collection.....	32
3.3	Mass concentration measurement .....	34
3.4	Acquisition of meteorological and gaseous pollutant data.....	34
3.5	Summary of aerosol sampling and online data collection .....	35
3.6	Chemical analysis.....	36
3.6.1	Water-soluble inorganic ions (WSIIs) .....	36
3.6.2	Water-soluble trace metals (WSTMs).....	37
3.6.3	Water-soluble organic carbon (WSOC).....	37
3.6.4	Levogluconan .....	37
3.6.5	Polycyclic aromatic hydrocarbons and homohopanes .....	38
3.6.6	Quinones .....	40
3.7	Oxidative potential.....	43
3.7.1	Extraction and pre-treatment.....	43
3.7.2	OP measurement .....	43
3.8	MPPD model.....	45

3.9	Source apportionment techniques .....	46
3.9.1	Positive Matrix Factorization model.....	46
3.9.2	Bivariate polar plots, air mass backward trajectories, and fire spot.....	47
3.10	Statistical analysis .....	48
<b>Chapter 4 Particulate-Bound Polycyclic Aromatic Hydrocarbons: Diurnal and Seasonal Variations, Size Distribution, Source Apportionment, and Lung Cancer Risk .....</b>		<b>49</b>
<b>4.1.</b>	<b>Introduction .....</b>	<b>49</b>
<b>4.2.</b>	<b>Results and discussions .....</b>	<b>52</b>
4.2.1.	Day and night concentrations of PAHs.....	52
4.2.2.	Seasonal variability of concentrations of PAHs.....	57
4.2.3.	Size distribution of PAHs in ambient particles .....	64
4.2.4.	PAHs as indicators of aerosol photochemical aging.....	73
4.2.5.	Source apportionment of PAHs .....	74
4.2.5.1.	PAH diagnostic ratios .....	74
4.2.5.2.	Positive matrix factorization/Bivariate polar plots (PMF-BPPs).....	78
4.2.6.	Health risk assessment of PAHs exposure .....	85
4.2.6.1.	BaP-toxic equivalent concentrations (BaPeq).....	85
4.2.6.2.	Lifetime excess cancer risk .....	88
4.2.6.3.	Source-specific LECR.....	90
<b>4.3.</b>	<b>Conclusions .....</b>	<b>94</b>
<b>Chapter 5 OP induced by Water and Methanol-Soluble Fractions of PM<sub>2.5</sub>: Diurnal and Seasonal Variations, Chemical Characterization, and Source Apportionment ...</b>		<b>97</b>
<b>5.1.</b>	<b>Introduction .....</b>	<b>97</b>
<b>5.2.</b>	<b>Results and discussions .....</b>	<b>100</b>
5.2.1.	Chemical characterizations: diurnal and seasonal variations.....	100
5.2.2.	Marine source contributions: diurnal and seasonal variations .....	107
5.2.3.	Aerosol acidity .....	110

5.2.3.1.	Ion balance .....	110
5.2.3.2.	Neutralization Factors (NFs).....	114
5.2.4.	Oxidative potential of PM <sub>2.5</sub> .....	117
5.2.4.1.	OP induced by water-and methanol soluble PM <sub>2.5</sub> : diurnal variations .....	117
5.2.4.2.	Chemical species associated with OP: day and night variations.....	120
5.2.4.3.	Graphical analysis of source dispersion of water-and methanol-soluble OP: diurnal variations.....	127
5.2.4.4.	OP induced by water-and methanol soluble PM <sub>2.5</sub> : seasonal variations ....	131
5.2.4.5.	Chemical species associated with OP: seasonal variations.....	134
5.2.4.6.	Graphical analysis of source dispersion of PM <sub>2.5</sub> mass concentration .....	142
5.2.4.7.	Graphical analysis of source dispersion of water-soluble OP: seasonal variations	144
5.2.4.8.	Graphical analysis of source dispersion of water-soluble OP: seasonal variations	147
5.2.4.9.	PMF model for source apportionment of PM <sub>2.5</sub> .....	151
5.2.4.10.	Source contribution to OP induced by water-and methanol-soluble fraction of PM <sub>2.5</sub>	167
<b>5.3.</b>	<b>Conclusion.....</b>	<b>172</b>
<b>Chapter 6 Particle Size Distribution of OP induced by Water and Methanol-Soluble Fractions: Chemical Characterization, Sources, and Respiratory Depositions.....</b>		<b>175</b>
<b>6.1.</b>	<b>Introduction .....</b>	<b>175</b>
<b>6.2.</b>	<b>Results and discussions .....</b>	<b>178</b>
6.2.1	Chemical characterization: trace metals, WSOC, and quinones.....	178
6.2.2	Validation of the MPPD model.....	185
6.2.3	Particle deposition fractions and doses in human respiratory system.....	186
6.2.4	Oxidative potential of ambient particles .....	190
6.2.4.1	OP induced by water-and methanol-soluble ultrafine, accumulation, coarse particles	190



6.2.4.2	Chemical species associated with OP: ultrafine, accumulation, and coarse particles	196
6.2.4.3	The response of DTT and AA assays to PM chemical compositions	204
6.2.4.4	Graphical analysis of source dispersion: PM mass concentration	204
6.2.4.5	Graphical analysis of source dispersion of OP: water-soluble fractions	208
6.2.4.6	Graphical analysis of source dispersion of OP: methanol-soluble fractions	212
6.2.4.7	OP induced by water-and methanol-soluble fractions of PM <sub>2.5</sub> and PM <sub>10</sub>	218
6.2.4.8	Chemical species associated with OP: PM <sub>2.5</sub> versus PM <sub>10</sub>	220
6.2.4.9	Graphical analysis of source dispersion of water-soluble OP: PM <sub>2.5</sub> versus PM <sub>10</sub>	226
6.2.4.10	Graphical analysis of source dispersion of methanol-soluble OP: PM <sub>2.5</sub> versus PM <sub>10</sub>	228
6.2.5	OP deposition in human respiratory tract	231
6.2.6	Relationship between particle deposition dose and OP	237
<b>6.3</b>	<b>Conclusion</b>	<b>242</b>
<b>Chapter 7 Contributions, Conclusions, and Recommendation for Future Work</b>		<b>246</b>
<b>7.1</b>	<b>Contributions and conclusions</b>	<b>246</b>
7.1.1	Lung cancer risk of PAH exposure	246
7.1.2	Effect of extraction solvents and acellular assays on OP measurement	248
7.1.3	OP size distribution and respiratory deposition	249
7.1.4	The relationship between particle deposition dose and OP	250
7.1.5	The reduction of OP of PM <sub>2.5</sub>	251
<b>7.2</b>	<b>Recommendations for future work</b>	<b>252</b>
<b>Bibliography</b>		<b>254</b>
<b>Appendices</b>		<b>284</b>

## List of Figures

Figure 1-1 Flowchart of the experimental work conducted in this study .....	13
Figure 2-1 Mechanism of DTT oxidation by PM (Cho et al., 2005) .....	16
Figure 2-2 Mechanism of AA oxidation by PM (Hedayat et al., 2015).....	18
Figure 2-3 Chemical structure of quinones: 1, 2-naphthoquinone, 1, 4-naphthoquinone, and 1, 4-anthraquinone.....	20
Figure 2-4 Chemical structure of levoglucosan (1,6-anhydro- $\beta$ -D-glucopyranos).....	22
Figure 2-5 Chemical structure of homohopane (17 $\alpha$ (H),21 $\beta$ (H)-22RS-Homohopane).....	23
Figure 3-1 Location of the sampling site: (a) Ningbo city in Zhejiang province, (b) UNNC in Ningbo.....	32
Figure 4-1 Comparison of averaged PAHs concentration based on aromatic rings: (a) Day, (b) Night.....	57
Figure 4-2 Comparisons of seasonal average PAHs concentration ( $\text{ng m}^{-3}$ ) based on aromatic rings.....	63
Figure 4-3 Size distribution ( $dC$ = mean concentration ( $\text{ng m}^{-3}$ ), $d\log D_p$ = logarithmic difference of aerodynamic diameter ( $D_p, \mu\text{m}$ )) of the mean mass concentration of PM size fractions collected in a residential/commercial site of Ningbo, China .....	65

Figure 4-4 Size distribution ( $dC$  = mean concentration ( $\text{ng m}^{-3}$ ),  $d\log D_p$  = logarithmic difference of aerodynamic diameter,  $D_p$  is average particle size,  $\mu\text{m}$ ) of individual LMW-PAHs (a-e) and total LMW-PAH (f) in ambient particle.....69

Figure 4-5 Size distribution ( $dC$  = mean concentration ( $\text{ng m}^{-3}$ ),  $d\log D_p$  = logarithmic difference of aerodynamic diameter,  $D_p$  is average particle size,  $\mu\text{m}$ ) of HMW-PAHs (a-n), total (k-n) 4PAHs (o), total HMW-PAHs (p), total (a-j)16 PAHs (g), and total (a-n) 20 PAHs (r).....70

Figure 4-6 Size distribution ( $dC$  = mean concentration ( $\text{ng m}^{-3}$ ),  $d\log D_p$  = logarithmic difference of aerodynamic diameter,  $D_p$  is average particle size,  $\mu\text{m}$ ) of PAHs based on aromatic rings: (a) two, (b) three, (c) four, (d) five, (e) six .....71

Figure 4-7 Plots of  $\log(\text{PAHs/PM})$  versus  $\log(D_p)$  based on aromatic rings: (a) two, (b) three, (c) four, (d) five, (e) six.....72

Figure 4-8 Sources of PAHs in  $\text{PM}_{2.5}$  derived from the PMF model: (a) vehicular exhaust, (b) coal combustion, (c) natural gas combustion, (d) biomass burning, (e) volatilization of unburnt fuel .....82

Figure 4-9 Time series source concentrations ( $\text{ng m}^{-3}$ ) derived from PMF model: (a) vehicular exhaust, (b) coal combustion, (c) natural gas combustion, (d) biomass burning, (e) volatilization of unburnt fuel.....83

Figure 4-10 Bivariate polar plots (BPPs) of five sources associated with annual  $\text{PM}_{2.5}$ -PAHs concentration ( $\text{ng m}^{-3}$ ) derived from PMF model (a) Vehicular exhaust (b) coal combustion, (c) natural gas combustion, (d) biomass burning, and (e) volatilization of unburnt fuel....84

Figure 4-11 Comparison of BaP<sub>eq</sub> of individual PAHs with (a) LMW, (b) HMW .....86

Figure 4-12 Annual averaged BaP<sub>eq</sub> (ng m<sup>-3</sup>) of 20 PAHs based on aromatic rings .....87

Figure 4-13 Comparison of average LECR of human exposure to 16 and 20 PAHs: (a) WHO unit risk, (b) EPA unit risk. Error bar present the standard deviation (level of variability of the data).....89

Figure 4-14 Source-specific contribution to PAH concentration (C) and LECR of 16 and 20 PAHs .....92

Figure 5-1 Day and night concentrations of WSIs in PM<sub>2.5</sub> particles collected residential area of Ningbo, China. Error bar present the standard deviation (level of variability of the data).....102

Figure 5-2 Seasonal concentrations of WSIs in PM<sub>2.5</sub> particles collected residential area of Ningbo, China. Error bar present the standard deviation (level of variability of the data)104

Figure 5-3 Day and night concentration of non-sea salts and their respective non-sea salt ionic fractions in PM<sub>2.5</sub> collected in a residential/commercial site of Ningbo, China. Error bar present the standard deviation (level of variability of the data).....108

Figure 5-4 Seasonal concentration of non-sea salts (a) and their respective non-sea salt ionic fractions (b) in PM<sub>2.5</sub> collected in a residential/commercial site of Ningbo, China. Error bar present the standard deviation (level of variability of the data).....109

Figure 5-5 Plot of anion equivalents (AE) vs cation equivalent WSIs in PM<sub>2.5</sub> in daytime and at night.....112

Figure 5-6 Plot of anion equivalents (AE) vs cation equivalent (CE) of WSIs in PM<sub>2.5</sub> in four seasons .....113

Figure 5-7 Neutralization factors of NH<sub>4</sub><sup>+</sup>, nss-K<sup>+</sup>, nss-Mg<sup>2+</sup>, and nss-Ca<sup>2+</sup> during the day and night. Error bar present the standard deviation (level of variability of the data) .....115

Figure 5-8 Neutralization factors of NH<sub>4</sub><sup>+</sup>, nss-K<sup>+</sup>, nss-Mg<sup>2+</sup>, and nss-Ca<sup>2+</sup> in four seasons. Error bar present the standard deviation (level of variability of the data).....116

Figure 5-9 Day and night extrinsic OP induced by water-soluble fractions of PM<sub>2.5</sub> measured in DTT (a) and AA (b) assays. Median (line across the box), mean (square within the box), first quartile (Q1) (bottom of the box), third quartile (Q3) (top of the box), outlier (square shown outside the box), whiskers shows minimum and maximum values .....118

Figure 5-10 Day and night extrinsic OP induced by methanol-soluble fractions of PM<sub>2.5</sub> measured in DTT (a) and AA (b) assays. Median (line across the box), mean (square within the box), first quartile (Q1) (bottom of the box), third quartile (Q3) (top of the box), outlier (square shown outside the box), whiskers shows minimum and maximum values.....120

Figure 5-11 Bivariate polar plots of extrinsic and intrinsic OP induced by water-soluble fractions of PM<sub>2.5</sub> during the day (a-d) and night (e-h) .....128

Figure 5-12 Bivariate polar plots of extrinsic and intrinsic OP induced by methanol-soluble fractions of PM<sub>2.5</sub> during the day (a-d) and night (e-h) .....129

Figure 5-13 Extrinsic (a, c) and intrinsic (b, d) OP of water-soluble fraction of PM<sub>2.5</sub> in DTT (a, b) and AA (c, d) assays. Median (line across the box), mean (square within the box), first

quartile (Q1) (bottom of the box), third quartile (Q3) (top of the box), outlier (square shown outside the box), whiskers shows minimum and maximum values .....	132
Figure 5-14 Extrinsic (a, c) and intrinsic (b, d) OP of methanol-soluble fraction of PM <sub>2.5</sub> in DTT (a, b) and AA (c, d) assays. Median (line across the box), mean (square within the box), first quartile (Q1) (bottom of the box), third quartile (Q3) (top of the box), outlier (square shown outside the box), whiskers shows minimum and maximum values .....	134
Figure 5-15 Bivariate polar plots of seasonal PM <sub>2.5</sub> concentration ( $\mu\text{g m}^{-3}$ ): (a) Autumn, (b) Winter, (c) Spring, (d) Summer .....	143
Figure 5-16 48-h back trajectory air masses and distribution of firespot during autumn (a), winter (b), spring (c) and summer (d) (Chen et al., 2022) .....	144
Figure 5-17 Bivariate polar plots of seasonal OP induced by water-soluble fractions of PM <sub>2.5</sub> : Autumn (a-d), Winter (e-h), Spring (i-m), Summer (m-p) .....	146
Figure 5-18 Bivariate polar plots of seasonal OP induced by methanol-soluble fractions of PM <sub>2.5</sub> : Autumn (a-d), Winter (e-h), Spring (i-m), Summer (m-p) .....	148
Figure 5-19 Daytime sources of PM <sub>2.5</sub> derived from PMF model: (a) IE, (b) BB, (c) SA, (d) ME, (e) VE, (f) RD .....	159
Figure 5-20 Nighttime sources of PM <sub>2.5</sub> derived from PMF model: (a) IE, (b) BB, (c) SA, (d) ME, (e) VE, (f) RD.....	160
Figure 5-21 Day and night source contributions to PM <sub>2.5</sub> mass concentration ( $\mu\text{g m}^{-3}$ ) derived from the PMF model .....	161

Figure 5-22 Annual sources of PM <sub>2.5</sub> derived from PMF model: (a) IE, (b) BB, (c) SA, (d) ME, (e) VE, (f) RD .....	162
Figure 5-23 Seasonal source contributions to PM <sub>2.5</sub> mass concentration (µg m <sup>-3</sup> ) derived from the PMF model.....	163
Figure 5-24 Bivariate polar plots of the factors derived from the PMF model attributed to PM <sub>2.5</sub> pollution during the day .....	164
Figure 5-25 Bivariate polar plots of the factors derived from the PMF model attributed to PM <sub>2.5</sub> pollution during the night.....	165
Figure 5-26 Bivariate polar plots of the factors derived from the PMF model attributed to PM <sub>2.5</sub> pollution in a year-round field campaign .....	166
Figure 5-27 Source contributions to day and night OP induced by water-soluble fractions of PM <sub>2.5</sub> : (a) extrinsic OP (DTTv, AAv), (b) Intrinsic OP (DTTm, AAm).....	169
Figure 5-28 Source contributions to Day and night OP induced by methanol-soluble fractions of PM <sub>2.5</sub> : (a) extrinsic OP (DTTv, AAv), (b) Intrinsic OP (DTTm, AAm) .....	170
Figure 5-29 Source contributions to the extrinsic OP of PM <sub>2.5</sub> induced by water-soluble fractions in a year-round field campaign .....	171
Figure 5-30 Seasonal source contributions to the extrinsic OP of PM <sub>2.5</sub> induced by methanol-soluble fractions : (a) DTTv, (b) AAv .....	171
Figure 6-1 Size distribution (dC = mean concentration (ng m <sup>-3</sup> ), dlogDp = logarithmic difference of aerodynamic diameter, Dp is average particle size, µm) of trace metals (a-j)	

and WSOC (k) in ambient particles collected in urban residential/commercial area of Ningbo, China .....	181
Figure 6-2 Size distribution of quinones in PM <sub>2.5</sub> and PM <sub>10</sub> collected in urban Ningbo, China. Error bar present the standard deviation (level of variability of the data) .....	183
Figure 6-3 Size distribution of quinones (a-c) and plot of log total quinones/PM versus log Dp (d-f).....	184
Figure 6-4 Comparison of experimental and modeled deposition fractions (DF) of ambient particles with aerodynamic size (Dp) of 0.005–15 μm in the whole human respiratory tract: (a) DP versus Dp for experimental and MPPD model, (b) Linear regression analysis of DF of experimental versus MPPD model. ....	186
Figure 6-5 Particle deposition fraction and lung-deposition doses in parts of the human lung (a) ET, (b) TB, (c) PL, and (d) TL .....	189
Figure 6-6 Modeled particle deposition fraction and doses in parts of the human respiratory tract (a) ET, (b) TB, (c) PL, and (d) TL .....	190
Figure 6-7 Size distribution of extrinsic OP (dOP = mean extrinsic OP (nmol min <sup>-1</sup> m <sup>-3</sup> ), dlogDp = logarithmic difference of aerodynamic diameter, Dp, μm) of water (a, b) and methanol (c, d): DTT (a, c), AA (b, d) assays.....	194
Figure 6-8 Bivariate polar plots of size-resolved PM mass concentration (μg m <sup>-3</sup> ) induced by water-soluble fractions: ultrafine (a, b), accumulation (c, d), coarse (e, f) particles ....	206



Figure 6-9 48-h back trajectories analysis with firespot at our study domain (the campus of the University of Nottingham Ningbo, China) (Chen et al., 2022).....	208
Figure 6-10 Bivariate polar plots of size-resolved concentrations of DTTv (nmol min <sup>-1</sup> m <sup>-3</sup> ) induced by water-soluble fractions: ultrafine (a, b), accumulation (c, d), coarse (e, f) particles .....	210
Figure 6-11 Bivariate polar plots of size-resolved concentrations of AAv (nmol min <sup>-1</sup> m <sup>-3</sup> ) induced by water-soluble fractions: ultrafine (a, b), accumulation (c, d), coarse (e, f) particles .....	211
Figure 6-12 Bivariate polar plots of size-resolved concentrations of DTTv (nmol min <sup>-1</sup> m <sup>-3</sup> ) induced by methanol-soluble fractions: ultrafine (a, b), accumulation (c, d), coarse (e, f) particles .....	215
Figure 6-13 Bivariate polar plots of size-resolved concentrations of AAv (nmol min <sup>-1</sup> m <sup>-3</sup> ) induced by methanol-soluble fractions: ultrafine (a, b), accumulation (c, d), coarse (e, f) particles .....	216
Figure 6-14 Size distribution of extrinsic OP (dOPv = mean extrinsic OP (nmol min <sup>-1</sup> m <sup>-3</sup> ), dlogDp = logarithmic difference of aerodynamic diameter) of water-soluble fractions of fine (≤ 2.5 μm) and coarse particles (2.5–10 μm) in DTT (a) and AA (b) assays. Median (line across the box), mean (square within the box), first quartile (Q1) (bottom of the box), third quartile (Q3) (top of the box), outlier (square shown outside the box), whiskers shows minimum and maximum values .....	219

Figure 6-15 Size distribution of extrinsic OP ( $dOP_v = \text{mean extrinsic OP (nmol min}^{-1} \text{ m}^{-3})$ ,  $d\log D_p = \text{logarithmic difference of aerodynamic diameter}$ ) of methanol-soluble fractions of fine ( $\leq 2.5 \mu\text{m}$ ) and coarse particles ( $2.5\text{--}10 \mu\text{m}$ ) in DTT (a) and AA (b) assays. Median (line across the box), mean (square within the box), first quartile (Q1) (bottom of the box), third quartile (Q3) (top of the box), outlier (square shown outside the box), whiskers shows minimum and maximum values .....219

Figure 6-16 Bivariate polar plots of extrinsic and intrinsic OP induced by water-soluble fractions of  $PM_{2.5}$  (a-d) and  $PM_{10}$  (e-h) .....227

Figure 6-17 Bivariate polar plots of extrinsic and intrinsic OP induced by methanol-soluble fractions of  $PM_{2.5}$  (a-d) and  $PM_{10}$  (e-h) .....230

Figure 6-18 OP deposition of fine ( $\leq 2.5 \mu\text{m}$ ) and coarse ( $2.5\text{--}10 \mu\text{m}$ ) particles in ET, TB, PL, and TL measured in DTT (a, b) and AA (c, d) assays .....231

Figure 6-19 OP deposition of PM size fraction in DTT assay: (a) ET, (b) TB, (c) PL, (d) TL .....235

Figure 6-20 OP deposition of PM size fraction in AA assay: (a) ET, (b) TB, (c) PL, (d) TL .....236

Figure 6-21 Comparison of DTT and AA measured OP deposition of ultrafine, accumulation, and coarse particles in the ET, TB, PL, and TL regions of human respiratory tract .....237

Figure 6-22 Association of lung-deposited dose and extrinsic OP of PM size fractions in DTT assay: (a)  $\leq 0.49 \mu\text{m}$ , (b)  $0.49\text{--}0.95 \mu\text{m}$ , (c)  $0.95\text{--}1.5 \mu\text{m}$ , (d)  $1.5\text{--}3 \mu\text{m}$ , (e)  $3\text{--}7.2 \mu\text{m}$ , and (f)  $\geq 7.2 \mu\text{m}$ .....238

Figure 6-23 Association of lung-deposited dose and extrinsic OP of PM size fractions in AA assay: (a)  $\leq 0.49 \mu\text{m}$ , (b)  $0.49\text{--}0.95 \mu\text{m}$ , (c)  $0.95\text{--}1.5 \mu\text{m}$ , (d)  $1.5\text{--}3 \mu\text{m}$ , (e)  $3\text{--}7.2 \mu\text{m}$ , and (f)  $\geq 7.2 \mu\text{m}$  .....241

Figure 8-1 Day and night intrinsic OP of water (a, b) and methanol (c, d)-soluble fraction of  $\text{PM}_{2.5}$  measured in DTT (a, c) and AA (b, d) assays. Median (line across the box), mean (square within the box), first quartile (Q1) (bottom of the box), third quartile (Q3) (top of the box), outlier (square shown outside the box), whiskers shows minimum and maximum values.....286

Figure 8:2 Seasonal source contributions to the extrinsic OP of  $\text{PM}_{2.5}$  induced by water-soluble fractions : (a)  $\text{DTTv}$ , (b)  $\text{AAv}$  .....294

Figure 8:3 Seasonal source contributions to the extrinsic OP of  $\text{PM}_{2.5}$  induced by methanol-soluble fractions : (a)  $\text{DTTv}$ , (b)  $\text{AAv}$  .....295

Figure 8-4 Seasonal source contributions to the intrinsic OP induced water-soluble fractions of  $\text{PM}_{2.5}$ : (a)  $\text{DTTm}$ , (b)  $\text{AAm}$  .....296

Figure 8-5 Seasonal source contributions to the intrinsic OP induced by methanol-soluble fractions of  $\text{PM}_{2.5}$ : (a)  $\text{DTTm}$ , (b)  $\text{AAm}$  .....297

Figure 8-6 Size distribution of intrinsic OP ( $dOP = \text{mean extrinsic OP } (\text{pmol min}^{-1} \mu\text{g}^{-1})$ ,  $d\log D_p = \text{logarithmic difference of aerodynamic diameter, } D_p, \mu\text{m}$ ) of water (a, b) and methanol (c, d): DTT (a, c), AA (b, d) assays.....300

Figure 8-7 Bivariate polar plots of size-resolved concentration of DTTm ( $\text{nmol min}^{-1} \mu\text{g}^{-1}$ ) induced by water-soluble fractions: ultrafine (a, b), accumulation (c, d), coarse (e, f) particles .....307

Figure 8-8 Bivariate polar plots of size-resolved concentration of AAm ( $\text{nmol min}^{-1} \mu\text{g}^{-1}$ ) induced by water-soluble fractions: ultrafine (a, b), accumulation (c, d), coarse (e, f) particles .....308

Figure 8-9 Bivariate polar plots of size-resolved concentration of DTTm ( $\text{nmol min}^{-1} \mu\text{g}^{-1}$ ) induced by methanol-soluble fractions: ultrafine (a, b), accumulation (c, d), coarse (e, f) particles .....309

Figure 8-10 Bivariate polar plots of size-resolved concentration of AAm ( $\text{nmol min}^{-1} \mu\text{g}^{-1}$ ) induced by methanol-soluble fractions: ultrafine (a, b), accumulation (c, d), coarse (e, f) particles .....310

Figure 8-11 Size distribution of intrinsic OP ( $dOP_v = \text{mean extrinsic OP } (\text{nmol min}^{-1} \text{m}^{-3})$ ,  $d\log D_p = \text{logarithmic difference of aerodynamic diameter}$ ) of water-soluble fractions of fine ( $\leq 2.5 \mu\text{m}$ ) and coarse particles ( $2.5\text{--}10 \mu\text{m}$ ) in DTT (a) and AA (b) assays. Median (line across the box), mean (square within the box), first quartile (Q1) (bottom of the box), third

quartile (Q3) (top of the box), outlier (square shown outside the box), whiskers shows minimum and maximum values .....311

Figure 8-12 Size distribution of intrinsic OP ( $dOP_v = \text{mean extrinsic OP (nmol min}^{-1} \text{ m}^{-3})$ ,  $d\log D_p = \text{logarithmic difference of aerodynamic diameter}$ ) of methanol-soluble fractions of fine ( $\leq 2.5 \mu\text{m}$ ) and coarse particles ( $2.5\text{--}10 \mu\text{m}$ ) in DTT (a) and AA (b) assays. Median (line across the box), mean (square within the box), first quartile (Q1) (bottom of the box), third quartile (Q3) (top of the box), outlier (square shown outside the box), whiskers shows minimum and maximum values .....311

Figure 8-13 Association of lung-deposited dose and intrinsic OP of PM size fractions in DTT assay: (a)  $\leq 0.49\mu\text{m}$ , (b)  $0.49\text{--}0.95 \mu\text{m}$ , (c)  $0.95\text{--}1.5 \mu\text{m}$ , (d)  $1.5\text{--}3 \mu\text{m}$ , (e)  $3\text{--}7.2 \mu\text{m}$ , and (f)  $\geq 7.2 \mu\text{m}$  .....312

Figure 8-14 Association of lung-deposited dose and intrinsic OP of PM size fractions in AA assay: (a)  $\leq 0.49\mu\text{m}$ , (b)  $0.49\text{--}0.95 \mu\text{m}$ , (c)  $0.95\text{--}1.5 \mu\text{m}$ , (d)  $1.5\text{--}3 \mu\text{m}$ , (e)  $3\text{--}7.2 \mu\text{m}$ , and (f)  $\geq 7.2 \mu\text{m}$  .....313

## List of Tables

Table 2.1 OP induced by water and methanol-soluble fraction of PM <sub>2.5</sub> in DTT and AA assays .....	25
Table 2.2 Association of OP and respiratory and cardiovascular health endpoints.....	18
Table 3.1 Summary of aerosol sampling field campaign and online data collection .....	35
Table 3.2 Categorizing ions for 20 PAHs and homohopanes for selected ion monitoring (SIM).....	40
Table 3.3 The experimental conditions for the MRM applied in the HPLC-MS/MS analysis of aquinone derivatives .....	42
Table 4.1 Day and night averaged mass concentration of PAHs in PM <sub>2.5</sub> .....	54
Table 4.2 Day and night averages of meteorological parameters .....	56
Table 4.3 Seasonal averages of meteorology parameters .....	60
Table 4.4 Seasonal averaged concentrations (mean ± standard deviation) of PM <sub>2.5</sub> -bound PAHs .....	61
Table 4.5 Day and night averaged diagnostic ratios of PAHs .....	75
Table 4.6 Seasonal average diagnostic ratios of PAHs.....	76
Table 5.1 Summary of averaged mass concentration of WSTMs, WSOC, Levoglucosan, quinones, homohopane, and gaseous pollutants during daytime and nighttime .....	103

Table 5.2 Summary of averaged mass concentration of WSTMs, WSOC, Levoglucosan, quinones, homohopane, and gaseous pollutants during across four seasons.....	105
Table 5.3 Pearson’s correlation (r) between OP induced by water-soluble fraction of PM <sub>2.5</sub> and chemical compositions during daytime .....	125
Table 5.4 Pearson’s correlation (r) between OP induced by water-soluble fraction of PM <sub>2.5</sub> and chemical compositions during nighttime .....	126
Table 5.5 Summary of potential sources associated with OP induced by water-and methanol-soluble fractions of PM <sub>2.5</sub> during the day and at night .....	130
Table 5.6 Pearson’s correlation (r) between OP induced by water-soluble fraction of PM <sub>2.5</sub> and chemical compositions in autumn .....	137
Table 5.7 Pearson’s correlation (r) between OP induced by water-soluble fraction of PM <sub>2.5</sub> and chemical compositions in winter .....	138
Table 5.8 Pearson’s correlation (r) between OP induced by water-soluble fraction of PM <sub>2.5</sub> and chemical compositions in spring .....	139
Table 5.9 Pearson’s correlation (r) between OP induced by water-soluble fraction of PM <sub>2.5</sub> and chemical compositions in summer .....	140
Table 5.10 Summary of potential sources associated with OP induced by water-and methanol-soluble fractions of PM <sub>2.5</sub> across four seasons .....	150
Table 6.1 Averaged concentrations (mean ± standard deviation) of WSTMs and WSOC in PM <sub>2.5</sub> and PM <sub>10</sub> .....	182

Table 6.2 Extrinsic OP induced by water-soluble PM in DTT and AA assays .....	191
Table 6.3 Extrinsic OP induced by methanol-soluble PM in DTT and AA assays .....	192
Table 6.4 Pearson's correlation (r) between OP induced by water-soluble fraction of $\leq 0.49$ $\mu\text{m}$ particles and chemical compositions .....	198
Table 6.5 Pearson's correlation (r) between OP induced by water-soluble fraction of 0.49–0.95 $\mu\text{m}$ particles and chemical compositions .....	199
Table 6.6 Pearson's correlation (r) between OP induced by water-soluble fraction of 0.95–1.5 $\mu\text{m}$ particles and chemical compositions .....	200
Table 6.7 Pearson's correlation (r) between OP induced by water-soluble fraction of 1.5–3 $\mu\text{m}$ particles and chemical compositions .....	201
Table 6.8 Pearson's correlation (r) between OP induced by water-soluble fraction of 3–7.2 $\mu\text{m}$ particles and chemical compositions .....	202
Table 6.9 Pearson's correlation (r) between OP induced by water-soluble fraction of $\geq 7.2$ $\mu\text{m}$ particles and chemical compositions .....	203
Table 6.10 Summary of potential sources associated with OP induced by water-and methanol-soluble fractions of ultrafine, accumulation , and coarse particles .....	217
Table 6.11 Pearson's correlation (r) between OP induced by water-soluble fraction of $\text{PM}_{2.5}$ and chemical compositions .....	222



Table 6.12 Pearson’s correlation (r) between OP induced by water-soluble fraction of PM <sub>10</sub> and chemical compositions .....	223
Table 6.13 Pearson’s correlation (r) between OP induced by methanol-soluble fraction of PM <sub>2.5</sub> and chemical compositions .....	224
Table 6.14 Pearson’s correlation (r) between OP induced by methanol-soluble fraction of PM <sub>10</sub> and chemical compositions .....	225
Table 6.15 Summary of potential sources associated with OP induced by water-and methanol-soluble fractions of PM <sub>2.5</sub> during the day and at night .....	229
Table 7.1 Pearson’s correlation (r) between OP induced by water-soluble fraction of PM <sub>2.5</sub> and LECR of PAHs .....	248
Table 8.1 Chemical structures of 20 PAHs investigated in this study .....	284
Table 8.2 BS Mapping of five factors for source apportionment of PAHs .....	285
Table 8.3 Summary of MLR model for source apportionment to PAH mass concentration and LECR .....	285
Table 8.4 Summary of regression coefficients of sources contribution to PAH mass concentration and LECR .....	285
Table 8.5 Pearson’s correlation (r) between OP induced by methanol-soluble fraction of PM <sub>2.5</sub> and chemical compositions during daytime .....	287

Table 8.6 Pearson's correlation (r) between OP induced by methanol-soluble fraction of PM <sub>2.5</sub> and chemical compositions during nighttime.....	288
Table 8.7 Pearson's correlation (r) between OP induced by methanol-soluble fraction of PM <sub>2.5</sub> and chemical compositions in autumn .....	289
Table 8.8 Pearson's correlation (r) between OP induced by methanol-soluble fraction of PM <sub>2.5</sub> and chemical compositions in winter .....	290
Table 8.9 Pearson's correlation (r) between OP induced by methanol-soluble fraction of PM <sub>2.5</sub> and chemical compositions in spring .....	291
Table 8.10 Pearson's correlation (r) between OP induced by methanol-soluble fraction of PM <sub>2.5</sub> and chemical compositions in summer .....	292
Table 8.11 Summary of correlation coefficients of source contribution DTTv (nmol min <sup>-1</sup> m <sup>-3</sup> ) induced by water-soluble fraction of PM <sub>2.5</sub> .....	293
Table 8.12 BS Mapping of six factors for source apportionment of PM <sub>2.5</sub> .....	293
Table 8.13 Intrinsic OP induced by water-soluble PM size fractions in DTT and AA assays .....	298
Table 8.14 Intrinsic OP induced by methanol-soluble PM size fractions in DTT and AA assays .....	299
Table 8.15 Pearson's correlation (r) between OP induced by methanol-soluble fraction of ≤ 0.49 μm particles and chemical compositions .....	301

Table 8.16 Pearson's correlation (r) between OP induced by methanol-soluble fraction of 0.49–0.95 $\mu\text{m}$ particles and chemical compositions .....	302
Table 8.17 Pearson's correlation (r) between OP induced by methanol-soluble fraction of 0.95–1.5 $\mu\text{m}$ particles and chemical compositions .....	303
Table 8.18 Pearson's correlation (r) between OP induced by methanol-soluble fraction of 1.5–3 $\mu\text{m}$ particles and chemical compositions .....	304
Table 8.19 Pearson's correlation (r) between OP induced by methanol-soluble fraction of 3–7.2 $\mu\text{m}$ particles and chemical compositions .....	305
Table 8.20 Pearson's correlation (r) between OP induced by methanol-soluble fraction of $\geq$ 7.2 $\mu\text{m}$ particles and chemical compositions .....	306

## List of symbols and abbreviations

### Symbols

Ag	Silver
Al	Aluminum
As	Arsenic
Ba	Barium
Bi	Bismuth
Ca <sup>2+</sup>	Calcium ion
Cd	Cadmium
Ce	Cerium
Cl <sup>-</sup>	Chloride ion
Co	Cobalt
CO	Carbon monoxide
Cr	Chromium
Cu	Copper
F <sup>-</sup>	Fluoride ion
Fe	Iron
H <sub>2</sub> O <sub>2</sub>	Hydrogen peroxide
H <sub>2</sub> SO <sub>4</sub>	Sulfuric acid
He	Helium
HNO <sub>3</sub>	Nitric acid
H <sub>2</sub> SO <sub>4</sub>	Sulfuric acid
K <sup>+</sup>	Potassium ion
Li <sup>+</sup>	Lithium ion
Mg <sup>2+</sup>	Magnesium ion
Mn	Manganese
Mo	Molybdenum
Na <sup>+</sup>	Sodium ion

$\text{NH}_4^+$	Ammonium ion
$\text{NH}_3 \cdot \text{H}_2\text{O}$	Ammonium hydroxide
$\text{NH}_4\text{HSO}_4$	Ammonium bi-sulfate
$\text{NH}_4\text{NO}_3$	Ammonium nitrate
$(\text{NH}_4)_2\text{SO}_4$	Ammonium sulfate
Ni	Nickel
$\text{NO}_3^-$	Nitrate ion
$\text{N}_2\text{O}_5$	Dinitrogen pentoxide
NO	Nitric Oxide
$\text{NO}_2$	Nitrogen dioxide
$\text{NO}_x$ (NO + $\text{NO}_2$ )	Nitrogen oxides
$\text{O}_2$	Oxygen
$\text{O}_3$	Ozone
$\cdot\text{OH}$	Hydroxyl radical
Pb	Lead
$\text{SO}_2$	Sulfur dioxide
$\text{SO}_3$	Sulfur trioxide
$\text{SO}_4^{2-}$	Sulfate ion
Sb	Strontium
Sr	Antimony
V	Vanadium
Zn	Zinc

#### Abbreviations

AA	Ascorbic Acid
AAv	Volume-Normaized OP in AA
AAm	Mass-Normalized OP in AA
ABL	Atmospheric Boundary Layer
ABW	Average Body Weight
Ace	Acenaphthene

Acy	Acenaphthylene
AE	Anion Equivalence
Ant	Anthracene
ANOVA	Analysis of Variance
AQ	Antraquinone
APCAP	Air Pollution Control Action Plan
PM	Particulate Matter
ASE	Accelerated Solvent Extraction
BaA	Benzo[a]anthracene
BaP	Benzo[a]pyrene
BbF	Benzo[b]fluoranthene
BcF	Benzo[c]fluorene
BkF	Benzo[k]fluoranthene
BghiP	Benzo-[ghi]perylene
BB	Biomass Burning
BD	Beilun District
BF	Breathing Frequency
BPPs	Bivariate Polar Plots
CA	Correlation Coefficient
CBD	Central Business District
CC	Coal Combustion
CE	Cation Equivalence
CF	Conversion Factor
Chr	Chrysene
CMB	Chemical Mass Balance
COPD	Chronic Obstructive Pulmonary Disease
CR	Carcinogenic Risks
CV	Coefficient of Variation
DahA	Dibenzo[a, h]anthracene

DBahPyr	Dibenzo[a, h]pyrene
DBalPyr	Dibenzo[a, l]pyrene
DBaePyr	Dibenzo[a, e]pyrene
DF	Deposition Fraction
DRs	Diagnostic Ratios
DTNB	5,5-Dithiobis(2-nitrobenzoic acid)
DTT	Dithiothreitol
DTTv	Volume-Normalized OP in DTT
DTTm	Mass-Normalized OP in DTT
ED	Exposure Duration
EF	Exposure Frequency
ELF	Epithelial Lining Fluid
EFs	Enrichment Factors
EPA	Environmental Protection Agency
ET	Exposure Time
ET	Extrathoracic
FIA	Flow Injection Analysis
Flt	Fluoranthene
Flu	Fluorene
FRC	Functional Residue Capacity
GC-FID	Gas Chromatography – Flame Ionization Detection
GC-MS	Gas Chromatography – Mass Spectrometry
GC-MSD	Gas Chromatography- Mass Selective Detector
GDAS	Global Data Assimilation System
GIS	Geographic Information System
GSD	Geometric Standard Deviation
HPLC-MSMS	High Performance Liquid Chromatography with tandem Mass Spectrometry

HMW	High Molecular Weight
HULIS	Humi-Like Substances
IC	Ion Chromatography
ICP-MS	Inductively Coupled Plasma- Mass Spectrometry
ICRP	International Commission on Radiological Protection
IE	Industrial Emissions
IGSNRR	Institute of Geographical Sciences and Natural Resources
IPyr	Indeno[1,2,3-cd]pyrene
IUR	Inhalation Unit Risk
Levo	Levoglucozan
LECR	Lifetime Excess Cancer Risk
LOD	Limit of Detection
LMW	Low Molecular Weight
MAs	Monosaccharide Anhydrides
MDL	Method Detection Limit
ME	Marine Emissions
MLR	Multiple Linear Regression
MPPD	Multiple-Path Particle Dosimetry
MSA	Methanesulfonic Acid
NaP	Naphthalene
NCEP	National Centre for Environmental Protection
NCR	Non-Carcinogenic Risk
NCRP	National Council on Radiation Protection
NFs	Neutralization Factors
NGC	Natural Gas Combustion



NOAA	National Ocean and Atmospheric Administration
NQ	Napthaquinone
NSS	Non-Sea Salt
OP	Oxidative Potential
PAHs	Polycyclic Aromatic Hydrocarbons
PBL	Planetary Boundary Layer
PL	Pulmonary
PCA	Principal Component Analysis
Phe	Phenanthrene
PMF	Positive Matrix Factorization
PRD	Pearl River Delta
Pyr	Pyrene
RD	Road Dust
RH	Relative Humidity
ROS	Reactive Oxygen Species
RSD	Relative Standard Deviations
SA	Secondary Aerosol
SIAs	Secondary Inorganic Aerosols
SIM	Selected Ion Monitoring
SNA	Sulfate, Nitrate and Ammonium
SOA	Secondary Organic Aerosols
TB	Tracheobroncial
TEF	Toxicity Equivalent Factors
TEQ	Toxicity Equivalent Quotient
TV	Tidal Volume
UNNC	University of Nottingham Ningbo China
UR	Unit Risk
URT	Upper Respiratory Tract

VE	Vehicular Emissions
VOCs	Volatile Organic Compounds
VUF	Volatilization Urbunt Fuel
WIZ	Wangchun Industrial Zone
WHO	World Health Organization
WSIIs	Water-Soluble Inorganic Ions
WSOC	Water-Soluble Organic Carbon
WSTMs	Water-Soluble Trace Metals
YRD	Yangtze River Delta
ZD	Zhenhai District

## Chapter 1 Introduction

### 1.1. Background

For a considerable period, air pollution in China has resulted in significant health impairments and other kinds of detrimental impacts on society (Liu et al., 2018). The issue of air pollution in China stems from elevated levels of pollutants, including PM, nitrogen oxides ( $\text{NO}_x = \text{NO} + \text{NO}_2$ ), and sulfur dioxide ( $\text{SO}_2$ ), carbon monoxide (CO), volatile organic compounds (VOCs), and ozone ( $\text{O}_3$ ), caused mainly by high levels of industrialization and energy consumption (Lihong and Jingyuan, 2011; Zhang et al., 2021). Air pollution cause serious health hazards, including chronic respiratory disease (Lakey et al., 2016), cardiovascular disease (Consensus et al., 2022), and cancer (Alemayehu et al., 2020). Moreover, air pollution can negatively affect wildlife (Honda and Suzuki, 2020), cause acid rain (Prakash et al., 2023), reduce visibility (Tian et al., 2016), cause climate change (Burr and Zhang, 2011), and lead to a reduction in the ozone layer (Womack et al., 2023). Air pollution can also pose economic consequences, such as increased healthcare expenditures and decreased productivity due to missed workdays caused by illness (Hopke and Hill, 2021).

Air pollution in China was initially attributed to coal combustion and industrial processes during the early stages of economic growth (Jin et al., 2016). However, with the rise in urbanization, vehicle emissions have become a significant contributor, particularly in megacities (Huang et al., 2018). In response to the heightened problem of air pollution, the Chinese Government established the Air Pollution Control Action Plan (APCAP) in 2013 (Cai et al., 2017), which aims to reduce air pollution in specific regions by 25% in Beijing-

Tianjin-Hebei, 20% in the Yangtze River Delta, and 15% in the Pear River Delta (Zhang et al., 2022). The Chinese Government has taken various steps to decrease air pollution, such as setting strict regulations for automobile, industrial, and coal-fired power plant emissions, advancing the usage of clean energy like wind and solar power, increasing investment in electric vehicles, developing public transportation like the metro, buses, and trains, creating a network of air quality monitoring stations throughout the country, and promoting eco-friendly behaviors and community-based initiatives (He et al., 2017).

The aforementioned actions have led to significant improvements in air quality in recent years, but there is still a problem with the emergence of fine particles (PM<sub>2.5</sub>) at a regional level (Wang et al., 2023; Xu et al., 2023). Consequently, PM<sub>2.5</sub> pollution has garnered significant attention nationwide in China, leading to its inclusion in the National Ambient Air Quality Standards (NAAQS, GB 3095-2012) (Zhao et al., 2016). The problem of air pollution, particularly PM<sub>2.5</sub> pollution, has received urgent attention due to research indicating that it causes approximately 4 million deaths globally every year, before individuals reach their average life expectancies (Thangavel et al., 2022). Studies have estimated that more than 1.36 million premature deaths occur annually due to human exposure to PM<sub>2.5</sub> pollution in the Western Pacific, with China being the largest contributor (Huang et al., 2021; Lelieveld et al., 2015).

In China, extensive nationwide monitoring stations are currently in place to measure the mass concentrations of PM<sub>2.5</sub> particles for regulatory purposes. However, it has been demonstrated through careful research that relying solely on mass concentration as a regulatory criterion may not effectively mitigate the health risks associated with fine

particles (Daellenbach et al., 2020; Wang et al., 2022). Given the significant differences in the chemical composition of PM arising from various emission sources, it is apparent that the mass concentration alone may not adequately reflect the toxicity levels (Farahani et al., 2022). This highlights the importance of using a more comprehensive and accurate metric that can effectively capture and evaluate the actual health risks presented by PM (Famiyeh et al., 2021). One such metric that has emerged as a promising alternative is the measurement of OP (Abrams et al., 2017; Campbell et al., 2021; Luo et al., 2023).

The OP of PM represents its ability to cause cellular damage through the generation of reactive oxygen species (ROS) (Wen et al., 2023), which can lead to inflammation and cell death (Ahmad et al., 2021; Li et al., 2022). Additionally, PM can also carry ROS that can adversely cause oxidative stress upon inhalation (Stevanovic et al., 2019). The high reactivity of ROS (such hydroxyl radical ( $\cdot\text{OH}$ ), hydrogen peroxide ( $\text{H}_2\text{O}_2$ ), organic peroxy radicals ( $\text{ROO}\cdot$ ), and superoxide radical ( $\text{O}_2^{\cdot-}$ ) primarily stems from the presence of unpaired electrons (Rao et al., 2020).

Numerous studies have indicated that particle size, chemical compositions, and sources of PM affects its ability to cause oxidative stress (An et al., 2022; Bates et al., 2019; Nishitahara et al., 2019), which can subsequently lead to various health endpoints. For example, previous research has consistently shown a significant correlation between OP of  $\text{PM}_{2.5}$  and emergency hospital visits for various cardiorespiratory conditions (Abrams et al., 2017). Moreover, several studies have established a causal link between OP and various health endpoints, such as asthma and congestive heart failure (Bates et al., 2015; Fang et al., 2016; Yang et al., 2016). Therefore, utilizing OP as a regulatory parameter could significantly

enhance our ability to accurately assess the toxicity of ambient particles and effectively safeguard public health (Calas et al., 2019; Yu et al., 2022). However, since the OP method is still in the developmental stage, the aim of this study is to contribute to its improvement by considering the effects of particle size, chemical compositions, and sources.

The chemical compositions of PM, particularly polycyclic aromatic hydrocarbons (PAHs), have been extensively established to cause lung cancer (Famiyeh et al., 2021). These compounds possess well-documented carcinogenic properties and tend to accumulate in the respiratory system upon inhalation (Famiyeh et al., 2021). Once inhaled, PAHs undergo metabolic activation facilitated by enzymes like cytochrome P450s (CYPs), consequently leading to DNA damage and the subsequent development of lung cancer (Famiyeh et al., 2021; Moorthy et al., 2015). PAHs have been found to be strongly associated with OP (Janssen et al., 2014), but it remains unclear whether the OP could directly contribute to the risk of developing lung cancer. This study contributes to existing knowledge by examining the correlation between specific PAHs and OP, and their association with the risk of lung cancer.

## 1.2. Statement of the problem

The research was conducted in the coastal hotspot city of Ningbo, China, which faces significant challenges with pollution originating from various sources such as vehicular traffic, commercial activities, industrial activities, and sea spray/marine emissions. Moreover, previous studies conducted in Ningbo have identified the influence of long-range transportation on the levels of aerosol pollution in the city (Chen et al., 2022; Xu et al., 2019). Moreover, most of the studies conducted in the city have primarily focused on analyzing the chemical composition of PM, including inorganic ions, trace metals, and

carbonaceous species (Liu et al., 2018; Tu et al., 2019). However, there is a significant gap in comprehensive research regarding the investigation of the effects of particle size, chemical composition, and sources on OP of PM (Wang et al., 2018). A previous study conducted by Chen et al. (2022) had a limited scope as it primarily focused on fine particles, had a small sample size, and utilized only one method for measuring OP. Moreover, the existing literature lacks clarity regarding the variation of OP in PM<sub>2.5</sub> during both daytime and nighttime periods (Ahmad et al., 2021; Ainur et al., 2023). This is primarily due to the fact that most studies have been focused solely on 24-hour aerosol sampling, which does not provide specific insights into diurnal fluctuations. Understanding these distinctions could aid in the formulation of improved public health policies and provide individuals with better guidance on reducing their exposure to PM<sub>2.5</sub> particles.

The current lung cancer risk assessment framework for PAHs fails to consider a wider range of highly carcinogenic PAHs, which may result in an underestimation of the actual level of risk (Iakovides et al., 2021). There is a significant lack of research specifically focused on examining this particular aspect.

The primary aim of this study is to identify areas in the research that have not been sufficiently addressed regarding the measurement of OP and the risk of lung cancer associated with particulate-PAHs.

The identified key research gaps were summarized as follows:

**(1) Lung cancer risk of PAH exposure**

(a) There are hundreds of different types of PAHs present in the air we breathe (Famiyeh et al., 2023). However, researchers have primarily focused their attention on the

Environmental Protection Agency (EPA) 16 priority PAHs that are known for their persistence, prevalence, and potential to harm a larger portion of the population (Famiyeh et al., 2021; Křůmal et al., 2013; Lee et al., 2022; Wang et al., 2011). The assessment of lung cancer risk has disregarded the impact of high carcinogenic PAHs, including 7H-benzo[c]fluorene and various dibenzopyrene derivatives. Their potential contribution has been neglected due to their low concentrations in the ambient environment (Famiyeh, Xu, et al., 2023). This can lead to an underestimation of the actual cancer risk associated with PAH exposure. Therefore, it is imperative to consider a broader range of PAHs to obtain a more accurate evaluation of the health risks.

- (b) A commonly observed error in the literature is the inappropriate estimation of cancer risk by multiplying the concentration of B[a]P<sub>eq</sub> (equivalent concentration of benzo[a]pyrene) by the unit risk recommended by the World Health Organization (WHO) (Pongpiachan et al., 2015). This approach can lead to a significant overestimation of risk. The correct procedure, as outlined by WHO, is to use the concentration of B[a]P (benzo[a]pyrene) alone as a surrogate for the entire mixture when estimating cancer risk. It is important to note that the WHO unit risk can only be applied when utilizing B[a]P as a marker for complex mixtures (Aquilina and Harrison, 2023). On the other hand, if the approach involves the use of B[a]P<sub>eq</sub> (such as the component-based potency factor approach), the appropriate unit risk to be used is the one recommended by the EPA.



## **(2) Effect of extraction solvents and acellular assays on OP measurement**

To determine the OP of PM, efficiently extracting its chemical compositions is crucial. The choice of extraction solvent is significant in obtaining accurate OP values. Water is a widely employed extraction medium for the isolation of hydrophilic chemical compounds present in PM when conducting OP measurement (Cui et al., 2023; Molina et al., 2023; Secrest et al., 2016). However, methanol can be used to extract both hydrophilic and hydrophobic chemicals, enabling the measurement of the OP of these chemical species (Chen et al., 2022; Famiyeh et al., 2023). While the impact of extracted chemicals on the OP of PM is acknowledged, the exact influence of specific chemicals remains uncertain. Given the potential variation in the effects of the extracted chemicals, it is imperative to assess OP using multiple assays, including dithiothreitol (DTT) and ascorbic acid (AA) assays with varying sensitivities to these chemicals (Famiyeh, Jia, et al., 2023). This approach will provide a more comprehensive understanding of the effects of these chemicals on OP. Moreover, this approach will determine the appropriate assay to be used for measuring the OP induced by water-soluble and methanol-soluble fractions of ambient particles.

## **(3) Effect of particle size on OP**

(a) The mass concentration is a commonly used metric for regulating PM<sub>2.5</sub> pollution.

However, research has demonstrated that PM<sub>2.5</sub> toxicity might not be best evaluated through this approach. For example, even though fine and ultrafine particles are typically more dangerous than coarse particles, some research have suggested that coarse particles may also have a severe impact on health (Deng et al., 2019; Famiyeh et al., 2023). The aforementioned discrepancy highlights the need to use OP as an effective metric for

providing comparative assessment of the toxicity of ultrafine, accumulation, and coarse particles. Furthermore, most previous investigations of OP have primarily focused on fine particles (PM<sub>2.5</sub>), and the relationship between particle size and OP remains unclear (Famiyeh, Jia, et al., 2023; Shang et al., 2022; Simonetti et al., 2018). There is limited literature comparing the OP induced by ultrafine ( $\leq 1.0 \mu\text{m}$ ), fine ( $\leq 2.5 \mu\text{m}$ ), and coarse (2.5–10  $\mu\text{m}$ ) particles using both DTT and AA assays.

(b) The assessment of OP deposition in specific regions of the human respiratory tract is considered a more accurate indicator of the health impacts related to exposure to PM, which can vary depending on particle size. However, there is limited research available that focuses on simulating OP deposition within the respiratory tract. For instance, Lyu et al. (2018) conducted a study in which they simulated OP deposition using the DTT assay and the MPPD model in the human respiratory tract. Since only one assay has been utilized for these investigations, it remains unclear whether different assays could measure similar levels of OP deposition of ultrafine, accumulation, and coarse particles.

#### **(4) The relationship between OP and doses of PM in human respiratory tract**

The degree to which PM exposure adversely impacts human health hinges on the particle's ability to trigger oxidative stress by consuming the antioxidants in the epithelial lining fluid (ELF) (Famiyeh, Jia, et al., 2023). When we breathe in PM particles, they can settle in different regions of human respiratory tract with different deposition efficiency and doses. However, the relationship between the deposition dose of the inhaled particle and OP in specific regions of the respiratory tract remain unclear (Famiyeh, Jia, et al., 2023). To accurately establish the relationship between OP and particle deposition dose, it is

insufficient to solely rely on acellular assays that only consider particles outside of cells. Such assays do not provide a precise estimation of the amount of PM present in the respiratory tract and its impact on human health. Therefore, in order to accurately predict the actual particle deposition dose in the human respiratory system and its association with OP, it is imperative to estimate the particle deposition dose using a realistic exposure scenarios.

#### **(5) The reduction of OP of PM<sub>2.5</sub>**

Due to the significant global health concerns linked to PM<sub>2.5</sub> pollution, it is of paramount importance to precisely estimate the contributions of various sources to its OP. This is indispensable for developing effective strategies aimed at mitigating the adverse impacts of PM on public health. Merely focusing on sources related to the mass concentration of ambient particles may prove insufficient in effectively reducing OP levels, as many studies have shown that the sources contributing to the PM<sub>2.5</sub> mass concentration and the OP can vary significantly (Daellenbach et al., 2020; Yixiang Wang et al., 2022). This assertion requires further investigation of the contributions of each source to both the mass concentration and OP of PM<sub>2.5</sub>.

#### 1.3. Aims of the study

The aims of the study were as follows:

- 1) investigating the effect of extraction solvents and acellular assays on the OP of PM;
- 2) investigating the effect of particle size, chemical composition, and sources on the OP levels of PM;
- 3) establishing the link between the deposition dose and OP of PM in the respiratory tract;

- 4) identifying the primary sources associated with the OP of PM<sub>2.5</sub> and lung cancer risk of PAHs.

#### 1.4. Specific objectives

This study aimed to systematically investigate PM ability to induce oxidative stress through ROS generation in Ningbo city. This study considered aerosols of varying sizes, ensuring a comprehensive assessment of OP using two assays. To achieve this, two acellular assays, DTT and AA, were employed to accurately measure OP levels and its respiratory depositions. Additionally, a thorough chemical characterization aimed to identify chemical species that OP was conducted, along with source apportionment analysis. Furthermore, the study assessed the lung cancer risk associated with particulate-bound PAHs, allowing for the identification of specific sources that can contribute to the risk level at our study domain.

The specific objectives investigated in this study were as follows:

- 1) analyzing the concentrations, diurnal and seasonal variations, and size distribution of chemical compositions of PM such as water-soluble inorganic ions, water-soluble trace metals, PAHs, quinones, levoglucosan, and homohopanes;
- 2) evaluating the lung cancer risk of particulate-bound PAHs, investigating the source dispersion characteristics, and estimating the source contributions;
- 3) assessing the source profiles, source dispersion, and estimating the source contribution to OP induced by water- and methanol-soluble fractions of PM<sub>2.5</sub> during daytime, nighttime, and by seasons;
- 4) investigating whether there is a link between OP and lung cancer risk caused by particulate-PAHs;

- 5) identifying the sources of PM<sub>2.5</sub> during the day, night, and seasons, and estimating the source contribution to the OP;
- 6) comparing OP induced by water-and methanol-soluble fractions of ultrafine ( $\leq 0.49$  and  $0.49\text{--}0.95\ \mu\text{m}$ ), accumulation ( $0.95\text{--}1.5$ ,  $1.5\text{--}3\ \mu\text{m}$ ), and coarse particles ( $3\text{--}7.2$ ,  $\geq 7.2\ \mu\text{m}$ );
- 7) comparing the OP induced by water-and methanol-soluble fractions of PM<sub>2.5</sub> and PM<sub>10</sub>;
- 8) estimating the particle deposition fractions and doses, and OP respiratory deposition;
- 9) identifying the dominant redox-active chemical species that induce OP of PM with varying size ranges.

#### 1.5. Research methodology

The flowchart presented in Figure 1-1 outlines the experimental methodology employed in this research project. The study commenced with the collection of PM samples, which spanned approximately one year. The chemical compositions of these PM samples, including water-soluble trace metals, inorganic ions, PAHs, water-soluble organic carbons, homohopanes, and levoglucosan were analyzed. This analysis was conducted using various techniques, namely Inductively Coupled Plasma-Mass Spectrometry (ICP-MS), Ion chromatography (IC), Gas Chromatography-Mass Selective Detector (GC-MSD), Thermal Optical Carbon (TOC) Analyzer, and High-Performance Liquid Chromatograph-Mass Spectrometry/Mass Spectrometry (HPLC-MS/MS). The OP induced by water and methanol-soluble fraction of the PM samples was assessed using DTT and AA assays. The dose of PM deposited in human respiratory tract was modeled using the MPPD model. Additionally, the

positive matrix factorization (PMF) model and bivariate polar plots (BPPs) were utilized to identify the sources of PAHs, PM<sub>2.5</sub>, and OP induced by PM with varying size ranges in ultrafine, accumulation, and coarse modes. The contribution of these source to lung cancer risk and OP was estimated using the multiple linear regression (MLR) model.

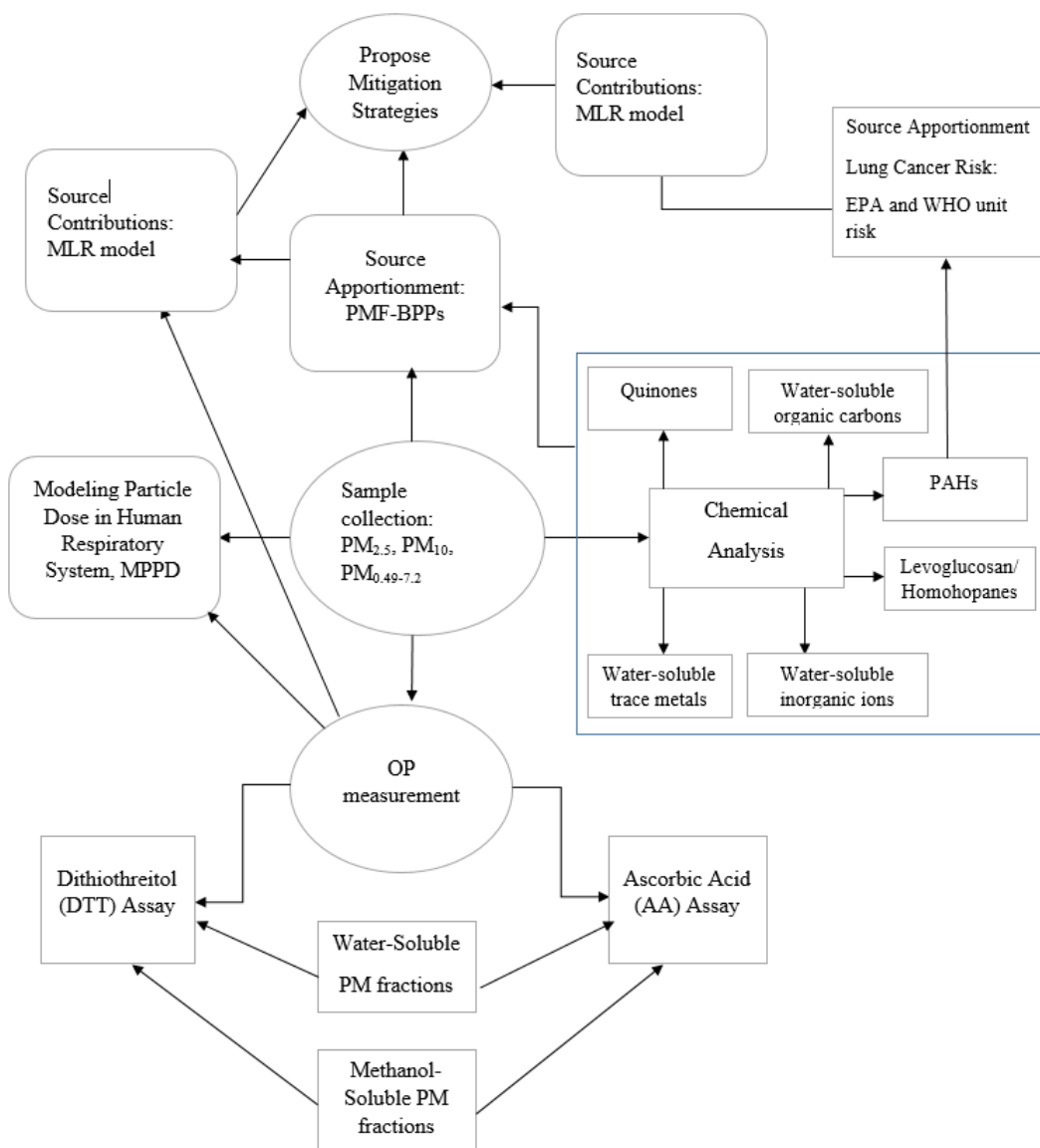


Figure 1-1 Flowchart of the experimental work conducted in this study

## 1.6. Thesis outline

**Chapter 1 Introduction.** This chapter provides background information on air pollution in China, with a specific focus on PM. The chapter introduces the concept of OP as a valuable metric for assessing the health risks associated with ambient particles. Additionally, the chapter outlines the research gaps, aims, objectives, and methodology used in this study.

**Chapter 2 Literature Review.** This chapter focuses on cell-free methods for measuring OP, specifically focusing more on DTT and AA assays that was employ in this study. It provides background information on the chemical species that induce OP and includes a literature review of studies conducted both within and outside of China. Additionally, it introduces a theoretical framework for utilizing the MPPD model to predict particle deposition fraction, doses, and OP deposition in the human respiratory tract. The chapter also presents information on the assessment of lung cancer risk associated with PAHs. Finally, it offers background information on the PMF model, MLR, and BPPs for source apportionment.

**Chapter 3 Materials and Methods.** This chapter presents the detailed experimental procedures used in the study, including aerosol sampling, chemical extraction and pre-treatment, and chemical analysis of inorganic ions, trace metals, PAHs, and quinones. The methods for measuring OP using the DTT and AA assays are described, and the statistical methods used for data analysis and source apportionment techniques, such as the PMF model, BPPs, and MLR, are provided.

**Chapter 4 Particulate-Bound Polycyclic Aromatic Hydrocarbons: Diurnal and Seasonal Variations, Size Distribution, Sources Apportionment, amd Lung Cancer Risk.** This chapter focuses primarily on the diurnal and seasonal variations, and size distribution of particulate-PAHs, and estimate the lifetime excess lung cancer risk (LECR) by comparing the WHO and EPA methodologies. PMF model was applied to identify sources of PAHs. The sources derived from PMF model was subjected to BPPs analysis to investigate the dispersion patterns and transport of PAHs to our monitoring station. MLR



was applied to identify the source contributions to the LECR of PAH exposure in PM<sub>2.5</sub> particles.

**Chapter 5 OP induced by Water and Methanol-Soluble Fractions of PM<sub>2.5</sub>: Diurnal and Seasonal Variations, Chemical Characterization, and Source Apportionment.** This chapter aimed to explore the daytime, nighttime, and seasonal patterns in the OP of PM<sub>2.5</sub> particles. The marine source contributions and aerosol acidity was investigated during the daytime, night, and seasons. Chemical species associated with OP were identified through Pearson's correlation analysis. By utilizing PMF-BPPs model, we successfully identified the sources and dispersion characteristics associated with PM<sub>2.5</sub> particles. Additionally, we employed MLR analysis to estimate the contributions of each source to the OP. We conducted a correlation analysis to investigate the existence of a link between OP and the risk of lung cancer caused by PAH exposure.

**Chapter 6 Particle Size Distribution of OP induced by Water and Methanol-Soluble Fractions: Chemical characterization, and Respiratory Depositions.** The level of chemical species such as trace metals, WSOC, and quinones were introduced. We utilized the MPPD model to estimate particle deposition efficiency and doses in the human respiratory system, as well as to investigate the size distribution of OP in ambient particles. Additionally, we studied the deposition of OP in various regions of the human respiratory tract. Lastly, we establish the link of the deposition dose and OP of PM with varying size ranges.

**Chapter 7 Contributions, Conclusions and recommendation for future works.** This chapter presents our contributions to the evaluation of the risk of lung cancer associated with

PAHs, OP measurement, and OP deposition in human respiratory tract. We have presented conclusions that focus on our key findings. In addition, we offer suggestions for future research, taking into consideration the limitations of the study.

## Chapter 2 Literature Review

### 2.1 OP for PM toxicological assessment

Many studies in the fields of epidemiology and toxicology have presented compelling evidence that establishes a strong link between the inhalation of ambient particles and the occurrence of respiratory and cardiopulmonary diseases, such as asthma, heart disease, and lung cancer (Kelly and Fussell, 2020; Thangavel et al., 2022). However, the precise mechanisms by which exposure to PM leads to the manifestation of diseases in humans are still not fully understood (Kobos and Shannahan, 2021). Recent research has used human biomarkers (such as 8-hydroxy-2'-deoxyguanosine, NO<sub>x</sub>, Uric acid, and Dopamine) (Kim et al., 2023), animal models (e.g., rat, rodent, etc.) (Ferreira et al., 2022; Mu et al., 2022), and DNA methylation (Ferrari et al., 2019) to gain valuable insights into the potential mechanisms underlying the toxicity of PM.

The exposure to PM can initiate oxidative stress in the body (Gangwar et al., 2020), which in turn may contribute to the initiation and progression of various diseases. This occurs when ROS in the body exceeds the natural antioxidant defenses, thereby disrupting the biochemical equilibrium (Mudway et al., 2020). OP describes how PM consumes antioxidants in the human ELF and produces ROS in the lungs (Shahpoury et al., 2022), and can be explored to understand the mechanism with which ambient particles can lead to diseases.

## 2.2 Acellular assays for OP measurement

Acellular assays are advantageous over cellular assays for measuring the OP of ambient particles due to several reasons. They are simpler and easier to perform as they do not require live cells. The cellular assays can become saturated when exposed to high concentrations of ambient particles and their chemical compositions (Wang et al., 2022). Acellular assays are cost-effective as they eliminate the need for expensive culture media and equipment. Cell-free assays can be designed to measure specific OPs of PM, which may not be measurable using cellular assays. They offer greater reproducibility by avoiding biological variability with live cells. Lastly, cell-free assays are more sensitive and can detect very low concentrations of oxidizing agents in PM (Shahpoury et al., 2022). In summary cell-free assays offer a simpler, cost-effective, automation-friendly, and more sensitive approach for measuring the OP of PM (Frezza et al., 2022; Rao et al., 2020; Xiong et al., 2017).

Cell-free assays can be categorized into two main types based on the OP methodology: antioxidant depletion assays and ROS generation assays. Antioxidant depletion assays measure the consumption of antioxidants over time when exposed to ambient particles, while ROS assays measure the levels of ROS generated. Commonly used antioxidant depletion assays for measuring OP include DTT and AA (Nishita-Hara et al., 2019; Perrone et al., 2019). The depletion of DTT and AA during OP measurement is presumed to correlate with the production of ROS (Fang et al., 2019). In contrast, assays such as the dichlorofluorescein diacetate (DCFH-DA) assay and electron paramagnetic resonance (EPR) directly measure ROS (Hedayat et al., 2015). In this study, both DTT and AA assays were employed to comparatively evaluate the OP of ambient particles. The selection of these two assays was

based on their user-friendliness, speed, high repeatability, and cost-effectiveness (Famiyeh, Jia, et al., 2023; Frezzini et al., 2022). Although AA assay has been utilized to determine the OP of PM, it has received less attention compared to the DTT assay. In Section 2.4, a comprehensive review of the literature on the comparison of OP measurement using DTT and AA assays is provided. The lack of consensus or comprehensive inter-laboratory comparison to validate this method impedes its progress and hinders its application as a more health-relevant metric for assessing human exposure to PM.

#### 2.2.1 Dithiothreitol (DTT) assay

Dithiothreitol, which is a strong reducing agent, frequently used as a surrogate for biological reducing agents to examine the rate at which antioxidants are consumed in human ELF upon exposure to chemical compositions of ambient particles. The DTT method established by Cho et al. (2005) remained the most widely employed assay to evaluate the OP of ambient particles (Chen et al., 2022; Cheng et al., 2021; Jiang et al., 2019; Molina et al., 2020; Nishita-Hara et al., 2019; Xiong et al., 2017).

The detailed procedures of DTT assay for OP measurement are described in section 3.4.2. Briefly, the oxidation of DTT involves electrons transfer from DTT to molecular oxygen ( $O_2$ ), which generates superoxide ( $O_2^-$ ) and DTT-disulphide. The chemical composition of PM, especially trace metals and quinones facilitates the electron transfer process, resulting in the formation of  $H_2O_2$ . Xiong et al. (2017) conducted thorough research that demonstrated a significant correlation ( $r = 0.91$ ) between the oxidation of DTT and the production of  $H_2O_2$ . To determine the remaining DTT, a thiol reagent such as 5,5'-ditiobis-2-nitrobenzoic acid (DTNB) is added, resulting in the formation of 2-nitro-5-thiobenzoic acid (TNB) (Hedayat

et al., 2015; Visentin et al., 2016). The detailed mechanism of DTT depletion and H<sub>2</sub>O<sub>2</sub> formation is shown in Figure 2-1.

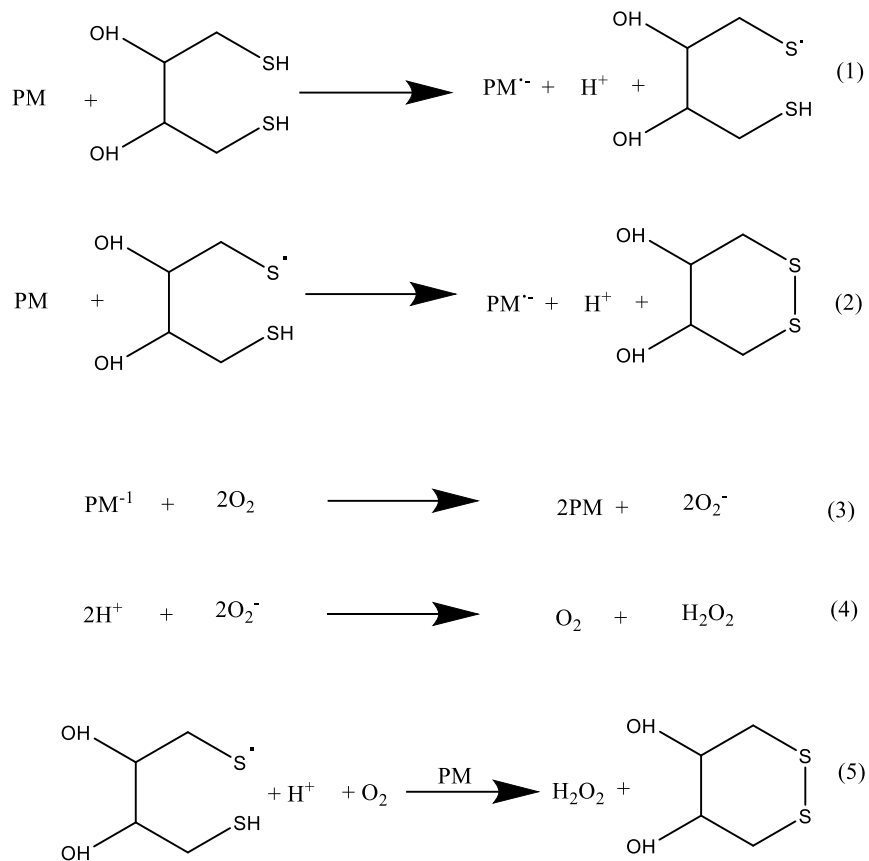


Figure 2-1 Mechanism of DTT oxidation by PM (Cho et al., 2005)

DTT is highly sensitive to a wide range of chemical species in ambient particles including trace metals (e.g., Fe, Cu, Mn, etc.) (Charrier and Anastasio, 2012; Fang et al., 2016), and carbonaceous species (e.g., WSOC, EC, OC) (Liu et al., 2018; Vreeland et al., 2017), Humic-like Substances (HULIS) (Cheng et al., 2021; Fang et al., 2019; Lyu et al., 2018; Yu et al., 2022), and quinones (H. Jiang et al., 2019; Rao et al., 2020), and black carbon (Rao et al., 2020). A strong positive correlation has been found between chemical species (such as PAH,

$\text{NH}_4^+$ ,  $\text{SO}_4^{2-}$ ,  $\text{K}^+$ ) and OP measured in the DTT assay (Kurihara et al., 2022; Ntziachristos et al., 2007; Xiong et al., 2017).

### 2.2.2 Ascorbic acid (AA) assay

In the ELF of the human lungs, AA serves as a natural antioxidant. Studies have reported that individuals with asthma have lower levels of ascorbic acid compared to individuals without the condition (Fang et al., 2019; Lin and Yu, 2020). The presence of certain chemical species, such as trace metals, in ambient particles can cause AA oxidation, generating dehydroascorbate (Rao et al., 2020). This oxidation process results in the formation of superoxide, which is further converted into  $\text{H}_2\text{O}_2$ . The generated  $\text{H}_2\text{O}_2$  then participates in the Fenton reaction. This ultimately leads to the production of  $\cdot\text{OH}$ , which then react with salicylic acid, resulting in the formation of 2, 3- and 2, 5-dihydroxybenzoates (DHBAs) (Hedayat et al., 2015). The summary of the mechanism of AA oxidation by PM is presented in Figure 2-2. The OP of PM can be quantified over time by measuring the absorbance of ascorbate at 265 nm. The detailed experimental procedure for measuring OP using the AA assay is presented in Section 3.7.2.

The depletion rate of AA is strongly influenced by water-soluble trace metals (e.g., Fe, Cu) (Rao et al., 2020). For example, AA has been found to exhibit a strong positive correlation with various metals emitted from non-exhaust traffic, such as Cu, Zn, Cr, Fe, Ni, Mn, Sn, Cd, and Pb (Bates et al., 2019; Pietrogrande et al., 2019). AA has been reported to be less sensitive to organic species (Fang et al., 2016). However, research has indicated that the addition of quinones into the reaction mixture containing AA can result in its depletion (Fang et al., 2016; Visentin et al., 2016).

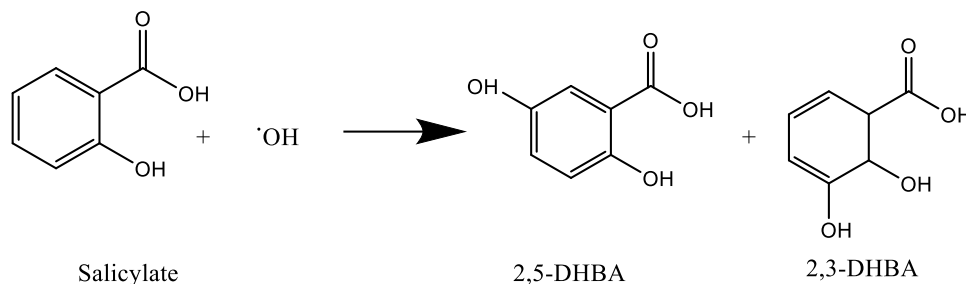
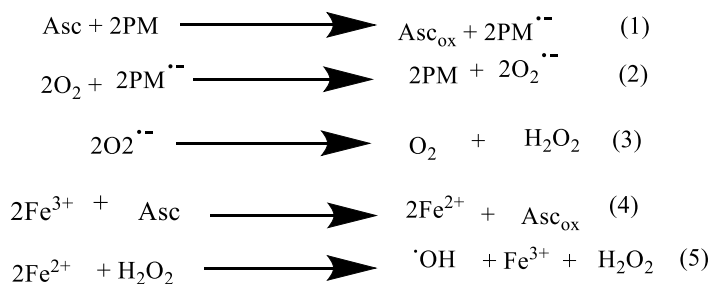


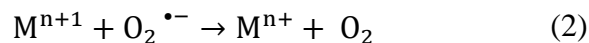
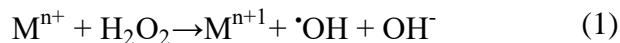
Figure 2-2 Mechanism of AA oxidation by PM (Hedayat et al., 2015)

### 2.3 OP induced by PM chemical compositions

The soluble fractions of trace metals influence the redox activity of ambient particles, subsequently leading to various health endpoints. For instance, trace elements such as Cu, Fe, Zn, and Mn contribute to immune system dysfunction and the development of inflammatory responses due to their ability to induce oxidative stress (Mahmoud et al., 2023; Mitra et al., 2022; Zheng et al., 2023). Moreover, elevated concentrations of these trace metals significantly impact the oxidative capacity of ambient aerosols. Cu stands out as having the highest OP in DTT assay among the trace metals, followed by Mn, Co, V, Ni, Pb, and Fe (Charrier and Anastasio, 2012). In urban environments with elevated levels of Fe in the ambient air, there is a significant depletion of DTT. This is due to the ability of Fe to oxidize  $\text{H}_2\text{O}_2$  to form  $\cdot\text{OH}$  radicals via Fenton (reaction 1) and Haber-Weiss reactions (reactions 2 and 3) (Cuypers et al., 2010; Fang et al., 2019), which enhance the OP activity.

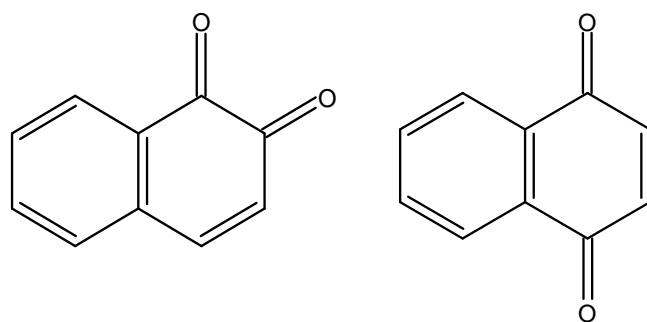


Furthermore, other metals such as Cu, Mn, Co, Ni, and V can also exhibit OP activity through similar mechanisms.



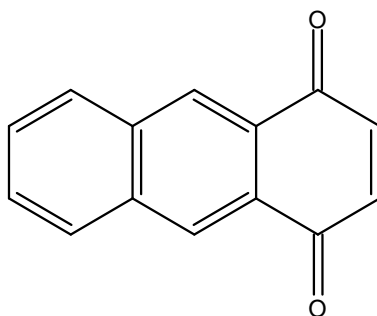
A strong correlation between WSOC and DTT-measured OP has been reported in previous studies (Fang et al., 2016; Verma et al., 2012). The OP induced by WSOC has been linked to catalytic oxidizers, such as humic-like substances (HULIS) (Fang et al., 2019; Verma et al., 2015). Previous studies have shown a correlation between PAH concentrations and OP induced by ambient particles in DTT assay (Charrier and Anastasio, 2012; Cho et al., 2005; Famiyeh et al., 2023; Xiong et al., 2017). This correlation is influenced by the variability of emission sources and the ability of PAHs to undergo oxidation (Cho et al., 2005).

Quinones are also generated through the photochemical oxidation of parent PAHs, specifically those with LMW, such as naphthalene (McWhinney et al., 2013). They chemical species possess high redox activity (Cho et al., 2004; Pei et al., 2018; Vreeland et al., 2017). Examples of quinones known for their high redox activity include 1, 2-naphthoquinone (1, 2-NQ), 1, 4-naphthoquinone (1, 4-NQ), and 1, 4-anthraquinone (1, 4-AQ) (Gao et al., 2020; Lyu et al., 2018; Xiong et al., 2017). The chemical structure of these quinones is depicted in Figure 2-3.



1, 2-NQ

1, 4-NQ



1, 4-AQ

Figure 2-3 Chemical structure of quinones: 1, 2-naphthoquinone, 1, 4-naphthoquinone, and 1, 4-anthraquinone

Although inorganic ions in ambient particles do not directly produce ROS or display redox activity, they are positively correlated with OP, especially with  $\text{SO}_4^{2-}$  and  $\text{NO}_3^-$  (Daellenbach et al., 2020; Fang et al., 2015). Specifically,  $\text{SO}_4^{2-}$  increase aerosol hygroscopicity and promotes the generation of  $\text{H}^+$  ions through aqueous phase reactions (Fang et al., 2017). The rise in aerosol acidity enhances the process of trace metal dissolution, ultimately leading to the formation of soluble metal sulfates (Fang et al., 2017). Consequently, this contributes to elevated levels of OP of PM.

The question of whether the summation of OP values for individual chemical components accurately represents the total OP is subject to ongoing debate. To address this, considerable

research has shown that the OP of ambient particle chemical compositions can have either a synergistic or an antagonistic effect on OP. Specifically, transition metals such as Cu, Fe, Mn, V, and Ni, as well as organic compounds such as WSOC, HULIS, and various quinones (such as 1, 2-NQ, 1, 4-NQ, and 1, 4-AQ), have the potential to interact with each other and induce either synergistic or antagonistic effects on OP. According to Yu et al. (2018), the interaction between Mn and quinones can have a synergistic effect on OP. However, this same interaction can result in an antagonistic effect on the production of  $\bullet\text{OH}$  radical. In contrast, when Mn interacts with HULIS, it produces an antagonistic effect. The presence of Cu, together with high concentrations of quinones and HULIS, leads to an antagonistic effect on OP (Pietrogrande et al., 2022). Fe shows a synergistic effect on OP when it interacts with quinones and HULIS (Pietrogrande et al., 2022; Yu et al., 2018), potentially due to the generation of  $\bullet\text{OH}$  radicals. According to a study by Yan et al. (2022), it was found that WSOC can form complexes with Cu or Mn, leading to synergistic effects on the generation of ROS. The complex interactions between chemical compositions and their associated OP pose a challenge in establishing a direct correlation between OP and specific chemical species in PM.

#### 2.4 Size distribution of PM chemical compositions

The mechanism of the size distribution of chemical compositions on the surfaces of the particles also plays a role in influencing the OP. One common approach used to study this mechanism involves plotting  $\log(\text{total } C/\text{PM})$  versus  $\log D_p$ , where  $C$  represents the mass concentration of the chemical species,  $\text{PM}$  represents the mass concentration of the ambient particle, and  $D_p$  represents the aerodynamic particle size. This method has been widely used

to investigate how chemical species including PAHs are distributed on the surfaces of ambient particles (Insian et al., 2022; Lv et al., 2016; Ray et al., 2019). When the slope of the regression line is near -1, it indicates adsorption. Conversely, if the slope value is greater than -1, it suggests multilayer adsorption, whereas a slope value less than -1 signifies absorption (Insian et al., 2022). The deposition of chemical species via adsorption is more prevalent on ultrafine and fine particles (Lv et al., 2016). However, multi-layer adsorption occurs when multiple layers of particles are deposited on the surface of ambient particles, particularly on coarse particles (Insian et al., 2022). The presence of multiple layers on particle surfaces increases the surface area available for chemical reactions, resulting in a higher production of ROS. Consequently, multi-layer adsorption can significantly contribute to an elevated OP of coarse particles compared to single-layer adsorption on fine particles. No studies have yet established a link between the size distribution of ambient particles chemical composition and their OP.

## 2.5 Occurrence of PM-induced OP in China and outside China

Extensive research has been conducted globally to investigate the OP induced by water-soluble fractions of ambient particles, with a specific emphasis on PM<sub>2.5</sub> (Cheng et al., 2021; Liu et al., 2020; Xing et al., 2023). The majority of the PM<sub>2.5</sub>-related OP studies were conducted in urban areas of China (Cheng et al., 2021; Liu et al., 2020; Ma et al., 2021; Secrest et al., 2016; Wang et al., 2019). Table 2.1 provides a comprehensive review of field studies conducted to assess the OP of PM. The OP values presented in the table are expressed as volume-normalized (OP<sub>v</sub>, in nmol min<sup>-1</sup> m<sup>-3</sup>) and mass-normalized (OP<sub>m</sub>, in pmol min<sup>-1</sup> μg<sup>-1</sup>) units. The table presents the assays used to assess OP, namely DTT and AA, as well as

a list of the chemical species that may potentially correlate with OP. The literature review indicates that the DTT assay is the most widely used for measuring OPs of PM.

Several studies have indicated that both OP<sub>v</sub> and OP<sub>m</sub> exhibit distinct seasonal variability. In a study conducted by Ma et al. (2021), they found a strong seasonality of DTT-measured OP of PM<sub>2.5</sub> in Nanjing. The study revealed that the highest OP<sub>v</sub> concentration occurred during winter (1.21 nmol min<sup>-1</sup> m<sup>-3</sup>). This was followed by spring (1.17 nmol min<sup>-1</sup> m<sup>-3</sup>), autumn (1.16 nmol min<sup>-1</sup> m<sup>-3</sup>), and summer (1.11 nmol min<sup>-1</sup> m<sup>-3</sup>). Molina et al. (2023) reported the OP<sub>v</sub> induced by water-soluble fraction of PM<sub>2.5</sub> in Santiago, Chile. The highest OP<sub>v</sub> was observed in winter (0.51 nmol min<sup>-1</sup> m<sup>-3</sup>), followed by autumn (0.43 nmol min<sup>-1</sup> m<sup>-3</sup>), spring (0.27 nmol min<sup>-1</sup> m<sup>-3</sup>), and summer (0.23 nmol min<sup>-1</sup> m<sup>-3</sup>). In contrast, Yu et al. (2019) reported a high OP<sub>v</sub> of PM<sub>2.5</sub> during the summer months in Beijing. Moreover, it has been consistently reported that OP<sub>m</sub> is higher during the summer months (Wang, et al., 2020). This increase in OP of PM during summer has been attributed to the generation of OP-active chemicals through photochemical aging processes (Famiyeh et al., 2023; Gao, et al., 2020; Hsiao et al., 2021). The aerosol generated through photochemical aging during summer is more OP active than aerosol that is freshly generated (Hsiao et al., 2021). Photochemical aged aerosols result from the oxidation of volatile and semivolatile organic compounds by oxidants such as •OH and NO<sub>3</sub> radicals, leading to the generation of organic peroxy radicals (RO<sub>2</sub>). These organic peroxy radicals then react with O<sub>3</sub> under intense solar radiation, resulting in the formation of hydroperoxides and organic peroxides. In the presence of sunlight, these compounds further decompose, giving rise to highly reactive

oxygen radicals, which react with VOCs to generate SOAs (Chen et al., 2021). These secondary chemicals, generated through photochemical reactions, exhibit high OP activity.

As shown in Table 2.1, the OP<sub>v</sub> induced by the water-soluble fraction of PM<sub>2.5</sub> varied across different locations. Specifically, Beijing, Wuhan, Inner Mongolia, and Lahore (Pakistan) exhibited higher OP<sub>v</sub> levels compared to Hangzhou, Xi'an, Santiago (Chile), Los Angeles (USA), and Yokohama (Italy). The observed differences in OP<sub>v</sub> can be attributed to variations in source types as well as chemical compositions.

The existing body of research on OP studies has primarily focused on examining OP derived from the water-soluble fraction of ambient particles. However, it is of utmost importance to acknowledge that PM also consist of water-insoluble hydrophobic components. These hydrophobic constituents have the potential to significantly contribute to the increased OP activity of PM. Therefore, it might be beneficial to consider employing alternative extraction solvents, such as methanol, to extract the hydrophobic fractions and investigate their OP levels (Chen et al., 2022). However, it is crucial to emphasize that the methanol extract will contain both hydrophilic and hydrophobic fractions (Verma et al., 2012). Therefore, the OP induced by the water-soluble and methanol-soluble fractions is not mutually exclusive, as both fractions contain hydrophilic chemical species (Famiyeh, Jia, et al., 2023).

Table 2.1 OP induced by water and methanol-soluble fraction of PM<sub>2.5</sub> in DTT and AA assays

Location (site description)	Study period	Dp ( $\mu\text{m}$ )	OPv	OPm	Assays	Extraction	Chemicals associated with OP	Reference
Santiago, Chile (urban)	June 2018- October 2019	$\leq 2.5$	0.38	15.0	DTT	Water	S, K, Fe, Br, As, Zn, Ca <sup>2+</sup> , Mn, Ba, Cu	(Molina et al., 2023)
Bern-Bollwerk, Switzerland (urban traffic)	June 2018- May 2019	$\leq 2.5$	1.10	N/A	DTT	Water	Cu, Zn, Sn, Sb, K <sup>+</sup> , Levogluconan	(Grange et al., 2022)
Changzhou, China (urban)	March- August 2021	$\leq 2.5$	1.00	16.8	DTT	Water	Mn, Cu, Zn, Fe, V, Ni, Ca <sup>2+</sup> , NH <sub>4</sub> <sup>+</sup> , OC, WSOC	(Cui et al., 2023)
Beijing, China (urban)	May 2015- April 2016	$\leq 2.5$	12.3	130.0	DTT	Water	Cr, Fe, Zn, Sb, WSOC	(Yu et al., 2019)
Wuhan, China (urban)	October 2011-July 2012	$\leq 2.5$	6.40	41.5	DTT	Water	EC, OC, NO <sub>3</sub> <sup>-</sup> , SO <sub>4</sub> <sup>2-</sup> , K <sup>+</sup>	(Liu et al., 2020)
Inner Mongolia, China (rural)	September- December 2012	$\leq 2.5$	5.32	15.5	DTT	Water	BC, Ca <sup>2+</sup> , As, NH <sub>4</sub> <sup>+</sup> , Fe, Sb, Ce, Cu, Pb, Sn, Zn, K <sup>+</sup>	(Secrest et al., 2016)
Lahore, Pakistan (urban)	February 2019	$\leq 2.5$	8.90	18.9	DTT	Water	Mg <sup>2+</sup> , Ca <sup>2+</sup> , Na <sup>+</sup> , K <sup>+</sup> , NH <sub>4</sub> <sup>+</sup> , NO <sub>3</sub> <sup>-</sup> , Cu, Fe, Mn, Sr, Mg, Al, Ti, V, OC, EC, WSOC	(Ahmad et al., 2021)
Xi'an, China (urban)	May- December 2017	$\leq 2.5$	0.53	10	DTT	Water	WSOC, SO <sub>2</sub> , NO <sub>2</sub> , EC, K <sup>+</sup>	(Wang et al., 2020)
Shanghai, China (urban)	November 2015-June 2016	0.056- 18	0.07- 0.19	40.0- 60.0	DTT	Water	Quinones, Fe, Mn, Cu, V, Pb, Ni, Co	(Guo et al., 2019)
Hong Kong, China (urban)	September 2011-August 2012	$\leq 2.5$	0.56	20.3	DTT	Water	Fe, Mn, OC, EC, WSOC, HULIS, SO <sub>4</sub> <sup>2-</sup>	(Cheng et al., 2021)

Milan, Italy (Milano Pascal: urban)	January- February 2020	$\leq 2.5$	0.62	13.0	DTT	Water	N/A	(Pietrogrande et al., 2022)
Milan, Italy (Milano Pascal: urban)	January- February 2020	$\leq 2.5$	1.08	29	AA	Water	N/A	(Pietrogrande et al., 2022)
Milan, Italy (Milano Pascal: urban)	January- February 2020	2.5–10	0.65	12	DTT	Water	NH <sub>4</sub> <sup>+</sup> , OC, EC, Levogluconan, Mannosan, Cl <sup>-</sup> , K <sup>+</sup> , Cr, Mn, Fe, Cu, Zn, Pb	(Pietrogrande et al., 2022)
Milan, Italy (Milano Pascal: urban)	January- February 2020	2.5–10	2.08	42	AA	Water	K <sup>+</sup> , Mg <sup>2+</sup> , OC, EC, Cr, Cu, Levogluconan, Mannosan	(Pietrogrande et al., 2022)
Atlanta, USA (urban)	November 2012-August 2013	$\leq 2.5$	0.93	60.0	DTT	Water	WSOC	(Vreeland et al., 2017)
Nanjing, China (urban)	March- December 2016	$\leq 2.5$	1.16	20.0	DTT	Water	V, Mn, Ni, Cu, As, Se, Cd, Ba, Pb, OC, EC, WSOC	(Ma et al., 2021)
Thessaloniki, Greece (urban traffic)	January-July 2013	$\leq 0.49$	1.13	24.5	DTT	Water	EC, NaP, Acy, Ace,	(Argyropoulos et al., 2016)
Shenzhen, China (urban)	November 2020- October 2021	$\leq 2.5$	0.99	30.2	DTT	Water	HULIS, WSOC, OC, Na <sup>+</sup> , Ca <sup>2+</sup> , Mg <sup>2+</sup>	(Xing et al., 2023)
Los Angeles, USA (urban)	September 2019- February 2020	$\leq 2.5$	1.09	61.5	DTT	Water	BC, Ba, Sb, Cd, Ag, Cd, Na <sup>+</sup> , Mg <sup>2+</sup> , V	(Shen et al., 2022)



Yokohama, Italy (Urban)	September 2020-Jun 2021	$\leq 2.5$	0.15	14.9	DTT	Water	K <sup>+</sup> , Mn, Pb, NH <sub>4</sub> <sup>+</sup> , SO <sub>4</sub> <sup>2-</sup> , OC	(Kurihara et al., 2022)
Hangzhou, China (urban)	December 2016- November 2017	$\leq 2.5$	0.62	6.39	DTT	Water	NH <sub>4</sub> <sup>+</sup> , NO <sub>3</sub> <sup>-</sup> , SO <sub>4</sub> <sup>2-</sup> , Ca <sup>2+</sup> , Mg <sup>2+</sup>	(Wang et al., 2019)
Salento's peninsula (suburban)	December 2014- October 2015	$\leq 2.5$	0.24	10.5	DTT	Water	K <sup>+</sup> , NO <sub>3</sub> <sup>-</sup> , Cd, Cu, Fe, Mn, V, OC, EC, POC, SOC	(Perrone et al., 2019)
Salento's peninsula (suburban)	December 2014- October 2015	$\leq 2.5$	0.15	6.5	AA	Water	NO <sub>3</sub> <sup>-</sup> , Ba, Cd, Ce, Cu, Fe, Mn, V, Zn, OC, EC, POC, SOC	(Perrone et al., 2019)
Salento's peninsula (suburban)	December 2014- October 2015	2.5–10	0.23	7.5	DTT	Water	K <sup>+</sup> , NH <sub>4</sub> <sup>+</sup> , Cu, Ba, Cd, Fe, OC, EC, POC,	(Perrone et al., 2019)
Salento's peninsula (suburban)	December 2014- October 2015	2.5–10	0.29	9.0	AA	Water	K <sup>+</sup> , NH <sub>4</sub> <sup>+</sup> , Ca <sup>2+</sup> , NO <sub>3</sub> <sup>-</sup> , SO <sub>4</sub> <sup>2-</sup> , Ba, Cd, Cr, Ni, Cu, Fe, Mn, V, OC, EC,	(Perrone et al., 2019)

OPv: nmol min<sup>-1</sup> m<sup>-3</sup>, OPm: pmol min<sup>-1</sup> μg<sup>-1</sup>, N/A: Not Available, BC: black carbon, SOC: secondary organic carbon, POC: primary organic carbon

The existing literature primarily focuses on 24-hour sampling campaigns when studying OP induced by PM<sub>2.5</sub> chemical compositions, resulting in a lack of understanding regarding its variations during the day and night (Ahmad et al., 2021; Ainur et al., 2023). Gaining a better understanding of these distinctions is crucial to support the development of improved public health policies and provide individuals with enhanced guidance to reduce their exposure to PM<sub>2.5</sub> particles. This present study conducted a comprehensive analysis of OP induced by the water- and methanol-soluble fractions of ambient particles. It employed both the DTT and AA assays, and considers OP variations during the day, and night, and across different seasons. This study compared the OP induced by ultrafine, accumulation, and coarse particles.

#### 2.6 Multiple-path particle dosimetry (MPPD) model

The MPPD model (also called whole lung model) is a mathematical model used to estimate the deposition fraction and doses of ambient particles in different regions of the respiratory system in humans and animals (Manojkumar et al., 2019). The MPPD model can make predictions of the particle deposited in the entire human respiratory system and in three different regions: the extrathoracic (ET), tracheobronchial (TB), and the pulmonary (PL) (Madureira et al., 2020). The model is designed to account for the complex structure of the respiratory tract and how airflow fluctuates during breathing in and out.

The model takes into consideration:

- 1) characteristics of the particles (size, shape, and density);
- 2) aerodynamic behaviors of the particle (inertia impaction, diffusion, and sedimentation);

- 3) anatomical structure (symmetric and asymmetric) of the respiratory tract. The model takes into account: functional residual capacity (FRC), and upper respiratory tract volume (URT) of the respiratory system;
- 4) exposure scenarios (aerosol concentration, exposure time, breathing frequency, tidal volume).

The MPPD model utilizes mathematical equations and computational algorithms to account for the interaction among particle characteristics, aerodynamic behavior, and anatomical factors in order to estimate particle deposition fraction in the ET, TB, and PL regions of the respiratory system (Manojkumar et al., 2019).

The MPDD model operates on the following assumptions:

- 1) ambient particles have a uniform spherical shape, making calculations and analysis easier;
- 2) ambient particles are uniformly distributed throughout the human respiratory system;
- 3) a steady-state condition is assumed, indicating that particle concentrations and other parameters remain constant as they pass through the respiratory system over time;
- 4) ambient particle interactions, including agglomeration or coagulation, are considered to be negligible and have no significant impact on particle behavior.

The accuracy of the results obtained from this model relies on the relevance of these assumptions (Ginsberg et al., 2007; Kuempel et al., 2015) for the particular system being examined. Furthermore, when comparing the MPDD model to other models such as the International Commission on Radiological Protection (ICRP) and the National Council on Radiation Protection (NCRP), it is worth noting that the MPDD model takes into account

both symmetric and asymmetric structures of the respiratory system (Asgharian, 2019). In contrast, the ICRP and NCRP models only consider the symmetric structure of the respiratory system.

The MPPD model offers several advantages (Hussein et al., 2013; Utembe and Sanabria, 2022). Firstly, it incorporates realistic breathing patterns, allowing for a more accurate representation of inhalation behavior. Secondly, it simulates the complex behavior of inhaled particles, providing a thorough understanding of particle dynamics within the respiratory system. Thirdly, it enables the prediction of region-specific dose, enhancing the evaluation of particle exposure on specific area of the human respiratory tract. Lastly, the model has undergone extensive validation against human data for various exposure scenarios and particle types, further attesting to its reliability and accuracy (Hofmann, 2011).

To validate the results of the MPPD model, several investigations have relied on experimental data from studies conducted by Heyder et al. (1986) and Kim and Fisher (1999), and Schiller et al. (1988). Hofmann (2011) provides extensively review of the validation of the MPPD model in the regional and the entire respiratory tract. The experiment conducted by Heyder et al. (1986) involves inhalation of a mixture of monodispersed aerosols with diameter in the range of 0.005–15  $\mu\text{m}$  through both their nose and mouth. Heyder et al. (1986) monitored the total and regional deposition fraction of the aerosol particles within the respiratory tract.

Both the experimental and modeled deposition fractions of aerosol particles in the human respiratory tract have demonstrated strong agreement, as shown by (Hofmann, 2011). This indicates the robustness of the MPPD model in predicting the deposition fractions and doses

of aerosol particles in the human respiratory tract. In the present study, the MPPD model was used to model the total deposition fraction of aerosol particles. The accuracy of these modeled results was validated by comparing them to the experimental data obtained from Heyder et al. (1986)

## 2.7 Respiratory deposition of ambient particles OP

Multiple research studies have indicated that the ambient particle deposition dose in the human respiratory tract is a more relevant factor to investigate the health-related risks, compared to the ambient concentration (Fang et al., 2019). The deposition dose of the particle is influenced by various factors, including the deposition fraction in different parts of the respiratory system, ambient concentration, and exposure conditions including exposure time, breathing frequency, and tidal volume. More information on how to estimate the deposition dose and related discussions is provided in Section 3.5 and 6.2.2.

The deposition fraction of coarse particles (2.5–10  $\mu\text{m}$ ) in the respiratory tract dominates in the upper airways, specifically in the ET region. Fine particles ( $\leq 2.5 \mu\text{m}$ ) tend to deposit more in both the tracheobronchial (TB) and pulmonary (PL) regions. Ultrafine particles (0.1–0.5  $\mu\text{m}$ ) exhibit a higher deposition fraction in the PL region and are subsequently transported into the bloodstream (Andrade et al., 2021). Elevated levels of oxidative stress in the upper airway, potentially caused by increased levels of ROS resulting from high doses of coarse particles, have a significant impact on the exacerbation of inflammation associated with neurodegenerative and nasal disorders (Fang et al., 2019). On the other hand, oxidative stress in the lower respiratory tract, likely resulting from higher levels of ROS induced by

high doses of smaller particles, contributes to the development of systemic or pulmonary diseases.

The size and surface area of particles have a significant impact on their OP (Fang et al., 2017). Decreasing particle size and increasing surface area facilitate chemical reactions on the particle surfaces to generate OP active chemicals. This, in turn, leads to an elevation of the OP. Moreover, a larger surface area provides more sites for chemical interactions with oxidants, resulting in the production of ROS. Extensive research has been conducted to investigate the effect of particle size on their associated health risk, and divergence findings have been reported. Some studies suggest that smaller-sized PM carries a higher risk to respiratory health due to its ability to penetrate deeper into the respiratory system compared to larger particles (Andrade et al., 2021). On the contrary, it has been suggested that larger particles may lead to higher levels of DNA degradation, hemolysis, and the release of pro-inflammatory cytokines. These particles could have more pronounced inhibitory effects on cell proliferation (Osornio-Vargas et al., 2011). Consequently, these larger particles may potentially contribute to a higher prevalence of respiratory health problems (Deng et al., 2019; Famiyeh et al., 2023). These divergent perspectives underscore the necessity for further research in order to comprehensively understand the precise health risks linked to the various sizes of PM.

## 2.8 Casual link OP and health endpoints

Numerous health endpoints have been linked to OP induced by ambient particles (Bates et al., 2019; Charrier and Anastasio, 2012; Fang et al., 2019; Lyu et al., 2018). For example, previous studies have provided compelling evidence of a strong association between

exposure to OP of PM and various health endpoints that include asthma, congestive heart failure, ischemic health failure, and chronic obstructive pulmonary diseases (COPD) (Bates et al., 2019; Corral et al., 2020). These studies indicate that OP represents a more reliable metric for assessing the health risk of PM exposure than the bulk mass concentration (Andrade et al., 2021; Bates et al., 2019). The generation of oxidative stress resulting from the excessive production of ROS is believed to be the mechanism by which PM induces OP, leading deterioration of human health. This oxidative stress can trigger inflammation and disrupt cellular balance (Delfino et al., 2011).

Table 2.2 Association of OP and respiratory and cardiovascular health endpoints

OP in cellular Assay	Health endpoints	Reference
DTT	FeNO	(Delfino et al., 2013; Janssen et al., 2015; Yang et al., 2016)
DTT	asthma/wheeze	(Fang et al., 2016; Yang et al., 2016)
AA	asthma/wheeze	(Janssen et al., 2015)
DTT	congestive health failure	(Bates et al., 2015; Fang et al., 2016)
DTT	ischemic health failure	(Abrams et al., 2017)
DTT	microvascular function	(Zhang et al., 2016)

According to a comprehensive literature review conducted by Bates et al. (2019), DTT-measured OP has demonstrated a stronger association with various health endpoints compared to other acellular assays. Table 2.2 shows studies reported in the literature that have linked OP measured in both DTT and AA assays to respiratory and cardiovascular diseases. Several biological endpoints such as as fraction of nitric oxide (FeNO), asthma,

and congestive health failure have specifically been found to be associated with DTT-measured OP (Bates et al., 2019; Rao et al., 2020). Yang et al. (2016) conducted a 14-year long-term study to establish the association between OP, measured via the DTT assay, and respiratory health in children. The study revealed a strong correlation between OP and asthma as well as rhinitis among children aged 14. The study also reported a strong association between OP and decline of lung function among children aged 12.

## 2.9 Methods for pollution source apportionment

### 2.9.1 Receptor modeling

Source apportionment methods, such as Positive Matrix Factorization (PMF) (Feng et al., 2022; Zong et al., 2018), Chemical Mass Balance (CMB) (Snyder et al., 2009; Tian et al., 2020), and Principal Component Analysis (PCA) (Campbell et al., 2021; Wang et al., 2015), are valuable for identifying the sources of air pollution (Famiyeh et al., 2021). These methods assist in reducing the complexity of a data set by minimizing the number of variables involved. We plan to use the PMF model to identify the sources of PAHs and PM<sub>2.5</sub> in Ningbo, as it offers advantages over the CMB and PCA models. In recent years, PMF has become a popular choice in studies because of its ability to provide reliable source profiles, allow for analysis of time series source emissions, and not require any prior knowledge of the emission sources of pollutants (Comero et al., 2009; Famiyeh et al., 2021; Liu et al., 2017). The PMF model can directly generate the contributions of each source to the mass concentrations when applied for the source apportionment of air pollutants, including PM<sub>2.5</sub> and PAHs (Feng et al., 2022). The CMB model requires a source profile database and prior knowledge of potential sources of air pollution (Clarke et al., 2012; Yang et al., 2013). The CMB model may generate incorrect source profiles when the chemical



compositions of the emission sources do not match those included in the database (Hopke, 2016). When the chemical compositions of the sources are similar, both the CMB and PCA models can encounter collinearity issues (Famiyeh et al., 2021).

The PMF model assumes that concentrations and sources of both pollutants must be non-negative and additive (Famiyeh et al., 2021; Lang et al., 2015). Although a specific sample size is not mandatory for conducting PMF analysis, it is advisable to increase the sample size to obtain reliable and accurate results. The sample data loaded in PMF model is decomposed into matrices consisting of the source profile and contributions, as represented in equation (2-1) (US-EPA, 2014; Yang et al., 2014). The values of  $X_{ij}$  and  $F_{kj}$  are determined by PMF to find the best fit for the concentration of  $i$ th chemical composition in the  $j$ th sample and the  $k$ th source contribution to the  $j$ th, respectively. Similarly,  $G_{ik}$  represents the concentration of the species of  $k$ th source, while  $E_{ij}$  represents the residual of the  $i$ th chemical composition in the  $j$ th sample. The base model runs generate the objective function ( $Q$ ), with the minimized value determined by the weight least-squares method, as shown in equation (2-2) (Chen et al., 2021). The quality of input data depends on the signal-to-noise ( $S/N$ ) of the PAHs. Species with  $S/N > 2.0$  and  $< 0.2$  are labeled as "strong" and "weak", respectively (Chen et al., 2021).

$$X_{ij} = \sum_{k=1}^p G_{ik} F_{kj} + E_{ij} \quad (2-1)$$

$$Q = \sum_{i=1}^n \sum_{j=1}^m \left[ \frac{X_{ij} - \sum_{k=1}^p G_{ik} F_{kj}}{Unc_{ij}} \right]^2 \quad (2-2)$$

The PMF model addresses the negative constraints by accounting for the uncertainty in the concentration profiles of the pollutants. To determine the uncertainty, equations (2-3) can be applied for chemical compositions with concentrations equal to or less than the method detection limit (MDL) (US-EPA, 2014), while equation (2-4) can be utilized for concentrations exceeding MDL (Zong et al., 2018). The error fraction in concentrations of each chemical species is represented by the coefficient of variation (CV, standard deviation divided by mean) in replicate analysis (Haque et al., 2019).

$$\text{Unc} = \frac{5}{6} \times \text{MDL} \quad (2-3)$$

$$\text{Unc} = \sqrt{(\text{concentration} \times \text{error fraction})^2 + (0.5 \times \text{MDL})^2} \quad (2-4)$$

## 2.9.2 Molecular biomarkers

### 2.9.2.1 Levoglucosan

Levoglucosan (1,6-anhydro- $\beta$ -D-glucopyranos, chemical structure shown in Figure 2-4) is a component of biomass burning emissions that can be employed to trace pollution resulting from such burning (Massimi et al., 2020). The combustion of biomass results in the production of levoglucosan, which has the potential to be transported over extended distances and deposited on the surfaces of ambient particles and other environmental media. Scientists can collect samples from these media and measure the concentration of levoglucosan to determine the extent of biomass burning in the area of interest (Liu et al., 2013). In this way, levoglucosan can be used as a reliable chemical marker for tracing the impact of biomass burning on air quality and the environment (Zdráhal et al., 2002).

Levoglucosan is a more reliable tracer of biomass burning than elemental potassium for several reasons. First, levoglucosan is only produced during biomass burning, whereas

potassium can be present in other sources of PM, such as soil dust, sea spray, and coal combustion (Giannoni et al., 2012; Yu et al., 2018). Moreover, it is worth noting that levoglucosan exhibits higher stability during atmospheric transport in comparison to potassium, as the latter tends to be easily scavenged from the air through both dry and wet deposition processes. Thus, for these reasons, levoglucosan is considered a better tracer for biomass burning compared to elemental potassium.

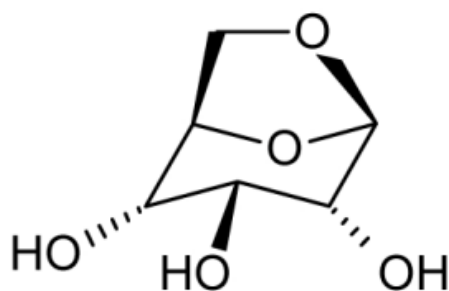


Figure 2-4 Chemical structure of levoglucosan (1,6-anhydro- $\beta$ -D-glucopyranos)

#### 2.9.2.2 Homohopanes

Homohopanes are organic compounds that are formed during the process of diagenesis, which is the transformation of buried organic matter into petroleum (Peters and Moldowan, 1991). Homohopanes are chemically stable compounds that can be used as molecular markers to identify and distinguish between different sources of organic matter. Recent studies have shown that the specific ratios of homohopanes in atmospheric samples can be used to differentiate between emissions from vehicular exhaust and coal combustion (Oros and Simoneit, 2000). This is because the ratios of specific homohopane compounds in vehicular exhaust emissions are significantly different from those in coal combustion emissions. For example, the ratio of C31 to C32 homohopanes is higher in coal combustion

emissions compared to vehicular exhaust emissions. Similarly, the ratio of C29 $\alpha\beta$  to C30 $\alpha\beta$  homohopanes is less than 1 in vehicular exhaust emissions compared to coal combustion emissions, which is greater than 1 (Tian et al., 2021).

The homohopane index was employed in this study to gain insights into the emissions from vehicular exhaust and coal combustion. It is calculated as the ratio of C31 $\alpha\beta$ S (17 $\alpha$ (H),21 $\beta$ (H)-22S-Homohopane) to the sum of C31 $\alpha\beta$ S and C31 $\alpha\beta$ R (17 $\alpha$ (H),21 $\beta$ (H)-22R-Homohopane) isomers (chemical structure of homohopane is shown in Figure 2-5). A higher homohopane index ratio (0.4–0.6) indicates a vehicular exhaust source, while a lower ratio (<0.4) suggests a coal combustion source (Křůmal et al., 2013; Tian et al., 2021; Wang et al., 2009).

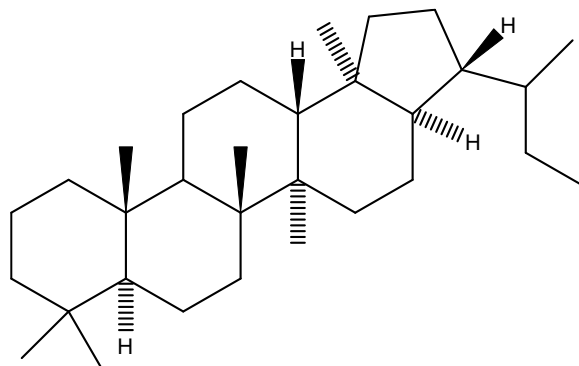


Figure 2-5 Chemical structure of homohopane (17 $\alpha$ (H),21  $\beta$  (H)-22RS-Homohopane)

### 2.9.2.3 PAHs

Certain types of PAHs can serve as source indicators. For example, PAHs, including naphthalene (NaP), fluorene (Flu), fluorene (Flt), pyrene (Pyr), anthracene (Ant), and phenanthrene (Phe), benzo[a]anthracene (BaA), benzo[k]fluoranthene (BkF), benzo[b]fluoranthene (BbF), and benzo[a]pyrene (BaP) are typically released into the atmosphere through combustion of coal and wood (Bai et al., 2020; Fan et al., 2019; Jamhari

et al., 2014). Chrysene (Chr), benzo[a]anthracene (BaA), benzo[a]pyrene (BaP), Pyr, and Flu can be emitted from natural gas combustion (Callén et al., 2014). PAHs containing 3-4 aromatic rings, such as acenaphthylene (Acy), acenaphthene (Ace), and Flu, are indicative of diesel engine emissions. PAHs with 5-6 aromatic rings, including BbF, BkF, benzo[g,h,i]perylene (BghiP), indeno[1,2,3-c,d]pyrene (IPyr), and dibenz[a,h]anthracene (DBahA), serve as tracers for gasoline exhaust engine emissions (Galvão et al., 2023; Wang et al., 2020).

In identifying the sources of PAHs, diagnostic ratios (DRs) such as  $\text{Flt}/(\text{Flt}+\text{Pyr})$ ,  $\text{IcdPyr}/(\text{IcdPyr}+\text{BghiP})$ ,  $\text{BaA}/(\text{BaA}+\text{Chr})$ , and  $\text{Ant}/(\text{Ant}+\text{Phe})$  are still regularly used (Byambaa et al., 2019; Elzein et al., 2019). However, it is important to recognize that these ratios solely provide qualitative source information and are influenced by weather conditions (Bosch et al., 2015). For example, the rate at which PAHs are removed from the atmosphere can alter their concentrations, affecting isomeric ratios in gaseous and particulate phases (Famiyeh et al., 2021). The photochemical reactions occurring between LMW PAHs and atmospheric oxidants, such as the  $\cdot\text{OH}$  radical, have the potential to significantly impact the accuracy and credibility of utilizing this method for PAH source apportionment (Masri et al., 2018; WHO, 2003). These reactions occur at varied rates depending on the individual LMW-PAHs (Tobiszewski and Namieśnik, 2012). Therefore, it is recommended to utilize diagnostic ratios of HMW-PAHs for source apportionment, as they possess greater atmospheric stability (Famiyeh et al., 2021). Specifically, HMW-PAHs like IcdPyr and BghiP are relatively resistant to photochemical degradation. Therefore, the utilization of isomeric ratios of  $\text{IcdPyr}/(\text{IcdPyr}+\text{BghiP})$ , provides a more precise and accurate approach

for identifying the sources of PAHs. As an example, Kubo et al. (2020) employed the diagnostic ratio of  $IcdPyr/(IcdPyr+BghiP)$  for PAH source apportionment during a seven-day continuous field sampling period.

#### 2.10 Source dispersion characteristics and transport to receptor site

Bivariate polar plots (BPPs) can serve as valuable tools for thorough examination and analysis of the geographical origins and dispersion characteristics of the concentration and OP induced by ambient particles. They offer information regarding the contribution of local sources to both PM concentration and the occurrence of OP. Bivariate polar plots can effectively illustrate the dispersion patterns of air pollutants to the receptor site by plotting the pollutant concentration at different wind directions and speeds (Carslaw and Beevers, 2013). This enables the identification of potential sources, spatial distribution, and transport of pollutants (Sooktawee et al., 2020).

The utilization of BPPs, in conjunction with the PMF model, offers a valuable and effective tool for the detailed analysis of air pollution sources (Palmisani et al., 2020). The precise location of the pollutant source, as well as its dispersion and transport to the receptor location, can be determined by applying BPPs to the sources derived from the PMF model (Khuzestani et al., 2018). In this study, the dispersion patterns of  $PM_{2.5}$  and PAH sources obtained from the PMF model were examined using BPPs. Furthermore, BPPs were employed to investigate the dispersion characteristics of OP induced by the water- and methanol-soluble fractions induced by ultrafine, accumulation, and coarse particles.

The analysis of air mass backward trajectories has been extensively studied to identify the long-range transport of pollutants (Huang et al., 2017; Xu et al., 2016). When combined

with fire spot analysis, it provides valuable information on the transport of biomass burning emissions to specific locations. In our study domain, extensive research has been conducted on air mass trajectories and fire spot analysis (Chen, 2022; Chen et al., 2022; Xu et al., 2019). The results consistently indicate the occurrence of regional transport of air pollution to our study domain.

#### 2.11 Lung cancer risk of particulate-bound PAHs

Humans get exposed to PAHs through inhalation, ingestion, and dermal contact (Bai et al., 2020; Idowu et al., 2019). The choice of the PAH exposure pathway for evaluating the cancer risk depends on the medium tainted (Famiyeh et al., 2021). Exposure to airborne PAHs is mainly due to inhalation. In this study, we evaluated the cancer risk posed by particulate-bound PAHs through inhalation (Famiyeh, Xu, et al., 2023). Assessing the cancer risk of airborne PAHs through all three exposure routes may result in an overestimation (Liu et al., 2018).

The estimation of lung cancer risks from PAHs relies on the established effectiveness of the Toxicity Equivalent Factor (TEF) approach, which is a crucial component within the EPA-developed component-based potency factor approach (Mo et al., 2019). The use of TEF to estimate the risk of lung cancer has been extensively utilized (Bai et al., 2020; Iakovides et al., 2019; Ma et al., 2017). Numerous authors have carried out a critical evaluation of the TEF of PAHs, and among all, the one proposed by Nisbet and LaGoy, (1992) is the most widely used for cancer risk assessment. The TEF of each PAH congener is expressed relative to BaP ( $1.0 \text{ ng m}^{-3}$ ). For example, the TEF of Pyr, Chr, and BghiP is 1/1000th, 1/100th,

and  $1/10^{\text{th}}$  of BaP, which shows their carcinogenic potency of 0.001, 0.01, and 0.1, respectively.

The current literature on PAH cancer risk assessment highlights a recurring error in estimating cancer risk (Aquilina and Harrison, 2023). Many studies improperly calculate the risk by multiplying the concentration of BaP<sub>eq</sub> (equivalent concentration of benzo[a]pyrene) by the unit risk ( $8.70 \times 10^{-2}$  per  $\mu\text{g m}^{-3}$ ) recommended by the World Health Organization (WHO) (Zhu et al., 2022). This approach could lead to a significant overestimation of the actual risk. However, the correct procedure, as outlined by the WHO, involves using the concentration of BaP (benzo[a]pyrene) alone as a surrogate for the entire mixture when estimating cancer risk (Aquilina and Harrison, 2023). It is essential to note that the WHO unit risk can only be appropriately applied when BaP serves as a marker for complex mixtures. Conversely, if the approach entails using BaP<sub>eq</sub>, such as in the component-based potency factor approach, the appropriate unit risk ( $6.0 \times 10^{-4}$  per  $\mu\text{g m}^{-3}$ ) recommended by the Environmental Protection Agency (EPA) in their recent report should be utilized (US EPA, 2017). Adhering to these guidelines could improve the accuracy of PAH cancer risk assessments and enhance the validity of the results.

Researchers have primarily concentrated on studying the lung cancer risk associated with only 16 out of the more than hundreds of PAHs present in the air. Highly carcinogenic PAHs like 7H-benzo[c]fluorene and several dibenzopyrene derivatives are not considered in calculating the risk of lung cancer (Iakovides et al., 2021), which could result in an underestimation. Including these PAHs might significantly increase the risk assessment of lung cancer (Famiyeh et al., 2021). Therefore, a wider range of PAHs should be considered



for accurate risk evaluation. In this study, we employed the WHO and EPA unit risk to estimate the lifetime excess cancer risk (LECR) of 16 priority PAHs. LECR describes the increased risk of developing cancer during a person's lifetime as a result of being exposed to PAHs. In this study, we improved the current risk assessment framework by including additional PAHs with high carcinogenic potential. The PAHs investigated are shown in Appendix (Table 8.1)

## 2.12 Source contribution to OP induced by PM<sub>2.5</sub> and lung cancer risk of PAHs

The use of MLR has been widely reported for estimating the contribution of different sources to the OP induced by PM<sub>2.5</sub> (Liu et al., 2018; Ma et al., 2021; Yu et al., 2022). This approach can also be employed to estimate the source contribution to PAH lung cancer risk (Masiol et al., 2012). The mass concentration of the chemical compositions in PM<sub>2.5</sub>, along with their associated uncertainties, can be initially utilized as input variables in the PMF model for source apportionment (as described in Section 2.9.1). A MLR analysis is performed using the dependent variables OP and LECR, and the independent variables consist of the sources derived from the PMF model. The relationships between the contributions of each source and the regression coefficient can be illustrated by Equation (2-5) (Liu et al., 2018).

$$y = \beta_1 X_1 + \beta_2 X_2 + \beta_3 X_3 + \dots + \beta_i X_i \quad (2-5)$$

where  $y = \text{OP (or LECR)}$ ,  $1-i = \text{different emission sources}$ ,  $\beta_1 - \beta_i = \text{regression coefficients}$ ,  $X_1 - X_i = \text{contribution of each source}$

In this study, both the PMF model and MLR were employed jointly to estimate the contribution of various sources to both OP induced by water- and methanol-soluble fractions of PM<sub>2.5</sub>, as well as the lung cancer risk associated with PAHs.

## Chapter 3 Materials and Methods

### 3.1 Study area

The study was conducted in Ningbo, a coastal city located in the eastern region of China. Ningbo is the second-largest city in Zhejiang province, positioned in the southern part of the Yangtze River Delta (YRD) region. Ningbo is well-known for its world-class port, which is one of the busiest in China and serves as a major hub for international trade. The annual cargo capacity of Ningbo-Zhoushan port is about 1.22 billion (Chen et al., 2022). Ningbo is home to approximately eight million people and covers an area of around 10,000 square kilometers.

The climate of the city is hot and humid during summers while cool and dry during winters (Liu et al., 2014; Tang et al., 2015). Ningbo exhibits a sub-tropical monsoon climate with dominant winds blowing from the northwest and southeast during the winter and summer seasons respectively (Chen et al., 2022). Ningbo has an average annual temperature of 18.1 °C with a relative humidity of 73%. The highest temperature is often observed in summer, reaching 28.9 °C, while the lowest temperature is experienced during winter, dropping to 5.35 °C. In winter, the relative humidity often reaches 69%, while in autumn, spring, and summer it reaches 70.6%, 71.9%, and 80.8%, respectively.

The city occasionally experiences episodes of heavy aerosol pollution, particularly during winter. These episodes are attributed to local emissions from commercial, industrial, residential, and rural activities, combined with long-range transport (Chen et al., 2022; Wang et al., 2018). The impact of long-range transport of aerosol pollution at our monitoring

station has been extensively studied (Chen et al., 2022; Xu et al., 2019). According to Xu et al. (2016), during times of severe pollution, aerosols travel from the northern region of China and Inner Mongolia to Ningbo. Chen et al. (2022) indicated that ship emissions from the East China Sea to Ningbo city contribute to aerosol pollution. Furthermore, a study conducted by Chen et al. (2022) revealed that aerosols have the potential to be transported from the northwest, specifically originating from mainland China. Approximately 80% of the air parcels observed were found to pass through Hangzhou Bay, which is situated in the northwest region. These air parcels transport pollutants emitted from biomass burning, thereby exacerbating the air quality. The city is home to various industries situated in its northern region, including photochemical, metallurgical, smelting, dyeing, and power plants. Furthermore, Ningbo boasts over five thousand firms engaged in metal smelting and processing (Chen et al., 2022).

The present study employed BPPs and long-range transport to analyze the dispersion characteristics and pollution transport to our study domain. The study area is classified as an intermediate transition zone that is affected by pollution from both natural and human activities. The selection of our study site was based on its predominantly residential and commercial characteristics, as well as the presence of pollution from various sources including industrial emissions, vehicular exhaust, biomass burning, marine emissions, secondary aerosol formation, and road dust.

In addition, the location of the site is situated 10 kilometers from the Central Business District (CBD) and less than 10 kilometers from the Wangchun industrial zone (WIZ) in the northwest (Chen et al., 2022). It is also 37 kilometers away from the two industrial hubs,

Zhenhai District (ZD) and Beilun District (BD) in the northeast, and 33 and 35 km from Ningbo-Zhoushan port and the East China Sea, respectively. Figure 3-1 illustrates the location of Ningbo ( $29.86^{\circ}$  N,  $121.54^{\circ}$  E) within the Zhejiang province (a), as well as the location of UNNC, Zhenhai District, and Beilun District, and Wangchun industrial zone within Ningbo (b).

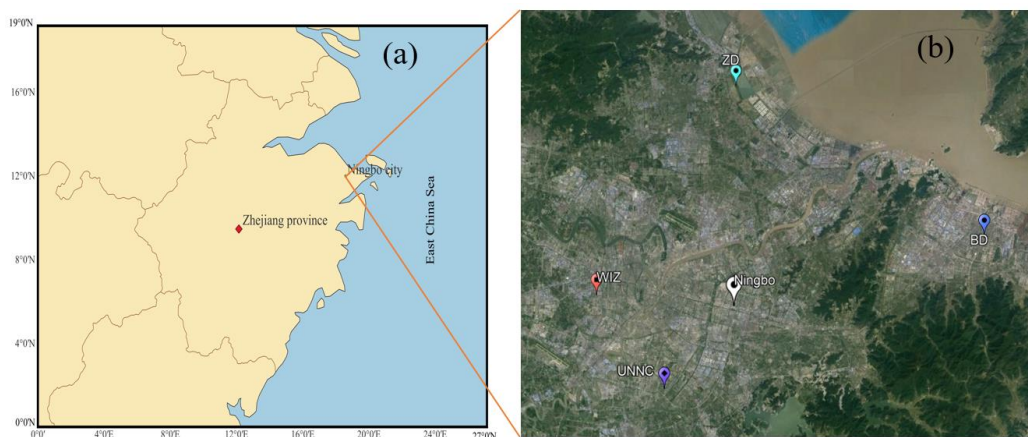


Figure 3-1 Location of the sampling site: (a) Ningbo city in Zhejiang province, (b) UNNC in Ningbo

### 3.2 Aerosol particle sample collection

To monitor aerosol levels, multiple aerosol samplers were set up on top of a four-story building (15 m above the ground) located at the campus of the University of Nottingham Ningbo China (UNNC,  $29.80^{\circ}$  N,  $121.56^{\circ}$  E). To prepare for sampling, the quartz filters were covered with aluminum foil, and prebaked at  $550^{\circ}\text{C}$  for six hours to remove impurities. The filters were then placed in a chamber to equilibrate at a temperature of  $23 \pm 2^{\circ}\text{C}$  and relative humidity of  $30 \pm 6\%$  for 24 hour. Fine particles ( $\leq 2.5 \mu\text{m}$ ) were collected on quartz filters (8×10 inches) using a high-volume aerosol sampler (TH-150C111, Tianhong Instrument Co. Ltd, Wuhan, China). The sampler operated at a flow rate of  $1.05 \text{ m}^3 \text{ min}^{-1}$  for 12 and 24-hour sampling events. Over the course of November 2020 to July 2021, a

sampling campaign was conducted for 12 hours each day and night (6:00 to 18:00 and 18:00 to 6:00, respectively). In each sampling event, 40 samples were collected, with an equal and representative 20 samples taken during both cold and warmer seasons. In addition, 120 samples were taken during the 24-hour integrated sampling campaign between October 2020 and August 2021. Out of these 120 samples, 30 samples were collected in each of the four seasons. On average, samples were collected every three days during each season. Furthermore, out of the 120 samples collected, 80 were gathered on weekdays and 40 were gathered on weekends. For each season, ten field blanks and five laboratory blanks were collected.

To collect both fine particles (FP,  $\leq 2.5 \mu\text{m}$ ) and coarse particles (CP,  $2.5\text{--}10 \mu\text{m}$ ) simultaneously, a universal air sampler (310 UAS<sup>TM</sup>, MSP Corporation, MN, USA) was used. The particles were collected onto quartz filters for 24 hours with a flow rate of  $285 \text{ L min}^{-1}$ . During the field campaign, which spanned from June 2021 to January 2022, a total of 30 fine particles and 30 coarse particles were collected. Specifically, 15 samples of each particle size were obtained during both the summer and winter seasons.

A high impactor aerosol sampler (Model 230, Tisch Environmental Inc., Ohio, USA) was used to collect six different sizes of PM simultaneously. Air was sucked in at a rate of  $1.12 \text{ m}^3 \text{ min}^{-1}$  and collected on quartz filters of dimensions  $5.6 \times 5.4$  inches. In winter, during the time period of January 2021 to February 2, 2021, and in summer, from June 2021 to August 2021, a total of 30 samples of PM of six different sizes were collected. For each PM size range in both winter and summer, 15 samples were collected within 24 hours.

### 3.3 Mass concentration measurement

To measure the masses of the aerosol samples, an electronic balance (Model: AL 104, Mettler Toledo, precision 0.1 mg) was employed. The weight of each sample was determined by taking the difference between the pre-collection weight of the filters and the post-collection weight. Mass concentration was calculated by dividing the sample mass by the corresponding air volume. After collection at the sampling site, the aerosol samples were immediately placed in zip-lock bags, wrapped in aluminum foil, and then transported to the analytical lab. To prevent volatilization, the samples were stored at  $-20^{\circ}\text{C}$  until chemical analysis. Notably, both the sampling site and the analytical lab are located within the same building at the University of Nottingham Ningbo China, minimizing the potential impact of volatile fraction loss during transportation.

### 3.4 Acquisition of meteorological and gaseous pollutants data

Meteorological data, including wind speed and direction, temperature, and relative humidity, were collected from a nearby air quality monitoring station ( $29.83^{\circ}\text{N}$ ,  $121.56^{\circ}\text{E}$ ), located less than 500 meters away from our sampling site ( $29.80^{\circ}\text{N}$ ,  $121.56^{\circ}\text{E}$ ). The concentrations of gaseous pollutants, such as  $\text{SO}_2$ ,  $\text{NO}_2$ , and  $\text{O}_3$  were obtained from the monitoring station. We excluded rainfall data from the analysis because the majority of our sampling was conducted on non-rainy days.

### 3.5 Summary of aerosol sampling and online data collection

Table 3.1 provides a summary of the aerosol sampling conducted in this study, as well as the online data collection from a nearby air monitoring station, which is discussed in Sections 3.2 and 3.4, respectively.

Table 3.1 Summary of aerosol sampling field campaign and online data collection

Sampler	Sampling Period	Sample Size	Purpose
High volume sampler	Oct 2020- Aug 2021	120 <sup>a</sup>	To collect PM <sub>2.5</sub> on pretreated quartz filter in a year-round field campaign during four seasons
High volume sampler	Nov-Dec 2020 Jun-Jul 2021	80 <sup>b</sup>	To collect PM <sub>2.5</sub> on pretreated quartz filter in a field campaign during during the day and at night
Universal Air Sampler	Jun-Aug 2021 Dec 2021-Jan 2022	60 <sup>c</sup>	To collect simultaneously PM <sub>2.5</sub> and PM <sub>10</sub> on pretreated quartz filter in a field campaign
Six-Stage High Volume Cascade Air Sampler	Jan-Feb 2021, Jun-Aug 2021	180 <sup>d</sup>	To collect PM size fractions in ultrafine ( $\leq 0.49$ , $0.49-0.95 \mu\text{m}$ ), fine ( $0.95-1.5$ , $1.5-3 \mu\text{m}$ ) and coarse ( $3-7.2$ , $\geq 7.2 \mu\text{m}$ ) modes
Ningbo Meteorological Bureau (Weather Station)	Online data collection occurred throughout the aerosol sampling period		To record meteorological data (relative humidity, wind speed/direction, temperature) and concentrations of gaseous pollutants (SO <sub>2</sub> , NO <sub>2</sub> , O <sub>3</sub> )

<sup>a</sup> Sampling was conducted approximately for 2-3 months in each season. 1 sample collected in every three days (Autumn: Oct-Dec 2020, Winter: Dec 2020-Mar 2021, Spring: Mar-Jul 2021, Summer: Jul-Aug 2021)

<sup>b</sup> Fourty samples were collected during the day and 40 samples at night (Nov-Dec 2020, Jun-Jul 2021)

<sup>c</sup> Thirty PM<sub>2.5</sub> and 30 PM<sub>10</sub> samples were conducted simultaneously for 4 weeks (Dec-Jan 2021, Jun-Aug 2021)

<sup>d</sup> Thirty samples of each of the six fractionated particle were collected in 4 weeks (Jan-Feb 2021, Jun-Aug 2021)



### 3.6 Chemical analysis

#### 3.6.1 Water-soluble inorganic ions (WSIIs)

A small part of the filter sample ( $3 \times 3 \text{ cm}^3$ ) was chopped into pieces and put in an ultrasonic bath with 20 mL of very clean water ( $18.2 \text{ M } \Omega\text{cm}$ ) for 90 minutes. After that, the solution was filtered using a  $0.45 \text{ } \mu\text{m}$  microporous membrane made of PTFE and kept in a refrigerator at  $4.0 \text{ } ^\circ\text{C}$  until it was examined through WSIIs. Ion Chromatograph (ICS-1600, Dionex, USA) was employed to identify five different anions ( $\text{F}^-$ ,  $\text{Cl}^-$ ,  $\text{NO}_2^-$ ,  $\text{NO}_3^-$ , and  $\text{SO}_4^{2-}$ ) and five cations ( $\text{Na}^+$ ,  $\text{NH}_4^+$ ,  $\text{K}^+$ ,  $\text{Mg}^{2+}$ , and  $\text{Ca}^{2+}$ ). The Ion Chromatograph included several components, such as an Autosampler (Dionex AS-DV), an Analytical column (Dionex, IonPac™ AS23 for anions, IonPac™ CS12A for cations,  $4 \times 250 \text{ mm}$ ), a Guard column (Dionex, IonPac™ AG23 for anions, IonPac™ CG12A for cations,  $4 \times 50 \text{ mm}$ ), and a self-regenerating Suppressor (Dionex, ASRSTM 300 for anions, Dionex, CSRSTM 300 for cations). The anions were detected using a constant eluent ( $4.5 \text{ mM Na}_2\text{CO}_3 + 0.8 \text{ mM NaHCO}_3$ ) at a flow rate of  $1 \text{ mL min}^{-1}$ , and the applied current of suppressor was  $25 \text{ mA}$ . The cations were tested using  $20 \text{ mM}$  Methanesulfonic acid (MSA) as an eluent at a flow rate of  $1 \text{ mL min}^{-1}$ , and the applied current was  $59 \text{ mA}$ .

Five blank filters spiked with  $200 \text{ } \mu\text{L}$  of  $200 \text{ ppb}$  of WSII were allowed to dry in a fumehood for four hours, then extracted and analyzed WSIIs to determine their recovery, which ranged from  $85.8$  to  $107.3\%$ . Five replicate analysis of WSIIs resulted in a precision  $<3\%$ . The method detection limit of WSIIs (MDL, three times the standard deviation of the blank). The MDLs of  $\text{F}^-$ ,  $\text{Cl}^-$ ,  $\text{NO}_2^-$ ,  $\text{NO}_3^-$ ,  $\text{SO}_4^{2-}$ ,  $\text{Na}^+$ ,  $\text{K}^+$ ,  $\text{Mg}^{2+}$ ,  $\text{Ca}^{2+}$ , and  $\text{NH}_4^+$  were  $0.05$ ,  $0.09$ ,  $0.04$ ,  $0.11$ ,  $0.09$ ,  $0.03$ ,  $0.012$ ,  $0.01$ ,  $0.02$ , and  $0.05 \text{ } \mu\text{g m}^{-3}$ , respectively. Finally, the

concentrations of the WSIs in the filter sample were calculated based on the calibration curve ( $r^2 \geq 0.98$ ) of the authentic standards of WSIs. The concentration of the field blank filters was subtracted from the sample filters.

### 3.6.2 Water-soluble trace metals (WSTMs)

The small filter with a size of  $3 \times 3 \text{ cm}^2$  was cut and submerged in a bath of 20 ml ultrapure water which was extracted at  $25 \text{ }^\circ\text{C}$  for 1-hour using ultrasonicator. The extracts were subjected to filtration using a microporous membrane made of  $0.45 \text{ }\mu\text{m}$  PTFE, and then kept at  $4 \text{ }^\circ\text{C}$  until the analysis of trace metals soluble in water was performed. Nitric acid ( $\text{HNO}_3$ , 2% w/v) was added to the extracts to make them acidic, and using ICP-MS (NexION<sup>TM</sup>300X), the concentration of eighteen water-soluble trace metals (Cu, Mn, Fe, Co, Ni, Cd, Zn, Ba, Cr, Al, As, Pb, V, Ag, Bi, Ce, Sr, and Sb) was quantified. The precision of the replicate analysis was  $<5\%$  and the MDL of WSIs was less than  $0.04 \text{ }\mu\text{g m}^{-3}$ .

### 3.6.3 Water-soluble organic carbon (WSOC)

To conduct WSOC analysis, a small filter sample ( $3 \times 3 \text{ cm}^2$ ) was taken and soaked in ultrapure water and extracted for 45 minutes at  $25 \text{ }^\circ\text{C}$  in an ultrasonic bath. The sample was then filtered using a  $0.45 \text{ }\mu\text{m}$  PTFE microporous membrane and stored at  $4 \text{ }^\circ\text{C}$  until further analysis. The WSOC in the extracts was analyzed using a Vario TOC analyzer (Vario TOC Cube, Elementar, Germany). The precision of the replicate analysis was  $< 3.5\%$ , and the MDL recorded was  $0.03 \text{ }\mu\text{g m}^{-3}$ .

### 3.6.4 Levoglucosan

The method used by Xu et al. (2018) was followed to extract and analyze the sample filters for biomass burning tracers. In short, the sample filters ( $3 \times 3 \text{ cm}^2$ ) were extracted with

4 ml of ultrapure water in an ultrasonic bath for 45 min at 25 °C. The extracts were then filtered using 0.45 µm PTFE syringe filters to eliminate insoluble contaminations and preserved at 4.0 °C. A High-Performance Liquid Chromatograph-Mass Spectrometry/Mass Spectrometry (HPLC-MS/MS) (Shimadzu 30A- ABSciex 3200 Q trap) that was equipped with Electrospray Ionization (ESI), an anion-exchange analytical column (Dionex, Carbopac MA1, 250 mm 4 mm), and a guard column (Dionex, Carbopac MA1, 50 mm 4 mm) was utilized to analyze levoglucosan (levo) in aerosol particles. The MDL of levoglucosan was 0.04 µg m<sup>-3</sup>. The precision of the replicate analysis was determined to be less than 5%.

### 3.6.5 Polycyclic aromatic hydrocarbons and homohopanes

A small part of the sample filter was cut to extract PAH and hopanes via accelerated solvent extraction method by using a blend of hexane and dichloromethane (1:1, v/v). The extracts were then concentrated to 1 ml using a rotatory evaporator (Biotage TurboVap II). The analysis was conducted for 20 PAHs (Naphthalene (Nap), Acenaphthylene (Acy), Acenaphthene (Ace), Fluorene (Flu), Phenanthrene (Phe), Anthracene (Ant), Fluoranthene (Flt), 7H-benzo [c]fluorene (7H-BcF), Pyrene (Pyr), Benzo [a]anthracene (BaA), Chrysene (Chr), Benzo [b]fluoranthene (BbF), Benzo [k]fluoranthene (BkF), Benzo [a]pyrene (BaP), indeno [1,2,3-cd]pyrene (InPyr), Dibenzo [a, h]anthracene (DBahA), and Benzo [g, h, i]pyrene (BghiP), Dibenzo [a, h]pyrene (DBahPyr), Dibenzo [a, l] pyrene (DBalPyr), Dibenzo [a,e]pyrene (DBaePyr)) and homohopanes (C31αβS and C31αβR) using a gas chromatography-mass selector detector (Agilent 7890B and 5977A respectively). The samples obtained from the filters and the standard PAH were enriched with d<sub>10</sub>-pyrene and d<sub>10</sub>-phenanthrene. The capillary column (HP-5MS, 0.25 µm×30 m × 0.25 mm) helped in the

separation of PAHs with a flow rate of  $1 \text{ mL min}^{-1}$  using helium gas as a carrier gas. After injecting samples of  $1 \mu\text{L}$  into the column in splitless mode, the temperature was set to  $290^\circ\text{C}$ . Then, a temperature program was followed, starting at  $80^\circ\text{C}$  for 1 min and increasing to  $240^\circ\text{C}$  at a rate of  $10^\circ\text{C min}^{-1}$ . It was then held for 10 mins, following which the temperature was increased to  $300^\circ\text{C}$  at a rate of  $5^\circ\text{C min}^{-1}$  and held for 2 mins. Selected ion monitoring (SIM) mode was used to monitor the parent and daughter ions. The identification of PAHs was based on  $m/z$  and retention time and their quantification through internal calibration of authentic standards.

For the purpose of quality control and assurance, the field blanks were analyzed in the same way as the PAHs in  $\text{PM}_{2.5}$  samples. The laboratory blank filters, which were spiked with a  $20 \mu\text{L}$  mixed standard solution containing 20 PAHs, were analyzed. The field blanks were analyzed in the same way as the  $\text{PM}_{2.5}$  samples for PAHs. The laboratory blank filters, spiked with a  $20 \mu\text{L}$  mixed standard solution containing 20 PAHs, were also analyzed. To correct for potential background contamination in the field, the results from the field samples were adjusted by subtracting the values obtained from the field blank samples. The recovery rates of all 20 PAHs were determined by analyzing the laboratory blank samples, which varied from 87.3% for Ant and BkF to 105.8%. These recovery rates are within the acceptable range (85-115%) established by the Association of Analytical Communities (AOAC) (He and Balasubramanian, 2009). The limit of detection (LOD) was determined as thrice the mean standard deviation of the blank sample values, which varied between 0.001 and  $0.009 \text{ ng m}^{-3}$ . To account for potential variations or changes in the instrument response,

internal standards (d<sub>10</sub>-pyrene and d<sub>10</sub>-phenanthrene) were introduced to both the PAH standards and samples.

Table 3.2 Categorizing ions for 20 PAHs and homohopanes for selected ion monitoring (SIM)

Time interval min	Ion Group	Number of Ions	Reference (m/z)	Ions	Targetted PAHs
3.8	Group 1	1	128		NaP
7.2	Group 2	3	152; 153; 166;		Ace, Acy, Flu
9.5	Group 3	2	176; 178;		Phe, Ant
12.2	Group 4	2	200; 202;		Flt, Pyr
15.5	Group 5	4	216, 226; 228; 234;		7H-BcF, BaA, Chr
18.5	Group 6	2	250; 252;		BbF, BkF, BaP
22.5	Group 7	2	276; 278;		IPyr, DBahA BghiP
30.4	Group 8	3	302		DBahPyr, DBalPyr, DBaePyr
35.7	Group 9	2	426		C31αβS, C31αβR

### 3.6.6 Quinones

The process of extracting and analyzing quinones was carried out using the method previously published by Chen et al. (2021). To summarize, filter samples (8×8 cm<sup>2</sup>) were cut and soaked in a mixture of pure dichloromethane and methanol (1:1 v/v) in an ultrasonic bath for 90 minutes at 25 °C. The extracted solution was then filtered through a 0.2 μm PTFE syringe filter and concentrated to about 1 ml under a gentle flow of nitrogen gas at 35 °C using a rotatory evaporator (Biotage TurboVap II). The extracted residues and standards dissolved in methanol (1 ml) were subsequently heated in air at 65 °C for 27 hours for derivatization.

The presence of quinones (1, 2-naphthoquinone (1, 2-NQ), 1,4-naphthoquinone (1, 4-NQ), 1, 4-anthraquinone (1, 4-AQ) in the samples was measured using a Shimadzu 30A high-performance liquid chromatograph (HPLC) tandem mass spectrometer (MS/MS) equipped with electrospray ionization (ESI). The LC system used consisted of a binary pump, an auto-sampler and a separation column (Agilent Zorbax Eclipse Plus C18 Column, 50×2.1mm i.d., 1.8µm), and the mobile phase consisted of 30% methanol (A) and 70% ammonium acetate (5 mmol/L) and formic acid (0.1%) in deionized water (B). The gradient was initially at 30% A followed by a linear gradient to 90% A in 3 minutes, an isocratic elution for 2.5 minutes, and then 30% A for 0.5 minutes. The tandem MS was utilized for analysis with multiple reaction monitoring (MRM), where the ionization mode used was positive.

The study focused on examining specific quinone derivatives such as 1, 2-NQ, 1, 4-NQ, and 1, 4-AQ, and the optimized parameters of the ionization source can be found in Table 3.3. The quinones in field blanks were subtracted from the that in field samples. Blanks filters were spiked with these three quinones and analyzed the same way as the sample to check for the recovery, which were in the range of 88.4 to 102.1%.

Table 3.3 The experimental conditions for the MRM applied in the HPLC-MS/MS analysis of aquinone derivatives

Quinone	Quinone Derivative	Parent Ion	Product Ion	De-clustering Potential (DP)	EP	Collison Entrance Potential (CEP)	Cell Collision Energy (CE)	Collision Cell Exit Potential (CXP)
				V	V	V	V	V
1, 2-NQ	1, 2-NQ-OCH <sub>3</sub>	189*	77*	55.4	8.8	16.144	45.6	2.3
		189	161	55.4	8.8	16.144	45.6	2.3
1, 4-NQ	1, 4-NQ-OCH <sub>3</sub>	189	77	55.0	8.8	16.144	45.6	2.3
		189	161	55.0	8.8	16.144	45.6	2.3
1, 4-AQ	1, 4-AQ-OCH <sub>3</sub>	239	211	55.0	8.8	18.203	45.6	2.3
		239	127	55.0	8.8	18.203	45.6	2.3

\* The labelled ion pairs were selected for quantifying the compound.

### 3.7 Oxidative potential

#### 3.7.1 Extraction and pre-treatment

A small part of the sample and blank filters ( $3 \times 3 \text{ cm}^2$ ) was cut and then exposed to ultrasonic treatment with 20 ml of water and methanol at 25 °C for 55 minutes. To prepare the water and methanol extracts for OP analysis, they were filtered through 0.45  $\mu\text{m}$  PTFE syringe filter. The methanol extract was reduced to approximately 1 ml using a Biotage TurboVap II rotatory evaporator by blowing with nitrogen at 35 °C. The final extract was then and reconstituted with methanol and stored at 4 °C until OP measurement.

#### 3.7.2 OP measurement

The concentration of OP in each sample was determined using DTT and AA tests following the procedures outlined by Wang et al. (2019) and Pietrogrande et al. (2018), respectively. The OP via DTT method was measured by adding 1.0 ml of PM extract (positive controls: Cu) to a Chelex<sup>TM</sup> 100 treated 0.1 M phosphate buffer solution (pH = 7.4, 4.5 ml) in an amber vial and incubating at 37 °C for 10 minutes. Next, 1.0 mM DTT assay (0.5 ml) was added and allowed to react for a specific period (10, 15, 20, 30, 35 min). After that, the reaction mixture (0.5 ml) was transferred to a clean centrifuged vial and mixed with 10% w/v TCA solution (0.5 ml) to stop the reaction. Then, DTNB (10.0 mM, 50  $\mu\text{l}$ ) was added to the reaction mixture and allowed to react with the excess DTT for 5 minutes. The final product, TNB, was formed by adding TE-buffer (2.0 ml). To measure the absorbance of TNB, the solution was analyzed using a UV/VIS double beam spectrophotometer (4802, Unico Instrument Co., Ltd, Shanghai) at a wavelength of 412 nm. The OP value was calculated using equation (3-1) (Cheng et al., 2021; Famiyeh et al., 2023;



Lin and Yu, 2011; Yu et al., 2022). The OP of the samples were then corrected with the OP of the blank filters ( $<0.5 \mu\text{M min}^{-1}$ ).

$$OP^{DTT} = \frac{A_o - A}{A_o \times t} DTT_o \quad (3-1)$$

where  $OP^{DTT}$  = consumption rate of DTTT ( $\mu\text{M min}^{-1}$ ),  $A_o$  = absorbance of the blank (i.e., without sample),  $A$  = absorbance of DTT + sample,  $t$  = reaction time (min),  $DTT_o$  = initial DTT concentration ( $\mu\text{M}$ ).

In order to determine the OP via AA method, the final sample extract (1.0 ml) (positive controls: phenanthrenequinone (PQ) in a phosphate buffer solution (0.1 M, pH = 7.4, Chelex<sup>TM</sup> 100 treated, 4.5 ml) was mixed with ascorbic acid (1.0 mM, 0.5 ml) and then left to mix for five minutes. The absorbance of ascorbate was then measured at 265 nm ( $\epsilon = 14,500 \text{ M}^{-1}\text{cm}^{-1}$  at pH = 7.4) using a UV/VIS double beam spectrophotometer (4802, Unico Instrument Co., Ltd., Shanghai) at time intervals of 0, 5, 10, 15, and 20 min. The OP was calculated by determining the slope of the linear plot of the blank corrected absorbance of the sample extract against the reaction time. The  $r^2$  value obtained from the linear plot was  $\geq 0.95$ , indicating an excellent linear AA consumption rate. The extrinsic and intrinsic OP were obtained by dividing the measured DTT and AA loss rate by the air volume and PM mass, respectively. Throughout the thesis, the extrinsic OP in the DTT and AA assays is represented as DTTv and AA<sub>v</sub>, respectively. Conversely, the intrinsic OP is represented as DTTm and AA<sub>m</sub>, respectively.

### 3.8 MPPD model

To predict the doses and OP deposition in human lungs, we first employed the Multiple-Path Particle Dosimetry Model (MPPD, v. 3.04) to predict the deposition fraction (DF) of the particles in the ET, TB, and PL regions. The OP deposition was calculated by multiplying the particle deposition fraction by the extrinsic OP frequency (shown in equation (3-2), as defined in Andrade et al. (2021) and Fang et al. (2017)). The approach used to estimate the deposition of OP in the human respiratory system was employed in our recent study (Famiyeh, Jia, et al., 2023).

The geometric standard deviation (GSD) of PM size fractions in accumulation ( $\leq 0.49$ ,  $0.49-0.95$ ,  $0.95-1.5$ ,  $1.5-3.0 \mu\text{m}$ ) and coarse ( $3-7.2$  and  $\geq 7.2 \mu\text{m}$ ) particles were greater than or equal to  $1.05 \mu\text{g m}^{-3}$ , indicating that they are polydisperse.

$$\text{OP deposition} = \text{Deposition fraction} \times \frac{\text{OP per m}^3}{\text{total OP per m}^3} \quad (3-2)$$

The deposition dose of the particles of varying size ranges was estimated according to equation (3-3). The doses in the respiratory system can depend on either the concentration of particles present in the air or the efficiency of their deposition, or both for the same age group. The present study used the same parameters as a study conducted in Beijing, China (Li et al., 2016) to determine the amount of inhaled particles in the lungs of adults. These parameters include a functional residual capacity (FRC, ml) of 2,950, upper respiratory tract volume (URT, ml) of 44.7, breathing frequency (BF, breath  $\text{min}^{-1}$ ) of 16, and tidal volume (TV, ml) of 537.5. Because the PM levels were lower in Ningbo compared to Shanghai and Beijing, the present study employed slightly lower effective particle density of  $1.13 \text{ g cm}^{-3}$  and  $1.36 \text{ g cm}^{-3}$  for accumulation and coarse mode particles (Li et al., 2016; Yin et al., 2015).

In the MPPD model, we considered a constant value for TV, BF, and ET. Hence, the key factors that determine the lung deposition dose for individuals of the same age group are the particle deposition efficiency and the concentration in the ambient air. The exposure time used in the MPPD is based on data provided in the Chinese Exposure Handbook (Duan et al., 2015), that recommends an average ET value of 221 minutes per day for adult population in China.

$$\text{Dose (D, } \mu\text{g day}^{-1}\text{)} = \text{DF} \times \text{C} \times \text{TV} \times \text{BF} \times \text{ET} \quad (3-3)$$

where DF, C, TV, BF, and ET are variables that represent the deposition fraction, concentration of the particle in ambient air, tidal volume, breathing frequency, and exposure time, respectively.

### 3.9 Source apportionment techniques

#### 3.9.1 Positive Matrix Factorization model

The PMF model was utilized in this study to determine the sources of PAHs and PM<sub>2.5</sub> in a year-round field campaign. In the study of PM<sub>2.5</sub> source apportionment, samples collected both during the daytime and at night were also taken into consideration. The PMF model requires two datasets - one for the concentration of the chemical species and another for their uncertainty. The dataset for the source apportionment of PAHs comprised the concentrations of 20 specific PAH congeners (Nap, Acy, Ace, Flu, Phe, Ant, Flt, 7H-BcF, Pyr, BaA, Chr, BbF, BkF, BaP, InPyr, DBahA, BghiP, DBahPyr, DBalPyr, DBaePyr). For PM<sub>2.5</sub> source apportionment, the dataset consisted of concentrations of F<sup>-</sup>, Cl<sup>-</sup>, NO<sub>3</sub><sup>-</sup>, SO<sub>4</sub><sup>2-</sup>, Na<sup>+</sup>, K<sup>+</sup>, Mg<sup>2+</sup>, Ca<sup>2+</sup>, NH<sub>4</sub><sup>+</sup>, Cu, Mn, Fe, Co, Ni, Cd, Zn, Ba, Cr, As, Pb, V, Ag, Bi, Ce, Sr, Sb, WSOC, Levoglucosan, PAHs, and quinones. The uncertainties of these chemical species

were calculated using the procedure outlined in Section 2.9.1, and also in our recent review publication (Famiyeh et al., 2021).

The selection of the number of factors derived from the PMF model was based on prioritizing the analysis with strong bootstrap mappings and avoiding any instances of unmapped bootstrap results. We performed PMF analysis using a range of factors, varying from two to eight. After examining the bootstrap summary, we were able to determine the optimal factors for source apportionment of PAHs and PM<sub>2.5</sub>. Further information on the selection of the number of factors has been provided in Sections 4.2.5.2 and 5.2.4.9 for source apportionment of PAHs and PM<sub>2.5</sub>, respectively.

### 3.9.2 Bivariate polar plots, air mass backward trajectories, and fire spot

In this study, BPPs were used to analyze the day and night variations, as well as seasonal changes, in the geographical origins, dispersion characteristics, and identification of local sources contributing to OP of ambient particles. The plots shows the trends in the variation of concentration of OP relative to wind speed and wind direction. In this study, the BPPs were generated using R statistical software and the openair package ([www.openair-project.org](http://www.openair-project.org)). The detailed description of BPPs can be found elsewhere (Carslaw & Bevers, 2013).

The air mass trajectories and fire spot analysis presented in this thesis were obtained from our recent study conducted at the same sampling domain (Chen et al., 2022). Briefly, the air masses were traced back 48 hours to assess their trajectories. These trajectories arrived at the sampling site every 6 hours throughout the entire sampling period, at an altitude of 500

meters above ground level. The fire spot data were obtained from the MODIS Collection 6 FIRMS Fire Archive data (<https://firms.modaps.eosdis.nasa.gov/download/>).

### 3.10 Statistical analysis

To compare the mean concentrations of chemical compositions and OP between daytime and nighttime, as well as between PM<sub>2.5</sub> and PM<sub>10</sub>, we performed a z-test. Furthermore, we compared the mean values across four seasons using an analysis of variance (ANOVA). These statistical analyses were conducted with a significance level set at  $p = 0.05$ . A Pearson correlation analysis was conducted to identify potential chemical species that can induce OP. The significance level for the correlation coefficient ( $r$ ) was set at  $p = 0.05$  and  $0.01$  to determine the statistically significant  $r$  values.

The MLR analysis was conducted to estimate the contributions of the various sources to LECR of PAHs and OP induced by PM<sub>2.5</sub>. The MLR was conducted using origin software (OriginLab Corporation, 2019). In MLR analysis, the sources derived from the PMF model were considered as independent variables, while the LECR and OP were considered as dependent variables. The sources with  $p$ -values greater than  $0.05$  were ignored in the MLR analysis. The source contribution to OP was determined by multiplying the absolute value of the standardized regression coefficient and OP, a method that has been employed in various studies (Liu et al., 2018; Ma et al., 2021; Wang et al., 2020).

## **Chapter 4 Particulate-Bound Polycyclic Aromatic Hydrocarbons: Diurnal and Seasonal Variations, Size Distribution, Source Apportionment, and Lung Cancer Risk**

### **4.1. Introduction**

The presence of PAHs in airborne particles can have harmful impacts on human health, including mutagenic and carcinogenic effects (Abdel-Shafy and Mansour, 2016). For example, about 1.6% of the documented lung cancer cases in China have been attributed to human exposure to PAHs (Wang et al., 2018; Zhang et al., 2009). In addition to that, multiple studies have provided evidence of a substantial link between the exposure to PAHs and a heightened likelihood of developing lung cancer (Zhang et al., 2019; Zhou et al., 2021). Therefore, effective collaboration among researchers, local, and regional authorities is crucial for developing methods to reduce both PAH exposure and the risk of developing lung cancer.

There are hundreds of PAHs present in the ambient environment, primarily emitted from vehicle exhaust, industrial processes, coal combustion, the burning of natural gas, and biomass burning (Famiyeh et al., 2021; Li et al., 2021). Nevertheless, researchers have primarily directed their attention towards the 16 priority PAHs due to their established toxicity, elevated concentrations, extended lifespan, and increased likelihood of exposure among the general population (Mo et al., 2019; Wang et al., 2020; Yadav et al., 2020). Within this group of priority PAHs, the biomarker most commonly utilized to assess PAH exposure is benzo[a]pyrene, which is known for its high cancer risk. Nonetheless, other

PAHs, such as 7H-benzo[c]fluorene and various dibenzopyrene derivatives (e.g., dibenzo [a, h]pyrene, dibenzo [a, l] pyrene, and dibenzo [a,e]pyrene), which exhibit even greater carcinogenic potential, have been predominantly excluded from assessments of lung cancer risk (Iakovides et al., 2021). Even though the ambient concentrations of these PAHs may be low, they can still pose a higher risk of lung cancer than BaP. Recent research conducted by Iakovides et al. (2021) has revealed that including these highly carcinogenic PAHs in the risk assessment model can lead to a significant increase in the risk of lung cancer. Therefore, it is essential for researchers to incorporate a wider range of PAHs into the framework of health risk assessment.

PAHs are found in both particulate and vapor phases, and their concentrations can vary throughout the day and across seasons, influenced by sources and meteorological conditions. However, the vapor phase predominantly contains low molecular weight PAHs (LMW-PAHs), which are generally less carcinogenic, with the exception of naphthalene (Famiyeh et al., 2021). In contrast, the particulate phase is composed of high molecular weight PAHs (HMW-PAHs) that carry a higher cancer risk. Furthermore, LMW-PAHs have reduced lipophilicity, which facilitates their absorption into the lower respiratory system and subsequent elimination from the body (Famiyeh et al., 2021). However, HMW-PAHs possess high lipophilicity, leading to their prolonged retention in the body (Ewing et al., 2006; Famiyeh et al., 2021). It is important to note that the presence of carcinogenic LMW-PAHs in the vapor phase may potentially lead to a slight underestimation of the actual risk levels when assessing lung cancer risk solely based on the particulate phase (Famiyeh et al., 2021).

An error commonly found in the literature is the incorrect estimation of cancer risk by multiplying the concentration of BaP-toxicity equivalent (BaP<sub>eq</sub>) with the unit risk ( $8.7 \times 10^{-2}$  per  $\mu\text{g m}^{-3}$ ) suggested by the World Health Organization (WHO) (Callén et al., 2014; Duan et al., 2023; Hong et al., 2016; Pongpiachan et al., 2015). This approach often leads to a significant overestimation of the risk. The proper method, according to the WHO, is to use the concentration of BaP alone as a surrogate for the entire mixture when estimating cancer risk. It is important to note that the WHO unit risk can only be applied when BaP is representative of complex mixtures (Aquilina and Harrison, 2023). However, if the component-based potency factor approach is utilized, specifically by considering BaP<sub>eq</sub> (equivalent concentration of benzo[a]pyrene), it is recommended to use the unit risk value ( $6.0 \times 10^{-4}$  per  $\mu\text{g m}^{-3}$ ) as recommended by the EPA in their recent report (US EPA, 2017).

The aim of this study was to improve the current method of assessing the risk of lung cancer caused by PAHs. This was achieved by incorporating highly carcinogenic PAHs into the assessment process. Furthermore, the study aimed to compare the risk assessment approaches adopted by the WHO and the EPA. This comparison aimed to identify the strengths and weaknesses of each approach, with the ultimate aim of advancing and refining PAH lung cancer risk assessment methodologies. Identifying potential sources of PAHs and accurately estimating the risk of lung cancer could provide valuable information for developing more effective control strategies to reduce the risk of lung cancer associated with PAHs. The methods utilized in this study possess substantial potential for evaluating the adverse impacts of PAH exposure across diverse urban areas, encompassing a wide range of highly carcinogenic PAHs.



The specific objectives were as follows:

- 1) comparing PAH concentrations during daytime, nighttime, and across seasons;
- 2) identifying PAH sources through the use of source apportionment methods such as diagnostic ratio and PMF model;
- 3) investigating source dispersion characteristic of PAHs derived from PMF model in our study domain;
- 4) evaluating the lifetime excess cancer risk (LECR) associated with PAH exposure using the unit risk values recommended by the WHO) and EPA;
- 5) comparing the LECR associated with exposure to 16 priority PAHs versus 20 PAHs, including four PAHs with a high cancer risk.
- 6) estimation of the contributions of different sources to the LECR associated with PAHs

## **4.2. Results and discussions**

### **4.2.1. Day and night concentrations of PAHs**

The results depicted in Table 4.1 showcase the concentrations of 20 PAHs (16 priority PAHs and 4 HMW-PAHs (7H-BcF, DBahPyr, DBalPy, and DBaePyr) during daytime and at night. The comparison of the mean concentrations of individual PAHs was achieved through paired z-statistics, with a significance level of  $p = 0.05$ . This study found that the concentration of most PAHs varied significantly between day and night ( $p \leq 0.05$ ), except for Chr, IPyr, 7H-BcF, and DBalPyr ( $p > 0.05$ ). There was no significant difference in the total concentration of 20 PAH between daytime and nighttime. However, the concentration during the day was slightly higher, which can be attributed to increased human activities.

The total concentration of the six LMW-PAHs exhibited significant variability ( $p \leq 0.05$ ) between day and night and were found to be more concentrated in  $PM_{2.5}$  during the day. This is supported by a higher day/night ratio of 3.59. It was observed that the proportion of LMW-PAHs to the total PAH concentration was much higher during the day (23.5%) than at night (7.44%). The high levels of low LMW-PAHs observed during the daytime can be partially attributed to the volatilization of unburnt fuel under high temperature and solar radiation conditions. For instance, the concentration of NaP significantly increased during the day ( $0.67 \pm 0.54 \text{ ng m}^{-3}$ ) compared to nighttime levels ( $0.15 \pm 0.08 \text{ ng m}^{-3}$ ), possibly due to volatilization from petroleum products (Galvão et al., 2023). Evaporation of petroleum product at gas filling station could potential increase the level of NaP during the daytime (Galvão et al., 2023). Additionally, NaP has been identified as a significant component of crude oil (Duan et al., 2023). The concentrations of NaP during the nighttime could be attributed to the extensive use of electricity generated from coal-fired plants for heating households, particularly in winter (Ravindra et al., 2008). The comparatively low concentration of LMW-PAHs at night can be explained by the absence of volatilization. Therefore, it is plausible that the concentration of NaP at nighttime could be potentially due to emissions from coal combustion for domestic heating (Ravindra et al., 2008). Moreover, the decreased concentration of LMW-PAHs at night may be partially attributed to nitrate radical oxidation, which is known to occur during this period (Ye et al., 2017). Furthermore, it was proposed by us that evaporation of LMW-PAHs from heavy fuel used in marine vessels operating in the Ningbo-Zhoushan port could potentially contribute to the level of LMW-PAHs.

Table 4.1 Day and night averaged mass concentration of PAHs in PM<sub>2.5</sub>

Concentrations	Day	Night	Day/Night
PM <sub>2.5</sub>	31.7 ± 15.7	22.9 ± 13.1	1.38
Napthalene (NaP) <sup>+</sup>	0.67 ± 0.54	0.15 ± 0.08	4.47
Acenaphthylene (Acy) <sup>+</sup>	0.11 ± 0.01	0.01 ± 0.02	11.0
Acenaphthene (Ace)	0.02 ± 0.01	0.02 ± 0.02	0.50
Fluorene (Flu)	0.03 ± 0.02	0.02 ± 0.01	1.5
Phenanthrene (Phe) <sup>+</sup>	0.16 ± 0.09	0.07 ± 0.04	2.29
Anthracene (Ant) <sup>+</sup>	0.07 ± 0.01	0.03 ± 0.03	2.33
Fluoranthene (Flt) <sup>+</sup>	0.15 ± 0.15	0.09 ± 0.12	1.67
Pyrene (Pyr) <sup>+</sup>	0.17 ± 0.09	0.06 ± 0.06	2.83
Benz[a]anthracene (BaA) <sup>+</sup>	0.23 ± 0.10	0.03 ± 0.02	7.67
Chrysene (Chr)	0.54 ± 0.47	0.53 ± 0.48	1.02
Benzo[b]fluoranthene (BbF) <sup>+</sup>	0.34 ± 0.22	0.52 ± 0.48	0.65
Benzo[k]fluoranthene (BkF) <sup>+</sup>	0.38 ± 0.24	0.59 ± 0.65	0.64
Benzo[a]pyrene (BaP) <sup>+</sup>	0.18 ± 0.12	0.12 ± 0.10	1.5
Indeno[1,2,3-c,d]pyrene (IPyr)	0.37 ± 0.24	0.36 ± 0.41	1.03
Dibenz[a,h]anthracene (DBahA) <sup>+</sup>	0.07 ± 0.03	0.11 ± 0.08	0.64
Benzo[g,h,i]perylene (BghiP) <sup>+</sup>	0.66 ± 0.42	1.01 ± 0.87	0.65
7H-benzo[c]fluorene (7H-BcF)	0.04 ± 0.04	0.03 ± 0.03	1.33
Dibenzo[a,h]pyrene (DBahPyr) <sup>+</sup>	0.17 ± 0.08	0.09 ± 0.09	1.89
Dibenzo[a,l]pyrene (DBalPyr)	0.06 ± 0.05	0.06 ± 0.06	1.00
Dibenzo[a,e]pyrene (DBaePyr) <sup>+</sup>	0.11 ± 0.02	0.01 ± 0.01	11.0
∑ <sub>6</sub> PAHs <sup>+</sup>	1.04 ± 0.63	0.29 ± 0.12	3.59
∑ <sub>14</sub> PAHs	3.37 ± 2.10	3.60 ± 2.89	0.94
∑ <sub>16</sub> PAHs	4.03 ± 2.31	3.71 ± 2.83	1.09
∑ <sub>4</sub> PAHs <sup>+</sup>	0.38 ± 0.14	0.19 ± 0.12	2.00
∑ <sub>20</sub> PAHs	4.41 ± 2.43	3.90 ± 2.92	1.13
∑ <sub>20</sub> PAHs/PM <sub>2.5</sub> <sup>+</sup>	0.14 ± 0.10	0.17 ± 0.12	0.82

PM<sub>2.5</sub>: µg m<sup>-3</sup>, PAHs: ng m<sup>-3</sup>, LMW = ∑<sub>6</sub>PAHs = NaP, Acy, Ace, Flu, Phe, Ant, ∑<sub>10</sub>PAHs = Flt, Pyr, BaA, Chr, BbF, BkF, BaP, IPyr, DahA, BghiP, HMW = ∑<sub>14</sub>PAHs = ∑<sub>10</sub>PAHs + ∑<sub>4</sub>PAHs = Flt, Pyr, BaA, Chr, BbF, BbF, BaP, IPyr, DahA, BghiP, 7H-BcF, DBahPyr, DBalPyr, DBaePyr, ∑<sub>4</sub>PAHs = 7H-BcF, DBahPyr, DBalPyr, DBaePyr, ∑<sub>16</sub>PAHs = EPA 16 priority PAHs, ∑<sub>20</sub>PAHs = ∑<sub>4</sub>PAHs+∑<sub>16</sub>PAHs, <sup>+</sup> p ≤ 0.05: (z-statistics, mean concentration between day and night statistically significant)

There was no significant variation (p > 0.05) in the concentration of HMW-PAHs like Chr, IPyr, 7H-BcF, and DBalPyr during the day and night periods, which is probably because

they are resistant to atmospheric changes and could have identical sources of emission both during the day and night. Furthermore, there was no noticeable difference in the total concentration of HMW-PAHs and 16 priority PAHs between daytime and nighttime. This is supported by the day-to-night ratio, which is approximately equal to 1. During the day, HMW-PAHs made up 76.4% of the total PAH concentration, which increased to 92.3% at night. BbK, BbF, DahA, and BghiP were the most dominant contributors to PAH concentration levels during both daytime and nighttime, indicating persistent emissions from petroleum combustion (Elzein et al., 2020).

The elevated levels of HMW-PAHs during nighttime may be attributed to the increased energy demand from coal-fired power plants for residential heating, particularly during the winter season. Moreover, the low wind speed ( $1.94 \pm 1.24 \text{ m s}^{-1}$ ), high humidity levels, and low ambient temperature ( $15.9 \pm 7.96 \text{ }^\circ\text{C}$  and  $77.1 \pm 13.0\%$ , respectively) (as shown in Table 4.2) during the night might have favored the accumulation and adsorption of PAHs on  $\text{PM}_{2.5}$  surfaces. The occurrence of temperature inversion, resulting from the low mixing layer height, could contribute to the nighttime levels of PAHs. However, the high wind speed ( $2.69 \pm 1.04 \text{ m s}^{-1}$ ), high ambient temperature, and low humidity levels ( $18.7 \pm 8.71 \text{ }^\circ\text{C}$  and  $64.8 \pm 15.5\%$ , respectively) (Table 4.2) during the day could have promoted the dispersion and dilution of PAH concentrations (Elzein et al., 2020).

Table 4.2 Day and night averages of meteorological parameters

	Unit	Day	Night	Day/Night
Temperature (Temp)	°C	18.7 ± 8.71	15.9 ± 7.96	1.18
+Relative humidity (RH)	%	64.8 ± 15.5	77.1 ± 13.0	0.84
+Wind velocity (WV)	ms <sup>-1</sup>	2.69 ± 1.04	1.93 ± 0.85	1.39

<sup>+</sup> p ≤ 0.05: (z-statistics, mean values statistically significant)

Figure 4-1 illustrates a comparison of PAH concentrations based on the number of aromatic rings present. PAHs with six, five, and four aromatic rings constitute a substantial proportion of the total concentration both during daytime and nighttime. This indicates a more significant contribution from pyrogenic sources (such as fossil fuel combustion) than from petrogenic sources, which typically contain PAHs with 2-3 aromatic rings. The dominant contribution of six-aromatic and five-aromatic ring PAHs implies emissions from petroleum and fossil fuel combustion (Elzein et al., 2020), respectively. The presence of high concentrations of four-aromatic ring PAHs suggests emissions from diesel exhaust and coal combustion (Callén et al., 2014; Ravindra et al., 2008). The higher levels of PAHs with 2-3 aromatic rings during daytime, compared to nighttime, suggest that petrogenic sources make a greater contribution during daytime hours. In contrast, the increased levels of PAHs with 5-6 aromatic rings during nighttime (as shown in Figure 4-1) indicate a higher contribution from fossil fuel combustion compared to daytime (Elzein et al., 2020).

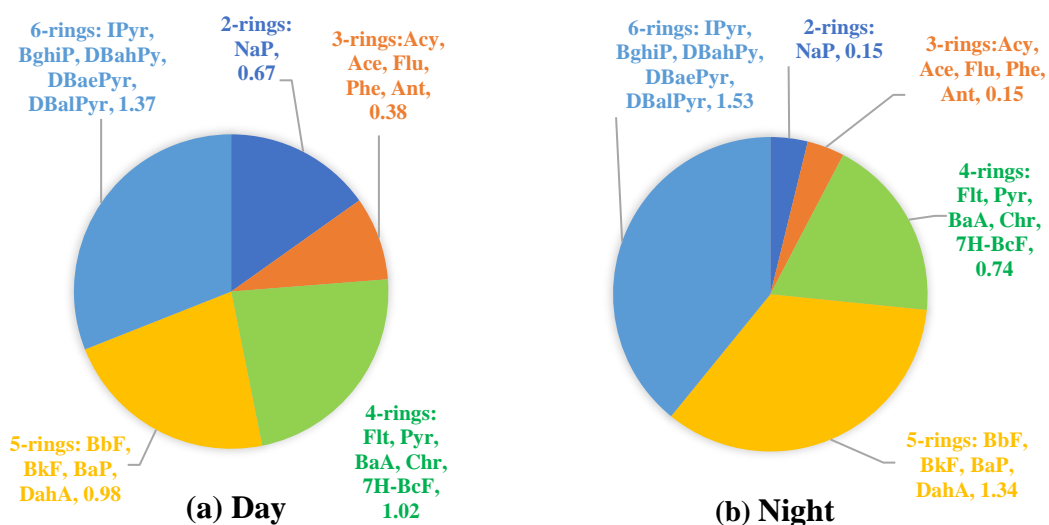


Figure 4-1 Comparison of averaged PAHs concentration based on aromatic rings: (a) Day, (b) Night

#### 4.2.2. Seasonal variability of concentrations of PAHs

The levels of individual PAHs exhibited significant seasonal variation ( $p \leq 0.05$ ), as determined by the analysis of variance (ANOVA). This seasonal variability was observed across all 20 PAHs examined. Among the 16 priority PAHs, the highest mean concentration was recorded in autumn ( $9.43 \pm 4.67 \text{ ng m}^{-3}$ ), followed closely by winter ( $9.26 \pm 6.02 \text{ ng m}^{-3}$ ), spring ( $4.35 \pm 2.10 \text{ ng m}^{-3}$ ), and summer ( $1.83 \pm 0.94 \text{ ng m}^{-3}$ ). A similar pattern was observed for both LMW-and HMW-PAHs, with autumn and winter concentrations surpassing the annual average, whereas spring and summer concentrations were comparatively lower. The seasonal pattern of PAH concentration is inconsistent with that reported in Ashan city (Wang et al., 2020) and Nanjing (He et al., 2014), where winter concentrations were highest, followed by spring, autumn, and summer. The PM<sub>2.5</sub> samples in autumn were collected in October to December 2020, shortly after the relaxation of Covid-19 lockdown measures. During this period, it is plausible that the higher levels of PAHs

observed in autumn can be attributed to the increase in traffic, industrial activities, and commercial operations, which were intensified to meet the heightened demand following the lockdown. Furthermore, the annual mean concentration of the 16 priority PAHs ( $6.21 \pm 5.11$  ng m<sup>-3</sup>) observed in our study was lower compared to other areas such as Anshan (Wang et al., 2020), Wuhan (Zhang et al., 2019), Nanjing (He et al., 2014), Shanghai (Liu et al., 2018), Taiwan (Chen et al., 2016), Hangzhou (Duan et al., 2023), and Beijing (Liu et al., 2019). However, it was higher than the concentrations reported in São Paulo, Brazil (Callén et al., 2014), and Bangi, Malaysia (Khan et al., 2015).

The predominant PAHs in PM<sub>2.5</sub> are the HMW-PAHs, with the exception of 7H-BcF and dibenzopyrene derivatives (DBahPyr, DBalPy, and DBaePyr), and they exhibit distinct seasonal variations. During the autumn and winter seasons, there is an increase in levels of Chr, BbF, BkF, BaP, IPyr, and BghiP, suggesting significant contributions from the combustion of coal (Fang et al., 2020) and gasoline exhaust emissions (Galvão et al., 2023). Throughout the entire duration of the field campaign, the consistent presence of substantial concentrations of BghiP indicates that vehicular emissions continuously contribute to PAH pollution (Wang et al., 2020). Specifically, the levels of BaP were highest during autumn ( $0.68 \pm 0.56$  ng m<sup>-3</sup>), followed by winter ( $0.48 \pm 0.46$  ng m<sup>-3</sup>), spring ( $0.19 \pm 0.15$  ng m<sup>-3</sup>), and summer ( $0.08 \pm 0.07$  ng m<sup>-3</sup>). The annual concentration of BaP ( $0.36 \pm 0.44$  ng m<sup>-3</sup>) was found to be below the permissible threshold (1.0 ng m<sup>-3</sup>) (Xing et al., 2020). There have been significant reduction in BaP levels in China over the past two decades, which can be attributed to the bans on open coal combustion for household heating and cooking purposes,

advancements in both domestic and industrial heating systems, and the use of alternative fuels that emit fewer PAHs (WHO, 2000).

The elevated levels of PAHs during cold seasons (autumn and winter) can be partially attributed to a lower mixing layer and periodic temperature inversion (Wang et al., 2020). The colder weather during this time, with temperatures ranging from  $9.83 \pm 4.99$  °C in winter to  $14.8 \pm 4.77$  °C in autumn (as shown in Table 4.3), promotes the accumulation and adsorption of PAHs onto ambient particles. Conversely, PAH concentrations decrease in summer, which is attributed to reduced fossil fuel usage (Ye et al., 2017). The warm seasons, characterized by higher ambient temperatures of  $19.7 \pm 4.91$  °C in spring and  $27.9 \pm 3.12$  °C in summer (as shown in Table 4.3), facilitate PAH degradation and increase the mixing layer height, resulting in lower PAH concentrations. The high solar radiation experienced during the summer season causes LMW-PAHs to evaporate and degrade through photochemical reactions (Famiyeh et al., 2021; Jiabao He et al., 2014), resulting in the production of oxygenated and nitrated PAHs. Furthermore, elevated temperatures further facilitate the degradation of LMW-PAHs by accelerating the reaction rates. Consequently, the combined influence of solar radiation and high temperatures during summer fosters favorable conditions for the evaporation and degradation of LMW-PAHs. The occurrence of regular rainfall during the summer season additionally plays a role in reducing PAH concentration (Chen et al., 2022). The significant levels of NaP, comprising 17.3% of the overall PAH concentration during summer, is likely attributed to the presence of unburnt fuel that vaporizes due to high temperatures and solar radiation (Roy et al., 2019).



Table 4.3 Seasonal averages of meteorology parameters

	Autumn	Winter	Spring	Summer	Annual
<sup>+</sup> Temperature (Temp)	14.8 ± 4.77	9.83 ± 4.99	19.7 ± 4.91	27.9 ± 3.12	18.0 ± 8.04
<sup>+</sup> Relative humidity (RH)	70.6 ± 14.7	69.0 ± 20.0	71.9 ± 21.9	80.8 ± 14.5	73.1 ± 18.7
<sup>+</sup> Wind velocity (WV)	2.47 ± 1.37	2.49 ± 1.68	2.24 ± 1.48	2.37 ± 1.85	2.39 ± 1.61

<sup>+</sup>p ≤ 0.05 (ANOVA, mean values statistically significant)

During warmer seasons, elevated levels of atmospheric oxidants (such as O<sub>3</sub> and •OH radicals), along with higher ambient temperatures and solar radiation, have the potential to induce the photochemical oxidation of NaP, leading to the formation of naphthoquinone derivatives (McWhinney et al., 2013). As indicated in Table 4.4, the low ratio of PAHs to PM<sub>2.5</sub> during the warm season (spring and summer) suggests the photochemical aging of PAHs (Lv et al., 2016), which may result in the generation of secondary PAHs, such as quinones.

The seasonal variability of PAH concentrations based on the number of aromatic rings is depicted in Figure 4-2. Five-aromatic ring PAHs were found to be the most abundant during autumn, four-aromatic ring PAHs during winter, six-aromatic ring PAHs during spring, and four and five-aromatic ring PAHs during summer. The predominance of five-aromatic ring PAHs implies a significant contribution from fossil fuel combustion (Elzein et al., 2020). During the winter season, there was a noticeable increase in the concentration of four-ring PAHs, which can be attributed to increase emissions from diesel exhaust and coal combustion (Callén et al., 2014; Ravindra et al., 2008). Lower temperatures lead to increased fuel consumption by the engine, which in turn leads to higher emissions of PAHs.

Table 4.4 Seasonal averaged concentrations (mean  $\pm$  standard deviation) of PM<sub>2.5</sub>-bound PAHs

Concentration	TEF <sup>a</sup>	Autumn	Winter	Spring	Summer	Annual
PM <sub>2.5</sub>		53.7 $\pm$ 19.4	64.6 $\pm$ 17.8	53.4 $\pm$ 16.6	34.9 $\pm$ 17.0	51.7 $\pm$ 20.5
Napthalene (NaP)	0.001	0.34 $\pm$ 0.15	0.32 $\pm$ 0.16	0.33 $\pm$ 0.12	0.43 $\pm$ 0.22	0.36 $\pm$ 0.17
Acenaphthylene (Acy) <sup>+</sup>	0.001	0.03 $\pm$ 0.02	0.05 $\pm$ 0.05	0.04 $\pm$ 0.07	0.02 $\pm$ 0.02	0.04 $\pm$ 0.04
Acenaphthene (Ace) <sup>+</sup>	0.001	0.07 $\pm$ 0.04	0.15 $\pm$ 0.09	0.05 $\pm$ 0.03	0.02 $\pm$ 0.02	0.07 $\pm$ 0.07
Fluorene (Flu) <sup>+</sup>	0.001	0.03 $\pm$ 0.52	0.04 $\pm$ 0.03	0.02 $\pm$ 0.01	0.03 $\pm$ 0.01	0.03 $\pm$ 0.01
Phenanthrene (Phe) <sup>+</sup>	0.001	0.24 $\pm$ 0.11	0.35 $\pm$ 0.31	0.13 $\pm$ 0.04	0.11 $\pm$ 0.03	0.21 $\pm$ 0.19
Anthracene (Ant) <sup>+</sup>	0.01	0.26 $\pm$ 0.14	0.35 $\pm$ 0.37	0.15 $\pm$ 0.05	0.13 $\pm$ 0.04	0.14 $\pm$ 0.11
Fluoranthene (Flt) <sup>+</sup>	0.001	0.31 $\pm$ 0.25	0.69 $\pm$ 0.67	0.19 $\pm$ 0.12	0.07 $\pm$ 0.03	0.32 $\pm$ 0.43
Pyrene (Pyr) <sup>+</sup>	0.001	0.46 $\pm$ 0.22	0.69 $\pm$ 0.67	0.19 $\pm$ 0.11	0.07 $\pm$ 0.04	0.36 $\pm$ 0.43
Benz[a]anthracene (BaA) <sup>+</sup>	0.1	0.44 $\pm$ 0.51	0.33 $\pm$ 0.33	0.09 $\pm$ 0.06	0.03 $\pm$ 0.03	0.23 $\pm$ 0.35
Chrysene (Chr) <sup>+</sup>	0.01	1.37 $\pm$ 0.70	1.31 $\pm$ 1.01	0.47 $\pm$ 0.24	0.19 $\pm$ 0.12	0.83 $\pm$ 0.81
Benzo[b]fluoranthene (BbF) <sup>+</sup>	0.1	1.12 $\pm$ 0.70	1.02 $\pm$ 0.53	0.53 $\pm$ 0.30	0.21 $\pm$ 0.17	0.72 $\pm$ 0.59
Benzo[k]fluoranthene (BkF) <sup>+</sup>	0.1	1.16 $\pm$ 0.79	1.35 $\pm$ 0.88	0.42 $\pm$ 0.27	0.16 $\pm$ 0.12	0.77 $\pm$ 0.78
Benzo[a]pyrene (BaP) <sup>+</sup>	1.0	0.68 $\pm$ 0.56	0.48 $\pm$ 0.46	0.19 $\pm$ 0.15	0.08 $\pm$ 0.07	0.36 $\pm$ 0.44
Indeno[1,2,3-c,d]pyrene (IPyr) <sup>+</sup>	0.1	0.83 $\pm$ 0.41	0.69 $\pm$ 0.48	0.42 $\pm$ 0.29	0.21 $\pm$ 0.18	0.54 $\pm$ 0.43
Dibenz[a,h]anthracene (DahA) <sup>+</sup>	1.0	0.19 $\pm$ 0.09	0.14 $\pm$ 0.09	0.13 $\pm$ 0.05	0.08 $\pm$ 0.04	0.14 $\pm$ 0.08
Benzo[g,h,i]perylene (BghiP) <sup>+</sup>	0.1	1.87 $\pm$ 0.95	1.58 $\pm$ 1.08	0.96 $\pm$ 0.60	0.58 $\pm$ 0.49	1.25 $\pm$ 0.95

7H-benzo[c]fluorene (7H-BcF) <sup>+</sup>	20	0.07 ± 0.03	0.09 ± 0.13	0.02 ± 0.01	0.01 ± 0.01	0.05 ± 0.07
Dibenzo[a,h]pyrene (DBahPyr) <sup>+</sup>	10	0.19 ± 0.13	0.17 ± 0.16	0.09 ± 0.07	0.04 ± 0.06	0.13 ± 0.13
Dibenzo[a,l]pyrene (DBalPyr) <sup>+</sup>	10	0.13 ± 0.11	0.04 ± 0.05	0.06 ± 0.04	0.03 ± 0.02	0.06 ± 0.07
Dibenzo[a,e]pyrene (DBaePyr)	1.0	0.01 ± 0.01	0.01 ± 0.02	0.01 ± 0.02	0.01 ± 0.02	0.01 ± 0.02
∑ <sub>6</sub> PAHs <sup>+</sup>		0.98 ± 0.39	0.96 ± 0.49	0.73 ± 0.20	0.73 ± 0.25	0.85 ± 0.37
∑ <sub>14</sub> PAHs <sup>+</sup>		8.83 ± 4.68	8.61 ± 5.89	3.80 ± 2.09	1.76 ± 1.34	5.75 ± 4.97
∑ <sub>16</sub> PAHs <sup>+</sup>		9.43 ± 4.67	9.26 ± 6.02	4.35 ± 2.10	1.83 ± 0.94	6.21 ± 5.11
∑ <sub>4</sub> PAHs <sup>+</sup>		0.39 ± 0.25	0.32 ± 0.32	0.19 ± 0.11	0.09 ± 0.08	0.25 ± 0.24
∑ <sub>20</sub> PAHs <sup>+</sup>		9.82 ± 4.89	9.57 ± 6.32	4.53 ± 2.19	2.49 ± 1.49	6.61 ± 5.24
∑ <sub>20</sub> PAHs/PM <sub>2.5</sub> <sup>+</sup>		0.18 ± 0.12	0.14 ± 0.08	0.08 ± 0.04	0.07 ± 0.05	0.13 ± 0.07

PM<sub>2.5</sub>: μg m<sup>-3</sup>, PAHs: ng m<sup>-3</sup>, LMW = ∑<sub>6</sub>PAHs=NaP, Acy, Ace, Flu, Phe, Ant, ∑<sub>10</sub>PAHs = Flt, Pyr, BaA, Chr, BbF, BbF, BaP, IPyr, DahA, BghiP, HMW = ∑<sub>14</sub>PAHs = ∑<sub>10</sub>PAHs + ∑<sub>4</sub>PAHs = Flt, Pyr, BaA, Chr, BbF, BbF, BaP, IPyr, DahA, BghiP, 7H-BcF, DBahPyr, DBalPyr, DBaePyr, ∑<sub>4</sub>PAHs = 7H-BcF, DBahPyr, DBalPyr, DBaePyr, ∑<sub>16</sub>PAHs = EPA 16 priority PAHs, ∑<sub>20</sub>PAHs = ∑<sub>4</sub>PAHs+∑<sub>16</sub>, PAHs, TEF: Toxicity Equivalent Factor (Iakovides et al., 2021; Soleimani et al., 2022), <sup>+</sup> p≤0.05 (ANOVA, mean concentrations statistically significant)

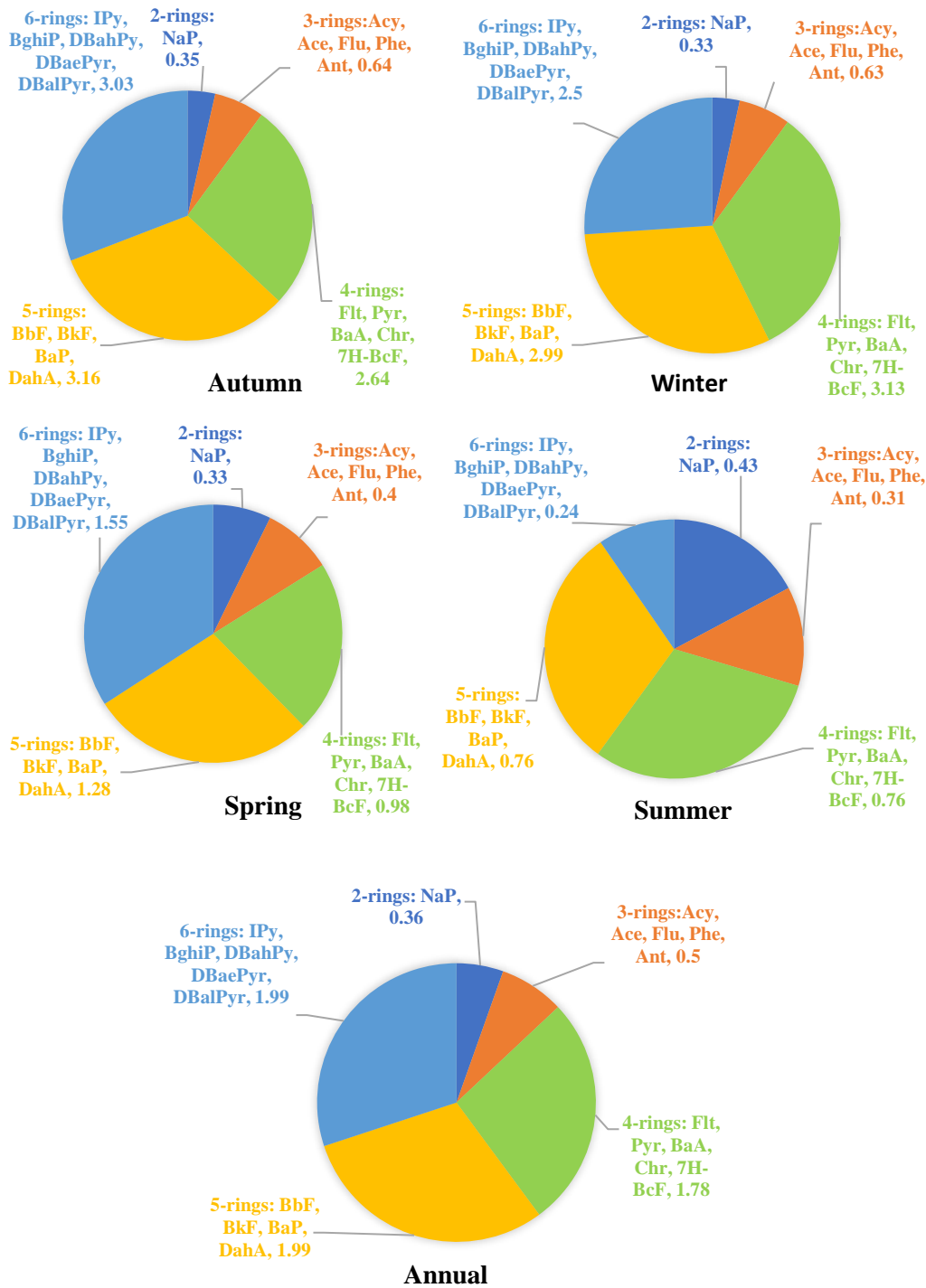


Figure 4-2 Comparisons of seasonal average PAHs concentration (ng m<sup>-3</sup>) based on aromatic rings

The persistent high concentrations of five and six-aromatic ring PAHs observed during the entire field campaign indicate a significant contribution from vehicular exhaust emissions to PAH pollution at the study site.

#### 4.2.3. Size distribution of PAHs in ambient particles

Analyzing the size distribution and peak concentration of PM and PAHs can help in determining their impact on human health. For example, smaller particles with higher levels of toxic chemicals, such as PAH, can be more dangerous to human health because they can penetrate deeper into the alveoli. Moreover, the size distribution of PM chemical compositions provides information about the potential sources and physicochemical properties (Do et al., 2021).

A common method extensively used to show the size distribution of ambient PM and chemical compositions involves plotting  $dC/d\log D_p$  against the particle diameter ( $D_p$ ) (Guo et al., 2018). As shown in Figure 4-4, ultrafine, accumulation, and coarse particles collected in Ningbo exhibited a bimodal size distribution with peak concentrations in accumulation particles (0.49–0.95, 0.95–1.5  $\mu\text{m}$ ) and coarse (3–7.2  $\mu\text{m}$ ) particles. In this plot,  $dC$  represents the mean concentration of PM,  $d\log D_p$  represents the logarithmic differences in aerodynamic diameter ( $D_p$ ).

The size distribution of both LMW- and HMW-PAHs can be found in Figure 4-4 and Figure 4-5, respectively. The concentrations of LMW-PAHs exhibited a bimodal distribution, peaking either in ultrafine, accumulation, or coarse particles. However, Acy displayed a unimodal distribution (Figure 4-4 b). Several PAHs such as NaP, Phe, Ant, and Flu also have bimodal distribution patterns, with peak concentrations in both accumulation

particles (0.95–1.5  $\mu\text{m}$ ) and coarse particles ( $\geq 0.72 \mu\text{m}$ ). The concentration of Ace peaks in ultrafine particles ( $\leq 0.49 \mu\text{m}$ ) and accumulation particles (1.5–3  $\mu\text{m}$ ) (Figure 4-4 c).

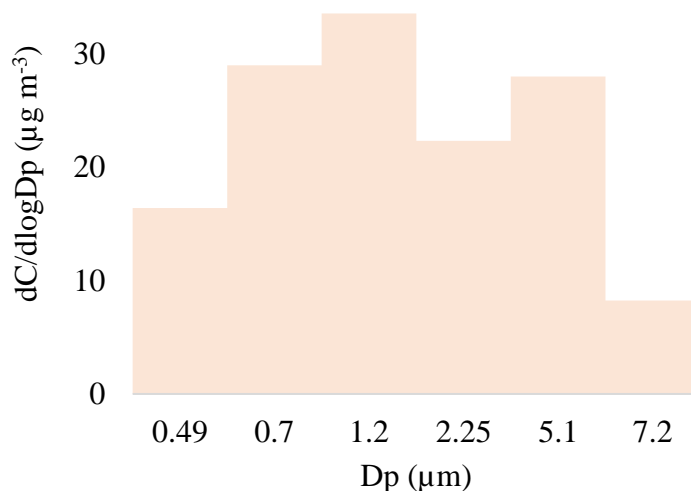


Figure 4-3 Size distribution ( $dC$  = mean concentration ( $\text{ng m}^{-3}$ ),  $d\log D_p$  = logarithmic difference of aerodynamic diameter ( $D_p$ ,  $\mu\text{m}$ )) of the mean mass concentration of PM size fractions collected in a residential/commercial site of Ningbo, China

The majority of HMW-PAHs showed unimodal distribution and had higher peak concentrations in ultrafine particles (0.49–0.95  $\mu\text{m}$ ), except for DBalPyr which exhibited bimodal distribution peaking in ultrafine particles (0.49–0.95  $\mu\text{m}$ ), followed by coarse particles ( $\geq 7.2 \mu\text{m}$ ). The results align with previous studies that indicate a greater concentration of HMW-PAHs in accumulation particles compared to coarse particles (Insian et al., 2022; Shen et al., 2019). Additionally, it was found that total PAH concentration peaked in ultrafine particle (Figure 4-5 r), which is in line with a previous study (Jamhari et al., 2021). The affinity of HMW-PAHs to associate with ultrafine particles facilitates their long-range transport due to their low vapor pressure (Drotikova et al., 2020). However, the peak concentration of LMW-PAHs in coarse particles suggests that during extended

transportation, they may undergo faster degradation through photochemical processes (Zhang et al., 2020). The predominant concentration of NaP in coarse particles suggests that they are susceptible to photochemical oxidation, leading to the formation of naphthoquinone derivatives (McWhinney et al., 2013). This photochemical oxidation process is especially pronounced during periods of warmer weather characterized by high levels of solar radiation, ambient temperature, and oxidants.

The distinct size distributions of LMW- and HMW-PAHs indicate that they may have different sources, and the mechanism controlling their size distribution in ambient particles may vary as well. Notably, PAHs like NaP, Flu, Phe, Ant, Flu, and Flt were present in the highest concentration in accumulation particles (0.95–1.5  $\mu\text{m}$ ). These specific PAHs serve as tracers of coal combustion, natural gas combustion, biomass burning, and diesel exhaust engine emissions (Callén et al., 2014; Fang et al., 2020; Ouyang et al., 2020; Wang et al., 2020), suggesting that these sources may be responsible for the origin of these particles. Additionally, HMW-PAHs come from sources such as gasoline exhaust, coal combustion, and natural gas combustion. Therefore, the highest concentration of HMW-PAHs in particles ranging from 0.49–0.95  $\mu\text{m}$  may indicate that gasoline exhaust, coal combustion, and natural gas combustion are potential sources of these particles at our study site.

The size distribution of PAH based on the number of aromatic rings is depicted in Figure 4-6 (a-e). Bimodal size distribution was observed for PAHs with 2-aromatic rings, wherein peak concentrations were found in both fine and coarse particles (Figure 4-6 a). Conversely, PAHs with 3-aromatic rings displayed bimodal distribution with peak concentrations only in ultrafine and accumulation particles (as shown in Figure 4-6 b). However, PAHs with 4,

5, and 6-aromatic rings exhibited unimodal distribution with highest concentrations in ultrafine particles (0.49–0.95  $\mu\text{m}$ ). As the ring number of PAHs increased, the peak concentration of PAH in ultrafine particles also increased; however, a decrease in peak concentration was observed in coarse particles. This trend is consistent with previous studies (Lv et al., 2016; Zhang et al., 2020). The similarity in size distribution of PAHs with 4, 5, and 6-aromatic rings suggests that they may possibly originate from the same sources and have the same controlling mechanism for their size distribution. The higher concentration of HMW-PAHs compared to LMW-PAHs in ultrafine (0.49–0.95  $\mu\text{m}$ ) and accumulation (0.95–1.5) particles demonstrate the "Kelvin effect" (Wang et al., 2018). This finding suggests that less volatile HMW-PAHs exhibit a greater tendency to condense onto finer particles (Insian et al., 2022; Wang et al., 2018). Moreover, HMW-PAHs tend to partition more in the particulate phase and adsorb more quickly onto smaller particles with larger surface areas (Wang et al., 2018).

The mechanism of PAH size distribution is affected by particle size. PAH size distribution in ultrafine particles is due to adsorption, while in accumulation particles, both adsorption and absorption occur (Lv et al., 2016). In coarse particles, the size distribution is through multilayer adsorption (Insian et al., 2022). Multiple studies have utilized the log (PAHs/PM) versus logDp plot to investigate the mechanism of PAH size distribution in ambient particles (Insian et al., 2022; Lv et al., 2016; Ray et al., 2019; Wang et al., 2018). The PAH size distribution controlling mechanism can be inferred from the slope of the regression line, wherein a slope value of approximately -1 indicates adsorption, while a slope value greater than -1 suggests multilayer adsorption, and a slope value less than -1 signifies



absorption (Insian et al., 2022). The plot for PAHs with 2-3 aromatic rings had regression line with a slope exceeding -1 (Figure 4-7 a), indicating that multilayer adsorption predominantly controls the size distribution of these LMW-PAHs in coarse particles ( $\geq 7.2$   $\mu\text{m}$ ). However, the high levels of 2 and 3-aromatic ring PAH found in ultrafine particles could be a result of adsorption. The slopes of the regression line for the 4-6 aromatic ring PAHs were near -1 (Figure 4-7 c-e). This indicates that the adsorption process predominantly controls the peak concentration of these PAHs in ultrafine particles. The high negative slopes observed in the regression line for 4, 5, and 6-aromatic ring PAHs suggest that these compounds have a significantly higher affinity for adsorption onto PM compared to 2 and 3-aromatic ring PAHs. The size distribution mechanism of 2, 3, 5, and 6-aromatic ring PAHs was consistent with previous studies (Insian et al., 2022), but the adsorption mechanism of 4-aromatic ring PAHs reported in this study conflicted with multilayer adsorption reported by Insian et al. (2022).

The adsorption was the primary mechanism controlling the size distribution of HMW-PAH in ambient particles. The slow mass transfer of HMW-PAHs increased their affinity to particle surfaces during the adsorption process (Ray et al., 2019). Moreover, the primary factor affecting the size distribution of HMW-PAHs is the adsorption mechanism, as they have limited ability to adapt to multiple equilibria because of their lower volatility (Insian et al., 2022).

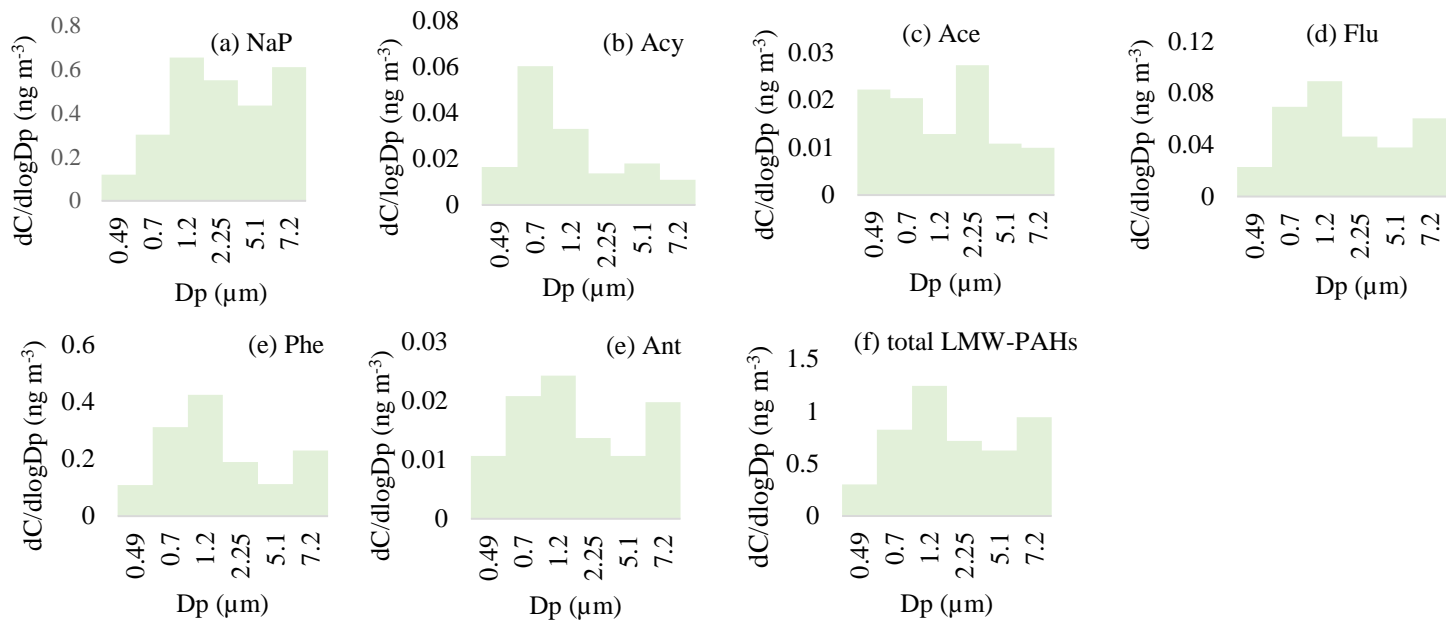


Figure 4-4 Size distribution ( $dC$  = mean concentration (ng m<sup>-3</sup>),  $d\log D_p$  = logarithmic difference of aerodynamic diameter,  $D_p$  is average particle size, μm) of individual LMW-PAHs (a-e) and total LMW-PAH (f) in ambient particle

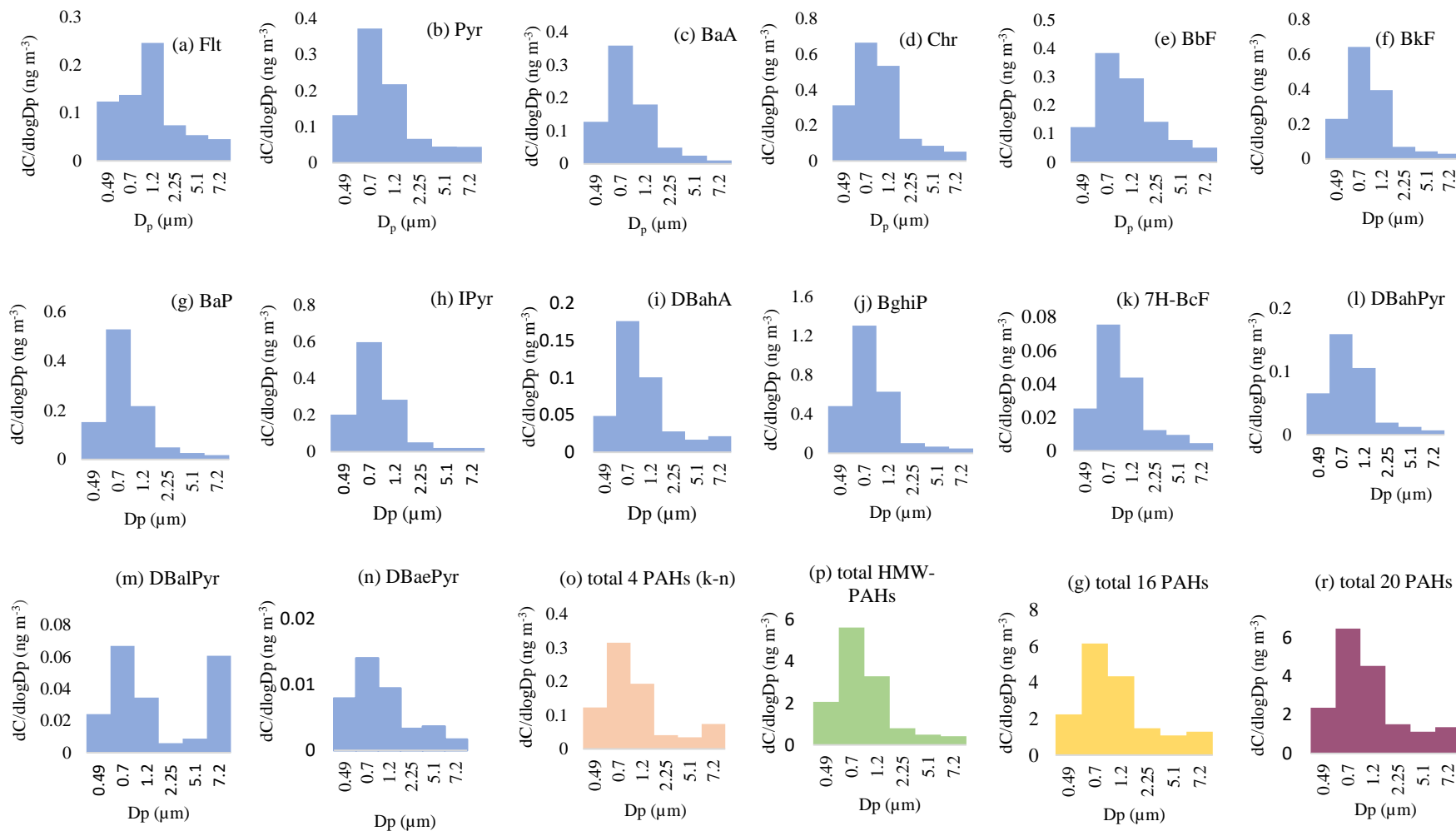


Figure 4-5 Size distribution ( $dC$  = mean concentration ( $\text{ng m}^{-3}$ ),  $d\log D_p$  = logarithmic difference of aerodynamic diameter,  $D_p$  is average particle size,  $\mu\text{m}$ ) of HMW-PAHs (a-n), total (k-n) 4PAHs (o), total HMW-PAHs (p), total (a-j) 16 PAHs (g), and total (a-n) 20 PAHs (r)

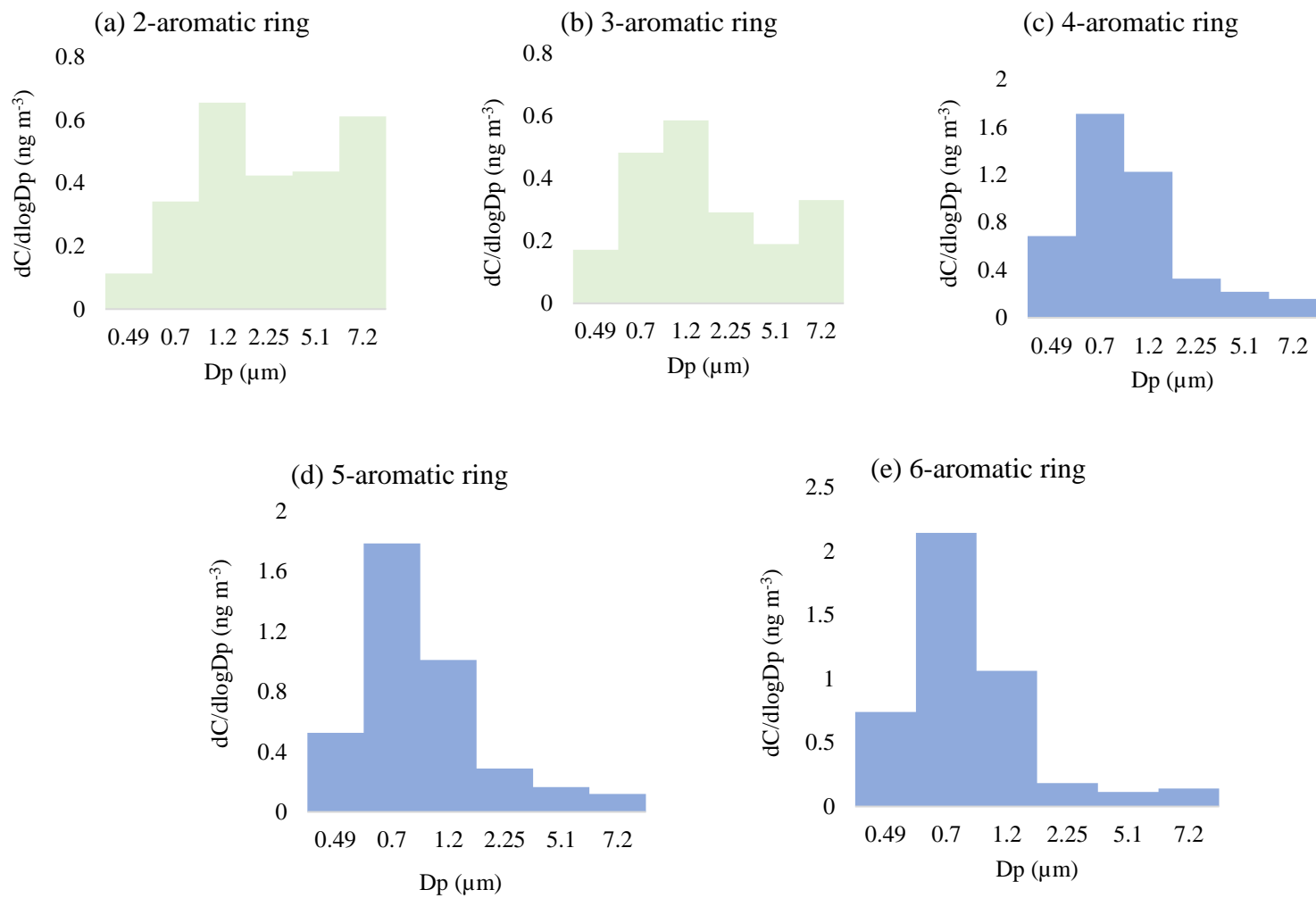


Figure 4-6 Size distribution ( $dC$  = mean concentration ( $\text{ng m}^{-3}$ ),  $d\log D_p$  = logarithmic difference of aerodynamic diameter,  $D_p$  is average particle size,  $\mu\text{m}$ ) of PAHs based on aromatic rings: (a) two, (b) three, (c) four, (d) five, (e) six

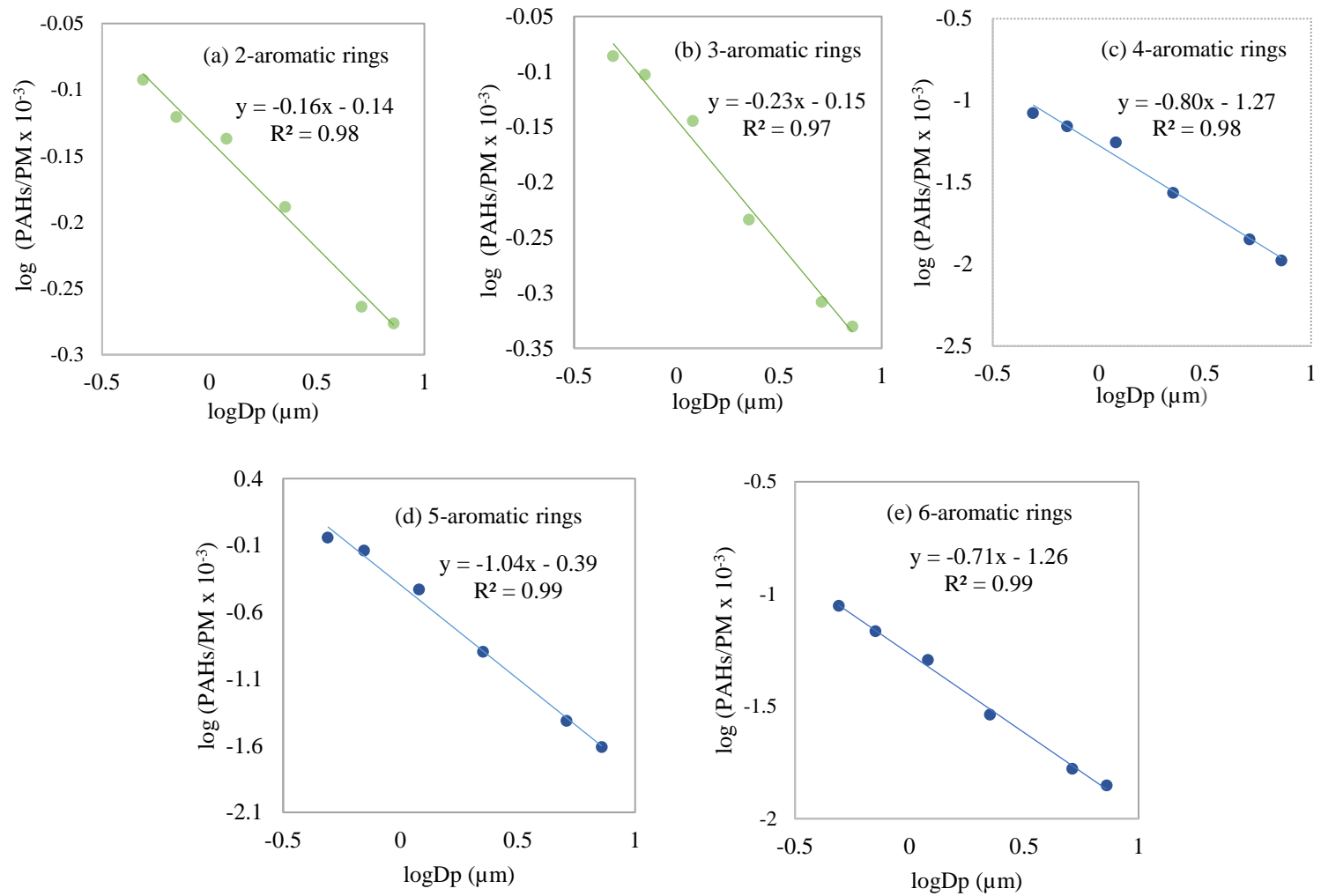


Figure 4-7 Plots of  $\log(\text{PAHs}/\text{PM})$  versus  $\log(D_p)$  based on aromatic rings: (a) two, (b) three, (c) four, (d) five, (e) six

#### 4.2.4. PAHs as indicators of aerosol photochemical aging

BaA has greater reactivity compared to Chr and may degrade quickly while being transported. Therefore, BaA/Chr has been extensively utilized to investigate the aging process of atmospheric aerosols (Esen et al., 2008; Wu et al., 2010). The high BaA/Chr ratio indicates freshly generated PAH, while a lower ratio indicates that the PAHs have undergone photochemical aging (Lv et al., 2016; Wu et al., 2010). The BaA/Chr ratio in daytime (0.29) was about twice higher compared to the nighttime (0.11). This indicates that during the day, sources including diesel exhaust vehicles emit fresh PAHs. Nevertheless, it is possible that during the night, a larger proportion of PAHs that have undergone aging as a result of daytime photochemical reactions may have persisted. Furthermore, it was also observed that summer have a lower BaA/Chr ratio (as shown in Table 4.6), indicating the occurrence of photochemical aging process.

Lv et al. (2016) have indicated that total LMW-PAH/PM<sub>2.5</sub> ratio can discriminate between freshly emitted and photochemically aged aerosols. A low total LMW-PAH/PM ratio suggests the presence of PAHs that have undergone photochemical aging, whereas a higher ratio indicates the presence of freshly emitted aerosols. The LMW-PAHs/PM<sub>2.5</sub> ratio was found to be three times lower at night (0.01) than during the day (0.03). This finding confirms that there are more photochemically aged aerosols present at night compared to during the day. The LMW-PAH/PM<sub>2.5</sub> ratios were lower in warmer seasons compared to colder seasons (as shown in Table 4.1). This finding indicates that aerosols experienced photochemical aging processes during the summer.

#### 4.2.5. Source apportionment of PAHs

##### 4.2.5.1. PAH diagnostic ratios

The diagnostic ratios (DRs) of PAHs in the atmospheric aerosol are often employed to provide qualitative source apportionment of PAHs to discriminate between pyrogenic and petrogenic sources (Cao et al., 2019; Famiyeh et al., 2021; Fang et al., 2020). While the diagnostic ratios can aid in identifying potential PAH emission sources, they are insufficient for quantifying the individual contributions of each source to overall PAH levels.

The mean DRs of PAH during the day, night, and different seasons are provided in Table 4.5 and Table 4.6, respectively. The results of the paired z-statistics and analysis of variance (ANOVA) for the mean diagnostic ratios indicate statistical significance, with a significance level of  $p \leq 0.05$ . This finding suggests the potential existence of disparities in the sources of PAH emissions during different times of the day and throughout various seasons.

A ratio of the sum of LMW to HMW-PAHs can differentiate between petrogenic and pyrogenic sources (Thang et al., 2019). If the ratio is greater than 1, it indicates a petrogenic source, while a ratio less than 1 indicates a pyrogenic source (Famiyeh et al., 2021). This study found that ratios below 1 are predominant during both daytime and nighttime, as well as in different seasons, suggesting a significant PAH emissions pyrogenic sources than petrogenic sources (Elzein et al., 2019). Moreover, to distinguish between petrogenic and pyrogenic sources, the BaA/(BaA + Chr) ratio was used, with a ratio of 0.2–0.35 indicating a pyrogenic source and a ratio below 0.2 indicating a petrogenic source (Galvão et al., 2023; Xing et al., 2020). The BaA/(BaA + Chr) ratio indicated that pyrogenic origin was the

dominant source during the day, whereas petrogenic was the dominant source during the night. Petrogenic sources are mainly release 2-3 aromatic ring PAHs into the ambient air through volatilization at high ambient temperatures and solar radiation. Volatilization of PAHs at night is unlikely, and the presence of 2-3 aromatic ring PAHs at night can be attributed to wood combustion for domestic heating (Sakizadeh, 2020), particularly in the rural areas of the city. The presence of 2-aromatic ring PAH such as NaP during nighttime may have resulted from coal combustion (Ravindra et al., 2008).

Table 4.5 Day and night averaged diagnostic ratios of PAHs

DR	Day	Night	Day/Night
BaA/(BaA + Chr) <sup>+</sup>	0.29	0.05	5.80
Ant/(An t+ Phe)	0.30	0.25	1.20
BaA/Chr <sup>+</sup>	0.29	0.11	2.64
Flu/(Flu + Pyr) <sup>+</sup>	0.16	0.27	0.59
Flt/(Flt + Pyr) <sup>+</sup>	0.40	0.52	0.77
IPyr/(IPyr + BghiP) <sup>+</sup>	0.35	0.26	1.35
BaP/BghiP <sup>+</sup>	0.30	0.14	2.14
BaP/(BaP + Chr) <sup>+</sup>	0.31	0.21	1.48
$\sum$ LMW/ $\sum$ HMW <sup>+</sup>	0.26	0.12	2.17

<sup>+</sup>p ≤0.05 (z-statistics, mean ratios statistically significant)

To further differentiate between pyrogenic and petrogenic sources, the Ant/(Ant + Phe) ratio was used. The ratio of Ant to (Ant + Phe) that was observed during the day, night, and seasons were higher than 0.1. This indicates that there are greater levels of PAH emissions from sources that are pyrogenic rather than petrogenic (Famiyeh et al., 2021). The Ant/(Ant + Phe) ratio being >0.1 through the field campaign suggest consistent PAH emission from vehicular exhaust (Liu et al., 2015). The Ant/(Ant + Phe) ratio consistently indicated the



presence of pyrogenic sources during both daytime and nighttime. In contrast, the BaA/(BaA + Chr) ratio revealed that petrogenic sources were predominantly present during the nighttime. This inconsistency emphasizes the need for a more robust techniques in determining the origin of PAHs.

Table 4.6 Seasonal average diagnostic ratios of PAHs

DR	Autumn	Winter	Spring	Summer	Annual
BaA/(BaA + Chr) <sup>+</sup>	0.20	0.19	0.16	0.15	0.17
Ant/(Ant + Phe) <sup>+</sup>	0.52	0.50	0.53	0.54	0.52
BaA/Chr <sup>+</sup>	0.28	0.22	0.19	0.17	0.21
Flu/(Flu + Pyr) <sup>+</sup>	0.08	0.09	0.11	0.32	0.15
Flt/(Flt + Pyr) <sup>+</sup>	0.42	0.50	0.49	0.47	0.45
IPyr/(IPyr + BghiP) <sup>+</sup>	0.30	0.30	0.30	0.27	0.29
BaP/BghiP <sup>+</sup>	0.34	0.27	0.19	0.15	0.24
BaP/(BaP + Chr) <sup>+</sup>	0.32	0.25	0.27	0.28	0.28
$\sum$ LMW/ $\sum$ HMW <sup>+</sup>	0.12	0.11	0.19	0.33	0.19

<sup>+</sup>p ≤ 0.05 (ANOVA, mean ratios statistically significant)

The ratio of Flt/(Flt + Pyr) can distinguish between different sources like biomass burning (0.50), coal combustion (>0.50), and vehicular exhaust (0.40–0.50) (Fang et al., 2020; Iakovides et al., 2019; Sofowote et al., 2010; Tobiszewski and Namieśnik, 2012). During the daytime, the Flt/(Flt + Pyr) ratio of 0.40 suggest dominant contribution from vehicular exhaust, while at night (0.52), coal and wood combustion dominate PAH emissions. The Flt/(Flt + Pyr) ratio in each season, autumn (0.42), winter (0.50), spring (0.49), and summer (0.47), suggests a consistent emissions of PAHs from vehicular exhaust throughout the study period. However, the high Flt/(Flt + Pyr) ratio in winter indicates a significant contribution from wood and coal combustion.

The ratio of BaP/BghiP was utilized to distinguish PAH emissions from diesel and gasoline exhaust. A ratio below 0.4 suggests that diesel exhaust emits more dominant PAHs than gasoline exhaust (Famiyeh et al., 2021; Gune et al., 2019). Diesel engines were found to emit higher levels of PAHs, characterized by ratios below 0.4, during different periods: daytime (0.30), nighttime (0.14), autumn (0.34), winter (0.27), spring (0.19), and summer (0.15). In order to differentiate further between PAH emissions from gasoline and diesel engines, we utilized the Flu/(Flu + Pyr) and BaP/(BaP + Chr) ratios. When the ratio is less than 0.5, it suggests that diesel engines emit more PAH than gasoline exhaust (Famiyeh et al., 2021). The findings of this study demonstrated that the ratios observed during the daytime, nighttime, autumn, winter, spring, and summer were all below 0.5. These findings provide additional evidence supporting the predominance PAH emissions from diesel exhaust over gasoline exhaust.

The use of IPyr/(IPyr + BghiP) in the study made it possible to distinguish between PAH emission from coal combustion and petroleum combustion. Ratios of 0.52 indicated that coal combustion had the predominant contribution, while ratios between 0.39 to 0.5 indicated that petroleum combustion was dominant (Famiyeh et al., 2021; Ouyang et al., 2020). The IPyr/(IPyr + BghiP) ratios reported in this study indicate a higher level of PAH emissions from petroleum combustion, specifically vehicular exhaust, compared to coal combustion.

The results obtained from the diagnostic ratios indicate that the PAH emissions from pyrogenic sources are higher than those of petrogenic sources. The increased levels of PAH observed during winter and at night-time can be attributed more to the combustion of wood and coal, combined with a lower planetary boundary layer during these periods. The PAH

diagnostic ratios suggest higher PAH emissions from vehicular exhaust than coal combustion. The diagnostic ratios of PAHs indicate that both pyrogenic sources, such as vehicular exhaust, coal combustion, and biomass burning, and petrogenic sources, such as the volatilization of unburned fuel, contribute to the levels of PAHs in our study area.

#### 4.2.5.2. Positive matrix factorization/Bivariate polar plots (PMF-BPPs)

The PMF model and BPPs were employed to identify the sources of PAHs. The PMF model calculates the signal-to-noise (S/N) ratio for each PAH congener, with PAH congeners having S/N ratios greater than 2.0 categorized as "strong" and those with ratios lower than 0.2 as "weak." (Chen et al., 2021). In this study, all 20 PAHs were included in the PMF analysis as their signal-to-noise (S/N) ratios ranged from 2.4 to 10. The model was executed with a range of 2 to 8 factors. The most favorable result was obtained with 5 factors. The Q (Robust) and Q (True) values were 1782.4 and 1792.5, respectively, consistently converging in all 20 Base Model Runs. The Q (theoretical) was calculated according to equation (4-1) (Callén et al., 2014). The minimum Q value was close to the theoretical value of Q (1800). The theoretical value of Q is 1.08 times the minimum Q value. This suggests an acceptable level of uncertainty in the input data (Callén et al., 2014).

At the 5-factor level, the Q/Q<sub>exp</sub> ratio was approximately 1 (0.93), but this ratio decreased as the number of factors exceeded 5. In addition, the bootstrap (BS) mapping demonstrated strong associations among the factors when employing 5 factors and conducting 100 runs. This is evidenced by all the bootstrap (BS) being unmapped, as shown in the Appendix (Table 8.2).

$$Q_{(\text{Theoretical})} = (\text{sample} \times \text{good species}) + \quad (4-1)$$

$$[(\text{samples} \times \text{weak species})/3] - (\text{samples} \times \text{factors estimated})$$

The PMF analysis revealed that vehicular exhaust, coal combustion, natural gas combustion, biomass burning, and volatilization of unburnt fuel were found to be the five sources associated with PAHs at our study domain. These five sources and their contributions to the total PAH mass concentration are shown in Figure 4-8. Figure 4-9 displays the time-series contributions of these five sources, as determined through the PMF model. Figure 4-10 showcases BPPs that visually depict the concentration profiles of these sources. This representation provides valuable insights into the dispersion patterns and transportation of PAHs to our monitoring site.

Factor 1 consists of elevated levels of specific PAHs, including Acy, Ace, and Flu (with loadings of 70.4%, 23.7%, and 28.9%, respectively). These PAHs are indicative of diesel engine emissions. It also includes BbF, BkF, BghiP, IPyr, and DBahA (with loadings of 51.9%, 36.7%, 60.4%, 59.5%, and 75.3%, respectively), which indicates PAH emission from gasoline exhaust (Galvão et al., 2023; Wang et al., 2020). Therefore, vehicular exhaust is identified as the source associated with factor 1 (as depicted in Figure 4-8 a). Vehicular exhaust emissions contributed 25% of the total PAH. Analysis of the PAH source data over a period of time consistently reveals the presence of vehicular exhaust emissions throughout all seasons, with a notable decrease observed during the later part of the field campaign in summer (as shown in Figure 4-9 a). The lower temperatures experienced during autumn and winter cause the engine to consume more fuel, leading to higher emissions of PAHs during these seasons. The analysis of the BPPs indicates the existence of PAH emissions originating

from nearby vehicular traffic, particularly under low wind speed atmospheric conditions. The transportation of high concentrations of PAHs from vehicular exhaust is observed from both the southwest and northwest directions, while lower concentrations are transported from the southeast direction, as represented in Figure 4-10 (a). There are freeways in close proximity to our study domain in these three areas.

The second factor displayed significant loadings for Flt, Pyr, Phe, 7H-BcF, Chr, BkF, and Ace. Flt, Pyr, Phe, Chr, and Ace are widely recognized as indicators of coal combustion (Fang et al., 2020; Wang et al., 2013). Coal combustion was identified as the secondary source of PAHs, contributing approximately 21.1% to the total PAH concentration, as depicted in Figure 4-8 (b). During winter, when coal-fired power plants experience a surge in coal demand for electricity generation, the concentration of PAHs associated with coal combustion reaches its peak, as depicted in Figure 4-9 (b). The BPPs in Figure 4-10 (b) provide evidence that PAHs resulting from coal combustion originate from northwest industrial facilities and are transported to our monitoring station by strong winds (Chen et al., 2022).

The high loadings of BaA, Chr, DBahPyr, BaP, BkF, DBaePyr, IPyr, and Ace in factor 3 strongly indicates the emission of PAHs resulting from natural gas combustion. Among these chemicals, BaA, BaP, and Chr are especially are key indicators to identify this particular source (Callén et al., 2014). PAH emissions from natural gas combustion contribute 33.6% to the overall PAH concentration. The highest concentration of PAHs resulting from natural gas combustion was observed during winter (as shown in Figure 4-9 c). The PAHs derived from the combustion of natural gas were transported to our monitoring

station from industrial facilities located in the northwest and southwest regions. The strong winds played a significant role in carrying these PAHs to our monitoring station (Figure 4-10 c). These industrial facilities use natural gas combustion for heat and power generation, as well as a reducing agent in metallurgical processes. Furthermore, the presence of PAHs associated with natural gas combustion at our monitoring station can be directly attributed to the utilization of natural gas as a fuel for household heating and cooking purposes.

Factor 4 is characterized by significant loadings of Ant (71.3%), Phe (34.8%), Flu (28.4%), Ace (25.1%), and Acy (22.7%). The high loadings of Ant, Phe, Flu, and Ace strongly suggests that biomass burning is a likely source of PAH emissions (Sakizadeh, 2020). Biomass burning accounts for approximately 9.66% of the total PAH concentration. The rise in PAH levels resulting from biomass burning during winter, as depicted in (Figure 4-9 d), suggests that wood is primarily used for residential heating, particularly in rural areas of the city. This is supported by the transport of PAH from the northwest to our monitoring station, observed during periods of both high and low wind speeds (as shown in Figure 4-10 d).

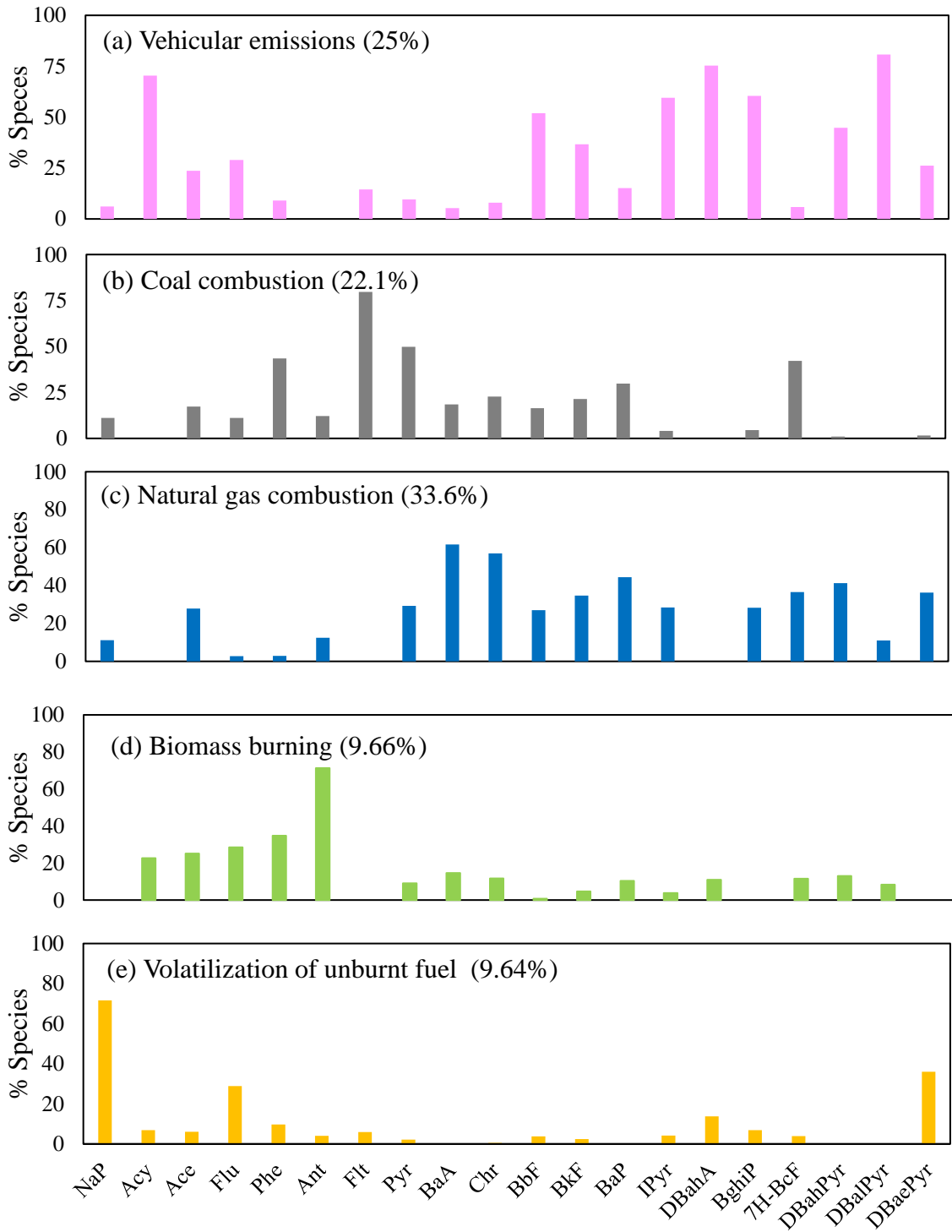


Figure 4-8 Sources of PAHs in PM<sub>2.5</sub> derived from the PMF model: (a) vehicular exhaust, (b) coal combustion, (c) natural gas combustion, (d) biomass burning, (e) volatilization of unburnt fuel

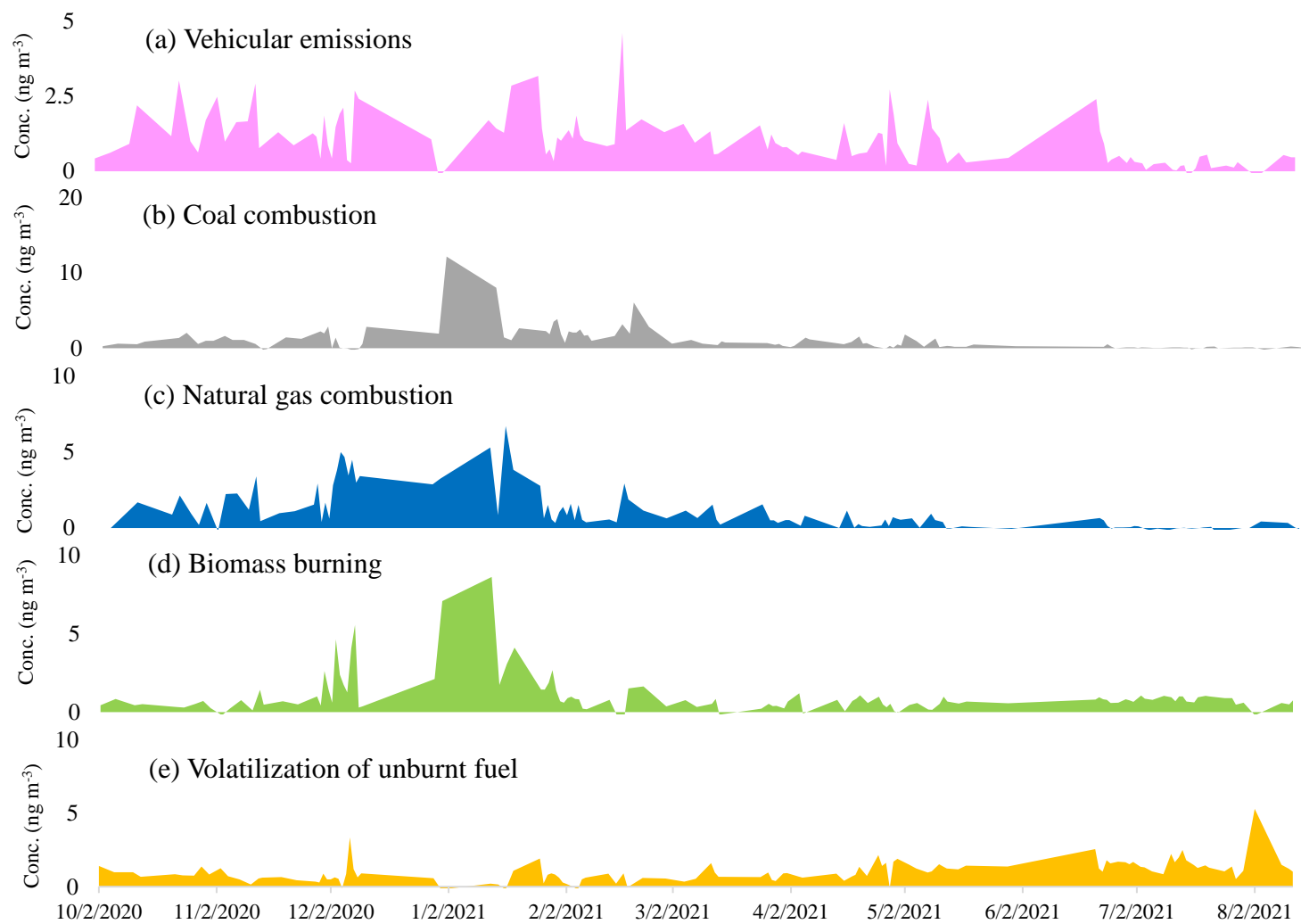


Figure 4-9 Time series source concentrations ( $\text{ng m}^{-3}$ ) derived from PMF model: (a) vehicular exhaust, (b) coal combustion, (c) natural gas combustion, (d) biomass burning, (e) volatilization of unburnt fuel



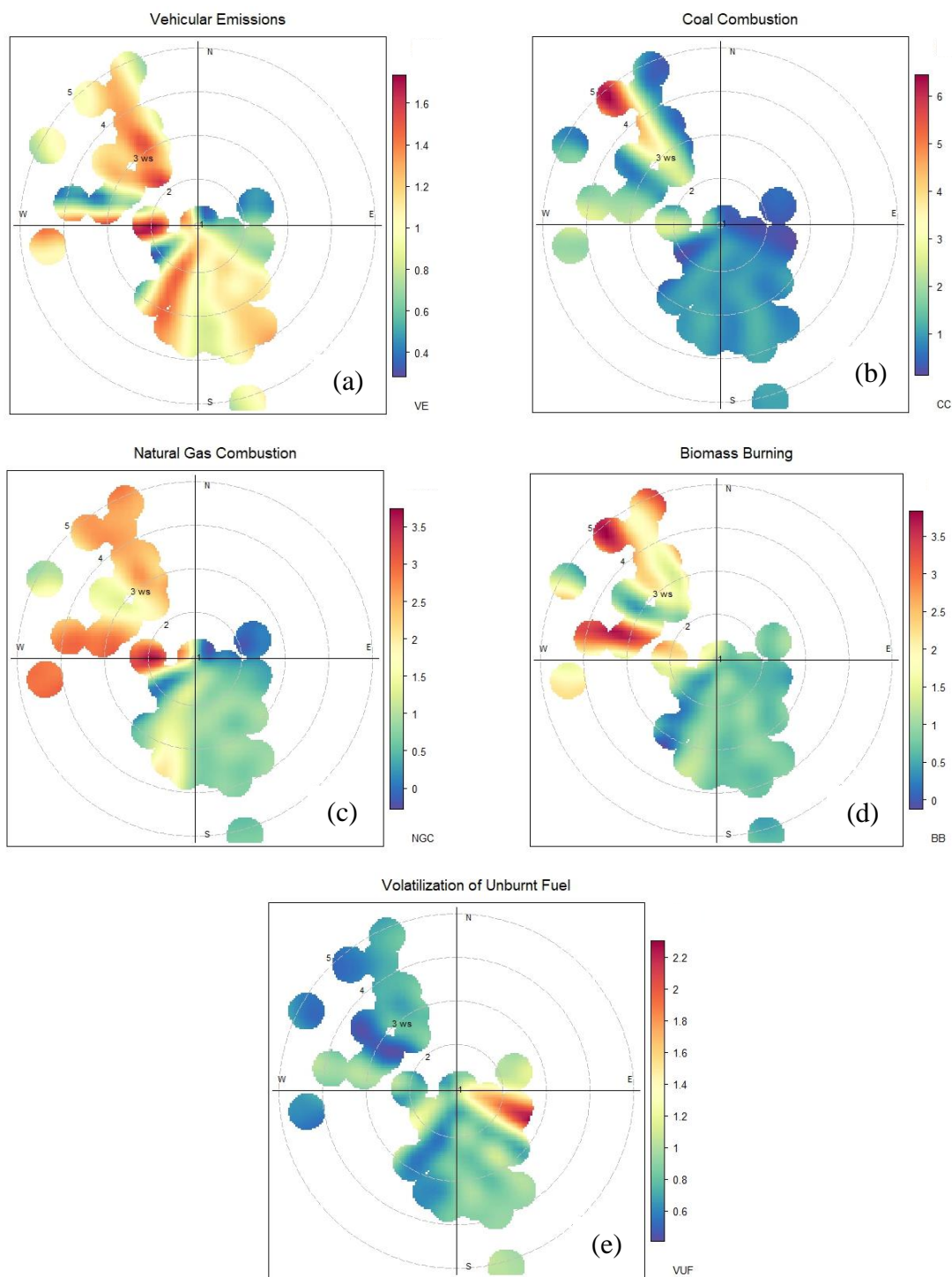


Figure 4-10 Bivariate polar plots (BPPs) of five sources associated with annual  $\text{PM}_{2.5}$ -PAHs concentration ( $\text{ng m}^{-3}$ ) derived from PMF model (a) Vehicular exhaust (b) coal combustion, (c) natural gas combustion, (d) biomass burning, and (e) volatilization of unburnt fuel

Factor 5 exhibits high loadings of NaP, DBaP, and Flu, with percentages of 71.6%, 36.0%, and 28.8%, respectively. The high loadings of NaP with peak concentrations in summer suggest vaporization of unburnt fuel (as shown in Figure 4-9 e). The evaporation of unburnt fuel accounted for 9.61% of the overall PAH concentration (Figure 4-8 d). Bivariate polar plots demonstrate that the PAHs associated with this source originate from the southeast. This suggests that these LMW-PAHs are transported from marine vessels located at the East China Sea and Ningbo-Zhoushan port. They reached our monitoring station at low wind speed, as evidenced in Figure 4-10 (e).

#### 4.2.6. Health risk assessment of PAHs exposure

##### 4.2.6.1. BaP-toxic equivalent concentrations (BaP<sub>TEQ</sub>)

To assess the relative toxic effects of different PAH congeners in comparison to BaP, we calculated the BaP-toxicity equivalent (BaP<sub>TEQ</sub>) by multiplying the concentration of each congener with its corresponding toxicity equivalent factor (TEF). The TEF for the 20 PAHs analyzed in this study can be found in Table 4.4. The overall potency of PAHs in terms of BaP<sub>TEQ</sub> was determined by calculating the sum of the BaP<sub>TEQ</sub> values, which is commonly referred to as the toxicity equivalent quotient (BaP<sub>TEQ</sub>). This is represented in Equation (4-2) (Ali-Taleshi et al., 2021; Hong et al., 2016).

$$\text{BaP}_{\text{TEQ}} = \sum_{i=1}^N \text{BaP}_{\text{eq}} = \sum_{i=1}^N (C_i \times \text{TEF}_i) \quad (4-2)$$

where N = number of PAH congeners, C<sub>i</sub> = concentration of ith PAH congener,

As shown in the Appendix (Figure 4-11 a), it is evident that the BaP<sub>TEQ</sub> values of the LMW-PAHs is dominated by Ant. However, the BaP<sub>TEQ</sub> of Ant is lower than those of the HMW-

PAHs, as shown in Appendix (Figure 4-11 b). The total BaP<sub>eq</sub> of the HMW-PAHs is approximately 1725 times higher than that of the LMW-PAHs. This difference in BaP<sub>eq</sub> values can be attributed to the contrasting partitioning behavior of these two types of PAHs in the particulate phase. LMW-PAHs partition more into the gaseous phase due to their higher vapor pressure, while HMW-PAHs partition into the particulate phase due to their lower vapor pressure (Famiyeh et al., 2021). Consequently, the BaP<sub>eq</sub> values of LMW-PAHs are lower, while those of HMW-PAHs remain high in the particulate phase. The BaP<sub>eq</sub> of HMW-PAHs is dominated by BaP, 7H-BcF, DBahPyr, and DBalPyr. HMW-PAHs, including DBahPyr, 7H-BcF, DBalPyr, BaP, DahA, and BghiP, dominate the total BaP<sub>eq</sub> of the 20 PAHs, accounting for 93.3%. The BaP<sub>eq</sub> values of the four additional PAHs (7H-BcF, DBahPyr, DBalPyr, and DBaePyr) constitute about 76.9% of the total BaP<sub>eq</sub>. The high BaP<sub>eq</sub> values of these four PAHs can be attributed to their high TEF values compared with other PAH congeners. This indicates that these four PAHs make a significant contribution to the overall toxicity of the 20 PAHs.

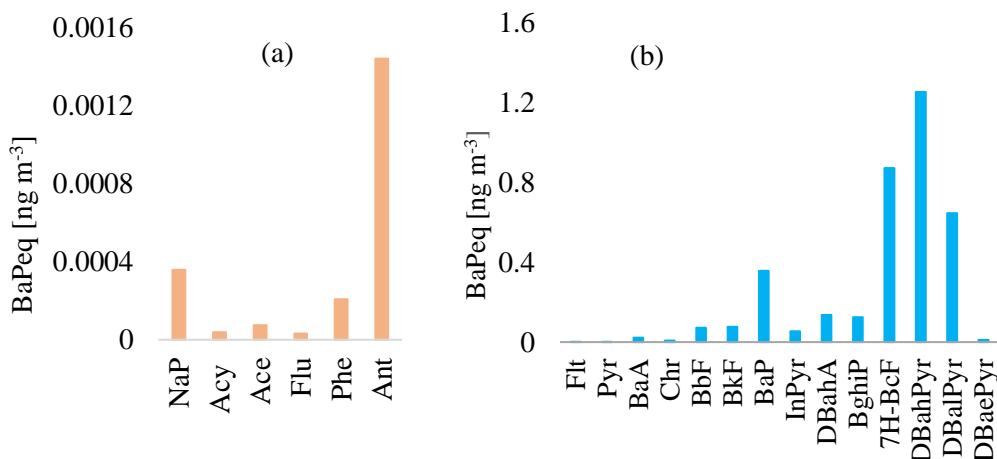


Figure 4-11 Comparison of BaP<sub>eq</sub> of individual PAHs with (a) LMW, (b) HMW

The BaPeq values of BaP and the 16 priority PAHs respectively account for 9.62% and 23.1% of the total BaPeq. BaP exhibited higher annual BaPeq levels compared to most other PAH congeners, with the exception of 7H-BcF, DBahPyr, and DBalPyr. The BaPeq of BaP ( $0.36 \text{ ng m}^{-3}$ ) and the 16 PAHs ( $0.86 \text{ ng m}^{-3}$ ) were lower than in Ashan (Wang et al., 2020), Beijing (Liu et al., 2020), Nanjing (Sun et al., 2016), Tangshan (Fang et al., 2020), and Hangzhou (Duan et al., 2023). However, the values reported in this study was higher than in Kong (Hong et al., 2016) and Malaysia (Khan et al., 2015). The BaPeq of 20 PAHs ( $3.72 \pm 3.69 \text{ ng m}^{-3}$ ) is about four times the BaPeq of the 16 priority PAHs. This suggests a high BaPeq for the four PAHs investigated in this study.

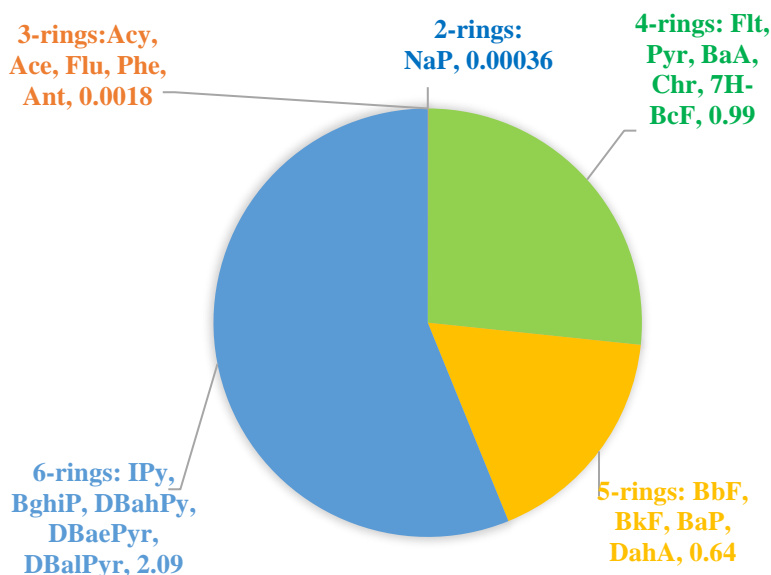


Figure 4-12 Annual averaged BaPeq ( $\text{ng m}^{-3}$ ) of 20 PAHs based on aromatic rings

The BaPeq of PAHs based on the number of aromatic rings is presented in Figure 4-12. The 6 aromatic ring PAHs dominated the total BaPeq constituting 56.2%, followed by 4-aromatic rings (26.6%), 5-aromatic rings (17.2%), 3-aromatic rings at (0.05%), and 2-aromatic rings (0.0097%). The high levels of BaPeq in PAHs with 4 to 6 rings suggest that

these PAHs could pose high health risk. Therefore, investigating their source-specific cancer risk and developing methods for mitigation could be of great interest in improving public health.

#### 4.2.6.2. Lifetime excess cancer risk

Figure 4-13 (a, b, respectively) displays the estimated LECR derived from the application of unit risk values for BaP based on the WHO and the EPA methods. The approach of the WHO is to use the concentration of BaP alone to represent the entire PAH mixture. Using this approach, we calculated LECR-BaP to be  $3.11 \times 10^{-6}$  (Figure 4-13 a). We employed Equation (4-3) (Duan et al., 2023) to estimate LECR of 16 and 20 PAHs by multiplying their  $BaP_{TEQ}$  by the WHO and EPA unit risk. The results are shown in Figure 4-13 (a) and (b), respectively.

$$LECR_{inh} = BaP_{TEQ} \times UR_{BaP} \quad (4-3)$$

The LECR calculated based on the WHO unit risk is approximately 14 times higher than values obtained using the EPA unit risk. As discussed, the use of the WHO unit risk and component-based potency approach leads to an overestimation of the LECR. The LECR-BaP is approximately 6.09 and 1.39 times higher than the LECR of the 16 and 20 PAHs, respectively, estimated based on the EPA unit risk. This suggests that incorporating four additional PAHs in the risk assessment model leads to a more accurate approximation of the LECR between the EPA and WHO approaches. Therefore, to achieve a closer estimation of the LECR between these approaches, it is advisable to include more highly carcinogenic PAHs in the component-based approach. We strongly advise future research to give priority to incorporating a broader range of PAHs in the risk assessment model. This will lead to

accurate estimation the estimation of LECR based on the component-based potency factor approach and the EPA unit risk.

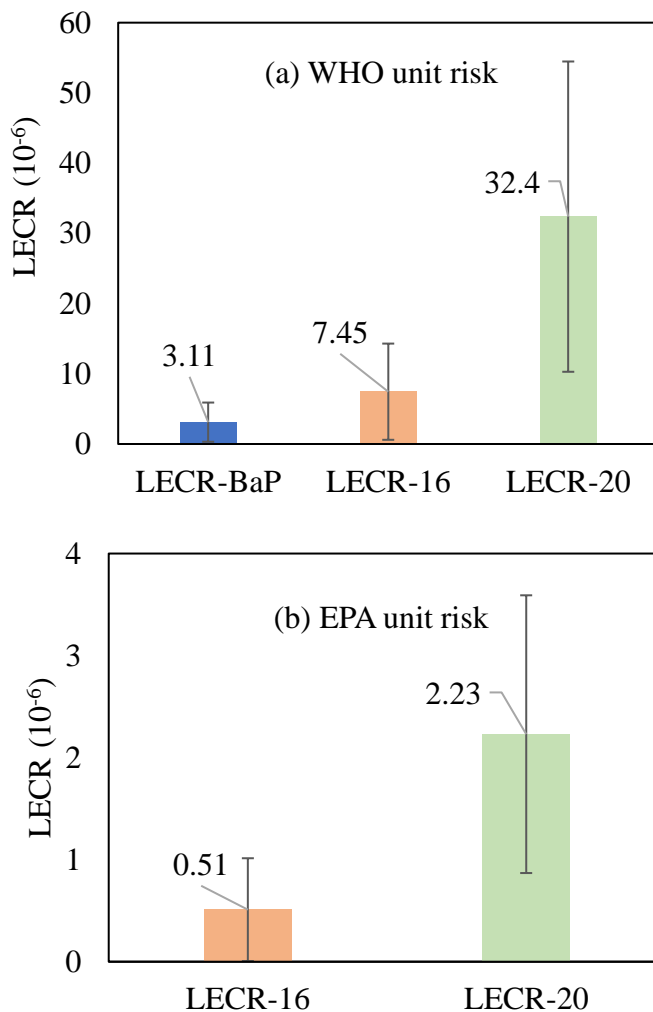


Figure 4-13 Comparison of average LECR of human exposure to 16 and 20 PAHs: (a) WHO unit risk, (b) EPA unit risk. Error bar present the standard deviation (level of variability of the data)

The mean LECR for the 16 priority PAHs ( $5.1 \times 10^{-7}$ ) estimated according to EPA unit risk falls below the acceptable threshold of  $1.00 \times 10^{-6}$ , indicating a negligible risk (Bai et al., 2020; Famiyeh et al., 2021). The mean LECR for the 20 PAHs estimated according to EPA unit ( $2.23 \times 10^{-6}$ ) and according to the WHO approach ( $3.11 \times 10^{-6}$ ) is between  $1.00 \times 10^{-6}$

<sup>6</sup> and  $1.00 \times 10^{-4}$ . This suggest that exposure to the 20 PAHs could poses a moderate level of risk to the population of Ningbo residing in our study domain (Gurkan Ayyildiz and Esen, 2020; US. EPA, 2004).

#### 4.2.6.3. Source-specific LECR

The contribution of each source to the concentration of PAH and LECR was determined through an MLR analysis. The PAH mass concentration and LECR were treated as the dependent variables, while the sources were considered as the independent variables. The summary of the MLR analysis is provided in the Appendix (Table 8.3 and Table 8.4).

Figure 4-14 provides an overview of the contributions of different sources to the concentrations and LECR of 16 and 20 PAHs. In terms of concentration, both sets of 16 and 20 PAHs exhibit similar patterns, with natural gas combustion being the dominant source contributor, followed by vehicular exhaust, coal combustion, biomass burning, and volatilization of unburnt fuel. The contributions to LECR for both 16 and 20 PAHs follow a slightly different trend, with natural gas combustion being the dominant source, followed by coal combustion, vehicular exhaust, biomass burning, and volatilization of unburnt fuel. Even though vehicular exhaust emits (25%) a higher concentration of PAHs compared to coal combustion (22.1%), the LECR associated with coal combustion is higher than that of vehicular exhaust (as shown in Figure 4-14). The observed disparities in PAH concentration and LECR between vehicular exhaust and coal combustion can be attributed to several factors. Firstly, there are variations in the compositions of PAHs released from each source. Additionally, differences in combustion conditions, emission control technologies, and

factors such as fuel type, combustion efficiency, and vehicle technology also contribute to these disparities (Shen et al., 2011).

There might be several points to support the fact that the LECR associated with coal combustion was higher than that of vehicular exhaust:

- 1) PAHs from coal combustion consist of more HMW-PAHs, such as 7H-BcF, Chr, BkF, etc., which have a higher cancer risk compared to vehicular exhaust. In contrast, vehicular exhaust, particularly from vehicles with diesel engines, consists of LMW-PAHs, such as Acy, Ace, Flu, etc., which have a lower cancer risk.
- 2) PAHs emitted from coal combustion were transported directly from an industrial facility located in the northwest region of Ningbo to our monitoring site, as depicted in Figure 4-10 (b). In contrast, PAH emissions from vehicular exhaust were more dispersed, as illustrated in Figure 4-10 (a). This dispersion could result in lower individual exposure.
- 3) The continuous generation of electricity from coal-fired plants for industrial operation and heating purposes could result in prolonged exposure to PAHs emitted during coal combustion. In contrast, the more intermittent emissions from vehicular exhaust could lead to a lower level of exposure.

The contributions of various sources to the concentrations of both the 16 PAHs and 20 PAHs did not exhibit significant variability, likely due to the low concentrations of the additional four PAHs. However, there was notable variation in the LECR for the 16 PAHs and the 20 PAHs across different sources. In particular, when comparing the LECR values of the 20 PAHs to the 16 priority PAHs, natural gas combustion, coal combustion, vehicular



exhaust, biomass burning, and volatilization of unburnt fuel exhibited LECR values that were respectively 4.03, 4.45, 5.71, 3.58, and 3.81 times higher. The predominance of vehicular exhaust and coal combustion in contributing to the 20 PAHs, as opposed to the 16 PAHs, suggests that these two sources emit these four PAHs to a greater extent than other sources. Coal combustion, vehicular exhaust, and tire wear contribute significantly to the level of 7H-Benzo[c]fluorene and dibenzopyrene derivatives in the ambient air (Bergvall and Westerholm, 2007; Richter-Brockmann and Achten, 2018; Sadiktsis et al., 2012).

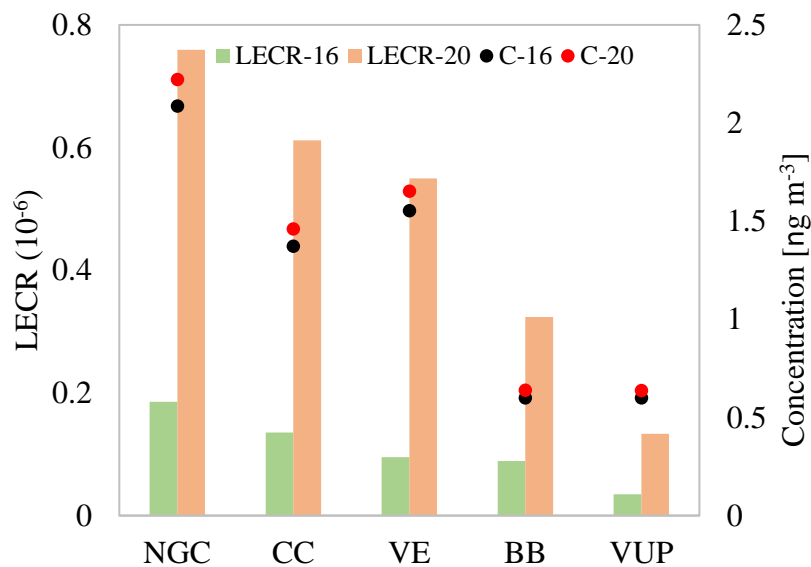


Figure 4-14 Source-specific contribution to PAH concentration (C) and LECR of 16 and 20 PAHs

To effectively reduce PAH concentrations and mitigate the risk of lung cancer, it is crucial to adopt a targeted strategy that addresses key sources. Specifically, this includes the implementation of measures to minimize PAH emissions from natural gas combustion, coal combustion, and vehicular emissions. When considering possible alternatives to natural gas combustion, biofuels, hydrogen, methanol, propane, and electric power are recommended due to their low emissions of PAHs (Osman et al., 2022). Biofuels provide a range of

environmental, economic, and sustainable benefits (Jeswani et al., 2020). Hydrogen combustion is considered a clean fuel option because it only produces water as a byproduct (Falfari et al., 2023). Methanol is characterized by its affordability and environmental friendliness (Araya et al., 2020). Propane is known for its cost-effectiveness, high energy output, and widespread availability (Hashem et al., 2023). In addition, renewable power sources like solar, wind, hydro, and geothermal do not produce PAH pollutants (Owusu and Asumadu-Sarkodie, 2016).

Several strategies can be employed to mitigate PAH emissions from vehicle exhaust. These strategies include adopting alternative fuels characterized by lower levels of PAHs, such as electric power, biofuels, and hydrogen (Sandaka and Kumar, 2023). Moreover, several other effective measures can be taken to decrease PAH emissions from vehicle exhaust. These measures encompass regular vehicle maintenance, the installation of three-way catalytic converters (TWC), the optimization of combustion and fuel injection processes, the promotion of sustainable transportation alternatives, and the reinforcement of environmental regulations and policies (Famiyeh et al., 2021; IARC, 2010). Promotion and advocacy of electric public transportation can play a crucial role in reducing PAH emissions.

Coal plays a pivotal role in China's electricity generation and industrial sectors. However, urgent action is required to address the adverse consequences of PAH emissions resulting from coal combustion. To effectively mitigate these emissions, a range of strategies can be adopted. These encompass improving combustion technologies, imposing rigorous emission standards, promoting the utilization of renewable energy sources, and making significant

investments in cleaner coal technologies, such as dedusters, electrostatic precipitation, and fabric filters (Scott et al., 2021).

### **4.3. Conclusions**

The findings of this study provide evidence of significant seasonal variations in the concentration and composition of PAHs. The highest levels of PAHs were observed during autumn, followed by winter, spring, and summer. The dominant contribution of PAHs with 5- and 6-aromatic rings to the overall PAH levels during night and cold seasons (autumn and winter) further suggests a significant impact from the combustion of fossil fuels, particularly coal and natural gas, which are utilized for industrial activities, electricity generation, and heating and cooking. The dominant contribution of 4-aromatic PAH rings during the day and winter suggests a significant contribution from vehicular exhaust emissions, particularly from diesel exhaust engines.

The size distribution patterns of PAHs varied depending on their molecular weight. PAHs with 2-3 aromatic rings showed a bimodal distribution, with high concentrations in accumulation and coarse particles. On the other hand, PAHs with 4-6 aromatic rings exhibited a unimodal distributions, with peak concentrations in ultrafine particles attributed to adsorption processes. The multilayer adsorption of certain PAHs in coarse particles also facilitates their photochemical oxidation with atmospheric oxidants, potentially leading to the formation of oxygenated and nitrated derivatives.

The diagnostic ratios of PAHs in our study area indicate that the levels of PAHs are contributed by both pyrogenic sources, such as vehicular exhaust, coal combustion, and biomass burning, as well as petrogenic sources, such as the volatilization of unburned fuel. Diesel engines were found to contribute more to PAH emissions than gasoline engines.

Moreover, the diurnal and seasonal variations in BaA/Chr and PAH/PM<sub>2.5</sub> ratios suggested the presence of photochemically aged aerosols, particularly during nighttime and summer.

The results of the PMF analysis identified five major sources of PAHs, including natural gas combustion, vehicular exhaust, coal combustion, biomass burning, and the volatilization of urban fuel. The BPPs analysis provided valuable information about the dispersion and transport characteristics of these sources at our study domain. Notably, coal combustion emissions were linked to an industrial facility in the northwest, while biomass burning activities were associated with wood combustion for heating and the burning of crop residues from rural areas. The PAHs associated with the volatilization of burnt fuel originated from the southeast of the East China Sea, indicating a significant contribution from marine vessel emissions.

The assessment of LECR for 16 and 20 PAHs using the WHO and EPA unit risk approaches revealed important findings. Initially, employing the WHO approach, which solely considers BaP concentration as a representative marker for the entire PAH mixture, the estimated LECR was  $3.11 \times 10^{-6}$ . However, when applying the component-based potency factor approach along with the WHO unit risk, the calculated LECR for 16 and 20 PAHs was significantly overestimated ( $7.45 \times 10^{-6}$  and  $32.4 \times 10^{-6}$ , respectively). These estimates were approximately 14 times higher than LECR estimated for 16 and 20 PAHs based on EPA unit risk ( $5.1 \times 10^{-7}$  and  $2.23 \times 10^{-6}$ , respectively). However, the LECR of 20 PAHs estimated based on the EPA unit risk closely aligned with the LECR estimated solely based on BaP concentration, according to WHO approach. Thus, it is crucial to adhere to the correct application of the EPA and WHO approaches. Furthermore, the inclusion of four

additional PAHs resulted in a moderate increase in the LECR, highlighting the importance of considering a broader range of PAHs in future research to more accurately assess the potential risk of developing lung cancer due to PAH exposure.

The three primary sources contributing to LECR were identified as natural gas combustion, coal combustion, and vehicular exhaust emissions. Therefore, the implementation of strict measures targeting these sources has the potential to effectively reduce PAH exposure levels and subsequently decrease the LECR, resulting in enhanced protection for the general population. These findings demonstrate that this study has provided a comprehensive and accurate assessment of PAH-related cancer risk by utilizing appropriate risk estimation methods, considering a broader range of PAHs, and identifying key sources associated with the risk. This research has made a significant contribution to the field of PAH cancer risk assessment and the development of mitigation strategies aimed at improving public health. The methods employed in this study can serve as a valuable framework for similar research in other cities.

## **Chapter 5 OP induced by Water and Methanol-Soluble Fractions of PM<sub>2.5</sub>: Diurnal and Seasonal Variations, Chemical Characterization, and Source Apportionment**

### **5.1. Introduction**

The chemical composition of PM<sub>2.5</sub>, which includes trace metals, inorganic ions, organic carbons, PAHs, and quinones, could exhibit significant variation throughout the day, night, and across seasons. This observed variation in the chemical composition of PM<sub>2.5</sub> can be attributed to the presence of diverse emission sources and the influence of different atmospheric conditions. Consequently, the OP induced by these chemicals is also likely to exhibit diurnal (Ahmad et al., 2021; Ainur et al., 2023) and seasonal variations (Cui et al., 2023; Molina et al., 2023). The extent of variability in OP within PM<sub>2.5</sub> particles throughout both the day and night remains poorly investigated (Ahmad et al., 2021; Ainur et al., 2023). The clarification of such differences could facilitate the development of more effective public health policies and guidance for individuals seeking to reduce their exposure to PM<sub>2.5</sub> particles. Thus, further research is necessary to determine potential discrepancies in the OP of PM<sub>2.5</sub> particles between daytime and nighttime and to improve our understanding of the associated health risks of exposure to PM<sub>2.5</sub> particles throughout the day.

To accurately measure OP, PM<sub>2.5</sub> chemical compositions must be extracted, and the choice of solvent significantly affects the consistency of OP values. This is because the solubility of the different chemical components of PM<sub>2.5</sub> varies depending on the solvent used (Famiyeh, Jia, et al., 2023). The use of water as the primary solvent for extracting

hydrophobic chemical species to measure their OP has been commonly employed in previous studies (Argyropoulos et al., 2016; Guo et al., 2019; Ma et al., 2021). The use of methanol extract both hydrophilic and hydrophobic chemical compositions (Chen et al., 2022; Pietrogrande et al., 2021). Therefore, the OP induced by the water- and methanol-soluble fractions may vary significantly due to differences in their chemical compositions (Famiyeh, Jia, et al., 2023). The exact impact of the chemicals extracted in these solvents on OP, as measured by DTT and AA assays, is still not clearly understood. In this study, the DTT and AA assays were chosen as OP measurement methods due to their capability to detect a diverse range of chemical species that can induce OP. (Charrier and Anastasio, 2012; Fang et al., 2016; Jiang et al., 2019; Visentin et al., 2016; Vreeland et al., 2017; Yu et al., 2022). This allows for the detection of several chemical compositions in PM<sub>2.5</sub> that induce OP.

The sources of these chemical species including fossil fuel combustion, vehicular exhaust, industrial emissions, and biomass burning could contribute to OP induced by PM<sub>2.5</sub> (Luo et al., 2023; Wen et al., 2023). Industries and vehicular exhaust are significant contributors to PM<sub>2.5</sub>, which can cause high OP due to their emission of redox-active chemical species like quinones and transition metals (Wang et al., 2020). Secondary aerosol formation through photochemical processes may lead to an increase in OP (Daellenbach et al., 2020; Saffari et al., 2015). In contrast, PM<sub>2.5</sub> from natural sources like sea salt, and road dust generally contain fewer redox-active chemical components (Liu et al., 2018; Park et al., 2018). However, the presence of inorganic ions from these sources can contribute to an increase aerosol acidity (Guo et al., 2023). This can leads to the dissolution of trace metals

and subsequent elevation of OP levels. (Fang et al., 2017). Therefore, the strategic positioning of our monitoring station near the Ningbo-Zhoushan port and the East China Sea is significant. It highlights the role of sea spray in releasing inorganic ions into the atmosphere, which can lead to an increase in aerosol acidity and subsequent elevation OP induced by PM<sub>2.5</sub>. The aim of this study is to compare the OP of PM<sub>2.5</sub> particles during daytime and nighttime and across different seasons using DTT and AA assays, while also identifying the potential chemical species and sources that contribute to the observed OP levels.

During this study, various molecular biomarkers including levoglucosan and homohopanes (discussed in Sections 2.9.2.1 and 2.9.2.2, respectively) were used, alongside the PMF model and BPPs analysis, to obtain a comprehensive source apportionment of PM<sub>2.5</sub> during different times of the day, night, and seasons. Additionally, the MLR analysis was applied to estimate the source contributions to the OP.

The specific objectives of the study were as follows:

- 1) comparing the diurnal and seasonal ambient concentrations of PM<sub>2.5</sub> chemical compositions such as water-soluble trace metals, inorganic ions, water-soluble organic carbons, quinones, and molecular tracers such as levoglucosan, and homohopanes;
- 2) investigating aerosol acidity, and marine source contributions to PM<sub>2.5</sub> pollution during daytime, nighttime, and across seasons;
- 3) comparing daytime and nighttime, and seasonal OP induced by water-and methanol soluble fraction of PM<sub>2.5</sub> and identifying their associated chemical species;



- 4) investigating the source dispersion characteristic of OP during the daytime, nighttime, and across seasons;
- 5) identifying the sources of PM<sub>2.5</sub> during the daytime and at nighttime, and across different seasons and estimate their contributions to the OP induced by water-and-methanol-soluble fraction.

The implementation of effective control measures by policymakers, specifically targeting the primary sources identified in this study that significantly contribute to PM<sub>2.5</sub> concentration and its associated OP, holds great potential for substantial reduction of PM<sub>2.5</sub> pollution and improvement of public health in Ningbo. Moreover, the methodologies utilized in this study can be successfully applied in other cities to assess the potential health risks associated with PM<sub>2.5</sub> pollution.

## **5.2. Results and discussions**

### 5.2.1. Chemical characterizations: diurnal and seasonal variations

This Section focuses on the chemical compositions of PM<sub>2.5</sub>, including inorganic ions, water-soluble trace metals, water-soluble organic carbon, and quinones, and presents the concentrations during the daytime, nighttime, and different seasons. The diurnal and seasonal concentrations of PAHs have been discussed in Chapter 4 (Sections 4.2.1 and 4.2.2, respectively). The main objective of analyzing these chemical species is to investigate their OP activity. These chemical species were utilized for source apportionment of PM<sub>2.5</sub> using the PMF model. The concentrations of source biomarkers such as levoglucosan and homohopanes, as well as gaseous pollutants like SO<sub>2</sub>, NO<sub>2</sub>, and O<sub>3</sub>, during the daytime, nighttime, and different seasons, have also been provided. The analysis of levoglucosan was conducted to trace the contributions of biomass burning to PM<sub>2.5</sub>, as outlined in Section

2.9.2.1. Conversely, the analysis of homohopanes was performed to differentiate between emissions from coal combustion and vehicular exhaust, as discussed in Section 2.9.2.2. The concentrations of SO<sub>2</sub>, NO<sub>2</sub>, and O<sub>3</sub> were analyzed because of their significant contributions to the formation of secondary aerosols, particularly sulfates and nitrates.

Figure 5-1 and Figure 5-2 shows the summary of the daytime and nighttime, and seasonal mass concentrations of inorganic ions in PM<sub>2.5</sub>, respectively. The daytime and nighttime concentrations of trace metals, levoglucosan, WSOC, and homohopanes (C31αβS and C31αβR), quinones (1, 2-NQ, 1, 4-NQ, and 1, 4-AQ), and gaseous pollutants (SO<sub>2</sub>, NO<sub>2</sub>, and O<sub>3</sub>) are shown in Table 5.1. The seasonal concentrations of these chemical compositions is shown in Table 5.2. The concentrations of these chemical compositions were compared between daytime and nighttime using z-statistics (p = 0.05), and seasonal variations were assessed using analysis of variance (ANOVA, p = 0.05). The variation in concentrations of these chemical species during both daytime and nighttime, as well as across seasons, is considered significant when the p-value is less than or equal to 0.05.

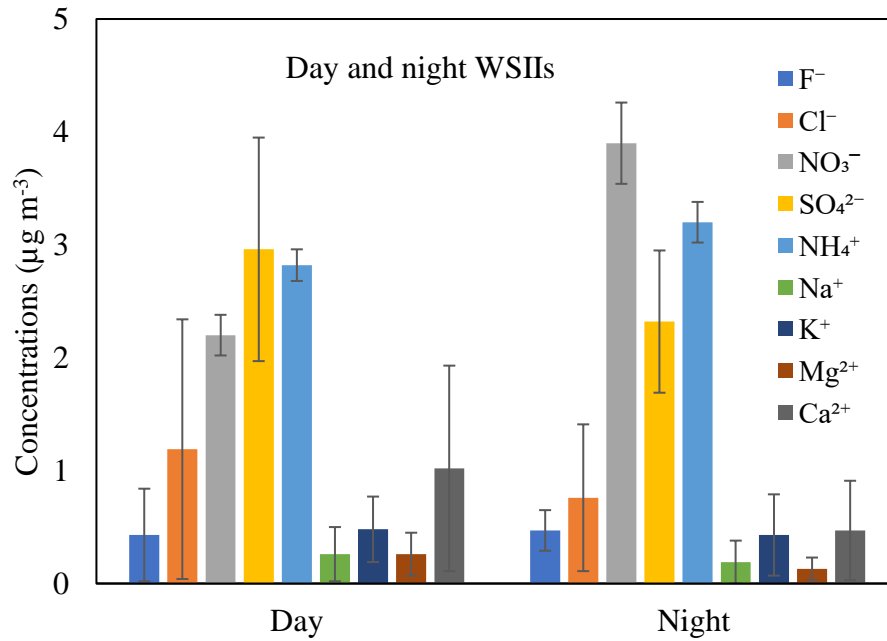


Figure 5-1 Day and night concentrations of WSIs in PM<sub>2.5</sub> particles collected residential area of Ningbo, China. Error bar present the standard deviation (level of variability of the data)

Table 5.1 Summary of averaged mass concentration of WSTMs, WSOC, Levoglucosan, quinones, homohopane, and gaseous pollutants during daytime and nighttime

Chemical compositions	Day	Night	Day/Night
Trace metals (ng m <sup>-3</sup> )			
Mn <sup>+</sup>	146.2 ± 89.9	181.3 ± 358.2	0.81
Co <sup>+</sup>	1.67 ± 1.34	0.86 ± 0.58	1.94
Ni	17.4 ± 8.51	14.2 ± 8.82	1.23
Cd	4.95 ± 5.23	6.27 ± 4.74	0.79
Zn <sup>+</sup>	655.9 ± 457.7	970.4 ± 370.1	0.66
Ba	38.9 ± 72.2	41.7 ± 81.6	0.93
Cr	20.4 ± 10.8	19.4 ± 12.2	1.05
Cu	51.7 ± 34.8	53.5 ± 74.4	0.97
As	16.3 ± 12.9	18.5 ± 12.9	0.88
Pb <sup>+</sup>	14.2 ± 13.6	23.0 ± 29.3	0.62
Fe <sup>+</sup>	612.1 ± 388.3	369.1 ± 316.6	1.66
Al <sup>+</sup>	442.8 ± 541.5	284.4 ± 279.8	1.56
V <sup>+</sup>	93.4 ± 84.6	112.3 ± 153.1	0.83
Ag <sup>+</sup>	1.30 ± 1.25	0.84 ± 0.61	1.55
Bi <sup>+</sup>	2.93 ± 5.67	4.60 ± 1.42	0.64
Ce <sup>+</sup>	0.74 ± 0.57	0.44 ± 0.33	1.68
Sr	9.05 ± 12.8	7.85 ± 11.1	1.15
Sb	2.51 ± 0.78	2.49 ± 1.09	1.01
ΣWSTMs (μg m <sup>-3</sup> )	2.32 ± 1.74	2.11 ± 1.72	1.09
Levoglucosan, WSOC, homohopanes			
Levo (ng m <sup>-3</sup> ) <sup>+</sup>	122.8 ± 5.90	124.6 ± 7.84	0.98
WSOC (μg m <sup>-3</sup> ) <sup>+</sup>	6.19 ± 4.56	7.05 ± 2.64	0.87
C31αβS (ng m <sup>-3</sup> ) <sup>+</sup>	0.19 ± 0.56	0.06 ± 0.04	3.17
C31αβR (ng m <sup>-3</sup> ) <sup>+</sup>	0.32 ± 0.85	0.17 ± 0.09	1.88
Quinones (ng m <sup>-3</sup> )			
1, 2-NQ	0.29 ± 0.14	0.24 ± 0.12	1.21
1, 4-NQ	0.06 ± 0.05	0.05 ± 0.03	1.20
1, 4-AQ <sup>+</sup>	0.08 ± 0.01	0.01 ± 0.02	8.00
ΣQuinones <sup>+</sup>	0.43 ± 0.07	0.30 ± 0.04	1.43
Gaseous pollutant (μg m <sup>-3</sup> )			
NO <sub>2</sub> <sup>+</sup>	29.4 ± 15.4	35.0 ± 20.5	0.84
SO <sub>2</sub>	9.44 ± 4.15	9.07 ± 2.93	1.04
O <sub>3</sub> <sup>+</sup>	77.9 ± 45.1	50.5 ± 34.8	1.54

<sup>+</sup> p ≤ 0.05: (z-statistics, mean concentration between day and night statistically significant)

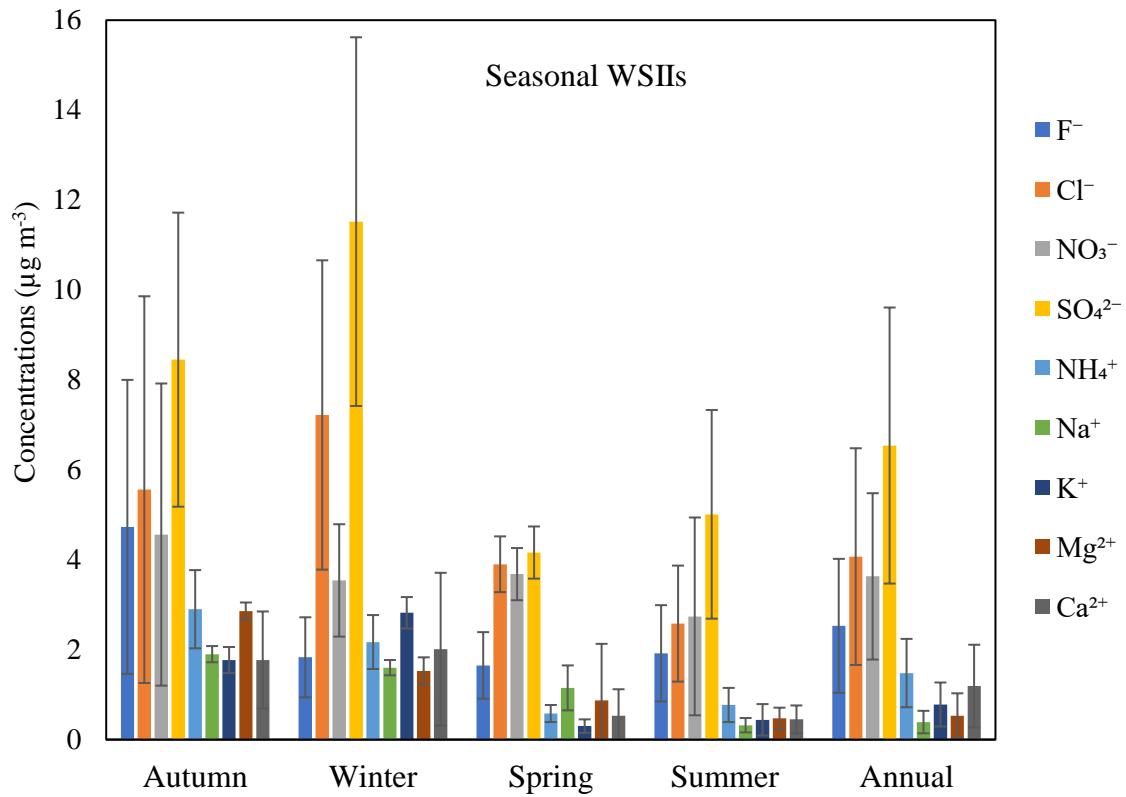


Figure 5-2 Seasonal concentrations of WSIs in  $\text{PM}_{2.5}$  particles collected residential area of Ningbo, China. Error bar present the standard deviation (level of variability of the data)

Table 5.2 Summary of averaged mass concentration of WSTMs, WSOC, Levoglucosan, quinones, homohopane, and gaseous pollutants during across four seasons

Chemical compositions	Autumn	Winter	Spring	Summer	Annual
Trace metals (ng m <sup>-3</sup> )					
Mn <sup>+</sup>	94.6 ± 39.9	69.4 ± 50.7	29.6 ± 28.7	18.9 ± 18.7	53.1 ± 34.5
Co <sup>+</sup>	0.54 ± 0.30	0.49 ± 0.34	0.82 ± 0.45	0.50 ± 0.36	0.59 ± 0.36
Ni <sup>+</sup>	6.67 ± 11.5	25.9 ± 15.9	41.4 ± 20.5	35.1 ± 19.8	27.3 ± 16.9
Cd <sup>+</sup>	1.71 ± 0.95	1.02 ± 0.51	0.31 ± 0.18	0.33 ± 0.22	0.84 ± 0.47
Zn <sup>+</sup>	851.1 ± 575.2	769.9 ± 527.9	201.1 ± 229.1	145.1 ± 143.2	216.8 ± 168.9
Ba <sup>+</sup>	32.1 ± 13.0	98.6 ± 107.0	47.7 ± 44.2	29.4 ± 22.7	51.9 ± 46.7
Cr <sup>+</sup>	48.0 ± 20.2	52.5 ± 24.1	16.3 ± 19.1	27.9 ± 13.9	36.2 ± 19.3
Cu <sup>+</sup>	15.4 ± 8.05	16.2 ± 11.1	4.04 ± 3.17	2.41 ± 1.18	9.51 ± 5.88
As <sup>+</sup>	51.8 ± 23.8	48.9 ± 29.5	20.9 ± 19.5	29.7 ± 23.8	37.8 ± 24.2
Pb <sup>+</sup>	17.7 ± 11.6	86.7 ± 56.3	45.3 ± 33.8	19.9 ± 11.9	42.4 ± 28.4
Fe <sup>+</sup>	257.5 ± 86.6	161.9 ± 149.8	200.9 ± 174.5	164.8 ± 90.7	196.3 ± 125.4
Al <sup>+</sup>	264.9 ± 131.8	199.0 ± 134.5	123.5 ± 65.3	89.1 ± 61.6	169.1 ± 98.3
V <sup>+</sup>	151.7 ± 77.8	198.2 ± 110.9	202.4 ± 172.9	137.3 ± 99.9	172.4 ± 115.4
Ag <sup>+</sup>	1.38 ± 1.00	2.58 ± 1.79	2.82 ± 2.97	2.29 ± 1.94	2.27 ± 1.93
Bi <sup>+</sup>	3.73 ± 1.54	10.2 ± 15.3	4.59 ± 1.24	3.78 ± 1.12	5.58 ± 4.80
Ce <sup>+</sup>	0.31 ± 0.09	0.34 ± 0.77	0.39 ± 0.65	0.17 ± 0.15	0.30 ± 0.42
Sr <sup>+</sup>	90.5 ± 127.7	233.6 ± 270.6	45.3 ± 50.1	27.7 ± 23.9	99.3 ± 118.1
Sb <sup>+</sup>	5.07 ± 2.03	4.53 ± 2.20	3.11 ± 3.20	5.61 ± 5.39	4.58 ± 3.21
Levoglucosan, WSOC, homohopanes					
Levo (ng m <sup>-3</sup> ) <sup>+</sup>	132.4 ± 9.20	127.4 ± 6.70	123.9 ± 4.38	124.1 ± 5.71	126.9 ± 6.62
WSOC (µg m <sup>-3</sup> ) <sup>+</sup>	6.02 ± 2.84	9.25 ± 2.89	5.89 ± 2.75	3.95 ± 1.89	6.28 ± 2.95
C31αβS <sup>+</sup> (ng m <sup>-3</sup> ) <sup>+</sup>	0.28 ± 0.14	0.11 ± 0.05	0.09 ± 0.07	0.06 ± 0.06	0.13 ± 0.13
C31αβR <sup>+</sup> (ng m <sup>-3</sup> ) <sup>+</sup>	0.04 ± 0.02	0.11 ± 0.09	0.03 ± 0.01	0.07 ± 0.04	0.06 ± 0.04

Quinones (ng m <sup>-3</sup> )					
1, 2-NQ <sup>+</sup>	0.53 ± 0.23	0.69 ± 0.34	0.59 ± 0.21	1.09 ± 0.46	0.72 ± 0.39
1, 4-NQ <sup>+</sup>	0.06 ± 0.03	0.12 ± 0.06	0.06 ± 0.02	0.09 ± 0.05	0.08 ± 0.05
1, 4-AQ <sup>+</sup>	0.48 ± 0.11	0.38 ± 0.34	0.13 ± 0.04	0.35 ± 0.10	0.34 ± 0.20
Gaseous pollutants (µg m <sup>-3</sup> )					
NO <sub>2</sub> <sup>+</sup>	42.7 ± 19.3	36.9 ± 20.5	30.0 ± 15.7	13.5 ± 9.12	34.6 ± 19.8
SO <sub>2</sub> <sup>+</sup>	9.41 ± 4.02	9.85 ± 2.77	7.82 ± 3.88	7.35 ± 1.67	8.88 ± 3.59
O <sub>3</sub> <sup>+</sup>	51.3 ± 37.2	58.2 ± 32.5	86.1 ± 43.4	70.6 ± 40.8	65.3 ± 40.7

<sup>+</sup>p ≤ 0.05 (ANOVA, mean concentrations statistically significant)

### 5.2.2. Marine source contributions: diurnal and seasonal variations

Acknowledging the potential contributions of aerosols from marine sources at our monitoring station, which is located in close proximity to the Ningbo-Zhoushan port and the East China Sea, we conducted an investigation to evaluate the potential impact of marine emissions. The non-sea salt (nss) content of WSIs such as  $K^+$ ,  $Ca^{2+}$ ,  $Mg^{2+}$ , and  $SO_4^{2-}$  was estimated using equation (5-1) (Guo et al., 2023). The assumption made is that the primary source of  $Na^+$  is the sea.

$$nss-X = X_i - Na^+_i \times \left( \frac{X}{Na^+} \right)_{sea} \quad (5-1)$$

where  $X_i$  and  $Na^+_i$  represent the concentration of the ion and  $Na^+$  in aerosol samples, respectively.  $(X/Na^+)_{sea}$  refers to the ratio of the ion and  $Na^+$  in seawater. According to the composition of seawater, the  $(X/Na^+)_{sea}$  ratios for  $Ca^{2+}$ ,  $K^+$ ,  $Mg^{2+}$ , and  $SO_4^{2-}$  are 0.0385, 0.037, 0.12, and 0.2516, respectively (Guo et al., 2023; Nair et al., 2005).

Figure 5-3 illustrates the concentrations of  $nss-SO_4^{2-}$ ,  $nss-Mg^{2+}$ ,  $nss-K^+$ , and  $nss-Ca^{2+}$ , as well as the corresponding ratios of  $nss-SO_4^{2-}/SO_4^{2-}$ ,  $nss-Mg^{2+}/Mg^{2+}$ ,  $nss-K^+/K^+$ , and  $nss-Ca^{2+}/Ca^{2+}$  during daytime and at night. The concentration of  $nss-SO_4^{2-}$  was higher during the day compared to at night, suggesting that secondary sulfate formation is more dominant during the day. This finding demonstrates a consistent pattern of higher concentrations of  $SO_4^{2-}$  during the daytime compared to nighttime. The observed increase can be attributed to intensified emissions of  $SO_2$  from anthropogenic activities, such as industrial sources and vehicular traffic, during the day in contrast to the night (Wang et al., 2019). More the high



temperatures and solar radiation, along with the presence of oxidants like  $\text{H}_2\text{O}_2$ ,  $\text{O}_3$ , and  $\cdot\text{OH}$ , facilitate the photochemical oxidation of  $\text{SO}_2$  to  $\text{SO}_4^{2-}$  during the day.

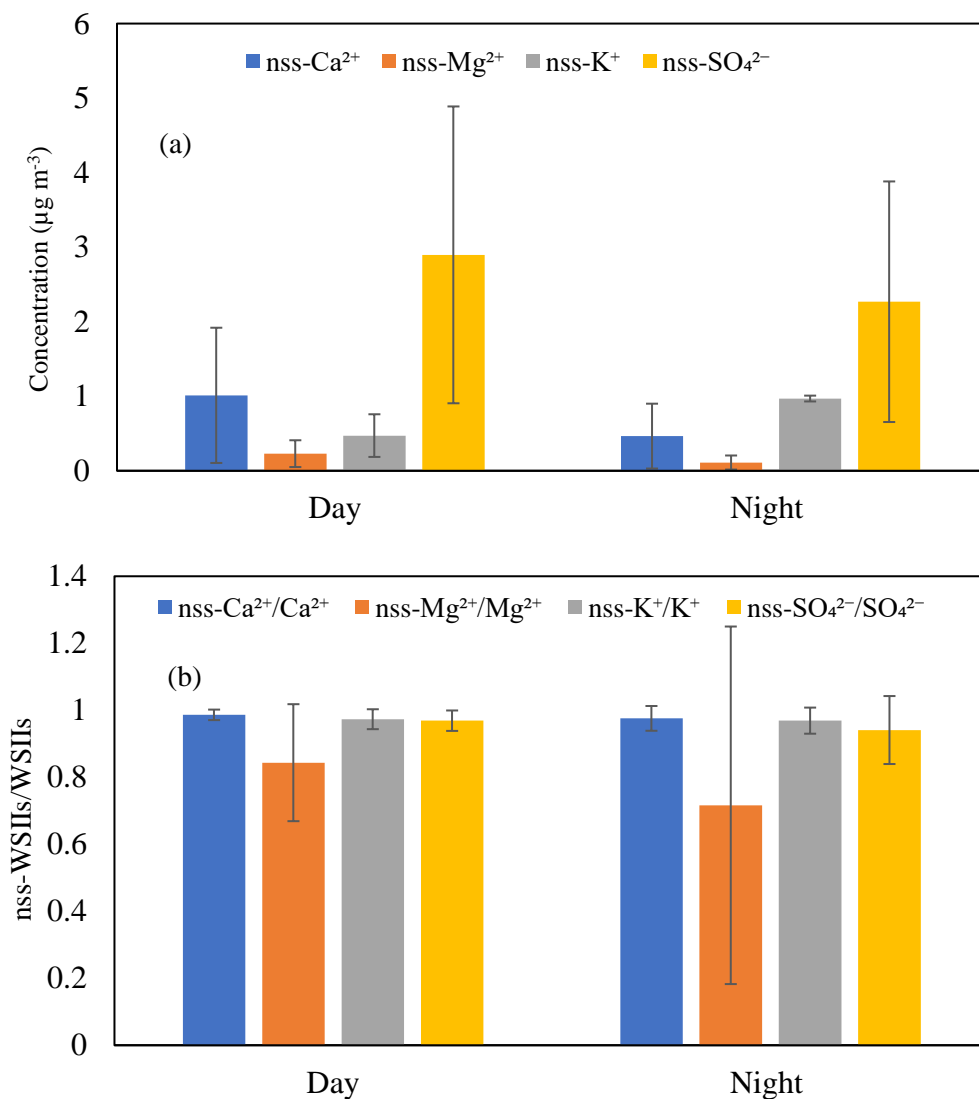


Figure 5-3 Day and night concentration of non-sea salts and their respective non-sea salt ionic fractions in  $\text{PM}_{2.5}$  collected in a residential/commercial site of Ningbo, China. Error bar present the standard deviation (level of variability of the data)

Higher ratios ( $\geq 0.94$ ) of nss- $\text{SO}_4^{2-}/\text{SO}_4^{2-}$ , nss- $\text{K}^{+}/\text{K}^{+}$  and nss- $\text{Ca}^{2+}/\text{Ca}^{2+}$  were observed during both day and night. This suggest a minor marine influence ( $\leq 6\%$ ) on these ions. A

lower ratio of  $\text{nss-Mg}^{2+}/\text{Mg}^{2+}$  was observed compared to other ions with lower values during the night than at day. This finding suggests that sea salt contribute more to  $\text{Mg}^{2+}$  in comparison to other ions during the day and at night.

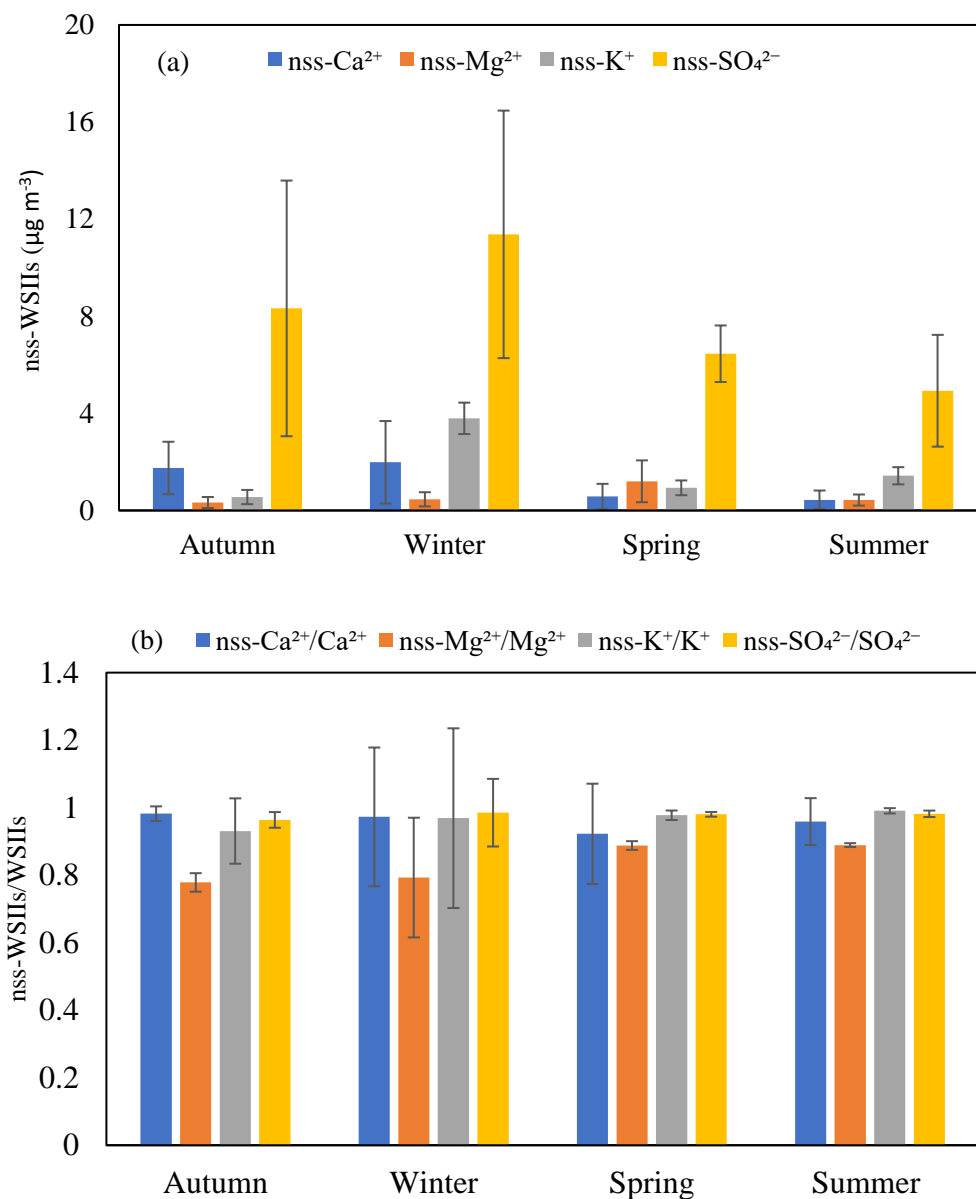


Figure 5-4 Seasonal concentration of non-sea salts (a) and their respective non-sea salt ionic fractions (b) in  $\text{PM}_{2.5}$  collected in a residential/commercial site of Ningbo, China. Error bar present the standard deviation (level of variability of the data)

The trends of  $\text{nss-SO}_4^{2-}/\text{SO}_4^{2-}$ ,  $\text{nss-Mg}^{2+}/\text{Mg}^{2+}$ ,  $\text{nss-K}^+/\text{K}^+$ , and  $\text{nss-Ca}^{2+}/\text{Ca}^{2+}$  are almost similar across all seasons, as depicted in Figure 5-4. The  $\text{nss-SO}_4^{2-}/\text{SO}_4^{2-}$ ,  $\text{nss-K}^+/\text{K}^+$ , and  $\text{nss-Ca}^{2+}/\text{Ca}^{2+}$  ratios were consistently  $\geq 0.93$  across all seasons, indicating a minor influence ( $\leq 7\%$ ). However, the  $\text{nss-Mg}^{2+}/\text{Mg}^{2+}$  ratio ranged from 0.78 to 0.89, suggesting a significantly greater contribution of sea salt to  $\text{Mg}^{2+}$  in comparison to other ions ( $\text{Ca}^{2+}$ ,  $\text{SO}_4^{2-}$ , and  $\text{K}^+$ ).

The presence of  $\text{nss-K}^+$  has often been used as an indicator of biomass burning sources. It was observed that concentrations of  $\text{nss-K}^+$  were higher during nighttime and winter periods. This suggests that biomass burning contributes more to the elevated levels of fine particles during these nocturnal hours and in the winter season. Moreover, the relatively higher concentrations of  $\text{nss-K}^+$  in autumn and spring can also be attributed to biomass burning, specifically the burning of straw during harvest periods in the region (Yang and Zhao, 2019). The emissions of  $\text{nss-K}^+$  can be linked to the transportation of air masses from agricultural areas to our monitoring site. Additionally, the higher values of  $\text{nss-Ca}^{2+}/\text{Ca}^{2+}$  ratios indicate that  $\text{Ca}^{2+}$  primarily originates from suspended dust particles instead of marine sources. Furthermore, during the sampling campaign, construction activities took place in close proximity to our study area during the daytime. These activities potentially contributed to higher levels of  $\text{nss-Ca}^{2+}$  during the daytime compared to nighttime.

### 5.2.3. Aerosol acidity

#### 5.2.3.1. Ion balance

Water-soluble inorganic ions play a pivotal role in the regulation of aerosol acidity. In this study, we employed ion balance analysis to comprehensively investigate aerosol acidity.

This analysis necessitates the calculation of both the anion equivalence (AE) and cation equivalence (CE) using the following equations (Meng et al., 2016; Yao et al., 2020):

$$AE = \frac{F^-}{19} + \frac{Cl^-}{35.5} + \frac{NO_3^-}{62} + \frac{SO_4^{2-}}{48} \quad (5-2)$$

$$CE = \frac{Na^+}{23} + \frac{NH_4^+}{18} + \frac{K^+}{39} + \frac{Mg^{2+}}{12} + \frac{Ca^{2+}}{20} \quad (5-3)$$

where,  $F^-$ ,  $Cl^-$ ,  $NO_3^-$ ,  $SO_4^{2-}$ ,  $Na^+$ ,  $NH_4^+$ ,  $K^+$ ,  $Mg^{2+}$ , and  $Ca^{2+}$  in equation (5-2) and (5-3) represent to the mass concentrations ( $\mu g m^{-3}$ ) of WSIIIs.

Figure 5-5 shows the relationship between AE and CE calculated from WSIIIs during daytime and nighttime. During both daytime and nighttime, respectively, a strong and moderate relationship with negligible intercept was observed between AE and CE. The slope of the regression line represents the ratio of anion/cation equivalents. A ratio greater than 1 indicates that the aerosol is acidic (Meng et al., 2016). The ratio of AE/CE during the daytime and nighttime were 0.99 and 1.54, respectively. The higher ratio observed at night suggests a deficiency of cations to neutralize the anions in  $PM_{2.5}$ . This indicates that aerosols collected at night were more acidic. In contrast, the ratio during the day is close to 1, indicating a sufficient presence of cations to balance the anions. This suggests that the aerosol is less acidic during the day compared to nighttime. The elevated relative humidity levels at night ( $77.1 \pm 13.0\%$ ) than daytime ( $64.8 \pm 15.8\%$ ) can potentially result in the dissolution of gaseous species (e.g.,  $SO_2$ ,  $NO_2$ ,  $HCl$ ,  $NO_3$ ,  $H_2SO_4$ , etc.), leading to an increase in aerosol acidity. Additionally, during nighttime, the water content of the aerosol increases, resulting in a decrease in pH (Glasow and Sander, 2001; Wang et al., 2019). Furthermore, the

nocturnal aerosols exhibit elevated levels of  $\text{NO}_3^-$ , which are approximately twice as high as the levels detected during daytime. This disparity in concentrations could potentially play a role in the increased acidity observed in aerosols during nighttime.

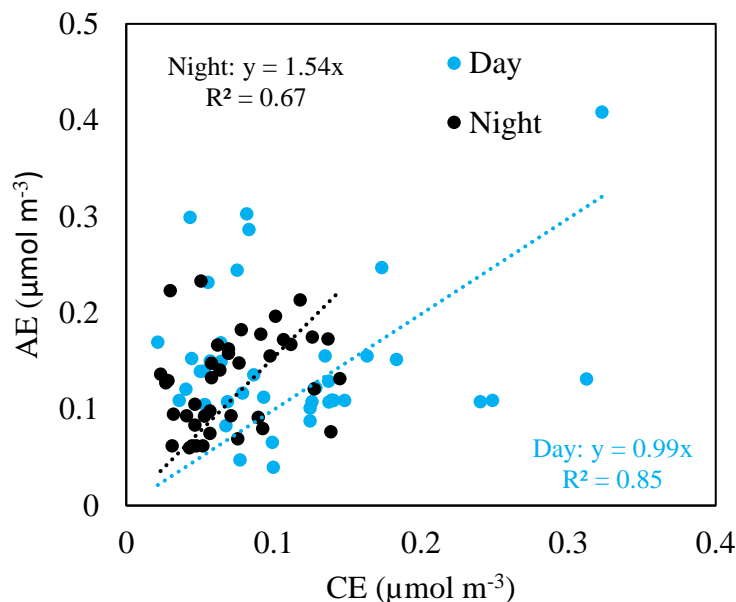


Figure 5-5 Plot of anion equivalents (AE) vs cation equivalent WSIs in PM<sub>2.5</sub> in daytime and at night

The ratio of AE to CE consistently exceeds 1 throughout all seasons (as shown in Figure 5-6), indicating a deficiency of cations in the aerosols to balance the anions. This finding suggests that the aerosols collected at our monitoring station during the year-long field campaign are consistently acidic. Additionally, it is important to note that the ratios were higher in warmer seasons compared to colder seasons, with summer showing the highest level of acidity, followed by spring, winter, and autumn. The heightened aerosol acidity in summer can be attributed to the combination of elevated relative humidity and solar radiation. The increased water vapor in the atmosphere during summer leads to the absorption of water by aerosol particles, resulting in their enhanced acidity (Zhou et al., 2012). This occurs because water vapor reacts with  $\text{SO}_2$  and  $\text{NO}_x$ , forming  $\text{H}_2\text{SO}_4$  and  $\text{HNO}_3$ , respectively.

Furthermore, solar radiation induces photochemical reactions, generating acidic species such as  $\text{H}_2\text{O}_2$  and organic acids (e.g., formic acids) in aerosol particles (Jiang et al., 2023). These compounds further contribute to the overall acidity of the aerosols collected at our study domain.

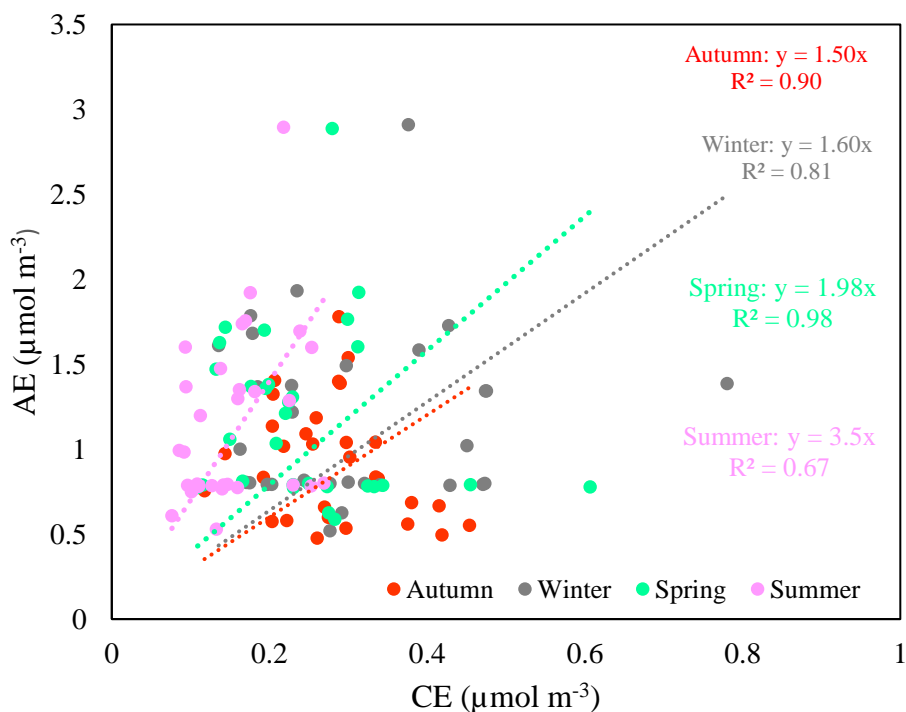


Figure 5-6 Plot of anion equivalents (AE) vs cation equivalent (CE) of WSIs in  $\text{PM}_{2.5}$  in four seasons

To determine the acidity of aerosols during different times of the day and across seasons, we investigated the ratio of  $[\text{NH}_4^+]/([\text{NO}_3^-]+[\text{SO}_4^{2-}])$  (Do et al., 2021). A ratio of less than 1 implies an insufficient amount of  $\text{NH}_4^+$  present in the aerosol. This partial neutralization of  $\text{NO}_3^-$  by  $\text{NH}_4^+$  suggests the potential formation of  $\text{NH}_4\text{HSO}_4$ , as  $\text{NH}_4^+$  tends to preferentially neutralize  $\text{SO}_4^{2-}$  over  $\text{NO}_3^-$  (Guo et al., 2020). In contrast, a ratio greater than 1 suggests an alkaline aerosol, where  $\text{NH}_4^+$  entirely neutralizes  $\text{SO}_4^{2-}$  and  $\text{NO}_3^-$  to form all three secondary

inorganic aerosols (SIAs):  $(\text{NH}_4)_2\text{SO}_4$  and  $\text{NH}_4\text{NO}_3$ , and  $\text{NH}_4\text{HSO}_4$  (Guo et al., 2023; Hong et al., 2022).

The ratio of  $[\text{NH}_4^+]$  to  $([\text{NO}_3^-] + [\text{SO}_4^{2-}])$  during the day and night was 0.56 and 0.51, respectively. This implies that the aerosols collected during these time periods were acidic. The ratios in autumn, winter, spring, and summer were 0.22, 0.14, 0.07, and 0.06, respectively. This finding confirms that the aerosols collected in our study domain were consistently acidic throughout all seasons, with the highest levels of acidity observed during the summer and spring.

#### 5.2.3.2. Neutralization Factors (NFs)

To assess the ability of major cations to neutralize  $\text{SO}_4^{2-}$  and  $\text{NO}_3^-$ , we estimated the neutralization factors (NFs) of  $\text{NH}_4^+$ , nss- $\text{Ca}^{2+}$ , nss- $\text{Mg}^{2+}$ , and nss- $\text{K}^+$ . The neutralization factors of these ions were estimated using the following equations (5-4 to 5-7) (Guo et al., 2023). The assumption is that  $\text{Na}^+$  and  $\text{Cl}^-$  predominantly exist in the form of sea salt. However, the ratios of  $\text{Na}^+/\text{Cl}^-$  during daytime (0.2), nighttime (0.25), and across different seasons (0.12–0.34) are lower than the ratio observed in seawater (1.1). This suggests that  $\text{Cl}^-$  originate from other sources, including coal combustion (Xu et al., 2016).

$$\text{NF} (\text{NH}_4^+) = \frac{[\text{NH}_4^+]}{(2[\text{nss-SO}_4^{2-}] + [\text{NO}_3^-] + [\text{Cl}^-] - [\text{Na}^+]/1.1)} \quad (5-4)$$

$$\text{NF} (\text{nss-K}^+) = \frac{[\text{nss-K}^+]}{(2[\text{nss-SO}_4^{2-}] + [\text{NO}_3^-] + [\text{Cl}^-] - [\text{Na}^+]/1.1)} \quad (5-5)$$

$$\text{NF} (\text{nss-Ca}^{2+}) = \frac{[\text{nss-Ca}^{2+}]}{([\text{nss-SO}_4^{2-}] + 2[\text{NO}_3^-] + 2[\text{Cl}^-] - 2[\text{Na}^+]/1.1)} \quad (5-6)$$

$$\text{NF (nss-Mg}^{2+}) = \frac{[\text{nss} - \text{Mg}^{2+}]}{([\text{nss-SO}_4^{2-}] + 2[\text{NO}_3^-] + 2[\text{Cl}^-] - 2[\text{Na}^+]) / 1.1} \quad (5-7)$$

The estimated NFs of  $\text{NH}_4^+$ ,  $\text{nss-K}^+$ ,  $\text{nss-Mg}^{2+}$ , and  $\text{nss-Ca}^{2+}$  during the day and at night are shown in Figure 5-7. The NF of  $\text{NH}_4^+$  during the day (0.04) and night (0.02) is extremely lower than 1, indicating a deficiency of  $\text{NH}_4^+$  to neutralize  $\text{SO}_4^{2-}$  and  $\text{NO}_3^-$ . The NFs of  $\text{nss-K}^+$  is higher at night compared to during the day, while the NFs of  $\text{nss-Ca}^{2+}$  shows the opposite trend with higher values during the day than at night.

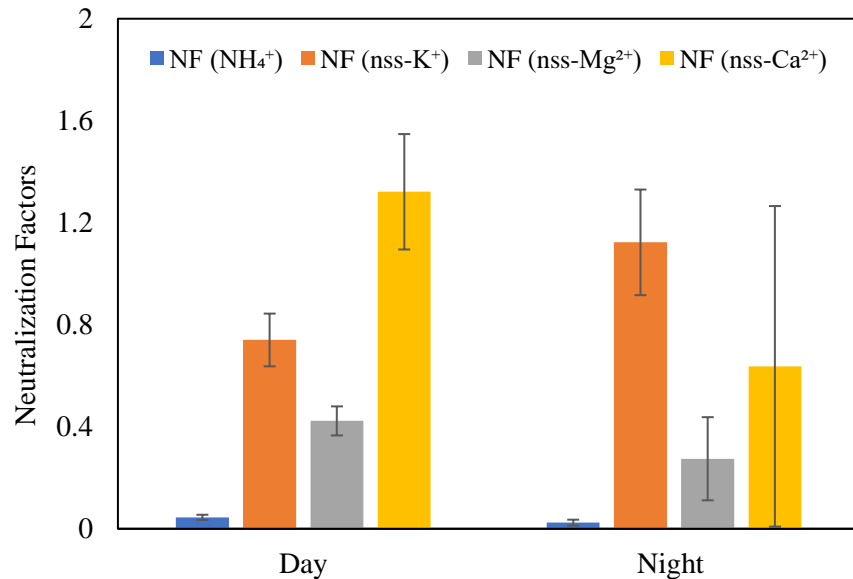


Figure 5-7 Neutralization factors of  $\text{NH}_4^+$ ,  $\text{nss-K}^+$ ,  $\text{nss-Mg}^{2+}$ , and  $\text{nss-Ca}^{2+}$  during the day and night. Error bar present the standard deviation (level of variability of the data)

This suggests that  $\text{nss-K}^+$  exhibits relatively higher neutralization of aerosol acidity during the night, whereas  $\text{nss-Ca}^{2+}$  has a greater effect during the day. This indicates that the monitoring station, which is surrounded by several construction activities during the day, contributed to the higher neutralization factors (NFs) of  $\text{Ca}^{2+}$ . The combustion of wood for domestic heating, especially in rural areas of the city, could have contributed to the high concentrations of  $\text{K}^+$  at night. Additionally, the long-range transport of  $\text{K}^+$  from other cities



and provinces could contribute to the high NFs observed at night. These factors potentially contribute to the observed NFs of  $\text{Ca}^{2+}$  and  $\text{K}^+$  during both day and night, respectively.

The NFs of  $\text{NH}_4^+$ ,  $\text{nss-K}^+$ ,  $\text{nss-Mg}^{2+}$ , and  $\text{nss-Ca}^{2+}$  in four seasons are shown in Figure 5-8. The NFs of  $\text{NH}_4^+$  consistently remained lower across all seasons. However, the NFs of  $\text{nss-K}^+$ ,  $\text{nss-Mg}^{2+}$ , and  $\text{nss-Ca}^{2+}$  were higher in winter compared to other seasons. The higher NFs of  $\text{nss-K}^+$  in winter can be attributed to increase wood combustion for domestic heating, while the considerably higher values in spring can be attributed to open burning of crop residues (Zhang et al., 2016; Zhao et al., 2017). The highest  $\text{nss-Ca}^{2+}$  levels in winter and autumn may be due to the strong dust effect from nearby construction areas and the proximity of freeways to our study domain. This is supported by slightly high wind speed in autumn and winter than in summer and spring (as shown in Table 4.3).

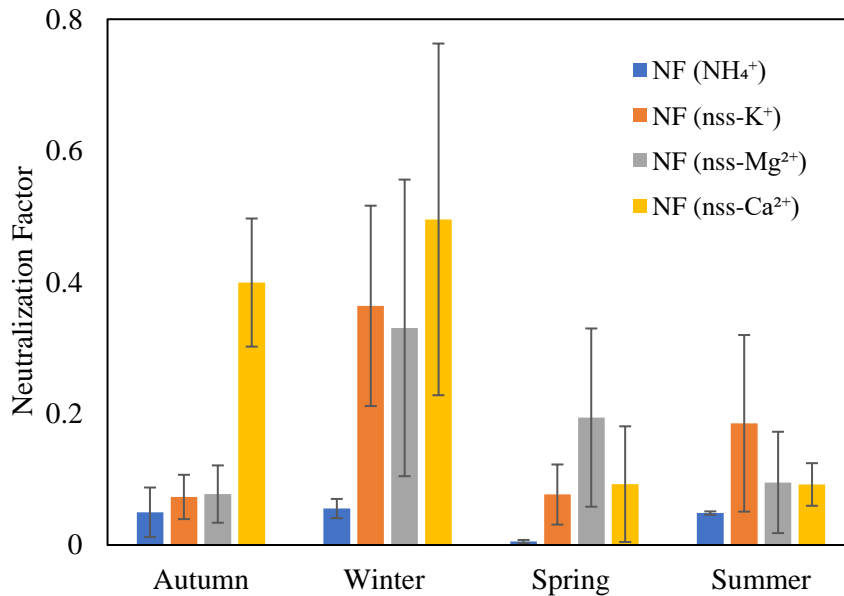


Figure 5-8 Neutralization factors of  $\text{NH}_4^+$ ,  $\text{nss-K}^+$ ,  $\text{nss-Mg}^{2+}$ , and  $\text{nss-Ca}^{2+}$  in four seasons. Error bar present the standard deviation (level of variability of the data)

#### 5.2.4. Oxidative potential of PM<sub>2.5</sub>

The water-soluble fraction of PM<sub>2.5</sub> contained hydrophilic chemical species such as trace metals, quinones, and WSOC, which are the main contributors to the OP in DTT assay (Xing et al., 2023). The methanol-soluble fraction of PM<sub>2.5</sub> comprises of both water-soluble and water-insoluble components, owing to its lower polarity than water. Therefore, similar chemical compositions may be extracted in both water and methanol PM fractions, indicating that the OP of the water and methanol soluble fractions are not mutually exclusive (Famiyeh, Jia, et al., 2023). However, as indicated by Verma et al., (2012), it is common for methanol fractions to contain higher concentrations of organic compounds in comparison to water-soluble fractions.

The OP induced by water and methanol extracts was expressed in terms of extrinsic values (OP per air volume, nmol min<sup>-1</sup> m<sup>-3</sup>) and intrinsic values (OP per PM mass, pmol min<sup>-1</sup> μg<sup>-1</sup>). Extrinsic OP of PM pertains to the ROS generation in human cells, mediated by chemical components, such as metal ions and organic compounds. The intrinsic OP of PM refers to its inherent ability of the particle to induce oxidative stress in human cells through ROS generation (Farahani et al., 2022). Measuring OP by air volume helps estimate human exposure to PM and the associated health risks, while OP per PM mass quantifies the ability of PM to generate OP (Borlaza et al., 2018; Verma et al., 2009).

##### 5.2.4.1. OP induced by water-and methanol soluble PM<sub>2.5</sub>: diurnal variations

The study assessed the OP induced by water-soluble and methanol-soluble fractions of PM<sub>2.5</sub> during the day and at night using two methods-DTT and AA assays. Specifically, the DTTv induced by water-soluble fractions showed values of  $0.39 \pm 0.10$  nmol min<sup>-1</sup>m<sup>-3</sup> for nighttime and  $0.25 \pm 0.13$  nmol min<sup>-1</sup>m<sup>-3</sup> for daytime (as shown in Figure 5-9 a), while AA v

values were  $0.31 \pm 0.22 \text{ nmol min}^{-1}\text{m}^{-3}$  for nighttime and  $0.23 \pm 0.09 \text{ nmol min}^{-1}\text{m}^{-3}$  for daytime (as shown in Figure 5-9 b). The high nighttime DTTv induced by water-soluble fraction of  $\text{PM}_{2.5}$  is consistent with the findings of a previous study carried out in Taiwan (Hsiao et al., 2021). Similarly, Ainur et al. (2023) reported that  $\text{PM}_{2.5}$  exhibited higher DTTv values during nighttime compared to daytime. In contrast, Ahmad et al. (2021) reported higher DTTv of  $\text{PM}_{2.5}$  during the daytime compared to nighttime in Lahore and Peshawar, Pakistan. This discrepancy can be attributed to variations in the contributions from various sources, differences in the duration of sample collection, and the diverse meteorological impacts. For example, Ahmad et al. (2021) conducted day and night OP analysis of  $\text{PM}_{2.5}$  particles collected only during cold seasons.

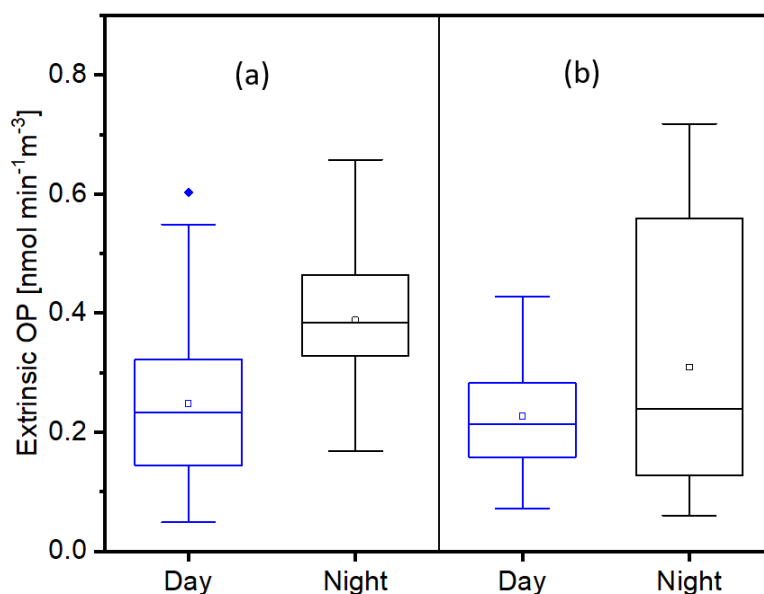


Figure 5-9 Day and night extrinsic OP induced by water-soluble fractions of  $\text{PM}_{2.5}$  measured in DTT (a) and AA (b) assays. Median (line across the box), mean (square within the box), first quartile (Q1) (bottom of the box), third quartile (Q3) (top of the box), outlier (square shown outside the box), whiskers shows minimum and maximum values

This study presents the levels of PM<sub>2.5</sub>-induced OP during both daytime and nighttime, determined through a 12-hour aerosol sampling campaign that included samples collected during both the cold and warm seasons. Furthermore, it is worth noting that the scarcity of literature on the OP of PM<sub>2.5</sub> during both daytime and nighttime poses a challenge for making a comprehensive comparison of our results with previous studies.

The methanol-soluble fraction results indicated slightly higher DTTv at night than during the day ( $0.23 \pm 0.12 \text{ nmol min}^{-1}\text{m}^{-3}$  for nighttime versus  $0.18 \pm 0.08 \text{ nmol min}^{-1}\text{m}^{-3}$  for daytime, as shown in Figure 5-10 a) and AA<sub>v</sub> ( $0.80 \pm 0.31 \text{ nmol min}^{-1}\text{m}^{-3}$  for nighttime versus  $0.74 \pm 0.24 \text{ nmol min}^{-1}\text{m}^{-3}$  for daytime, shown in Figure 5-10 b) assays. The intrinsic OP induced by water- and methanol-soluble PM<sub>2.5</sub> fractions measured in both DTT and AA assays revealed higher values during the nighttime compared to the daytime, as illustrated in Appendix (Figure 8-1). The observed increase in intrinsic OP of PM<sub>2.5</sub> in DTT and AA assays during the night could be linked to high OP and low concentration of PM<sub>2.5</sub> particles (Famiyeh, Jia, et al., 2023). To examine the potential chemical species that induce OP of PM<sub>2.5</sub> during daytime and nighttime, a Pearson correlation analysis was conducted (Section 5.2.4.2).

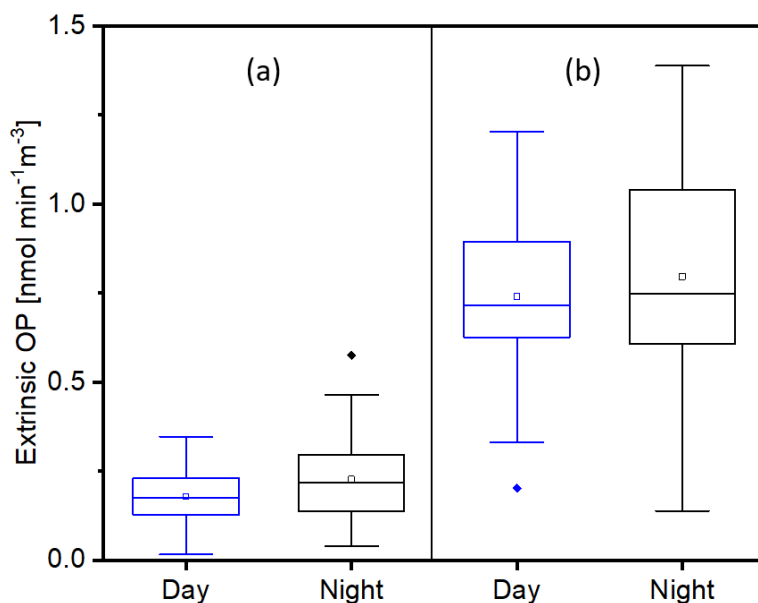


Figure 5-10 Day and night extrinsic OP induced by methanol-soluble fractions of PM<sub>2.5</sub> measured in DTT (a) and AA (b) assays. Median (line across the box), mean (square within the box), first quartile (Q1) (bottom of the box), third quartile (Q3) (top of the box), outlier (square shown outside the box), whiskers shows minimum and maximum values

#### 5.2.4.2. Chemical species associated with OP: day and night variations

The total concentrations of water-soluble trace metals and quinones (such as 1, 2-NQ and 1, 4-NQ) indicated in Table 5.1, as well as the total PAHs presented in Table 4.1, exhibited similar levels during both daytime and nighttime periods. Although human activities are generally lower at nighttime, the combination of a lower mixing layer height, low wind speed, and high relative humidity contribute to poor diffusion and dispersion of these chemicals species (Do et al., 2023). Therefore, these chemical species tend to accumulate more in PM<sub>2.5</sub>, thus contributing to their elevated levels during nighttime (Virgilio et al., 2018). This could contribute to the increase in OP levels at night. For example, at night, AA<sub>v</sub> induced by methanol-soluble fractions exhibit strong and moderate correlation with ambient temperatures and relative humidity, respectively, as shown in the Appendix (Table 8.6).

In Chapter 4 (Sections 4.2.4), we presented evidence demonstrating that the aerosols collected at nighttime are photochemical aged, while those collected during the daytime comprised of a higher proportion of freshly emitted aerosols from human activities, including traffic emissions. This is supported by lower BaA/Chr, LMW-PAHs/PM<sub>2.5</sub> (Lv et al., 2016; Wu et al., 2010). The aerosols that undergo photochemical aging are produced during the day and become more OP active during the night due to stable meteorological conditions. For instance, when VOCs and LMW-PAHs are released, they experience photochemical oxidation in response to intense solar radiation and the presence of oxidizing agents during daytime hours (Jin et al., 2016). This indicates that secondary quinones are generated during the photochemical oxidation of LMW-PAHs (Wang et al., 2018). The reactive properties of these OP chemicals appeared to be more active during nighttime when sunlight is not present. This provides an explanation for the high levels of OP observed in the photochemically aged aerosols collected during nighttime. This is consistent with the findings of Hsiao et al. (2021), which indicated that photochemically aged aerosols exhibit high OP activity.

To identify specific chemical species that are responsible for the OP of PM<sub>2.5</sub> during both daytime and nighttime, Pearson's correlation analysis was performed between OP and the concentration of various chemical species. The analysis revealed that the DTTv induced by water-soluble fraction of PM<sub>2.5</sub> during the day exhibit a strong correlation with trace metals, such as Co, Ni, Ba, Sr, and As, as well as a moderate correlation with Mn, Cu, Al, Fe, Ag, V, Ce, and Sr, (as displayed in Table 5.3). Moreover, it correlated with Ca<sup>2+</sup>, Mg<sup>2+</sup>, Na<sup>+</sup>, K<sup>+</sup>, 1, 4-NQ, and 1, 4-AQ. Conversely, at night, DTTv exhibited a moderate correlation with Ni,

V, 1, 2-NQ, WSOC,  $\text{NO}_3^-$ , and strongly correlated with  $\text{F}^-$  (as displayed in Table 5.4). The correlation observed between nighttime DTTv and chemical species such as WSOC and  $\text{NO}_3^-$  indicates a substantial contribution of secondary aerosols to the elevated OP during nighttime, which may not be as pronounced during the daytime. The reaction between  $\text{NO}_3$  radical and biogenic VOCs at night could lead to SOA formation consisting of low-volatile organic nitrates (Zaveri et al., 2010). This could potentially contribute to the high OP levels at night. This reaction is particularly pronounced at night, where the oxidation of volatile/semivolatile organics is primarily controlled by nitrate radicals instead of other oxidants, such as ozone.

The AAv induced by water-soluble fraction of  $\text{PM}_{2.5}$  during the day exhibit moderate correlation with Cu, Pb, Ag, Bi, Sb,  $\text{Na}^+$ , and  $\text{K}^+$  (as shown in Table 5.3). At nighttime, a moderate correlation was observed with trace metals such as Ni, As, and Pb, and strong correlation with quinone 1, 2-NQ ( $r = 0.82$ ) (as represented Table 5.4). These findings suggest that the presence of these elements, along with the quinone 1, 2-NQ, may have played a role in the nighttime increase of AAv levels. However, it is possible that unanalyzed chemical species, such as HULIS, and high molecular weight quinones, may contribute to the observed discrepancies in daytime and nighttime DTTv and AAv induced by water-soluble fractions of  $\text{PM}_{2.5}$ .

During the day, the DTTv of the methanol extract showed a strong correlation with As, Cr, and  $\text{Cl}^-$ , and a moderate correlation with Co and  $\text{SO}_4^{2-}$ , as shown in the Appendix (Table 8.5). At night, the DTTv induced by methanol-soluble fraction exhibited a strong correlation with WSOC and  $\text{O}_3$  (as shown in Table 8.6). This finding suggests that secondary aerosols

formed through the daytime oxidation of VOCs by ozone (Berezina et al., 2020) persist in the ambient air at night and contribute to elevated OP levels.

The AAv of the methanol-soluble fraction correlated strongly with Cu and moderately with Fe, Zn, Ce, Sr, and  $\text{SO}_4^{2-}$  during the day (as depicted in Table 8.5), while at night, it correlated strongly with  $\text{NO}_3^-$ , WSOC, and Ce, and moderately with Zn, Pb, Ag, and 7H-BcF. There was no correlation observed between AAv and quinones during both daytime and nighttime, which suggests that the AA assay exhibited greater sensitivity to trace metals compared to quinones.

The correlation between OP and  $\text{PM}_{2.5}$  concentration was found to be weak, as consistent with a previous study by Xing et al., (2023). A moderate correlation was specifically observed for the nighttime DTTv induced by water-soluble fraction of  $\text{PM}_{2.5}$ . However, a consistently moderate-to-strong correlation was observed for the majority of chemical compositions and intrinsic OP. Based on the correlation analysis, chemical species, including PAHs (such as DBalPyr and DBaePyr), WSOCs, trace metals (e.g., Cu, Mn, Ni, Cd, Zn, Ce, Pb, Ag, Ba, Bi, and As), inorganic ions ( $\text{Na}^+$ ,  $\text{Mg}^{2+}$ ,  $\text{Ca}^{2+}$ ,  $\text{K}^+$ ,  $\text{NO}_3^-$ ), and quinones (e.g., 1, 4-NQ), may contribute to the intrinsic OP. For example, strong correlations were found between PAHs (e.g., DBalPyr and DBaePyr) and DTTm, although it remains unclear whether PAHs can directly exhibit OP effect through electron transfer reactions. However, their correlation suggests that they may act as proxies for highly reactive sources of specific quinones with high OP activity (Janssen et al., 2014). Consequently, the co-occurrence of high concentrations of PAHs and quinones could potentially elevate the OP levels induced by  $\text{PM}_{2.5}$  particles.



To sum up, the elevated OP at night can be attributed to photochemically generated aerosols. These aerosols are generated during the day and persist at night, becoming more OP active due to favorable atmospheric conditions. These conditions include low temperature and high relative humidity, which promote their accumulation on pre-existing particles (Do et al., 2023). During nighttime, the occurrence of oxidation of biogenic VOCs by NO<sub>3</sub> radical, lead to SOA formation, which could potentially contribute to the elevated levels of OP during nighttime (Ng et al., 2017).

Aerosols collected during both daytime and nighttime have been demonstrated to exhibit acidity, with nighttime aerosols being more acidic. The initial hypothesis was that the high aerosol acidity at night would contribute to the levels of OP through the dissolution of metals. However, the results of Pearson's correlation analysis revealed only a moderate correlation between nighttime OP and trace metals, while a strong correlation was observed between daytime OP and trace metals. Specifically, nighttime OP exhibited a moderate correlation with trace metals such as Ni, V, As, Pb, and As, as shown in Table 5.4. In contrast, daytime OP showed a moderate to strong correlation with several trace metals including Mn, Co, Ni, Ba, Cu, As, V, Ag, and Zn, as shown in Table 5.3. Therefore, it can be concluded that the higher levels of OP observed at night are primarily attributed to the secondary generation of aerosols through the photochemical aging process, rather than being influenced by the dissolution of trace metals due to high aerosol acidity.

Table 5.3 Pearson's correlation (r) between OP induced by water-soluble fraction of PM<sub>2.5</sub> and chemical compositions during daytime

	DTTv	DTTm	AAv	AAm	PM <sub>2.5</sub>	F <sup>-</sup>	Cl <sup>-</sup>	NO <sub>3</sub> <sup>-</sup>	SO <sub>4</sub> <sup>2-</sup>	NH <sub>4</sub> <sup>+</sup>	Na <sup>+</sup>	K <sup>+</sup>	Mg <sup>2+</sup>	Ca <sup>2+</sup>	Mn	Co	Ni	Cd	Zn	Ba	Cr	Cu	Al	As	Pb	Fe	V	Ag	Bi	Ce	Sr	Sb	1,4-NQ	1,2-NQ	1,4-AQ	WSOC	O <sub>3</sub>	Temp	RH						
DTTv	1																																												
DTTm	0.28	1																																											
AAv	0.14	0.51*	1																																										
AAm	0.15	0.89**	0.8*	1																																									
PM <sub>2.5</sub>	0.31	-0.73	-0.21	-0.64	1																																								
F <sup>-</sup>	-0.04	-0.17	-0.65	-0.32	0.28	1																																							
Cl <sup>-</sup>	-0.39	-0.12	0	-0.05	0.34	0.18	1																																						
NO <sub>3</sub> <sup>-</sup>	-0.02	-0.27	0.35	-0.06	0.65*	-0.42	0.16	1																																					
SO <sub>4</sub> <sup>2-</sup>	-0.11	-0.16	-0.02	-0.05	0.56*	0.52*	0.18	-0.19	1																																				
NH <sub>4</sub> <sup>+</sup>	0.31	-0.73	-0.21	-0.64	0.98**	-0.08	-0.19	0.2	0.21	1																																			
Na <sup>+</sup>	0.54*	0.75**	0.67*	0.87**	-0.4	-0.07	-0.01	-0.16	0.08	-0.4	1																																		
K <sup>+</sup>	0.6*	0.51*	0.59*	0.62*	0.46	-0.3	-0.54	-0.27	0.05	0.06	0.74*	1																																	
Mg <sup>2+</sup>	0.75**	-0.02	-0.28	-0.14	0.45	0.35	-0.29	-0.27	-0.14	0.31	0.25	0.38	1																																
Ca <sup>2+</sup>	0.67*	-0.03	-0.41	-0.2	0.75**	0.56*	-0.18	-0.38	0.02	0.24	0.21	0.26	0.97**	1																															
Mn	0.67*	0.21	0.18	0.2	0.44	-0.11	-0.59	-0.48	-0.01	0.31	0.42	0.86**	0.64*	0.55*	1																														
Co	0.74**	0.11	-0.13	0.03	0.87**	0.28	-0.39	-0.37	-0.04	0.3	0.43	0.59*	0.94**	0.9**	0.76**	1																													
Ni	0.79**	-0.09	0.04	-0.15	0.61*	-0.28	-0.44	0.3	-0.23	0.61*	-0.01	0.33	0.55*	0.41	0.42	0.53*	1																												
Cd	0.25	0.1	0.21	0.07	0.39	-0.46	-0.55	-0.27	-0.31	0.12	-0.04	0.5*	0.14	0.01	0.66*	0.13	0.18	1																											
Zn	0.39	0.2	0.53*	0.21	0.32	-0.41	-0.39	-0.46	0.06	0.32	0.25	0.73**	0.17	0.08	0.82**	0.32	0.26	0.75**	1																										
Ba	0.76**	-0.03	-0.02	-0.04	0.41	0.15	-0.39	-0.27	-0.04	0.41	0.32	0.62*	0.92**	0.84**	0.84**	0.9**	0.55*	0.41	0.46	1																									
Cr	0.21	-0.07	0.3	0.08	0.55*	-0.41	-0.3	-0.29	0.2	0.55*	0.19	0.63*	0.07	-0.03	0.67*	0.29	0.27	0.44	0.86**	0.34	1																								
Cu	0.55*	0.54*	0.63*	0.69*	-0.01	-0.16	-0.34	-0.2	0.17	-0.01	0.88**	0.94**	0.37	0.29	0.72**	0.6*	0.25	0.19	0.54*	0.55*	0.54*	1																							
Al	0.6*	-0.05	0.28	0.06	0.67*	-0.37	-0.46	-0.12	0.08	0.67*	0.27	0.73**	0.41	0.27	0.79**	0.58*	0.65*	0.41	0.78**	0.62*	0.88**	0.65*	1																						
As	0.76**	0.3	0.44	0.38	0.87**	-0.22	-0.55	0.13	-0.18	0.16	0.59*	0.78**	0.59*	0.44	0.7**	0.66**	0.52*	0.34	0.34	0.71**	0.26	0.76**	0.58*	1																					
Pb	0.45	0.33	0.58*	0.5*	0.77**	-0.36	-0.46	-0.28	0.18	0.23	0.61*	0.94**	0.22	0.11	0.83**	0.46	0.26	0.5*	0.84**	0.52*	0.83**	0.88**	0.83**	0.64*	1																				
Fe	0.59*	0.17	0.27	0.21	0.41	-0.25	-0.56	-0.43	0.08	0.41	0.4	0.87**	0.47	0.36	0.96**	0.64*	0.42	0.62*	0.9**	0.71*	0.84**	0.74**	0.9**	0.63*	0.92**	1																			
V	0.5*	0.26	-0.08	0.05	-0.11	-0.17	-0.41	0.19	-0.64	-0.11	-0.03	0.06	0.44	0.34	0.11	0.31	0.61*	0.21	-0.13	0.3	-0.37	-0.06	-0.03	0.3	-0.2	-0.04	1																		
Ag	0.63*	0.4	0.57*	0.51*	0.25	-0.39	-0.34	-0.23	0.06	0.25	0.67*	0.92**	0.35	0.23	0.82**	0.57*	0.43	0.4	0.81**	0.58*	0.79**	0.89**	0.87**	0.68*	0.94**	0.9**	-0.05	1																	
Bi	0.4	0.23	0.52*	0.4	0.33	-0.38	-0.45	-0.27	0.21	0.33	0.52*	0.89**	0.18	0.07	0.8**	0.44	0.28	0.47	0.85**	0.48	0.9**	0.83**	0.89**	0.58*	0.99**	0.92**	-0.25	0.93**	1																
Ce	0.69*	0.18	0.2	0.19	0.32	-0.05	-0.6	-0.41	0.07	0.32	0.43	0.86**	0.65*	0.56*	0.98**	0.75**	0.41	0.63*	0.76**	0.86**	0.61*	0.74**	0.76**	0.77**	0.82**	0.93**	0.08	0.79**	0.78**	1															
Sr	0.74**	0.02	-0.25	-0.1	0.31	0.43	-0.29	-0.42	0.06	0.31	0.31	0.48	0.97**	0.97**	0.63*	0.95**	0.46	0.17	0.29	0.93**	0.19	0.47	0.47	0.57*	0.35	0.58*	0.27	0.45	0.31	0.74**	1														
Sb	0.34	0.2	0.53*	0.36	0.36	-0.52	-0.35	-0.24	0.12	0.36	0.43	0.81**	0.09	-0.04	0.73*	0.33	0.3	0.49	0.89**	0.38	0.95**	0.72**	0.88**	0.44	0.94**	0.88**	-0.25	0.92**	0.97**	0.68*	0.2	1													
1,4-NQ	0.66*	0.5*	0.38	0.44	-0.18	-0.32	-0.36	0.28	-0.53	-0.18	0.42	0.43	0.47	0.32	0.29	0.42	0.61*	0.23	0.02	0.43	-0.2	0.38	0.16	0.63*	0.16	0.17	0.86**	0.31	0.07	0.3	0.33	0.03	1												
1,2-NQ	0.31	-0.73	-0.21	-0.64	0.45	-0.08	-0.19	0.2	0.21	0.67	-0.4	0.06	0.31	0.24	0.31	0.3	0.68*	0.12	0.32	0.41	0.55*	-0.01	0.67*	0.16	0.23	0.41	-0.11	0.25	0.33	0.32	0.31	0.36	-0.18	1											
1,4-AQ	0.6*	-0.21	-0.3	-0.26	0.43	0.3	-0.03	-0.18	-0.14	0.43	0.18	0.23	0.92**	0.89**	0.5*	0.87**	0.5*	-0.04	0.1	0.82**	0.15	0.29	0.43	0.44	0.15	0.38	0.25	0.32	0.15	0.49	0.88	0.11	0.28	0.43	1										
WSOC	-0.34	0.19	0.01	0.13	0.5*	-0.1	-0.15	-0.15	-0.28	-0.49	-0.06	-0.06	-0.33	-0.33	-0.07	-0.37	-0.6	0.34	-0.02	-0.29	-0.22	-0.16	-0.39	0.01	-0.07	-0.12	-0.19	-0.23	-0.12	-0.03	-0.33	-0.16	-0.21	-0.49	-0.45	1									
O <sub>3</sub>	0.34	0.51*	0.14	0.43	-0.27	0	-0.51	-0.66	-0.19	-0.27	0.47	0.69*	0.49	0.44	0.74**	0.58*	0.07	0.6*	0.54*	0.59*	0.27	0.54*	0.3	0.41	0.54*	0.61*	0.34	0.5*	0.46	0.69	0.54*	0.39	0.42	-0.27	0.27	0.07	1								
Temp	0.68*	0.36	0.26	0.29	-0.05	-0.3	-0.52	0.38	-0.54	-0.05	0.28	0.37	0.47	0.31	0.27	0.41	0.68*	0.21	-0.05	0.41	-0.22	0.3	0.18	0.69*	0.11	0.15	0.86**	0.38	0.04	0.3	0.31	-0.02	0.95**	-0.05	0.26	-0.11	0.29	1							
RH	0.28	0.33	0.07	0.18	-0.17	-0.47	-0.57	-0.22	-0.79	-0.17	0.04	0.35	0.29	0.13	0.46	0.26	0.28	0.73**	0.39	0.33	0.1	0.11	0.19	0.33	0.21	0.36	0.66*	0.24	0.17	0.38	0.19	0.21	0.58*	-0.17	0.12	0.28	0.68*	0.55*	1						

\* At 0.05 level (two-tailed), the correlation is significant

\*\* At 0.01 level (two-tailed), the correlation is significant

Table 5.4 Pearson's correlation (r) between OP induced by water-soluble fraction of PM<sub>2.5</sub> and chemical compositions during nighttime

	DTTv	DTTm	AAv	AAm	PM <sub>2.5</sub>	F <sup>-</sup>	Cl <sup>-</sup>	NO <sub>3</sub> <sup>-</sup>	SO <sub>4</sub> <sup>2-</sup>	NH <sub>4</sub> <sup>+</sup>	Na <sup>+</sup>	K <sup>+</sup>	Mg <sup>2+</sup>	Ca <sup>2+</sup>	Mn	Co	Ni	Cd	Zn	Ba	Cr	Cu	Al	As	Pb	Fe	V	Ag	Bi	Ce	Sr	Sb	1,4-NQ	1,2-NQ	1,4-AQ	WSOC	O <sub>3</sub>	Temp	
DTTv	1																																						
DTTm	-0.02	1																																					
AAv	-0.26	-0.6	1																																				
AAm	-0.69	-0.03	0.61*	1																																			
PM <sub>2.5</sub>	0.61*	-0.71	0.31	-0.41	1																																		
F <sup>-</sup>	0.73**	0.11	-0.28	-0.26	0.52*	1																																	
Cl <sup>-</sup>	-0.22	0.04	-0.12	-0.03	-0.29	-0.26	1																																
NO <sub>3</sub> <sup>-</sup>	0.62*	0.15	-0.17	-0.16	0.81**	0.07	-0.17	1																															
SO <sub>4</sub> <sup>2-</sup>	-0.16	-0.2	0.12	0.09	-0.09	0.13	0.34	0.13	1																														
NH <sub>4</sub> <sup>+</sup>	0.06	-0.18	0.09	-0.38	0.61*	-0.24	0.05	-0.38	0.04	1																													
Na <sup>+</sup>	-0.49	-0.13	0	0.33	-0.2	0.01	0	-0.02	0.06	-0.33	1																												
K <sup>+</sup>	0.07	-0.29	0.17	0.04	0.42	-0.4	0.12	0.22	0.5*	0	-0.2	1																											
Mg <sup>2+</sup>	0.02	-0.11	0.2	0.54*	0.51*	-0.3	0.32	0.53*	0.62*	-0.26	0.02	0.67*	1																										
Ca <sup>2+</sup>	-0.2	-0.11	0.39	0.67*	-0.14	-0.34	0.57*	0.11	0.63*	-0.22	0.11	0.48	0.84**	1																									
Mn	-0.23	0.26	-0.06	0.04	-0.25	0.03	-0.04	0.17	-0.15	-0.01	-0.21	-0.21	-0.04	-0.12	1																								
Co	0.18	-0.06	0.12	0.03	0.69*	0.8**	-0.28	0.1	0.33	-0.15	-0.09	-0.12	-0.15	-0.12	0.06	1																							
Ni	0.54*	-0.28	0.54*	-0.04	0.5*	0.18	-0.43	0.16	-0.1	-0.04	-0.19	0.1	-0.14	-0.18	-0.1	0.56*	1																						
Cd	0.01	0.63*	-0.49	-0.21	0.55*	0.5*	0.03	0.16	-0.24	-0.1	-0.14	-0.53	-0.34	-0.35	0.67*	0.36	-0.03	1																					
Zn	-0.02	0.5*	-0.37	-0.22	-0.31	0.18	-0.04	0.08	-0.25	0.21	-0.33	-0.18	-0.23	-0.31	0.65*	0.13	-0.06	0.77**	1																				
Ba	-0.12	0.25	-0.07	0.04	-0.27	-0.02	0.11	-0.19	-0.04	0.15	-0.03	0.12	0.02	0.13	-0.1	-0.02	-0.11	0.12	0.55*	1																			
Cr	0.08	-0.21	0.08	0.11	0.02	0.3	0.06	0.06	0.32	-0.39	0.22	-0.06	0.12	0.23	0.26	0.48	0.45	0.15	-0.14	-0.32	1																		
Cu	-0.14	-0.22	0.44	0.47	-0.04	0.07	0.22	0.04	0.53*	-0.27	0.27	0.13	0.45	0.69*	-0.16	0.35	0.24	-0.21	-0.19	0.29	0.54*	1																	
As	0.26	-0.03	0.58*	-0.13	0.14	0.83**	-0.26	-0.15	0.29	0.09	-0.27	-0.21	-0.24	-0.17	0.05	0.89**	0.37	0.35	0.2	0.07	0.32	0.23	1																
Pb	-0.16	-0.15	0.67*	0.12	0.63*	0.3	-0.22	-0.13	-0.04	-0.15	-0.16	-0.17	-0.21	-0.17	0.73**	0.39	0.19	0.38	0.29	-0.21	0.59*	0.04	0.39	1															
Fe	0.29	0.05	-0.32	-0.26	0	0.8**	-0.2	0.07	0.06	-0.21	0.04	-0.34	-0.38	-0.39	0.2	0.79**	0.49*	0.57*	0.21	-0.22	0.62*	0.05	0.69**	0.45	1														
V	0.58*	-0.13	0	-0.17	0.72**	-0.04	-0.2	-0.12	-0.33	-0.09	-0.14	0	-0.21	-0.13	-0.11	0.13	0.75**	-0.06	-0.03	0.03	0.48	0.18	0.08	0.16	0.33	1													
Ag	-0.16	-0.28	0.32	0.32	-0.07	0.39	0.14	0.06	0.67*	-0.3	0.3	0.1	0.35	0.52*	-0.05	0.62*	0.24	-0.05	-0.15	0.14	0.68*	0.89**	0.48*	0.28	0.36	0.06	1												
Bi	-0.27	-0.17	0.49*	0.55*	-0.12	-0.22	0.3	0.04	0.41	-0.26	0.34	0.2	0.56*	0.8**	-0.11	0.05	0.08	-0.28	-0.18	0.35	0.39	0.93**	-0.07	-0.04	-0.24	0.12	0.73**	1											
Ce	0.09	0.53*	-0.35	-0.19	-0.37	0.6	-0.16	-0.07	-0.19	-0.03	-0.1	-0.3	-0.36	-0.32	0.21	0.51*	0.13	0.71	0.71**	0.6*	-0.04	-0.02	0.54*	0.17	0.48	0.09	0.11	-0.12	1										
Sr	-0.27	-0.02	0.35	0.44	-0.21	-0.18	0.28	-0.04	0.32	-0.13	0.25	0.21	0.46	0.68*	-0.13	0.02	-0.02	-0.18	0.08	0.69*	0.15	0.84**	-0.03	-0.13	-0.3	0.06	0.62*	0.92**	0.15	1									
Sb	0.38	-0.11	-0.21	-0.37	0.64*	0.61*	-0.36	0	0.01	0.03	-0.28	-0.19	-0.41	-0.51	0.34	0.65*	0.52	0.41	0.18	-0.41	0.55*	-0.19	0.65*	0.64*	0.85**	0.36	0.13	-0.46	0.24	-0.55	1								
1,4-NQ	-0.43	0.22	0.02	0.53*	-0.39	0.14	-0.13	-0.08	-0.03	-0.23	0.53*	-0.1	-0.08	0.03	-0.19	0.18	-0.02	0.12	0.18	0.51*	-0.12	0.33	0.07	-0.28	0.06	-0.11	0.22	0.32	0.38	0.45	-0.31	1							
1,2-NQ	0.61*	-0.71	0.82**	-0.41	0.78**	0.02	-0.29	0.1	-0.09	0.31	-0.2	0.09	0.05	-0.14	-0.25	0.02	0.4	-0.43	-0.31	-0.27	0.02	-0.04	0.14	-0.04	0	0.32	-0.07	-0.12	-0.37	-0.21	0.22	-0.39	1						
1,4-AQ	-0.13	0.09	-0.05	0.05	-0.23	-0.25	0.25	-0.09	0.14	0.36	-0.11	-0.05	-0.15	0.03	0.03	-0.01	0.15	0.05	0.26	0.33	0.1	0.33	-0.09	-0.06	-0.04	0.17	0.2	0.29	0.02	0.36	-0.06	0.07	-0.23	1					
WSOC	0.65*	0.06	-0.19	-0.08	0.09	-0.05	-0.04	0.56*	-0.01	-0.43	0.21	0.22	0.44	0.17	-0.41	-0.31	-0.27	-0.3	-0.19	0.2	-0.36	0.06	-0.38	-0.54	-0.38	-0.23	-0.05	0.14	-0.13	0.22	-0.53	0.15	0.09	-0.2	1				
O <sub>3</sub>	-0.24	0.25	-0.19	0.22	-0.08	0.04	-0.34	0.15	-0.23	-0.25	0.31	-0.29	-0.06	-0.23	-0.01	-0.31	-0.49	-0.02	-0.15	-0.27	-0.36	-0.33	-0.22	-0.21	-0.21	-0.47	-0.36	-0.28	-0.22	-0.32	-0.21	0.28	-0.08	-0.41	0.39	1			
Temp	-0.44	0.18	0.08	0.35	-0.23	-0.4	-0.19	-0.48	-0.17	0.23	0.23	-0.22	-0.28	-0.11	-0.15	-0.5	-0.42	-0.33	-0.26	-0.05	-0.34	-0.17	-0.32	-0.18	-0.5	-0.2	-0.32	-0.05	-0.3	-0.05	-0.36	0.12	-0.23	0.11	-0.08	0.53*	1		
RH	-0.08	-0.04	0.01	0.02	-0.08	-0.58	0.13	-0.42	-0.01	0.38	0.08	0.2	-0.05	0.15	-0.14	-0.41	0.07	-0.34	0.02	0.38	0.07	0.22	-0.35	-0.12	-0.34	0.45	0	0.34	-0.13	0.41	-0.25	0	-0.08	0.61	-0.2	-0.36	0.42	1	

\*At 0.05 level (two-tailed), the correlation is significant

\*\* At 0.01 level (two-tailed), the correlation is significant

#### 5.2.4.3. Graphical analysis of source dispersion of water-and methanol-soluble OP: diurnal variations

The BPPs displayed in Figure 5-11 show the diverse dispersion patterns of daytime and nighttime OP induced by water-soluble fractions of PM<sub>2.5</sub>. During the day, the DTTv levels are primarily influenced by traffic emissions on freeways and road dust in the southwest area, which is in close proximity to our study domain. Conversely, at night, industrial emissions from the Wangchun industrial zone and Beilun industrial park become dominant source contributing to the DTTv levels. In addition, marine aerosols and sea salt aerosols also play a significant role in contributing to the DTTv levels during nighttime hours. The DTTm in both daytime and nighttime is influence by industrial emissions from the Wangchun industrial zone. During the daytime, AAv resulting from water-soluble fractions is primarily driven by industrial and vehicular traffic in the Wangchun industrial zone and on the freeway, respectively. Conversely, nighttime AAv is characterized by the dominance of marine and sea salt aerosols, as well as vehicular traffic. Moreover, DTTm and AAm exhibit a similar pattern, with industrial emissions in the Wangchun industrial zone being the most dominant source during both day and night.

The source dispersion patterns of the methanol-soluble fractions are shown in Figure 5-12. This patterns varies with the OP induced by water-soluble fraction, suggesting diversion emission sources. The DTTv induced by methanol-soluble fractions is dominated by industrial emission in the northwest, which is Wangchun industrial zone, vehicular traffic in the southwest, where there is close proximity of nearby freeway to our sampling domain. The DTTv induced by methanol-soluble fractions at night is predominantly dominated by industrial emissions in the northwest of the Wangchun industrial zone.

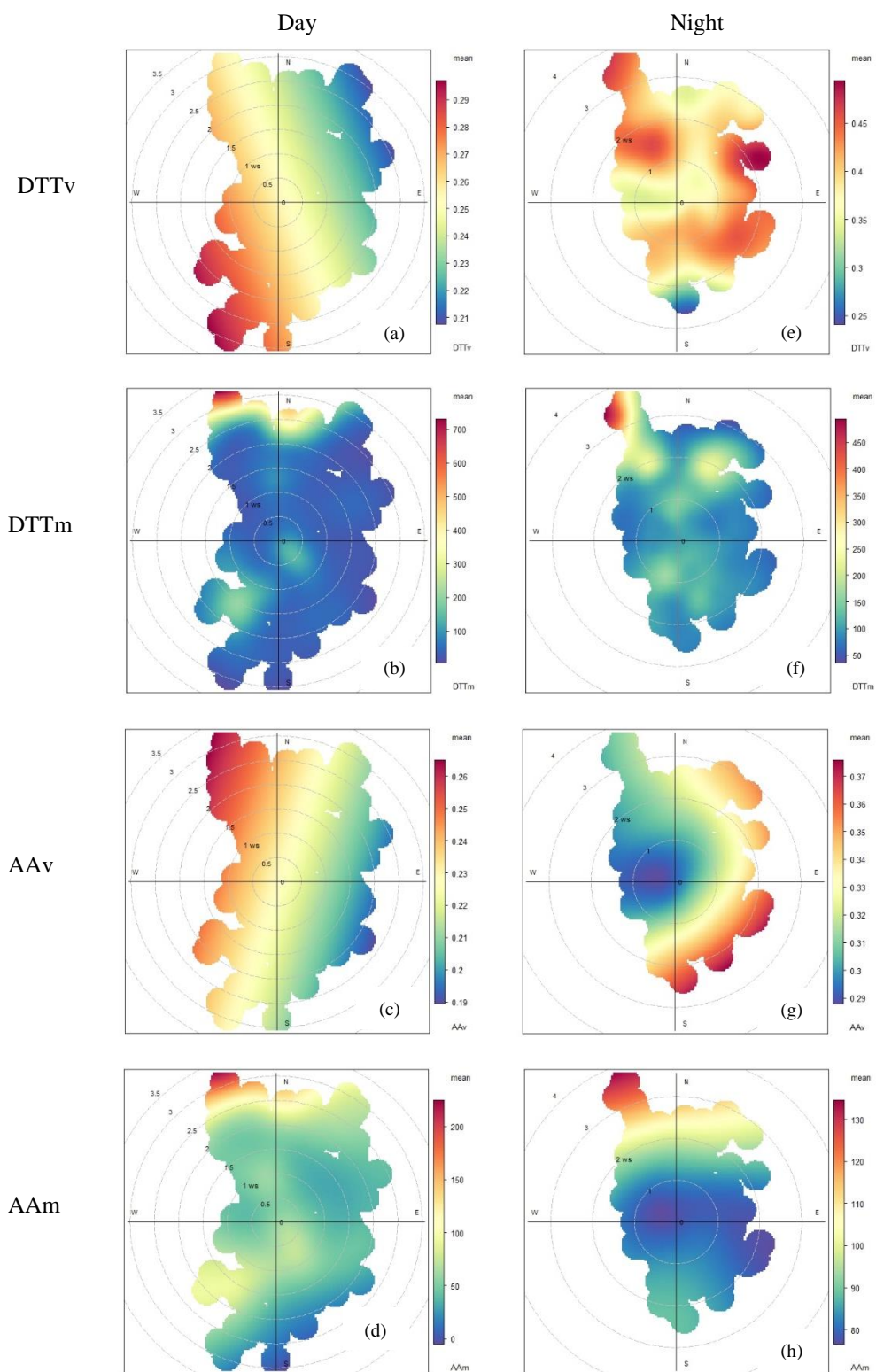


Figure 5-11 Bivariate polar plots of extrinsic and intrinsic OP induced by water-soluble fractions of  $PM_{2.5}$  during the day (a-d) and night (e-h)

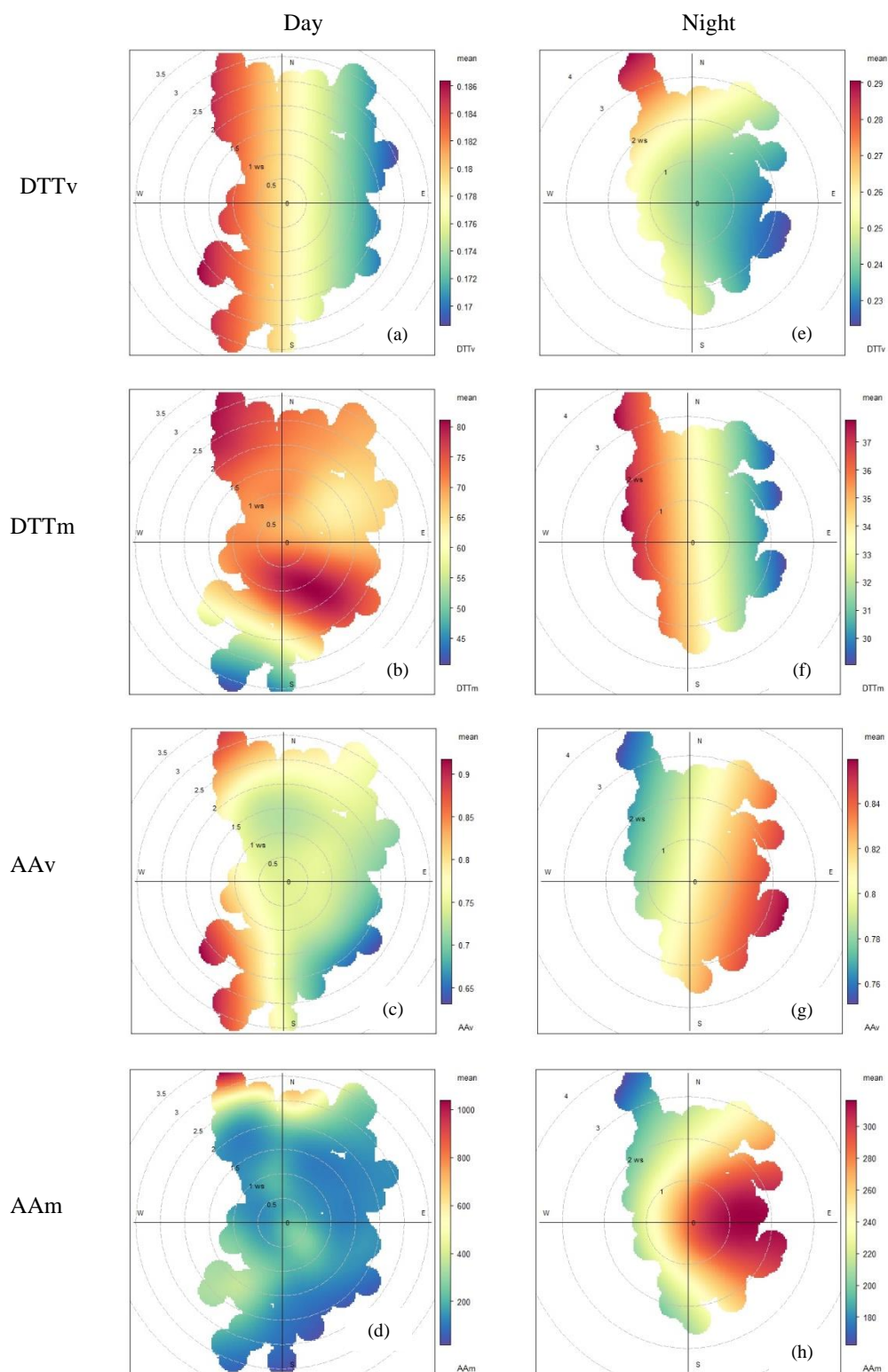


Figure 5-12 Bivariate polar plots of extrinsic and intrinsic OP induced by methanol-soluble fractions of  $PM_{2.5}$  during the day (a-d) and night (e-h)

Similarly, the corresponding DTTm during the day and night is predominated by industrial emissions in the northwest. Industrial emissions from the Zhenhai industrial park and vehicular traffic in the southeast also influence the DTTm during the day, whereas vehicular traffic in the southeast dominates the DTTm at night.

Table 5.5 Summary of potential sources associated with OP induced by water-and methanol-soluble fractions of PM<sub>2.5</sub> during the day and at night

Water-soluble fractions	Day	Night
DTTv	vehicular traffic, industrial	industrial, vehicular traffic, marine, sea salt
AAv	industrial, vehicular traffic	industrial, marine, sea salt,
Methanol-soluble fractions		
DTTv	industrial, vehicular traffic	industrial
AAv	industrial, vehicular traffic	vehicular traffic, marine, sea salt, industrial

During the day, the AAv is dominated by two potential sources: industrial emissions from the northwest and vehicular traffic from the southeast. In contrast, at night, the AAv is dominated by vehicular traffic in the southeast and marine and sea salt aerosol from the Ningbo-Zhoushan port and East China Sea, which are approximately 33 and 35 km away from our study domain, respectively. Similar source dispersion patterns were observed for both AAv and AAm during the night, with AAm being sourced at ground level during periods of low wind speed (Figure 5-12 h). Table 5.5 presents a summary of potential sources identified from the bivariate plots that are associated with the extrinsic OP measured in DTT and AA assays. The findings consistently indicate the contribution of vehicular traffic and industrial emissions to DTTv and AAv during the day. In contrast, during the night, DTTv

and AAv are influenced by industrial emissions, vehicular traffic, marine sources, and sea salt.

#### 5.2.4.4. OP induced by water-and methanol soluble PM<sub>2.5</sub>: seasonal variations

The DTTv induce by water-soluble fraction of PM<sub>2.5</sub> displayed significant seasonal variations (ANOVA,  $p \leq 0.05$ ), as shown in Figure 5-13 (a). The mean DTTv in autumn was  $1.19 \pm 0.26 \text{ nmol min}^{-1} \text{ m}^{-3}$ , while it was  $1.31 \pm 0.49 \text{ nmol min}^{-1} \text{ m}^{-3}$  in winter and  $1.00 \pm 0.37 \text{ nmol min}^{-1} \text{ m}^{-3}$  in spring and  $1.22 \pm 0.19 \text{ nmol min}^{-1} \text{ m}^{-3}$  in summer. The mean levels of DTTv were found to be higher in winter, followed by summer, autumn, and spring. It is noteworthy that several studies have reported elevated levels of DTTv during the winter season (Campbell et al., 2021; Li et al., 2021; Molina et al., 2023; Shen et al., 2022; Xing et al., 2023). In contrast, Yu et al. (2019) reported high DTTv in summer than other seasons. These results emphasize the importance of exploring the factors that contribute to the variations in the OP of PM<sub>2.5</sub> during different seasons. Therefore, it is necessary to identify the key chemical species that contribute to the seasonality of the OP of PM.

The annual mean DTTv induced by the water-soluble fraction of PM<sub>2.5</sub> was determined to be  $1.18 \pm 0.39 \text{ nmol min}^{-1} \text{ m}^{-3}$ . This value was compared to the results from similar studies conducted both within and outside of China, as presented in the literature review chapter (Table 2.1). The yearly DTTv of PM<sub>2.5</sub> is less than those measured in Beijing (Yu et al., 2019), Wuhan (Liu et al., 2020), Patiala (India) (Patel and Rastogi, 2018), and Inner Mongolia (Secrest et al., 2016). However, it is higher than those in Santiago, Chile (Molina et al., 2023), Hangzhou (Wang et al., 2019), Hong Kong (Cheng et al., 2021), Milan (Italy) (Pietrogrande et al., 2022). The DTTv level is similar to that observed in Nanjing (Ma et al., 2021), Shenzhen (Xing et al., 2023), Los Angeles (USA) (Shen et al., 2022), and Bern-Bollwerk (Switzerland) (Grange et al., 2022). These comparisons suggest that the OP



induced by water-soluble fraction of PM<sub>2.5</sub> in the present study falls within the range of OP values observed in different geographical locations, highlighting the need for regional context when assessing the OP of PM<sub>2.5</sub>.

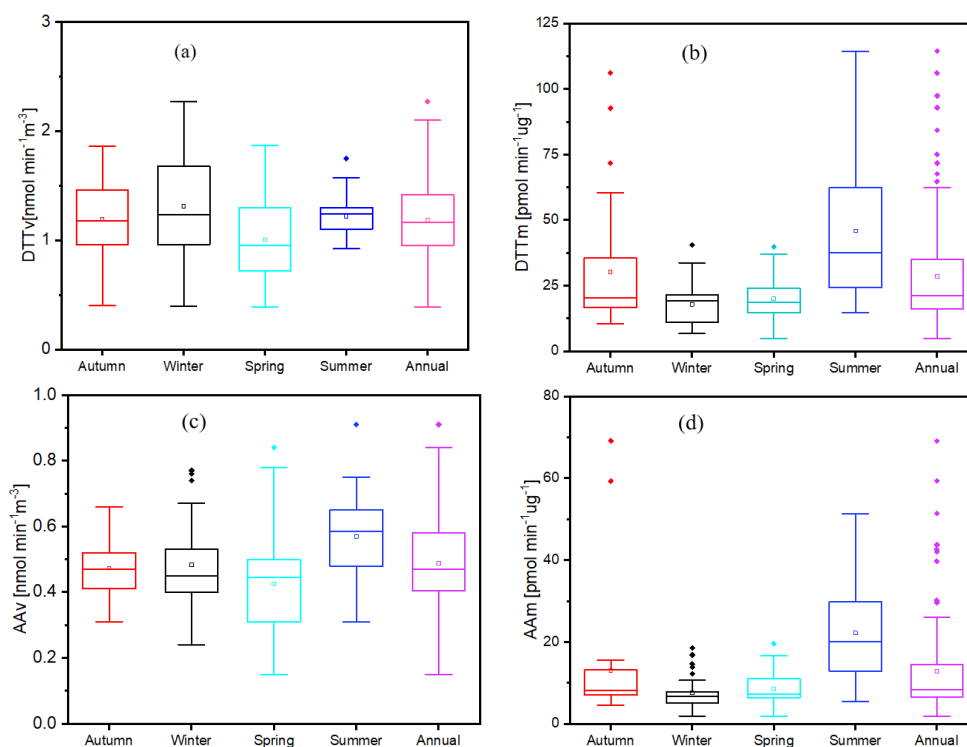


Figure 5-13 Extrinsic (a, c) and intrinsic (b, d) OP of water-soluble fraction of PM<sub>2.5</sub> in DTT (a, b) and AA (c, d) assays. Median (line across the box), mean (square within the box), first quartile (Q1) (bottom of the box), third quartile (Q3) (top of the box), outlier (square shown outside the box), whiskers shows minimum and maximum values

The corresponding DTTm (as shown in Figure 5-13 b) exhibited significant seasonal difference, with higher values reported in summer due to high levels of OP and a lower mass concentration of PM<sub>2.5</sub> during this season. The mean DTTm reported in this study was  $28.5 \pm 21.5$  pmol min<sup>-1</sup> μg<sup>-1</sup>, which is lower than the values in Beijing (Yu et al., 2019), Wuhan (Liu et al., 2020), and Los Angeles (Shen et al., 2022). However, it is higher than the values reported in Inner Mongolia (Secrest et al., 2016), Milan (Pietrogrande et al., 2022), Pakistand (Ahmad et al., 2021), and Hangzhou (Wang et al., 2019) (as shown in Table 2.1).

The AAv induced by water-soluble fraction of PM<sub>2.5</sub> exhibited significant seasonal variation. During autumn, winter, spring, and summer, the mean AAv ranged from  $0.43 \pm 0.17 \text{ nmol min}^{-1} \text{ m}^{-3}$  to  $0.57 \pm 0.13 \text{ nmol min}^{-1} \text{ m}^{-3}$ . The highest AAv was observed in summer, which was higher than the annual mean AAv of  $0.49 \pm 0.14 \text{ nmol min}^{-1} \text{ m}^{-3}$ , as represented in Figure 5-13 (c). Similarly, Weichenthal et al. (2019) reported higher AAv of PM<sub>2.5</sub> in the summer compared to other seasons. The AAm values in this study exhibited seasonal trends, with higher values observed during the summer, followed by autumn, winter, and spring (as depicted in Figure 5-13 d).

The DTTv induced by methanol-soluble fraction of PM<sub>2.5</sub> exhibited significant seasonal variability ( $p \leq 0.05$ ). As per Figure 5-14 (a), the highest mean values were observed in summer, followed by winter, spring, and autumn. The highest DTTv induced by the methanol-soluble fraction during the summer season aligns with the findings of previous studies (Weichenthal et al., 2019; Yu et al., 2021). However, Chen et al. (2021) reported a contrasting results, as they found that the highest DTTv induced by the methanol-soluble fraction occurred during the winter season.

Throughout the year, there was a significant seasonal variation observed in the AAv levels ( $p \leq 0.05$ ). The AAv was higher in summer ( $4.97 \pm 1.30 \text{ nmol min}^{-1} \text{ m}^{-3}$ ), followed by winter ( $4.88 \pm 1.11 \text{ nmol min}^{-1} \text{ m}^{-3}$ ), autumn ( $4.29 \pm 1.55 \text{ nmol min}^{-1} \text{ m}^{-3}$ ), and spring ( $2.52 \pm 0.95 \text{ nmol min}^{-1} \text{ m}^{-3}$ ) (as shown in Figure 5-14 c). Figure 5-14 illustrates the seasonal variation of DTTm induced by methanol-soluble fraction, revealing higher values in summer. Similarly, the AAm induced by methanol-soluble fraction was highest in summer (as shown in Figure 5-14 d). Therefore, the study has demonstrated that OP induced by both the water-soluble and methanol-soluble fractions of PM<sub>2.5</sub> exhibit varying levels of extrinsic

and intrinsic OP across different seasons. In this study, Pearson's correlation analysis was conducted to identify potential chemical species that could influence the seasonality of the OP induced by both water- and methanol-soluble fractions of PM<sub>2.5</sub>.

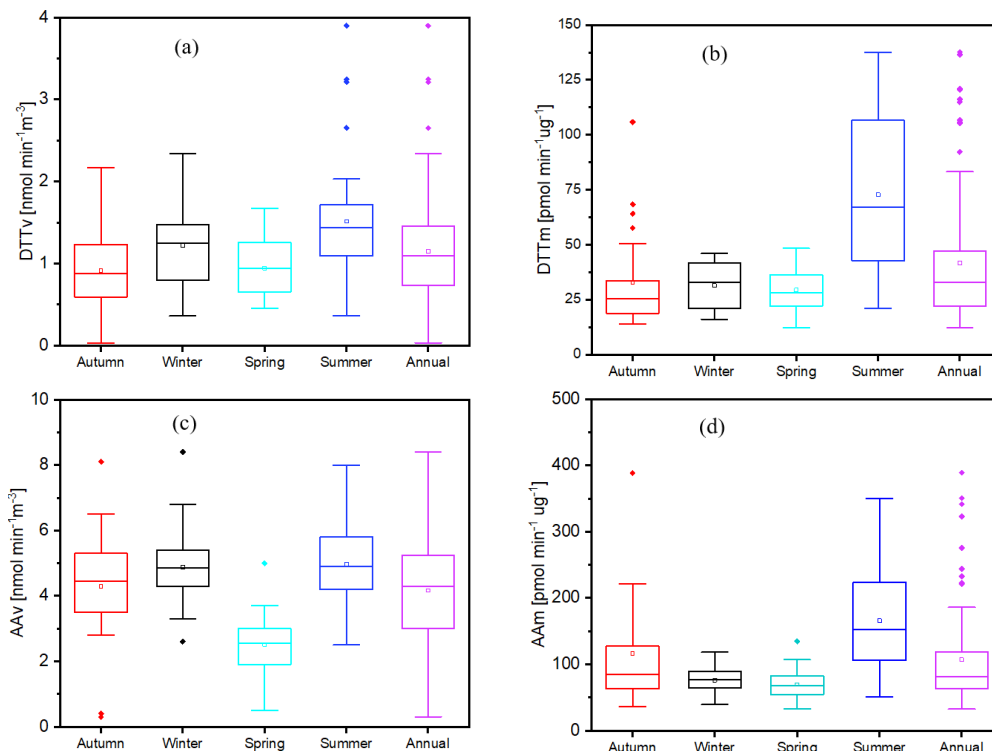


Figure 5-14 Extrinsic (a, c) and intrinsic (b, d) OP of methanol-soluble fraction of PM<sub>2.5</sub> in DTT (a, b) and AA (c, d) assays. Median (line across the box), mean (square within the box), first quartile (Q1) (bottom of the box), third quartile (Q3) (top of the box), outlier (square shown outside the box), whiskers shows minimum and maximum values

#### 5.2.4.5. Chemical species associated with OP: seasonal variations

The seasonal variation in the OP of PM<sub>2.5</sub> can be attributed to multiple factors. Elevated ambient temperatures and increased solar radiations can generally lead to the formation of secondary chemicals (e.g., quinones) with significant redox activity, ultimately resulting in an increase in OP values, especially in summer (Famiyeh, Jia, et al., 2023; Hsiao et al., 2021). Furthermore, during the summer season, high relative humidity can promote the accumulation of pollutants on pre-existing particles (Luo et al., 2023). The synergistic effects

of high temperatures and solar radiations, and high relative humidity, and elevated levels of NO<sub>2</sub> and VOCs, collectively contribute to the formation of SOAs with high OP activity (Zhai et al., 2023). Moreover, in warmer seasons, the volatilization of organic compounds and their subsequent oxidation by oxidants such as <sup>•</sup>OH, NO<sub>x</sub>, and O<sub>3</sub> contribute to SOA formation (Molina et al., 2023). As demonstrated in Chapter 4 (Sections 4.2.4), we present compelling evidence indicating that the aerosols collected during the summer are photochemically aged. These processes contribute to elevated levels of OP during the summer months (Famiyeh, Jia, et al., 2023; Hsiao et al., 2021).

The correlation between the chemical composition of PM<sub>2.5</sub> and OP varied throughout the seasons. In the autumn season, DTTv correlated strongly with Cu, As, as well as a moderate correlation with Cd, 1, 4-NQ, and NO<sub>3</sub><sup>-</sup> (as presented in Table 5.6). In contrast, during the winter season, a moderate-to-strong correlation between trace metals (Co, Cu, V, Cr, and Fe) and DTTv was observed (shown in Table 5.7). During winter, the increased levels of DTTv can be mainly attributed to the presence of Fe and Cu, which play a significant role in the Fenton reaction (Campbell et al., 2021; Luo et al., 2023). These metals serve as catalysts, facilitating the conversion of H<sub>2</sub>O<sub>2</sub> to <sup>•</sup>OH, a highly reactive oxidative species that plays a crucial role in the generation of SOA with high OP activity.

As demonstrated in Sections 5.2.3.1 (Figure 5-6), aerosols collected at our study domain exhibited significant acidity in the summer season, followed by spring, winter, and autumn. This acidity contribute to the dissolution of trace metals and subsequently increased the OP activity of PM<sub>2.5</sub> throughout all seasons. This finding provides evidence of the moderate-to-strong correlation between DTTv and trace metals across all seasons, particularly in winter,

where Cu, Mn, Co, and V exhibited a moderate-to-strong correlation. This contribute to the high DTTv induce by water-soluble fraction of PM<sub>2.5</sub> in winter.

According to the results presented in Table 5.8, a strong correlation is observed between WSOC and DTTv during the summer season. This finding suggests the possible contribution of SOA to the elevated levels of DTTv observed during this time period (Cui et al., 2023). Previous studies have also frequently employed WSOC as a tracer for SOA (Cui et al., 2023; Farahani et al., 2022; Lovett et al., 2018), especially summer. The AAv induced by water-soluble fraction of PM<sub>2.5</sub> in summer exhibited moderate-to-strong correlation with Pb, Ag, Ce, Sr (as shown in Table 5.9). The high AAv observed during the summer season can be attributed to these non-exhaust trace metals. Additionally, the aging of summer aerosols through photochemical processes could contribute to the elevated AAv levels.

The DTTv induced by methanol-soluble fraction of PM<sub>2.5</sub> in autumn exhibited moderate-to-strong correlation with several water-soluble trace metals (e.g., Cd, Cr, Cu, Ba, Ce, Sr), inorganic ions (e.g., Ca<sup>2+</sup>, Mg<sup>2+</sup>), PAHs (e.g., NaP, Phe, Ant, Flt, Pyr, BkF, BahA, etc.), and quinones (e.g., 1, 4-NQ, 1, 2-NQ, 1, 4-AQ), as shown in Appendix (Table 8.7), whereas in winter it correlated moderate-to-strong with organics such as PAHs (Ant, 7H-BcF), quinone (1, 4-AQ), and WSOC (as shown in Table 8.8).

Table 5.6 Pearson's correlation (r) between OP induced by water-soluble fraction of PM<sub>2.5</sub> and chemical compositions in autumn

	DTTv	DTTm	AAv	AAm	PM2.5	F <sup>-</sup>	Cl <sup>-</sup>	NO <sub>3</sub> <sup>-</sup>	SO <sub>4</sub> <sup>2-</sup>	NH <sub>4</sub> <sup>+</sup>	Na <sup>+</sup>	K <sup>+</sup>	Mg <sup>2+</sup>	Ca <sup>2+</sup>	Mn	Co	Ni	Cd	Zn	Ba	Cr	Cu	Al	As	Pb	Fe	V	Ag	Bi	Ce	Sr	Sb	WSOC	1,4-NQ	1,2-NQ	1,4-AQ	O <sub>3</sub>	Temp	RH								
DTTv	1																																														
DTTm	0	1																																													
AAv	0.5*	0.26	1																																												
AAm	-0.32	0.9**	0.15	1																																											
PM2.5	-0.16	-0.07	-0.04	0.25	1																																										
F <sup>-</sup>	0.06	-0.11	0.34	-0.09	-0.26	1																																									
Cl <sup>-</sup>	0.03	-0.26	0.47	-0.19	-0.09	0.56*	1																																								
NO <sub>3</sub> <sup>-</sup>	0.62*	-0.15	-0.39	-0.34	-0.37	-0.17	-0.07	1																																							
SO <sub>4</sub> <sup>2-</sup>	0.01	-0.19	-0.06	-0.14	0.28	-0.53	0.17	0.41	1																																						
NH <sub>4</sub> <sup>+</sup>	-0.16	-0.07	-0.04	0.25	0.85**	-0.29	-0.15	-0.3	0.44	1																																					
Na <sup>+</sup>	-0.16	-0.07	-0.04	0.25	0.75**	-0.26	-0.09	-0.37	0.28	1	1																																				
K <sup>+</sup>	0.07	-0.73	-0.03	-0.59	0.4	-0.22	-0.03	-0.07	0.37	0.4	0.4	1																																			
Mg <sup>2+</sup>	0.11	-0.8	-0.24	-0.73	0.27	-0.05	0.03	-0.07	0.14	0.27	0.27	0.72**	1																																		
Ca <sup>2+</sup>	0.1	-0.8	-0.35	-0.75	0.15	-0.12	0.03	0.05	0.1	0.15	0.15	0.65*	0.95**	1																																	
Mn	-0.2	-0.77	-0.25	-0.52	0.49	-0.17	0.17	0.02	0.47	0.49	0.49	0.89**	0.7**	0.69*	1																																
Co	-0.42	0.64*	0.08	0.89**	0.63*	-0.19	-0.19	-0.47	0.05	0.63*	0.63*	-0.19	-0.4	-0.48	-0.1	1																															
Ni	0.66*	-0.16	-0.15	-0.14	0.14	-0.14	0.24	0.76**	0.7**	0.14	0.14	0.09	-0.13	-0.1	0.27	-0.1	1																														
Cd	0.54*	-0.62	-0.02	-0.52	0.28	-0.15	0.34	0.45	0.72**	0.28	0.28	0.62*	0.29	0.27	0.7**	-0.28	0.78**	1																													
Zn	-0.06	-0.62	0.55*	-0.48	0.14	0.14	0.19	-0.16	0.11	0.14	0.14	0.84**	0.56*	0.54*	0.79**	-0.17	-0.07	0.4	1																												
Ba	0.1	-0.93	-0.1	-0.85	0.2	-0.03	0.16	-0.02	0.27	0.2	0.2	0.86**	0.9	0.84**	0.8**	-0.53	0.02	0.56*	0.69*	1																											
Cr	-0.12	-0.63	-0.29	-0.48	0.24	-0.35	0.05	0.36	0.58*	0.24	0.24	0.77**	0.36	0.43	0.85**	-0.19	0.52*	0.82**	0.65*	0.59*	1																										
Cu	0.72**	-0.48	-0.18	-0.43	0.12	-0.09	0.34	0.71**	0.72**	0.12	0.12	0.37	0.15	0.18	0.54*	-0.29	0.93**	0.91**	0.23	0.35	0.73**	1																									
Al	-0.23	-0.64	0.08	-0.44	0.2	-0.07	0.54*	-0.01	0.52*	0.2	0.2	0.54*	0.26	0.24	0.66**	-0.23	0.36	0.78**	0.43	0.57*	0.69*	0.57*	1																								
As	0.78**	-0.43	0.29	-0.44	0.12	0.17	0.25	0.24	0.2	0.12	0.12	0.66*	0.34	0.36	0.58*	-0.23	0.33	0.55*	0.76**	0.47	0.6*	0.5*	0.26	1																							
Pb	-0.18	-0.26	0.26	-0.07	0.27	-0.01	0.66*	-0.16	0.32	0.27	0.27	0.15	-0.06	-0.01	0.33	0.03	0.28	0.52*	0.1	0.17	0.36	0.37	0.82**	0.08	1																						
Fe	-0.28	-0.73	-0.14	-0.55	0.05	-0.03	0.46	0.1	0.33	0.05	0.05	0.57*	0.33	0.43	0.73**	-0.36	0.28	0.69*	0.58*	0.6*	0.79**	0.55*	0.9**	0.38	0.71**	1																					
V	-0.16	-0.34	0.67	-0.26	-0.31	0.7**	0.31	-0.15	-0.48	-0.31	-0.31	0.22	0.03	0.05	0.21	-0.25	-0.21	0.02	0.62*	0.2	0.19	-0.02	0.18	0.44	0.03	0.38	1																				
Ag	0.22	-0.23	-0.4	-0.39	-0.36	-0.28	-0.06	0.89**	0.5*	-0.36	-0.36	0.17	0.12	0.27	0.25	-0.42	0.61*	0.42	0.17	0.14	0.52*	0.65*	0.02	0.4	-0.22	0.21	-0.07	1																			
Bi	-0.32	-0.58	-0.46	-0.46	-0.1	-0.14	0.02	0.44	0.34	-0.1	-0.1	0.55*	0.21	0.32	0.68*	-0.3	0.41	0.61*	0.61*	0.43	0.88**	0.62*	0.55*	0.45	0.19	0.76**	0.45	0.59*	1																		
Ce	-0.14	-0.93	-0.24	-0.79	0.08	0.12	0.23	0.01	0.07	0.08	0.08	0.61*	0.62*	0.6*	0.65*	-0.58	0.08	0.57*	0.48	0.82**	0.56*	0.37	0.73**	0.22	0.41	0.77**	0.37	-0.01	0.54*	1																	
Sr	0.13	-0.86	-0.27	-0.78	0.25	-0.13	0.12	0.06	0.24	0.25	0.25	0.73**	0.96**	0.98**	0.76**	-0.47	0.03	0.43	0.56*	0.91**	0.51*	0.31	0.39	0.41	0.12	0.5*	0	0.24	0.33	0.68*	1																
Sb	-0.08	-0.68	-0.11	-0.56	0.13	-0.18	0.04	0.18	0.49	0.13	0.13	0.88**	0.47	0.43	0.84**	-0.26	0.3	0.72**	0.82**	0.72**	0.89**	0.56*	0.63*	0.64*	0.16	0.68*	0.36	0.4	0.81**	0.59*	0.51*	1															
WSOC	-0.51	-0.56	-0.58	-0.44	-0.07	-0.28	-0.05	0.25	0.51*	-0.07	-0.07	0.45	0.43	0.41	0.58*	-0.26	0.2	0.41	0.36	0.53*	0.57*	0.39	0.46	-0.05	-0.01	0.49	0.04	0.43	0.67*	0.5*	0.44	0.65*	1														
1,4-NQ	-0.54	-0.44	-0.11	0.53*	0.54*	-0.54	-0.67	-0.22	0.45	0.87**	0.56*	0.22	0.69*	0.28	0.33	0.54*	-0.21	0.12	-0.18	0.34	-0.08	-0.22	0.05	-0.32	-0.43	0.22	-0.09	-0.67	-0.45	0.34	0.11	0.09	0.56*	1													
1,2-NQ	-0.27	-0.08	-0.27	0.11	0.66*	-0.34	-0.18	-0.39	0.18	0.63*	0.63*	0.13	0.33	0.18	0.19	0.36	-0.07	0.06	-0.17	0.22	-0.04	-0.11	0.01	-0.41	-0.2	-0.24	-0.46	-0.43	-0.23	0.17	0.17	0.04	0.26	0.86**	1												
1,4-AQ	0.75**	-0.66	-0.21	-0.62	0.37	-0.42	0.17	0.03	0.56*	0.37	0.37	0.54*	0.72**	0.69*	0.72**	-0.28	0.32	0.63*	0.44	0.81**	0.59*	0.5*	0.44	0.37	0	0.33	-0.32	0.38	0.33	0.5*	0.81**	0.69	0.6*	0.45	0.45	1											
O <sub>3</sub>	-0.39	0.79**	0.13	0.8**	0.06	-0.03	-0.13	-0.39	-0.22	0.06	0.06	-0.7	-0.74	-0.8	-0.67	0.6*	-0.22	-0.49	-0.71	-0.75	-0.61	-0.48	-0.24	-0.78	0.08	-0.46	-0.28	-0.6	-0.53	-0.48	-0.8	-0.65	-0.32	0.32	0.32	-0.42	1										
Temp	-0.28	0.74**	-0.11	0.71**	-0.29	0.24	-0.29	-0.03	-0.53	-0.29	-0.29	-0.67	-0.66	-0.64	-0.62	0.44	-0.22	-0.66	-0.35	-0.85	-0.44	-0.44	-0.63	-0.3	-0.36	-0.47	0.21	-0.08	-0.14	-0.65	-0.78	-0.5	-0.38	-0.47	-0.47	-0.92	0.53*	1									
RH	-0.3	0.1	-0.32	0.32	0.28	0.18	-0.04	0.19	-0.09	0.28	0.28	0.02	-0.23	-0.13	0.24	0.42	0.33	0.11	0.24	-0.26	0.32	0.28	-0.1	0.35	-0.02	0.12	0.37	0.22	0.43	-0.15	-0.18	0.13	-0.09	-0.38	-0.38	-0.49	-0.08	0.52*	1								

\*At 0.05 level (two-tailed), the correlation is significant

\*\* At 0.01 level (two-tailed), the correlation is significant

Table 5.7 Pearson's correlation (r) between OP induced by water-soluble fraction of PM<sub>2.5</sub> and chemical compositions in winter

	DTTv	DTTm	AAv	AAm	PM2.5	F <sup>-</sup>	Cl <sup>-</sup>	NO <sub>3</sub> <sup>-</sup>	SO <sub>4</sub> <sup>2-</sup>	NH <sub>4</sub> <sup>+</sup>	Na <sup>+</sup>	K <sup>+</sup>	Mg <sup>2+</sup>	Ca <sup>2+</sup>	Mn	Co	Ni	Cd	Zn	Ba	Cr	Cu	Al	As	Pb	Fe	V	Ag	Bi	Ce	Sr	Sb	WSOC	1,4-NQ	1,2-NQ	1,4-AQ	O <sub>3</sub>	Temp	RH							
DTTv	1																																													
DTTm	0.78**	1																																												
AAv	0.02	0.09	1																																											
AAm	-0.42	0.12	-0.13	1																																										
PM2.5	0.2	-0.43	-0.16	-0.81	1																																									
F <sup>-</sup>	-0.06	-0.43	-0.32	-0.48	0.62*	1																																								
Cl <sup>-</sup>	-0.09	-0.09	0.09	-0.17	0.14	0.47	1																																							
NO <sub>3</sub> <sup>-</sup>	0.42	-0.35	-0.25	-0.32	0.62*	0.01	-0.32	1																																						
SO <sub>4</sub> <sup>2-</sup>	-0.52	-0.67	-0.27	0.18	0.03	0.04	-0.29	0.36	1																																					
NH <sub>4</sub> <sup>+</sup>	0.2	-0.73	-0.16	-0.81	0.42	0.82**	0.19	0.66*	0.12	1																																				
Na <sup>+</sup>	0.2	-0.43	-0.19	-0.89	0.66*	0.62*	0.14	0.62*	0.03	0.95**	1																																			
K <sup>+</sup>	-0.2	-0.55	-0.16	-0.51	0.64*	0.76**	0.33	0.4	0.32	0.64*	0.64*	1																																		
Mg <sup>2+</sup>	0.15	-0.34	0.06	-0.69	0.69*	0.41	-0.17	0.44	0	0.69*	0.69*	0.64*	1																																	
Ca <sup>2+</sup>	0.14	-0.38	-0.06	-0.7	0.8**	0.51*	0.03	0.43	-0.11	0.8**	0.8**	0.6*	0.94**	1																																
Mn	0.46	-0.57	-0.06	-0.8	0.88**	0.49*	-0.05	0.69*	0.31	0.88**	0.88**	0.7**	0.78*	0.77**	1																															
Co	0.72**	-0.4	-0.12	-0.54	0.76**	0.29	-0.08	0.85**	0.15	0.76**	0.76**	0.68*	0.82*	0.78**	0.81**	1																														
Ni	0.03	-0.22	0.01	-0.41	0.53*	-0.08	-0.12	0.9**	0.19	0.53*	0.53*	0.43	0.48	0.45	0.66*	0.87**	1																													
Cd	-0.15	-0.38	-0.08	-0.48	0.47	0.02	-0.2	0.69*	0.63	0.47	0.47	0.41	0.29	0.19	0.72**	0.51*	0.68*	1																												
Zn	-0.25	-0.52	-0.14	-0.55	0.51*	0.34	-0.13	0.5*	0.67	0.51*	0.51*	0.55*	0.37	0.26	0.78**	0.41	0.43	0.9**	1																											
Ba	-0.02	0	0.08	-0.08	-0.05	0.37	0.35	-0.4	-0.33	-0.05	-0.05	0.37	0.45	0.45	-0.05	0.09	-0.21	-0.49	-0.32	1																										
Cr	0.64**	-0.23	-0.26	-0.15	0.43	-0.07	-0.23	0.95**	0.36	0.43	0.43	0.35	0.22	0.2	0.52*	0.75**	0.9*	0.66*	0.43	-0.44	1																									
Cu	0.61*	-0.34	0	-0.07	0.26	0.4	0.33	0.25	0.15	0.26	0.26	0.78**	0.47	0.72**	0.27	0.58*	0.38	0.05	0.03	0.57*	0.29	1																								
Al	0.29	0.1	-0.19	-0.39	0.44	-0.03	-0.14	0.79**	-0.1	0.44	0.44	0.33	0.44	0.43	0.51*	0.79**	0.89**	0.45	0.25	-0.09	0.83**	0.29	1																							
As	0.14	0.03	-0.42	-0.24	0.34	-0.07	-0.37	0.73**	0.03	0.34	0.34	0.07	0.3	0.33	0.45	0.59*	0.68*	0.4	0.29	-0.25	0.72**	-0.1	0.84**	1																						
Pb	0.1	0.64*	-0.19	-0.06	0.1	-0.3	-0.24	0.71**	0.22	0.1	0.1	0.06	-0.09	-0.17	0.24	0.4	0.74**	0.62*	0.38	-0.57	0.86**	-0.02	0.77**	0.7**	1																					
Fe	0.63*	-0.36	-0.23	-0.52	0.74**	0.19	-0.15	0.92**	0.19	0.74*	0.74**	0.54*	0.68*	0.72**	0.81**	0.96**	0.91**	0.6*	0.47	-0.07	0.82**	0.38	0.84**	0.75**	0.53*	1																				
V	0.76**	0.14	0.06	-0.35	0.19	-0.21	-0.12	0.59*	-0.1	0.19	0.19	0.14	0.27	0.22	0.41	0.54*	0.78**	0.48	0.31	-0.12	0.66*	0.04	0.87**	0.79**	0.78**	0.64*	1																			
Ag	-0.09	-0.18	-0.3	0.08	0.31	-0.21	-0.17	0.85**	0.24	0.31	0.31	0.19	0.15	0.21	0.29	0.69*	0.8**	0.38	0.07	-0.3	0.89**	0.36	0.72**	0.6*	0.66*	0.74**	0.46	1																		
Bi	-0.06	-0.13	0.09	-0.01	0.14	0.33	0.34	0.1	0.05	0.14	0.14	0.68*	0.31	0.22	0.09	0.39	0.24	-0.03	-0.07	0.49*	0.18	0.94**	0.17	-0.29	-0.03	0.16	-0.08	0.24	1																	
Ce	0.09	-0.33	-0.17	-0.61	0.77**	0.28	-0.11	0.82**	0.06	0.77**	0.77**	0.58*	0.8**	0.83**	0.83**	0.96**	0.84**	0.49	0.42	0.1	0.69*	0.4	0.82**	0.72**	0.4	0.98**	0.64*	0.61*	0.18	1																
Sr	-0.03	-0.09	0.13	-0.08	0.06	0.45	0.4	-0.24	-0.18	0.06	0.06	0.59*	0.45	0.41	0.02	0.23	-0.07	-0.35	-0.24	0.89**	-0.25	0.83**	-0.04	-0.38	-0.45	0	-0.2	-0.13	0.83**	0.12	1															
Sb	-0.37	-0.65	-0.42	-0.32	0.53*	0.51*	-0.11	0.54*	0.8	0.53*	0.53*	0.67*	0.31	0.25	0.69*	0.44	0.34	0.76**	0.88**	-0.28	0.48	0.24	0.16	0.21	0.29	0.45	0.04	0.22	0.14	0.38	-0.1	1														
WSOC	0.44	-0.58	-0.33	-0.58	0.78**	0.59*	0.13	0.6*	0.43	0.78**	0.78**	0.59*	0.29	0.37	0.79*	0.51*	0.44	0.7**	0.8**	-0.39	0.52*	0.05	0.32	0.38	0.35	0.58*	0.23	0.25	-0.08	0.52*	-0.28	0.83**	1													
1,4-NQ	-0.54	-0.22	0.43	0.65*	-0.24	0.14	0.45	-0.55	0.47	0.12	-0.49	-0.68	0.23	-0.7	-0.87	0.22	-0.44	-0.06	-0.35	0.33	-0.76	0.09	-0.78	-0.66	-0.75	-0.54	0.45	-0.56	0.54*	0.11	0.43	-0.23	-0.56	1												
1,2-NQ	-0.73	-0.49	0.22	0.52*	-0.39	0.14	0.36	-0.47	0.26	-0.37	-0.37	-0.06	-0.47	-0.41	-0.38	-0.49	-0.57	-0.45	-0.21	0.12	-0.49	0.04	-0.7	-0.59	-0.54	-0.56	-0.54	-0.36	0.04	-0.56	0.12	-0.04	-0.11	0.67*	1											
1,4-AQ	-0.27	-0.39	-0.05	-0.2	0.21	0.81**	0.66*	-0.33	0.17	0.23	0.23	0.62*	0.02	0.06	0.12	-0.14	-0.43	-0.14	0.22	0.6*	-0.48	0.38	-0.45	-0.55	-0.58	-0.28	-0.47	-0.54	0.41	-0.2	0.55*	0.4	0.35	0.51*	0.54*	1										
O <sub>3</sub>	0.67*	0.29	0.28	-0.78	0.48	0.28	0	0.11	-0.61	0.48	0.48	0.2	0.57*	0.54*	0.44	0.35	0.25	0.04	0.12	0.2	0	-0.05	0.44	0.31	0.07	0.31	0.46	-0.21	-0.04	0.46	0.12	-0.14	0.16	-0.56	-0.56	-0.06	1									
Temp	0.05	-0.07	-0.2	-0.05	0.28	-0.36	-0.2	0.54*	0.01	0.28	0.28	-0.39	-0.13	0.06	0.19	0.23	0.41	0.28	0.05	-0.64	0.48	-0.47	0.35	0.57*	0.41	0.44	0.31	0.56*	-0.6	0.33	-0.74	0	0.31	-0.25	-0.25	-0.59	-0.08	1								
RH	0.02	0.35	0.14	0.54*	-0.52	-0.94	-0.39	0.06	0.01	-0.52	-0.52	-0.8	-0.56	-0.57	-0.5	-0.31	0.06	-0.01	-0.34	-0.56	0.14	-0.49	-0.01	0.09	0.32	-0.17	0.09	0.32	-0.42	-0.31	-0.61	-0.42	-0.43	-0.07	-0.07	-0.76	-0.43	0.57*	1							

\*At 0.05 level (two-tailed), the correlation is significant

\*\* At 0.01 level (two-tailed), the correlation is significant





Table 5.9 Pearson's correlation (r) between OP induced by water-soluble fraction of PM<sub>2.5</sub> and chemical compositions in summer

	DTTv	DTTm	AAv	AAm	PM2.5	F <sup>-</sup>	Cl <sup>-</sup>	NO <sub>3</sub> <sup>-</sup>	SO <sub>4</sub> <sup>2-</sup>	NH <sub>4</sub> <sup>+</sup>	Na <sup>+</sup>	K <sup>+</sup>	Mg <sup>2+</sup>	Ca <sup>2+</sup>	Mn	Co	Ni	Cd	Zn	Ba	Cr	Cu	Al	As	Pb	Fe	V	Ag	Bi	Ce	Sr	Sb	WSOC	1,4-NQ	1,2-NQ	1,4-AQ	O <sub>3</sub>	Temp	RH											
DTTv	1																																																	
DTTm	0.69*	1																																																
AAv	-0.07	0.22	1																																															
AAm	0.31	0.86**	0.44	1																																														
PM2.5	-0.23	-0.83	-0.16	-0.9	1																																													
F <sup>-</sup>	-0.28	-0.09	-0.14	0.19	-0.16	1																																												
Cl <sup>-</sup>	-0.32	-0.74	0.52*	-0.76	0.88**	-0.43	1																																											
NO <sub>3</sub> <sup>-</sup>	0.03	-0.6	-0.3	-0.67	0.85**	0.06	0.59*	1																																										
SO <sub>4</sub> <sup>2-</sup>	0.15	-0.51	-0.1	-0.76	0.83**	-0.35	0.73**	0.66*	1																																									
NH <sub>4</sub> <sup>+</sup>	-0.23	-0.83	-0.16	-0.9	0.82**	-0.19	0.88**	0.63*	0.92**	1																																								
Na <sup>+</sup>	-0.23	-0.83	-0.16	-0.9	0.44	-0.16	0.84	0.85**	0.83**	0.95**	1																																							
K <sup>+</sup>	0.48	0.57*	0.47	0.52*	-0.31	-0.21	-0.15	-0.18	-0.14	-0.31	-0.31	1																																						
Mg <sup>2+</sup>	-0.28	-0.82	-0.23	-0.84	0.9**	0.04	0.71**	0.8**	0.75**	0.9**	0.9**	-0.61	1																																					
Ca <sup>2+</sup>	-0.35	-0.49	-0.46	-0.43	0.41	0.55*	0.09	0.52*	0.22	0.41	0.41	-0.7	0.63*	1																																				
Mn	-0.45	-0.45	-0.34	-0.32	0.24	0.6*	-0.02	0.25	0.13	0.24	0.24	-0.78	0.54*	0.93**	1																																			
Co	-0.02	-0.57	-0.11	-0.73	0.83**	-0.01	0.69*	0.77**	0.8**	0.83**	0.83**	-0.35	0.85**	0.6*	0.44	1																																		
Ni	-0.16	-0.52	-0.21	-0.5	0.65*	0.39	0.36	0.77**	0.55*	0.65*	0.65*	-0.39	0.76**	0.86**	0.72*	0.8**	1																																	
Cd	0.24	-0.27	-0.23	-0.4	0.63*	0.01	0.38	0.88**	0.58*	0.63*	0.63*	0.08	0.55*	0.47	0.17	0.69*	0.77**	1																																
Zn	0.24	-0.48	-0.09	-0.72	0.84**	-0.44	0.78**	0.76**	0.87**	0.84**	0.84**	0.05	0.67*	0.01	-0.2	0.72**	0.36	0.63*	1																															
Ba	0.14	-0.52	0	-0.72	0.9**	-0.42	0.85**	0.8**	0.91**	0.9**	0.9**	-0.08	0.77**	0.19	0	0.83**	0.55*	0.69*	0.94**	1																														
Cr	0.37	0.13	-0.13	0.03	0.01	0.43	-0.19	0.2	0.07	0.01	0.01	-0.34	0.26	0.39	0.4	0.36	0.32	0.09	0.03	0.08	1																													
Cu	0.57*	-0.05	0.05	-0.27	0.42	-0.41	0.41	0.45	0.51*	0.42	0.42	0.58*	0.12	-0.48	-0.67	0.18	-0.09	0.41	0.77**	0.57	-0.17	1																												
Al	0.41	0.5	0.22	0.45	-0.37	-0.09	-0.31	-0.11	-0.24	-0.37	-0.37	0.49*	-0.35	-0.35	-0.43	-0.23	-0.23	0.14	-0.03	-0.16	-0.13	0.24	1																											
As	0.22	-0.34	-0.08	-0.53	0.69*	-0.08	0.5*	0.68*	0.88**	0.69*	0.69*	0.08	0.6	0.33	0.2	0.73**	0.71	0.75**	0.7**	0.77**	0.05	0.47	-0.11	1																										
Pb	0.63*	0.31	0.78**	0.05	-0.04	-0.32	0.07	-0.05	0.18	-0.04	-0.04	0.46	-0.17	-0.66	-0.68	-0.03	-0.46	-0.14	0.43	0.2	0.26	0.69*	0.27	0.01	1																									
Fe	-0.17	-0.37	0.09	-0.36	0.36	0.4	0.25	0.16	0.48	0.36	0.36	-0.05	0.34	0.23	0.34	0.41	0.38	0.04	0.23	0.23	0.22	0.13	-0.39	0.54*	0.13	1																								
V	0.63*	0.29	0.01	0	0	-0.36	-0.02	0	0.35	0	0	0.57*	-0.16	-0.59	-0.61	-0.09	-0.31	0.09	0.44	0.22	-0.15	0.77**	0.47	0.35	0.72**	0.19	1																							
Ag	0.28	-0.14	0.62*	-0.33	0.43	-0.26	0.38	0.3	0.74**	0.43	0.43	0.41	0.23	-0.19	-0.21	0.32	0.22	0.38	0.6*	0.55*	-0.25	0.66*	0.02	0.82**	0.29	0.58*	0.71**	1																						
Bi	0.42	0.19	-0.07	-0.04	-0.09	-0.15	-0.09	-0.08	0.12	-0.09	-0.09	0.31	-0.14	-0.47	-0.47	-0.08	-0.37	-0.11	0.31	0.02	0	0.56*	0.59*	0.03	0.73**	0.15	0.83**	0.34	1																					
Ce	0.69*	0.25	0.55*	-0.02	0.16	-0.46	0.2	0.22	0.5*	0.16	0.16	0.45	0.1	-0.43	-0.5	0.23	-0.06	0.32	0.61*	0.5*	0.07	0.71**	0.6*	0.45	0.68*	0.04	0.82**	0.59*	0.68*	1																				
Sr	0.25	-0.23	0.61*	-0.4	0.58*	-0.17	0.48	0.51*	0.78**	0.58*	0.58*	0.41	0.34	-0.02	-0.13	0.5*	0.42	0.6*	0.69*	0.67*	-0.18	0.68*	-0.03	0.91**	0.22	0.58*	0.56*	0.95**	0.21	0.52*	1																			
Sb	-0.37	-0.56	-0.19	-0.48	0.47	0.47	0.24	0.43	0.4	0.47	0.47	-0.74	0.75**	0.87**	0.92**	0.68**	0.81**	0.31	0.11	0.29	0.45	-0.43	-0.29	0.4	-0.47	0.46	-0.41	-0.01	-0.25	-0.18	0.07	1																		
WSOC	0.78*	-0.46	-0.36	-0.75	0.8**	-0.18	0.57*	0.82**	0.9**	0.8**	0.8**	-0.16	0.75**	0.41	0.21	0.86**	0.68*	0.79**	0.85**	0.86**	0.18	0.5*	-0.05	0.86**	0.13	0.34	0.32	0.59*	0.21	0.48	0.7**	0.45	1																	
1,4-NQ	0.2	-0.33	0.1	0.23	0.22	0.34	0.22	0.47	-0.48	0.64*	0.45	-0.87	0.55*	0.67*	0.55*	0.44	0.78**	0.45	0.34	0.54*	0.22	-0.55	0.22	0.35	-0.01	0.44	-0.89	-0.56	-0.77	0.44	0.22	0.52*	0.22	1																
1,2-NQ	-0.06	-0.19	-0.5	-0.23	0.32	0.18	0.2	0.63*	0.09	0.36	0.36	-0.21	0.39	0.72**	0.37	0.48	0.67*	0.72**	0.14	0.28	0.06	-0.18	0.03	0.19	-0.53	-0.43	-0.51	-0.3	-0.47	-0.24	-0.06	0.33	0.37	0.67*	1															
1,4-AQ	0.3	-0.33	-0.65	-0.55	0.68*	-0.1	0.3	0.85**	0.62*	0.63*	0.63*	-0.24	0.65*	0.55*	0.31	0.75**	0.83**	0.92**	0.64*	0.72**	0.29	0.3	-0.04	0.7*	-0.13	-0.04	0.05	0.26	-0.12	0.27	0.44	0.44	0.84**	0.68*	0.68*	1														
O <sub>3</sub>	0.01	-0.08	0.06	-0.19	0.17	-0.02	0.16	0.11	0.34	0.17	0.17	-0.54	0.45	0.54*	0.61*	0.58*	0.5*	0.18	0.06	0.28	0.45	-0.48	-0.03	0.26	-0.27	0.09	-0.31	-0.1	-0.21	0.09	-0.08	0.73**	0.34	0.33	0.33	0.29	1													
Temp	-0.03	0.66*	-0.17	0.34	-0.63	-0.35	-0.47	-0.75	-0.46	-0.63	-0.63	0.05	-0.64	-0.38	-0.23	-0.68	-0.65	-0.58	-0.56	-0.6	-0.53	-0.34	0.1	-0.5	-0.18	-0.42	0.06	-0.2	0.05	-0.23	-0.4	-0.46	-0.51	-0.4	-0.4	-0.42	-0.15	1												
RH	0.23	0.52*	0.15	0.61*	-0.53	-0.21	-0.38	-0.33	-0.65	-0.53	-0.53	0.18	-0.51	-0.41	-0.44	-0.6	-0.55	-0.3	-0.39	-0.39	0.02	-0.13	0.23	-0.71	0.09	-0.85	-0.21	-0.65	-0.19	-0.1	-0.67	-0.58	-0.61	0.04	0.04	-0.22	-0.26	0.28	1											

\*At 0.05 level (two-tailed), the correlation is significant

The correlation observed between DTTv and WSOC during winter suggests a possible contribution of biomass burning (Farahani et al., 2022; Hakimzadeh et al., 2020). During the summer, both DTTv and AAv induced by methanol-soluble fraction showed weak correlation with most trace metals. Furthermore, during the summer season, DTTv exhibited a weak correlation with WSOC, whereas AAv demonstrated a strong correlation with WSOC (as shown in Table 8.10). This indicates that WSOC may play a significant role in contributing to the high AAv. The correlation of OP and WSOC has been reported in several studies (Fang et al., 2016; Verma et al., 2012). However, the specific chemical species responsible for the high DTTv during the summer season remain unclear. Therefore, it is plausible that the elevated DTTv levels observed during the summer season could be attributed to photochemically aged aerosols (Famiyeh, Jia, et al., 2023; Hsiao et al., 2021), as well as other unanalyzed chemical species such as water-insoluble trace metals (WITMs), water-insoluble organic carbons (WIOCs), and HMW-quinones (Fang et al., 2016).

Overall, the OP showed moderate-to-strong correlation with several chemical species, including Cu, Fe, Cd, As, Ag, Pb, V, Ce, quinones,  $\text{Ca}^{2+}$ ,  $\text{Mg}^{2+}$ ,  $\text{Na}^+$ ,  $\text{K}^+$ , 1, 2-NQ,  $\text{NO}_3^-$ ,  $\text{SO}_4^{2-}$ , WSOC, and PAHs. These chemical species can be attributed to a variety of sources, such as vehicular emissions, industrial emissions, sea spray, road dust, and secondary aerosol. Nevertheless, establishing a conclusive link between the OP of  $\text{PM}_{2.5}$  and its sources cannot rely solely on correlation. This is because a strong correlation does not necessarily indicate causality (Veld et al., 2023). Therefore, we employed a more robust technique consisting of a PMF model coupled with BPPs, and MLR to accurately identify the sources of  $\text{PM}_{2.5}$  and determine their contributions to the OP.

#### 5.2.4.6. Graphical analysis of source dispersion of PM<sub>2.5</sub> mass concentration

Figure 5-15 displays the dispersion patterns of PM<sub>2.5</sub> mass concentration across four seasons. In autumn, the concentration of PM<sub>2.5</sub> is predominantly found in the northeast and southeast, indicating significant contributions from the Beilun and Zhenhai industrial zones, as well as vehicular traffic emissions from a nearby freeway adjacent to our study area. This suggests that industrial and vehicular emissions are the primary sources of PM<sub>2.5</sub> in autumn. The concentration patterns in winter show similarities, with dominant contributions from industrial and vehicular traffic emissions. In spring, the concentration of PM<sub>2.5</sub> is predominantly influenced by industrial emissions from the Wangchun industrial zone and vehicular traffic emissions from a freeway close to our study area in the southwest. In summer, the highest concentration is observed in the southwest, indicating that vehicular traffic emissions, which is in close proximity to our sampling domain.

The bivariate plot confirms that industrial and vehicular traffic exhaust emissions are the predominant sources contributing to PM<sub>2.5</sub> in Ningbo. However, it is important to emphasize that long-range transport of PM<sub>2.5</sub> during different seasons can also contribute to its levels. This aspect was explored through air mass trajectory analysis, as shown in Figure 5-16.

The analysis of air mass trajectory and fire spot distribution reveals that during the winter season, more than 80% of the air masses originate from the northwestern region of China and pass through Hangzhou Bay before reaching the study area. This finding suggests that aerosols transported over medium distances, potentially containing pollutants from regional biomass burning activities, could significantly contribute to the

heightened levels of PM<sub>2.5</sub> concentrations during winter. Additionally, during winter, air mass transport (43.1%) originates from Inner Mongolia to our study domain. Another observation is that in autumn, there is air mass transport (18.3%) from Northern China, particularly Hebei Province, to our study domain. It is worth noting that throughout all seasons, there is a consistent inflow of air masses from the East China Sea to our study domain.

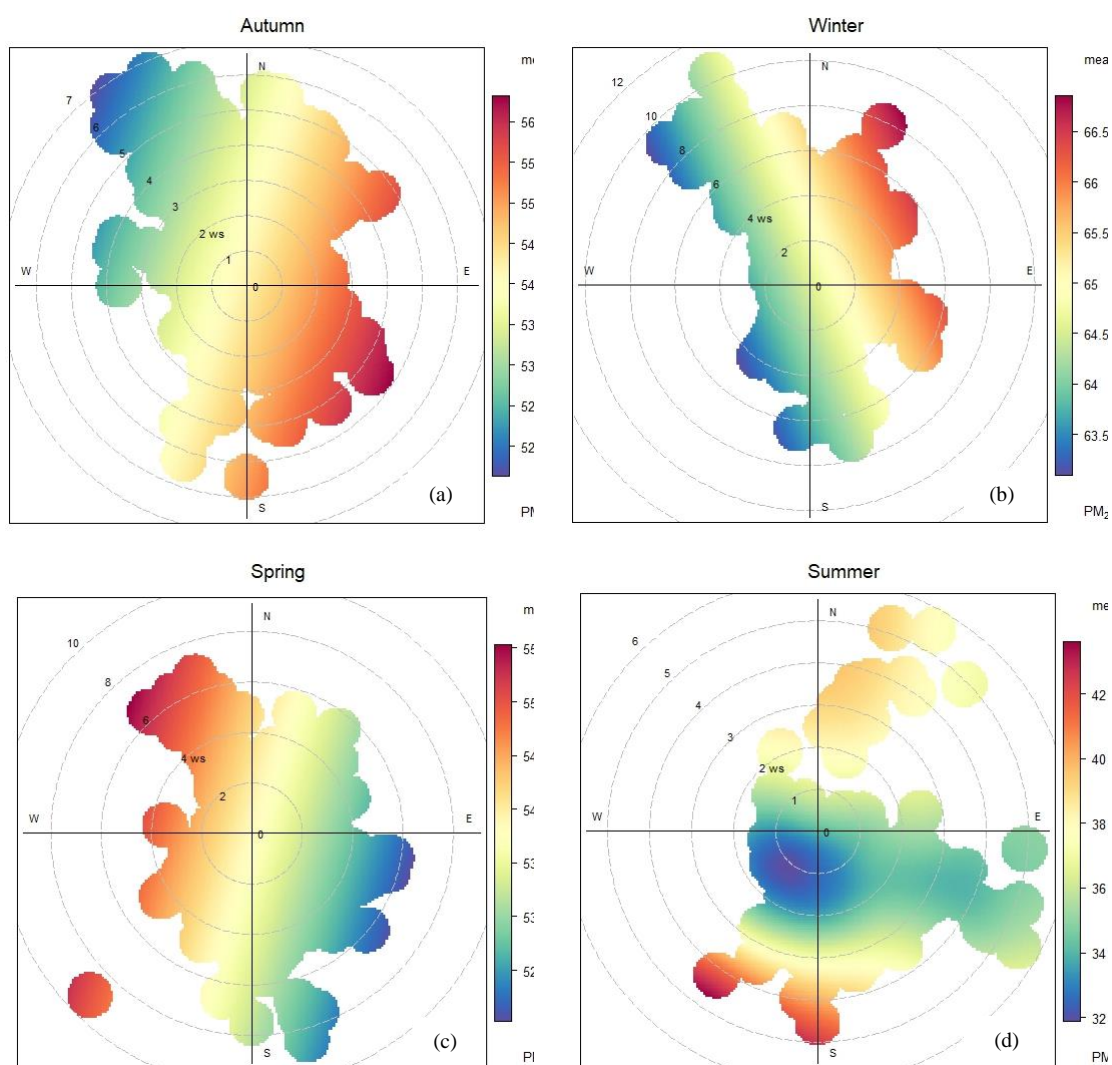


Figure 5-15 Bivariate polar plots of seasonal PM<sub>2.5</sub> concentration ( $\mu\text{g m}^{-3}$ ): (a) Autumn, (b) Winter, (c) Spring, (d) Summer

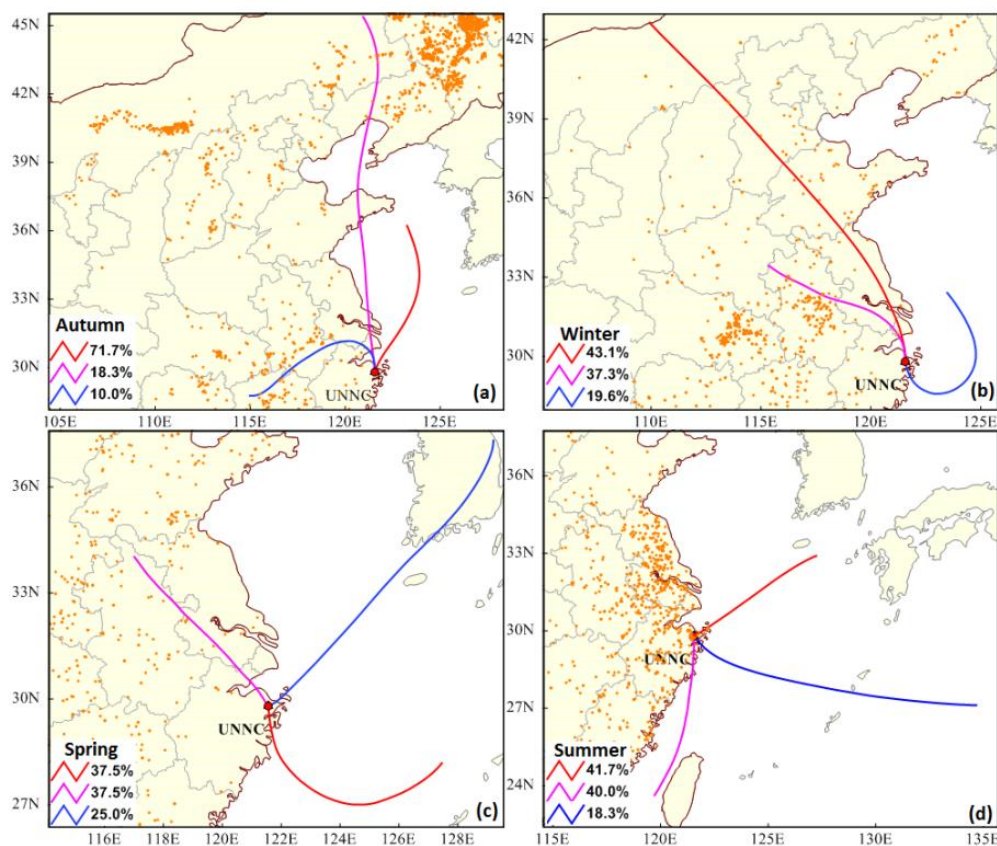


Figure 5-16 48-h back trajectory air masses and distribution of firespot during autumn (a), winter (b), spring (c) and summer (d) (Chen et al., 2022)

ing, (d) Summer

#### 5.2.4.7. Graphical analysis of source dispersion of water-soluble OP: seasonal variations

Figure 5-17 presents the BPPs of OP induced by water-soluble fractions of  $PM_{2.5}$  across different seasons. The dispersion characteristics of the OP exhibit variation across different seasons, indicating distinct source contributions. In autumn, the dominant source of DTTv is observed in the northwest, west, and southwest regions (as shown in Figure 5-17 a), suggesting the contribution of industrial emissions from the Wangchun industrial zone, as well as vehicular traffic from a nearby freeway within our study area. In winter, the dominant sources of DTTv are industrial emissions from the northwest of the Wangchun industrial zone and minor contributions from the Zhenhai industrial park in

the northeast. In spring, the potential sources of DTTv can be attributed to industrial emissions in the Zhenhai and Beilun industrial parks, as well as contributions from marine and sea salt aerosols originating from the Ningbo-Zhoushan port and the East China Sea. In summer, the DTTv is possibly associated with industrial emissions from the Zhenhai Industrial Park in the northeast and vehicular traffic emissions during both low and high wind speeds in the southeast region of a freeway proximal to our study area.

The above results suggest consist contribution of industrial emissions to DTTv induced by water-soluble fractions of PM<sub>2.5</sub>. The corresponding DTTm results display comparable patterns of source dispersion, with the exception of autumn where the contribution of vehicular traffic in the southwest region diminishes (Figure 5-17 b), and summer where the contribution of vehicular traffic emissions increases notably during periods of low wind speed (Figure 5-17 n).

In autumn, the AAv concentrations were highest in the southeast, south, southwest, and northeast regions (as shown in Figure 5-17 c), indicating potential contributions from vehicular traffic and industrial emissions. The corresponding AAm concentrations in autumn (Figure 5-17 d) were dominated by industrial emissions from Zhenhai and Beilun industrial park, as well as vehicular traffic emissions from the nearby freeway. Additionally, marine and sea salt aerosols from the Ningbo-Zhoushan port and the East China Sea were also identified as significant contributors to the AAm levels in autumn. In winter, both AAv and AAm were dominated in the south, southwest, and southeast (as shown in Figure 5-17 g), which could suggest dominant vehicular exhaust emissions from the freeways in close proximity to our study domain.

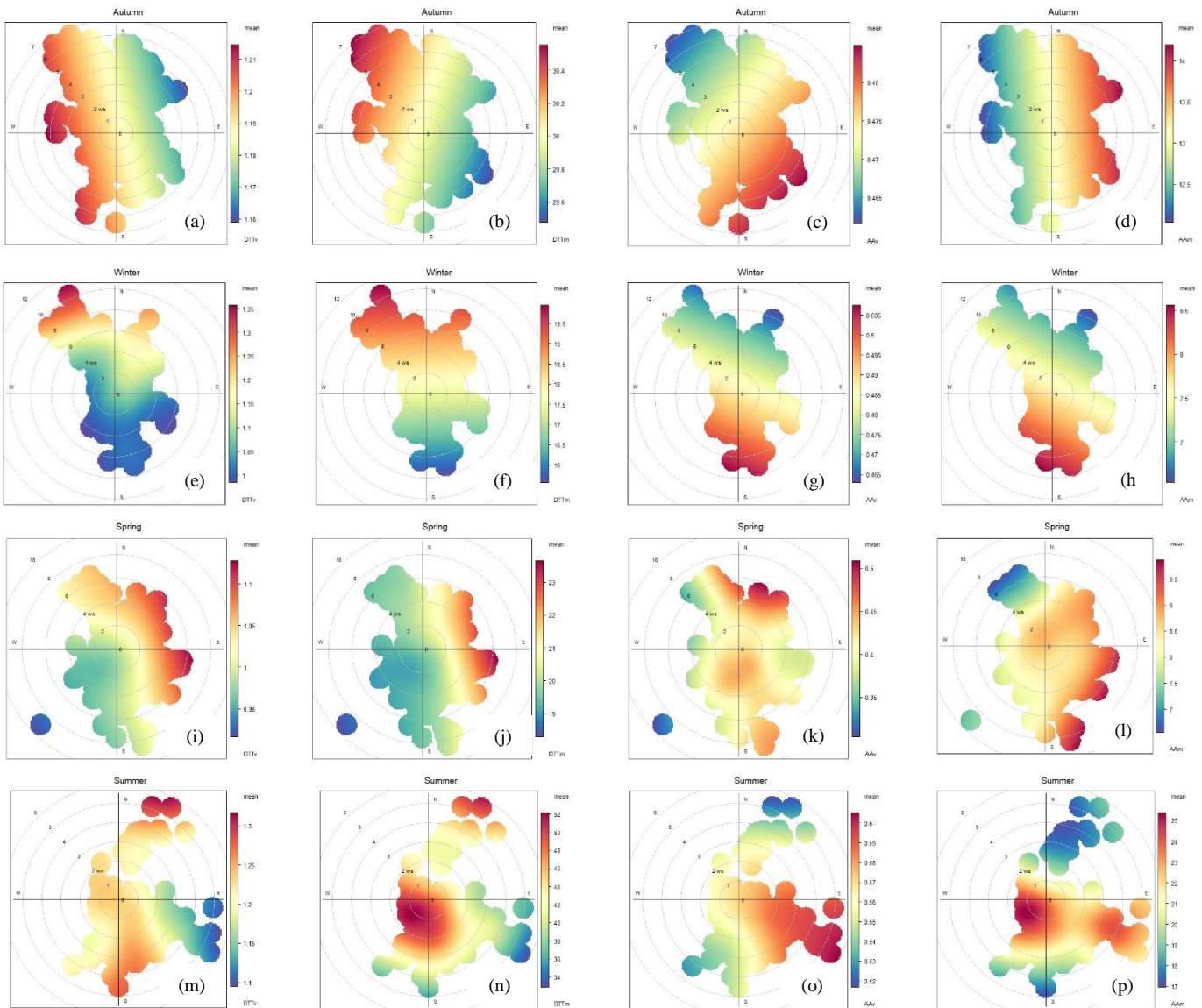


Figure 5-17 Bivariate polar plots of seasonal OP induced by water-soluble fractions of  $PM_{2.5}$ : Autumn (a-d), Winter (e-h), Spring (i-m), Summer (m-p)

The spring AAv is dominated by industrial emissions in the northeast of Zhenhai and Beilun industrial park, and minor vehicular exhaust contributions at low and high wind speed. The corresponding AAm concentrations are dominant in the southeast and northeast, indicating the significant contribution of vehicular traffic exhaust emissions, industrial emissions, and marine and sea salt aerosols from the Ningbo-Zhoushan port

and the East China Sea. In contrast, the AAv concentrations in summer are highest in the southeast region, whereas the corresponding AAm concentrations are dominant in the southeast and southwest regions. The AAv and AAm levels in the southeast reveal potential contributions from marine and sea salt aerosols, while the AAm concentrations in the southwest region, particularly during periods of low wind speed, suggest the influence of vehicular traffic exhaust emissions.

#### 5.2.4.8. Graphical analysis of source dispersion of water-soluble OP: seasonal variations

Figure 5-18 shows the dispersion patterns of OP induced by methanol-soluble fractions of PM<sub>2.5</sub>. In autumn, the concentrations of DTTv peaked in the northeast and southeast regions, indicating potential sources from industrial emissions originating from Zhenhai and Beilun industrial park, vehicular traffic from nearby freeways in the southeast, and marine and sea salt aerosols from the Ningbo-Zhoushan port and the East China Sea. The AAv concentrations, on the other hand, were dominant in the northwest and west regions, suggesting potential emissions from industrial facilities in the Wangchun industrial zone, as well as vehicular traffic from highways and nearby freeways. As for the DTTm and AAm levels in autumn, they can be associated with industrial emissions. Specifically, the DTTm concentrations can be attributed to industrial emissions from both the Wangchun industrial zone and Zhenhai industrial park. The AAm in autumn can be attributed to industrial emissions from both Zhenhai and Beilun industrial park, with potential contributions from marine and sea salt aerosols.



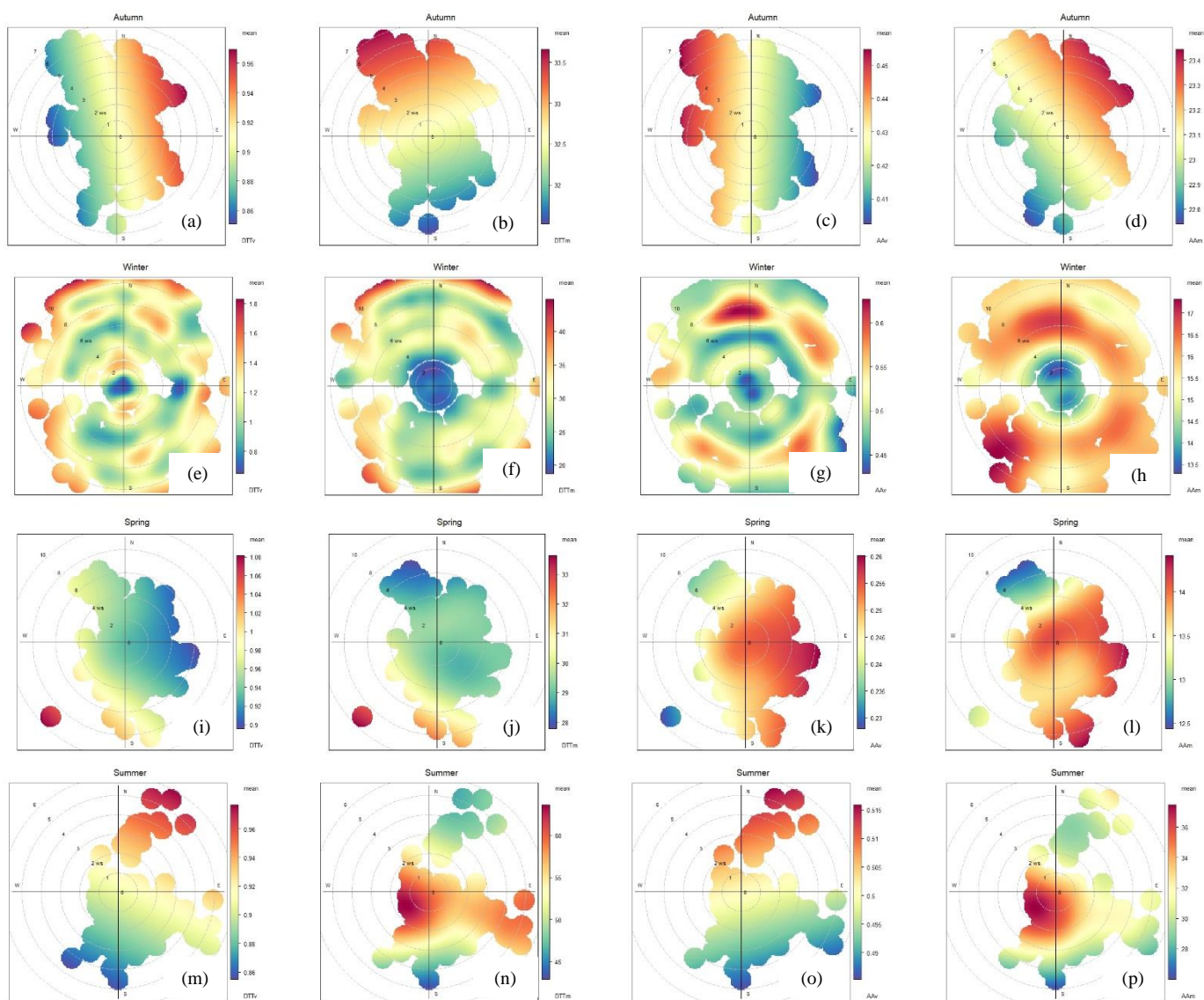


Figure 5-18 Bivariate polar plots of seasonal OP induced by methanol-soluble fractions of  $PM_{2.5}$ : Autumn (a-d), Winter (e-h), Spring (i-m), Summer (m-p)

The concentrations of DTTv, DTTm, AAv, and AAm induced by methanol-soluble fractions of  $PM_{2.5}$  (as shown in Figure 5-18 e-h) in winter were found to be predominant in all directions, indicating multiple sources and locations. Specifically, the elevated levels of DTTv and AAv can be attributed to industrial emissions originating from both

the Wangchun industrial zone and Zhenhai industrial park, as well as vehicular traffic on nearby freeways.

Furthermore, the sources of AAv and AAm include similar contributions from these sources, along with potential influences from marine and sea salt aerosols. In the spring season, the dispersion patterns of DTTv and DTTm (as shown in Figure 5-18 i and j, respectively) were found to be similar, with a prevalence in the southwest direction. This observation suggests that vehicular traffic contributions from nearby freeways play a significant role. Similar patterns were between AAv and AAm in spring (as shown in Figure 5-18 k and l, respectively), with peak concentrations occurring in all directions during periods of low wind speed. Moreover, the concentration peaks in the southeast were attributed to vehicular traffic, while those in the northeast were associated with industrial emissions from the Beilun and Zhenhai industrial park. The dominant concentrations in the east further indicate contributions from marine and sea salt aerosols. These findings provide compelling evidence for the contributions of vehicular traffic, industrial emissions, and marine sources to the elevated levels of DTTv, DTTm, AAv, and AAm concentrations during the spring season.

In the summer, both DTTv and AAv displayed similar dispersion patterns (as shown in Figure 5-18 m and o, respectively), with concentrations predominantly observed in the northwest direction. This observation strongly suggests that industrial emissions from the Zhenhai industrial park are the major contributing factor. Similarly, DTTm and AAm also exhibited similar patterns (as shown in Figure 5-18 n and p, respectively), with elevated concentrations occurring during periods of low wind speed. These elevated

concentrations were primarily attributed to vehicular traffic activities on nearby freeways, which were within a few meters of our sampling domain. Additionally, the peak concentrations of DTTm in the southeast direction may indicate contributions from marine and sea salt aerosols.

Table 5.10 Summary of potential sources associated with OP induced by water-and methanol-soluble fractions of PM<sub>2.5</sub> across four seasons

Water-soluble fractions	Autumn	Winter	Spring	Summer
DTTv	industrial, vehicular traffic	industrial	industrial, marine, and sea salt	industrial, vehicular traffic
AAv	vehicular traffic, industrial	vehicular traffic	industrial, vehicular traffic	vehicular traffic, marine, and sea salt
Methanol-soluble fractions	Autumn	Winter	Spring	Summer
DTTv	industrial, vehicular traffic, marine, and sea salt	industrial, vehicular traffic	vehicular traffic	industrial
AAv	industrial, vehicular traffic	industrial, vehicular traffic	vehicular traffic	industrial

Table 5.10 presents a comprehensive summary of the potential sources attributed to DTTv and AAv, explored through the water- and methanol-soluble fractions of PM<sub>2.5</sub>, across all four seasons. The results of the bivariate polar plots analysis reveal consistent

contributions of industrial emissions to DTTv induced by water-soluble fractions throughout all seasons. Conversely, vehicular traffic demonstrates a consistent dominance in AAv during autumn and winter, with an additional contribution from marine and sea salt aerosols in AAv during the summer, alongside vehicular traffic. In the case of the methanol-soluble fraction, vehicular traffic and industrial emissions emerge as the key contributors to DTTv during spring and summer, respectively. For autumn and winter, industrial and vehicular traffic emissions consistently dominate both DTTv and AAv induced by the methanol-soluble fractions of PM<sub>2.5</sub>, with the further influence of marine and sea salt aerosols on DTTv during autumn. These findings provide robust evidence on the seasonal variations in sources contributing to DTTv and AAv, emphasizing the significant roles played by industrial emissions, vehicular traffic, and marine sources in the levels of these pollutants across different seasons.

#### 5.2.4.9. PMF model for source apportionment of PM<sub>2.5</sub>

In this study, the PMF model was utilized to identify the sources of PM<sub>2.5</sub> during different time periods, including daytime, nighttime, and throughout a year-round field campaign encompassing all four seasons. The concentrations and uncertainties of chemical species such as F<sup>-</sup>, Cl<sup>-</sup>, NO<sub>3</sub><sup>-</sup>, SO<sub>4</sub><sup>2-</sup>, Na<sup>+</sup>, K<sup>+</sup>, Mg<sup>2+</sup>, Ca<sup>2+</sup>, NH<sub>4</sub><sup>+</sup>, Cu, Mn, Fe, Co, Ni, Cd, Zn, Ba, Cr, As, Pb, V, Ag, Bi, Ce, Sr, Sb, WSOC, Levoglucosan, LMW-PAHs, HMW-PAHs, and quinones analyzed in daytime, nighttime, and year-round aerosol samples were incorporated into the PMF model. All 31 chemical species were included in the PMF analysis as their signal-to-noise (S/N) ratios exceeded 2.

The model was executed using a range of 2 to 8 factors, and the most favorable outcome was obtained with 6 factors. The Q (Robust) and Q (True) values were

consistently converging in all 31 iterations of the Base Model Runs, resulting in values of 3505.4 and 3794.1, respectively. The Q Theoretical was calculated according to equation (4-1) (Callén et al., 2014). The minimum Q value closely approached the theoretical value of Q (3000). Specifically, the theoretical value of Q was calculated as 0.98 times the minimum Q value. This suggests that there is an acceptable level of uncertainty in the input data (Callén et al., 2014). The Q/Qexp ratio at the 6-factor level was close to 1 (0.97); however, it decreased as the number of factors exceeded 6, indicating that the 6-factor solution represents the optimized solution for the input data. Moreover, the bootstrap (BS) mapping for the 6 factors and 150 runs were all unmapped (as shown in the Appendix Table 8.12).

The daytime and nighttime factor loadings of the 31 chemical species are depicted in Figure 5-19 and Figure 5-20, respectively. The factor loading of chemical species related to each emission source during the annual field campaign is depicted in Figure 5-22. The six sources of PM<sub>2.5</sub> derived from the PMF model include industrial emissions, biomass burning, secondary aerosol, marine emissions, vehicular emissions, and road dust. The results of the PMF model indicate that these sources are present consistently both during the day and night, as well as across various seasons. However, the contributions of these sources to PM<sub>2.5</sub> mass concentrations vary during day and night, and across seasons (as shown in Figure 5-21, and Figure 5-23, respectively). The specific details of each of the six sources of PM<sub>2.5</sub> derived from the PMF model are outlined below.

### (1) Industrial emissions (IE)

The daytime  $PM_{2.5}$  associated with IE is characterized by high loadings of Ni, Cd, Cr, Pd, V, PAHs, and quinones, as shown in Appendix (Figure 5-19 a). In contrast, during the night, the IE is marked by elevated loadings of Mn, Co, Zn, Cr, Pb, Fe, As, and Bi, as shown in Appendix (Figure 5-20 a). The presence of PAHs and quinones during the day can be primarily attributed to combustion sources, such coal combustion from coal-fired power plants. Furthermore, the elements Ni, V, and Mn are indicative of heavy oil combustion (Xu et al., 2021), while Co, As, Cd and Cr are associated with coal combustion (Do et al., 2023). The elevated levels of Mn and Fe suggest emissions from the iron and steel industry (Peli et al., 2021). During both daytime and nighttime, IE contributes 25.9% ( $8.21 \mu\text{g m}^{-3}$ ) and 29.9% ( $6.84 \mu\text{g m}^{-3}$ ), respectively, to the total  $PM_{2.5}$  mass concentration, which is  $31.7 \mu\text{g m}^{-3}$  during the day and  $22.9 \mu\text{g m}^{-3}$  at night. This suggests higher IE  $PM_{2.5}$  mass loading during the daytime than at night. As shown in Figure 5-24, IE contribution during the day originates largely from northwest, suggesting dominant contribution of industries from Wangchun industrial zone. In contrast, during the night, the dominant contribution of IE comes from both the northwest and northeast (as shown in Figure 5-25), suggesting contribution of industries from the Wangchun industrial zone and the Zhenhai industrial park.

Throughout the entire year, the IE is dominated by high loadings of trace metals such as Ni, Cd, As, Pb, and V (Liu et al., 2019), as well as PAHs (as shown in Figure 5-22 a). Throughout the year-round field campaign, the industrial sector was identified as the primary source of the  $PM_{2.5}$  mass concentration, representing 26.4% ( $13.7 \mu\text{g m}^{-3}$ ) of the

total PM mass concentration ( $51.7 \mu\text{g m}^{-3}$ ). The high IE throughout the year is dominated in winter season ( $17.1 \mu\text{g m}^{-3}$ ), as depicted in Figure 5-23 (a), and with the greatest emission originating from northwest (Figure 5-25).

## (2) Biomass burning (BB)

Biomass burning emissions during the day are associated with high loadings of WSOC, Levo,  $\text{F}^-$ , and  $\text{K}^+$  (as shown in Figure 5-19 b). Conversely, during the night, BB emissions are traced by high loadings of Levo,  $\text{K}^+$ , and quinones (as shown in Figure 5-20). The contribution of BB to  $\text{PM}_{2.5}$  pollution is 11.2% ( $3.55 \mu\text{g m}^{-3}$ ) during the day and increases to 17.8 % ( $4.07 \mu\text{g m}^{-3}$ ) at night (as shown in Figure 5-21). This suggests an increase in biomass burning (BB) emissions during nighttime, potentially attributed to the combustion of wood for domestic heating, particularly in rural areas of the city.

During the year-long campaign, we monitored  $\text{PM}_{2.5}$  emissions from BB. The data revealed high loadings of Levo,  $\text{Cl}^-$ ,  $\text{K}^+$ , and quinones. The BB emissions contribute approximately 14.3% ( $7.4 \mu\text{g m}^{-3}$ ) to the total annual  $\text{PM}_{2.5}$  pollution. By season, BB emissions dominated in spring ( $9.3 \mu\text{g m}^{-3}$ ), followed by autumn ( $8.2 \mu\text{g m}^{-3}$ ) (as shown in Figure 5-23) . This can be attributed to the burning of agriculture residues by farmers in rural areas during this period. The percentage contribution of BB emissions to  $\text{PM}_{2.5}$  pollution in Ningbo is relatively higher than other cities, including Beijing and Tianjin (4.5%) (Huang et al., 2017), and Changzhou (10.7%) (Li et al., 2023).

## (3) Secondary aerosols (SA)

During the daytime, SA accounted for 24.9 % ( $7.89 \mu\text{g m}^{-3}$ ) of the total concentration of  $\text{PM}_{2.5}$  particles, which is characterized by high loadings of  $\text{Cl}^-$ ,  $\text{NO}_3^-$ ,  $\text{SO}_4^{2-}$ ,  $\text{NH}_4^+$ , and

WSOC. However, during nighttime, SA were mainly loaded with  $\text{NO}_3^-$ ,  $\text{SO}_4^{2-}$ ,  $\text{NH}_4^+$ , and PAHs, and contributed 22.3% ( $5.11 \mu\text{g m}^{-3}$ ) to nighttime  $\text{PM}_{2.5}$  pollution (as shown in Figure 5-21). This indicates a decrease in SA contribution to  $\text{PM}_{2.5}$  pollution during nighttime compared to daytime. The dispersion characteristics of SA during the day and at night are shown in Figure 5-24 and Figure 5-25, respectively. This suggests a significant contribution of precursor gases, such as  $\text{SO}_2$  and  $\text{NO}_2$ , from industries and vehicular traffic, in the formation of secondary aerosols in our study domain. Throughout the entire one year-field campaign, SA contributed 24.1% ( $12.5 \mu\text{g m}^{-3}$ ) of the total  $\text{PM}_{2.5}$  pollution, and was characterized by high loadings of  $\text{Cl}^-$ ,  $\text{NO}_3^-$ ,  $\text{SO}_4^{2-}$ ,  $\text{NH}_4^+$ , WSOC, and quinones. It is important to note that  $\text{Cl}^-$  is not directly emitted from secondary processes. However, it can play a role in initiating the oxidation of VOCs (Choi et al., 2020; Le Breton et al., 2018). Secondary inorganic aerosols are primarily formed from reactions involving  $\text{NO}_3^-$ ,  $\text{SO}_4^{2-}$ , and  $\text{NH}_4^+$  (Huang et al., 2017; Liu et al., 2019). The SA emissions were highest in winter ( $16.9 \mu\text{g m}^{-3}$ ), followed by autumn ( $12.7 \mu\text{g m}^{-3}$ ), spring ( $11.6 \mu\text{g m}^{-3}$ ), and summer ( $8.80 \mu\text{g m}^{-3}$ ) (as shown in Figure 5-23). This can be attributed to the high concentrations of secondary inorganic species such as  $\text{NO}_3^-$ ,  $\text{SO}_4^{2-}$ , and  $\text{NH}_4^+$  in colder seasons than in warmer seasons.

#### (4) Marine emissions (ME)

The high loadings of  $\text{Cl}^-$ ,  $\text{Na}^+$ ,  $\text{Ca}^{2+}$ ,  $\text{NO}_3^-$ ,  $\text{SO}_4^{2-}$ , and  $\text{Mg}^{2+}$  were found to be indicative of the presence of  $\text{PM}_{2.5}$  emissions from sea spray during the day (Figure 5-19 d). At night, sea spray emissions were identified through elevated levels of  $\text{F}^-$ ,  $\text{Cl}^-$ ,  $\text{NO}_3^-$ ,  $\text{SO}_4^{2-}$ ,



and  $\text{Na}^+$  (Figure 5-20 d). The moderate loadings of V and Ni during daytime and at night can be attributed to emissions from marine vessels (Celo et al., 2015; Chen et al., 2022).

#### (5) Vehicular emissions (VE)

The  $\text{PM}_{2.5}$  emissions from VE during the day and at night is characterized by elevated levels of trace metals (Ni, Cd, Zn, Cr, Cu, As, Pb, Fe, V, Ag), PAHs, and quinones. Chemical compositions associated with VE during the day and night were similar, as shown in Figure 5-19 (e) and Figure 5-20 (e), respectively. During the daytime, VE accounts for 19.7% ( $6.25 \mu\text{g m}^{-3}$ ) of the total  $\text{PM}_{2.5}$  pollution. During nighttime hours, the contribution of VE to the overall pollution from  $\text{PM}_{2.5}$  amounts to approximately 14.3% ( $3.27 \mu\text{g m}^{-3}$ ). This suggests that  $\text{PM}_{2.5}$  pollution from VE is lower during nighttime compared to daytime. However, despite the reduced traffic emissions at night, it is possible that the lower mixing layer height and reduced wind speed contributed to the levels of chemical species associated with VE observed during this time. Figure 5-22 (e) shows the concentration profile of chemical species associated with  $\text{PM}_{2.5}$  pollution from VE, including Ni, Cd, Cr, Cu, Ag, Bi, PAHs, and quinones. Copper is also linked to non-exhaust emissions, primarily resulting from brake wear, as it is commonly used in brake pads (Clemente et al., 2023; Hsiao et al., 2021; Shen et al., 2022). VE contributes 21.4% ( $11.1 \mu\text{g m}^{-3}$ ) to the total  $\text{PM}_{2.5}$  pollution. The contribution of VE to  $\text{PM}_{2.5}$  pollution in the present study was similar to previous studies conducted in Ningbo (21%,  $11.2 \mu\text{g m}^{-3}$ ) (Li et al., 2018). Furthermore, the contribution of VE to  $\text{PM}_{2.5}$  mass concentration was lower than in Zhengzhou (17.3%,  $20.6 \mu\text{g m}^{-3}$ ) (Liu et al., 2019), and in Beijing (24.9%,  $24.8$

$\mu\text{g m}^{-3}$ ) (Huang et al., 2017), but higher than in Nanjing (10.7%,  $7.35 \mu\text{g m}^{-3}$ ) (Zhan et al., 2023).

By using the homohopane index ( $\text{C31}\alpha\beta\text{S}/(\text{C31}\alpha\beta\text{S} + \text{C31}\alpha\beta\text{R})$ ) ratio (as explained in Section 2.9.2.2), we were able to discriminate between vehicular emissions (0.4–0.6) and coal combustion ( $< 0.4$ ) (Křůmal et al., 2013; Wang et al., 2009). The homohopane index values during the daytime (0.37), nighttime (0.40), autumn (0.88), winter (0.50), spring (0.75), and summer (0.46), indicate that vehicular emissions contribute more to  $\text{PM}_{2.5}$  pollution than coal combustion at our study domain. This is expected because most of the industrial facilities in Ningbo are located in the northwest (specifically in the Wangchun industrial zone, 10 km away) and the northeast (specifically in the Zhenhai and Beilun industrial park, 37 km away). Our study area is in close proximity to several freeways that experience high levels of road traffic. This increases the likelihood of vehicular emissions being transported over short distances into our study domain.

#### (6) Road dust (RD)

The impact of RD on  $\text{PM}_{2.5}$  pollution can be assessed by examining the levels of  $\text{Ca}^{2+}$ ,  $\text{Mg}^{2+}$ , Fe, and Mn (Guo et al., 2023; Liu et al., 2019). These crustal elements have been widely used as tracers of road dust (Shen et al., 2022). The results of the PMF analysis indicate that RD contributes 12.8% to the total  $\text{PM}_{2.5}$  pollution during the day 12.8% ( $4.06 \mu\text{g m}^{-3}$ ) and 9.5% at night ( $2.18 \mu\text{g m}^{-3}$ ) (as shown in Figure 5-21). The higher contribution of RD during the day, as opposed to at night, can be attributed to construction activities that took place a few meters away from monitoring station, predominantly during the day. Furthermore, the stronger daytime wind speed ( $2.69 \text{ m s}^{-1}$ ) compared to

the nighttime wind speed ( $1.93 \text{ m s}^{-1}$ ) contributed to the resuspension of road dust particles that could potentially be transported into our study domain (Chen et al., 2022). During the day, road dust (RD) is transported from freeways in the southwest and southeast, whereas at night, RD is transported from the northwest (as shown in Figure 5-24 and Figure 5-25, respectively). The annual contribution of RD to the  $\text{PM}_{2.5}$  mass concentration is estimated to be 3.09% ( $2.3 \text{ } \mu\text{g m}^{-3}$ ) (as shown in Figure 5-23). The contribution of RD to  $\text{PM}_{2.5}$  mass concentration did not exhibit significant seasonality.

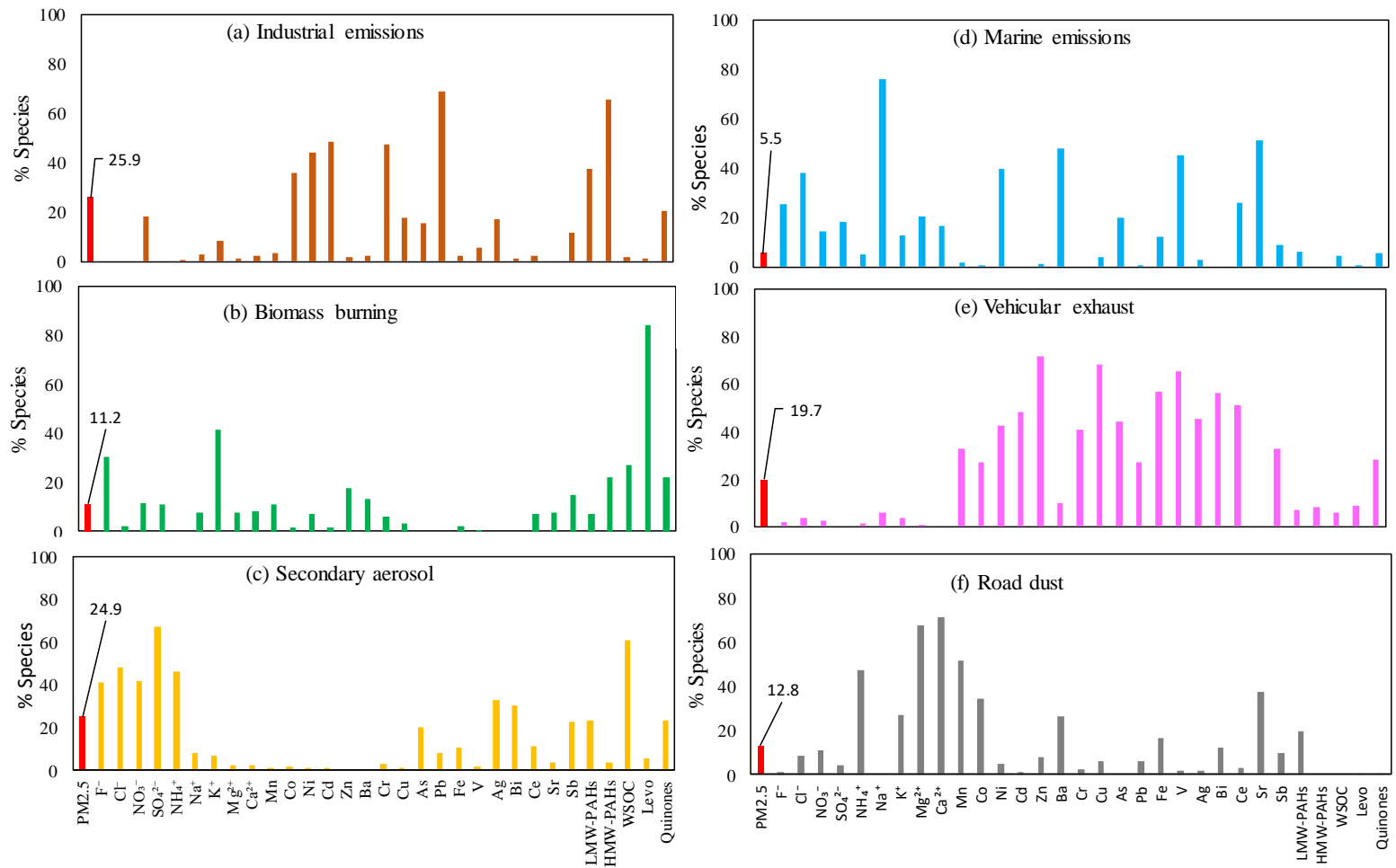


Figure 5-19 Daytime sources of PM<sub>2.5</sub> derived from PMF model: (a) IE, (b) BB, (c) SA, (d) ME, (e) VE, (f) RD

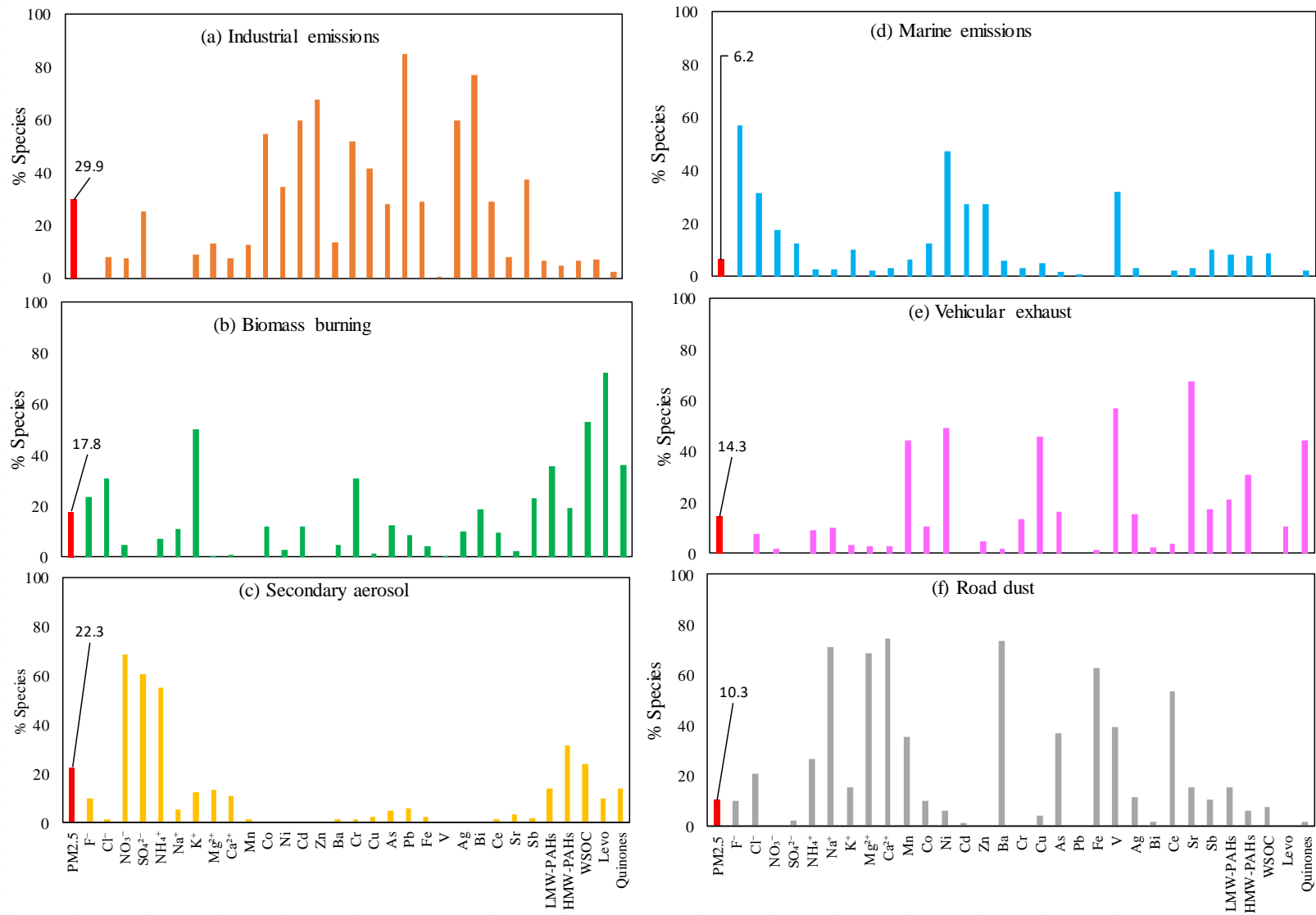


Figure 5-20 Nighttime sources of PM<sub>2.5</sub> derived from PMF model: (a) IE, (b) BB, (c) SA, (d) ME, (e) VE, (f) RD

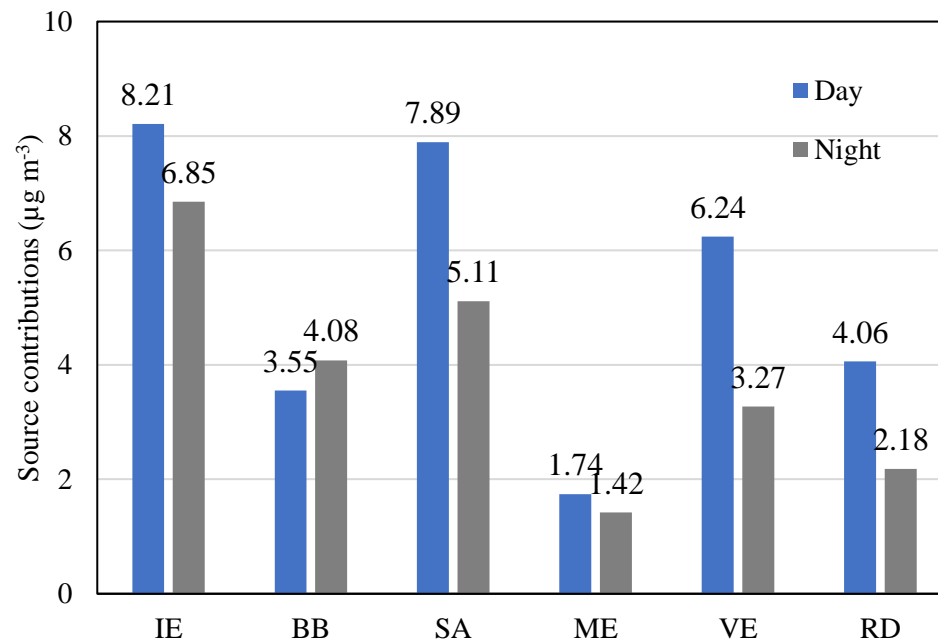


Figure 5-21 Day and night source contributions to PM<sub>2.5</sub> mass concentration (µg m<sup>-3</sup>) derived from the PMF model

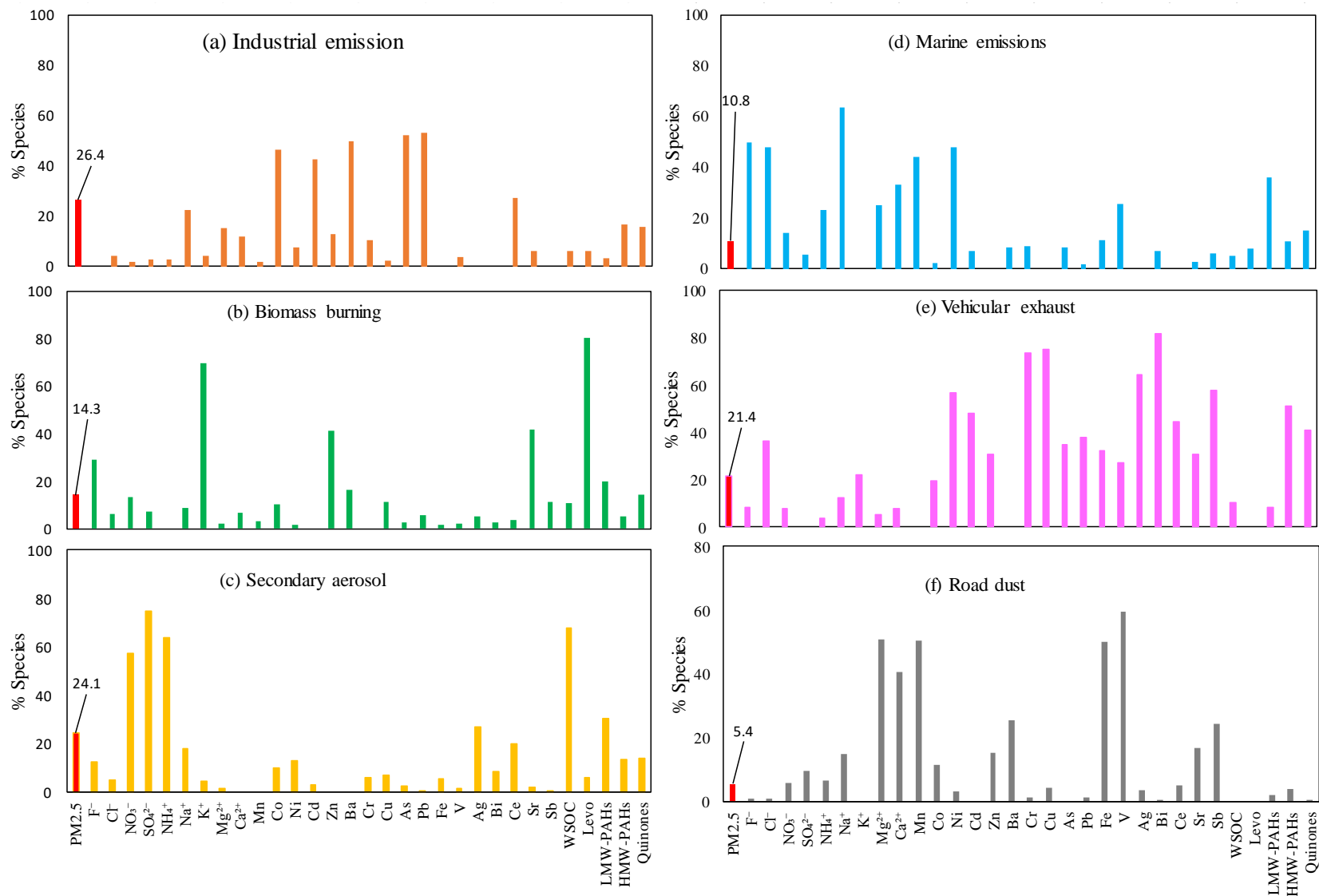


Figure 5-22 Annual sources of PM<sub>2.5</sub> derived from PMF model: (a) IE, (b) BB, (c) SA, (d) ME, (e) VE, (f) RD

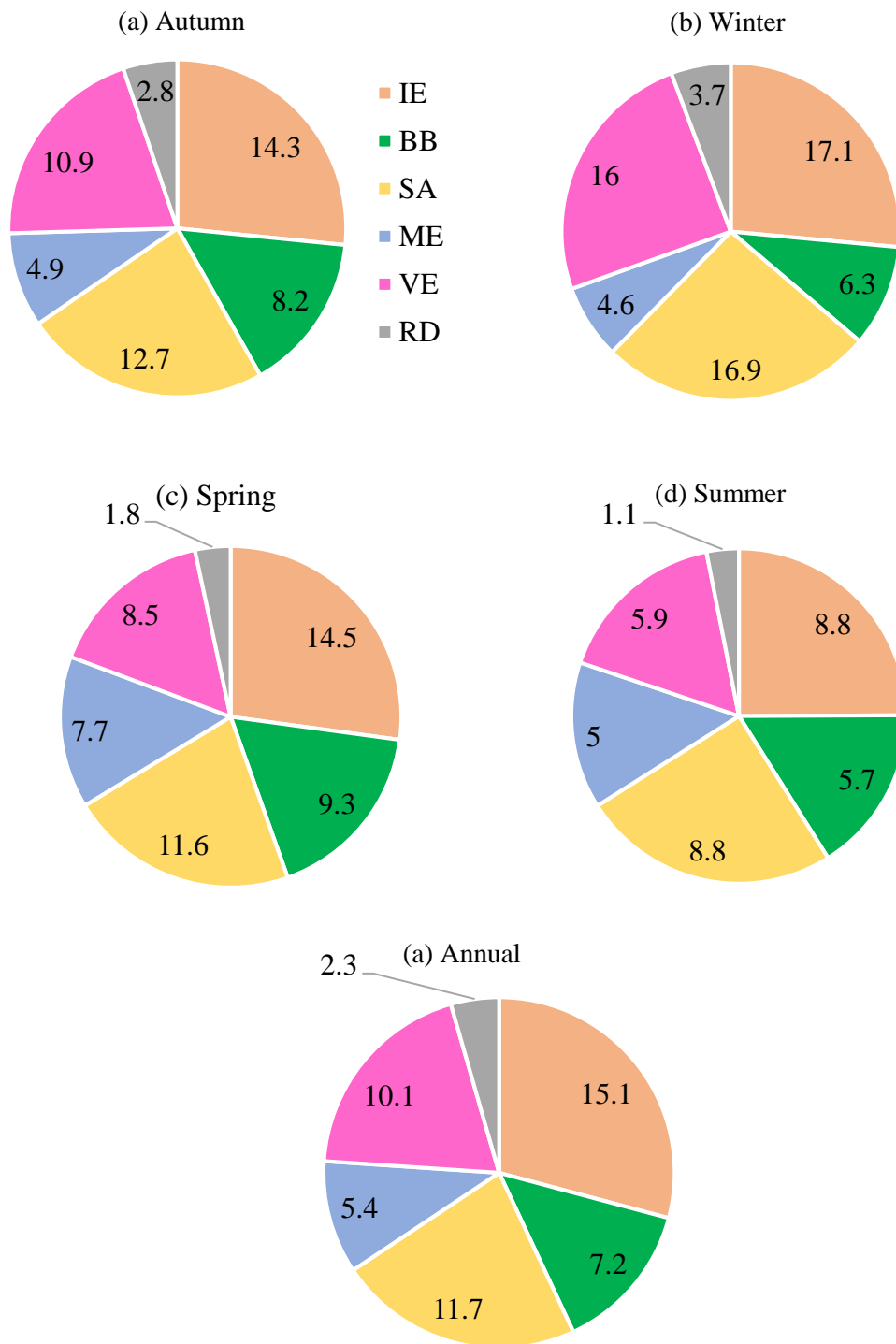


Figure 5-23 Seasonal source contributions to PM<sub>2.5</sub> mass concentration ( $\mu\text{g m}^{-3}$ ) derived from the PMF model



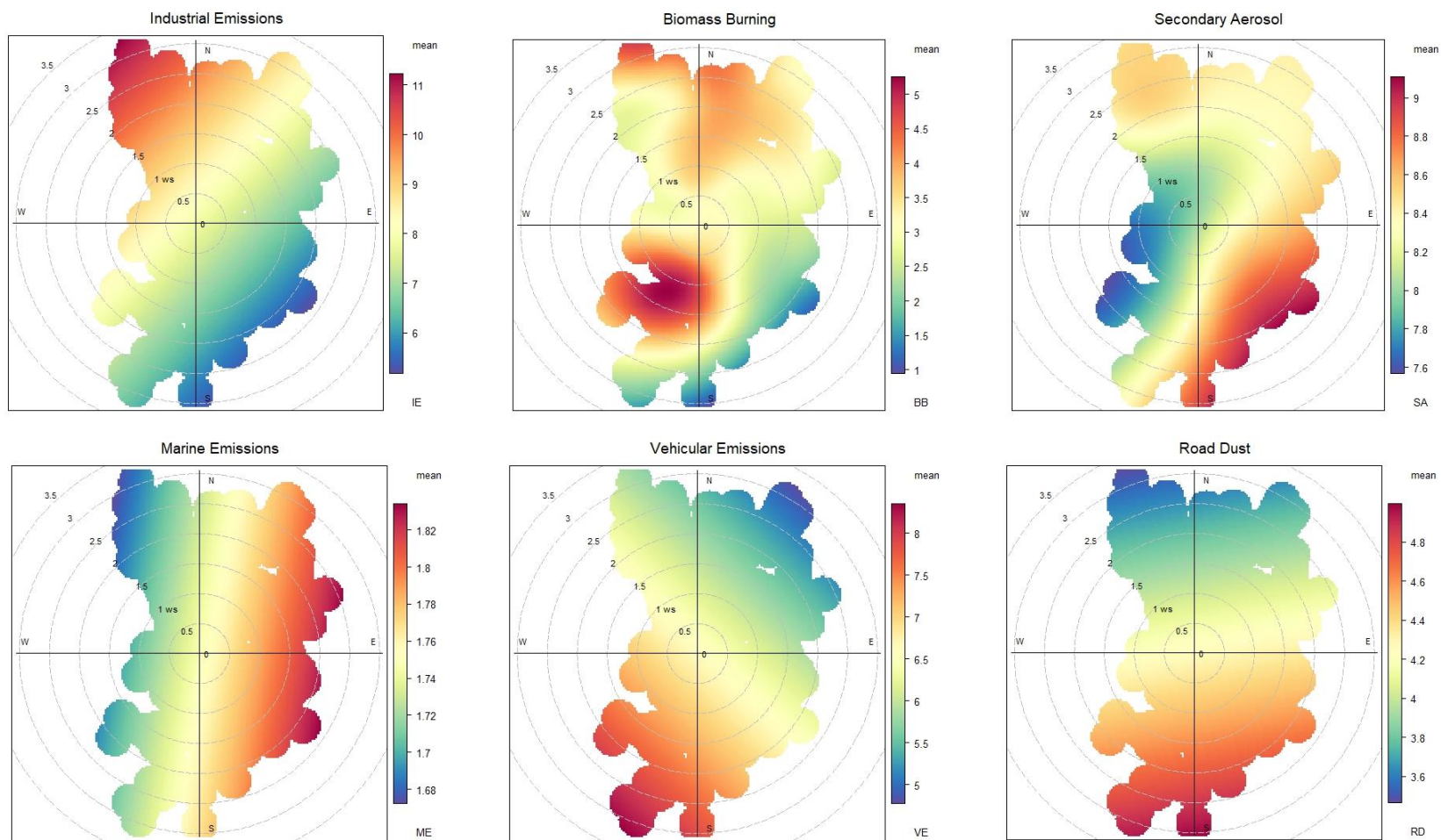


Figure 5-24 Bivariate polar plots of the factors derived from the PMF model attributed to PM<sub>2.5</sub> pollution during the day

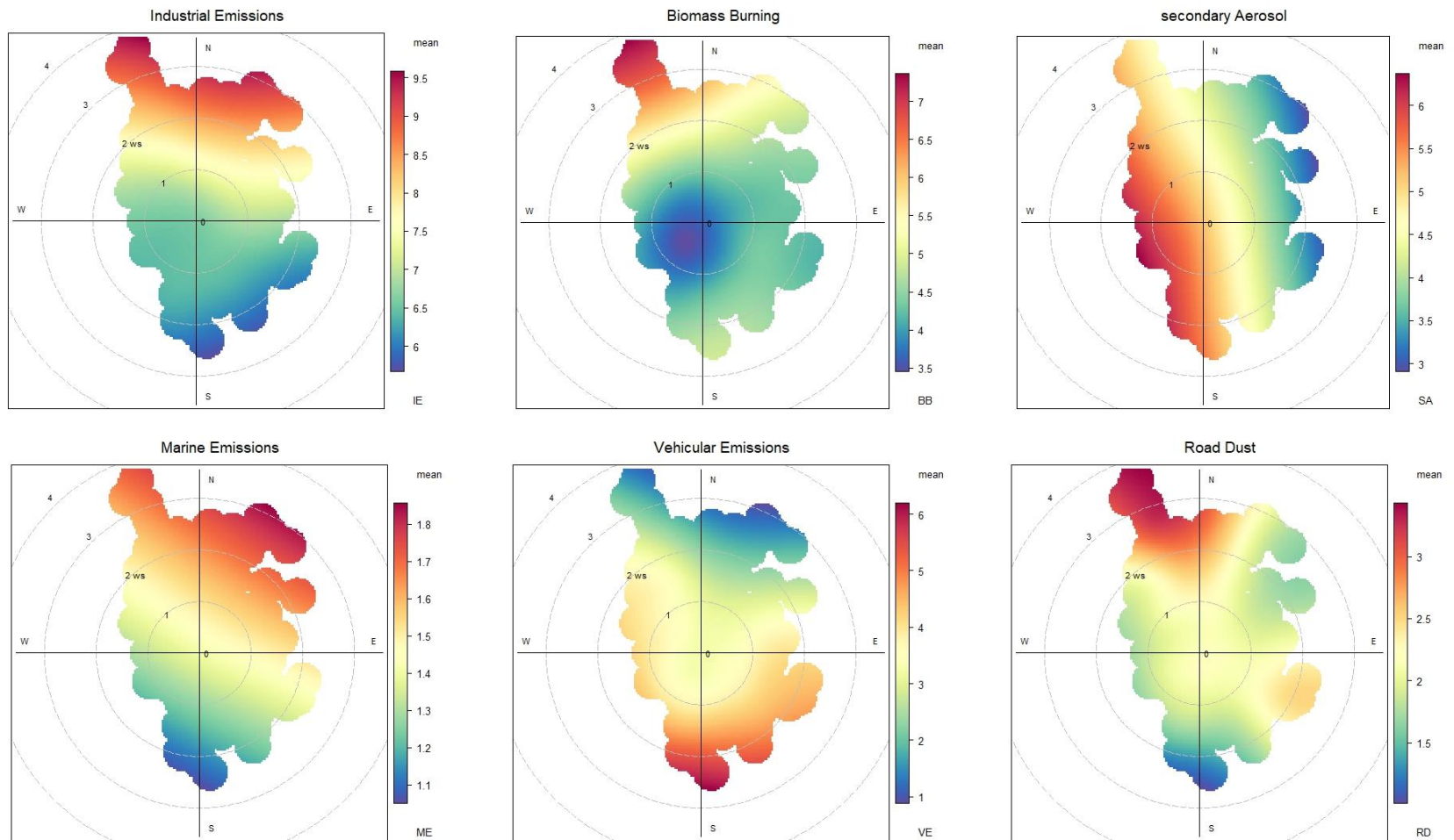


Figure 5-25 Bivariate polar plots of the factors derived from the PMF model attributed to PM<sub>2.5</sub> pollution during the night

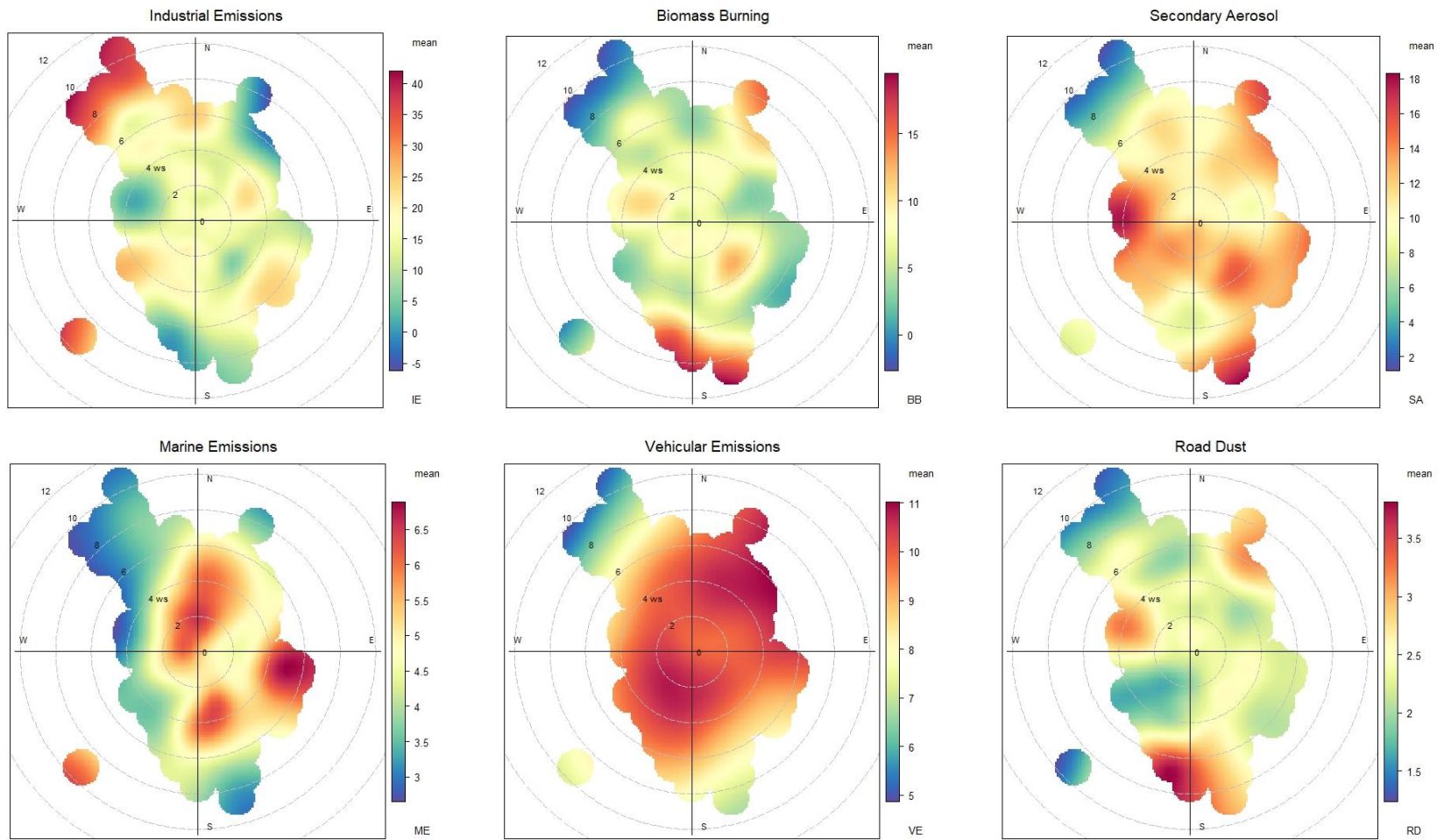


Figure 5-26 Bivariate polar plots of the factors derived from the PMF model attributed to PM<sub>2.5</sub> pollution in a year-round field campaign

#### 5.2.4.10. Source contribution to OP induced by water-and methanol-soluble fraction of PM<sub>2.5</sub>

Multiple linear regression was performed to estimate the contribution of different sources to the OP induced by water-and methanol-soluble fractions of PM<sub>2.5</sub>. The six sources identified through the PMF model were treated as independent variables, while OP was treated as the dependent variable. The contribution of each source was estimated from the absolute value of the standardized regression coefficient. Table 8.11 presents the summary of the multiple linear regression analysis conducted to estimate the source contributions to DTTv induced by water-soluble fractions of daytime and nighttime PM<sub>2.5</sub>.

Three sources dominated daytime DTTv: ME (0.069 nmol min<sup>-1</sup>m<sup>-3</sup>), IE (0.066 nmol min<sup>-1</sup>m<sup>-3</sup>), and RD (0.039 nmol min<sup>-1</sup>m<sup>-3</sup>). During nighttime DTTv, the main dominant sources were ME (0.124 nmol min<sup>-1</sup>m<sup>-3</sup>), SA (0.093 nmol min<sup>-1</sup>m<sup>-3</sup>), and IE (0.057 nmol min<sup>-1</sup>m<sup>-3</sup>). This suggests that ME, which increases aerosol acidity, elevates the OP levels. The aerosol collected in our study domain during both daytime and nighttime was found to be acidic. This acidity leads to the dissolution of trace metals emitted from IE and VE. As a result, the acidity of the aerosol increases their capacity to elevate OP levels (Fang, Guo, et al., 2017; Guo et al., 2023). This is supported by our findings of a moderate-to-strong correlation between trace metals (e.g., Co, Ni, Ba, Sr, As, Mn, Cu, Fe, Ag, Ce, Sr) and DTTv during the day. The consistent contribution of IE to DTTv during both day and night aligns with our findings from the bivariate polar plots.

The significant contribution of RD to daytime DTTv was attributed to construction activities during the sampling campaign. RD during the day contains trace metals such as Fe and Mn, which contribute to the OP activity through the Fenton reaction (Campbell et al.,

2021; Luo et al., 2023). During the nighttime, SA significantly contributes to DTTv. The daytime AAv induced by water-soluble fraction is dominated by SA and ME, whereas at night is dominated by SA, ME, and BB (as shown in Figure 5-27 a). This suggest consistent contribution of SA and ME to AAv during the daytime and at night. The AAv induced by methanol-soluble fraction of PM<sub>2.5</sub> during the day is dominated by IE, ME, and VE, and during the night is dominated by VE and RD (as shown in Figure 5-28).

The contributions of different sources to the concentrations of DTTv and AAv induced by the water-soluble fraction during a year-round field campaign are shown in Figure 5-29 and Figure 5-30, respectively. DTTv is mainly dominated by SA, with a concentration of 0.30 nmol min<sup>-1</sup>m<sup>-3</sup>, followed by RD (0.25 nmol min<sup>-1</sup>m<sup>-3</sup>), IE (0.21 nmol nmol min<sup>-1</sup>m<sup>-3</sup>), ME (0.16 nmol min<sup>-1</sup>m<sup>-3</sup>), and VE (0.15 nmol min<sup>-1</sup>m<sup>-3</sup>). The contribution of sources to AAv is mainly dominated by SA, with a concentration of 0.18 nmol min<sup>-1</sup>m<sup>-3</sup>. The seasonal contributions of these sources to DTTv and AAv are shown in Appendix (Figure 8:2). The contribution of SA to DTTv is dominant in autumn, winter, and summer, whereas in AAv it is dominant in winter and summer.

The contribution of sources to DTTv induced by the methanol-soluble fraction is dominated by ME, SA, and VE. In contrast, AAv is primarily influenced by RD, ME, and VE, as demonstrated in Figure 5-30. These findings suggest a consistent contribution of RD and VE to the OP induced by the methanol-soluble fractions of PM<sub>2.5</sub>. The contribution of RD can be linked to Fe and Mn, both of which play an active role in elevating the OP of ambient particles through the Fenton reaction. Furthermore, the OP of VE can be associated with various trace metals, including Ni, Cd, Zn, Cr, Cu, As, Pb, Fe, V, and Ag. It is not

surprising that in Ningbo, being a coastal and industrial city, IE and ME significantly contribute to the overall OP activity of ambient particles.

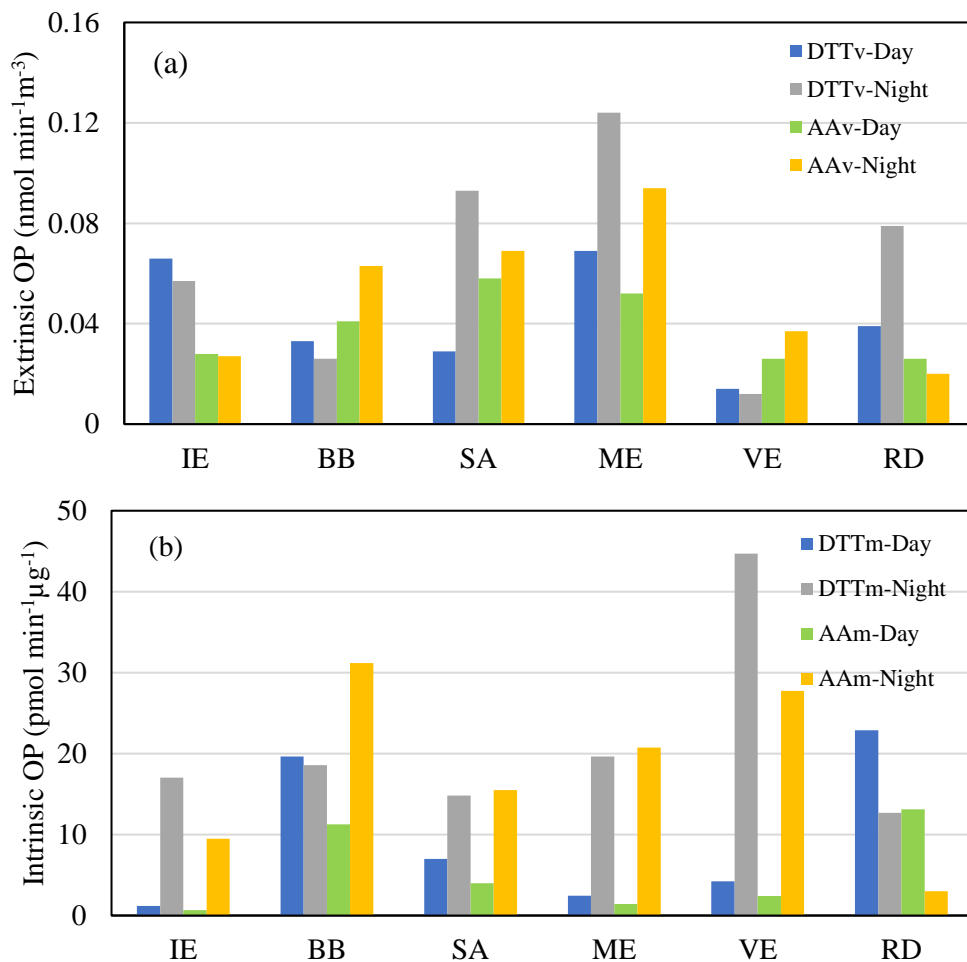


Figure 5-27 Source contributions to day and night OP induced by water-soluble fractions of PM<sub>2.5</sub>: (a) extrinsic OP (DTTv, AAv), (b) Intrinsic OP (DTTm, AAm)

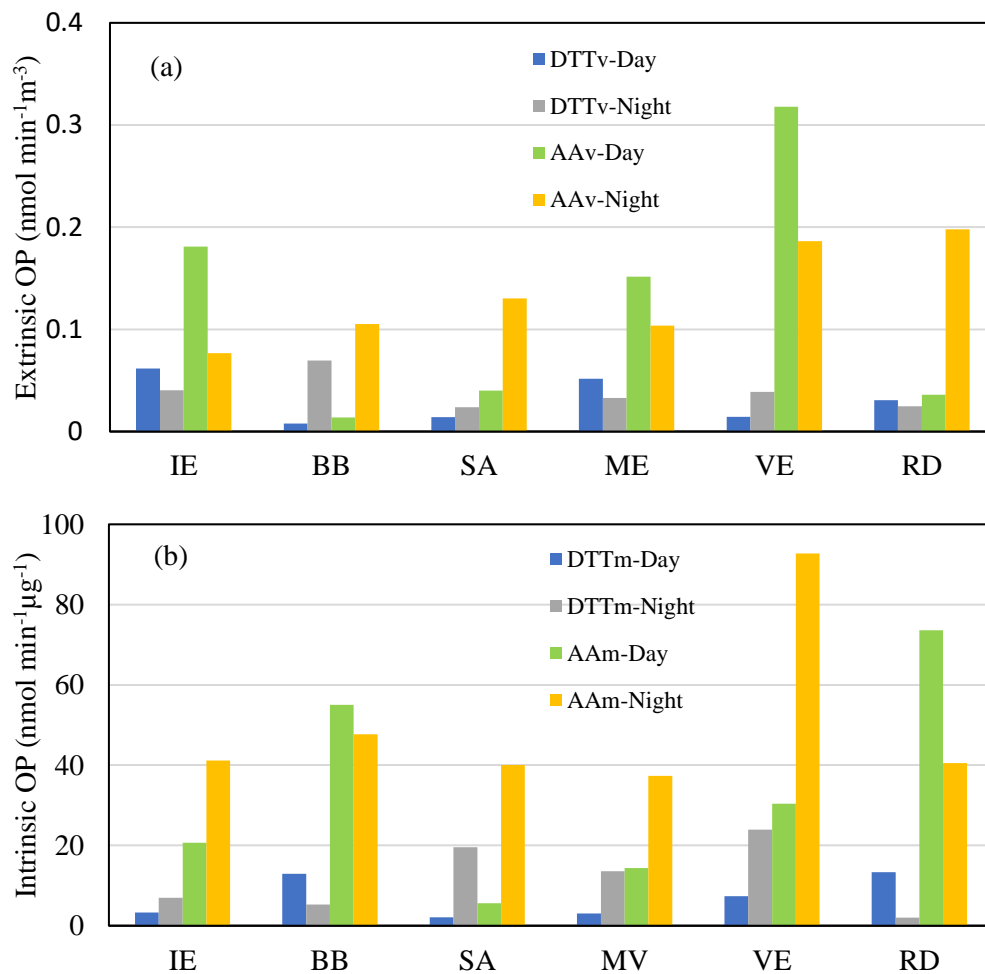


Figure 5-28 Source contributions to Day and night OP induced by methanol-soluble fractions of PM<sub>2.5</sub>: (a) extrinsic OP (DTTv, AAv), (b) Intrinsic OP (DTTm, AAm)

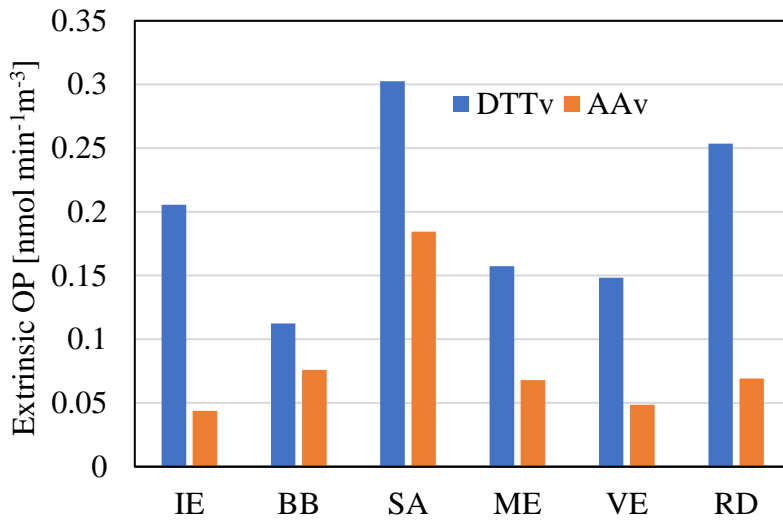


Figure 5-29 Source contributions to the extrinsic OP of PM<sub>2.5</sub> induced by water-soluble fractions in a year-round field campaign

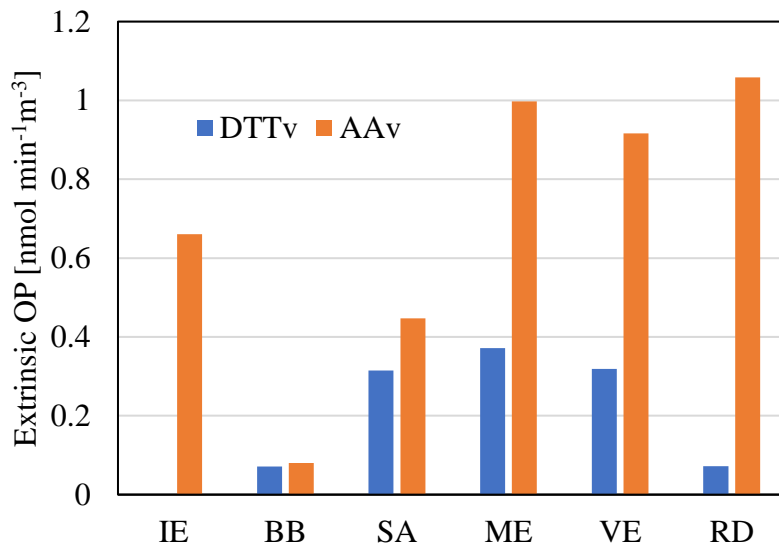


Figure 5-30 Seasonal source contributions to the extrinsic OP of PM<sub>2.5</sub> induced by methanol-soluble fractions : (a) DTTv, (b) AAv



### 5.3. Conclusion

The OP induced by the water- and methanol-soluble fractions of  $PM_{2.5}$  exhibited distinct variations between daytime and nighttime, with higher values observed at night. This increase in OP during nighttime can be attributed to the presence of photochemically aged aerosols, as evidenced by low BaA/Chr and LMW-PAHs/ $PM_{2.5}$  ratios. These aerosols are formed during the day through the photochemical oxidation of volatile/semivolatile organics in the presence of oxidants like ozone, but persisted in the ambient air at night, characterized by favorable meteorological conditions such as lower temperatures, reduced sunlight, low wind speed, and higher relative humidity. Additionally, the aerosols collected throughout the sampling campaign consistently showed high aerosol acidity. The acidity of the aerosol contributes to the dissolution of trace metals, thus elevating the OP of these metals, as evidenced during the day, where OP correlated strongly with trace metals.

The OP exhibited distinct seasonal variations, with DTTv induced by water-soluble fractions dominating in winter, while AAv dominated in summer. Moreover, the DTTv and AAv induced by the methanol-soluble fraction dominated in summer. The high DTTv in winter was attributed to its strong correlation with trace metals including Cu, Co, V, Cr, and Fe. The high DTTv and AAv in summer were attributed to photochemically aged aerosols, driven by a strong correlation of OP with  $O_3$  at high ambient temperatures, solar radiation, and relative humidity.

The dispersion characteristics of the OP were investigated to identify potential local sources that contribute to OP. The analysis revealed a consistent contribution of industrial emissions to the OP induced by both water- and methanol-soluble fractions of  $PM_{2.5}$  during

the day. The analysis also revealed a potential contribution of marine and sea salt aerosols to the OP at night, which is consistent with the high aerosol acidity observed during nighttime. The bivariate polar plots revealed distinct source dispersion patterns of OP across different seasons, suggesting diverse contributions from various emission sources. Moreover, the analysis consistently demonstrated dominant contributions from industrial emissions throughout all seasons. The analysis of air mass backward trajectories has provided insights into the influence of long-range transport on the PM<sub>2.5</sub> levels in Ningbo city from multiple sources, including Inner Mongolia, the East China Sea, Northern China, and Taiwan.

The PMF model was employed in this study to identify the sources of PM<sub>2.5</sub>. The comprehensive analysis revealed six distinct source contributors to PM<sub>2.5</sub> mass concentration: industrial emissions, biomass burning, secondary aerosol formation, marine/sea salt, vehicular emissions, and road dust. During the daytime, the three dominant sources of PM<sub>2.5</sub> were industrial emissions, secondary aerosol formation, and vehicular emissions, whereas during the nighttime, they were industrial emissions, secondary aerosol formation, and biomass burning. The year-round analysis PM<sub>2.5</sub> mass concentration was dominated by industrial emissions, secondary aerosol, and vehicular emissions, which were dominant in winter and autumn, suggesting extensive use of fossil fuel during these seasons for electricity generation to heat households and offices.

The contributions of various sources of PM<sub>2.5</sub> to the OP were estimated using MLR analysis. The results revealed that daytime DTTv was mainly influenced by marine/sea salt, industrial emissions, and road dust, whereas at night is dominated by secondary aerosol, biomass burning, and marine/sea salt dominated the contributions to AAv at night. During a

year-round field campaign, the main contributors to DTTv were secondary aerosol, industrial emissions, and road dust, which differed from the patterns observed for the mass concentration. Moreover, DTTv induced by methanol-soluble fractions was primarily influenced by secondary aerosol, marine/sea salt, and vehicular emissions, while AAv was associated with road dust, marine/sea salt, vehicular emissions, and industrial emissions. These results imply that the contributions of different sources vary to some extent for both the mass concentration and the OP of  $PM_{2.5}$ . However, we observed that industrial emissions and vehicular emissions significantly contribute to both the mass concentration and the OP. Additionally, marine/sea salt and road dust make minor contributions to the PM mass concentration, but have a significant impact on the OP. Therefore, to effectively target the reduction of potential health risks associated with  $PM_{2.5}$ , a comprehensive source apportionment approach that considers both mass concentration and OP should be considered. The consistent contribution of industrial emissions and marine/sea salt to the OP of  $PM_{2.5}$  in Ningbo is not surprising, given the city's status as an industrial and coastal hotspot.

## **Chapter 6 Particle Size Distribution of OP induced by Water and Methanol-Soluble Fractions: Chemical Characterization, Sources, and Respiratory Depositions**

### **6.1. Introduction**

A significant amount of research has been dedicated to investigating the deposition of particles in different regions of the human respiratory tract through both laboratory and field measurements (Deng et al., 2019; Fang et al., 2017; Guo et al., 2019; Kim and Jaques, 2004; Lin et al., 2019). The results have shown that coarse particles have a tendency to settle in the nasal passages and head airway. Although they can be exhaled, it is important to note that these particles may contain harmful chemical species such as trace metals, PAHs, quinones, which can cross synapses in the olfactory system and reach the brain (Maher et al., 2016). Such consequences can be detrimental, resulting in impairments in the olfactory function and the emergence of brain lesions (Calderón-Garcidueñas et al., 2010). However, fine particles have a higher propensity to penetrate more deeply into the respiratory tract, specifically reaching the tracheobronchial and pulmonary regions (Li et al., 2016). The presence of these particles has been linked to the initiation of inflammatory responses. Consequently, this association has the potential to contribute to the development of both pulmonary and systemic diseases (Li et al., 2017). Numerous studies have consistently shown that smaller particles, especially ultrafine particles, possess high toxicity due to their capacity to evade clearance mechanisms, enter the bloodstream, and accumulate in the

pulmonary interstitial sites (Schraufnagel, 2020). This evasive behavior allows them to effectively evade the phagocytic action of alveolar macrophages and contribute to prolonged inflammation in the lungs (Lyu et al., 2018).

The deposition of particles in the respiratory system is greatly influenced by breathing pattern, flow rate, as well as the size and shape of the particles (Manojkumar et al., 2019; Rissler et al., 2017). The adverse health effects related to inhaled particles are likely influenced by the dose within the respiratory system, but may predominantly depend on the concentration of toxic chemical constituents present. For example, Chen et al. (2022) demonstrated that  $PM_{2.5}$  with similar mass concentrations or doses exhibits different OP values, which may be attributed to variations in chemical compositions. However, it is not yet evident how particle doses in particular regions of the respiratory system and the OP are interconnected (Famiyeh, Jia, et al., 2023). Moreover, the deposition of OP in various regions of the human respiratory tract is often regarded as a more accurate assessment of the harmful effects of PM exposure. However, the variation of OP deposition with particle size depending on the type of acellular assay used remains unclear. Only a limited number of studies have simulate the deposition of OP within the respiratory system and establish potential associations with specific chemical species (Lyu et al., 2018; Wu et al., 2021). To address the existing knowledge gap, this study utilized multiple-path particle dosimetry (MPPD, detailed in Sections 2.5 and 3.8) as well as the DTT and AA assays to conduct a comparative assessment of OP deposition in different regions of the human respiratory tract. By employing these methods, we have determined the most appropriate assay type for measuring the deposition of ultrafine, accumulation, and coarse particles in the respiratory

system for the first time. This comprehensive approach enhances our understanding of OP deposition in the human respiratory tract, providing valuable insights for future research and risk assessment. It also assists in selecting the appropriate assay for a specific particle size. While numerous studies have examined the OP of fine particles (Borlaza et al., 2018; Chen et al., 2022; Shang et al., 2022), there is a limited research evaluating the OP of particles across different size ranges, including ultrafine, accumulation, and coarse particles (Simonetti et al., 2018), using multiple acellular assays, including DTT and AA.. Moreover, the studies by Perrone et al. (2019) and Veld et al. (2023) highlight a significant gap in the research literature. Specifically, there are limited studies that utilize both the DTT and AA assays to provide a comparative assessment of OP deposition in fine particles ( $\leq 2.5 \mu\text{m}$ ) and coarse particles ( $2.5\text{--}10 \mu\text{m}$ ) (Grange et al., 2022). This limits our understanding of the OP deposition of fine and coarse particles in human respiratory tract.

The aim of the study is to modeled the doses and OP deposition of the inhaled particles in human respiratory system through realistic exposure scenarios and determine whether there is a link between particle deposition doses and OP induced by ambient particles. The results obtained from this research have the potential to significantly contribute towards addressing the lack of understanding regarding the potential health risk associated with ultrafine, accumulation, and coarse particles in specific regions of the human respiratory tract.

The specific objectives of this study were as follows:

- 1) analyzing the concentrations and size distribution of PM chemical compositions, such as water-soluble trace metals, water-soluble organic carbons, and quinones;

- 2) modeling the deposition fractions and doses of ultrafine, accumulation, and coarse particles in the human respiratory tract;
- 3) comparing the OP induced by water-and methanol-soluble fractions of ultrafine, accumulation, and coarse particles;
- 4) modeling the source dispersion patterns of the concentrations of OP induced by water-and methanol-soluble fractions of ultrafine, accumulation, and coarse particles in our study domain;
- 5) identifying chemical species associated with OP induced by water-and methanol soluble fraction of ultrafine, accumulation, and coarse particles;
- 6) modeling OP deposition of ultrafine, accumulation, and coarse particles in the human respiratory tract;
- 7) establishing the link between particle deposition dose and OP induced by ultrafine, accumulation, and coarse particles in specific region of the human respiratory tract.

## **6.2. Results and discussions**

### **6.2.1 Chemical characterization: trace metals, WSOC, and quinones**

This section is dedicated to introducing the mass concentrations of key chemical species, such as trace metals, WSOC, and quinones in PM size fractions, that were analyzed in this study. The primary aim is to study OP activity of these chemical species (Sections 6.2.4.2 and 6.2.4.3). The size distribution of trace metal and WSOC concentrations is shown in Figure 6-1. Most of the trace metals (e.g Cu, Fe, Ni, Mn, V, etc.) exhibited unimodal size distribution with peak concentrations in accumulation particles (0.95–1.5  $\mu\text{m}$ ). The trace

metals As and V exhibit a unimodal size distribution with peak concentrations in ultrafine particles (0.49–0.95  $\mu\text{m}$ ).

The concentrations of trace metals and WSOC in  $\text{PM}_{2.5}$  and  $\text{PM}_{10}$  are shown in Table 6.1. The concentration of WSOC exhibited a unimodal size distribution, peaking in the accumulation particles range of 0.95–1.5  $\mu\text{m}$  (as shown in Figure 6-1 k). The concentrations of WSOC in  $\text{PM}_{2.5}$  and  $\text{PM}_{10}$  were found to be similar, showing no significant variability ( $p \leq 0.05$ ).

There were clear differences in the size distribution of quinone in ambient particles. The concentrations of 1, 4-NQ peaked in fine particles ( $\leq 2.5 \mu\text{m}$ ), whereas 1, 2-NQ and 1, 4-NQ peaked in coarse particles (2.5–10  $\mu\text{m}$ ), as shown in Figure 6-2. According to Figure 6-3 (a-c), 1, 4-NQ had concentrations peaked in accumulation particles that ranged from 0.95–1.5  $\mu\text{m}$  in diameter. However, both 1, 2-NQ and 1, 4-AQ exhibited a bimodal size distribution. 1, 2-NQ was predominantly concentrated in coarse particles (5.0–7.2  $\mu\text{m}$ ), followed accumulation particles (0.95–1.5  $\mu\text{m}$ ). In contrast, 1, 4-AQ had the highest concentration in accumulation particles (0.95–1.5  $\mu\text{m}$ ), followed by coarse particles ( $\geq 7.2 \mu\text{m}$ ).

The plot of  $\log(\text{quinones}/\text{PM})$  against the  $\log D_p$  graph was employed to investigate the mechanism of the size distribution of 1, 4-NQ, 1, 2-NQ, and 1, 4-AQ in ultrafine, accumulation, and coarse particles. This deepens our understanding of the mechanism behind the size distribution of quinones on the surface of ambient particles. A similar approach was employed in Chapter 4 to study the mechanism governing the size distribution of PAHs in ambient particles, as illustrated in Figure 4-7. These plots provided us with an



understanding of how LMW-PAHs can be vaporized and oxidized, resulting in the formation of secondary quinones. These quinones are then subsequently condensed onto particle surfaces. The results showed that the slope of the regression line of 1, 4-NQ and 1, 2-NQ was close to -1, indicating that adsorption is the main mechanism that control their size distribution in accumulation particles. The highest concentration of 1, 2-NQ in particles with diameter ranging between 5.0 and 7.2  $\mu\text{m}$  can be attributed to multilayer adsorption. In addition, the reason behind the highest level of 1, 4-AQ in coarse particles with diameter  $\geq 7.2 \mu\text{m}$  is because of multilayer adsorption, which is evident from the slope of the regression line being higher than -1.

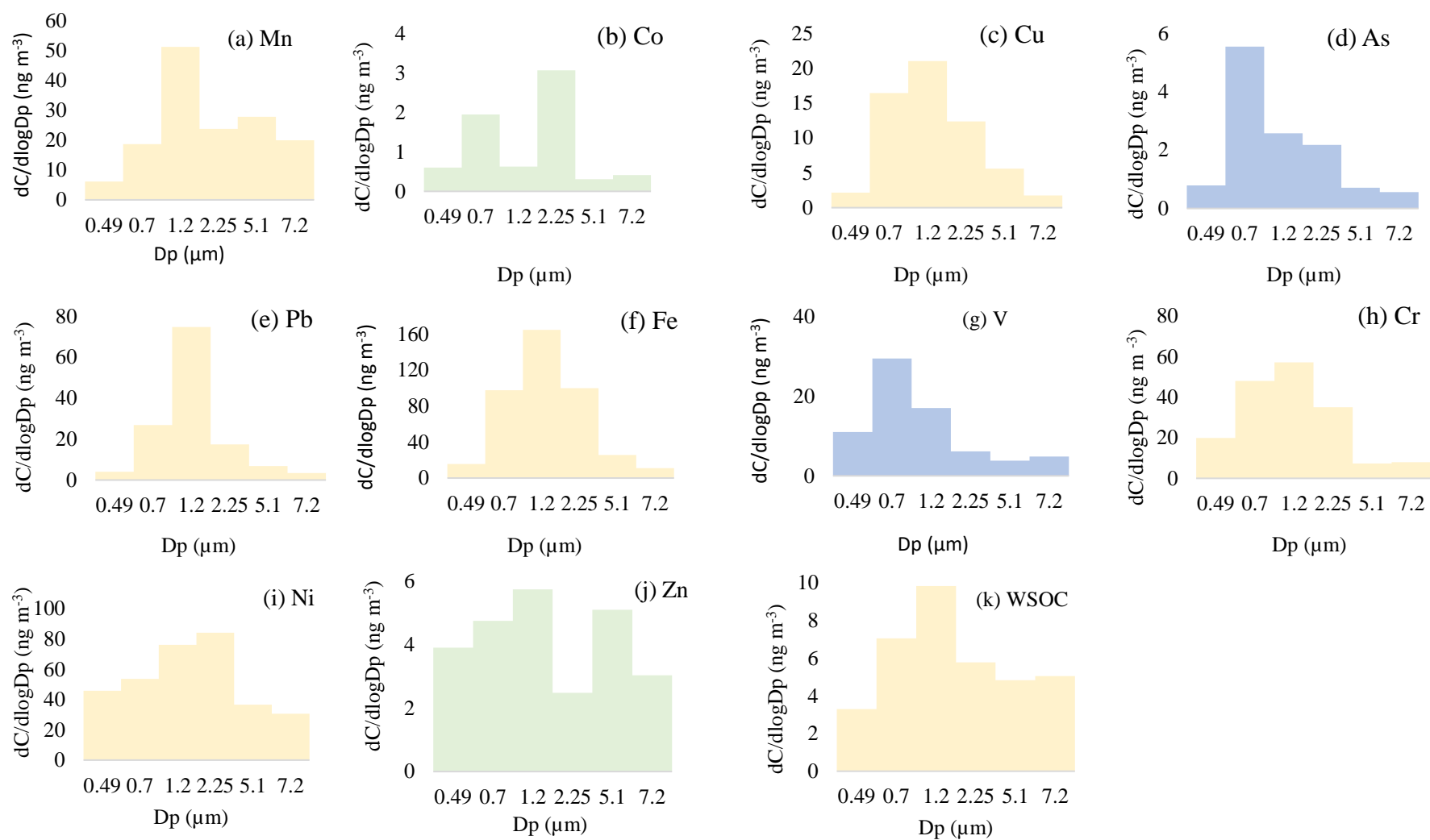


Figure 6-1 Size distribution ( $dC$  = mean concentration ( $\text{ng m}^{-3}$ ),  $d\log D_p$  = logarithmic difference of aerodynamic diameter,  $D_p$  is average particle size,  $\mu\text{m}$ ) of trace metals (a-j) and WSOC (k) in ambient particles collected in urban residential/commercial area of Ningbo, China

Table 6.1 Averaged concentrations (mean  $\pm$  standard deviation) of WSTMs and WSOC in PM<sub>2.5</sub> and PM<sub>10</sub>

WSTMs	PM <sub>2.5</sub>	PM <sub>10</sub>	PM <sub>2.5</sub> /PM <sub>10</sub>
<sup>+</sup> Mn	21.4 $\pm$ 21.0	9.19 $\pm$ 12.1	2.33
Co	0.19 $\pm$ 0.12	0.16 $\pm$ 0.11	1.19
<sup>+</sup> Ni	1.39 $\pm$ 0.60	0.59 $\pm$ 0.57	2.36
<sup>+</sup> Cd	0.59 $\pm$ 0.49	0.15 $\pm$ 0.14	3.93
<sup>+</sup> Zn	501.1 $\pm$ 324.2	191.2 $\pm$ 142.0	2.62
Ba	13.6 $\pm$ 12.4	16.2 $\pm$ 10.7	0.84
<sup>+</sup> Cr	118.7 $\pm$ 146.2	69.1 $\pm$ 117.8	1.72
<sup>+</sup> Cu	7.21 $\pm$ 4.46	2.55 $\pm$ 1.94	2.83
<sup>+</sup> As	4.28 $\pm$ 3.47	2.11 $\pm$ 2.37	2.03
<sup>+</sup> Pb	3.25 $\pm$ 3.60	0.55 $\pm$ 0.94	5.91
<sup>+</sup> Fe	29.2 $\pm$ 22.3	13.3 $\pm$ 11.8	2.19
<sup>+</sup> Al	7.61 $\pm$ 7.89	1.55 $\pm$ 1.48	4.91
<sup>+</sup> V	1.25 $\pm$ 0.54	0.95 $\pm$ 0.36	1.32
Ag	0.79 $\pm$ 0.97	0.33 $\pm$ 0.27	2.39
<sup>+</sup> Bi	0.42 $\pm$ 0.43	0.78 $\pm$ 0.12	0.54
<sup>+</sup> Ce	0.24 $\pm$ 0.19	0.69 $\pm$ 0.73	0.35
<sup>+</sup> Sr	3.43 $\pm$ 1.49	6.91 $\pm$ 12.3	0.49
<sup>+</sup> Sb	1.24 $\pm$ 1.22	0.34 $\pm$ 0.33	3.65
WSOC	5.42 $\pm$ 0.66	5.05 $\pm$ 0.70	1.07

WSTMs: water-soluble trace metals, ng m<sup>-3</sup>,

WSOC: water-soluble organic carbons,  $\mu$ g m<sup>-3</sup>,

<sup>+</sup> p  $\leq$  0.05: (z-statistics, mean concentration statistically significant)

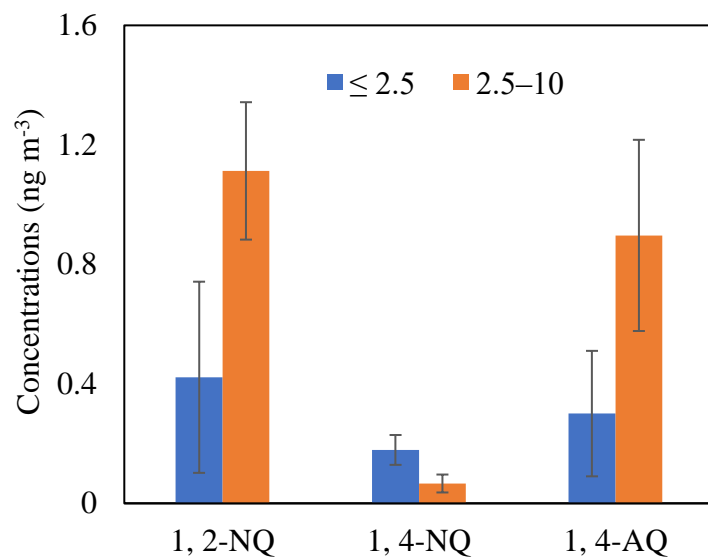


Figure 6-2 Size distribution of quinones in PM<sub>2.5</sub> and PM<sub>10</sub> collected in urban Ningbo, China. Error bar present the standard deviation (level of variability of the data)

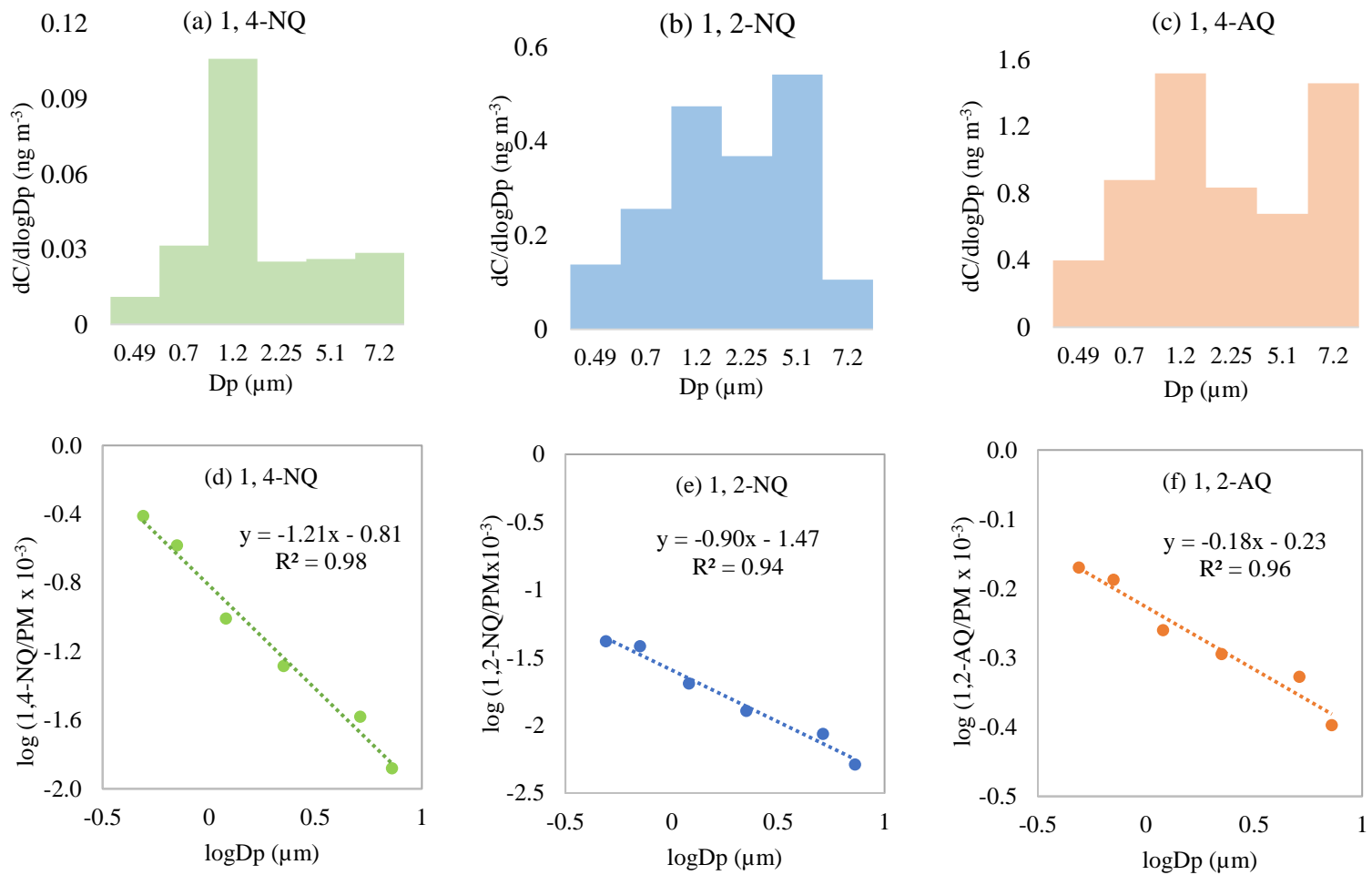


Figure 6-3 Size distribution of quinones (a-c) and plot of log total quinones/PM versus log Dp (d-f)

### 6.2.2 Validation of the MPPD model

Extensive validation of the MPPD model has been conducted in previous studies to ensure its accuracy and reliability in accurately modeling particle deposition in the human respiratory tract (Hofmann, 2011). To further confirm the robustness of MPPD, a brief exercise was conducted to compare the modeled and experimental deposition fractions of ambient particles ranging in size from 0.005 to 15  $\mu\text{m}$  in the respiratory tract of humans. The experimental data was taken from Heyder et al. (1986). The results of this comparison are presented in Figure 6-4.

In the upper airways, smaller particles exhibited low deposition fraction due to their low inertia (Morawska and Buonanno, 2021), while larger particles have higher deposition fraction due to increased momentum and inertia. Specifically, particles with a diameter greater than 0.4  $\mu\text{m}$  exhibit higher deposition in the upper airways due to their high inertial impaction. The high deposition fraction of particles with a diameter below 0.4  $\mu\text{m}$  can be attributed to their increased surface area and the influence of Brownian diffusion. As the particle diameter exceeds 5  $\mu\text{m}$ , the deposition fraction remains constant. This could be attributed to the increase in particle density, which in turn leads to gravitational settling that balances the effect of inertial impaction in the upper airways.

As shown in Figure 6-4 (b), the experimental and modeled deposition fractions yielded excellent agreement, with an  $R^2$  value close to 1 (0.99). This finding confirms the validity and robustness of the MPPD model in accurately simulating the deposition fraction and doses of ambient particles in the human respiratory tract. This justifies our decision to utilize

the MPPD model in this study for modeling particle deposition doses and OP deposition in the human respiratory tract.

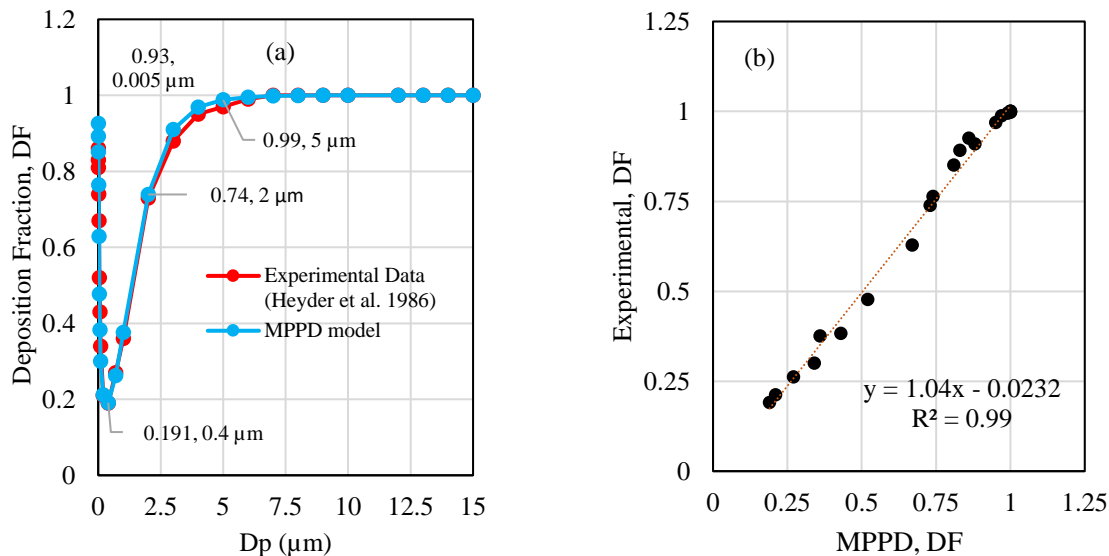


Figure 6-4 Comparison of experimental and modeled deposition fractions (DF) of ambient particles with aerodynamic size ( $D_p$ ) of 0.005–15  $\mu\text{m}$  in the whole human respiratory tract: (a) DP versus  $D_p$  for experimental and MPPD model, (b) Linear regression analysis of DF of experimental versus MPPD model.

### 6.2.3 Particle deposition fractions and doses in human respiratory system

By utilizing equation (3-3) (Deepthi et al., 2019; Lv et al., 2021), we were able to compute the dose of PM size fractions ( $\mu\text{g day}^{-1}$ ) that can be deposited in the human respiratory tract every day through the inhalation route. The MPPD model was first utilized to estimate the particle deposition fraction in the ET, TB, PL and TL regions of the human respiratory tract. The deposited dose is influenced by multiple factors, such as the ambient concentration of particles inhaled, deposition fraction, exposure time, and the breathing rate of the individual (Hammer et al., 2020). However, within the same group, the particle dose

varies depending on the ambient concentrations and deposition fractions within the human respiratory tract.

The deposition fraction and doses of ultrafine ( $\leq 0.49$ ,  $0.49\text{--}0.95\ \mu\text{m}$ ), accumulation ( $0.95\text{--}1.5$ ,  $1.5\text{--}3\ \mu\text{m}$ ), and coarse ( $3\text{--}7.2$ ,  $\geq 7.2\ \mu\text{m}$ ) particles in different regions of the human respiratory tract is depicted in Figure 6-5. Ultrafine ( $\leq 0.49\ \mu\text{m}$ ) particles tend to have higher deposition dose in the TB and PL regions of the respiratory system (as shown in Figure 6-5 b and c, respectively). Accumulation particles within the size range of  $1.5\text{--}3\ \mu\text{m}$ , which also have a high deposition fraction, tend to have high doses in the alveoli. The deposition of these particles in the alveoli is predominantly controlled by Brownian diffusion (Hofmann, 2011). Therefore, the high doses of these particles in the alveoli allows for their deep penetration into the lungs and bloodstream, which can lead to a range of health complications, including chronic obstructive pulmonary disease (COPD), heart disease, and lung cancer (Parris et al., 2019). The deposition of these particles in the ET region (as shown in Figure 6-5 a) and the total deposition (TL) (as shown in Figure 6-5 d) was minimal, suggesting that they are likely cleared from the upper airways. Although only a small amount of ultrafine and accumulation mode particles are deposited in the upper airway, if retained, they have the potential to trigger several health problems, such as irritation, inflammation, sinusitis, and nasal congestion (Schraufnagel, 2020). Moreover, accumulation ( $0.95$  to  $1.5\ \mu\text{m}$ ) particles contains higher concentrations of trace metals (Mn, Fe, Cu, Zn, Cr, Pb) and quinones (1, NQ, 1, 4-AQ, and 1, 2-NQ), as shown in Figure 6-1 and Figure 6-3, respectively), suggesting that these particles could pose a significant health risk in various regions of the respiratory tract, particularly in the PL region. Therefore, accumulation



particles with high deposition dose and contains high concentration of toxic chemical species in the PL region could pose high health risk than ultrafine and coarse particles in this region.

Coarse particles with size ranging from 3 to 7.2  $\mu\text{m}$ , have high deposition dose in the ET and TL regions (Figure 6-5 a and d, respectively) due to their high ambient concentration and deposition fraction. The deposition of these particles in the upper airway is mainly controlled by inertial impaction (Darquenne, 2020). The inhalation and deposition of coarse particles in the human respiratory tract, especially in the ET region, have been linked to numerous detrimental health effects. These adverse outcomes include the onset of respiratory symptoms, exacerbation of asthma, and chronic bronchitis (Brunekreef and Forsberg, 2005). Moreover, these coarse particles tend to have high deposition dose in the alveoli (Figure 6-5 c), which can be attributed to the mechanism of sedimentation (Darquenne, 2012). However, coarse particles in the size range of  $\geq 7.2 \mu\text{m}$  tend to have a low deposition dose in all three regions of the lungs. This is attributed to their low ambient concentration, despite their high deposition fractions. This suggests that the concentration of particles in the ambient air strongly influences their doses in the human respiratory tract. Thus, providing support for the need of regulating and reducing the concentration of PM in order to minimize their deposition doses and reduce the health risk in human respiratory tract.

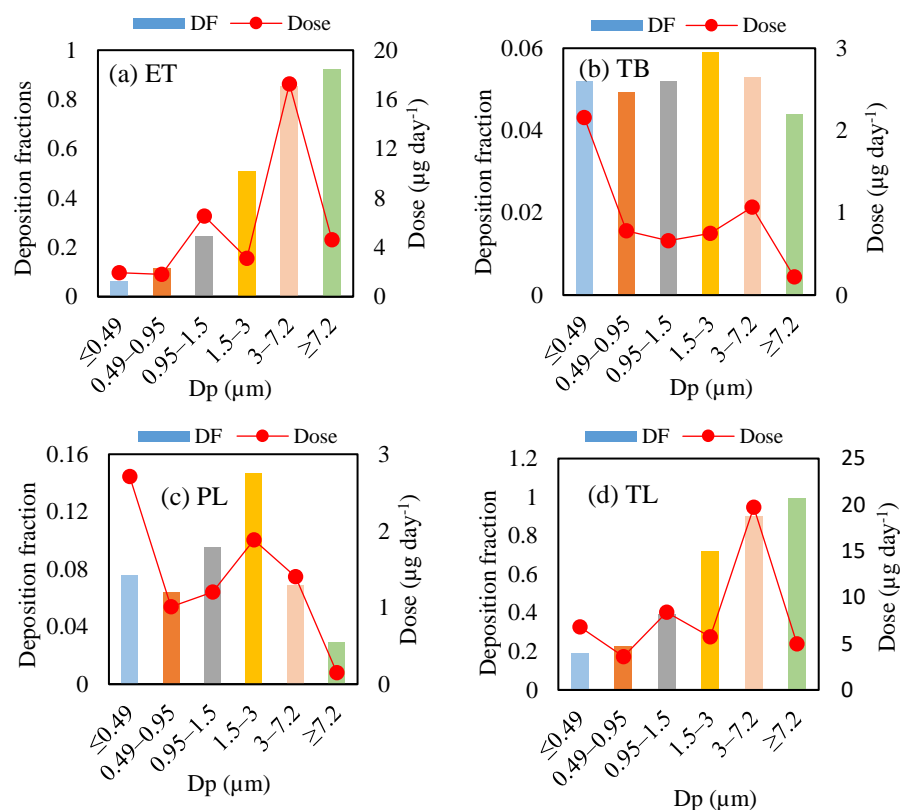


Figure 6-5 Particle deposition fraction and lung-deposition doses in parts of the human lung (a) ET, (b) TB, (c) PL, and (d) TL

Figure 6-6 presents a comparison of the deposition fraction and doses of fine ( $\leq 2.5 \mu\text{m}$ ) and coarse ( $2.5\text{--}10 \mu\text{m}$ ) particles. In the ET region, the deposition fraction of coarse particles exceeded that of fine particles, as anticipated. Despite this difference, the doses of both particle types were similar. The doses of fine and coarse particles in the ET region can be attributed to their elevated ambient concentration and high deposition fraction, respectively. However, the deposition doses of fine particles in both the pulmonary and whole respiratory tract were found to exceed those of coarse particles, as expected. Fine particles ( $\leq 2.5 \mu\text{m}$ ) have high levels of trace metals (as shown in Table 6.1), whereas coarse particles have high levels of 1, 2-NQ and 1, 4-AQ (as shown in Figure 6-2). This suggests that the high deposition of trace metals could result in an increased health risk associated with fine

particles in the PL regions, while quinones could significantly contribute to the heightened health risk of coarse particles.

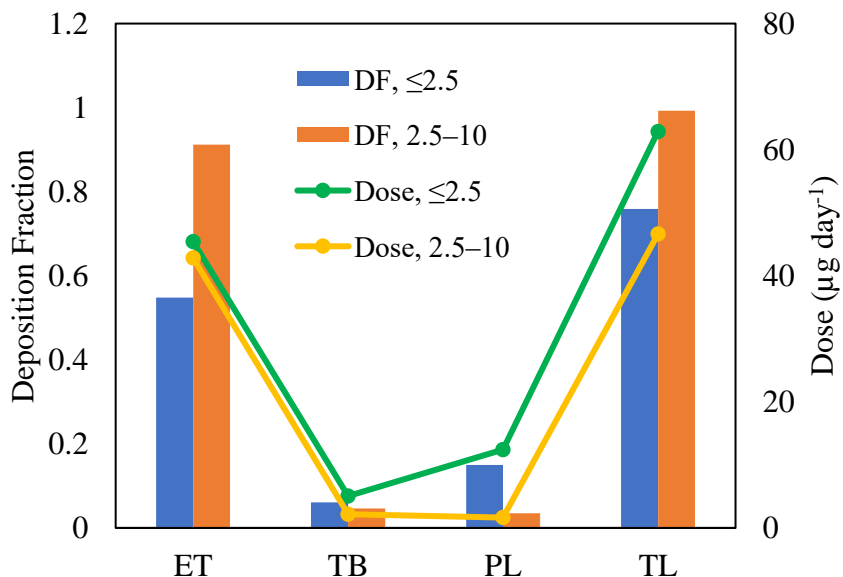


Figure 6-6 Modeled particle deposition fraction and doses in parts of the human respiratory tract (a) ET, (b) TB, (c) PL, and (d) TL

#### 6.2.4 Oxidative potential of ambient particles

This chapter presents the findings on the OP induced by water- and methanol-soluble fractions of ultrafine, accumulation, and coarse particles. The OP induced by water- and methanol-soluble fractions of PM<sub>2.5</sub> and PM<sub>10</sub> were compared.

##### 6.2.4.1 OP induced by water- and methanol-soluble ultrafine, accumulation, coarse particles

The extrinsic OP induced by water- and methanol-soluble fractions of ultrafine, accumulation, and coarse particles are shown in Table 6.2 and Table 6.3, respectively. The water-soluble fraction of ultrafine particles ( $\leq 0.49 \mu\text{m}$ ) exhibited the highest extrinsic OP values in both DTT and AA assays. The mean DTTv of water-soluble fractions for these particles were  $36.4 \pm 3.0 \text{ nmol min}^{-1} \text{ m}^{-3}$ , with higher values observed in summer compared

to winter. Specifically, the DTTv in winter was  $34.7 \pm 2.75 \text{ nmol min}^{-1} \text{ m}^{-3}$ , while in summer it was  $38.1 \pm 2.33 \text{ nmol min}^{-1} \text{ m}^{-3}$ . According to Hsiao et al. (2021), the elevated OP detected by the DTT assay in the summer could be attributed to the photochemical aging of aerosol particles due to high level of solar radiation and ozone (Famiyeh, Jia, et al., 2023). This is consistent with our earlier findings that aerosol collected during summer at our study domain are photochemically aged.

In Thessaloniki, Greece, the DTTv values for ultrafine ( $\leq 0.49 \mu\text{m}$ ) particles in urban traffic were found to be  $1.09 \pm 0.62 \text{ nmol min}^{-1} \text{ m}^{-3}$  and  $1.16 \pm 0.54 \text{ nmol min}^{-1} \text{ m}^{-3}$  during the warm and cold seasons, respectively. The DTTv values from the urban background were  $0.84 \pm 0.25 \text{ nmol min}^{-1} \text{ m}^{-3}$  and  $3.10 \pm 0.49 \text{ nmol min}^{-1} \text{ m}^{-3}$  during the warm and cold seasons, respectively (Argyropoulos et al., 2016). Despite the limited literature available, our study has found significantly higher DTTv values for ultrafine particles in Ningbo city.

Table 6.2 Extrinsic OP induced by water-soluble PM in DTT and AA assays

Dp ( $\mu\text{m}$ )	DTTv ( $\text{nmol min}^{-1} \text{ m}^{-3}$ )	AAv ( $\text{nmol min}^{-1} \text{ m}^{-3}$ )
$\leq 0.49$	$36.4 \pm 3.05$	$9.64 \pm 5.84$
0.49–0.95	$13.5 \pm 1.78$	$3.45 \pm 2.89$
0.95–1.5	$13.8 \pm 0.85$	$2.17 \pm 1.83$
1.5–3	$13.2 \pm 1.23$	$2.07 \pm 1.52$
3–7.2	$13.9 \pm 0.97$	$5.45 \pm 4.53$
$\geq 7.2$	$13.2 \pm 2.11$	$4.34 \pm 3.52$

Ultrafine particles:  $\leq 0.49, 0.49\text{--}0.95 \mu\text{m}$ , accumulation particles:  $0.95\text{--}1.5, 1.5\text{--}3 \mu\text{m}$ , coarse particles:  $3\text{--}7.2, \geq 7.2 \mu\text{m}$

The mean of AAv of water-soluble fractions ultrafine particles ( $\leq 0.49 \mu\text{m}$ ) was  $9.64 \pm 5.84 \text{ nmol min}^{-1} \text{ m}^{-3}$ , with higher values observed in summer compared to winter. The AAv

were higher in  $\leq 0.49 \mu\text{m}$  particles, followed by coarse particles ( $\geq 7.2 \mu\text{m}$ ). The coefficient of variation (CV) for the OP induced by water-soluble fraction in DTT across all particle sizes exhibited limited variability ranging from 15% to 30%. In contrast, AAv had limited to moderate variability ranging from 27% to 84% across all particle sizes. These findings suggest that water-soluble chemical compositions that induce OP in DTT assay were consistently present in ambient particles. In contrast, the the chemical species that induce OP in AA assay may not be consistently present through the field campaign. This is supported by the high and lower OP values induced by the water-soluble fraction in DTT and AA assay, respectively. This finding suggests that AA is less responsive to water-soluble chemical species, while DTT displays high sensitivity.

Table 6.3 Extrinsic OP induced by methanol-soluble PM in DTT and AA assays

Dp ( $\mu\text{m}$ )	DTTv ( $\text{nmol min}^{-1}\text{m}^{-3}$ )	AAv ( $\text{nmol min}^{-1}\text{m}^{-3}$ )
$\leq 0.49$	$28.9 \pm 9.61$	$72.9 \pm 21.3$
0.49–0.95	$12.8 \pm 3.36$	$21.9 \pm 7.64$
0.95–1.5	$12.8 \pm 2.64$	$21.1 \pm 12.8$
1.5–3	$12.1 \pm 3.15$	$20.2 \pm 7.80$
3–7.2	$11.5 \pm 3.44$	$32.3 \pm 19.5$
$\geq 7.2$	$12.3 \pm 2.67$	$40.2 \pm 11.2$

Ultrafine particles:  $\leq 0.49, 0.49\text{--}0.95 \mu\text{m}$ , accumulation particles:  $0.95\text{--}1.5, 1.5\text{--}3 \mu\text{m}$ , coarse particles:  $3\text{--}7.2, \geq 7.2 \mu\text{m}$

The extrinsic OP induced by methanol-soluble of  $\leq 0.49 \mu\text{m}$  particles dominated both in DTT and AA assays (as shown in Table 6.3). The DTTv induced by methanol-soluble fractions for other particle size ranges were at similar levels. The elevated AAv levels during

summer ( $85.7 \pm 11.9 \text{ nmol min}^{-1} \text{ m}^{-3}$ ) compared to winter ( $60.2 \pm 21.2 \text{ nmol min}^{-1} \text{ m}^{-3}$ ) could be attributed to the photochemical aging process (Famiyeh, Jia, et al., 2023). With the exception of ultrafine particles with a size of  $\leq 0.49 \mu\text{m}$ , it was observed that coarse particles exhibited higher AAv levels in comparison to ultrafine (0.49–0.95  $\mu\text{m}$ ) and accumulation (0.95–1.5, 1.5–3  $\mu\text{m}$ ) particles. The AAv values consistently surpassed the DTTv values for the same PM size fractions, indicating that the AA assay is more sensitive to the chemical composition extracted in methanol-soluble fraction than the DTT assay. The CV for DTTv and AAv were within the range from 20% to 60%.

To accurately compare the OP of ultrafine, accumulation, and coarse particles, their respective size distributions were considered. Figure 6-7 (also shown in our recent publication, Famiyeh et al. (2023)) displays the size distribution of DTTv and AAv of water-soluble fractions (a, b, respectively). The DTTv and AAv exhibited a unimodal size distribution with peak concentration in accumulation particles (0.95–1.5  $\mu\text{m}$ ). The unimodal distribution of DTTv with a peak concentration in accumulation particles is consistent with a study by Lyu et al. (2018). The high peak value observed in the DTT assay for particles ranging from 0.95 to 1.5  $\mu\text{m}$  exhibits similar size distribution patterns with trace metals (Mn, Zn, Cu, Pb, Cr, and Fe), and quinones (1,4-NQ, 1,4-AQ, and 1,2-NQ) (as shown in Figure 6-1 and Figure 6-3, respectively).

The AAv induced by water-soluble fraction exhibited trimodal distribution (as shown in Figure 6-7 b), peaked in  $\leq 0.49 \mu\text{m}$  particles, 3–7.2, and  $\geq 7.2$ , suggesting dominant AAv of coarse particles, followed by ultrafine particles. The AAv peaking in coarse particles is in line with a study conducted by Simonetti et al. (2018). This suggests that AAv might be more

sensitive to chemical species in coarse particles, followed by ultrafine, and accumulation particles. For example, the high AAv of coarse particles can be partially attributed to high concentration of coarse quinones such 1, 2-NQ and 1, 4-AQ (Figure 6-3 b, c, respectively). In contrast, DTT assay might be more sensitive to the chemical species in accumulation particles, followed by ultrafine, and coarse particles.

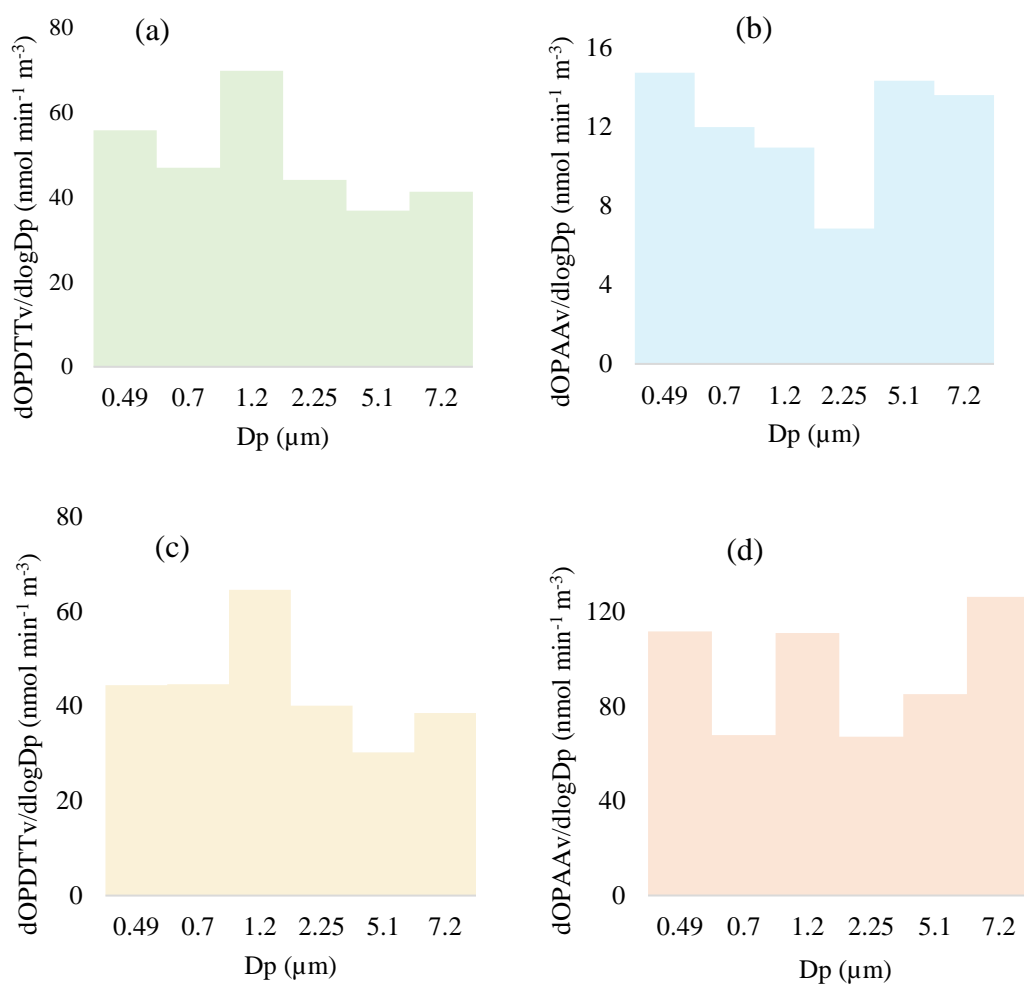


Figure 6-7 Size distribution of extrinsic OP (dOP = mean extrinsic OP (nmol min<sup>-1</sup> m<sup>-3</sup>), dlogDp = logarithmic difference of aerodynamic diameter, Dp, μm) of water (a, b) and methanol (c, d): DTT (a, c), AA (b, d) assays

The levels of intrinsic OP induced by water-soluble PM fractions in DTT and AA assays are presented in the Appendix (as shown in Table 8.13). The mean DTTm of water-soluble fractions was found to be high for ultrafine particles ( $\leq 0.49 \mu\text{m}$ ) at  $46.9 \pm 45.9 \text{ pmol min}^{-1} \mu\text{g}^{-1}$ , followed by coarse particles ( $\geq 7.2 \mu\text{m}$ ) at  $39.5 \pm 20.8 \text{ pmol min}^{-1} \mu\text{g}^{-1}$ . The mean AAm of water-soluble fraction was higher in coarse particles ( $\geq 7.2 \mu\text{m}$ ,  $18.9 \pm 19.3 \text{ pmol min}^{-1} \mu\text{g}^{-1}$ ), followed by ultrafine particles ( $\leq 0.49 \mu\text{m}$ ,  $17.1 \pm 20.9 \text{ pmol min}^{-1} \mu\text{g}^{-1}$ ). The DTTm consistently exhibited higher values than AAm across the water-soluble PM size fractions.

The mean DTTm and AAm induced by the methanol-soluble fractions were higher in coarse and ultrafine particles compared to accumulation particles, as shown in Appendix (Table 8.14). The AAm consistently exhibited higher values than DTTm across the methanol-soluble PM size fractions. The CVs for DTTm and AAm ranged from 53% to 112%. The moderate to high CVs observed in intrinsic OP can be attributed to the variability in PM mass concentration (68.6% to 79.1%) during the sampling campaign.

The DTTm showed a bimodal size distribution, with peak concentrations observed in coarse particles ( $\geq 7.2 \mu\text{m}$ ) and accumulation particles ( $0.95\text{--}1.5 \mu\text{m}$ ) both in water- and methanol-soluble fractions (as shown in Figure 8-6 a, c, respectively). As reported in Figure 6-7 (a, c), DTTv induced by water-soluble and methanol-soluble fractions showed a unimodal size distribution. The diverse size distribution of DTTv and DTTm suggest that they are associated with different chemical compositions. The AAm induced by the water-soluble and methanol-soluble fraction exhibited peak concentrations in coarse particles with a size of  $\geq 7.2 \mu\text{m}$  (as shown in Figure 8-6 b, d, respectively), which is consistent with AAv reported in Figure 6-7 (b, d).



#### 6.2.4.2 Chemical species associated with OP: ultrafine, accumulation, and coarse particles

The Pearson's correlation between chemical compositions and OP varies significantly depending on particle size. DTTv induced by the water-soluble fraction showed a weak correlation with quinones and trace metals across most particle sizes, except for accumulation particles (1.5–3  $\mu\text{m}$ ) and coarse particles (3–7.2  $\mu\text{m}$ ). The high peak concentrations of DTTv in the 1.5–3  $\mu\text{m}$  range can be attributed to its correlation with Cu, Zn, Co, and  $\text{O}_3$  (as shown in Table 6.7). Conversely, DTTv in the 3–7.2  $\mu\text{m}$  particles correlates with 1, 4-NQ and  $\text{O}_3$  (as shown in Table 6.8). The correlation between  $\text{O}_3$  and DTTv suggests that the contribution of photochemical aging process to the OP induced by these particles (Gao et al., 2020). This process takes place during the summer, characterized by high solar radiation, relative humidity, ambient temperature, and elevated ambient concentrations of  $\text{O}_3$ . The occurrence of the OP, driven by  $\text{O}_3$  at high temperatures, solar radiation, and relative humidity, has been reported by Chen et al. (2022). Moreover, aerosol aging process can promote the formation of quinones through the oxidation of LMW-PAHs, resulting in an elevation of OP levels (Famiyeh, Jia, et al., 2023; Hsiao et al., 2021).

The AAv induced by the water-soluble fraction of ultrafine particles particles with a size of  $\leq 0.49 \mu\text{m}$  exhibited a strong correlation with  $\text{O}_3$ , suggesting the influence of a photochemical process. The AA value induced by accumulation particles (0.49 to 0.95  $\mu\text{m}$ ) exhibited a moderate-to-strong correlation with trace metals such as Cu, Pb, Fe, Cr, and Co, as well as a moderate correlation with Mn, V, and As. The strong correlation of AAv with trace metals is consistent with a study by Fang et al. (2016). The AAv exhibited strong correlation with trace metals, while DTTv exhibit weak correlation. This suggest that the

high DTTv induced by water-soluble fractions of PM can be attributed to water-soluble organics, including HULIS (Cheng et al., 2021; Famiyeh et al., 2023).

The elevated AAv of the water-soluble fraction of coarse particles, ranging in size from 3–7.2  $\mu\text{m}$ , can be attributed to their moderate-to-strong correlation with trace metals such as Fe, Mn, V, Co, Ni, As, as well as  $\text{O}_3$  (as shown in Table 6.8). Furthermore, the multilayer adsorption of LMW-PAHs (2-3 aromatic rings), such as NaP and Ant, on particles ranging from 3–7.2  $\mu\text{m}$  (as demonstrated in Figure 4-7) can lead to their evaporation and subsequent oxidation, thereby contributing to secondary formation of 1, 2-NQ and 1, 4-AQ. Therefore, the high AAv values of 3–7.2  $\mu\text{m}$  particles could potentially be attributed to the peak concentration of 1, 4-AQ (as shown in Figure 6-3).

The concentrations of DTTv and AAv induced by the methanol-soluble fraction exhibited a limited correlation with trace metals, quinones, and PAHs across all six particle size ranges, as shown in the Appendix (Table 8.15 to Table 8.20). This finding implies that further investigation into the potential contribution of other chemical compositions, such as water-insoluble trace metals, high molecular weight quinones, and HULIS (which were not examined in this study), is warranted. These chemical species could potentially play a role in the observed values of OP induced by the methanol-soluble fraction of ultrafine, accumulation, and coarse particles. Therefore, it is crucial to conduct extensive characterization of these chemical species and explore their OP activity in future studies.

Table 6.4 Pearson's correlation (r) between OP induced by water-soluble fraction of  $\leq 0.49 \mu\text{m}$  particles and chemical compositions

	DTTv	DTTm	AAv	AAm	PM0.49	Cu	Pb	Fe	Mn	Al	V	Cr	Zn	Co	Ni	As	WSOC	1,4-NQ	1,2-NQ	1,4-AQ	O <sub>3</sub>	Temp	RH	
DTTv	1																							
DTTm	0.54*	1																						
AAv	0.53*	-0.22	1																					
AAm	0.74**	0.37	0.78**	1																				
PM0.49	-0.43	-0.92	0.28	-0.33	1																			
Cu	-0.52	-0.45	-0.46	-0.76	0.53*	1																		
Pb	-0.82	-0.68	-0.46	-0.81	0.65*	0.73**	1																	
Fe	-0.4	-0.54	-0.32	-0.57	0.45	0.41	0.73**	1																
Mn	-0.68	-0.63	-0.41	-0.75	0.69*	0.77**	0.95**	0.72**	1															
Al	0.09	-0.31	-0.11	-0.25	0.35	0.38	0.28	0.65*	0.43	1														
V	-0.58	-0.47	-0.5	-0.69	0.45	0.83**	0.66*	0.38	0.68*	0.52*	1													
Cr	-0.37	-0.2	-0.51	-0.65	0.32	0.71**	0.74**	0.59*	0.83**	0.34	0.46	1												
Zn	-0.45	-0.53	-0.37	-0.71	0.65*	0.73**	0.84**	0.79**	0.94**	0.61*	0.59	0.86**	1											
Co	-0.49	-0.4	-0.49	-0.58	0.27	0.62*	0.59*	0.63*	0.55*	0.64*	0.84**	0.33	0.5	1										
Ni	-0.51	-0.29	-0.59	-0.63	0.3	0.76**	0.67*	0.51*	0.75**	0.6*	0.9**	0.67*	0.68*	0.8**	1									
As	-0.26	-0.25	-0.31	-0.47	0.24	0.42	0.61*	0.74**	0.64*	0.32	0.14	0.83**	0.71**	0.22	0.42	1								
WSOC	0.37	0.69*	0.14	0.58*	-0.62	-0.34	-0.64	-0.82	-0.58	-0.5	-0.31	-0.31	-0.66	-0.44	-0.2	-0.4	1							
1,4-NQ	-0.19	0	0.03	0.09	-0.2	-0.43	-0.28	-0.3	-0.4	-0.33	-0.19	-0.55	-0.5	-0.23	-0.26	-0.31	0.18	1						
1,2-NQ	-0.04	0.08	-0.26	-0.07	-0.12	-0.28	0.1	0.5	0.13	0.47	0.02	-0.02	0.21	0.35	0.15	0.04	-0.39	-0.08	1					
1,4-AQ	0.34	0.36	0.07	0.25	-0.43	-0.32	-0.16	0.05	-0.26	-0.33	-0.55	0.09	-0.21	-0.27	-0.39	0.28	0.08	-0.38	-0.01	1				
O <sub>3</sub>	0.77**	0.26	0.79**	0.85**	-0.18	-0.63	-0.77	-0.64	-0.73	-0.3	-0.63	-0.67	-0.66	-0.63	-0.76	-0.62	0.37	-0.02	-0.21	0.28	1			
Temp	0.15	0.09	-0.13	0.08	-0.36	-0.31	-0.09	0.32	-0.15	0.32	0	-0.06	-0.12	0.31	0.18	0.21	-0.08	0.19	0.4	0.33	-0.08	1		
RH	-0.32	-0.32	-0.35	-0.47	0.05	-0.01	0.27	0.59*	0.14	0.39	0.23	-0.05	0.19	0.48	0.17	0.19	-0.66	0.41	0.49	-0.13	-0.43	0.57*	1	

\*At 0.05 level (two-tailed), the correlation is significant

\*\* At 0.01 level (two-tailed), the correlation is significant

Table 6.5 Pearson's correlation (r) between OP induced by water-soluble fraction of 0.49–0.95  $\mu\text{m}$  particles and chemical compositions

	DTTv	DTTm	AAv	AAm	PM0.49-0.95	Cu	Pb	Fe	Mn	V	Cr	Zn	Co	Ni	As	WSOC	1,4-NQ	1,2-NQ	1,4-AQ	O <sub>3</sub>	Temp	RH	
DTTv	1																						
DTTm	0.22	1																					
AAv	-0.25	-0.68	1																				
AAm	-0.67	-0.15	0.55*	1																			
0.49-0.95	0.24	-0.75	0.62*	-0.25	1																		
Cu	0.05	-0.52	0.87**	0.29	0.66*	1																	
Pb	0.11	-0.53	0.71**	0.06	0.72**	0.81**	1																
Fe	-0.24	-0.49	0.76**	0.35	0.54*	0.78**	0.83**	1															
Mn	-0.37	-0.56	0.6*	0.46	0.27	0.44	0.66*	0.56*	1														
V	-0.09	-0.6	0.69*	0	0.83**	0.72**	0.6*	0.53*	0.17	1													
Cr	-0.02	-0.61	0.82**	0.25	0.69*	0.84**	0.97**	0.83**	0.75**	0.62*	1												
Zn	-0.45	-0.46	0.69*	0.63*	0.17	0.52*	0.56*	0.51*	0.91**	0.23	0.68*	1											
Co	0.27	-0.58	0.7**	-0.01	0.81**	0.75**	0.83**	0.64*	0.49	0.63*	0.82**	0.33	1										
Ni	0.39	-0.08	0.33	-0.14	0.48	0.34	0.06	0.07	-0.42	0.51*	0.07	-0.37	0.43	1									
As	0.25	-0.51	0.63*	-0.09	0.74**	0.83**	0.96**	0.79**	0.53*	0.6*	0.9**	0.41	0.83**	0.15	1								
WSOC	0.13	-0.14	0	-0.13	0.06	0.06	-0.05	-0.26	0.05	0.08	0	-0.07	0.24	0.1	-0.01	1							
1,4-NQ	0.23	-0.16	0.09	-0.12	0.24	0.12	0.03	-0.2	-0.14	0.32	0.1	-0.24	0.25	0.4	0.07	0.69*	1						
1,2-NQ	0.19	0.09	-0.45	-0.64	0.12	-0.16	-0.12	-0.24	-0.46	0.22	-0.25	-0.49	-0.24	-0.02	0.04	-0.06	0.16	1					
1,4-AQ	0.34	0.33	-0.44	-0.29	-0.22	-0.41	-0.47	-0.64	-0.54	-0.15	-0.44	-0.53	-0.37	0.27	-0.38	0.11	0.61*	0.41	1				
O <sub>3</sub>	-0.19	-0.34	0.15	-0.26	0.4	0.24	0.34	0.28	0.31	0.46	0.29	0.14	0.44	-0.01	0.4	0.35	-0.01	0.28	-0.44	1			
Temp	-0.32	-0.14	-0.22	-0.09	-0.08	-0.37	-0.24	-0.2	-0.05	-0.07	-0.21	-0.18	-0.19	-0.27	-0.34	0.52*	0.31	-0.03	-0.06	0.15	1		
RH	-0.06	-0.38	0.13	0.05	0.15	-0.01	-0.11	-0.22	-0.05	0.16	0	0.03	-0.14	0.01	-0.16	0.34	0.56*	0	0.38	-0.37	0.51*	1	

\*At 0.05 level (two-tailed), the correlation is significant

\*\* At 0.01 level (two-tailed), the correlation is significant

Table 6.6 Pearson's correlation (r) between OP induced by water-soluble fraction of 0.95–1.5 µm particles and chemical compositions

	DTTv	DTTm	AAv	AAm	PM0.95-1.5	Cu	Pb	Fe	Mn	V	Cr	Zn	Co	Ni	As	WSOC	O <sub>3</sub>	Temp	RH	1,4-NQ	1,2-NQ	1,4-AQ	
DTTv	1																						
DTTm	0.05	1																					
AAv	0.38	-0.31	1																				
AAm	0.35	0.35	0.65*	1																			
10.95-1.5	0.07	-0.92	0.56*	-0.16	1																		
Cu	0.2	-0.55	0.66*	0.28	0.57*	1																	
Pb	-0.49	-0.48	0.33	-0.01	0.41	0.52*	1																
Fe	0.31	-0.25	0.44	0.29	0.25	0.58*	0.52*	1															
Mn	0.42	-0.52	0.69*	0.24	0.58*	0.76**	0.33	0.62*	1														
V	-0.37	-0.65	0.27	-0.23	0.65*	0.56*	0.69*	0.38	0.38	1													
Cr	0.03	-0.64	0.53*	0.09	0.58*	0.72**	0.76**	0.73**	0.76**	0.69*	1												
Zn	0.38	-0.39	0.52*	0.32	0.36	0.74**	0.45	0.85**	0.75**	0.41	0.79**	1											
Co	0.08	-0.75	0.64*	-0.03	0.88**	0.68*	0.33	0.14	0.64*	0.57*	0.48	0.25	1										
Ni	0.33	0.11	-0.18	-0.22	-0.13	-0.01	-0.42	-0.08	0.3	-0.01	0.03	0	0.02	1									
As	0.2	-0.27	0.42	0.08	0.39	0.45	0.15	0.38	0.54*	0.1	0.24	0.17	0.61*	0.02	1								
WSOC	-0.14	0.39	0.01	0.28	-0.21	-0.53	-0.21	-0.44	-0.41	-0.52	-0.57	-0.56	-0.2	-0.43	-0.07	1							
O <sub>3</sub>	-0.27	-0.58	0.07	-0.35	0.58*	0.2	0.39	0.19	0.21	0.51*	0.25	0.15	0.43	-0.24	0.25	0.06	1						
Temp	-0.15	0.05	0.07	0.19	0	-0.47	-0.12	-0.44	-0.22	-0.22	-0.17	-0.32	-0.17	-0.2	-0.5	0.57*	0.03	1					
RH	0.08	-0.03	0.37	0.56*	0.1	0	-0.02	-0.03	0.07	-0.03	0.12	0.09	-0.01	-0.21	-0.25	0.14	-0.41	0.55*	1				
1, 4-NQ	0.18	0.03	-0.19	-0.16	-0.12	0.4	-0.16	-0.02	0.14	-0.06	-0.13	0.1	0.09	0.32	0.19	-0.3	-0.04	-0.65	-0.49	1			
1, 2-NQ	-0.1	0.59*	0.15	0.48	-0.32	-0.22	-0.21	-0.2	-0.2	-0.09	-0.35	-0.16	-0.24	-0.03	-0.27	0.43	-0.27	0.26	0.36	-0.14	1		
1, 4-AQ	0.25	-0.07	0.37	0.3	0.14	0.15	0	0.31	0.15	-0.18	0.01	0.18	0.11	-0.47	0.46	0.04	0.08	-0.02	0.18	-0.17	-0.16	1	

\*At 0.05 level (two-tailed), the correlation is significant

\*\* At 0.01 level (two-tailed), the correlation is significant

Table 6.7 Pearson's correlation (r) between OP induced by water-soluble fraction of 1.5–3 μm particles and chemical compositions

	DTTv	DTTm	AAv	AAm	PM1.5-3	Cu	Pb	Fe	Mn	V	Cr	Zn	Co	Ni	As	WSOC	1,4-NQ	1,2-NQ	1,4-AQ	O <sub>3</sub>	Temp	RH	
DTTv	1																						
DTTm	0.1	1																					
AAv	-0.08	-0.48	1																				
AAm	-0.04	0.52*	0.42	1																			
PM1.5-3	0.13	-0.8	0.54*	-0.47	1																		
Cu	0.67*	-0.29	0.59*	0.19	0.45	1																	
Pb	0.35	-0.47	0.57*	-0.18	0.78**	0.73**	1																
Fe	0.05	-0.1	-0.25	-0.45	0.15	-0.06	0.15	1															
Mn	0.07	-0.6	0.15	-0.5	0.58*	0.24	0.39	0.65*	1														
V	0.42	0.24	-0.06	0.14	-0.03	0.26	0.2	0.41	0.49	1													
Cr	0.31	-0.45	0.55*	-0.13	0.76**	0.72**	0.89**	0.12	0.48	0.31	1												
Zn	0.6*	-0.31	0.56*	0.21	0.38	0.91**	0.5*	-0.22	0.13	0	0.51*	1											
Co	0.59*	0.12	0.28	0.17	0.35	0.54*	0.65*	0.03	0.17	0.67*	0.62*	0.27	1										
Ni	-0.36	-0.2	0.26	-0.18	0.39	0.1	0.58*	0.03	0.05	-0.23	0.55*	-0.06	0.08	1									
As	0.35	-0.27	0.34	-0.16	0.61*	0.59*	0.68*	0.41	0.74**	0.6*	0.78**	0.45	0.6*	0.26	1								
WSOC	0.18	-0.05	0.24	0.25	0.01	0.45	0.31	-0.15	0.03	0.31	0.53*	0.23	0.26	0.29	0.14	1							
1,4-NQ	-0.16	0.58*	-0.28	0.23	-0.3	-0.23	-0.12	-0.34	-0.4	0.09	0.1	-0.3	0.18	0.4	-0.03	0.35	1						
1,2-NQ	0.36	-0.21	0.21	-0.01	0.15	0.54*	0.22	0.45	0.26	-0.06	0.21	0.62*	-0.15	-0.11	0.27	0.03	-0.52	1					
1,4-AQ	-0.05	-0.08	-0.42	-0.45	-0.07	-0.37	-0.09	-0.28	-0.33	-0.36	-0.31	-0.43	-0.15	0.09	-0.56	-0.1	0.03	-0.54	1				
O <sub>3</sub>	0.81**	0.24	-0.35	-0.27	0.14	0.31	0.22	0.24	0.02	0.24	0.16	0.3	0.47	-0.26	0.31	-0.24	-0.02	0.29	-0.02	1			
Temp	-0.24	0	-0.11	0.02	-0.11	-0.29	-0.37	-0.39	-0.53	-0.68	-0.2	-0.07	-0.49	0.02	-0.57	0.08	0.27	0.02	0.13	-0.08	1		
RH	-0.34	0.09	0.46	0.66*	-0.14	0.02	-0.26	-0.54	-0.35	-0.26	0	0.21	-0.2	-0.03	-0.17	0.26	0.31	0.01	-0.49	-0.43	0.57*	1	

\*At 0.05 level (two-tailed), the correlation is significant

\*\* At 0.01 level (two-tailed), the correlation is significant

Table 6.8 Pearson's correlation (r) between OP induced by water-soluble fraction of 3–7.2 μm particles and chemical compositions

	DTTv	DTTm	AAv	AAm	PM3-7.2	Cu	Pb	Fe	Mn	V	Cr	Zn	Co	Ni	As	WSOC	1,4-NQ	1,2-NQ	1,4-AQ	O <sub>3</sub>	Temp	RH	
DTTv	1																						
DTTm	-0.34	1																					
AAv	0.31	-0.49	1																				
AAm	0.2	0.54*	0.39	1																			
PM3-7.2	0.52*	-0.89	0.25	-0.52	1																		
Cu	0.15	-0.7	0.47	-0.23	0.56*	1																	
Pb	-0.1	-0.24	0.33	-0.02	0.09	0.45	1																
Fe	0.26	-0.51	0.79**	0.14	0.38	0.31	0.19	1															
Mn	0.28	-0.68	0.63*	-0.14	0.57*	0.46	0.35	0.84**	1														
V	0.14	-0.63	0.61*	-0.19	0.47	0.45	0.32	0.88**	0.74**	1													
Cr	-0.41	-0.34	-0.08	-0.58	0.34	0.19	0.35	0.26	0.32	0.46	1												
Zn	-0.01	-0.32	0.48	0.1	0.14	0.81**	0.73**	0.29	0.46	0.35	0.09	1											
Co	0.2	-0.57	0.63*	0.05	0.4	0.92**	0.58*	0.46	0.59*	0.5*	0.04	0.94**	1										
Ni	0.19	-0.59	0.57*	-0.05	0.46	0.85**	0.77**	0.48	0.66*	0.56*	0.25	0.92**	0.94**	1									
As	0.13	-0.47	0.65*	0.07	0.35	0.39	0.57*	0.84**	0.8**	0.85**	0.3	0.52*	0.59*	0.7**	1								
WSOC	0.36	-0.16	-0.22	-0.33	0.36	-0.16	-0.36	0.32	0.23	0.45	0.26	-0.37	-0.23	-0.16	0.18	1							
1,4-NQ	0.6*	0.42	-0.29	0.34	-0.18	-0.53	-0.13	-0.27	-0.22	-0.4	-0.49	-0.33	-0.39	-0.3	-0.24	0.26	1						
1,2-NQ	-0.14	0.09	0.29	0.33	-0.26	0.26	0.09	0.2	0.35	-0.01	-0.39	0.54*	0.48	0.33	0.25	-0.35	-0.15	1					
1,4-AQ	-0.55	0.23	-0.25	-0.12	-0.19	-0.27	-0.2	0.19	0.05	0.27	0.3	-0.21	-0.24	-0.23	0.29	0.35	-0.33	0.15	1				
O <sub>3</sub>	0.51*	-0.09	0.71**	0.6*	-0.11	0.15	0.24	0.32	0.16	0.18	-0.62	0.3	0.38	0.29	0.29	-0.28	0.27	0.24	-0.5	1			
Temp	0.19	-0.19	-0.02	-0.08	0.24	0.07	-0.19	-0.3	-0.07	-0.51	-0.07	-0.13	-0.08	-0.12	-0.52	-0.41	0.05	-0.1	-0.65	-0.08	1		
RH	-0.22	-0.48	0.02	-0.45	0.45	0.49	-0.25	-0.07	0.07	-0.05	0.28	0.07	0.21	0.09	-0.24	-0.22	-0.69	0.01	-0.06	-0.43	0.57*	1	

\*At 0.05 level (two-tailed), the correlation is significant

\*\* At 0.01 level (two-tailed), the correlation is significant

Table 6.9 Pearson's correlation (r) between OP induced by water-soluble fraction of  $\geq 7.2 \mu\text{m}$  particles and chemical compositions

	DTTv	DTTm	AAv	AAm	PM7.2	Cu	Pb	Fe	Mn	V	Cr	Zn	Co	Ni	As	WSOC	1,4-NQ	1,2-NQ	1,4-AQ	O <sub>3</sub>	Temp	RH	
DTTv	1																						
DTTm	-0.09	1																					
AAv	0.27	0.01	1																				
AAm	0.13	0.01	0.84**	1																			
PM7.2	0.46	-0.84	-0.01	-0.11	1																		
Cu	0.09	-0.37	-0.11	-0.07	0.15	1																	
Pb	-0.39	0.05	0.11	0.38	-0.36	-0.09	1																
Fe	-0.11	-0.53	-0.36	-0.39	0.68*	-0.25	-0.15	1															
Mn	0.24	-0.67	-0.09	-0.09	0.42	0.59*	-0.14	-0.08	1														
V	0.13	0.2	-0.05	0.21	-0.17	-0.01	0.43	-0.06	-0.19	1													
Cr	0.1	0.36	-0.17	-0.32	-0.3	0.33	-0.07	-0.21	-0.04	0.49	1												
Zn	0.12	-0.25	-0.17	-0.18	0.09	0.73**	-0.52	-0.31	0.72**	-0.3	0.16	1											
Co	0.06	-0.08	0.57*	0.71**	-0.09	0.2	0.3	-0.24	0.15	0.53*	0.25	0.09	1										
Ni	-0.42	-0.14	-0.52	-0.56	0	0.42	-0.44	0.23	0.27	-0.2	0.37	0.62*	-0.04	1									
As	-0.68	0.22	0.23	0.18	-0.37	-0.22	0.38	0.07	-0.63	0.12	0.07	-0.51	0.14	0.01	1								
WSOC	0.08	0.32	-0.51	-0.27	-0.1	-0.08	-0.41	0.05	-0.23	0.36	0.14	0.17	-0.14	0.27	-0.16	1							
1,4-NQ	-0.29	-0.28	0.1	0.11	0.34	0.03	-0.16	0.52*	-0.37	-0.32	-0.38	-0.15	-0.08	0.18	0.46	-0.02	1						
1,2-NQ	-0.45	0.14	-0.35	-0.37	-0.37	0.04	-0.21	-0.16	0.25	0.03	0.32	0.44	0.05	0.64*	0.08	0.33	-0.39	1					
1,4-AQ	0.02	0.34	0.35	-0.15	-0.11	-0.45	-0.38	0.01	-0.44	-0.41	0.11	-0.29	-0.29	-0.08	0.37	-0.23	0.12	0.03	1				
O <sub>3</sub>	0.38	-0.49	0.66*	0.26	0.51*	0.14	-0.23	0.03	0.33	-0.5	-0.2	0.09	0.09	-0.23	-0.07	-0.7	0.18	-0.36	0.45	1			
Temp	-0.88	0	-0.08	0.03	-0.36	0	0.51*	0.04	-0.27	-0.27	-0.31	-0.23	-0.17	0.12	0.71**	-0.31	0.44	0.07	0.01	-0.15	1		
RH	-0.26	0.13	-0.39	-0.33	0.07	-0.25	-0.38	0.44	-0.45	-0.48	-0.39	-0.08	-0.58	0.27	0.07	0.36	0.66*	-0.16	0.14	-0.43	0.57*	1	

\*At 0.05 level (two-tailed), the correlation is significant

\*\* At 0.01 level (two-tailed), the correlation is significant



#### 6.2.4.3 The response of DTT and AA assays to PM chemical compositions

The results of the study demonstrate the selective sensitivity of the DTT and AA assays towards the chemical constituents of PM<sub>2.5</sub> samples, which is influenced by their solubility. As demonstrated in Chapter 5 and herein, the DTT assay consistently shows higher OP levels induced by water-soluble fraction compared to the AA assay. This can be attributed to DTT's sensitivity to a wide range of water-soluble chemical species, including trace metals, HMW-quinones, and HULIS (Bates et al., 2015; Famiyeh, Jia, et al., 2023). In contrast, the AA assay exhibits higher OP induced by methanol-soluble fractions compared to the DTT assay. The elevated OP induced by methanol-soluble fraction in the AA assay can be attributed to its strong sensitivity to non-vehicular exhaust trace metals and LMW-quinones soluble in methanol (Bates et al., 2019; Pietrogrande et al., 2019). Hence, it is crucial to carefully select the appropriate assay based on the chemical species of interest and the solvent used for extraction (Bates et al., 2015). Moreover, these findings underscore the importance of prudent assay selection and interpretation to accurately assess the OP of ambient particles. The results of this study strongly support the suitability of the DTT assay for exploring the OP induced by water-soluble fractions. Conversely, the AA assay is recommended for assessing the OP induced by methanol-soluble fractions of ambient particles. It is worth noting that utilizing multiple assays enables the identification of various chemical species that contribute to the oxidative potential of ambient particles.

#### 6.2.4.4 Graphical analysis of source dispersion: PM mass concentration

Figure 6-8 presents the dispersion patterns of the concentrations of ultrafine, accumulation, and coarse particles collected at our study domain. The data indicates that

particles within size ranges of  $\leq 0.49 \mu\text{m}$ ,  $0.49\text{--}0.95 \mu\text{m}$ , and  $0.95\text{--}1.5 \mu\text{m}$  showed similar dispersion patterns, with higher concentrations observed in the northwest (NW) (Figure 6-8 a, b, c, respectively), suggesting a potential source from the Wangchun industrial zone, which is situated about 12 km away from our study domain. The Ningbo Lishe airport, located approximately 9 km northwest of our study area, implies that emissions from the airport in this direction may contribute to the levels of these particles. The highest concentrations of these particles were detected during periods of high wind speeds ( $\geq 4 \text{ ms}^{-1}$ ), suggesting the release of buoyant plumes from industrial sources via chimneys (Carslaw and Beevers, 2013; Chen et al., 2021). The elevated concentrations of these particles in the northeast (NE) region suggest potential emissions from industrial facilities in the Zhenhai and Beiliun Districts. Moreover, the high concentrations of particles in northwest and northeast regions suggest potential source from highway traffic located less than 200 km away from our study domain (Chen et al., 2022). There is a potential source of  $\leq 0.49 \mu\text{m}$  particles in the southeast (SE) region, specifically from a freeway that is located near our study domain. The high concentration of particles  $\leq 0.49 \mu\text{m}$  in the northeast and southeast suggest a potential source from marine vessels and sea salt aerosol originating from the Ningbo-Zhoushan port and the East China Sea. These findings suggest that industrial sources and vehicular traffic are two potential sources contributing to the mass concentrations of  $\leq 0.49 \mu\text{m}$ ,  $0.49\text{--}0.95 \mu\text{m}$ , and  $0.95\text{--}1.5 \mu\text{m}$ .

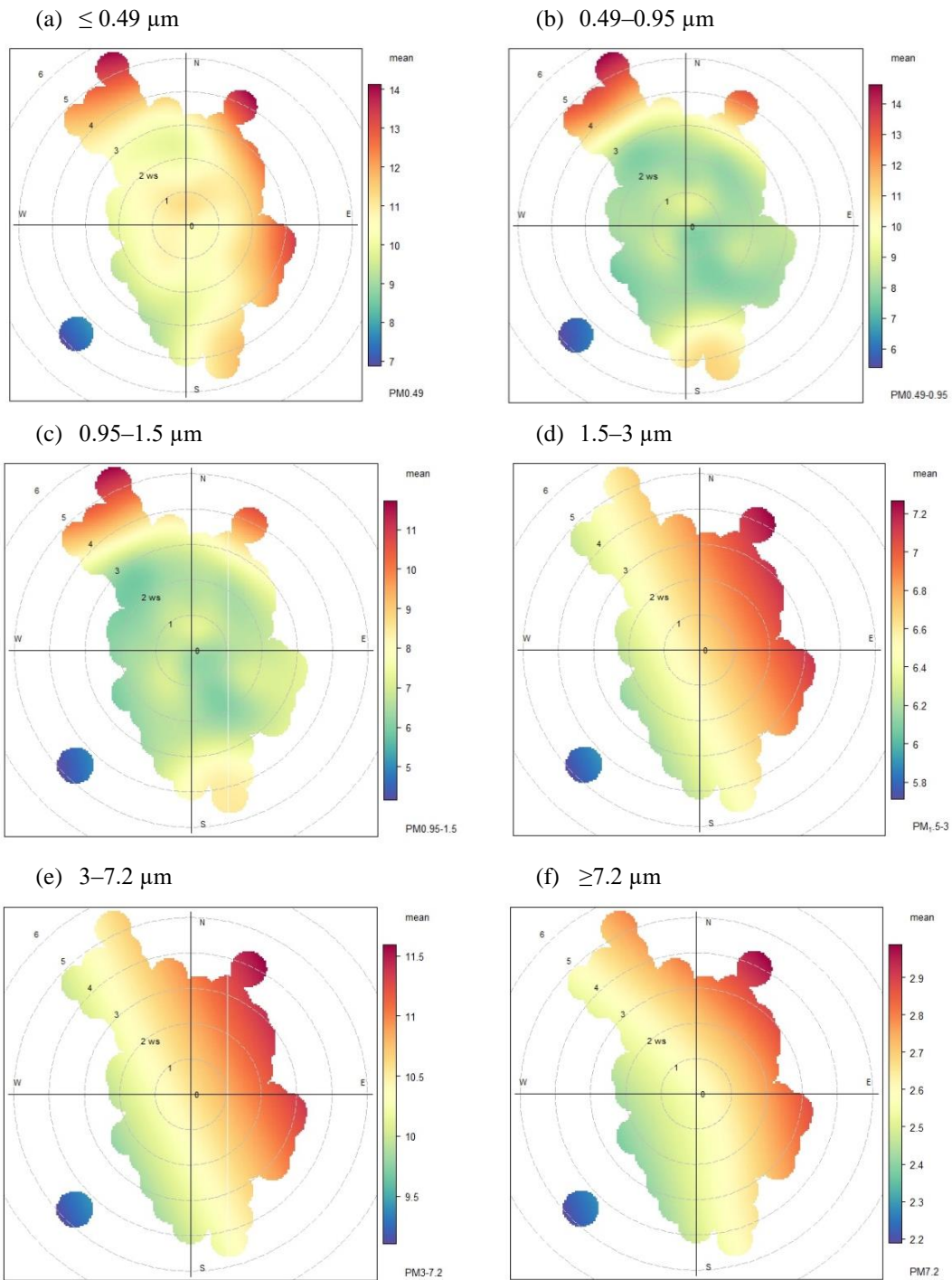


Figure 6-8 Bivariate polar plots of size-resolved PM mass concentration ( $\mu\text{g m}^{-3}$ ) induced by water-soluble fractions: ultrafine (a, b), accumulation (c, d), coarse (e, f) particles

The dispersion patterns of both accumulation particles (1.5–3  $\mu\text{m}$ ) and coarse particles (3–7.2  $\mu\text{m}$  and  $\geq 7.2$   $\mu\text{m}$ ) showed similarities (as illustrated in Figure 6-8 d-f). Higher concentrations of these particles were observed in both the northeast and southeast regions, suggesting potential sources from industrial facilities in the Zhenhai and Beiliun Districts and freeways. The findings indicate that an increase in wind speed (4  $\text{m s}^{-1}$ ) is linked to an elevated concentration of coarse particles on freeways, suggesting that both vehicle movement and wind force play significant roles in the suspension of road dust and the accumulation of high levels of coarse particles transported to our study domain. Moreover, the elevated concentrations of 1.5–3  $\mu\text{m}$ ) and coarse particles (3–7.2  $\mu\text{m}$  and  $\geq 7.2$   $\mu\text{m}$ ) observed in the southeast region indicate a potential sources from marine vessels and sea salt (SS) aerosols, considering the close proximity of the Ningbo-Zhoushan port and East China Sea, located approximately 33 km and 35 km from our study domain, respectively.

The analysis of air mass trajectories reveals the regional transport of air masses from Northern China, Southern China, and the East China Sea to the study domain. This evidence is supported by Figure 6-9, which highlights the trajectory of an air mass originating from Jiangsu Province (indicated by the pink color) and passing through a region with a high concentration of fire spots. This suggests the potential transport of pollutants from biomass burning to our study area, which may contribute to the level of ultrafine particles ( $\leq 0.49$   $\mu\text{m}$ , and 0.49–0.95  $\mu\text{m}$ ) as well as accumulation particles (0.95–1.5  $\mu\text{m}$ ). Furthermore, our analysis consistently reveals the transport of air masses from the East China Sea (indicated by the blue color) through key areas such as the Ningbo-Zhoushan port and Beilun and Zhenhai Districts to our study area. This is consistent with the bivariate polar plots shown in

Figure 6-8 (d-f). This transport contributes to the level of accumulation particles ( $1.5\text{--}3\ \mu\text{m}$ ) as well as coarse particles. The most dominant trajectory of the air masses, constituting 42.9% of the total, originated from the East China Sea. Initially, these air masses followed a south-easterly direction, and subsequently shifted to a southerly direction before reaching our study domain.

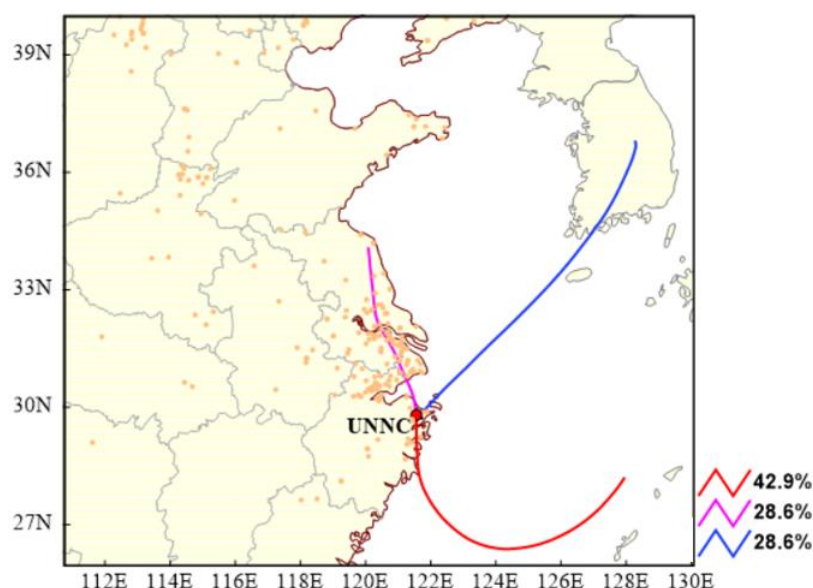


Figure 6-9 48-h back trajectories analysis with firespot at our study domain (the campus of the University of Nottingham Ningbo, China) (Chen et al., 2022)

#### 6.2.4.5 Graphical analysis of source dispersion of OP: water-soluble fractions

The source dispersion patterns of DTTv and AAv induced by water-soluble fractions of size-resolved PM varies across the same particle size ranges (as shown in Figure 6-10 and Figure 6-11, respectively). The corresponding DTTm and AAm are shown in Figure 8-7 and Figure 8-8, respectively. The source dispersion pattern of DTTv for particles with a size of  $\leq 0.49\ \mu\text{m}$  (Figure 6-10 a) is similar to that of the mass concentration (as shown in Figure 6-8 a), suggesting that similar sources contribute to both the mass concentration and DTTv

of particles with a size of  $\leq 0.49 \mu\text{m}$ . Therefore, the high DTTv in the northwest can be associated with emissions from the Wangchun industrial zone and Ningbo Lishe airport. The corresponding DTTm of  $\leq 0.49 \mu\text{m}$  particles (as shown in Appendix, Figure 8-7 a) exhibited different patterns, with higher concentrations in the north and southwest. The corresponding AAv of  $\leq 0.49 \mu\text{m}$  exhibited different patterns (Figure 6-11 a), with high values in the southwest (SW) region. The observed pattern in the distribution of AAv at high wind speed ( $> 4 \text{ ms}^{-1}$ ) can be attributed to the presence of buoyant plumes, which are likely originating from vehicular traffic. This observation is in line with expectations, as the ring expressway of Ningbo city is situated approximately 2 km away from our study area, towards the southwest and south. In addition to emissions from the Wangchun industrial zone and easterly wind (as shown in Figure 8-8 a), this source also contributes to the corresponding AAm levels of particles with a diameter of  $\leq 0.49 \mu\text{m}$ .

The dispersion patterns of the concentration of accumulation particles ( $0.95\text{--}1.5 \mu\text{m}$ ) exhibited varies with DTTv and AAv (as shown in Figure 6-10 c and Figure 6-11 c, respectively). The distribution of DTTv is dominated in the northeast and southeast regions, while AAv is dominant in the southerly and southwest regions. This indicates a divergent source of DTTv and AAv. Specifically, DTTv can be attributed to emissions from industries in Beilun and Zhenhai District, vehicular traffic, and marine and sea salt aerosols from the Ningbo-Zhoushan port and East China Sea. In contrast, the elevated levels of AAv primarily result from road traffic, specifically due to the presence of nearby freeways in the southwest area.

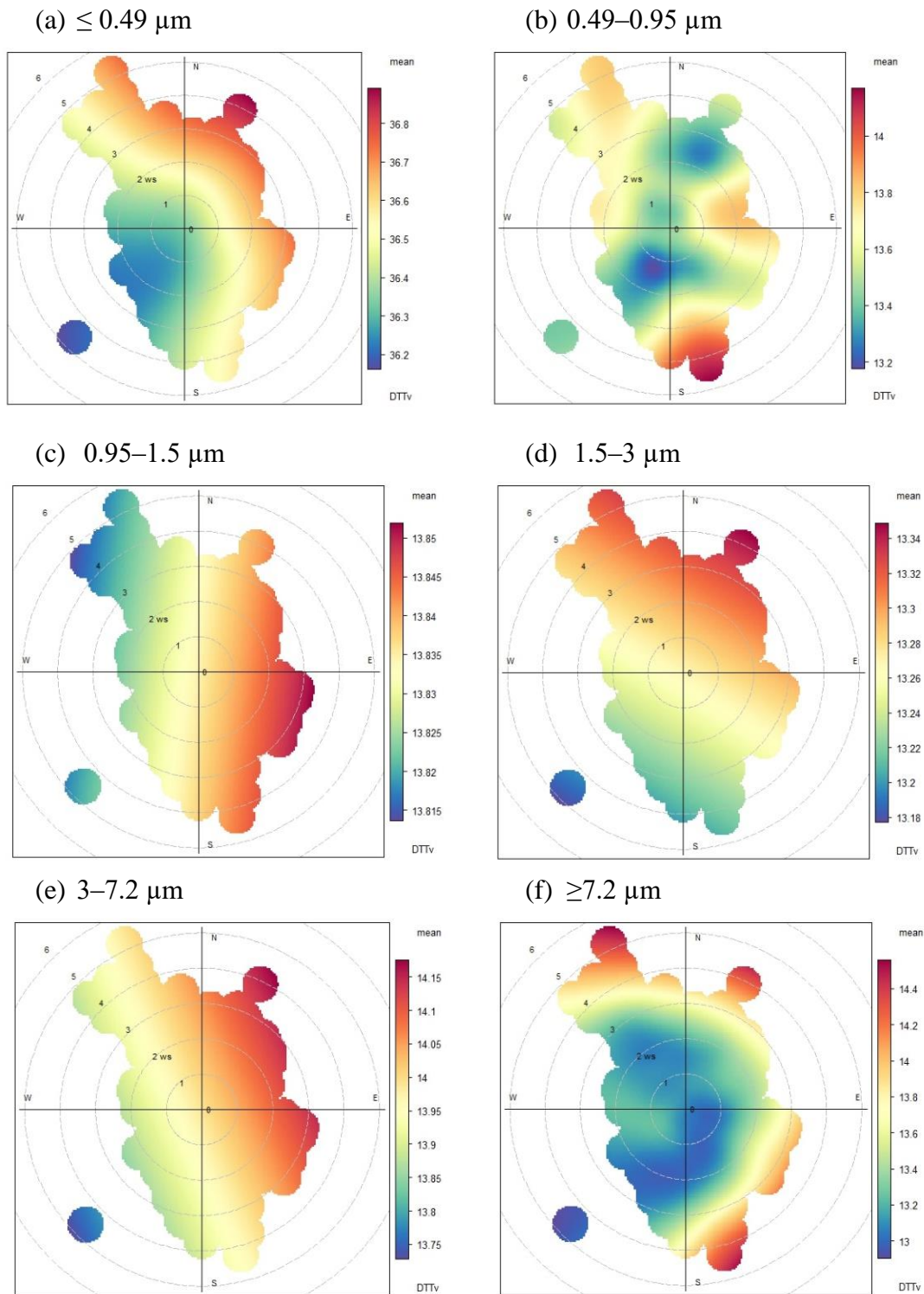


Figure 6-10 Bivariate polar plots of size-resolved concentrations of DTTv ( $\text{nmol min}^{-1}\text{m}^{-3}$ ) induced by water-soluble fractions: ultrafine (a, b), accumulation (c, d), coarse (e, f) particles

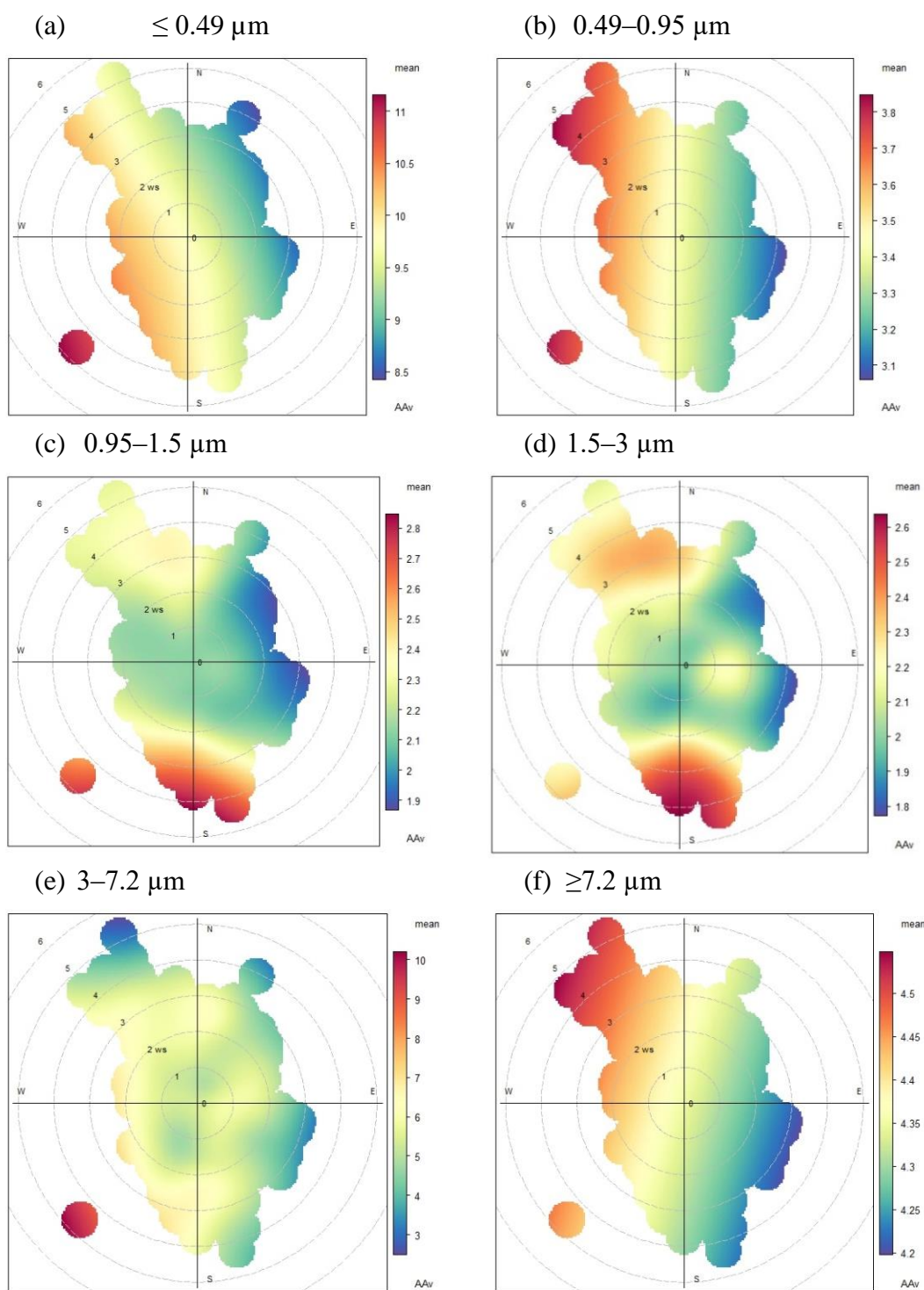


Figure 6-11 Bivariate polar plots of size-resolved concentrations of AAV ( $\text{nmol min}^{-1}\text{m}^{-3}$ ) induced by water-soluble fractions: ultrafine (a, b), accumulation (c, d), coarse (e, f) particles



The DTTv of accumulation (1.5–3  $\mu\text{m}$ ) and coarse particles (Figure 6-10, d-f) showed similar distribution patterns as their corresponding mass concentrations. This suggests that they have similar sources to DTTv and concentrations. These particles are primarily influenced by industrial emissions from the Wangchun industrial zone, as well as Beilun and Zhenhai industrial parks, as well as vehicular traffic from nearby freeways. The AAv of these particles exhibited different source dispersion patterns to their mass concentrations. Specifically, the AAv of particles with a size range of  $\leq 1.5\text{--}3\ \mu\text{m}$  is primarily influenced by southerly winds, while AAv of coarse particles with sizes ranging from  $3\text{--}7.2\ \mu\text{m}$  and  $\geq 7.2\ \mu\text{m}$  are dominant in the southwest and northwest regions. This suggests that the suspension of road dust in freeway few meters from our study domain due to vehicular movement and high wind speeds contributes to the AAv of particles in the  $3\text{--}7.2\ \mu\text{m}$  range. The elevated levels of particles  $\geq 7.2\ \mu\text{m}$  in the AAv are primarily attributed to industrial emissions originating from the Wangchun industrial zone, as well as the suspension of road dust caused by traffic activity. These pollutant sources are then transported to our study area during periods of high wind speeds.

#### 6.2.4.6 Graphical analysis of source dispersion of OP: methanol-soluble fractions

The dispersion patterns of DTTv induced by methanol-soluble fraction-induced (as illustrated in Figure 6-12) differed slightly from the patterns observed in the mass concentrations (as shown in Figure 6-8). Furthermore, the DTTv and AAv (Figure 6-13) displayed distinct source dispersion patterns. The DTTv of ultrafine particles, specifically those with sizes  $\leq 0.49\ \mu\text{m}$  and  $0.49\text{--}0.95\ \mu\text{m}$ , exhibited comparable source dispersion patterns (Figure 6-12 a and b, respectively). The high DTTv of these particles were

predominantly observed in the northwest and northeast regions, indicating the influence of industrial emissions from the Wangchun industrial zone and Zhenhai industrial park, as well as vehicular traffic from highways in the northeast and northwest.

The corresponding AAv of  $\leq 0.49 \mu\text{m}$  particles dominated in all directions (as shown in Figure 6-13 a), suggesting contributions of several emission sources including industrial, vehicular traffic, marine, and sea salt aerosols. The AAv of  $0.49\text{--}0.95 \mu\text{m}$  particles clearly reveals a dominant source originating from the southeast and northeast (as shown in Figure 6-13 b). This observation provides strong evidence of contributions of industrial emissions from the Beilun industrial park, marine aerosols, sea salt, and road traffic from nearby freeways to AAv of  $0.49\text{--}0.95 \mu\text{m}$  particles. The corresponding DTTm of  $0.49\text{--}0.95 \mu\text{m}$  particles displayed distinct distribution patterns compared to AAv. The DTTm of these ultrafine particles showed increased concentration with decreasing wind speeds (as shown in Appendix, Figure 8-9 b), indicating dominant contribution of ground-level sources, particularly from nearby traffic within close proximity of our study domain.

The DTTv of  $\leq 0.95\text{--}1.5 \mu\text{m}$  and  $\leq 1.5\text{--}3 \mu\text{m}$  particles exhibited similar distribution pattern, with peak concentrations in the northwest at high wind speed and in the north at low wind speed (as shown in Figure 6-12), suggest industrial emissions from Wangchun industrial zone and vehicular traffic. This pattern is different from AAv of the same particle size ranges. Specifically, AAv of  $\leq 0.95\text{--}1.5 \mu\text{m}$  is concentrated in the southwest (as shown in Figure 6-13 c) attributed to vehicular traffic in freeway close to our study domain. The AAv of  $\leq 0.95\text{--}1.5 \mu\text{m}$  peaked in southwest, suggesting the contribution of vehicular traffic.

The distribution pattern of DTTv for accumulation particles with sizes  $\leq 0.95\text{--}1.5\ \mu\text{m}$  and  $\leq 1.5\text{--}3\ \mu\text{m}$  exhibited similarities, with peak concentrations observed in the northwest during high wind speeds and in the north during low wind speeds (as illustrated in Figure 6-12). This observation indicates potential contributions from industrial emissions originating from the Wangchun industrial zone and vehicular traffic from highway. In contrast, the source distribution pattern of DTTv differs from the AAv pattern observed for particles within the same size ranges. Specifically, the AAv of accumulation particles ( $\leq 0.95\text{--}1.5\ \mu\text{m}$ ) dominated in the southwest (Figure 6-13 c), which can be attributed to vehicular traffic on the nearby freeway. In contrast, the AAv of particles within the  $\leq 1.5\text{--}3\ \mu\text{m}$  dominated in the southeast (Figure 6-13 d), indicating contributions vehicular traffic.

The DTTv values of coarse particles in the size range of  $3\text{--}7.2\ \mu\text{m}$  and  $\geq 7.2\ \mu\text{m}$  display similar source dispersion patterns (Figure 6-12 e and f, respectively). However, the dispersion patterns of both DTTv and AAv in these particles vary, indicating diverse response of these assays to various sources. Specifically, DTTv of  $3\text{--}7.2\ \mu\text{m}$  particles dominated in the northeast, with minor distribution in northwest and southeast regions (Figure 6-12 e). In contrast, AAv dominated in northwest at high wind speed, possibly associated with industrial emissions and wind-driven transport of dust particles from highways. At low wind speeds, AAv of  $3\text{--}7.2\ \mu\text{m}$  particles is concentrated in the north and southwest, suggesting the contribution of dust particles from nearby freeways due to vehicular movement. In contrast, the DTTv of particles with sizes  $\geq 7.2\ \mu\text{m}$  is more concentrated in the northwest and northeast (Figure 6-12 f), while the corresponding AAv is dominated in the southwest, northeast, and southeast regions (Figure 6-13 f).

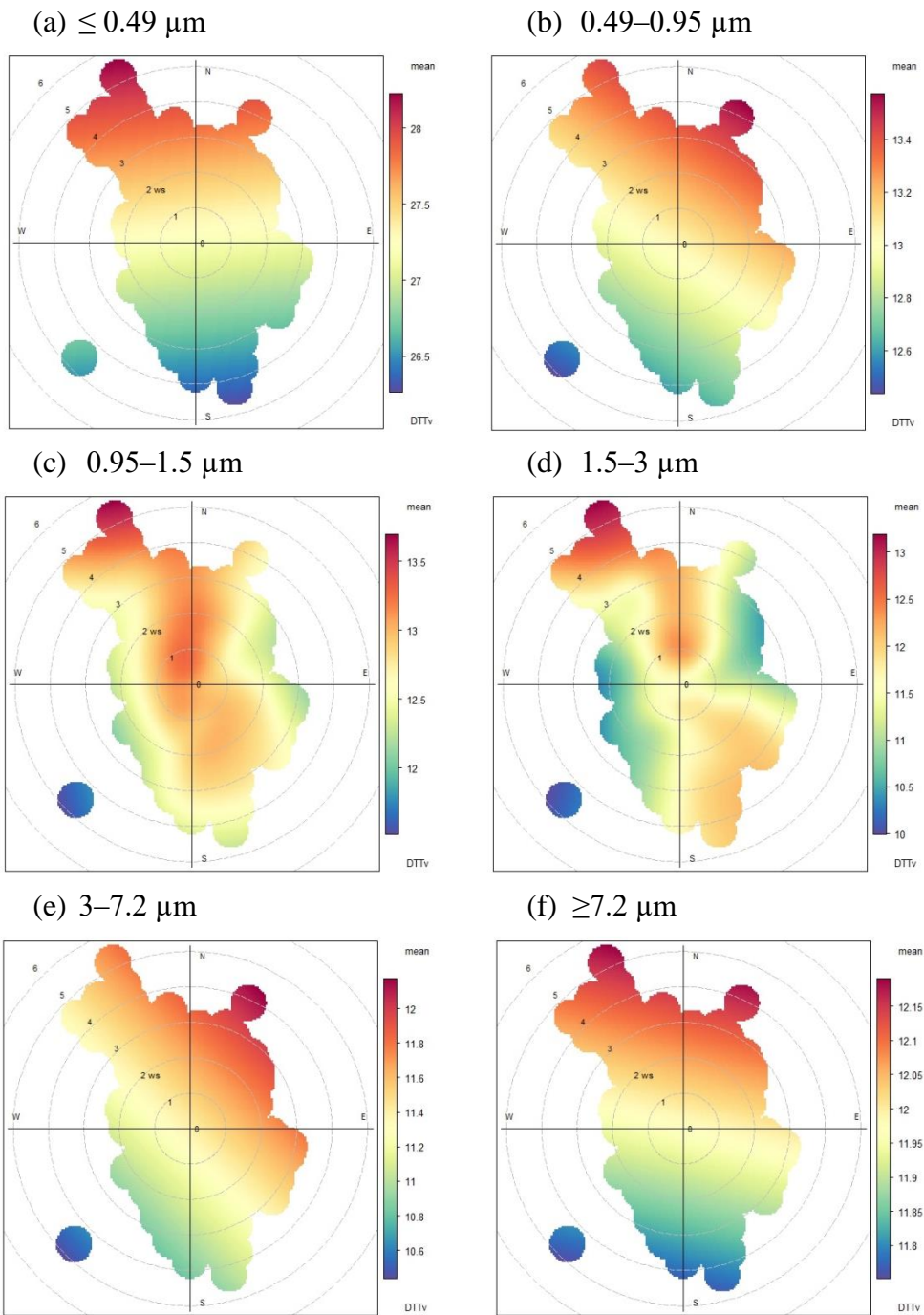


Figure 6-12 Bivariate polar plots of size-resolved concentrations of DTTv ( $\text{nmol min}^{-1}\text{m}^{-3}$ ) induced by methanol-soluble fractions: ultrafine (a, b), accumulation (c, d), coarse (e, f) particles

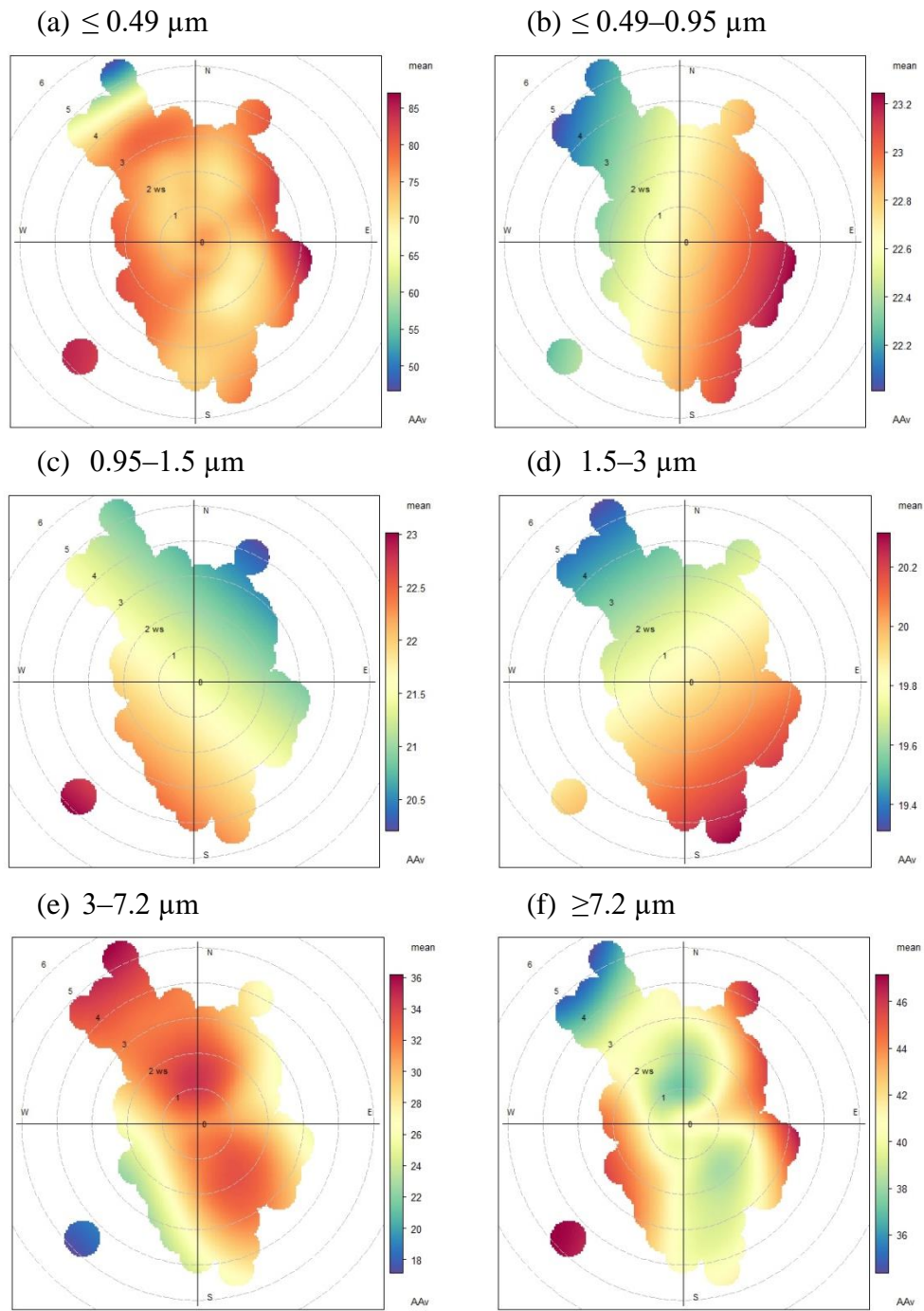


Figure 6-13 Bivariate polar plots of size-resolved concentrations of AAV ( $\text{nmol min}^{-1}\text{m}^{-3}$ ) induced by methanol-soluble fractions: ultrafine (a, b), accumulation (c, d), coarse (e, f) particles

Table 6.10 Summary of potential sources associated with OP induced by water-and methanol-soluble fractions of ultrafine, accumulation , and coarse particles

Water-soluble fractions	≤0.49	0.49–0.95	0.95–1.5	1.5–3	3–7.2	≥7.2
DTTv	industrial, vehicular traffic, marine, sea salt	vehicular traffic	industrial, vehicular traffic, marine, sea salt	industrial, vehicular traffic, marine, sea salt	industrial, marine, sea salt, vehicular traffic	vehicular traffic, road dust, industrial
AAv	vehicular traffic, road dust	industrial, vehicular, road dust,	vehicular traffic, road dust	vehicular traffic, road dust	road dust, vehicur traffic	industrial, vehicular traffic, road dust
Methanol-soluble fractions	≤0.49	0.49–0.95	0.95–1.5	1.5–3	3–7.2	≥7.2
DTTv	industrial, vehicular traffic	industrial, vehicular traffic	industrial, vehicular traffic	industrial, vehicular traffic	industrial, vehicular traffic, marine, sea salt	industrial, vehicular traffic, marine, sea salt
AAv	industrial, vehicular traffic, road dust, marine, sea salt	industrial, marine, sea salt, vehicular traffic	vehicular traffic, road dust	vehicular, marine, sea salt	industrial, vehicular traffic	vehicular traffic, industrial, marine, sea salt

Ultrafine particles: ≤ 0.49, 0.49–0.95 μm, accumulation particles: 0.95–1.5, 1.5–3 μm, coarse particles: 3–7.2, ≥7.2 μm

This indicates that AAv with a size of  $\geq 7.2 \mu\text{m}$  is primarily influenced by dust particles from freeways in the southwest and southeast, industrial emissions in Beilun and Zhenhai industrial park, in addition to contributions from marine aerosols and sea salt originating from the East China Sea and Ningbo-Zhoushan port. In contrast, DTTv  $\geq 7.2 \mu\text{m}$  is significantly dominated by industrial emissions from Wangchun industrial zone and Zhenhai industrial park, and vehicular traffic and road dust transport from highways.

#### 6.2.4.7 OP induced by water- and methanol-soluble fractions of PM<sub>2.5</sub> and PM<sub>10</sub>

The DTTv and AAv induced by water- and methanol-soluble fractions of PM<sub>2.5</sub> and PM<sub>10</sub> are presented in Figure 6-14 and Figure 6-15, respectively. The corresponding intrinsic OP are shown in the Appendix (Figure 8-11 and Figure 8-12, respectively). The DTTv and AAv values induced by the water-soluble and methanol-soluble fractions of PM<sub>2.5</sub> and PM<sub>10</sub> show significant differences (z-statistics,  $p \leq 0.05$ ), with PM<sub>10</sub> exhibiting higher values compared to PM<sub>2.5</sub>. Specifically, the mean DTTv induced by the water-soluble fractions of PM<sub>2.5</sub> and PM<sub>10</sub> were  $1.77 \pm 1.62 \text{ nmol min}^{-1}\text{m}^{-3}$  and  $3.95 \pm 2.01 \text{ nmol min}^{-1}\text{m}^{-3}$ , respectively. The mean AAv values for PM<sub>2.5</sub> and PM<sub>10</sub> were  $1.23 \pm 0.23 \text{ nmol min}^{-1}\text{m}^{-3}$  and  $3.36 \pm 0.45 \text{ nmol min}^{-1}\text{m}^{-3}$ , respectively. The DTTv induced by the methanol-soluble fraction of PM<sub>2.5</sub> and PM<sub>10</sub> were  $2.17 \pm 0.93 \text{ nmol min}^{-1}\text{m}^{-3}$  and  $3.26 \pm 2.87 \text{ nmol min}^{-1}\text{m}^{-3}$ , respectively. The AAv values for PM<sub>2.5</sub> and PM<sub>10</sub> were  $2.96 \pm 1.62 \text{ nmol min}^{-1}\text{m}^{-3}$  and  $3.57 \pm 0.91 \text{ nmol min}^{-1}\text{m}^{-3}$ , respectively.

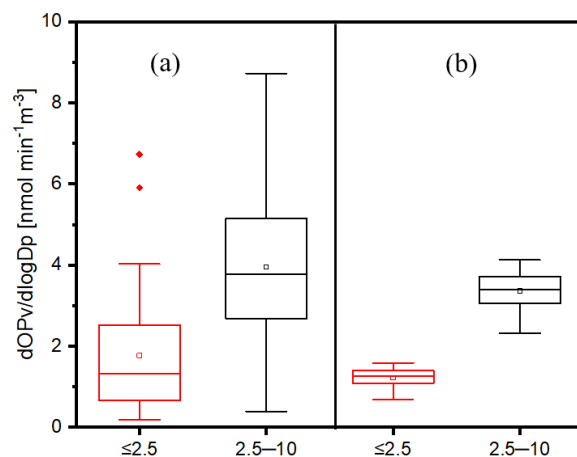


Figure 6-14 Size distribution of extrinsic OP ( $dOP_v = \text{mean extrinsic OP (nmol min}^{-1} \text{ m}^{-3})$ ,  $d\log D_p = \text{logarithmic difference of aerodynamic diameter}$ ) of water-soluble fractions of fine ( $\leq 2.5 \mu\text{m}$ ) and coarse particles ( $2.5\text{--}10 \mu\text{m}$ ) in DTT (a) and AA (b) assays. Median (line across the box), mean (square within the box), first quartile (Q1) (bottom of the box), third quartile (Q3) (top of the box), outlier (square shown outside the box), whiskers shows minimum and maximum values

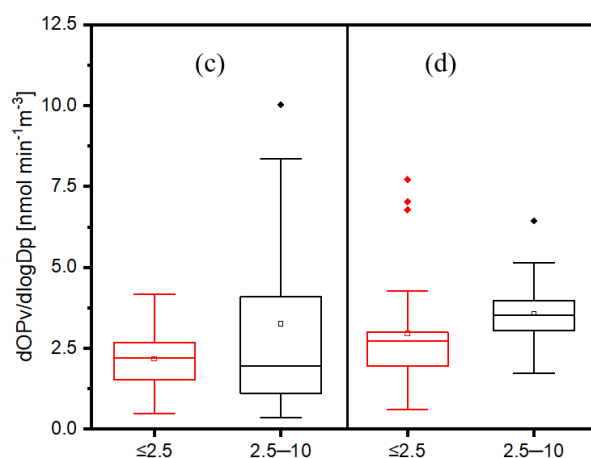


Figure 6-15 Size distribution of extrinsic OP ( $dOP_v = \text{mean extrinsic OP (nmol min}^{-1} \text{ m}^{-3})$ ,  $d\log D_p = \text{logarithmic difference of aerodynamic diameter}$ ) of methanol-soluble fractions of fine ( $\leq 2.5 \mu\text{m}$ ) and coarse particles ( $2.5\text{--}10 \mu\text{m}$ ) in DTT (a) and AA (b) assays. Median (line across the box), mean (square within the box), first quartile (Q1) (bottom of the box), third quartile (Q3) (top of the box), outlier (square shown outside the box), whiskers shows minimum and maximum values



In a study conducted by Perrone et al. (2019) in Peninsula, Italy, the researchers compared the OP of the water-soluble fraction of PM<sub>2.5</sub> and PM<sub>10</sub>. The findings of their study revealed the following observations. The values of DTT<sub>v</sub> were reported to be similar for both PM<sub>2.5</sub> and PM<sub>10</sub>. However, the AAv was found to be higher in PM<sub>10</sub> compared to PM<sub>2.5</sub>. The study conducted by Veld et al. (2023) in Barcelona, Spain reported higher values of DTT<sub>v</sub> and AAv for PM<sub>10</sub> compared to PM<sub>2.5</sub>, which is consistent with the findings of our study.

#### 6.2.4.8 Chemical species associated with OP: PM<sub>2.5</sub> versus PM<sub>10</sub>

As demonstrated in this study, PM<sub>10</sub> particles consistently exhibited higher OP values than PM<sub>2.5</sub> in both water- and methanol-soluble fractions. This can be attributed to several factors. The presence of high concentrations of OP-induced chemicals such as 1, 2-NQ and 1, 4-AQ in PM<sub>10</sub> could contribute to the high OP activity (as shown in Figure 6-2). Moreover, this study for the first time provides evidence to suggest that a multilayer adsorption mechanism of the chemical compositions of coarse particles play a key role in controlling the OP. This adsorption mechanism enables more efficient reactions between LMW-PAHs, such as NaP and Ant, in coarse particles and atmospheric oxidants. As a result, this leads to the formation of quinones such as 1, 2-NQ and 1, 4-AQ with high concentrations in coarse particles, thereby elevating the OP levels.

In order to identify the primary chemical species responsible for the OP induced by water- and methanol-soluble fractions of PM<sub>2.5</sub> and PM<sub>10</sub>, a Pearson's correlation analysis was performed. The study found that the DTT<sub>v</sub> of PM<sub>2.5</sub> showed a moderate-to-strong correlation with Mn, Cd, Sr, Co, Pb, V, Al, and Ce, as well as 1, 2-NQ (as depicted in Table 6.11). The DTT<sub>v</sub> of PM<sub>10</sub> exhibit a strong correlation with quinones (1, 2-NQ and 1, 4-AQ), strong with

Fe, and moderate with Cu (as shown in Table 6.12). The strong correlation between the OP levels of PM<sub>10</sub> and the presence of Fe and Cu suggests that the Fenton reaction plays a significant role in increasing the OP levels of PM<sub>10</sub>. (Fang et al., 2019). Moreover, the present of Fe and quinones cause synergistic effect, increasing the OP of PM<sub>10</sub> (Pietrogrande et al., 2022; Yu et al., 2018). There was a weak correlation observed between AAv induced by water-soluble fractions of PM<sub>10</sub> and PM<sub>2.5</sub> and trace metals, and quinones. However, the AAv of PM<sub>10</sub> showed a moderate correlation with O<sub>3</sub>, suggesting contribution of photochemical aging processes to the high AAv. Several studies have associated the generation of OP with photochemically aged aerosols (Chen et al., 2022; Famiyeh et al., 2023; Hsiao et al., 2021).

The DTTv and AAv values induced by the methanol-soluble fraction of PM<sub>2.5</sub> showed a weak correlation with water-soluble trace metals and quinones. However, the DTTv and AAv values of PM<sub>10</sub> exhibited a moderate correlation with quinones and WSOCs. Therefore, the high DTTv induced by PM<sub>10</sub> can be attributed to the presence of 1, 2-NQ and WSOCs. In summer, SOA makes up a large part of WSOC and shows high OP activity (Park et al., 2011). Furthermore, WSOC has been used as a tracer for SOA during this season (Farahani et al., 2022; Lovett et al., 2018; Taghvaei et al., 2019).

Table 6.11 Pearson's correlation (r) between OP induced by water-soluble fraction of PM<sub>2.5</sub> and chemical compositions

	DTTv	DTTm	AAv	AAm	PM2.5	Mn	Co	Ni	Cd	Zn	Ba	Cr	Cu	Al	As	Pb	Fe	V	Ag	Bi	Ce	Sr	Sb	WSOC	1,4-NQ	1,2-NQ	1,4-AQ	O3	Temp	RH	
DTTv	1																														
DTTm	0.71**	1																													
AAv	-0.62	-0.52	1																												
AAm	-0.33	0.25	0.27	1																											
PM2.5	0.55*	0.35	-0.2	-0.4	1																										
Mn	0.53*	0.15	0.19	-0.18	0.36	1																									
Co	0.57*	0.07	0.03	-0.29	0.11	0.8**	1																								
Ni	0.28	-0.03	0.32	-0.15	-0.16	0.68*	0.81**	1																							
Cd	0.69*	0.34	-0.02	-0.31	0.79**	0.76**	0.65*	0.36	1																						
Zn	0.33	-0.16	0.18	-0.39	-0.09	0.59*	0.92**	0.83**	0.45	1																					
Ba	0.19	0.17	0.22	0.32	0.08	0.76**	0.39	0.41	0.37	0.12	1																				
Cr	-0.06	-0.24	0.31	0.07	-0.45	0.14	0.62*	0.62*	0.06	0.78**	-0.1	1																			
Cu	0.48*	0.16	0.15	-0.25	0.11	0.66*	0.86*	0.91**	0.6*	0.85**	0.27	0.63*	1																		
Al	0.65*	0.69*	-0.01	0.07	0.46	0.64*	0.39	0.5*	0.61*	0.17	0.5*	-0.14	0.55*	1																	
As	0.17	-0.15	0.39	-0.22	0.11	0.52*	0.77**	0.63*	0.6*	0.85**	0.1	0.77**	0.76**	0.12	1																
Pb	0.5*	0.26	-0.11	-0.55	0.61*	0.26	0.42	0.33	0.69*	0.46	-0.23	0.23	0.65*	0.38	0.59*	1															
Fe	0.35	0.01	0.28	-0.26	0.15	0.79**	0.85**	0.85**	0.66*	0.82**	0.49*	0.54*	0.91**	0.44	0.82**	0.56*	1														
V	0.62*	0.36	-0.15	-0.05	0.12	0.6*	0.78**	0.4	0.59*	0.66**	0.28	0.47	0.51*	0.28	0.64*	0.25	0.53*	1													
Ag	0.53*	0.21	0.16	-0.13	0.34	0.97**	0.7**	0.64*	0.67*	0.46	0.79**	-0.01	0.56*	0.71**	0.33	0.13	0.66*	0.51*	1												
Bi	0.49*	0.25	-0.05	-0.37	0.57*	0.75**	0.43	0.37	0.7**	0.25	0.65*	-0.26	0.45	0.55*	0.26	0.43	0.66*	0.26	0.72**	1											
Ce	0.81**	0.65*	-0.22	-0.28	0.66*	0.73**	0.49*	0.41	0.78**	0.25	0.48*	-0.25	0.54*	0.88**	0.2	0.54*	0.53*	0.42	0.76**	0.8*	1										
Sr	0.51*	0.49*	-0.09	0.06	-0.07	0.3	0.66*	0.59*	0.39	0.67*	-0.01	0.7**	0.75**	0.4	0.66*	0.52*	0.58*	0.71**	0.19	0.06	0.34	1									
Sb	0.49*	0.26	0.25	-0.18	0.57*	0.67*	0.69*	0.5*	0.9**	0.61*	0.25	0.38	0.73**	0.54*	0.83**	0.74**	0.76**	0.64*	0.54*	0.51*	0.61*	0.61*	1								
WSOC	-0.44	0.01	0.21	0.67*	-0.32	-0.57	-0.59	-0.42	-0.55	-0.56	-0.29	-0.11	-0.55	-0.14	-0.48	-0.54	-0.72	-0.39	-0.46	-0.8	-0.52	-0.23	-0.45	1							
1,4-NQ	0.35	0.01	0.28	-0.26	0.15	0.79**	0.85**	0.85**	0.66*	0.82**	0.49*	0.54*	0.91**	0.44	0.82**	0.56*	0.98**	0.53*	0.66*	0.66*	0.53*	0.58*	0.76**	-0.72	1						
1,2-NQ	0.55*	0.35	-0.2	-0.4	0.98**	0.36	0.11	-0.16	0.79**	-0.09	0.08	-0.45	0.11	0.46	0.11	0.61*	0.15	0.12	0.34	0.57*	0.66*	-0.07	0.57*	-0.32	0.15	1					
1,4-AQ	0.33	-0.16	0.18	-0.39	-0.09	0.59*	0.92**	0.83**	0.45	0.98**	0.12	0.78**	0.85**	0.17	0.85**	0.46	0.82**	0.66*	0.46	0.25	0.25	0.67*	0.61*	-0.56	0.82**	-0.09	1				
O3	0.38	0.21	0.16	-0.05	0.65*	0.8**	0.35	0.19	0.75**	0.06	0.78**	-0.34	0.23	0.56*	0.2	0.17	0.47	0.3	0.8**	0.82**	0.7**	-0.11	0.55*	-0.43	0.47	0.65*	0.06	1			
Temp	0.11	-0.25	0.18	0.03	0.07	0.69*	0.52*	0.23	0.39	0.32	0.73**	0.09	0.12	0	0.3	-0.28	0.41	0.48*	0.65*	0.42	0.15	-0.12	0.25	-0.37	0.41	0.07	0.32	0.65*	1		
RH	-0.06	-0.37	0.08	-0.01	-0.47	0.33	0.46	0.63*	-0.13	0.44	0.44	0.4	0.42	-0.02	0.12	-0.22	0.44	-0.01	0.33	0.14	-0.09	0.03	-0.16	-0.28	0.44	-0.47	0.44	-0.01	0.41	1	

\*At 0.05 level (two-tailed), the correlation is significant

\*\* At 0.01 level (two-tailed), the correlation is significant

Table 6.12 Pearson's correlation (r) between OP induced by water-soluble fraction of PM<sub>10</sub> and chemical compositions

	DTTv	DTTm	AAv	AAm	PM <sub>10</sub>	Mn	Co	Ni	Cd	Zn	Ba	Cr	Cu	Al	As	Pb	Fe	V	Ag	Bi	Ce	Sr	Sb	WSOC	1,4-NQ	1,2-NQ	1,4-AQ	O <sub>3</sub>	Temp	RH		
DTTv	1																															
DTTm	0.75**	1																														
AAv	0.38	0.26	1																													
AAm	0.2	0.76**	0.29	1																												
PM <sub>10</sub>	0.51*	0.01	0.13	-0.46	1																											
Mn	-0.09	0.06	-0.32	0.1	-0.15	1																										
Co	0.32	0.03	0.37	-0.19	0.12	0.48*	1																									
Ni	0	0	-0.15	-0.04	-0.07	0.94**	0.72**	1																								
Cd	0.18	-0.11	0.25	-0.3	0.15	0.47	0.95**	0.74**	1																							
Zn	0.44	0.06	-0.18	0.06	-0.11	0.97**	0.61*	0.94**	0.55*	1																						
Ba	-0.05	0.11	0.01	0.25	-0.01	-0.36	-0.39	-0.47	-0.47	-0.32	1																					
Cr	-0.08	0.09	-0.34	0.14	-0.17	0.99**	0.42	0.92**	0.4	0.96**	-0.35	1																				
Cu	0.62*	0.03	-0.03	-0.05	-0.02	0.89**	0.82**	0.98**	0.82**	0.92**	-0.44	0.85**	1																			
Al	-0.01	-0.14	0.03	-0.16	-0.06	0.78**	0.85**	0.94**	0.9**	0.81**	-0.47	0.73**	0.95**	1																		
As	-0.36	-0.17	-0.02	0.13	-0.59	0.45	0.28	0.37	0.09	0.56*	0.11	0.46	0.38	0.33	1																	
Pb	0.05	-0.06	-0.03	-0.15	0.01	0.84**	0.83**	0.97**	0.87**	0.86**	-0.52	0.79**	0.98**	0.99**	0.28	1																
Fe	0.73*	0.1	-0.13	0.15	-0.18	0.84**	0.46	0.75**	0.3	0.92**	-0.09	0.85**	0.74**	0.58*	0.77**	0.62*	1															
V	-0.16	0.08	-0.11	0.29	-0.26	0.86**	0.37	0.75**	0.26	0.9**	0.03	0.87**	0.72**	0.58*	0.73**	0.61*	0.95**	1														
Ag	-0.18	0.12	-0.42	0.28	-0.36	0.89**	0.17	0.71**	0.08	0.86**	-0.09	0.92**	0.63*	0.47	0.65*	0.53*	0.9**	0.91**	1													
Bi	0.04	-0.07	-0.01	-0.16	-0.01	0.82**	0.85**	0.96**	0.89**	0.84**	-0.5	0.77**	0.98**	0.99**	0.29	0.96**	0.61*	0.6*	0.5*	1												
Ce	0.04	-0.05	0.19	-0.07	-0.21	0.67*	0.89**	0.8**	0.79**	0.79**	-0.36	0.63*	0.87**	0.86**	0.66*	0.83**	0.74**	0.66*	0.51*	0.85**	1											
Sr	-0.44	-0.25	0.09	0.12	-0.63	-0.16	-0.12	-0.24	-0.31	-0.04	0.37	-0.14	-0.21	-0.21	0.8**	-0.3	0.27	0.24	0.18	-0.27	0.21	1										
Sb	0.06	-0.01	0.03	-0.08	-0.08	0.83**	0.87**	0.96**	0.87**	0.88**	-0.43	0.79**	0.99**	0.98**	0.41	0.98**	0.7**	0.68*	0.56*	0.99**	0.91**	-0.15	1									
WSOC	-0.76	-0.43	-0.25	0.13	-0.27	0.26	-0.4	0.09	-0.3	0.17	0.27	0.28	0	0	0.25	-0.02	0.19	0.43	0.39	-0.04	-0.16	0.2	-0.05	1								
1,4-NQ	-0.01	0.1	-0.13	0.15	-0.18	0.84**	0.46	0.75**	0.3	0.92**	-0.09	0.85**	0.74**	0.58*	0.77**	0.62*	0.99**	0.95**	0.9**	0.61*	0.74**	0.27	0.7	0.19	1							
1,2-NQ	0.75*	0.01	0.13	-0.46	0.78**	-0.15	0.12	-0.07	0.15	-0.11	-0.01	-0.17	-0.02	-0.06	-0.59	0.01	-0.18	-0.26	-0.36	-0.01	-0.21	-0.63	-0.08	-0.27	-0.18	1						
1,4-AQ	0.82*	0.06	-0.18	0.06	-0.11	0.97**	0.61*	0.94**	0.55*	0.69*	-0.32	0.96**	0.92**	0.81**	0.56*	0.86**	0.92**	0.9**	0.86**	0.84**	0.79**	-0.04	0.88**	0.17	0.92**	-0.11	1					
O <sub>3</sub>	0.26	-0.04	0.69*	-0.12	0.25	0.16	0.8**	0.44	0.84**	0.27	-0.4	0.1	0.54*	0.66*	-0.09	0.6*	0.05	0.06	-0.22	0.62*	0.55*	-0.31	0.6*	-0.22	0.05	0.25	0.25	1				
Temp	-0.27	-0.55	0.09	-0.49	-0.06	0.26	0.54*	0.48*	0.69*	0.25	-0.73	0.22	0.47	0.67*	0.01	0.61*	0	-0.02	-0.06	0.65*	0.46	-0.19	0.54*	0	0	-0.06	0.25	0.65*	1			
RH	-0.41	-0.65	0.06	-0.51	-0.25	-0.59	-0.13	-0.47	-0.08	-0.55	-0.11	-0.6	-0.45	-0.23	0.07	-0.35	-0.48	-0.56	-0.54	-0.32	-0.12	0.46	-0.34	-0.11	-0.48	-0.25	-0.55	-0.01	0.41	1		

\*At 0.05 level (two-tailed), the correlation is significant

\*\* At 0.01 level (two-tailed), the correlation is significant

Table 6.13 Pearson's correlation (r) between OP induced by methanol-soluble fraction of PM<sub>2.5</sub> and chemical compositions

	DTTv	DTTm	AAv	AAm	PM2.5	Mn	Co	Ni	Cd	Zn	Ba	Cr	Cu	Al	As	Pb	Fe	V	Ag	Bi	Ce	Sr	Sb	WSOC	1,4-NQ	1,2-NQ	1,4-AQ	O <sub>3</sub>	Temp	RH		
DTTv	1																															
DTTm	0.4	1																														
AAv	0.39	0.44	1																													
AAm	-0.41	0.55*	0.3	1																												
PM2.5	0.04	0.15	-0.22	-0.25	1																											
Mn	-0.04	-0.2	-0.57	-0.43	0.36	1																										
Co	0.11	-0.26	-0.15	-0.41	0.11	0.8**	1																									
Ni	-0.07	-0.33	-0.02	-0.27	-0.16	0.68*	0.81**	1																								
Cd	-0.08	-0.09	-0.35	-0.33	0.79**	0.76**	0.65*	0.36	1																							
Zn	0.11	-0.41	0.04	-0.49	-0.09	0.59*	0.92**	0.83**	0.45	1																						
Ba	-0.16	-0.06	-0.71	-0.05	0.08	0.76**	0.39	0.41	0.37	0.12	1																					
Cr	-0.19	-0.53	0.18	-0.1	-0.45	0.14	0.62*	0.62*	0.06	0.78**	-0.1	1																				
Cu	-0.05	-0.23	0.11	-0.23	0.11	0.66*	0.86**	0.91**	0.6*	0.85**	0.27	0.63*	1																			
Al	-0.29	0.26	-0.15	0.21	0.46	0.64*	0.39	0.5*	0.61*	0.17	0.5*	-0.14	0.55*	1																		
As	-0.22	-0.58	-0.13	-0.41	0.11	0.52*	0.77**	0.63*	0.6*	0.85**	0.1	0.77**	0.76**	0.12	1																	
Pb	0.06	-0.01	0.34	-0.22	0.61*	0.26	0.42	0.33	0.69*	0.46	-0.23	0.23	0.65*	0.38	0.59*	1																
Fe	-0.03	-0.35	-0.18	-0.4	0.15	0.79**	0.85**	0.85**	0.66*	0.82**	0.49*	0.54*	0.91**	0.44	0.82**	0.56*	1															
V	-0.03	0.01	-0.21	-0.09	0.12	0.6*	0.78**	0.4	0.59*	0.66*	0.28	0.47	0.51*	0.28	0.64*	0.25	0.53*	1														
Ag	-0.03	-0.1	-0.58	-0.36	0.34	0.97**	0.7**	0.64*	0.67*	0.46	0.79**	-0.01	0.56*	0.71**	0.33	0.13	0.66*	0.51*	1													
Bi	0.22	0.14	-0.33	-0.35	0.57*	0.75**	0.43	0.37	0.7**	0.25	0.65*	-0.26	0.45	0.55*	0.26	0.43	0.66*	0.26	0.72**	1												
Ce	0.05	0.37	-0.15	-0.06	0.66*	0.73**	0.49*	0.41	0.78**	0.25	0.48*	-0.25	0.54*	0.88**	0.2	0.54*	0.53*	0.42	0.76**	0.8**	1											
Sr	-0.21	0.07	0.32	0.27	-0.07	0.3	0.66*	0.59*	0.39	0.67*	-0.01	0.7**	0.75**	0.4	0.66*	0.52*	0.58*	0.71**	0.19	0.06	0.34	1										
Sb	-0.34	-0.31	-0.27	-0.25	0.57	0.67*	0.69*	0.5*	0.9**	0.61*	0.25	0.38	0.73**	0.54*	0.83**	0.74**	0.76**	0.64*	0.54*	0.51*	0.61*	0.61*	1									
WSOC	-0.56	-0.05	-0.01	0.56*	-0.32	-0.57	-0.59	-0.42	-0.55	-0.56	-0.29	-0.11	-0.55	-0.14	-0.48	-0.54	-0.72	-0.39	-0.46	-0.8	-0.52	-0.23	-0.45	1								
1,4-NQ	-0.03	-0.35	-0.18	-0.4	0.15	0.79**	0.85**	0.85**	0.66*	0.82**	0.49*	0.54*	0.91**	0.44	0.82**	0.56*	0.89**	0.53*	0.66*	0.66*	0.53*	0.58*	0.76*	-0.72	1							
1,2-NQ	0.04	0.15	-0.22	-0.25	0.56*	0.36	0.11	-0.16	0.79**	-0.09	0.08	-0.45	0.11	0.46	0.11	0.61*	0.15	0.12	0.34	0.57*	0.66*	-0.07	0.57*	-0.32	0.15	1						
1,4-AQ	0.11	-0.41	0.04	-0.49	-0.09	0.59*	0.92**	0.83**	0.45	0.89**	0.12	0.78**	0.85**	0.17	0.85**	0.46	0.82**	0.66*	0.46	0.25	0.25	0.67*	0.61*	-0.56	0.82**	-0.09	1					
O <sub>3</sub>	-0.13	-0.07	-0.76	-0.31	0.65*	0.8**	0.35	0.19	0.75**	0.06	0.78**	-0.34	0.23	0.56*	0.2	0.17	0.47	0.3	0.8**	0.82**	0.7*	-0.11	0.55*	-0.43	0.47	0.65*	0.06	1				
Temp	0.08	-0.35	-0.8	-0.5	0.07	0.69*	0.52*	0.23	0.39	0.32	0.73**	0.09	0.12	0	0.3	-0.28	0.41	0.48*	0.65*	0.42	0.15	-0.12	0.25	-0.37	0.41	0.07	0.32	0.65*	1			
RH	0.32	-0.25	-0.03	-0.27	-0.47	0.33	0.46	0.63*	-0.13	0.44	0.44	0.4	0.42	-0.02	0.12	-0.22	0.44	-0.01	0.33	0.14	-0.09	0.03	-0.16	-0.28	0.44	-0.47	0.44	-0.01	0.41	1		

\*At 0.05 level (two-tailed), the correlation is significant

\*\* At 0.01 level (two-tailed), the correlation is significant

Table 6.14 Pearson's correlation (r) between OP induced by methanol-soluble fraction of PM<sub>10</sub> and chemical compositions

	DTTv	DTTm	AAv	AAm	PM <sub>10</sub>	Mn	Co	Ni	Cd	Zn	Ba	Cr	Cu	Al	As	Pb	Fe	V	Ag	Bi	Ce	Sr	Sb	WSOC	1,4-NQ	1,2-NQ	1,4-AQ	O <sub>3</sub>	Temp	RH	
DTTv	1																														
DTTm	0.66	1																													
AAv	-0.31	-0.35	1																												
AAm	-0.42	-0.06	0.85**	1																											
PM <sub>10</sub>	0.65	0.17	-0.25	-0.5	1																										
Mn	0.33	0.74**	-0.43	-0.19	-0.15	1																									
Co	0.04	0.16	-0.59	-0.48	0.12	0.48*	1																								
Ni	0.28	0.62*	-0.52	-0.32	-0.07	0.94**	0.72**	1																							
Cd	0.1	0.16	-0.54	-0.48	0.15	0.47	0.95**	0.74**	1																						
Zn	0.3	0.67*	-0.48	-0.27	-0.11	0.97**	0.61*	0.94**	0.55*	1																					
Ba	0.23	0.02	0.53*	0.45	-0.01	-0.36	-0.39	-0.47	-0.47	-0.32	1																				
Cr	0.33	0.75**	-0.39	-0.15	-0.17	0.78**	0.42	0.92**	0.4	0.96**	-0.35	1																			
Cu	0.25	0.57*	-0.56	-0.36	-0.02	0.89**	0.82**	0.98**	0.82**	0.92**	-0.44	0.85**	1																		
Al	0.16	0.38	-0.46	-0.34	-0.06	0.78**	0.85**	0.94**	0.9**	0.81**	-0.47	0.73**	0.95**	1																	
As	-0.23	0	-0.06	0.03	-0.59	0.45	0.28	0.37	0.09	0.56*	0.11	0.46	0.38	0.33	1																
Pb	0.24	0.49*	-0.55	-0.39	0.01	0.84**	0.83**	0.97**	0.87**	0.86**	-0.52	0.79**	0.98**	0.99**	0.28	1															
Fe	0.23	0.55*	-0.37	-0.18	-0.18	0.89**	0.46	0.77**	0.3	0.92**	-0.09	0.85**	0.74**	0.58*	0.77	0.62*	1														
V	0.22	0.61*	-0.13	0.06	-0.26	0.86**	0.37	0.75**	0.26	0.9**	0.03	0.87**	0.72**	0.58*	0.73	0.61*	0.95**	1													
Ag	0.25	0.68*	-0.23	0.02	-0.36	0.89**	0.17	0.71**	0.08	0.86**	-0.09	0.92**	0.63*	0.47	0.65	0.53*	0.9**	0.91**	1												
Bi	0.22	0.46	-0.55	-0.39	-0.01	0.82**	0.85**	0.96**	0.89**	0.84**	-0.5	0.77**	0.98**	0.99**	0.29	0.87**	0.61*	0.6*	0.5*	1											
Ce	-0.06	0.2	-0.53	-0.38	-0.21	0.67*	0.89**	0.8**	0.79**	0.79**	-0.36	0.63*	0.87**	0.86**	0.66	0.83**	0.74**	0.66*	0.51*	0.85**	1										
Sr	-0.49	-0.47	0.28	0.23	-0.63	-0.16	-0.12	-0.24	-0.31	-0.04	0.37	-0.14	-0.21	-0.21	0.8	-0.3	0.27	0.24	0.18	-0.27	0.21	1									
Sb	0.17	0.46	-0.54	-0.36	-0.08	0.83**	0.87**	0.96**	0.87**	0.88**	-0.43	0.79**	0.99**	0.98**	0.41	0.98**	0.7**	0.68*	0.56*	0.99**	0.91**	-0.15	1								
WSOC	0.79**	0.13	0.66*	0.52*	-0.27	0.26	-0.4	0.09	-0.3	0.17	0.27	0.28	-0.23	0	0.25	-0.02	0.19	0.43	0.39	-0.04	-0.16	0.2	-0.05	1							
1,4-NQ	0.23	0.55*	-0.37	-0.18	-0.18	0.84**	0.46	0.75**	0.3	0.92**	-0.09	0.85**	0.74**	0.58*	0.77	0.62*	0.89**	0.95**	0.9**	0.61**	0.74**	0.27	0.7	0.19	1						
1,2-NQ	0.65*	0.17	-0.25	-0.5	0.55*	-0.15	0.12	-0.07	0.15	-0.11	-0.01	-0.17	-0.02	-0.06	-0.59	0.01	-0.18	-0.26	-0.36	-0.01	-0.21	-0.63	-0.08	-0.27	-0.18	1					
1,4-AQ	0.3	0.67*	-0.48	-0.27	-0.11	0.97**	0.61*	0.94**	0.55*	0.77**	-0.32	0.96**	0.92**	0.81**	0.56	0.86**	0.92**	0.9**	0.86**	0.84**	0.79**	-0.04	0.88**	0.17	0.92**	-0.11	1				
O <sub>3</sub>	-0.15	-0.11	-0.15	-0.17	0.25	0.16	0.8**	0.44	0.84**	0.25	-0.4	0.1	0.54*	0.66*	-0.09	0.6*	0.05	0.06	-0.22	0.62*	0.55*	-0.31	0.6*	-0.22	0.05	0.25	0.25	1			
Temp	-0.22	-0.27	-0.21	-0.33	-0.06	0.26	0.54*	0.48*	0.69*	0.25	-0.73	0.22	0.47	0.67*	0.01	0.61*	0	-0.02	-0.06	0.58*	0.46	-0.19	0.54*	0	0	-0.06	0.25	0.65*	1		
RH	-0.51	-0.92	0.18	-0.13	-0.25	-0.59	-0.13	-0.47	-0.08	-0.55	-0.11	-0.6	-0.45	-0.23	0.07	-0.35	-0.48	-0.56	-0.54	-0.32	-0.12	0.46	-0.34	-0.11	-0.48	-0.25	-0.55	-0.01	0.41	1	

\*At 0.05 level (two-tailed), the correlation is significant

\*\* At 0.01 level (two-tailed), the correlation is significant

#### 6.2.4.9 Graphical analysis of source dispersion of water-soluble OP: PM<sub>2.5</sub> versus PM<sub>10</sub>

Figure 6-16 illustrates the source dispersion characteristics of OP induced by water-soluble fractions of PM<sub>2.5</sub> and PM<sub>10</sub>. The DTTv induced by water-soluble PM<sub>2.5</sub> dominates in the west, southwest, northeast, east, and southeast (Figure 6-16 a), while PM<sub>10</sub>-induced DTTv is primarily dominant in the southwest (Figure 6-16 e). These findings suggest that multiple sources contribute to PM<sub>2.5</sub>-induced DTTv, including industrial emissions from Beilun and Zhenhai industrial parks, road traffic from freeways in the southwest and southeast, as well as marine and sea salt contributions from Ningbo-Zhoushan port and East China Sea. In contrast, road dust suspension from freeways in the southwest, during high wind speeds, is the main contributor to PM<sub>10</sub>-induced DTTv. The DTTv and DTTm induced by water-soluble PM<sub>2.5</sub> exhibit similar source dispersion patterns (Figure 6-16 a and b, respectively). Similarly, DTTv and DTTm induced by PM<sub>10</sub> showed similar patterns (Figure 6-16 e and f, respectively). These findings suggest that similar sources contribute to both DTTv and DTTm in these ambient particles.

The AAv induced by water-soluble fractions of PM<sub>2.5</sub> and PM<sub>10</sub> shows diverse source dispersion patterns (Figure 6-16 c and g, respectively), consistent with AAm induced by water-soluble PM<sub>2.5</sub> and PM<sub>10</sub> (Figure 6-16 d and h, respectively). AAv and AAm induced by PM<sub>2.5</sub> are dominant in all directions during low wind speeds, indicating the contribution nearby source, especially vehicular traffic emissions from surrounding freeways. Marine and sea salt aerosols from Ningbo-Zhoushan port and the East China Sea also contribute to AAm of PM<sub>2.5</sub>. In contrast, road dust and vehicular traffic emissions from nearby freeways in the southwest consistently contribute to OP induced by PM<sub>10</sub> (Figure 6-16 e-h).

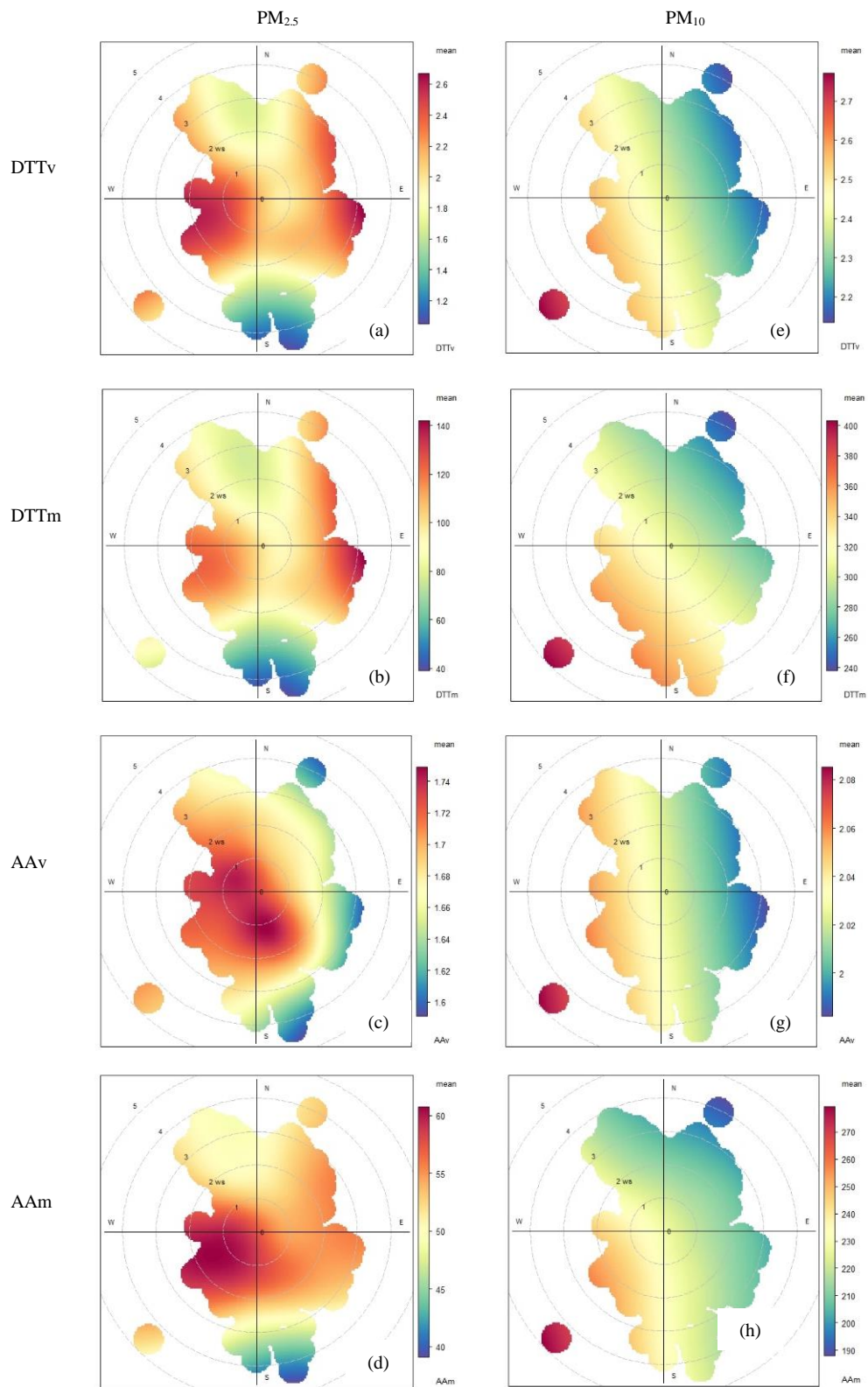


Figure 6-16 Bivariate polar plots of extrinsic and intrinsic OP induced by water-soluble fractions of  $PM_{2.5}$  (a-d) and  $PM_{10}$  (e-h)



#### 6.2.4.10 Graphical analysis of source dispersion of methanol-soluble OP: PM<sub>2.5</sub> versus PM<sub>10</sub>

Figure 6-17 displays the source dispersion induced by methanol-soluble fractions of PM<sub>2.5</sub> and PM<sub>10</sub>. The DTTv induced by methanol-soluble fractions of PM<sub>2.5</sub> and PM<sub>10</sub> exhibited similar source dispersion patterns with high concentrations in southwest, suggesting contribution of vehicular traffic and road dust from nearby freeways close to the study domain (Figure 6-17 c and e, respectively). The DTTv of methanol-soluble fractions of PM<sub>2.5</sub> is in contrast to that induced by water-soluble fractions. However, the DTTv induced by both water-and methanol-soluble fractions of PM<sub>10</sub> exhibited similar source dispersion patterns, suggesting similar source contribution, including vehicular traffic and road dust. The DTTm induced by methanol-soluble fractions of PM<sub>2.5</sub> and PM<sub>10</sub> exhibited similar patterns (Figure 6-17 b and f, respectively). This patterns varies considerably with corresponding water-soluble fractions. Specifically, DTTm of the methanol-soluble fraction is concentrated in west and southwest, which occurs at low wind speed. This suggest dominant contribution of road traffic in nearby freeway. The high DTTm in the southwest occurs at high wind speed and can be attributed to road dust transport, which is more concentrated in the case of PM<sub>10</sub> (Figure 6-17 f).

The AAv induced by methanol-soluble fractions of PM<sub>2.5</sub> and PM<sub>10</sub> (Figure 6-17 c and g, respectively) exhibited source dispersion patterns which is highly concentrated in the southwest, attributed to to vehicular traffic and road dust in nearby freeway. This trend is different for water-and methanol-soluble fractions of PM<sub>2.5</sub>, but similar in the case of PM<sub>10</sub>. The AAv and AAm exhibited different patterns of methanol-soluble of PM<sub>2.5</sub>, but the pattern is similar for PM<sub>10</sub>. The AAv and AA induced by methanol-soluble fractions of PM<sub>2.5</sub> and

PM<sub>10</sub> can be attributed to road traffic and road dust in nearby freeways. The AAv induced by the methanol-soluble fractions of both PM<sub>2.5</sub> and PM<sub>10</sub> (Figure 6-17 c and g, respectively) displays consistent patterns of source dispersion, primarily concentrated in the southwest. This phenomenon can be attributed to the combined influence of road traffic emission and road dust transported from nearby freeways. In contrast, AAm induced by the methanol-soluble fractions of PM<sub>2.5</sub> and PM<sub>10</sub> exhibits more diverse dispersion patterns. Specifically, AAm induced by PM<sub>2.5</sub> is primarily influenced by road traffic emissions and road dust, with additional minor contributions from industrial sources, as well as marine and sea spray aerosols. However, AAm induced by PM<sub>10</sub> is mainly dominated by emissions from road traffic and road dust sources.

Table 6.15 Summary of potential sources associated with OP induced by water-and methanol-soluble fractions of PM<sub>2.5</sub> during the day and at night

Water-soluble fractions	PM <sub>2.5</sub>	PM <sub>10</sub>
DTTv	vehicular traffic, industrial, marine, sea salt	vehicular traffic, road dust
AAv	vehicular traffic	vehicular traffic, road dust
Methanol-soluble fractions		
DTTv	vehicular, road dust	vehicular, road dust
AAv	vehicular, road dust	vehicular, road dust

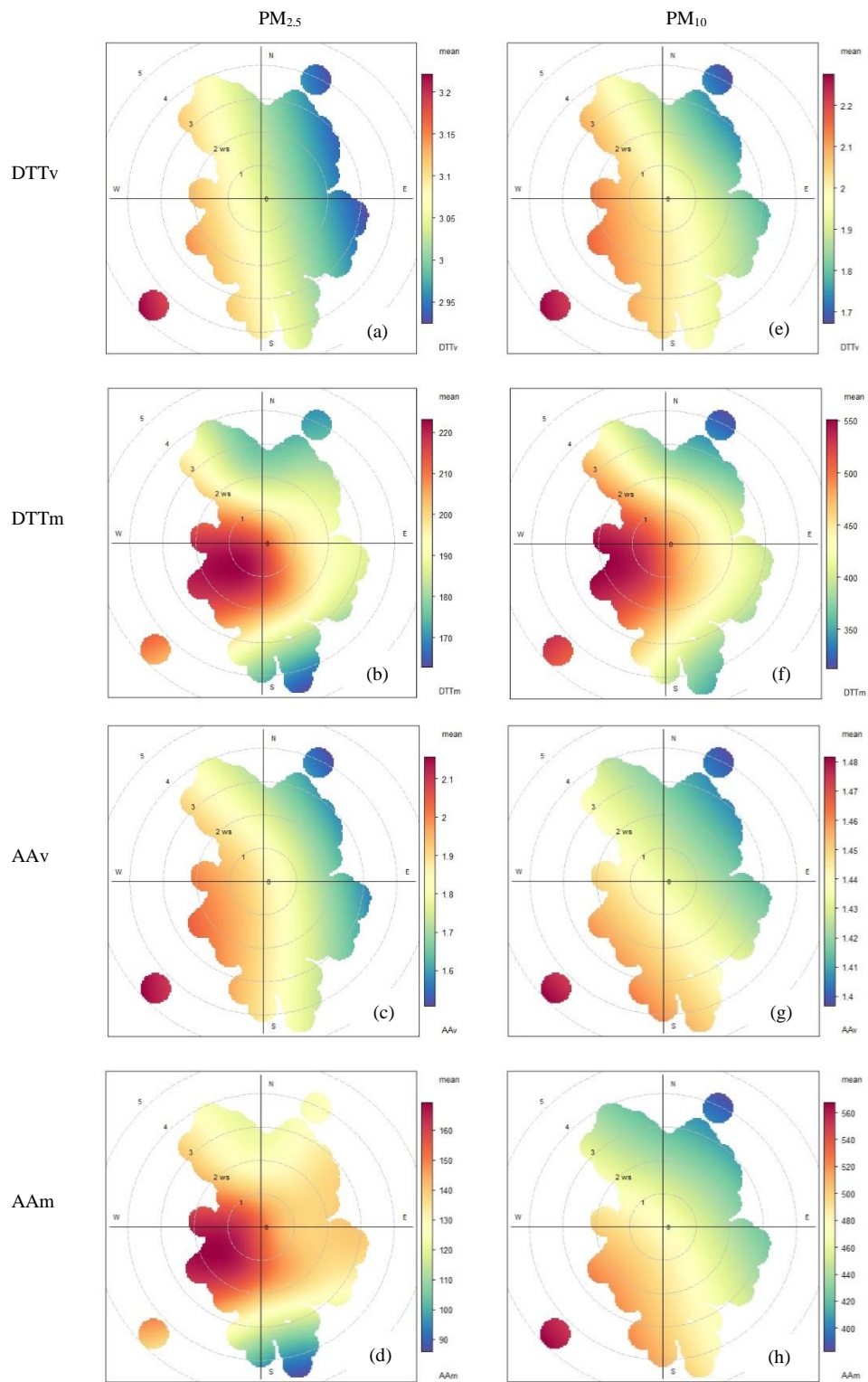


Figure 6-17 Bivariate polar plots of extrinsic and intrinsic OP induced by methanol-soluble fractions of  $PM_{2.5}$  (a-d) and  $PM_{10}$  (e-h)

### 6.2.5 OP deposition in human respiratory tract

It is established in this study that the chemical composition of PM varies among particles of different sizes (Famiyeh, Jia, et al., 2023). This variation in chemical composition has a significant impact on the ability of these particles to cause OP in the various regions of the human respiratory tract (Fang et al., 2017; Guo et al., 2019). As a result, the OP deposition of ambient particles can vary across different regions of the respiratory tract. Figure 6-18 depicts the comparison of OP deposition of PM<sub>2.5</sub> and PM<sub>10</sub> particles in the ET, TB, PL, and TL regions of the human respiratory tract. The patterns of OP deposition of ultrafine, accumulation, and coarse particles measured in both DTT and AA assays are shown in Figure 6-19 and Figure 6-20, respectively.

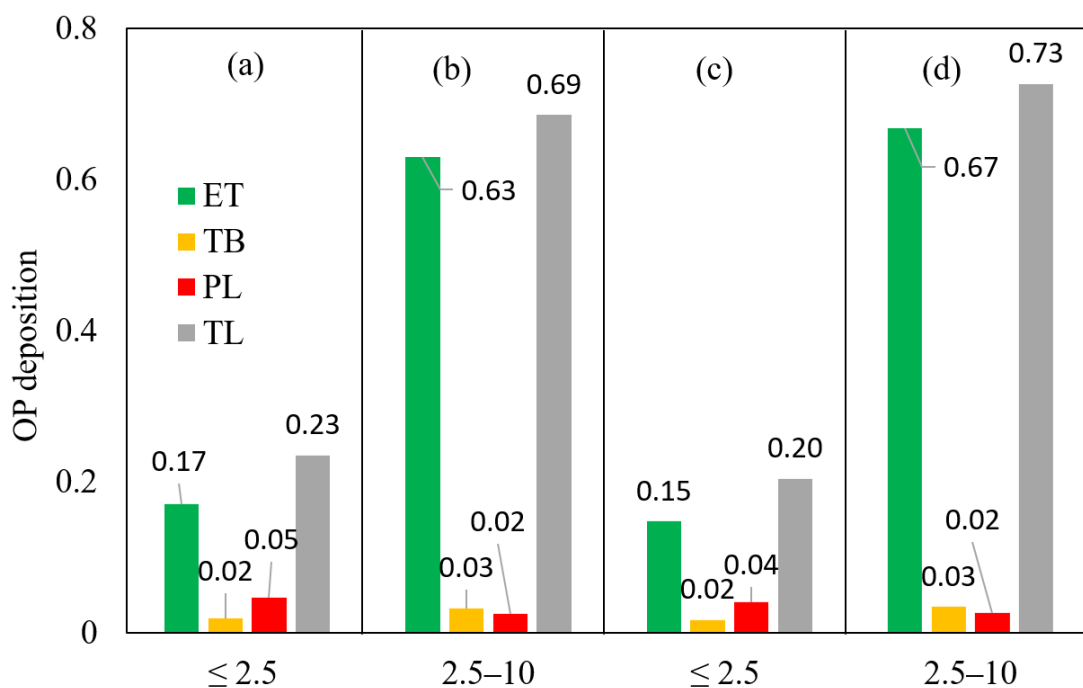


Figure 6-18 OP deposition of fine ( $\leq 2.5 \mu\text{m}$ ) and coarse ( $2.5\text{--}10 \mu\text{m}$ ) particles in ET, TB, PL, and TL measured in DTT (a, b) and AA (c, d) assays

Coarse particles had a higher deposition fraction in the ET region, resulting in their dominance in OP deposition. The results of previous studies are consistent with our findings, which suggest that coarse particles due to their high deposition fraction have a higher OP deposition in the ET region and TL regions than ultrafine and accumulation particles (Fang et al., 2017; Lyu et al., 2018). In accordance with the findings in Figure 6-18, the OP deposition of PM<sub>10</sub> in ET and TL was found to be lower in the DTT assay compared to the AA assay. In contrast, the OP deposition of PM<sub>2.5</sub> in ET and TL regions are slightly higher in DTT assay than in AA assay. This is consistent with our findings shown in Figure 6-19 and Figure 6-20.

The OP deposition of accumulation particles (1.5–3 μm) were found to be higher in the PL region when measured using the DTT assay compared to the AA assay. As revealed by the AA assay, coarse particles with a size range of 3 to 7.2 μm tend to exhibit elevated levels of OP deposition in the PL region (as shown in Figure 6-20 c) in comparison to those estimated by DTT assay (as shown in Figure 6-19 c). The trend of OP deposition induced by ultrafine, accumulation, and coarse particles particles in both the PL region and TL reported in this study is contrary to the results of Fang et al. (2017). According to Fang et al. (2017), ultrafine particles have lower OP deposition in the PL region compared to accumulation particles, while accumulation particles exhibit higher OP deposition than coarse particles in the TL region.

The health impacts resulting from the same mix of PM can vary across different regions of the respiratory tract. The complexity of the health risk can be exacerbated by the chemical compositions in the PM under varying exposure scenarios (Famiyeh, Jia, et al., 2023). Due to the low concentrations of trace metals in coarse particles and their weak association with

the extrinsic OP, the high OP deposition of coarse particles in the ET and TL might not be linked to water-soluble metals. Thus, quinones such as 1, 2-NQ and 1, 4-AQ, which concentrations peak in coarse particles and exhibit strong correlation with OP might contribute to the high OP deposition and health risk of these particles.

Our findings indicate that ultrafine ( $\leq 0.49 \mu\text{m}$ ) and accumulation ( $0.95\text{--}1.5 \mu\text{m}$ ) particles could pose health risks in the TB and PL regions (Famiyeh et al., 2023; Fang et al., 2017). This is because of the high concentration of trace metals, PAHs, and quinones in these particles, as well as their high OP deposition. The results presented above have convincingly demonstrated that establishing a connection between OP depositions particles and composition of toxic chemicals can yield significant insights into associated health risks. In particular, when ultrafine particles and accumulation particles with toxic chemical compositions such as trace metals, PAHs, and quinones are inhaled into the human respiratory system, they have the potential to cause a range of health issues, including respiratory irritation, anemia, kidney failure, brain damage, and lung cancer. These detrimental effects can be attributed to the oxidative stress induced by these particles or potentially by other biochemical mechanisms.

Coarse particles, on the other hand, could pose severe health risks in the ET region due to their high OP deposition. The high deposition fraction and doses of coarse particles, along with their OP deposition in the ET region, can cause elevated AA depletion in the upper airways of asthmatic patients (Liu et al., 2022). The low level of AA in asthmatic patients aligns with our observation that coarse particles exhibit higher OP deposition when measured using the AA assay compared to the DTT assay (Famiyeh, Jia, et al., 2023). Therefore, exposure to coarse particles is more likely to result in severe respiratory

conditions such as asthma, chronic obstructive pulmonary disease, and other respiratory diseases than exposure to ultrafine and accumulation particles (Brunekreef and Forsberg, 2005). This has been supported by research, such as a study in the United States which found a significant association between exposure to coarse particles and emergency room visits by asthmatic patients (Malig et al., 2013).

Figure 6-21 presents a comparison of the OP deposition measured by the DTT and AA. This provides valuable insights into the OP deposition of different particle sizes. It indicates that ultrafine particles have a similar predicted OP deposition when measured by both assays. This suggests that the health risks associated with ultrafine particles may be consistent regardless of the assay used to measure OP deposition. The differences in OP deposition predictions between the DTT and AA assays for accumulation and coarse particles are significant. The DTT assay predicts a higher OP deposition for accumulation particles, while the AA assay predicts a higher OP deposition for coarse particles. Therefore, when assessing health risks associated with accumulation and coarse particles, it is essential to consider the type of assay used to measure OP deposition in order to obtain a comprehensive understanding of their potential effects on human health.

By considering the differences in OP deposition predictions for different particle sizes, different assays, health risk assessments can be more accurately informed. This can lead to better targeted mitigation strategies and interventions to reduce the potential health impacts of PM. Additionally, it highlights the importance of employing multiple assays and considering particle size when assessing the health risks associated with human exposure to ambient particles.

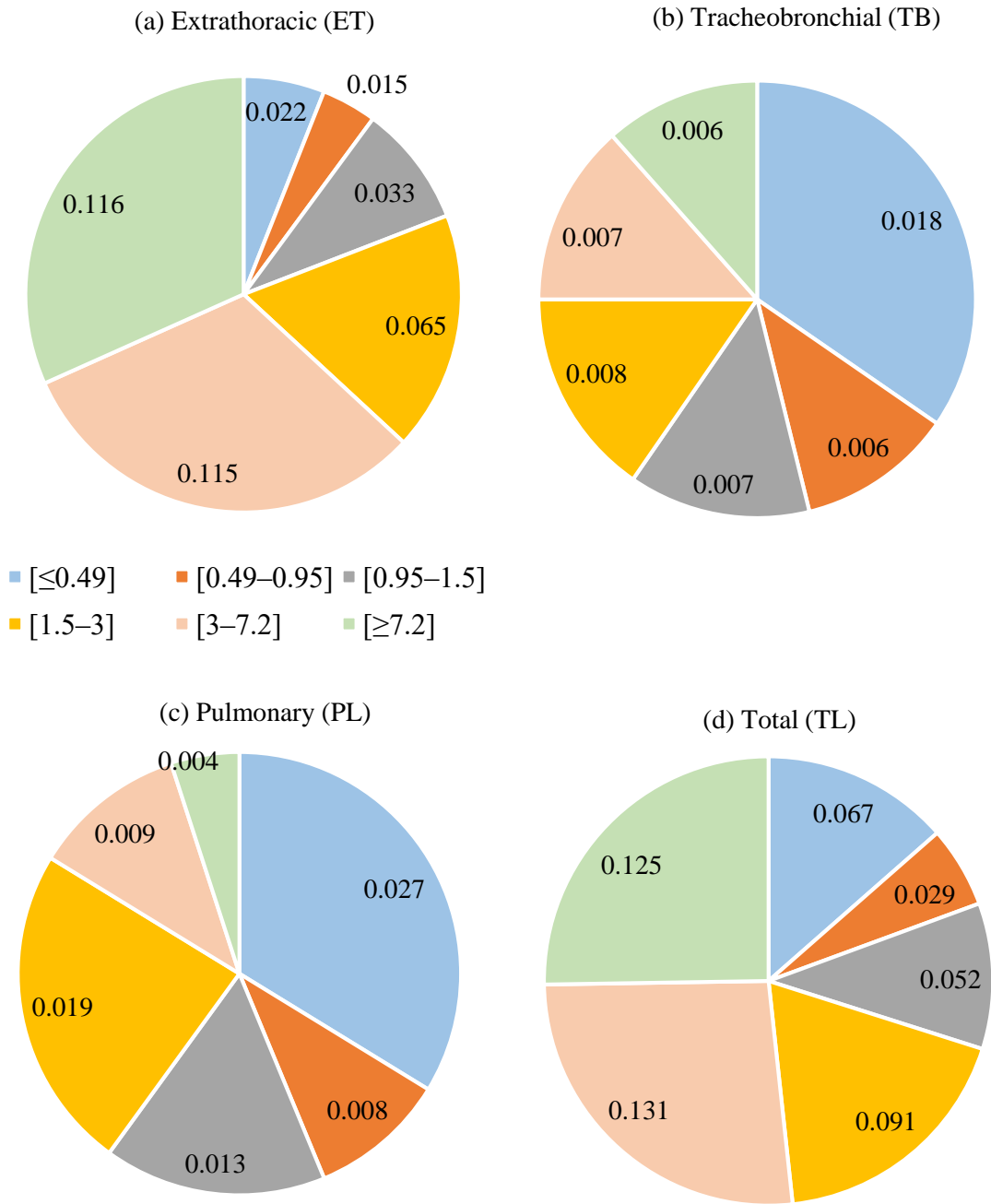


Figure 6-19 OP deposition of PM size fraction in DTT assay: (a) ET, (b) TB, (c) PL, (d) TL



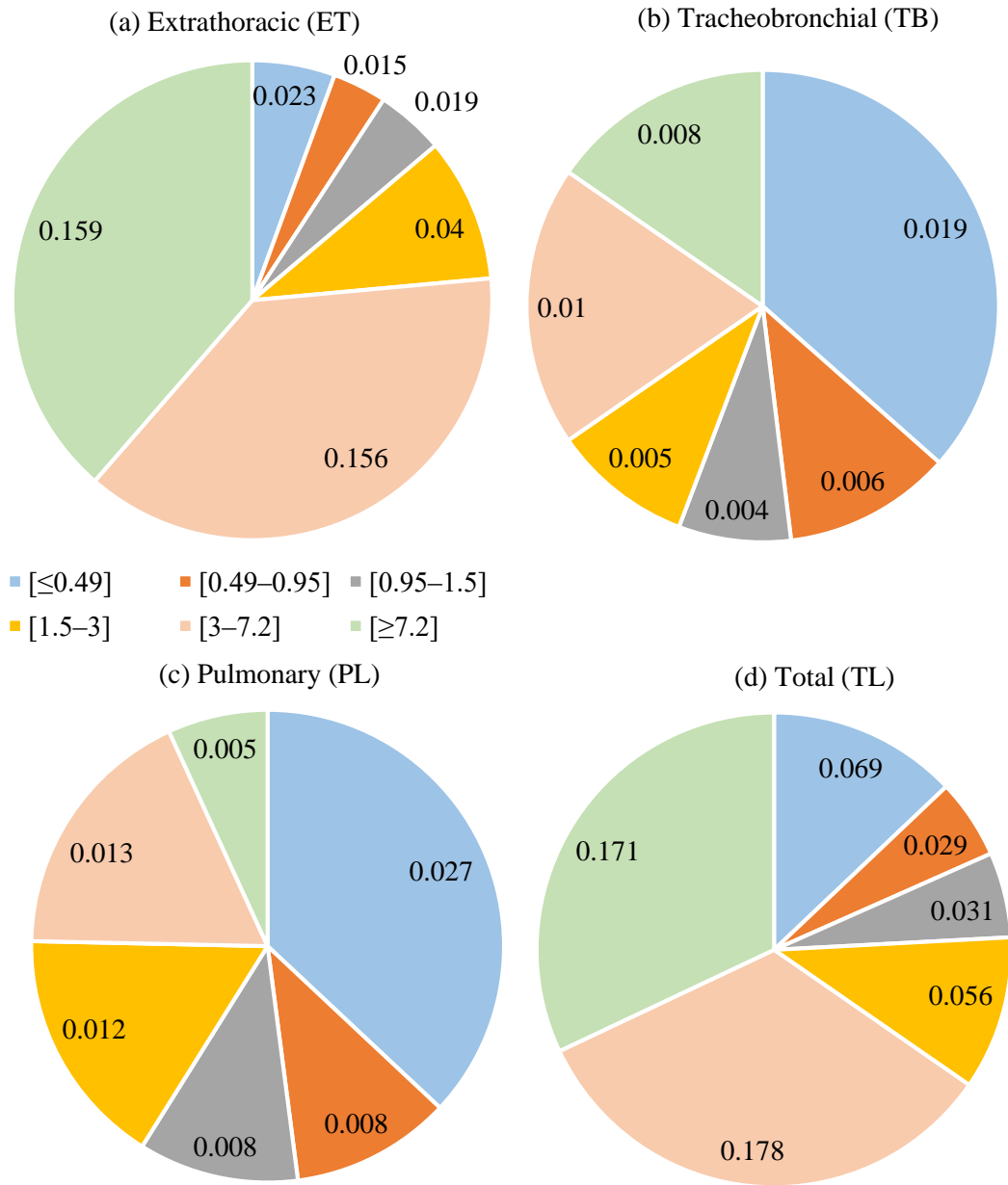


Figure 6-20 OP deposition of PM size fraction in AA assay: (a) ET, (b) TB, (c) PL, (d) TL

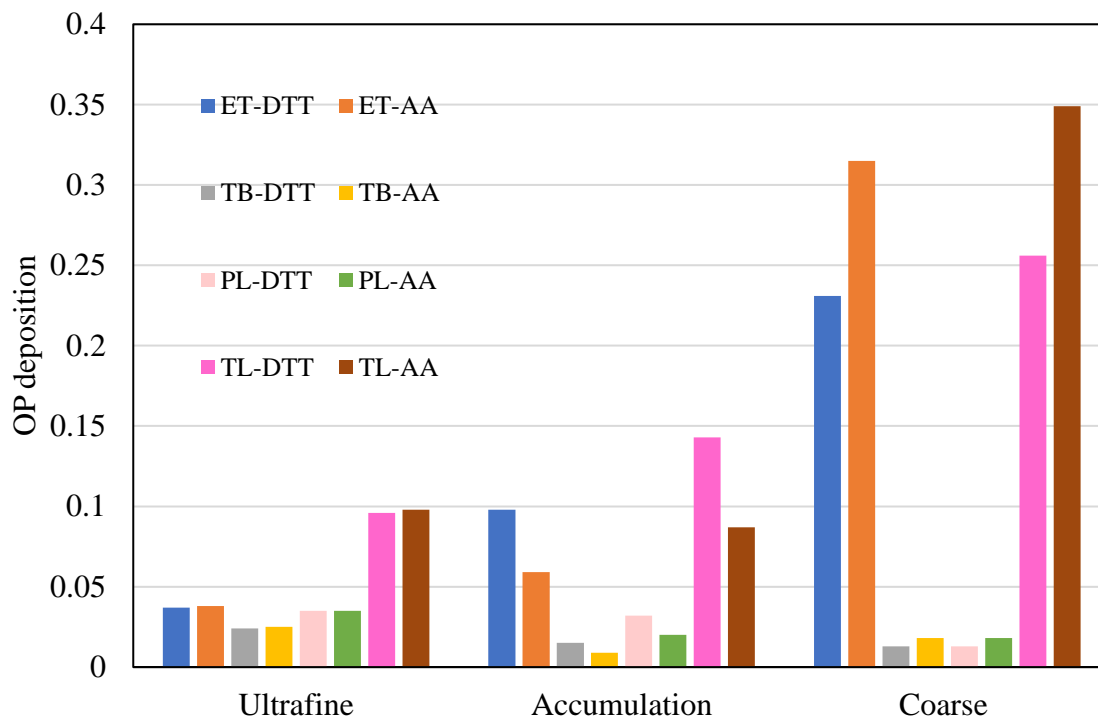


Figure 6-21 Comparison of DTT and AA measured OP deposition of ultrafine, accumulation, and coarse particles in the ET, TB, PL, and TL regions of human respiratory tract

#### 6.2.6 Relationship between particle deposition dose and OP

In this study, we examined for the first time the association between the particle deposition doses and the extrinsic OP of PM size fractions, as measured in DTT and AA assays. Figure 6-22 and Figure 6-23 (as shown in our recent publication Famiyeh et al. (2023)) illustrate the relationship between the deposition dose and OP measured in DTT and AA, respectively. Our findings suggest a weak relationship between DTTv and deposition doses, as evidenced by  $r^2$  values ranging from 0.08 to 0.23. In contrast, we found no association between deposition doses and AA<sub>v</sub>. Our results support the argument that the deposition dose, which is estimated based on particle concentration in the ambient air, cannot be solely used as a measure to determine the ability of the particle to induce oxidative stress.

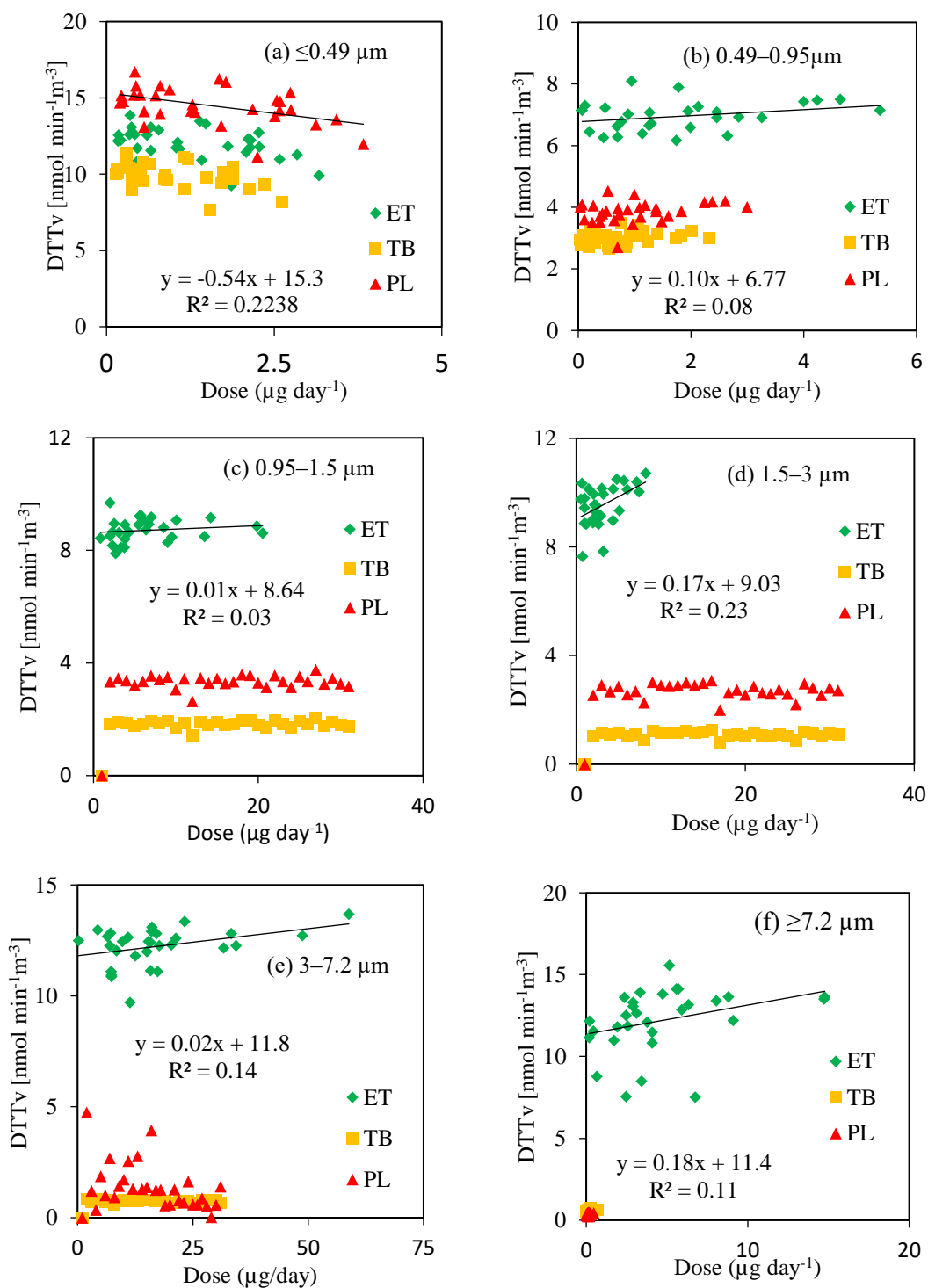


Figure 6-22 Association of lung-deposited dose and extrinsic OP of PM size fractions in DTT assay: (a)  $\leq 0.49 \mu\text{m}$ , (b)  $0.49-0.95 \mu\text{m}$ , (c)  $0.95-1.5 \mu\text{m}$ , (d)  $1.5-3 \mu\text{m}$ , (e)  $3-7.2 \mu\text{m}$ , and (f)  $\geq 7.2 \mu\text{m}$

Although the DTT measured extrinsic OP of accumulation and coarse particle typically increases at higher deposition doses in the ET region, it was observed that the OP of ultrafine particles ( $\leq 0.49 \mu\text{m}$ ) decreases with higher deposition doses. However, the DTTv of ultrafine particles ( $0.49\text{--}0.95 \mu\text{m}$ ) and accumulation particles in the TB and P regions remained relatively constant as the deposition doses increased. As shown Table 6.4, DTTv induced by  $\leq 0.49 \mu\text{m}$  particles correlate negatively with quinones (1, 4-NQ, and 1, 2-NQ) and trace metals (e.g., Cu, Fe, Mn). This suggests that the antagonistic interactions between these chemical species contribute to the decrease in DTTv as their dose in the respiratory tract increases (Pietrogrande, et al., 2022; Yan et al., 2022). The antagonistic and synergistic interactions among these chemical compositions and their effects on OP could be further investigated.

Our finding of no correlation between AAv and deposition doses suggests that the substances causing OP detected by AA may not be significant contributors to the dose of each PM size fraction collected at our study domain. Previous research has revealed that AA measurements can detect OP that arises from transitional metal ions like  $\text{Fe}^{2+}$  and  $\text{Cu}^{2+}$ , as well as specific quinones with double aromatic rings (Fang et al., 2016; Pietrogrande et al., 2019). In contrast, DTT assays are capable of measuring OP from a wider range of organic compounds and certain metals (Fang et al., 2016). Based on the chemical species detectable by both AA and DTT assays and the absence of a correlation between AAv and deposition doses, it is reasonable to infer that the relationship between DTTv of the water-soluble fraction and doses is influenced more by transitional metals and other water-soluble organic components than by small-sized quinones (Famiyeh, Jia, et al., 2023). Further evidence supporting this inference can be observed in the OP levels detected in each water-soluble

fraction through AA measurements, which were significantly lower compared to those detected by DTT assays. This suggests that DTT assay is more sensitive in detecting the OP of similar chemical species compared to the AA assay of PM water-soluble fractions.

To investigate the relationship between deposition dose and intrinsic OP, a power function was used to fit the data. The results of the relationship between deposition doses and intrinsic OP, as measured in DTT and AA assays, are presented in the Appendix (Figure 8-13 and Figure 8-14, respectively). The study has shown that there was a stronger correlation between deposition doses and DTT<sub>m</sub> compared to AA<sub>m</sub> of the same PM size fraction. In addition, an increase in deposition dose led to a decrease in both DTT<sub>m</sub> and AA<sub>m</sub> across all particle sizes. By considering the decline of intrinsic OP, it can be suggested that particle deposition dose does not significantly contribute to intrinsic OP or has only a minor influence (Wang et al., 2020). However, there is a strong correlation between particle deposition dose and intrinsic OP, rather than extrinsic OP, indicating the inherent ability of PM to consistently induce oxidative stress. More importantly, analyzing the relationship between OP and the dose of particles deposited can help identify specific respiratory airway regions with a high potential for health risks. As expected, in the alveoli, high doses of ultrafine particles ( $\leq 0.49 \mu\text{m}$ ) exhibit slightly higher OP, whereas accumulation and coarse particles are more concentrated in the ET region.

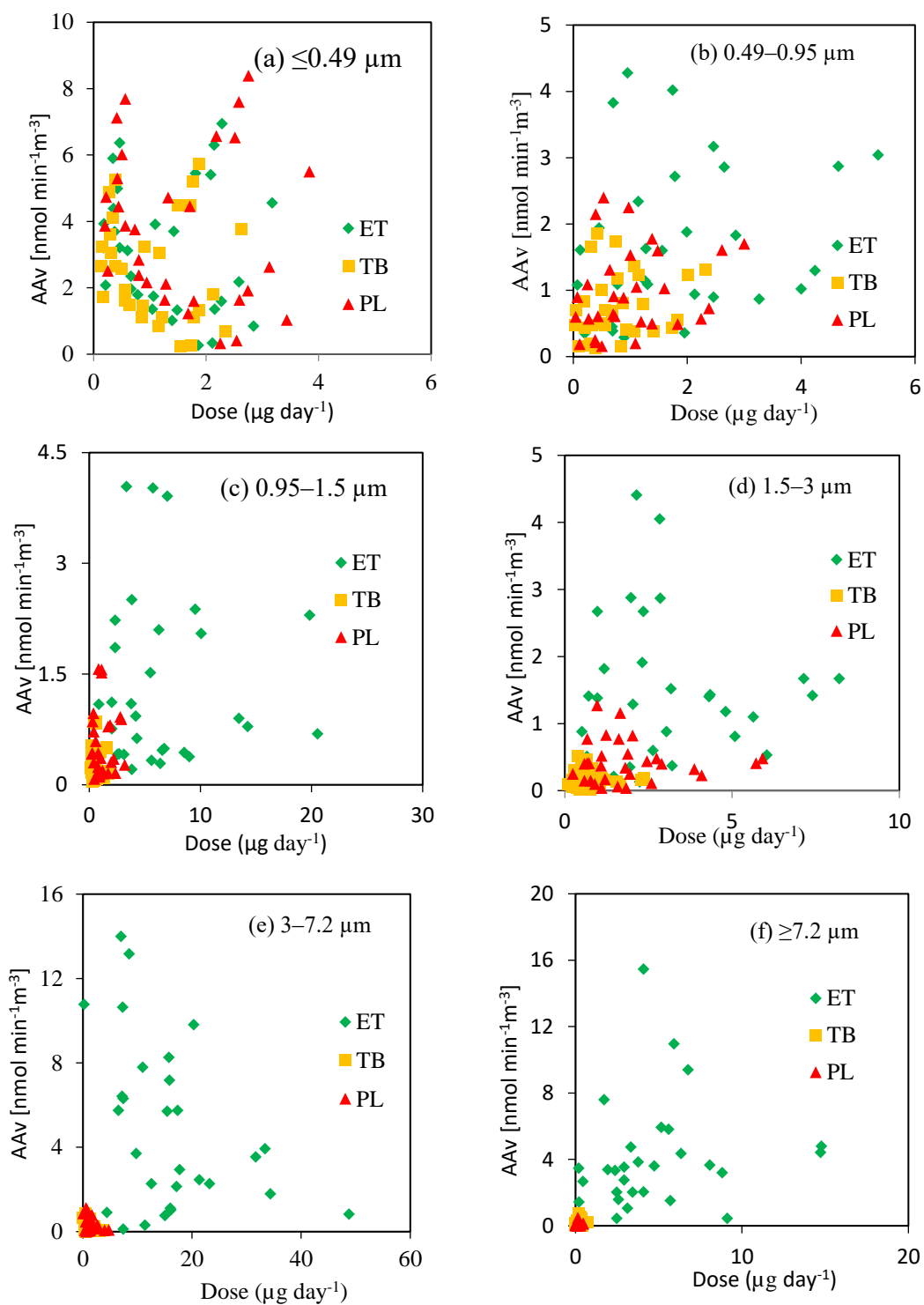


Figure 6-23 Association of lung-deposited dose and extrinsic OP of PM size fractions in AA assay: (a)  $\leq 0.49 \mu\text{m}$ , (b)  $0.49-0.95 \mu\text{m}$ , (c)  $0.95-1.5 \mu\text{m}$ , (d)  $1.5-3 \mu\text{m}$ , (e)  $3-7.2 \mu\text{m}$ , and (f)  $\geq 7.2 \mu\text{m}$

### 6.3 Conclusion

This chapter presents compelling evidence that particle size and chemical composition have a significant impact on the OP of PM. The analysis revealed that PM<sub>10</sub> demonstrated significantly higher OP values compared to PM<sub>2.5</sub> in both the DTT and AA assays. The OP of PM<sub>2.5</sub> is primarily linked to vehicular traffic, industrial emissions, and marine and sea salt aerosols. On the other hand, PM<sub>10</sub> is mainly associated with road dust and vehicular traffic emissions from nearby freeways. Moreover, this study has provided compelling evidence for the first time that the mechanism of multilayer adsorption not only facilitates the oxidation of LMW-PAHs, but also leads to increased levels of quinones in PM<sub>10</sub>. This ultimately contribute to understanding of the high OP of PM<sub>10</sub> than PM<sub>2.5</sub>.

The DTT and AA assays demonstrated that the water-soluble fractions of PM size fractions in the range of 0.95–1.5  $\mu\text{m}$  predominated over the ultrafine and coarse particles in terms of inducing OP. The high DTT values induced by the water-soluble fraction of particles in the 0.95–1.5  $\mu\text{m}$  range can be attributed to various sources, including vehicular traffic, road dust, industrial emissions, and marine and sea salt aerosols. Similarly, the DTT values induced by the methanol-soluble fraction of particles in the same size range are primarily linked to industrial emissions and vehicular traffic. The AA assay consistently demonstrated that ultrafine particles ( $\leq 0.49 \mu\text{m}$ ) and coarse particles ( $\geq 7.2 \mu\text{m}$ ) exhibited significantly higher OP compared to accumulation particles. The higher AA values induced by the water-soluble fraction of ultrafine particles ( $\leq 0.49 \mu\text{m}$ ) can be potentially attributed to vehicular traffic. Conversely, the higher AA values induced by the coarse particles ( $\geq 7.2 \mu\text{m}$ ) result from a combination of sources, including industrial emissions, vehicular traffic, and road dust.

The above findings suggest that the DTT and AA assays exhibit divergent responses to variations in particle size, chemical compositions, and sources. For example, the DTT assay demonstrated higher OP values for the water-soluble fractions, while the AA assay showed higher values for the methanol-soluble fractions. The higher DTT values induced by the water-soluble fraction can be attributed to its sensitivity to a wider range of water-soluble chemical species, such as trace metals, quinones, and HULIS, compared to the AA assay. On the other hand, the higher AA<sub>v</sub> induced by the methanol-soluble fraction compared to DTT<sub>v</sub> suggest that the AA assay exhibited higher sensitivity to water-insoluble chemical species that were extracted in methanol. These findings highlight the importance of understanding the chemical composition of particles in order to accurately assess their potential to cause oxidative stress and associated health risks.

The relationship between the deposition doses and OP varies depending particle size, chemical compositions, and the type of assay employed. Specifically, the DTT assay demonstrates a weak association, whereas the AA assay does not show any association. The decline in DTT<sub>v</sub> as doses of particles with a size of  $\leq 0.49 \mu\text{m}$  increases can be attributed to the antagonistic interactions between quinones, such as 1,4-NQ and 1,2-NQ, and trace metals like Cu, Fe, and Mn. Furthermore, it is noteworthy that both the AA assay and the DTT assay exhibit similar patterns of OP deposition for ultrafine particles in the human respiratory system. However, the AA assay predicted a greater OP deposition for coarse particles compared to the DTT assay. In contrast, DTT assay predicted high OP deposition of accumulation particles than AA assay, particularly in the alveoli. This underscores the importance of carefully selecting the appropriate assay type when investigating the potential health risks associated with PM. Furthermore, when selecting the assay type, it is crucial to



consider both the particle size, chemical compositions, and the specific regions of interest in the respiratory tract.

The comprehensive results of this study demonstrate that ambient particles with high deposition fraction and OP could significantly contribute to increased respiratory deposition and potentially pose adverse health effects. The elevated OP deposition of accumulation particles in the alveolar region as predicted by both DTT is particularly concerning due to its association with various health outcomes, including respiratory irritation, anemia, kidney failure, brain damage, and lung cancer. Moreover, the higher OP deposition of coarse particles in the upper respiratory regions of the respiratory tract could contribute to the development of respiratory diseases, asthma, and chronic obstructive pulmonary disease.

The significance of this study lies in its comprehensive examination of the overall health impact of PM, ultrafine, accumulation, and coarse particles, across various regions of the respiratory tract. The study has demonstrated that coarse particles have a greater capacity to induce oxidative stress and inflammation in the entire respiratory tract. This underscores the necessity for continuous monitoring and investigation into the sources of coarse particles. In order to advance air quality management and improve public health outcomes related to these particles, conducting a long-term field campaign to measure their OP and estimate contributions from various sources is essential. It is important to highlight that the ELF located in the upper airways contains a significant concentration of AA. Consequently, employing the AA assay to assess the deposition of OP caused by coarse particles in the upper airways holds more relevance compared to using the DTT assay. This outcome has the potential to enhance the accuracy of methods used to measure the OP

associated with exposure to coarse particles in the respiratory tract, particularly in the upper airways.

This study makes a significant contribution to our understanding of the potential health risks associated with ultrafine, accumulation, and coarse particles. Using DTT and AA assays, we investigated the deposition of their OP in the human respiratory tract. Our findings established a clear link between the deposition dose and OP, indicating that particle size and chemical composition are major contributors to OP rather than the dose alone in the human respiratory tract. Additionally, the diverse patterns of OP deposition observed through the DTT and AA assays emphasize the importance of considering particles with varying size ranges, particularly ultrafine, fine, and coarse particles, when designing strategies to reduce human exposure and minimize the associated health risks. Therefore, we recommend that interventions and policies aimed at mitigating the health risks of ambient particles should give careful consideration to particles in ultrafine, accumulation, and coarse mode.

## **Chapter 7 Contributions, Conclusions, and Recommendation for Future Work**

### **7.1 Contributions and conclusions**

This chapter synthesized the main findings from the three experimental chapters (Chapters 4, 5, and 6) and explored their implications for assessing the potential health risks linked to PM through lung cancer risk assessment and OP measurement. Specifically, Chapter 4 investigated lung cancer risk of PAHs and identified source contributions. Chapter 5 primarily focused on characterizing PM chemical compositions and investigating their OP activity, sources, and diurnal and seasonal variations. Chapter 6 delved into the OP of six size-fractionated PM, PM<sub>2.5</sub>, and PM<sub>10</sub>, and investigated their respiratory deposition to gain an understanding of their potential health risks to humans.

The research contributions and conclusions were summarized according to the following topics:

#### **7.1.1 Lung cancer risk of PAH exposure**

This study made significant contributions to the assessment of lung cancer risk associated with PAHs. Specifically, by including highly carcinogenic PAHs such as 7H-benzo[c]fluorene and various dibenzopyrene derivatives in addition to the traditional 16 priority PAHs, a four-fold increase in the lung cancer risk was observed. These findings emphasized the necessity for future research to consider including a broader range of PAHs in order to more accurately approximate the true risk level associated with PAH exposure. Additionally, our study addressed the common error reported in the literature regarding the estimation of lung cancer risk due to PAH exposure. The use of the WHO unit risk method

necessitated the use of BaP as a marker for complex mixtures, involving a simple multiplication of the BaP concentration by the WHO unit risk. However, the Environmental Protection Agency (EPA) adopted a component-based potency factor approach to assess the lung cancer risk of PAHs. The use of the component-based potency factor approach, in conjunction with the WHO unit risk, resulted in a substantial overestimation of cancer risk. Specifically, this approach overestimated the risk by approximately 14 times compared to the estimates derived from the EPA unit risk. These findings highlighted the significant disparities between the two approaches and underscored the need for a critical examination of current risk assessment methodologies. Our findings revealed that including additional PAHs in the component-based potency factor approach resulted in a close estimation of the lung cancer risk according to both EPA and WHO approaches. This led to a more accurate assessment of the lung cancer risk associated with PAH exposure.

Due to the strong correlation between PAHs and OP, we were intrigued to explore the relationship between OP and PAH lung cancer risk. This allowed us to assess whether OP associated with PAHs contributed to the risk of developing lung cancer. We focused on PAHs that exhibited a moderate to strong correlation with DTTv. For example, in autumn, the majority of PAHs (Nap, Flu, Phe, Ant, Flt, Pyr, Chr, BkF, BbF, BaP, IPyr, DBahA, BghiP, 7H-BcF, DBahPyr) shown in Appendix, Table 8.7, exhibited a moderate-to-strong correlation with OP. This investigation was conducted by performing Pearson's correlation analysis between DTTv and the toxicity equivalent concentration of each PAH, as well as the estimated LECR of 15 PAHs. The findings of this analysis are presented in Table 7.1 (reported only in this chapter).

Table 7.1 Pearson's correlation (r) between OP induced by water-soluble fraction of PM<sub>2.5</sub> and LECR of PAHs

	DTTv	NaP	Flu	Phe	Ant	Flt	Pyr	Chr	BbF	BkF	BaP	IPyr	DBahA	BghiP	7H-BcF	DBahPyr	LECR
DTTv	1																
NaP	-0.3	1															
Flu	0.32	0	1														
Phe	-0.2	0.51*	0.22	1													
Ant	-0.17	0.51*	0.06	0.92**	1												
Flt	-0.25	0.46	0.09	0.94**	0.98**	1											
Pyr	-0.25	0.5*	0.04	0.9**	0.98**	0.99**	1										
Chr	-0.3	0.53*	-0.06	0.83**	0.94**	0.96**	0.97**	1									
BbF	-0.59	0.68*	-0.38	0.58*	0.73**	0.71**	0.76**	0.78**	1								
BkF	-0.38	0.46	-0.18	0.65*	0.78**	0.76**	0.78**	0.76**	0.87**	1							
BaP	-0.27	0.55*	-0.19	0.67*	0.87**	0.86**	0.92**	0.96**	0.84**	0.76**	1						
IPyr	-0.38	0.75**	-0.26	0.59*	0.77**	0.74**	0.81**	0.86**	0.89**	0.68*	0.94**	1					
DBahA	-0.12	0.77**	-0.34	0.34	0.53*	0.43	0.51*	0.58*	0.7**	0.41	0.7**	0.86**	1				
BghiP	-0.36	0.74*	-0.24	0.63*	0.81**	0.78**	0.84**	0.89**	0.9**	0.72**	0.95**	0.99**	0.85**	1			
7H-BcF	0.02	0.43	0.04	0.67*	0.86**	0.8**	0.85**	0.79**	0.68*	0.72**	0.85**	0.77**	0.64*	0.79**	1		
DBahPyr	-0.31	0.79**	-0.3	0.31	0.53*	0.45	0.54*	0.59*	0.83**	0.58*	0.74**	0.9**	0.93**	0.88**	0.68*	1	
LECR	-0.13	0.6*	-0.1	0.61*	0.83**	0.77**	0.83**	0.82**	0.82**	0.75**	0.9**	0.9**	0.8**	0.91**	0.96**	0.85**	1

\*At 0.05 level (two-tailed), the correlation is significant

\*\* At 0.01 level (two-tailed), the correlation is significant

The results revealed no significant correlation between DTTv and LECR. This suggest that the lung cancer risk of PAHs is not as result of OP. Therefore, the lung cancer risk of PAHs can be linked soley to oxidation of PAHs by enzymes such as cytochrome P450 (CYPs) (Famiyeh et al., 2021). This enzymatic oxidation converts PAHs into reactive epoxides that have the potential cause DNA mutations, and subsequently lung cancer (Famiyeh et al., 2021; Kim et al., 2013; Shiizaki et al., 2017).

### 7.1.2 Effect of extraction solvents and acellular assays on OP measurement

The existing literature have extensively covered the OP generated by the water-soluble fraction of PM<sub>2.5</sub>. However, most of these studies have predominantly relied on the DTT assay as the primary method for measuring OP. This reliance on a single assay and the water-soluble fraction has limited the ability of the identification of more chemical species with

high OP activity. In our study, we used two extraction solvents, water and methanol, which allowed us to capture both hydrophilic and hydrophobic chemical species present in PM. Additionally, we employed two assays, DTT and AA, which exhibited different sensitivities towards the chemical species in PM. The DTT assay showed a higher response to the OP induced by the water-soluble fraction of PM, while the AA assay exhibited a high response to the methanol-soluble fractions. The higher DTT response to the OP induced by the water-soluble fraction observed in this study was attributed to the greater sensitivity of this assay to a wide range of water-soluble chemical species, including trace metals, high molecular weight quinones, and HULIS. The elevated OP induced by the methanol-soluble fractions in the AA assay was attributed to its strong response to water-insoluble chemical compositions in methanol. Therefore, we conclude that the careful selection of the appropriate assay based on the chemical species of interest and the solvent used for extraction is highly needed for accurate assessment of OP. Moreover, our study effectively demonstrated that the utilization of the DTT and AA assays, along with two extraction solvents, has significantly enhanced our understanding of the sensitivity of these assays towards the chemical species in PM

### 7.1.3 OP size distribution and respiratory deposition

The existing literature has primarily focused on the OP of PM<sub>2.5</sub>, creating a lack of clarity regarding the influence of particle size on the OP. To fill this knowledge gap, our study conducted a comparative assessment of the OP induced by ultrafine, accumulation, and coarse mode particles. This study has revealed for the first time that the effect of particle on OP and respiratory deposition depends on the type of assay used. Below were our key findings and conclusions:

- 1) The DTT assay exhibited a unimodal size distribution peaking in accumulation particles, whereas the AA assay exhibited a trimodal distribution peaking in coarse and ultrafine particles;
- 2) The high response of AA assay to coarse particle was in lign with their high respiratory deposition in the upper airways. This suggests that the high deposition fraction and doses of coarse particles, along with their high OP deposition in the upper airways, contribute to the low levels of AA in the epithelial lining fluid (ELF) of asthmatic patients when exposed to these particles. Therefore, the study demonstrated that AA prediction of high OP deposition of coarse particles in the ELF is more relevant than DTT prediction of low OP deposition. In contrast, DTT assay predicted high OP deposition of accumulation particles. The two assays predicted similar levels of OP deposition in the respiratory tract. These results lead us to the conclusion that when investigating the potential health risks of ambient particles, the choice of assay should depend on the size of the particle.

#### 7.1.4 The relationship between particle deposition dose and OP

This study investigated, for the first time, the potential link between particle deposition dose and OP induced by these particles. The following summarizes the findings and conclusions of this investigation:

- 1) Our findings revealed a weak correlation between particle deposition dose and OP measured in DTT assays, as well as no correlation with OP measured in AA assays.
- 2) The absence of a correlation between AAv and particle deposition doses suggests that the substances detected by the AA assay does not significantly contribute to the dose of each PM size fraction collected at the site. This is consistent with our findings that the AA assay exhibits a weak response to chemical species in water-soluble

fractions, which is evident in the low OP values. In contrast, DTT assays have been found to respond to a wider range of water-soluble chemical species, as evidenced by their high OP values than AA assay.

#### 7.1.5 The reduction of OP of PM<sub>2.5</sub>

Given the significant health risks associated with PM<sub>2.5</sub>, it was crucial to develop effective strategies for reducing exposure and mitigating its health impact. The current regulation of PM<sub>2.5</sub> primarily focused on mass concentration, may sufficiently address the health risks posed by PM<sub>2.5</sub>. This study investigated the source contributions to mass concentration and OP by conducting a year-round field campaign. The findings and conclusions of our study were as follows:

- 1) The mass concentration of PM<sub>2.5</sub> is dominated by industrial emissions, secondary aerosol, and vehicular emissions.
- 2) The OP induced by water-soluble fraction of PM<sub>2.5</sub> in DTT assay is dominated by secondary aerosol, industrial emissions, and road dust.
- 3) The OP induced by water-soluble fractions of PM<sub>2.5</sub> in AA assay is dominated by secondary aerosol.
- 4) The OP induced by methanol-soluble fractions of PM<sub>2.5</sub> in DTT assay is dominated by marine/sea spray, secondary aerosol, and vehicular emissions.
- 5) The OP induced by methanol-soluble fractions of PM<sub>2.5</sub> in AA assay is dominated by road dust, marine/sea spray, and vehicular emissions.

The above findings revealed that the source contributions to the PM<sub>2.5</sub> mass concentration and OP vary with the type of assay and extraction solvent used for OP measurement. This leads to the conclusion that targeting the mass concentration alone, as in the current



method for regulating PM<sub>2.5</sub> pollution, would not significantly reduce the health risk. Therefore, we suggest that future regulation efforts should adopt the results of both the source contributions of the mass concentration and OP in order to mitigate the health risks associated with PM<sub>2.5</sub>.

## **7.2 Recommendations for future work**

Based on the findings of this study, several compelling recommendations can be made for future research:

- 1) It is recommended that future investigations should compare the levels of OP across multiple sites in Ningbo, China, including both residential, industrial, and rural areas. This comparative analysis will provide valuable insights into the spatial distribution of OP and its potential association with different pollution sources in these areas.
- 2) Future investigations should consider both gaseous and particulate PAHs when assessing the risk of lung cancer. By taking into account both forms of PAHs, researchers will obtain a more comprehensive understanding of their overall contribution to the development of lung cancer and related health risks.
- 3) Future studies should conduct detailed analysis of the carbonaceous components, such as elemental carbon (EC) and organic carbon (OC), present in PM. This analysis will help identify the sources of these components and evaluate their specific contributions to OP. Additionally, it is crucial to estimate the proportion of SOA in PM and investigate its potential association with OP.
- 4) It is worth noting that the chemical composition of ambient particles, when extracted separately with water and methanol, resulted in different measured OP values for

each solvent that are not mutually exclusive. To address this discrepancy, it is strongly recommended that future investigations prioritize the extraction of water-soluble chemical compositions, followed by methanol extraction to capture water-insoluble chemical compositions. This sequential approach will enable accurate and comprehensive measurement of OP for both water-soluble and water-insoluble chemical components.

- 5) Future investigations should compare the levels of OP in ambient particles between indoor and outdoor environments. This comparison is crucial in understanding the potential sources and variations of OP in different environments and can aid in the development of targeted measures to mitigate OP and improve the overall health of populations exposed to both indoor and outdoor pollution sources.
- 6) In terms of diurnal variations of OP, it is highly recommended to ensure accurate representation by collecting a large sample size that encompasses all seasons and accounts for potential seasonal variations in OP during both daytime and nighttime. Moreover, conducting a comparison of the OP of PM at different times of the day, including morning, afternoon, and night, would be of particular interest. The results of such studies will help individuals in managing their exposure to ambient particles.

## Bibliography

- Abdel-Shafy, H. I., & Mansour, M. S. M. (2016). A review on polycyclic aromatic hydrocarbons: Source, environmental impact, effect on human health and remediation. *Egypt. J. Pet.*, 25(1), 107–123. <https://doi.org/10.1016/j.ejpe.2015.03.011>
- Abrams, J. Y., Weber, R. J., Klein, M., Sarnat, S. E., Chang, H. H., Strickland, M. J., Verma, V., Fang, T., Bates, J. T., Mulholland, J. A., Russell, A. G., & Tolbert, P. E. (2017). Associations between Ambient Fine Particulate Oxidative Potential and Cardiorespiratory Emergency Department Visits. *Environ. Health Perspect.*, 125(12), 129001. <https://doi.org/10.1289/EHP3048>
- Ahmad, M., Yu, Q., Chen, J., Cheng, S., Qin, W., & Zhang, Y. (2021). Chemical characteristics, oxidative potential, and sources of PM<sub>2.5</sub> in wintertime in Lahore and Peshawar, Pakistan. *J. Environ. Sci.*, 102, 148–158. <https://doi.org/10.1016/j.jes.2020.09.014>
- Ainur, D., Chen, Q., Sha, T., Zarak, M., Dong, Z., Guo, W., Zhang, Z., Dina, K., & An, T. (2023). Outdoor Health Risk of Atmospheric Particulate Matter at Night in Xi'an, Northwestern China. *Environ Sci. Technol.*, 57(25), 9252–9265. <https://doi.org/10.1021/acs.est.3c02670>
- Alemayehu, Y. A., Asfaw, S. L., & Terfie, T. A. (2020). Exposure to urban particulate matter and its association with human health risks. *Environ Sci. Pollut. Res.*, 27(22), 27491–27506. <https://doi.org/10.1007/s11356-020-09132-1>
- Ali-Taleshi, M. S., Squizzato, S., Riyahi Bakhtiari, A., Moeinaddini, M., & Masiol, M. (2021). Using a hybrid approach to apportion potential source locations contributing to excess cancer risk of PM<sub>2.5</sub>-bound PAHs during heating and non-heating periods in a megacity in the Middle East. *Environ. Res.*, 201(July), 111617. <https://doi.org/10.1016/j.envres.2021.111617>
- An, J., Liu, H., Wang, X., Talifu, D., Abulizi, A., Maihemuti, M., Li, K., Bai, H., Luo, P., & Xie, X. (2022). Oxidative potential of size-segregated particulate matter in the dust-storm impacted Hotan, northwest China. *Atmos. Environ.*, 280(January), 119142. <https://doi.org/10.1016/j.atmosenv.2022.119142>
- Andrade, C., Molina, C., S, L. F., Manzano, C. A., A, R. T., & G, M. A. L. (2021). Exploring the oxidative potential and respiratory deposition of size-segregated particulate matter at an urban site. *J. S. Am. Earth Sci.*, 105, 102957. <https://doi.org/10.1016/j.jsames.2020.102957>
- Aquilina, N. J., & Harrison, R. M. (2023). Evaluation of the cancer risk from PAHs by inhalation: Are current methods fit for purpose? *Environ. Int.*, 177(March), 107991. <https://doi.org/10.1016/j.envint.2023.107991>
- Argyropoulos, G., Besis, A., Voutsas, D., Samara, C., Sowlat, M. H., Hasheminassab, S., & Sioutas, C. (2016). Source apportionment of the redox activity of urban quasi-ultrafine particles (PM<sub>0.49</sub>) in Thessaloniki following the increased biomass burning due to the economic crisis in Greece. *Sci. Total Environ.*, 568, 124–136. <https://doi.org/10.1016/j.scitotenv.2016.05.217>

- Asgharian, B. (2019). *Multiple Path Particle Dosimetry ( MPPD ) model and its Applications*.
- Bai, L., Chen, W., He, Z., Sun, S., & Qin, J. (2020). Pollution characteristics, sources and health risk assessment of polycyclic aromatic hydrocarbons in PM<sub>2.5</sub> in an office building in northern areas, China. *Sustain. Cities Soc.*, 53(July 2019), 101891. <https://doi.org/10.1016/j.scs.2019.101891>
- Bates, J. T., Fang, T., Verma, V., Zeng, L., Weber, R. J., Tolbert, P. E., Abrams, J. Y., Sarnat, S. E., Klein, M., Mulholland, J. A., & Russell, A. G. (2019). Review of Acellular Assays of Ambient Particulate Matter Oxidative Potential: Methods and Relationships with Composition, Sources, and Health Effects [Review-article]. *Environ. Sci. Technol.*, 53(8), 4003–4019. <https://doi.org/10.1021/acs.est.8b03430>
- Bates, J. T., Weber, R. J., Abrams, J., Verma, V., Fang, T., Klein, M., Strickland, M. J., Sarnat, S. E., Chang, H. H., Mulholland, J. A., Tolbert, P. E., & Russell, A. G. (2015). Reactive Oxygen Species Generation Linked to Sources of Atmospheric Particulate Matter and Cardiorespiratory Effects. *Environ Sci. Technol*, 49(22), 13605–13612. <https://doi.org/10.1021/acs.est.5b02967>
- Berezina, E., Moiseenko, K., Skorokhod, A., Pankratova, N. V., Belikov, I., Belousov, V., & Elansky, N. F. (2020). Impact of VOCs and NO<sub>x</sub> on Ozone Formation in Moscow. *Atmosphere*, 11(11), 1262. <https://doi.org/10.3390/atmos11111262>
- Bergvall, C., & Westerholm, R. (2007). Identification and Determination of Highly Carcinogenic Dibenzopyrene Isomers in Air Particulate Samples from a Street Canyon, a Rooftop, and a Subway Station in Stockholm. *Environ Sci. Technol.*, 41(3), 731–737. <https://doi.org/10.1021/es062232p>
- Borlaza, L. J. S., Cosep, E. M. R., Kim, S., Lee, K., Joo, H., Park, M., Bate, D., Cayetano, M. G., & Park, K. (2018). Oxidative potential of fine ambient particles in various environments. *Environ.Pollut.*, 243, 1679–1688. <https://doi.org/10.1016/j.envpol.2018.09.074>
- Bosch, C., Andersson, A., Kruså, M., Bandh, C., Hovorková, I., Klánová, J., Knowles, T. D. J., Pancost, R. D., Evershed, R. P., & Gustafsson, Ö. (2015). Source Apportionment of Polycyclic Aromatic Hydrocarbons in Central European Soils with Compound-Specific Triple Isotopes ( $\delta^{13}C$ ,  $\Delta^{14}C$ , and  $\delta^2H$ ). *Environ. Sci. Technol.*, 49(13), 7657–7665. <https://doi.org/10.1021/acs.est.5b01190>
- Brunekreef, B., & Forsberg, B. (2005). Epidemiological evidence of effects of coarse airborne particles on health. *Eur. Respir. J*, 26(2), 309–318. <https://doi.org/10.1183/09031936.05.00001805>
- Burr, M. J., & Zhang, Y. (2011). Source apportionment of fine particulate matter over the Eastern U.S. Part I: source sensitivity simulations using CMAQ with the Brute Force method. *Atmos. Pollut. Res.*, 2(3), 300–317. <https://doi.org/10.5094/APR.2011.036>
- Byambaa, B., Yang, L., Matsuki, A., Nagato, E. G., Gankhuyag, K., Chuluunpurev, B., Banzragch, L., Chonokhuu, S., Tang, N., & Hayakawa, K. (2019). Sources and characteristics of polycyclic aromatic hydrocarbons in ambient total suspended particles in Ulaanbaatar City, Mongolia. *Int. J. Environ. Res. Public Health*, 16(3), 442. <https://doi.org/10.3390/ijerph16030442>
- Cai, S., Wang, Y., Zhao, B., Wang, S., Chang, X., & Hao, J. (2017). The impact of the “Air

- Pollution Prevention and Control Action Plan” on PM<sub>2.5</sub> concentrations in Jing-Jin-Ji region during 2012–2020. *Sci. Total Environ.*, 580(2017), 197–209. <https://doi.org/10.1016/j.scitotenv.2016.11.188>
- Calas, A., Uzu, G., Besombes, J. L., Martins, J. M. F., Redaelli, M., Weber, S., Charron, A., Albinet, A., Chevrier, F., Brulfert, G., Mesbah, B., Favez, O., & Jaffrezo, J. L. (2019). Seasonal variations and chemical predictors of oxidative potential (OP) of particulate matter (PM), for seven urban French sites. *Atmos.*, 10(11), 1–20. <https://doi.org/10.3390/atmos10110698>
- Calderón-Garcidueñas, L., Franco-Lira, M., Henríquez-Roldán, C., Osnaya, N., González-Maciel, A., Reynoso-Robles, R., Villarreal-Calderon, R., Herritt, L., Brooks, D., Keefe, S., Palacios-Moreno, J., Villarreal-Calderon, R., Torres-Jardón, R., Medina-Cortina, H., Delgado-Chávez, R., Aiello-Mora, M., Maronpot, R. R., & Doty, R. L. (2010). Urban air pollution: Influences on olfactory function and pathology in exposed children and young adults. *Exp. Toxicol. Pathol.*, 62(1), 91–102. <https://doi.org/10.1016/j.etp.2009.02.117>
- Callén, M. S., Iturmendi, A., & López, J. M. (2014). Source apportionment of atmospheric PM<sub>2.5</sub>-bound polycyclic aromatic hydrocarbons by a PMF receptor model. Assessment of potential risk for human health. *Environ. Pollut.*, 195, 167–177. <https://doi.org/10.1016/j.envpol.2014.08.025>
- Campbell, S. J., Wolfer, K., Utinger, B., Westwood, J., Zhang, Z.-H., Bukowiecki, N., Steimer, S. S., Vu, T. V., Xu, J., Straw, N., Thomson, S., Elzein, A., Sun, Y., Liu, D., Li, L., Fu, P., Lewis, A. C., Harrison, R. M., Bloss, W. J., ... Kalberer, M. (2021). Atmospheric conditions and composition that influence PM<sub>2.5</sub> oxidative potential in Beijing, China. *Atmos. Chem. Phys.*, 21(7), 5549–5573. <https://doi.org/10.5194/acp-21-5549-2021>
- Cao, W., Yin, L., Zhang, D., Wang, Y., Yuan, J., Zhu, Y., & Dou, J. (2019). Contamination, sources, and health risks associated with soil PAHs in rebuilt land from a Coking Plant, Beijing, China. *Int. J. Environ. Res. Public Health*, 16(4). <https://doi.org/10.3390/ijerph16040670>
- Carslaw, D. C., & Beevers, S. D. (2013). Characterising and understanding emission sources using bivariate polar plots and k-means clustering. *Environ. Model Softw.*, 40, 325–329. <https://doi.org/10.1016/j.envsoft.2012.09.005>
- Celo, V., Dabek-Zlotorzynska, E., & McCurdy, M. (2015). Chemical Characterization of Exhaust Emissions from Selected Canadian Marine Vessels: The Case of Trace Metals and Lanthanoids. *Environ Sci. Technol.*, 49(8), 5220–5226. <https://doi.org/10.1021/acs.est.5b00127>
- Charrier, J. G., & Anastasio, C. (2012). On dithiothreitol (DTT) as a measure of oxidative potential for ambient particles: Evidence for the importance of soluble \newline transition metals. *Atmos. Chem. Phys.*, 12(19), 9321–9333. <https://doi.org/10.5194/acp-12-9321-2012>
- Chen, C., Ju, Y., Cheng, Y., Wang, M., Paolo, F., Albarico, J. B., Chen, C., & Dong, C. (2022). Potential sources and toxicity risks of polycyclic aromatic hydrocarbons in surface sediments of commercial ports in Taiwan. *Mar. Pollut. Bull.*, 181(June), 113924. <https://doi.org/10.1016/j.marpolbul.2022.113924>

- Chen, K. (2022). Oxidative potential of urban haze in a coastal area: chemical characterisation, source identification and lung deposition. *PhD Thesis*.
- Chen, K., Metcalfe, S. E., Yu, H., Xu, J., Xu, H., Ji, D., Wang, C., Xiao, H., & He, J. (2021). Characteristics and source attribution of PM<sub>2.5</sub> during 2016 G20 Summit in Hangzhou: Efficacy of radical measures to reduce source emissions. *J. Environ. Sci.*, *106*, 47–65. <https://doi.org/10.1016/j.jes.2021.01.010>
- Chen, K., Xu, J., Famiyeh, Lord, Sun, Y., Ji, D., Xu, H., Wang, C., Metcalfe, S. E., Betha, R., Behera, S. N., Jia, C., Xiao, H., & He, J. (2022). Chemical constituents, driving factors, and source apportionment of oxidative potential of ambient fine particulate matter in a Port City in East China. *J. Hazard. Mater.*, *440*(May), 129864. <https://doi.org/10.1016/j.jhazmat.2022.129864>
- Chen, T., Liu, J., Ma, Q., Chu, B., Zhang, P., Ma, J., Liu, Y., Zhong, C., Liu, P., Wang, Y., Mu, Y., & He, H. (2021). Measurement report: Effects of photochemical aging on the formation and evolution of summertime secondary aerosol in Beijing. *Atmos. Chem. Phys.*, *21*(2), 1341–1356. <https://doi.org/10.5194/acp-21-1341-2021>
- Chen, Y. C., Chiang, H. C., Hsu, C. Y., Yang, T. T., Lin, T. Y., Chen, M. J., Chen, N. T., & Wu, Y. S. (2016). Ambient PM<sub>2.5</sub>-bound polycyclic aromatic hydrocarbons (PAHs) in Changhua County, central Taiwan: Seasonal variation, source apportionment and cancer risk assessment. *Environ. Pollut.*, *218*, 372–382. <https://doi.org/10.1016/j.envpol.2016.07.016>
- Cheng, Y., Ma, Y., Dong, B., Qiu, X., & Hu, D. (2021). Pollutants from primary sources dominate the oxidative potential of water-soluble PM<sub>2.5</sub> in Hong Kong in terms of dithiothreitol (DTT) consumption and hydroxyl radical production. *J. Hazard. Mater.*, *405*(September 2020), 124218. <https://doi.org/10.1016/j.jhazmat.2020.124218>
- Cho, A. K., Di Stefano, E., You, Y., Rodriguez, C. E., Schmitz, D. A., Kumagai, Y., Miguel, A. H., Eiguren-Fernandez, A., Kobayashi, T., Avol, E., & Froines, J. R. (2004). Determination of Four Quinones in Diesel Exhaust Particles, SRM 1649a, and Atmospheric PM 2.5 Special Issue of Aerosol Science and Technology on Findings from the Fine Particulate Matter Supersites Program. *Aerosol Sci. Technol.*, *38*(sup1), 68–81. <https://doi.org/10.1080/02786820390229471>
- Cho, A. K., Sioutas, C., Miguel, A. H., Kumagai, Y., Schmitz, D. A., Singh, M., Eiguren-Fernandez, A., & Froines, J. R. (2005). Redox activity of airborne particulate matter at different sites in the Los Angeles Basin. *Environ. Res.*, *99*(1), 40–47. <https://doi.org/10.1016/j.envres.2005.01.003>
- Choi, M. S., Qiu, X., Zhang, J., Wang, S., Li, X., Sun, Y., Chen, J., & Ying, Q. (2020). Study of Secondary Organic Aerosol Formation from Chlorine Radical-Initiated Oxidation of Volatile Organic Compounds in a Polluted Atmosphere Using a 3D Chemical Transport Model. *Environ. Sci. Technol.*, *54*(21), 13409–13418. <https://doi.org/10.1021/acs.est.0c02958>
- Clarke, K., Romain, A. C., Locoge, N., & Redon, N. (2012). Application of chemical mass balance methodology to identify the different sources responsible for the olfactory annoyance at a receptor-site. *Chem. Eng. Trans.*, *30*, 79–84. <https://doi.org/10.3303/CET1230014>
- Clemente, Gil-Moltó, J., Yubero, E., Juárez, N., Nicolás, J. F., Crespo, J., & Galindo, N.

- (2023). Sensitivity of PM10 oxidative potential to aerosol chemical composition at a Mediterranean urban site: ascorbic acid versus dithiothreitol measurements. *Air Qual Atmos Health*, 0123456789. <https://doi.org/10.1007/s11869-023-01332-1>
- Comero, S., Capitani, L., & Gawlik, B. M. (2009). *Positive Matrix Factorisation (PMF) An introduction to the chemometric evaluation of environmental monitoring data using PMF*. <https://doi.org/10.2788/2497>
- Consensus, E., Force, T., Shi, X., & Duan, G. (2022). Recommendations of Controlling and Preventing Acute Health Risks of Fine Particulate Matter Pollution — China , 2021. *China CDC Wkly*, 4(16), 329–341.
- Corral, A. F., Dadashazar, H., Stahl, C., Edwards, E.-L., Zuidema, P., & Sorooshian, A. (2020). Source Apportionment of Aerosol at a Coastal Site and Relationships with Precipitation Chemistry: A Case Study over the Southeast United States. *Atmosphere*, 11(11), 1212. <https://doi.org/10.3390/atmos11111212>
- Cui, Y., Zhu, L., Wang, H., Zhao, Z., Ma, S., & Ye, Z. (2023). Characteristics and Oxidative Potential of Ambient PM2.5 in the Yangtze River Delta Region: Pollution Level and Source Apportionment. *Atmosphere*, 14(3), 425. <https://doi.org/10.3390/atmos14030425>
- Cuyppers, A., Plusquin, M., Remans, T., Jozefczak, M., Keunen, E., Gielen, H., Opdenakker, K., Nair, A. R., Munters, E., Artois, T. J., Nawrot, T., Vangronsveld, J., & Smeets, K. (2010). Cadmium stress: an oxidative challenge. *BioMetals*, 23(5), 927–940. <https://doi.org/10.1007/s10534-010-9329-x>
- Daellenbach, K. R., Uzu, G., Jiang, J., Cassagnes, L. E., Leni, Z., Vlachou, A., Stefenelli, G., Canonaco, F., Weber, S., Segers, A., Kuenen, J. J. P., Schaap, M., Favez, O., Albinet, A., Aksoyoglu, S., Dommen, J., Baltensperger, U., Geiser, M., El Haddad, I., ... Prévôt, A. S. H. (2020). Sources of particulate-matter air pollution and its oxidative potential in Europe. *Nature*, 587(7834), 414–419. <https://doi.org/10.1038/s41586-020-2902-8>
- Darquenne, C. (2012). Aerosol deposition in health and disease. *J. Aerosol. Med. Pulm Drug Deliv.*, 25(3), 140–147. <https://doi.org/10.1089/jamp.2011.0916>
- Darquenne, C. (2020). Deposition Mechanisms. *J. Aerosol. Med. Pulm Drug Deliv.*, 33(4), 181–185. <https://doi.org/10.1089/jamp.2020.29029.cd>
- Deepthi, Y., Shiva Nagendra, S. M., & Gummadi, S. N. (2019). Characteristics of indoor air pollution and estimation of respiratory dosage under varied fuel-type and kitchen-type in the rural areas of Telangana state in India. *Sci. Total Environ.*, 650, 616–625. <https://doi.org/10.1016/j.scitotenv.2018.08.381>
- Delfino, R. J., Staimer, N., Tjoa, T., Gillen, D. L., Schauer, J. J., & Shafer, M. M. (2013). Airway inflammation and oxidative potential of air pollutant particles in a pediatric asthma panel. *J Expo Sci Environ Epidemiol.*, 23(5), 466–473. <https://doi.org/10.1038/jes.2013.25>
- Delfino, R. J., Staimer, N., & Vaziri, N. D. (2011). Air pollution and circulating biomarkers of oxidative stress. *Air Qual Atmos Health*, 4(1), 37–52. <https://doi.org/10.1007/s11869-010-0095-2>
- Deng, Q., Deng, L., Miao, Y., Guo, X., & Li, Y. (2019). Particle deposition in the human lung: Health implications of particulate matter from different sources. *Environ. Res.*,

- 169(July 2018), 237–245. <https://doi.org/10.1016/j.envres.2018.11.014>
- Di Virgilio, G., Hart, M. A., & Jiang, N. (2018). Meteorological controls on atmospheric particulate pollution during hazard reduction burns. *Atmos. Chem. Phys.*, 18(9), 6585–6599. <https://doi.org/10.5194/acp-18-6585-2018>
- Do, T. Van, Vuong, Q. T., & Choi, S. D. (2021). Day–night variation and size distribution of water-soluble inorganic ions in particulate matter in Ulsan, South Korea. *Atmos. Res.*, 247(May 2020), 105145. <https://doi.org/10.1016/j.atmosres.2020.105145>
- Do, T. Van, Vuong, Q. T., Lee, S.-J., Song, C.-K., & Choi, S.-D. (2023). Comparison of characteristics and sources of water-soluble inorganic ions, trace elements, and polycyclic aromatic hydrocarbons in PM<sub>2.5</sub> on polluted and normal days in Ulsan, South Korea. *Air Qual Atmos Health*, 16(6), 1239–1256. <https://doi.org/10.1007/s11869-023-01340-1>
- Drotikova, T., Ali, A. M., Halse, A. K., Reinardy, H. C., & Kallenborn, R. (2020). Polycyclic aromatic hydrocarbons (PAHs) and oxy- and nitro-PAHs in ambient air of the Arctic town Longyearbyen, Svalbard. *Atmos. Chem. Phys.*, 20(16), 9997–10014. <https://doi.org/10.5194/acp-20-9997-2020>
- Duan, Xiaoli, Zhao Xiuge, Wang Beibei, Chen Yiting, C. S. (2015). *Highlights of the Chinese Exposure Factors Handbook (Adults)*. <https://doi.org/10.1016/c2014-0-03838-5>
- Duan, L., Yu, H., Wang, Q., Cao, Y., Wang, G., Sun, X., Li, H., Lin, T., & Guo, Z. (2023). PM<sub>2.5</sub>-bound polycyclic aromatic hydrocarbons of a megacity in eastern China: Source apportionment and cancer risk assessment. *Sci. Total Environ.*, 869(October 2022), 161792. <https://doi.org/10.1016/j.scitotenv.2023.161792>
- Elzein, A., Dunmore, R. E., Ward, M. W., Hamilton, J. F., & Lewis, A. C. (2019). Variability of polycyclic aromatic hydrocarbons and their oxidative derivatives in wintertime Beijing, China. *Atmos. Chem. Phys.*, 19(13), 8741–8758. <https://doi.org/10.5194/acp-19-8741-2019>
- Elzein, A., Stewart, G. J., Swift, S. J., Nelson, B. S., Crilley, L. R., Alam, M. S., Reyes-Villegas, E., Gadi, R., Harrison, R. M., Hamilton, J. F., & Lewis, A. C. (2020). A comparison of PM<sub>2.5</sub>-bound polycyclic aromatic hydrocarbons in summer Beijing (China) and Delhi (India). *Atmos. Chem. Phys.*, 20(22), 14303–14319. <https://doi.org/10.5194/acp-20-14303-2020>
- Esen, F., Tasdemir, Y., & Vardar, N. (2008). Atmospheric concentrations of PAHs, their possible sources and gas-to-particle partitioning at a residential site of Bursa, Turkey. *Atmos. Res*, 88(3–4), 243–255. <https://doi.org/10.1016/j.atmosres.2007.11.022>
- Ewing, P., Blomgren, B., Ryrfeldt, A., & Gerde, P. (2006). Increasing Exposure Levels Cause an Abrupt Change in the Absorption and Metabolism of Acutely Inhaled Benzo(a)pyrene in the Isolated, Ventilated, and Perfused Lung of the Rat. *Toxicol. Sci.*, 91(2), 332–340. <https://doi.org/10.1093/toxsci/kfj104>
- Falfari, S., Cazzoli, G., Mariani, V., & Bianchi, G. M. (2023). Hydrogen Application as a Fuel in Internal Combustion Engines. *Energies*, 16(6), 2545. <https://doi.org/10.3390/en16062545>
- Famiyeh, Lord, Chen, K., Xu, J., Sun, Y., Guo, Q., Wang, C., Lv, J., Tang, Y.-T., Yu, H., Snape, C., & He, J. (2021). A review on analysis methods, source identification, and



- cancer risk evaluation of atmospheric polycyclic aromatic hydrocarbons. *Sci. Total Environ.*, 789, 147741. <https://doi.org/10.1016/j.scitotenv.2021.147741>
- Famiyeh, Lord, Jia, C., Chen, K., Tang, Y.-T., Ji, D., He, J., & Guo, Q. (2023). Size distribution and lung-deposition of ambient particulate matter oxidative potential: A contrast between dithiothreitol and ascorbic acid assays. *Environ. Pollut.*, 336(August), 122437. <https://doi.org/10.1016/j.envpol.2023.122437>
- Famiyeh, Lord, Xu, H., Chen, K., Tang, Y., Ji, D., Xiao, H., Tong, L., Jia, C., Guo, Q., & He, J. (2023). Breathing in danger: Unveiling the link between human exposure to outdoor PM<sub>2.5</sub>-bound polycyclic aromatic hydrocarbons and lung cancer risk in an urban residential area of China. *Sci. Total Environ.*, 167762. <https://doi.org/10.1016/j.scitotenv.2023.167762>
- Fan, X., Chen, Z., Liang, L., & Qiu, G. (2019). Atmospheric PM 2.5 -Bound Polycyclic Aromatic Hydrocarbons (PAHs) in Guiyang City, Southwest China: Concentration, Seasonal Variation, Sources and Health Risk Assessment. *Arch. Environ. Contam. Toxicol.*, 76(1), 102–113. <https://doi.org/10.1007/s00244-018-0563-5>
- Fang, B., Zhang, L., Zeng, H., Liu, J., Yang, Z., Wang, H., Wang, Q., & Wang, M. (2020). PM<sub>2.5</sub>-Bound Polycyclic Aromatic Hydrocarbons: Sources and Health Risk during Non-Heating and Heating Periods (Tangshan, China). *Int. J. Environ. Res.*, 17(2), 483. <https://doi.org/10.3390/ijerph17020483>
- Fang, T., Verma, V., Guo, H., King, L. E., Edgerton, E. S., & Weber, R. J. (2015). A semi-automated system for quantifying the oxidative potential of ambient particles in aqueous extracts using the dithiothreitol (DTT) assay: Results from the Southeastern Center for Air Pollution and Epidemiology (SCAPE). *Atmospheric Measurement Techniques*, 8(1), 471–482. <https://doi.org/10.5194/amt-8-471-2015>
- Fang, Ting, Guo, H., Zeng, L., Verma, V., Nenes, A., & Weber, R. J. (2017). Highly Acidic Ambient Particles, Soluble Metals, and Oxidative Potential: A Link between Sulfate and Aerosol Toxicity. *Environ Sci. Technol.*, 51(5), 2611–2620. <https://doi.org/10.1021/acs.est.6b06151>
- Fang, Ting, Lakey, P. S. J., Weber, R. J., & Shiraiwa, M. (2019). Oxidative Potential of Particulate Matter and Generation of Reactive Oxygen Species in Epithelial Lining Fluid [Research-article]. *Environ Sci. Technol.*, 53(21), 12784–12792. <https://doi.org/10.1021/acs.est.9b03823>
- Fang, Ting, Verma, V., T Bates, J., Abrams, J., Klein, M., Strickland, J. M., Sarnat, E. S., Chang, H. H., Mulholland, A. J., Tolbert, E. P., Russell, G. A., & Weber, J. R. (2016). Oxidative potential of ambient water-soluble PM<sub>2.5</sub> in the southeastern United States: Contrasts in sources and health associations between ascorbic acid (AA) and dithiothreitol (DTT) assays. *Atmos. Chem. Phys.*, 16(6), 3865–3879. <https://doi.org/10.5194/acp-16-3865-2016>
- Fang, Ting, Zeng, L., Gao, D., Verma, V., Stefaniak, A. B., & Weber, R. J. (2017). Ambient Size Distributions and Lung Deposition of Aerosol Dithiothreitol-Measured Oxidative Potential: Contrast between Soluble and Insoluble Particles. *Environ Sci. Technol.*, 51(12), 6802–6811. <https://doi.org/10.1021/acs.est.7b01536>
- Farahani, V. J., Altuwayjiri, A., Pirhadi, M., Verma, V., Ruprecht, A. A., Diapouli, E., Eleftheriadis, K., & Sioutas, C. (2022). The oxidative potential of particulate matter

- (PM) in different regions around the world and its relation to air pollution sources. *Environ. Sci. Atmos.*, 2(5), 1076–1086. <https://doi.org/10.1039/D2EA00043A>
- Feng, X., Feng, Y., Chen, Y., Cai, J., Li, Q., & Chen, J. (2022). Source apportionment of PM<sub>2.5</sub> during haze episodes in Shanghai by the PMF model with PAHs. *J. Clean. Prod.*, 330(November 2021), 129850. <https://doi.org/10.1016/j.jclepro.2021.129850>
- Ferrari, L., Carugno, M., & Bollati, V. (2019). Particulate matter exposure shapes DNA methylation through the lifespan. *Clin. Epigenetics*, 11(1), 129. <https://doi.org/10.1186/s13148-019-0726-x>
- Ferreira, A. P. S., Ramos, J. M. O., Gamaro, G. D., Gioda, A., Gioda, C. R., & Souza, I. C. C. (2022). Experimental rodent models exposed to fine particulate matter (PM<sub>2.5</sub>) highlighting the injuries in the central nervous system: A systematic review. *Atmos. Pollut. Res.*, 13(5), 101407. <https://doi.org/10.1016/j.apr.2022.101407>
- Frezzini, M. A., De Francesco, N., Massimi, L., & Canepari, S. (2022). Effects of operating conditions on PM oxidative potential assays. *Atmos. Environ.*, 268(October 2021), 118802. <https://doi.org/10.1016/j.atmosenv.2021.118802>
- Galvão, E. S., Paiva, H. B., Menezes, H. C., de Almeida Albuquerque, T. T., & Cardeal, Z. de L. (2023). Cancer risk assessment and source apportionment of the gas- and particulate-phase of the polycyclic aromatic hydrocarbons in a metropolitan region in Brazil. *Chemosphere*, 311(Pt 1), 136872. <https://doi.org/10.1016/j.chemosphere.2022.136872>
- Gangwar, R. S., Bevan, G. H., Palanivel, R., Das, L., & Rajagopalan, S. (2020). Oxidative stress pathways of air pollution mediated toxicity: Recent insights. *Redox Biol.*, 34(March), 101545. <https://doi.org/10.1016/j.redox.2020.101545>
- Gao, D., J. Godri Pollitt, K., A. Mulholland, J., G. Russell, A., & J. Weber, R. (2020). Characterization and comparison of PM<sub>2.5</sub> oxidative potential assessed by two acellular assays. *Atmos. Chem. Phys.*, 20(9), 5197–5210. <https://doi.org/10.5194/acp-20-5197-2020>
- Gao, D., Ripley, S., Weichenthal, S., & Godri Pollitt, K. J. (2020). Ambient particulate matter oxidative potential: Chemical determinants, associated health effects, and strategies for risk management. *Free. Radic. Biol. Med.*, 151(April), 7–25. <https://doi.org/10.1016/j.freeradbiomed.2020.04.028>
- Giannoni, M., Martellini, T., Del Bubba, M., Gambaro, A., Zangrando, R., Chiari, M., Lepri, L., & Cincinelli, A. (2012). The use of levoglucosan for tracing biomass burning in PM<sub>2.5</sub> samples in Tuscany (Italy). *Environ. Pollut.*, 167(April 2010), 7–15. <https://doi.org/10.1016/j.envpol.2012.03.016>
- Ginsberg, G. L., Asgharian, B., Kimbell, J. S., Ultman, J. S., & Jarabek, A. M. (2007). Modeling Approaches for Estimating the Dosimetry of Inhaled Toxicants in Children. *J. Toxicol. Environ. Health*, 71(3), 166–195. <https://doi.org/10.1080/15287390701597889>
- Grange, S. K., Uzu, G., Weber, S., Jaffrezo, J., & Hueglin, C. (2022). Linking Switzerland's PM<sub>10</sub> and PM<sub>2.5</sub> oxidative potential (OP) with emission sources. *Atmos. Chem. Phys.*, February, 1–31. <https://doi.org/https://doi.org/10.5194/acp-2021-979>
- Gune, M. M., Ma, W.-L., Sampath, S., Li, W., Li, Y.-F., Udayashankar, H. N., Balakrishna, K., & Zhang, Z. (2019). Occurrence of polycyclic aromatic hydrocarbons (PAHs) in air

- and soil surrounding a coal-fired thermal power plant in the south-west coast of India. *Environ. Sci. Pollut. Res.*, 26(22), 22772–22782. <https://doi.org/10.1007/s11356-019-05380-y>
- Guo, H., Li, M., Lyu, Y., Cheng, T., Xv, J., & Li, X. (2019). Size-resolved particle oxidative potential in the office, laboratory, and home: Evidence for the importance of water-soluble transition metals. *Environ. Pollut.*, 246, 704–709. <https://doi.org/10.1016/j.envpol.2018.12.094>
- Guo, M., Lyu, Y., Xu, T., Yao, B., Song, W., Li, M., Yang, X., Cheng, T., & Li, X. (2018). Particle size distribution and respiratory deposition estimates of airborne perfluoroalkyl acids during the haze period in the megacity of Shanghai. *Environ. Pollut.*, 234, 9–19. <https://doi.org/10.1016/j.envpol.2017.10.128>
- Guo, Q., Chen, K., & Xu, G. (2023). Characteristics and Sources of Water-Soluble Inorganic Ions in PM<sub>2.5</sub> in Urban Nanjing, China. *Atmosphere*, 14(1), 135. <https://doi.org/10.3390/atmos14010135>
- Guo, W., Zhang, Z., Zheng, N., Luo, L., Xiao, H., & Xiao, H. (2020). Chemical characterization and source analysis of water-soluble inorganic ions in PM<sub>2.5</sub> from a plateau city of Kunming at different seasons. *Atmos. Res.*, 234(October 2019), 104687. <https://doi.org/10.1016/j.atmosres.2019.104687>
- Gurkan Ayyildiz, E., & Esen, F. (2020). Atmospheric Polycyclic Aromatic Hydrocarbons (PAHs) at Two Sites, in Bursa, Turkey: Determination of Concentrations, Gas–Particle Partitioning, Sources, and Health Risk. *Arch. Environ. Contam. Toxicol.*, 78(3), 350–366. <https://doi.org/10.1007/s00244-019-00698-7>
- Hakimzadeh, M., Soleimani, E., Mousavi, A., Borgini, A., De Marco, C., Ruprecht, A. A., & Sioutas, C. (2020). The impact of biomass burning on the oxidative potential of PM<sub>2.5</sub> in the metropolitan area of Milan. *Atmos. Environ.*, 224(January), 117328. <https://doi.org/10.1016/j.atmosenv.2020.117328>
- Hammer, T., Gao, H., Pan, Z., & Wang, J. (2020). Relationship between aerosols exposure and lung deposition dose. *Aerosol and Air Qual. Res.*, 20(5), 1083–1093. <https://doi.org/10.4209/aaqr.2020.01.0033>
- Haque, M. M., Kawamura, K., Deshmukh, D. K., Fang, C., Song, W., Mengying, B., & Zhang, Y. L. (2019). Characterization of organic aerosols from a Chinese megacity during winter: Predominance of fossil fuel combustion. *Atmos. Chem. Phys.*, 19(7), 5147–5164. <https://doi.org/10.5194/acp-19-5147-2019>
- He, J., Chen, K., & Xu, J. (2017). Urban Air Pollution and Control. In *Encyc. Sust. Technol.* (Vol. 2, pp. 243–257). Elsevier. <https://doi.org/10.1016/B978-0-12-409548-9.10182-4>
- He, Jiabao, Fan, S., Meng, Q., Sun, Y., Zhang, J., & Zu, F. (2014). Polycyclic aromatic hydrocarbons (PAHs) associated with fine particulate matters in Nanjing, China: Distributions, sources and meteorological influences. *Atmos. Environ.*, 89, 207–215. <https://doi.org/10.1016/j.atmosenv.2014.02.042>
- He, Jun, & Balasubramanian, R. (2009). Determination of Atmospheric Polycyclic Aromatic Hydrocarbons Using Accelerated Solvent Extraction. *Anal. Lett.*, 42(11), 1603–1619. <https://doi.org/10.1080/00032710902993886>
- Hedayat, F., Stevanovic, S., Miljevic, B., Bottle, S., & Ristovski, Z. D. (2015). Review-Evaluating The Molecular Assays for Measuring Oxidative Potential of Particulate

- Matter. *Chem. Ind. Chem. Eng*, 21(1–2), 201–210. <https://doi.org/10.2298/CICEQ140228031H>
- Heyder, J., Gebhart, J., Rudolf, G., Schiller, C. F., & Stahlhofen, W. (1986). Deposition of particles in the human respiratory tract in the size range 0.005–15  $\mu\text{m}$ . *J. Aerosol. Sci.*, 17(5), 811–825. [https://doi.org/10.1016/0021-8502\(86\)90035-2](https://doi.org/10.1016/0021-8502(86)90035-2)
- Hofmann, W. (2011). Modelling inhaled particle deposition in the human lung-A review. *J. Aerosol. Sci.*, 42(10), 693–724. <https://doi.org/10.1016/j.jaerosci.2011.05.007>
- Honda, M., & Suzuki, N. (2020). Toxicities of Polycyclic Aromatic Hydrocarbons for Aquatic Animals. *Int. J. Environ. Res. Public Health*, 17(4), 1363. <https://doi.org/10.3390/ijerph17041363>
- Hong, W.-J., Jia, H., Ma, W.-L., Sinha, R. K., Moon, H.-B., Nakata, H., Minh, N. H., Chi, K. H., Li, W.-L., Kannan, K., Sverko, E., & Li, Y.-F. (2016). Distribution, Fate, Inhalation Exposure and Lung Cancer Risk of Atmospheric Polycyclic Aromatic Hydrocarbons in Some Asian Countries. *Environ Sci. Technol*, 50(13), 7163–7174. <https://doi.org/10.1021/acs.est.6b01090>
- Hong, X., Yang, K., Liang, H., & Shi, Y. (2022). Characteristics of Water-Soluble Inorganic Ions in PM 2.5 in Typical Urban Areas of Beijing, China. *ACS Omega*, 7(40), 35575–35585. <https://doi.org/10.1021/acsomega.2c02919>
- Hopke, P. K. (2016). Review of receptor modeling methods for source apportionment. *Journal of the Air & Waste Management Association*, 66(3), 237–259. <https://doi.org/10.1080/10962247.2016.1140693>
- Hopke, P. K., & Hill, E. L. (2021). Health and charge benefits from decreasing PM2.5 concentrations in New York State: Effects of changing compositions. *Atmos. Pollut. Res.*, 12(3), 47–53. <https://doi.org/10.1016/j.apr.2021.01.018>
- Hsiao, T., Chou, L., Pan, S., Young, L., Chi, K., & Chen, A. Y. (2021). Chemically and temporally resolved oxidative potential of urban fine. *Environ. Pollut.*, 291(September), 118206. <https://doi.org/10.1016/j.envpol.2021.118206>
- Hu, M., Peng, J., Sun, K., Yue, D., Guo, S., Wiedensohler, A., & Wu, Z. (2012). Estimation of size-resolved ambient particle density based on the measurement of aerosol number, mass, and chemical size distributions in the winter in Beijing. *Environ. Sci. Technol.*, 46(18), 9941–9947. <https://doi.org/10.1021/es204073t>
- Huang, L., Liu, X., Wang, Z., Zhu, Y., & Hu, J. (2021). Size Distributions and Seasonal Variations of Water-Soluble Inorganic Particulate Matter at a Suburban Site in Nanjing, China. *J. Hazard. Toxic Radioact. Waste*, 25(4), 04021029. [https://doi.org/10.1061/\(asce\)hz.2153-5515.0000635](https://doi.org/10.1061/(asce)hz.2153-5515.0000635)
- Huang, R. J., Cheng, R., Jing, M., Yang, L., Li, Y., Chen, Q., Chen, Y., Yan, J., Lin, C., Wu, Y., Zhang, R., El Haddad, I., Prevot, A. S. H., O'Dowd, C. D., & Cao, J. (2018). Source-Specific Health Risk Analysis on Particulate Trace Elements: Coal Combustion and Traffic Emission As Major Contributors in Wintertime Beijing. *Environ Sci. Technol*, 52(19), 10967–10974. <https://doi.org/10.1021/acs.est.8b02091>
- Huang, X., Liu, Z., Liu, J., Hu, B., Wen, T., Tang, G., Zhang, J., Wu, F., Ji, D., Wang, L., & Wang, Y. (2017). Chemical characterization and source identification of PM2.5 at multiple sites in the Beijing–Tianjin–Hebei region, China. *Atmos. Chem. Phys.*, 17(21), 12941–12962. <https://doi.org/10.5194/acp-17-12941-2017>

- Hussein, T., Löndahl, J., Paasonen, P., Koivisto, A. J., Petäjä, T., Hämeri, K., & Kulmala, M. (2013). Modeling regional deposited dose of submicron aerosol particles. *Sci. Total Environ.*, 458–460, 140–149. <https://doi.org/10.1016/j.scitotenv.2013.04.022>
- Iakovides, M., Iakovides, G., & Stephanou, E. G. (2021). Atmospheric particle-bound polycyclic aromatic hydrocarbons, n-alkanes, hopanes, steranes and trace metals: PM2.5 source identification, individual and cumulative multi-pathway lifetime cancer risk assessment in the urban environment. *Sci. Total Environ.*, 752, 141834. <https://doi.org/10.1016/j.scitotenv.2020.141834>
- Iakovides, M., Stephanou, E. G., Apostolaki, M., Hadjicharalambous, M., Evans, J. S., Koutrakis, P., & Achilleos, S. (2019). Study of the occurrence of airborne Polycyclic Aromatic Hydrocarbons associated with respirable particles in two coastal cities at Eastern Mediterranean: Levels, source apportionment, and potential risk for human health. *Atmos. Res.*, 213(May), 170–184. <https://doi.org/10.1016/j.atmosenv.2019.05.059>
- IARC monographs on the evaluation of carcinogenic risks to humans. (2010). *IARC Monographs on the Evaluation of Carcinogenic Risks to Humans*, 93, 9–38. <https://doi.org/10.1136/jcp.48.7.691-a>
- Idowu, O., Semple, K. T., Ramadass, K., O'Connor, W., Hansbro, P., & Thavamani, P. (2019). Beyond the obvious: Environmental health implications of polar polycyclic aromatic hydrocarbons. *Environ. Int.*, 123(December 2018), 543–557. <https://doi.org/10.1016/j.envint.2018.12.051>
- Insian, W., Yabueng, N., Wiriya, W., & Chantara, S. (2022). Size-fractionated PM-bound PAHs in urban and rural atmospheres of northern Thailand for respiratory health risk assessment. *Environ. Pollut.*, 293(November 2021), 118488. <https://doi.org/10.1016/j.envpol.2021.118488>
- Jamhari, A. A., Latif, M. T., Wahab, M. I. A., Othman, M., Hamid, H. H. A., Tekasakul, P., Hata, M., Furuchi, M., & Rajab, N. F. (2021). Size-segregated atmospheric polycyclic aromatic hydrocarbons down to PM0.1 in urban tropical environment: Temporal distribution, potential sources and human health risk. *Urban Clim.*, 40(October), 100996. <https://doi.org/10.1016/j.uclim.2021.100996>
- Jamhari, A. A., Sahani, M., Latif, M. T., Chan, K. M., Tan, H. S., Khan, M. F., & Mohd Tahir, N. (2014). Concentration and source identification of polycyclic aromatic hydrocarbons (PAHs) in PM10 of urban, industrial and semi-urban areas in Malaysia. *Atmos. Environ.*, 86, 16–27. <https://doi.org/10.1016/j.atmosenv.2013.12.019>
- Janssen, N. A. H., Strak, M., Yang, A., Hellack, B., Kelly, F. J., Kuhlbusch, T. A. J., Harrison, R. M., Brunekreef, B., Cassee, F. R., Steenhof, M., & Hoek, G. (2015). Associations between three specific a-cellular measures of the oxidative potential of particulate matter and markers of acute airway and nasal inflammation in healthy volunteers. *Occup Environ. Med.*, 72(1), 49–56. <https://doi.org/10.1136/oemed-2014-102303>
- Janssen, N. A. H., Yang, A., Strak, M., Steenhof, M., Hellack, B., Gerlofs-Nijland, M. E., Kuhlbusch, T., Kelly, F., Harrison, R., Brunekreef, B., Hoek, G., & Cassee, F. (2014). Oxidative potential of particulate matter collected at sites with different source characteristics. *Sci. Total Environ.*, 472, 572–581.

- <https://doi.org/10.1016/j.scitotenv.2013.11.099>
- Jeswani, H. K., Chilvers, A., & Azapagic, A. (2020). Environmental sustainability of biofuels: a review. *Proceedings of the Royal Society A: Mathematical, Physical and Engineering Sciences*, 476(2243). <https://doi.org/10.1098/rspa.2020.0351>
- Jiang, H., Sabbir Ahmed, C. M., Canchola, A., Chen, J. Y., & Lin, Y. H. (2019). Use of dithiothreitol assay to evaluate the oxidative potential of atmospheric aerosols. *Atmos.*, 10(10), 1–21. <https://doi.org/10.3390/atmos10100571>
- Jiang, Y., Xia, M., Wang, Z., Zheng, P., Chen, Y., & Wang, T. (2023). Photochemical aging of aerosols contributes significantly to the production of atmospheric formic acid. *June*.
- Jin, Y., Andersson, H., & Zhang, S. (2016). Air pollution control policies in China: A retrospective and prospects. *Int. J. Environ. Res. Public Health*, 13(12). <https://doi.org/10.3390/ijerph13121219>
- Kelly, F. J., & Fussell, J. C. (2020). Toxicity of airborne particles - established evidence, knowledge gaps and emerging areas of importance: Topical aspects of particle toxicity. *Philos. Trans. Royal Soc.*, 378(2183). <https://doi.org/10.1098/rsta.2019.0322>
- Khan, M. F., Latif, M. T., Lim, C. H., Amil, N., Jaafar, S. A., Dominick, D., Mohd Nadzir, M. S., Sahani, M., & Tahir, N. M. (2015). Seasonal effect and source apportionment of polycyclic aromatic hydrocarbons in PM2.5. *Atmos. Environ.*, 106, 178–190. <https://doi.org/10.1016/j.atmosenv.2015.01.077>
- Khuzestani, R. B., Schauer, J. J., Shang, J., Cai, T., Fang, D., Wei, Y., Zhang, L., & Zhang, Y. (2018). Source apportionments of PM2.5 organic carbon during the elevated pollution episodes in the Ordos region, Inner Mongolia, China. *Environ. Sci. Pollut. Res.*, 25(13), 13159–13172. <https://doi.org/10.1007/s11356-018-1514-4>
- Kim, C. S., & Fisher, D. M. (1999). Deposition Characteristics of Aerosol Particles in Sequentially Bifurcating Airway Models. *Aerosol Sci. Technol.*, 31(2–3), 198–220. <https://doi.org/10.1080/027868299304255>
- Kim, C. S., & Jaques, P. A. (2004). Analysis of total respiratory deposition of inhaled ultrafine particles in adult subjects at various breathing patterns. *Aerosol Sci. Technol.*, 38(6), 525–540. <https://doi.org/10.1080/02786820490465513>
- Kim, J., Kim, N. Y., & Kim, W. J. (2023). Biomarkers of particulate matter exposure in patients with chronic obstructive pulmonary disease: a systematic review. *J. Thorac. Dis.*, 15(6), 3453–3465. <https://doi.org/10.21037/jtd-23-78>
- Kim, K.-H., Jahan, S. A., Kabir, E., & Brown, R. J. C. (2013). A review of airborne polycyclic aromatic hydrocarbons (PAHs) and their human health effects. *Environ. Int.*, 60, 71–80. <https://doi.org/10.1016/j.envint.2013.07.019>
- Kobos, L., & Shannahan, J. (2021). Particulate matter inhalation and the exacerbation of cardiopulmonary toxicity due to metabolic disease. *Exp. Biol. Med.*, 246(7), 822–834. <https://doi.org/10.1177/1535370220983275>
- Křůmal, K., Mikuška, P., & Večeřa, Z. (2013). Polycyclic aromatic hydrocarbons and hopanes in PM1 aerosols in urban areas. *Atmos. Environ.*, 67, 27–37. <https://doi.org/10.1016/j.atmosenv.2012.10.033>
- Kubo, T., Bai, W., Nagae, M., & Takao, Y. (2020). Seasonal Fluctuation of Polycyclic Aromatic Hydrocarbons and Aerosol Genotoxicity in Long-Range Transported Air Mass Observed at the Western End of Japan. *Int. J. Environ. Res.*, 17(4), 1210.

- <https://doi.org/10.3390/ijerph17041210>
- Kuempel, E. D., Sweeney, L. M., Morris, J. B., & Jarabek, A. M. (2015). Advances in Inhalation Dosimetry Models and Methods for Occupational Risk Assessment and Exposure Limit Derivation. *J. Occup. Environ. Hyg.*, *12*(sup1), S18–S40. <https://doi.org/10.1080/15459624.2015.1060328>
- Kurihara, K., Iwata, A., Horwitz, S. G. M., Ogane, K., Sugioka, T., Matsuki, A., & Okuda, T. (2022). Contribution of Physical and Chemical Properties to Dithiothreitol-Measured Oxidative Potentials of Atmospheric Aerosol Particles at Urban and Rural Sites in Japan. *Atmosphere*, *13*(2). <https://doi.org/10.3390/atmos13020319>
- Lakey, P. S. J., Berkemeier, T., Tong, H., Arangio, A. M., Lucas, K., Pöschl, U., & Shiraiwa, M. (2016). Chemical exposure-response relationship between air pollutants and reactive oxygen species in the human respiratory tract. *Sci. Rep.*, *6*(1), 32916. <https://doi.org/10.1038/srep32916>
- Lang, Y.-H., Li, G.-L., Wang, X.-M., & Peng, P. (2015). Combination of Unmix and PMF receptor model to apportion the potential sources and contributions of PAHs in wetland soils from Jiaozhou Bay, China. *Mar. Pollut. Bull.*, *90*(1–2), 129–134. <https://doi.org/10.1016/j.marpolbul.2014.11.009>
- Le Breton, M., Hallquist, Å. M., Kant Pathak, R., Simpson, D., Wang, Y., Johansson, J., Zheng, J., Yang, Y., Shang, D., Wang, H., Liu, Q., Chan, C., Wang, T., Bannan, T. J., Priestley, M., Percival, C. J., Shallcross, D. E., Lu, K., Guo, S., ... Hallquist, M. (2018). Chlorine oxidation of VOCs at a semi-rural site in Beijing: Significant chlorine liberation from ClNO<sub>2</sub> and subsequent gas- and particle-phase Cl-VOC production. *Atmos. Chem. Phys.*, *18*(17), 13013–13030. <https://doi.org/10.5194/acp-18-13013-2018>
- Lee, G., Jang, Y.-C., Choi, K., Kim, H., Ji, S., Kim, B., Kwon, Y., & Shin, H.-S. (2022). Occurrence, Distribution and Risk Assessment of PAHs in Road Dust Sediment in Daejeon Metropolitan City, South Korea. *Environ. Eng. Res.*, *28*(2), 220043–0. <https://doi.org/10.4491/eer.2022.043>
- Lelieveld, J., Evans, J. S., Fnais, M., Giannadaki, D., & Pozzer, A. (2015). The contribution of outdoor air pollution sources to premature mortality on a global scale. *Nature*, *525*(7569), 367–371. <https://doi.org/10.1038/nature15371>
- Li, J., Li, J., Wang, G., Ho, K. F., Han, J., Dai, W., Wu, C., Cao, C., & Liu, L. (2022). In-vitro oxidative potential and inflammatory response of ambient PM<sub>2.5</sub> in a rural region of Northwest China: Association with chemical compositions and source contribution. *Environ. Res.*, *205*, 112466. <https://doi.org/10.1016/j.envres.2021.112466>
- Li, M., Hu, M., Guo, Q., Tan, T., Du, B., Huang, X., He, L., Guo, S., Wang, W., Fan, Y., & Xu, D. (2018). Seasonal Source Apportionment of PM<sub>2.5</sub> in Ningbo, a Coastal City in Southeast China. *Aerosol and Air Qual. Res.*, *18*(11), 2741–2752. <https://doi.org/10.4209/aaqr.2018.01.0011>
- Li, Q., Zhang, K., Li, R., Yang, L., Yi, Y., Liu, Z., Zhang, X., Feng, J., Wang, Q., Wang, W., Huang, L., Wang, Y., Wang, S., Chen, H., Chan, A., Latif, M. T., Ooi, M. C. G., Manomaiphiboon, K., Yu, J., & Li, L. (2023). Underestimation of biomass burning contribution to PM<sub>2.5</sub> due to its chemical degradation based on hourly measurements of organic tracers: A case study in the Yangtze River Delta (YRD) region, China. *Sci.*

- Li, W., Park, R., Alexandrou, N., Dryfhout-Clark, H., Brice, K., & Hung, H. (2021). Multi-year Analyses Reveal Different Trends, Sources, and Implications for Source-Related Human Health Risks of Atmospheric Polycyclic Aromatic Hydrocarbons in the Canadian Great Lakes Basin. *Environ. Sci. Technol.* <https://doi.org/10.1021/acs.est.0c07079>
- Li, X.-Y., Hao, L., Liu, Y.-H., Chen, C.-Y., Pai, V. J., & Kang, J. X. (2017). Protection against fine particle-induced pulmonary and systemic inflammation by omega-3 polyunsaturated fatty acids. *Biochim. Biophys. Acta - Gen. Subj.*, 1861(3), 577–584. <https://doi.org/10.1016/j.bbagen.2016.12.018>
- Li, X., Yan, C., Patterson, R. F., Zhu, Y., Yao, X., Zhu, Y., Ma, S., Qiu, X., Zhu, T., & Zheng, M. (2016). Modeled deposition of fine particles in human airway in Beijing, China. *Atmos. Environ.*, 124, 387–395. <https://doi.org/10.1016/j.atmosenv.2015.06.045>
- Li, Z., Nie, D., Chen, M., Ge, P., Liu, Z., Ma, X., Ge, X., & Gu, R. (2021). Seasonal variation of oxidative potential of water-soluble components in PM<sub>2.5</sub> and PM<sub>1</sub> in the Yangtze River Delta, China. *Air Quality, Atmosphere and Health*, 14(11), 1825–1836. <https://doi.org/10.1007/s11869-021-01056-0>
- Lihong, Y., & Jingyuan, W. (2011). The Effects of Energy Production on Environment in China. *Energy Procedia*, 5, 779–784. <https://doi.org/10.1016/j.egypro.2011.03.137>
- Lin, C.-W., Huang, S.-H., Chang, K.-N., Kuo, Y.-M., Wu, H.-D., Lai, C.-Y., & Chen, C.-C. (2019). Experimental Measurements of Regional Lung Deposition in Taiwanese. *Aerosol and Air Qual. Res.*, 19(4), 832–839. <https://doi.org/10.4209/aaqr.2018.06.0213>
- Lin, M., & Yu, J. Z. (2020). Assessment of interactions between transition metals and atmospheric organics: ascorbic acid depletion and hydroxyl radical formation in organic-metal mixtures. *Environ. Sci. Technol.*, 54(3), 1431–1442. <https://doi.org/10.1021/acs.est.9b07478>
- Lin, P., & Yu, J. Z. (2011). Generation of reactive oxygen species mediated by Humic-like substances in atmospheric aerosols. *Environ. Sci. Technol.*, 45(24), 10362–10368. <https://doi.org/10.1021/es2028229>
- Liu, D., Li, J., Zhang, Y., Xu, Y., Liu, X., Ding, P., Shen, C., Chen, Y., Tian, C., & Zhang, G. (2013). The use of levoglucosan and radiocarbon for source apportionment of PM<sub>2.5</sub> carbonaceous aerosols at a background site in East China. *Environ. Sci. Processes Impacts*, 47(18), 10454–10461. <https://doi.org/10.1021/es401250k>
- Liu, D., Lin, T., Syed, J. H., Cheng, Z., Xu, Y., Li, K., Zhang, G., & Li, J. (2017). Concentration, source identification, and exposure risk assessment of PM<sub>2.5</sub>-bound parent PAHs and nitro-PAHs in atmosphere from typical Chinese cities. *Sci. Rep.*, 7(1), 1–12. <https://doi.org/10.1038/s41598-017-10623-4>
- Liu, D., Xu, Y., Chaemfa, C., Tian, C., Li, J., Luo, C., & Zhang, G. (2014). Concentrations, seasonal variations, and outflow of atmospheric polycyclic aromatic hydrocarbons (PAHs) at Ningbo site, Eastern China. *Atmos. Pollut. Res.*, 5(2), 203–209. <https://doi.org/10.5094/APR.2014.025>
- Liu, J., Man, R., Ma, S., Li, J., Wu, Q., & Peng, J. (2015). Atmospheric levels and health



- risk of polycyclic aromatic hydrocarbons (PAHs) bound to PM 2.5 in Guangzhou, China. *Mar. Pollut. Bull.*, *100*(1), 134–143. <https://doi.org/10.1016/j.marpolbul.2015.09.014>
- Liu, K., Hua, S., & Song, L. (2022). PM2.5 Exposure and Asthma Development: The Key Role of Oxidative Stress. *Oxid. Med. Cell.*, *2022*, 1–12. <https://doi.org/10.1155/2022/3618806>
- Liu, Q., Lu, Z., Xiong, Y., Huang, F., Zhou, J., & Schauer, J. J. (2020). Oxidative potential of ambient PM2.5 in Wuhan and its comparisons with eight areas of China. *Sci. Total Environ.*, *701*, 134844. <https://doi.org/10.1016/j.scitotenv.2019.134844>
- Liu, W. J., Xu, Y. S., Liu, W. X., Liu, Q. Y., Yu, S. Y., Liu, Y., Wang, X., & Tao, S. (2018). Oxidative potential of ambient PM2.5 in the coastal cities of the Bohai Sea, northern China: Seasonal variation and source apportionment. *Environ. Pollut.*, *236*, 514–528. <https://doi.org/10.1016/j.envpol.2018.01.116>
- Liu, W. Y., Yu, Z. Bin, Qiu, H. Y., Wang, J. B., Chen, X. Y., & Chen, K. (2018). Association between ambient air pollutants and preterm birth in Ningbo, China: A time-series study. *BMC Pediatrics*, *18*(1), 1–9. <https://doi.org/10.1186/s12887-018-1282-9>
- Liu, Weijian, Xu, Y., Zhao, Y., Liu, Q., Yu, S., Liu, Y., Wang, X., Liu, Y., Tao, S., & Liu, W. (2019). Occurrence, source, and risk assessment of atmospheric parent polycyclic aromatic hydrocarbons in the coastal cities of the Bohai and Yellow Seas, China. *Environ. Pollut.*, *254*, 113046. <https://doi.org/10.1016/j.envpol.2019.113046>
- Liu, Wenling, Xu, Z., & Yang, T. (2018). Health Effects of Air Pollution in China. *Int. J. Environ. Res.*, *15*(7), 1471. <https://doi.org/10.3390/ijerph15071471>
- Liu, X., Jiang, N., Yu, X., Zhang, R., Li, S., Li, Q., & Kang, P. (2019). Chemical characteristics, sources apportionment, and risk assessment of pm2.5 in different functional areas of an emerging megacity in China. *Aerosol and Air Qual. Res.*, *19*(10), 2222–2238. <https://doi.org/10.4209/aaqr.2019.02.0076>
- Liu, Yankun, Yu, Y., Liu, M., Lu, M., Ge, R., Li, S., Liu, X., Dong, W., & Qadeer, A. (2018). Characterization and source identification of PM2.5-bound polycyclic aromatic hydrocarbons (PAHs) in different seasons from Shanghai, China. *Sci. Total Environ.*, *644*, 725–735. <https://doi.org/10.1016/j.scitotenv.2018.07.049>
- Liu, Yunwei, Qin, N., Liang, W., Chen, X., Hou, R., Kang, Y., Guo, Q., Cao, S., & Duan, X. (2020). Polycycl. Aromatic Hydrocarbon Exposure of Children in Typical Household Coal Combustion Environments: Seasonal Variations, Sources, and Carcinogenic Risks. *Int. J. Environ. Res. Public Health*, *17*(18), 6520. <https://doi.org/10.3390/ijerph17186520>
- Lovett, C., Sowlat, M. H., Saliba, N. A., Shihadeh, A. L., & Sioutas, C. (2018). Oxidative potential of ambient particulate matter in Beirut during Saharan and Arabian dust events. *Atmos. Environ.*, *188*(1994), 34–42. <https://doi.org/10.1016/j.atmosenv.2018.06.016>
- Luo, Y., Zeng, Y., Xu, H., Li, D., Zhang, T., Lei, Y., Huang, S., & Shen, Z. (2023). Connecting oxidative potential with organic carbon molecule composition and source-specific apportionment in PM2.5 in Xi'an, China. *Atmos. Environ.*, *306*(February), 119808. <https://doi.org/10.1016/j.atmosenv.2023.119808>
- Lv, H., Li, H., Qiu, Z., Zhang, F., & Song, J. (2021). Assessment of pedestrian exposure and

- deposition of PM<sub>10</sub>, PM<sub>2.5</sub> and ultrafine particles at an urban roadside: A case study of Xi'an, China. *Atmos. Pollut. Res.*, *12*(4), 112–121. <https://doi.org/10.1016/j.apr.2021.02.018>
- Lv, Y., Li, X., Ting Xu, T., Tao Cheng, T., Yang, X., Min Chen, J., Iinuma, Y., & Herrmann, H. (2016). Size distributions of polycyclic aromatic hydrocarbons in urban atmosphere: Sorption mechanism and source contributions to respiratory deposition. *Atmos. Chem. Phys.*, *16*(5), 2971–2983. <https://doi.org/10.5194/acp-16-2971-2016>
- Lyu, Y., Guo, H., Cheng, T., & Li, X. (2018). Particle Size Distributions of Oxidative Potential of Lung-Deposited Particles: Assessing Contributions from Quinones and Water-Soluble Metals. *Environ. Sci. Technol.*, *52*(11), 6592–6600. <https://doi.org/10.1021/acs.est.7b06686>
- Ma, X., Nie, D., Chen, M., Ge, P., Liu, Z., Ge, X., Li, Z., & Gu, R. (2021). The relative contributions of different chemical components to the oxidative potential of ambient fine particles in nanjing area. *Int. J. Environ. Res. Public Health*, *18*(6), 1–17. <https://doi.org/10.3390/ijerph18062789>
- Ma, Y., Liu, A., Egodawatta, P., McGree, J., & Goonetilleke, A. (2017). Quantitative assessment of human health risk posed by polycyclic aromatic hydrocarbons in urban road dust. *Sci. Total Environ.*, *575*, 895–904. <https://doi.org/10.1016/j.scitotenv.2016.09.148>
- Madureira, J., Slezakova, K., Silva, A. I., Lage, B., Mendes, A., Aguiar, L., Pereira, M. C., Teixeira, J. P., & Costa, C. (2020). Assessment of indoor air exposure at residential homes: Inhalation dose and lung deposition of PM<sub>10</sub>, PM<sub>2.5</sub> and ultrafine particles among newborn children and their mothers. *Sci. Total Environ.*, *717*, 137293. <https://doi.org/10.1016/j.scitotenv.2020.137293>
- Maher, B. A., Ahmed, I. A. M., Karloukovski, V., MacLaren, D. A., Foulds, P. G., Allsop, D., Mann, D. M. A., Torres-Jardón, R., & Calderon-Garciduenas, L. (2016). Magnetite pollution nanoparticles in the human brain. *PNAS*, *113*(39), 10797–10801. <https://doi.org/10.1073/pnas.1605941113>
- Mahmoud, N., Al-Shahwani, D., Al-Thani, H., & Isaifan, R. J. (2023). Risk Assessment of the Impact of Heavy Metals in Urban Traffic Dust on Human Health. *Atmosphere*, *14*(6), 1049. <https://doi.org/10.3390/atmos14061049>
- Malig, B. J., Green, S., Basu, R., & Broadwin, R. (2013). Coarse particles and respiratory emergency department visits in California. *Am. J. Epidemiol.*, *178*(1), 58–69. <https://doi.org/10.1093/aje/kws451>
- Manojkumar, N., Srimuruganandam, B., & Shiva Nagendra, S. M. (2019). Application of multiple-path particle dosimetry model for quantifying age specified deposition of particulate matter in human airway. *Ecotoxicolo. Environ. Saf.*, *168*(July 2018), 241–248. <https://doi.org/10.1016/j.ecoenv.2018.10.091>
- Masiol, M., Hofer, A., Squizzato, S., Piazza, R., Rampazzo, G., & Pavoni, B. (2012). Carcinogenic and mutagenic risk associated to airborne particle-phase polycyclic aromatic hydrocarbons: A source apportionment. *Atmos. Environ.*, *60*, 375–382. <https://doi.org/10.1016/j.atmosenv.2012.06.073>
- Masri, S., Li, L., Dang, A., Chung, J. H., Chen, J.-C., Fan, Z.-H. (Tina), & Wu, J. (2018). Source characterization and exposure modeling of gas-phase polycyclic aromatic

- hydrocarbon (PAH) concentrations in Southern California. *Atmos. Environ.*, *177*(1994), 175–186. <https://doi.org/10.1016/j.atmosenv.2018.01.014>
- Massimi, L., Simonetti, G., Buiarelli, F., Di Filippo, P., Pomata, D., Riccardi, C., Ristorini, M., Astolfi, M. L., & Canepari, S. (2020). Spatial distribution of levoglucosan and alternative biomass burning tracers in atmospheric aerosols, in an urban and industrial hot-spot of Central Italy. *Atmos. Res.*, *239*(February), 104904. <https://doi.org/10.1016/j.atmosres.2020.104904>
- McWhinney, R. D., Zhou, S., & Abbatt, J. P. D. (2013). Naphthalene SOA: redox activity and naphthoquinone gas–particle partitioning. *Atmos. Chem. Phys.*, *13*(19), 9731–9744. <https://doi.org/10.5194/acp-13-9731-2013>
- Meng, C. C., Wang, L. T., Zhang, F. F., Wei, Z., Ma, S. M., Ma, X., & Yang, J. (2016). Characteristics of concentrations and water-soluble inorganic ions in PM<sub>2.5</sub> in Handan City, Hebei province, China. *Atmos. Res.*, *171*, 133–146. <https://doi.org/10.1016/j.atmosres.2015.12.013>
- Mitra, S., Chakraborty, A. J., Tareq, A. M., Emran, T. Bin, Nainu, F., Khusro, A., Idris, A. M., Khandaker, M. U., Osman, H., Alhumaydhi, F. A., & Simal-Gandara, J. (2022). Impact of heavy metals on the environment and human health: Novel therapeutic insights to counter the toxicity. *J. King Saud Univ. Sci.*, *34*(3), 101865. <https://doi.org/10.1016/j.jksus.2022.101865>
- Mo, Z., Wang, Z., Mao, G., Pan, X., Wu, L., Xu, P., Chen, S., Wang, A., Zhang, Y., Luo, J., Ye, X., Wang, X., Chen, Z., & Lou, X. (2019). Characterization and health risk assessment of PM<sub>2.5</sub>-bound polycyclic aromatic hydrocarbons in 5 urban cities of Zhejiang Province, China. *Sci. Rep.*, *9*(1), 1–11. <https://doi.org/10.1038/s41598-019-43557-0>
- Molina, C., Andrade, C., Manzano, C. A., Richard Toro, A., Verma, V., & Leiva-Guzmán, M. A. (2020). Dithiothreitol-based oxidative potential for airborne particulate matter: an estimation of the associated uncertainty. *Environ. Sci. Pollut. Res.*, *27*(23), 29672–29680. <https://doi.org/10.1007/s11356-020-09508-3>
- Molina, C., Manzano, C. A., Toro A., R., & Leiva G, M. A. (2023). The oxidative potential of airborne particulate matter in two urban areas of Chile: More than meets the eye. *Environ. Int.*, *173*(November 2022), 107866. <https://doi.org/10.1016/j.envint.2023.107866>
- Moorthy, B., Chu, C., & Carlin, D. J. (2015). Polycyclic aromatic hydrocarbons: From metabolism to lung cancer. *Toxicol. Sci.*, *145*(1), 5–15. <https://doi.org/10.1093/toxsci/kfv040>
- Morawska, L., & Buonanno, G. (2021). The physics of particle formation and deposition during breathing. *Nat. Rev. Phys.*, *3*(5), 300–301. <https://doi.org/10.1038/s42254-021-00307-4>
- Mu, N., Wang, H., Chen, D., Wang, F., Ji, L., Zhang, C., Li, M., & Lu, P. (2022). A Novel Rat Model of Dry Eye Induced by Aerosol Exposure of Particulate Matter. *Investig. Ophthalmol. Vis. Sci.*, *63*(1), 39. <https://doi.org/10.1167/iovs.63.1.39>
- Mudway, I. S., Kelly, F. J., & Holgate, S. T. (2020). Oxidative stress in air pollution research. *Free Radic Biol Med.*, *151*(January), 2–6. <https://doi.org/10.1016/j.freeradbiomed.2020.04.031>

- Nair, P. R., Parameswaran, K., Abraham, A., & Jacob, S. (2005). Wind-dependence of sea-salt and non-sea-salt aerosols over the oceanic environment. *J. Atmos Sol Terr Phys.*, *67*(10), 884–898. <https://doi.org/10.1016/j.jastp.2005.02.008>
- Ng, N. L., Brown, S. S., Archibald, A. T., Atlas, E., Cohen, R. C., Crowley, J. N., Day, D. A., Donahue, N. M., Fry, J. L., Fuchs, H., Griffin, R. J., Guzman, M. I., Herrmann, H., Hodzic, A., Iinuma, Y., Jimenez, J. L., Kiendler-Scharr, A., Lee, B. H., Luecken, D. J., ... Zaveri, R. A. (2017). Nitrate radicals and biogenic volatile organic compounds: oxidation, mechanisms, and organic aerosol. *Atmos. Chem. Phys.*, *17*(3), 2103–2162. <https://doi.org/10.5194/acp-17-2103-2017>
- Nisbet, I. C. T., & LaGoy, P. K. (1992). Toxic equivalency factors (TEFs) for polycyclic aromatic hydrocarbons (PAHs). *Regul. Toxicol. Pharmacol.*, *16*(3), 290–300. [https://doi.org/10.1016/0273-2300\(92\)90009-X](https://doi.org/10.1016/0273-2300(92)90009-X)
- Nishita-Hara, C., Hirabayashi, M., Hara, K., Yamazaki, A., & Hayashi, M. (2019). Dithiothreitol-Measured Oxidative Potential of Size-Segregated Particulate Matter in Fukuoka, Japan: Effects of Asian Dust Events. *GeoHealth*, *3*(6), 160–173. <https://doi.org/10.1029/2019gh000189>
- Ntziachristos, L., Froines, J. R., Cho, A. K., & Sioutas, C. (2007). Relationship between redox activity and chemical speciation of size-fractionated particulate matter. *Part. Fibre Toxicol.*, *4*, 1–12. <https://doi.org/10.1186/1743-8977-4-5>
- Oros, D. R., & Simoneit, B. R. T. (2000). Identification and emission rates of molecular tracers in coal smoke particulate matter. *Fuel*, *79*(5), 515–536. [https://doi.org/10.1016/S0016-2361\(99\)00153-2](https://doi.org/10.1016/S0016-2361(99)00153-2)
- Osman, A. I., Mehta, N., Elgarahy, A. M., Hefny, M., Al-Hinai, A., Al-Muhtaseb, A. H., & Rooney, D. W. (2022). Hydrogen production, storage, utilisation and environmental impacts: a review. *Environ. Chem. Lett*, *20*(1), 153–188. <https://doi.org/10.1007/s10311-021-01322-8>
- Osornio-Vargas, A. R., Serrano, J., Rojas-Bracho, L., Miranda, J., García-Cuellar, C., Reyna, M. A., Flores, G., Zuk, M., Quintero, M., Vázquez, I., Sánchez-Pérez, Y., López, T., & Rosas, I. (2011). In vitro biological effects of airborne PM<sub>2.5</sub> and PM<sub>10</sub> from a semi-desert city on the Mexico–US border. *Chemosphere*, *83*(4), 618–626. <https://doi.org/10.1016/j.chemosphere.2010.11.073>
- Ouyang, R., Yang, S., & Xu, L. (2020). Analysis and risk assessment of PM<sub>2.5</sub>-bound PAHs in a comparison of indoor and outdoor environments in a middle school: A case study in Beijing, China. *Atmosphere*, *11*(9). <https://doi.org/10.3390/ATMOS11090904>
- Owusu, P. A., & Asumadu-Sarkodie, S. (2016). A review of renewable energy sources, sustainability issues and climate change mitigation. *Cogent Eng.*, *3*(1), 1167990. <https://doi.org/10.1080/23311916.2016.1167990>
- Palmisani, J., Di Gilio, A., Franchini, S. A., Cotugno, P., Miniero, D. V., D’Ambruoso, P., & de Gennaro, G. (2020). Particle-Bound PAHs and Elements in a Highly Industrialized City in Southern Italy: PM<sub>2.5</sub> Chemical Characterization and Source Apportionment after the Implementation of Governmental Measures for Air Pollution Mitigation and Control. *Int J Environ Res Public Health*, *17*(13), 4843. <https://doi.org/10.3390/ijerph17134843>
- Park, M., Joo, H. S., Lee, K., Jang, M., Kim, S. D., Kim, I., Borlaza, L. J. S., Lim, H., Shin,

- H., Chung, K. H., Choi, Y. H., Park, S. G., Bae, M. S., Lee, J., Song, H., & Park, K. (2018). Differential toxicities of fine particulate matters from various sources. *Sci. Rep.*, 8(1), 1–11. <https://doi.org/10.1038/s41598-018-35398-0>
- Park, S. S., Ko, J. M., & Cho, S. Y. (2011). Investigation of possible sources of water-soluble organic carbon particles observed with an online monitoring system. *Atmos. Environ.*, 45(19), 3257–3266. <https://doi.org/10.1016/j.atmosenv.2011.03.038>
- Parris, B. A., O'Farrell, H. E., Fong, K. M., & Yang, I. A. (2019). Chronic obstructive pulmonary disease (COPD) and lung cancer: common pathways for pathogenesis. *J. Thorac Dis*, 11(S17), S2155–S2172. <https://doi.org/10.21037/jtd.2019.10.54>
- Patel, A., & Rastogi, N. (2018). Seasonal variability in chemical composition and oxidative potential of ambient aerosol over a high altitude site in western India. *Sci. Total Environ.*, 644, 1268–1276. <https://doi.org/10.1016/j.scitotenv.2018.07.030>
- Pei, J., Wang, Y., & Yu, K. (2018). Sensitive determination of quinones by high-performance liquid chromatography-electrospray ionization-tandem mass spectrometry with methanol derivatization. *Anal. Sci.*, 34(3), 335–340. <https://doi.org/10.2116/analsci.34.335>
- Peli, M., Bostick, B. C., Barontini, S., Lucchini, R. G., & Ranzi, R. (2021). Profiles and species of Mn, Fe and trace metals in soils near a ferromanganese plant in Bagnolo Mella (Brescia, IT). *Sci. Total Environ.*, 755(Pt 2), 143123. <https://doi.org/10.1016/j.scitotenv.2020.143123>
- Perrone, M. R., Bertoli, I., Romano, S., Russo, M., Rispoli, G., & Pietrogrande, M. C. (2019). PM2.5 and PM10 oxidative potential at a Central Mediterranean Site: Contrasts between dithiothreitol- and ascorbic acid-measured values in relation with particle size and chemical composition. *Atmos. Environ.*, 210(April), 143–155. <https://doi.org/10.1016/j.atmosenv.2019.04.047>
- Peters, K. E., & Moldowan, J. M. (1991). Effects of source, thermal maturity, and biodegradation on the distribution and isomerization of homohopanes in petroleum. *Org. Geochem.*, 17(1), 47–61. [https://doi.org/10.1016/0146-6380\(91\)90039-M](https://doi.org/10.1016/0146-6380(91)90039-M)
- Pietrogrande, M. C., Bacco, D., Trentini, A., & Russo, M. (2021). Effect of filter extraction solvents on the measurement of the oxidative potential of airborne PM2.5. *Environ. Sci. Pollut. Res.*, 28(23), 29551–29563. <https://doi.org/10.1007/s11356-021-12604-7>
- Pietrogrande, M. C., Bertoli, I., Manarini, F., & Russo, M. (2019). Ascorbate assay as a measure of oxidative potential for ambient particles: Evidence for the importance of cell-free surrogate lung fluid composition. *Atmos. Environ.*, 211, 103–112. <https://doi.org/10.1016/j.atmosenv.2019.05.012>
- Pietrogrande, M. C., Demaria, G., Colombi, C., Cuccia, E., & Dal Santo, U. (2022). Seasonal and Spatial Variations of PM10 and PM2.5 Oxidative Potential in Five Urban and Rural Sites across Lombardia Region, Italy. *Int. J. Environ. Res. Public Health*, 19(13), 7778. <https://doi.org/10.3390/ijerph19137778>
- Pietrogrande, M. C., Perrone, M. R., Manarini, F., Romano, S., Udisti, R., & Becagli, S. (2018). PM10 oxidative potential at a Central Mediterranean Site: Association with chemical composition and meteorological parameters. *Atmos. Environ.*, 188(June), 97–111. <https://doi.org/10.1016/j.atmosenv.2018.06.013>
- Pietrogrande, M. C., Romanato, L., & Russo, M. (2022). Synergistic and Antagonistic

- Effects of Aerosol Components on Its Oxidative Potential as Predictor of Particle Toxicity. *Toxics*, 10(4), 196. <https://doi.org/10.3390/toxics10040196>
- Pietrogrande, M. C., Russo, M., & Zagatti, E. (2019). Review of PM oxidative potential measured with acellular assays in urban and rural sites across Italy. *Atmos.*, 10(10), 8–11. <https://doi.org/10.3390/atmos10100626>
- Pongpiachan, S., Tipmanee, D., Khumsup, C., Kittikoon, I., & Hirunyatrakul, P. (2015). Assessing risks to adults and preschool children posed by PM<sub>2.5</sub>-bound polycyclic aromatic hydrocarbons (PAHs) during a biomass burning episode in Northern Thailand. *Sci. Total Environ.*, 508, 435–444. <https://doi.org/10.1016/j.scitotenv.2014.12.019>
- Prakash, J., Agrawal, S. B., & Agrawal, M. (2023). Global Trends of Acidity in Rainfall and Its Impact on Plants and Soil. *J. Soil Sci. Plant Nutr.*, 23(1), 398–419. <https://doi.org/10.1007/s42729-022-01051-z>
- Rao, L., Zhang, L., Wang, X., Xie, T., Zhou, S., Lu, S., Liu, X., Lu, H., Xiao, K., Wang, W., & Wang, Q. (2020). Oxidative potential induced by ambient particulate matters with acellular assays: A review. *Processes*, 8(11), 1–21. <https://doi.org/10.3390/pr8111410>
- Ravindra, K., Sokhi, R., & Vangrieken, R. (2008). Atmospheric polycyclic aromatic hydrocarbons: Source attribution, emission factors and regulation. *Atmos. Environ.*, 42(13), 2895–2921. <https://doi.org/10.1016/j.atmosenv.2007.12.010>
- Ray, D., Ghosh, A., Chatterjee, A., Ghosh, S. K., & Raha, S. (2019). Size-specific pahs and associated health risks over a tropical urban metropolis: Role of long-range transport and meteorology. *Aerosol and Air Qual. Res.*, 19(11), 2446–2463. <https://doi.org/10.4209/aaqr.2019.06.0312>
- Richter-Brockmann, S., & Achten, C. (2018). Analysis and toxicity of 59 PAH in petrogenic and pyrogenic environmental samples including dibenzopyrenes, 7H-benzo[c]fluorene, 5-methylchrysene and 1-methylpyrene. *Chemosphere*, 200, 495–503. <https://doi.org/10.1016/j.chemosphere.2018.02.146>
- Rissler, J., Gudmundsson, A., Nicklasson, H., Swietlicki, E., Wollmer, P., & Löndahl, J. (2017). Deposition efficiency of inhaled particles (15-5000 nm) related to breathing pattern and lung function: an experimental study in healthy children and adults. *Part. Fibre Toxicol.*, 14(1), 10. <https://doi.org/10.1186/s12989-017-0190-8>
- Roy, R., Jan, R., Gunjal, G., Bhor, R., Pai, K., & Satsangi, P. G. (2019). Particulate matter bound polycyclic aromatic hydrocarbons: Toxicity and health risk assessment of exposed inhabitants. *Atmos. Environ.*, 210(November 2018), 47–57. <https://doi.org/10.1016/j.atmosenv.2019.04.034>
- Sadiktsis, I., Bergvall, C., Johansson, C., & Westerholm, R. (2012). Automobile Tires—A Potential Source of Highly Carcinogenic Dibenzopyrenes to the Environment. *Environ Sci. Technol.*, 46(6), 3326–3334. <https://doi.org/10.1021/es204257d>
- Saffari, A., Hasheminassab, S., Wang, D., Shafer, M. M., Schauer, J. J., & Sioutas, C. (2015). Impact of primary and secondary organic sources on the oxidative potential of quasi-ultrafine particles (PM<sub>0.25</sub>) at three contrasting locations in the Los Angeles Basin. *Atmos. Environ.*, 120, 286–296. <https://doi.org/10.1016/j.atmosenv.2015.09.022>
- Sakizadeh, M. (2020). Spatial distribution and source identification together with environmental health risk assessment of PAHs along the coastal zones of the USA. *Environ. Geochem. Health*, 42(10), 3333–3350. <https://doi.org/10.1007/s10653-020->

00578-3

- Sandaka, B. P., & Kumar, J. (2023). Alternative vehicular fuels for environmental decarbonization: A critical review of challenges in using electricity, hydrogen, and biofuels as a sustainable vehicular fuel. *Chem. Eng. J. Adv.*, *14*(January), 100442. <https://doi.org/10.1016/j.cej.2022.100442>
- Schiller, C. H. F., Gebhart, J., Heyder, J., Rudolf, G., & Stahlhofen, W. (1988). Deposition of Monodisperse Insoluble Aerosol Particles in the 0.005 to 0.2  $\mu\text{m}$  Size Range Within the Human Respiratory Tract. *Ann Occup Hyg*, *32*(inhaled\_particles\_VI), 41–49. [https://doi.org/10.1093/annhyg/32.inhaled\\_particles\\_VI.41](https://doi.org/10.1093/annhyg/32.inhaled_particles_VI.41)
- Schraufnagel, D. E. (2020). The health effects of ultrafine particles. *Exp Mol Med*, *52*(3), 311–317. <https://doi.org/10.1038/s12276-020-0403-3>
- Scott, M., Sander, R., Nemet, G., & Patz, J. (2021). Improving Human Health in China Through Alternative Energy. *Front. Public Health*, *9*(April). <https://doi.org/10.3389/fpubh.2021.613517>
- Secrest, M. H., Schauer, J. J., Carter, E. M., Lai, A. M., Wang, Y., Shan, M., Yang, X., Zhang, Y., & Baumgartner, J. (2016). The oxidative potential of PM<sub>2.5</sub> exposures from indoor and outdoor sources in rural China. *Sci. Total Environ.*, *571*, 1477–1489. <https://doi.org/10.1016/j.scitotenv.2016.06.231>
- Shahpoury, P., Zhang, Z. W., Filippi, A., Hildmann, S., Lelieveld, S., Mashtakov, B., Patel, B. R., Traub, A., Umbrio, D., Wietzoreck, M., Wilson, J., Berkemeier, T., Celo, V., Dabek-Zlotorzynska, E., Evans, G., Harner, T., Kerman, K., Lammel, G., Noroozifar, M., ... Tong, H. (2022). Inter-comparison of oxidative potential metrics for airborne particles identifies differences between acellular chemical assays. *Atmos. Pollut. Res.*, *13*(12), 101596. <https://doi.org/10.1016/j.apr.2022.101596>
- Shang, J., Zhang, Y., Schauer, J. J., Chen, S., Yang, S., Han, T., Zhang, D., Zhang, J., & An, J. (2022). Prediction of the oxidation potential of PM<sub>2.5</sub> exposures from pollutant composition and sources. *Environ. Pollut.*, *293*(April 2021), 118492. <https://doi.org/10.1016/j.envpol.2021.118492>
- Shen, J., Taghvaei, S., La, C., Oroumiyeh, F., Liu, J., Jerrett, M., Weichenthal, S., Del Rosario, I., Shafer, M. M., Ritz, B., Zhu, Y., & Paulson, S. E. (2022). Aerosol Oxidative Potential in the Greater Los Angeles Area: Source Apportionment and Associations with Socioeconomic Position. *Environ Sci. Technol.*, *56*(24), 17795–17804. <https://doi.org/10.1021/acs.est.2c02788>
- Shen, R., Wang, Y., Gao, W., Cong, X., Cheng, L., & Li, X. (2019). Size-segregated particulate matter bound polycyclic aromatic hydrocarbons (PAHs) over China: Size distribution, characteristics and health risk assessment. *Sci. Total Environ.*, *685*, 116–123. <https://doi.org/10.1016/j.scitotenv.2019.05.436>
- Shiizaki, K., Kawanishi, M., & Yagi, T. (2017). Modulation of benzo[a]pyrene–DNA adduct formation by CYP1 inducer and inhibitor. *Genes and Environ.*, *39*(1), 14. <https://doi.org/10.1186/s41021-017-0076-x>
- Simon Araya, S., Liso, V., Cui, X., Li, N., Zhu, J., Sahlin, S. L., Jensen, S. H., Nielsen, M. P., & Kær, S. K. (2020). A Review of The Methanol Economy: The Fuel Cell Route. *Energies*, *13*(3), 596. <https://doi.org/10.3390/en13030596>
- Simonetti, G., Conte, E., Perrino, C., & Canepari, S. (2018). Oxidative potential of size-

- segregated PM in an urban and an industrial area of Italy. *Atmos. Environ.*, 187, 292–300. <https://doi.org/10.1016/j.atmosenv.2018.05.051>
- Snyder, D. C., Rutter, A. P., Collins, R., Worley, C., & Schauer, J. J. (2009). Insights into the Origin of Water Soluble Organic Carbon in Atmospheric Fine Particulate Matter. *Aerosol Sci Technol.*, 43(11), 1099–1107. <https://doi.org/10.1080/02786820903188701>
- Sofowote, U. M., Allan, L. M., & McCarry, B. E. (2010). Evaluation of PAH diagnostic ratios as source apportionment tools for air particulates collected in an urban-industrial environment. *J. Environ. Monit.*, 12(2), 417–424. <https://doi.org/10.1039/B909660D>
- Soleimani, M., Ebrahimi, Z., Mirghaffari, N., Moradi, H., Amini, N., Poulsen, K. G., & Christensen, J. H. (2022). Seasonal trend and source identification of polycyclic aromatic hydrocarbons associated with fine particulate matters (PM<sub>2.5</sub>) in Isfahan City, Iran, using diagnostic ratio and PMF model. *Environ Sci. Pollut. Res.*, 29(18), 26449–26464. <https://doi.org/10.1007/s11356-021-17635-8>
- Sooktaewee, S., Kanabkaew, T., Boonyapitak, S., Patpai, A., & Piemyai, N. (2020). Characterising particulate matter source contributions in the pollution control zone of mining and related industries using bivariate statistical techniques. *Sci. Rep.*, 10(1), 21372. <https://doi.org/10.1038/s41598-020-78445-5>
- Stevanovic, S., Gali, N. K., Salimi, F., Brown, R. A., Ning, Z., Cravigan, L., Brimblecombe, P., Bottle, S., & Ristovski, Z. D. (2019). Diurnal profiles of particle-bound ROS of PM<sub>2.5</sub> in urban environment of Hong Kong and their association with PM<sub>2.5</sub>, black carbon, ozone and PAHs. *Atmos. Environ.*, 219(April), 117023. <https://doi.org/10.1016/j.atmosenv.2019.117023>
- Sun, S., Xia, Z., Wang, T., Wu, M., Zhang, Q., Yin, J., Zhou, Y., Yang, H., Wang, W., Yu, Y., Xu, J., & Chen, C. (2016). Pollution Level, Sources, and Lung Cancer Risk of PM<sub>10</sub>-Bound Polycyclic Aromatic Hydrocarbons (PAHs) in Summer in Nanjing, China. *J. Chem.*, 2016, 1–10. <https://doi.org/10.1155/2016/4546290>
- Taghvaei, S., Sowlat, M. H., Diapouli, E., Manousakas, M. I., Vasilatou, V., Eleftheriadis, K., & Sioutas, C. (2019). Source apportionment of the oxidative potential of fine ambient particulate matter (PM<sub>2.5</sub>) in Athens, Greece. *Sci. Total Environ.*, 653, 1407–1416. <https://doi.org/10.1016/j.scitotenv.2018.11.016>
- Talib Hashem, G., Al-Dawody, M. F., & Sarris, I. E. (2023). The characteristics of gasoline engines with the use of LPG: An experimental and numerical study. *Int. J. Thermofluids*, 18(March), 100316. <https://doi.org/10.1016/j.ijft.2023.100316>
- Tang, Y.-T., Chan, F. K. S., & Griffiths, J. (2015). City profile: Ningbo. *Cities*, 42(PA), 97–108. <https://doi.org/10.1016/j.cities.2014.10.001>
- Thang, P. Q., Kim, S.-J., Lee, S.-J., Ye, J., Seo, Y.-K., Baek, S.-O., & Choi, S.-D. (2019). Seasonal characteristics of particulate polycyclic aromatic hydrocarbons (PAHs) in a petrochemical and oil refinery industrial area on the west coast of South Korea. *Atmos. Environ.*, 198(November 2018), 398–406. <https://doi.org/10.1016/j.atmosenv.2018.11.008>
- Thangavel, P., Park, D., & Lee, Y.-C. (2022). Toxicity of airborne particles—established evidence, knowledge gaps and emerging areas of importance. *Int. J. Environ. Res. Public Health*, 19(12), 7511. <https://doi.org/10.3390/ijerph19127511>



- Tian, M., Wang, H., Chen, Y., Yang, F., Zhang, X., Zou, Q., Zhang, R., Ma, Y., & He, K. (2016). Characteristics of aerosol pollution during heavy haze events in Suzhou, China. *Atmos. Chem. Phys.*, *16*(11), 7357–7371. <https://doi.org/10.5194/acp-16-7357-2016>
- Tian, S., Liu, Y., Wang, J., Wang, J., Hou, L., Lv, B., Wang, X., Zhao, X., Yang, W., Geng, C., Han, B., & Bai, Z. (2020). Chemical compositions and source analysis of PM<sub>2.5</sub> during autumn and winter in a heavily polluted city in China. *Atmosphere*, *11*(4). <https://doi.org/10.3390/atmos11040336>
- Tian, Y., Liu, X., Huo, R., Shi, Z., Sun, Y., Feng, Y., & Harrison, R. M. (2021). Organic compound source profiles of PM<sub>2.5</sub> from traffic emissions, coal combustion, industrial processes and dust. *Chemosphere*, *278*, 130429. <https://doi.org/10.1016/j.chemosphere.2021.130429>
- Tobiszewski, M., & Namieśnik, J. (2012). PAH diagnostic ratios for the identification of pollution emission sources. *Environ. Pollut.*, *162*, 110–119. <https://doi.org/10.1016/j.envpol.2011.10.025>
- Tu, X., Lu, Y., Yao, R., & Zhu, J. (2019). Air quality in Ningbo and transport trajectory characteristics of primary pollutants in autumn and winter. *Atmos*, *10*(3). <https://doi.org/10.3390/atmos10030120>
- US-EPA. (2014). EPA Positive Matrix Factorization (PMF)<sub>5.0</sub> Fundamentals and. *Environmental Protection Agency Office of Research and Development, Publishing House Washington, DC 20460*, 136.
- US. EPA. (2004). Risk assessment guidance for superfund (RAGS). Volume I. Human health evaluation manual (HHEM). Part E. Supplemental guidance for dermal risk assessment. *Us Epa*, *1*(540/R/99/005). <https://doi.org/EPA/540/1-89/002>
- US EPA. (2017). Toxicological Review of Benzo[A]Pyrene (Final Report). *EPA, Washington, DC, EPA/635/R-17/003F*, 1–9. [www.epa.gov/iris/0Ahttps://cfpub.epa.gov/ncea/iris/iris\\_documents/documents/toxreviews/0136tr.pdf](https://www.epa.gov/iris/0Ahttps://cfpub.epa.gov/ncea/iris/iris_documents/documents/toxreviews/0136tr.pdf)
- Utembe, W., & Sanabria, N. (2022). Lung Dosimetry Modelling in Nanotoxicology: A Critical Analysis of the State of the Art. *Environ. Sci. Proc.*, *2*. <https://doi.org/10.3390/ecas2022-12801>
- Veld, M., Pandolfi, M., Amato, F., Pérez, N., Reche, C., Dominutti, P., Jaffrezzo, J., Alastuey, A., Querol, X., & Uzu, G. (2023). Discovering oxidative potential (OP) drivers of atmospheric PM<sub>10</sub>, PM<sub>2.5</sub>, and PM<sub>1</sub> simultaneously in North-Eastern Spain. *Sci. Total Environ.*, *857*(August 2022), 159386. <https://doi.org/10.1016/j.scitotenv.2022.159386>
- Verma, V., Fang, T., Xu, L., Peltier, R. E., Russell, A. G., Ng, N. L., & Weber, R. J. (2015). Organic aerosols associated with the generation of reactive oxygen species (ROS) by water-soluble PM<sub>2.5</sub>. *Environ Sci. Technol.*, *49*(7), 4646–4656. <https://doi.org/10.1021/es505577w>
- Verma, V., Ning, Z., Cho, A. K., Schauer, J. J., Shafer, M. M., & Sioutas, C. (2009). Redox activity of urban quasi-ultrafine particles from primary and secondary sources. *Atmos. Environ.*, *43*(40), 6360–6368. <https://doi.org/10.1016/j.atmosenv.2009.09.019>
- Verma, V., Rico-Martinez, R., Kotra, N., King, L., Liu, J., Snell, T. W., & Weber, R. J. (2012). Contribution of water-soluble and insoluble components and their hydrophobic/hydrophilic subfractions to the reactive oxygen species-generating

- potential of fine ambient aerosols. *Environ. Sci. Pollut. Res.*, *46*(20), 11384–11392. <https://doi.org/10.1021/es302484r>
- Visentin, M., Pagnoni, A., Sarti, E., & Pietrogrande, M. C. (2016). Urban PM<sub>2.5</sub> oxidative potential: Importance of chemical species and comparison of two spectrophotometric cell-free assays. *Environ. Pollut.*, *219*, 72–79. <https://doi.org/10.1016/j.envpol.2016.09.047>
- von Glasow, R., & Sander, R. (2001). Variation of sea salt aerosol pH with relative humidity. *Geophys. Res. Lett.*, *28*(2), 247–250. <https://doi.org/10.1029/2000GL012387>
- Vreeland, H., Weber, R., Bergin, M., Greenwald, R., Golan, R., Russell, A. G., Verma, V., & Sarnat, J. A. (2017). Oxidative potential of PM<sub>2.5</sub> during Atlanta rush hour: Measurements of in-vehicle dithiothreitol (DTT) activity. *Atmos. Environ.*, *165*, 169–178. <https://doi.org/10.1016/j.atmosenv.2017.06.044>
- Wang, G., Kawamura, K., Xie, M., Hu, S., Gao, S., Cao, J., An, Z., & Wang, Z. (2009). Size-distributions of n -hydrocarbons, PAHs and hopanes and their sources in the urban, mountain and marine atmospheres over East Asia. *Atmos. Chem. Phys. Discuss.*, *9*(3), 13859–13888. <https://doi.org/10.5194/acpd-9-13859-2009>
- Wang, Haiting, Ding, J., Xu, J., Wen, J., Han, J., Wang, K., Shi, G., Feng, Y., Ivey, C. E., Wang, Y., Nenes, A., Zhao, Q., & Russell, A. G. (2019). Aerosols in an arid environment: The role of aerosol water content, particulate acidity, precursors, and relative humidity on secondary inorganic aerosols. *Sci. Total Environ.*, *646*, 564–572. <https://doi.org/10.1016/j.scitotenv.2018.07.321>
- Wang, Honglei, Zhu, B., Shen, L., Xu, H., An, J., Xue, G., & Cao, J. (2015). Water-soluble ions in atmospheric aerosols measured in five sites in the Yangtze River Delta, China: Size-fractionated, seasonal variations and sources. *Atmos. Environ.*, *123*, 370–379. <https://doi.org/10.1016/j.atmosenv.2015.05.070>
- Wang, Jialing, Wu, L., Sun, J., Zhang, S., & Zhong, J. (2023). Characteristics of PM<sub>2.5</sub> and secondary inorganic pollution formation during the heating season of 2021 in Beijing. *Front. Environ. Sci.*, *10*(January 2013), 1–13. <https://doi.org/10.3389/fenvs.2022.1028468>
- Wang, Jiaqi, Jiang, H., Jiang, H., Mo, Y., Geng, X., Li, J., Mao, S., Bualert, S., Ma, S., Li, J., & Zhang, G. (2020). Source apportionment of water-soluble oxidative potential in ambient total suspended particulate from Bangkok: Biomass burning versus fossil fuel combustion. *Atmos. Environ.*, *235*(May), 117624. <https://doi.org/10.1016/j.atmosenv.2020.117624>
- Wang, Jingpeng, Lin, X., Lu, L., Wu, Y., Zhang, H., Lv, Q., Liu, W., Zhang, Y., & Zhuang, S. (2019). Temporal variation of oxidative potential of water soluble components of ambient PM<sub>2.5</sub> measured by dithiothreitol (DTT) assay. *Sci. Total Environ.*, *649*, 969–978. <https://doi.org/10.1016/j.scitotenv.2018.08.375>
- Wang, Q., Shao, M., Zhang, Y., Wei, Y., Hu, M., & Guo, S. (2009). Source apportionment of fine organic aerosols in Beijing. *Atmos. Chem. Phys.*, *9*(21), 8573–8585. <https://doi.org/10.5194/acp-9-8573-2009>
- Wang, R., Liu, G., Sun, R., Yousaf, B., Wang, J., Liu, R., & Zhang, H. (2018). Emission characteristics for gaseous- and size-segregated particulate PAHs in coal combustion flue gas from circulating fluidized bed (CFB) boiler. *Environ. Pollut.*, *238*, 581–589.

- <https://doi.org/10.1016/j.envpol.2018.03.051>
- Wang, Shibao, Ji, Y., Zhao, J., Lin, Y., & Lin, Z. (2020). Source apportionment and toxicity assessment of PM<sub>2.5</sub>-bound PAHs in a typical iron-steel industry city in northeast China by PMF-ILCR. *Sci. Total Environ.*, *713*, 136428. <https://doi.org/10.1016/j.scitotenv.2019.136428>
- Wang, Shunyao, Ye, J., Soong, R., Wu, B., Yu, L., Simpson, A. J., & Chan, A. W. H. (2018). Relationship between chemical composition and oxidative potential of secondary organic aerosol from polycyclic aromatic hydrocarbons. *Atmos. Chem. Phys.*, *18*(6), 3987–4003. <https://doi.org/10.5194/acp-18-3987-2018>
- Wang, Wei, Huang, M., Kang, Y., Wang, H., Leung, A. O. W., Cheung, K. C., & Wong, M. H. (2011). Polycyclic aromatic hydrocarbons (PAHs) in urban surface dust of Guangzhou, China: Status, sources and human health risk assessment. *Sci. Total Environ.*, *409*(21), 4519–4527. <https://doi.org/10.1016/j.scitotenv.2011.07.030>
- Wang, Weifeng, Yu, J., Cui, Y., He, J., Xue, P., Cao, W., Ying, H., Gao, W., Yan, Y., Hu, B., Xin, J., Wang, L., Liu, Z., Sun, Y., Ji, D., & Wang, Y. (2018). Characteristics of fine particulate matter and its sources in an industrialized coastal city, Ningbo, Yangtze River Delta, China. *Atmos. Res.*, *203*(December), 105–117. <https://doi.org/10.1016/j.atmosres.2017.11.033>
- Wang, X.-T., Miao, Y., Zhang, Y., Li, Y.-C., Wu, M.-H., & Yu, G. (2013). Polycyclic aromatic hydrocarbons (PAHs) in urban soils of the megacity Shanghai: Occurrence, source apportionment and potential human health risk. *Sci. Total Environ.*, *447*, 80–89. <https://doi.org/10.1016/j.scitotenv.2012.12.086>
- Wang, X., Zong, Z., Tian, C., Chen, Y., Luo, C., Tang, J., Li, J., & Zhang, G. (2018). Assessing on toxic potency of PM<sub>2.5</sub>-bound polycyclic aromatic hydrocarbons at a national atmospheric background site in North China. *Sci. Total Environ.*, *612*, 330–338. <https://doi.org/10.1016/j.scitotenv.2017.08.208>
- Wang, Yixiang, Puthussery, J. V., Yu, H., Liu, Y., Salana, S., & Verma, V. (2022). Sources of cellular oxidative potential of water-soluble fine ambient particulate matter in the Midwestern United States. *J. Hazard. Mater.*, *425*(November 2021), 127777. <https://doi.org/10.1016/j.jhazmat.2021.127777>
- Wang, Yuqin, Wang, M., Li, S., Sun, H., Mu, Z., Zhang, L., Li, Y., & Chen, Q. (2020). Study on the oxidation potential of the water-soluble components of ambient PM<sub>2.5</sub> over Xi'an, China: Pollution levels, source apportionment and transport pathways. *Environ. Int.*, *136*(January), 105515. <https://doi.org/10.1016/j.envint.2020.105515>
- Wang, Yuqin, Zhang, Y., Schauer, J. J., de Foy, B., Cai, T., & Zhang, Y. (2020). Impacts of Sources on PM<sub>2.5</sub> Oxidation Potential during and after the Asia-Pacific Economic Cooperation Conference in Huairou, Beijing. *Environ Sci. Technol.*, *54*(5), 2585–2594. <https://doi.org/10.1021/acs.est.9b05468>
- Weichenthal, S., Shekarrizfard, M., Traub, A., Kulka, R., Al-Rijleh, K., Anowar, S., Evans, G., & Hatzopoulou, M. (2019). Within-City Spatial Variations in Multiple Measures of PM<sub>2.5</sub> Oxidative Potential in Toronto, Canada [Research-article]. *Environ Sci. Technol.*, *53*(5), 2799–2810. <https://doi.org/10.1021/acs.est.8b05543>
- Wen, W., Hua, T., Liu, L., Liu, X., Ma, X., Shen, S., & Deng, Z. (2023). Oxidative Potential Characterization of Different PM<sub>2.5</sub> Sources and Components in Beijing and the

- Surrounding Region. *Int. J. Environ. Res. Public Health*, 20(6), 5109. <https://doi.org/10.3390/ijerph20065109>
- WHO. (2000). Air Quality Guidelines : Polycyclic aromatic hydrocarbons. *Air Quality Guidelines, 1*, 1–24.
- WHO. (2003). Selected nitro-and nitro-oxy-polycyclic aromatic hydrocarbons. *Environ. Health Criteria*, 229(2003), 86.
- Womack, C. C., Chace, W. S., Wang, S., Baasandorj, M., Fibiger, D. L., Franchin, A., Goldberger, L., Harkins, C., Jo, D. S., Lee, B. H., Lin, J. C., McDonald, B. C., McDuffie, E. E., Middlebrook, A. M., Moravek, A., Murphy, J. G., Neuman, J. A., Thornton, J. A., Veres, P. R., & Brown, S. S. (2023). Midlatitude Ozone Depletion and Air Quality Impacts from Industrial Halogen Emissions in the Great Salt Lake Basin. *Environ. Sci. Technol.*, 57(5), 1870–1881. <https://doi.org/10.1021/acs.est.2c05376>
- Wu, N., Lu, B., Chen, J., & Li, X. (2021). Size distributions of particle-generated hydroxyl radical ( $\cdot\text{OH}$ ) in surrogate lung fluid (SLF) solution and their potential sources. *Environ. Pollut.*, 268, 115582. <https://doi.org/10.1016/j.envpol.2020.115582>
- Wu, S.-P., Wang, X.-H., Yan, J.-M., Zhang, M.-M., & Hong, H.-S. (2010). Diurnal Variations of Particle-bound PAHs at a Traffic Site in Xiamen, China. *Aerosol and Air Qual. Res.*, 10(5), 497–506. <https://doi.org/10.4209/aaqr.2010.05.0040>
- Xing, C., Wang, Y., Yang, X., Zeng, Y., Zhai, J., Cai, B., Zhang, A., Fu, T.-M., Zhu, L., Li, Y., Wang, X., & Zhang, Y. (2023). Seasonal variation of driving factors of ambient PM<sub>2.5</sub> oxidative potential in Shenzhen, China. *Sci. Total Environ.*, 862(1088), 160771. <https://doi.org/10.1016/j.scitotenv.2022.160771>
- Xing, X., Chen, Z., Tian, Q., Mao, Y., Liu, W., Shi, M., Cheng, C., Hu, T., Zhu, G., Li, Y., Zheng, H., Zhang, J., Kong, S., & Qi, S. (2020). Characterization and source identification of PM<sub>2.5</sub>-bound polycyclic aromatic hydrocarbons in urban, suburban, and rural ambient air, central China during summer harvest. *Ecotoxicol. Environ. Saf.*, 191(January), 110219. <https://doi.org/10.1016/j.ecoenv.2020.110219>
- Xiong, Q., Yu, H., Wang, R., Wei, J., & Verma, V. (2017). Rethinking Dithiothreitol-Based Particulate Matter Oxidative Potential: Measuring Dithiothreitol Consumption versus Reactive Oxygen Species Generation. *Environ. Sci. Technol.*, 51(11), 6507–6514. <https://doi.org/10.1021/acs.est.7b01272>
- Xu, J.-W., Lin, J., Luo, G., Adeniran, J., & Kong, H. (2023). Foreign emissions exacerbate PM<sub>2.5</sub> pollution in China through nitrate chemistry. *Atmos. Chem. Phys.*, 23(7), 4149–4163. <https://doi.org/10.5194/acp-23-4149-2023>
- Xu, J., He, J., Xu, H., Ji, D., Snape, C., Yu, H., Jia, C., Wang, C., & Gao, J. (2018). Simultaneous measurement of multiple organic tracers in fine aerosols from biomass burning and fungal spores by HPLC-MS/MS. *RSC Advances*, 8(59), 34136–34150. <https://doi.org/10.1039/C8RA04991B>
- Xu, J., Jia, C., He, J., Xu, H., Tang, Y. T., Ji, D., Yu, H., Xiao, H., & Wang, C. (2019). Biomass burning and fungal spores as sources of fine aerosols in Yangtze River Delta, China – Using multiple organic tracers to understand variability, correlations and origins. *Environ. Pollut.*, 251, 155–165. <https://doi.org/10.1016/j.envpol.2019.04.090>
- Xu, J., Jia, C., Yu, H., Xu, H., Ji, D., Wang, C., Xiao, H., & He, J. (2021). Characteristics, sources, and health risks of PM<sub>2.5</sub>-bound trace elements in representative areas of

- Northern Zhejiang Province, China. *Chemosphere*, 272, 129632. <https://doi.org/10.1016/j.chemosphere.2021.129632>
- Xu, J. S., Xu, H. H., Xiao, H., Tong, L., Snape, C. E., Wang, C. J., & He, J. (2016). Aerosol composition and sources during high and low pollution periods in Ningbo, China. *Atmos. Res.*, 178–179, 559–569. <https://doi.org/10.1016/j.atmosres.2016.05.006>
- Yadav, A., Behera, S. N., Nagar, P. K., & Sharma, M. (2020). Spatio-seasonal Concentrations, Source Apportionment and Assessment of Associated Human Health Risks of PM<sub>2.5</sub>-bound Polycyclic Aromatic Hydrocarbons in Delhi, India. *Aerosol and Air Qual. Res.*, 20(12), 2805–2825. <https://doi.org/10.4209/aaqr.2020.04.0182>
- Yan, Y., Zhao, T., Huang, W., Fang, D., Zhang, X., Zhang, L., Huo, P., Xiao, K., Zhang, Y., & Zhang, Y. (2022). The complexation between transition metals and water-soluble organic compounds (WSOC) and its effect on reactive oxygen species (ROS) formation. *Atmos. Environ.*, 287(November 2021), 119247. <https://doi.org/10.1016/j.atmosenv.2022.119247>
- Yang, A., Janssen, N. A. H., Brunekreef, B., Cassee, F. R., Hoek, G., & Gehring, U. (2016). Children's respiratory health and oxidative potential of PM<sub>2.5</sub>: the PIAMA birth cohort study. *Occup Environ Med.*, 73(3), 154–160. <https://doi.org/10.1136/oemed-2015-103175>
- Yang, A., Jedynska, A., Hellack, B., Kooter, I., Hoek, G., Brunekreef, B., Kuhlbusch, T. A. J., Cassee, F. R., & Janssen, N. A. H. (2014). Measurement of the oxidative potential of PM<sub>2.5</sub> and its constituents: The effect of extraction solvent and filter type. *Atmos. Environ.*, 83, 35–42. <https://doi.org/10.1016/j.atmosenv.2013.10.049>
- Yang, B., Zhou, L., Xue, N., Li, F., Li, Y., Vogt, R. D., Cong, X., Yan, Y., & Liu, B. (2013). Source apportionment of polycyclic aromatic hydrocarbons in soils of Huanghuai Plain, China: Comparison of three receptor models. *Sci. Total Environ.*, 443, 31–39. <https://doi.org/10.1016/j.scitotenv.2012.10.094>
- Yang, D., Qi, S., Zhang, Y., Xing, X., Liu, H., Qu, C., Liu, J., & Li, F. (2013). Levels, sources and potential risks of polycyclic aromatic hydrocarbons (PAHs) in multimedia environment along the Jinjiang River mainstream to Quanzhou Bay, China. *Mar. Pollut. Bull.*, 76(1–2), 298–306. <https://doi.org/10.1016/j.marpolbul.2013.08.016>
- Yang, Y., & Zhao, Y. (2019). Quantification and evaluation of atmospheric pollutant emissions from open biomass burning with multiple methods: a case study for the Yangtze River Delta region, China. *Atmos. Chem. Phys.*, 19(1), 327–348. <https://doi.org/10.5194/acp-19-327-2019>
- Yao, Q., Liu, Z., Han, S., Cai, Z., Liu, J., Hao, T., Liu, J., Huang, X., & Wang, Y. (2020). Seasonal variation and secondary formation of size-segregated aerosol water-soluble inorganic ions in a coast megacity of North China Plain. *Environ Sci. Pollut. Res.*, 27(21), 26750–26762. <https://doi.org/10.1007/s11356-020-09052-0>
- Ye, Z., Li, Q., Ma, S., Zhou, Q., Gu, Y., Su, Y., Chen, Y., Chen, H., Wang, J., & Ge, X. (2017). Summertime Day-Night Differences of PM<sub>2.5</sub> Components (Inorganic Ions, OC, EC, WSOC, WSON, HULIS, and PAHs) in Changzhou, China. *Atmos.*, 8(12), 189. <https://doi.org/10.3390/atmos8100189>
- Yin, Z., Ye, X., Jiang, S., Tao, Y., Shi, Y., Yang, X., & Chen, J. (2015). Size-resolved effective density of urban aerosols in Shanghai. *Atmos. Environ.*, 100, 133–140.

- <https://doi.org/10.1016/j.atmosenv.2014.10.055>
- Yu, H., Puthussery, J. V., Wang, Y., & Verma, V. (2021). Spatiotemporal Variability in the Oxidative Potential of Ambient Fine Particulate Matter in Midwestern United States. *Atmos. Chem. Phys.*, *June*, 1–33. <https://doi.org/10.5194/acp-2021-376>
- Yu, H., Wei, J., Cheng, Y., Subedi, K., & Verma, V. (2018). Synergistic and Antagonistic Interactions among the Particulate Matter Components in Generating Reactive Oxygen Species Based on the Dithiothreitol Assay. *Environ Sci. Technol.*, *52*(4), 2261–2270. <https://doi.org/10.1021/acs.est.7b04261>
- Yu, J., Yan, C., Liu, Y., Li, X., Zhou, T., & Zheng, M. (2018). Potassium: A Tracer for Biomass Burning in Beijing? *Aerosol and Air Qual. Res.*, *18*(9), 2447–2459. <https://doi.org/10.4209/aaqr.2017.11.0536>
- Yu, Q., Chen, J., Qin, W., Ahmad, M., Zhang, Y., Sun, Y., Xin, K., & Ai, J. (2022). Oxidative potential associated with water-soluble components of PM<sub>2.5</sub> in Beijing: The important role of anthropogenic organic aerosols. *J. Hazard. Mater.*, *433*(March), 128839. <https://doi.org/10.1016/j.jhazmat.2022.128839>
- Yu, S. Y., Liu, W. J., Xu, Y. S., Yi, K., Zhou, M., Tao, S., & Liu, W. X. (2019). Characteristics and oxidative potential of atmospheric PM<sub>2.5</sub> in Beijing: Source apportionment and seasonal variation. *Sci. Total Environ.*, *650*, 277–287. <https://doi.org/10.1016/j.scitotenv.2018.09.021>
- Yu, Y., Cheng, P., Li, Y., Gu, J., Gong, Y., Han, B., Yang, W., Sun, J., Wu, C., Song, W., & Li, M. (2022). The association of chemical composition particularly the heavy metals with the oxidative potential of ambient PM<sub>2.5</sub> in a megacity (Guangzhou) of southern China. *Environ. Res.*, *213*, 113489. <https://doi.org/10.1016/j.envres.2022.113489>
- Zaveri, R. A., Berkowitz, C. M., Brechtel, F. J., Gilles, M. K., Hubbe, J. M., Jayne, J. T., Kleinman, L. I., Laskin, A., Madronich, S., Onasch, T. B., Pekour, M. S., Springston, S. R., Thornton, J. A., Tivanski, A. V., & Worsnop, D. R. (2010). Nighttime chemical evolution of aerosol and trace gases in a power plant plume: Implications for secondary organic nitrate and organosulfate aerosol formation, NO<sub>3</sub> radical chemistry, and N<sub>2</sub>O<sub>5</sub> heterogeneous hydrolysis. *J. Geophys. Res.*, *115*(12), 1–22. <https://doi.org/10.1029/2009JD013250>
- Zdráhal, Z., Oliveira, J., Vermeylen, R., Claeys, M., & Maenhaut, W. (2002). Improved method for quantifying levoglucosan and related monosaccharide anhydrides in atmospheric aerosols and application to samples from urban and tropical locations. *Environ Sci. Technol.*, *36*(4), 747–753. <https://doi.org/10.1021/es015619v>
- Zhai, M., Kuang, Y., Liu, L., He, Y., Luo, B., Xu, W., Tao, J., Zou, Y., Li, F., Yin, C., Li, C., Xu, H., & Deng, X. (2023). Insights into characteristics and formation mechanisms of secondary organic aerosols in the Guangzhou urban area. *Atmos. Chem. Phys.*, *23*(9), 5119–5133. <https://doi.org/10.5194/acp-23-5119-2023>
- Zhan, Y., Xie, M., Zhao, W., Wang, T., Gao, D., Chen, P., Tian, J., Zhu, K., Li, S., Zhuang, B., Li, M., Luo, Y., & Zhao, R. (2023). Quantifying the seasonal variations in and regional transport of PM<sub>2.5</sub> in the Yangtze River Delta region, China: characteristics, sources, and health risks. *Atmos. Chem. Phys.*, *23*(17), 9837–9852. <https://doi.org/10.5194/acp-23-9837-2023>
- Zhang, Libo, Liu, Y., & Hao, L. (2016). Contributions of open crop straw burning emissions

- to PM 2.5 concentrations in China. *Environ. Res. Lett.*, 11(1), 014014. <https://doi.org/10.1088/1748-9326/11/1/014014>
- Zhang, Lulu, Yang, L., Zhou, Q., Zhang, X., Xing, W., Wei, Y., Hu, M., Zhao, L., Toriba, A., Hayakawa, K., & Tang, N. (2020). Size distribution of particulate polycyclic aromatic hydrocarbons in fresh combustion smoke and ambient air: A review. *J. Environ. Sci.*, 88, 370–384. <https://doi.org/10.1016/j.jes.2019.09.007>
- Zhang, Xian, Staimer, N., Tjoa, T., Gillen, D. L., Schauer, J. J., Shafer, M. M., Hasheminassab, S., Pakbin, P., Longhurst, J., Sioutas, C., & Delfino, R. J. (2016). Associations between microvascular function and short-term exposure to traffic-related air pollution and particulate matter oxidative potential. *Environ. Health*, 15(1), 81. <https://doi.org/10.1186/s12940-016-0157-5>
- Zhang, Xiaoping, Lin, M., Wang, Z., & Jin, F. (2021). The impact of energy-intensive industries on air quality in China's industrial agglomerations. *J. Geogr. Sci.*, 31(4), 584–602. <https://doi.org/10.1007/s11442-021-1860-x>
- Zhang, Yangyang, Tang, A., Wang, C., Ma, X., Li, Y., Xu, W., Xia, X., Zheng, A., Li, W., Fang, Z., Zhao, X., Peng, X., Zhang, Y., Han, J., Zhang, L., Collett, J. L., & Liu, X. (2022). PM2.5 and water-soluble inorganic ion concentrations decreased faster in urban than rural areas in China. *J. Environ. Sci.*, 122, 83–91. <https://doi.org/10.1016/j.jes.2021.09.031>
- Zhang, Yanxu, Tao, S., Shen, H., & Ma, J. (2009). Inhalation exposure to ambient polycyclic aromatic hydrocarbons and lung cancer risk of Chinese population. *PANS*, 106(50), 21063–21067. <https://doi.org/10.1073/pnas.0905756106>
- Zhang, Yuan, Zheng, H., Zhang, L., Zhang, Z., Xing, X., & Qi, S. (2019). Fine particle-bound polycyclic aromatic hydrocarbons (PAHs) at an urban site of Wuhan, central China: Characteristics, potential sources and cancer risks apportionment. *Environ. Pollut.*, 246, 319–327. <https://doi.org/10.1016/j.envpol.2018.11.111>
- Zhao, B., Su, Y., He, S., Zhong, M., & Cui, G. (2016). Evolution and comparative assessment of ambient air quality standards in China. *J. Integr. Environ. Sci.*, 13(2–4), 1–18. <https://doi.org/10.1080/1943815X.2016.1150301>
- Zhao, H., Zhang, X., Zhang, S., Chen, W., Tong, D., & Xiu, A. (2017). Effects of Agricultural Biomass Burning on Regional Haze in China: A Review. *Atmosphere*, 8(5), 88. <https://doi.org/10.3390/atmos8050088>
- Zheng, K., Zeng, Z., Tian, Q., Huang, J., Zhong, Q., & Huo, X. (2023). Epidemiological evidence for the effect of environmental heavy metal exposure on the immune system in children. *Sci. Total Environ.*, 868(December 2022), 161691. <https://doi.org/10.1016/j.scitotenv.2023.161691>
- Zhou, S., Zhu, Q., Liu, H., Jiang, S., Zhang, X., Peng, C., Yang, G., Li, J., Cheng, L., Zhong, R., Zeng, Q., Miao, X., & Lu, Q. (2021). Associations of polycyclic aromatic hydrocarbons exposure and its interaction with XRCC1 genetic polymorphism with lung cancer: A case-control study. *Environ. Pollut.*, 290(May), 118077. <https://doi.org/10.1016/j.envpol.2021.118077>
- Zhou, Y., Xue, L., Wang, T., Gao, X., Wang, Z., Wang, X., Zhang, J., Zhang, Q., & Wang, W. (2012). Characterization of aerosol acidity at a high mountain site in central eastern China. *Atmos. Environ.*, 51, 11–20. <https://doi.org/10.1016/j.atmosenv.2012.01.061>

- Zhu, C., Li, J., Liu, Z., Wang, J., & Chen, J. (2022). Polycyclic aromatic hydrocarbons (PAHs) in gas, PM<sub>2.5</sub>, and frost samples in a severely polluted rural site of the North China Plain: Distribution, source, and risk assessment. *Sci. Total Environ.*, 844(January), 156919. <https://doi.org/https://doi.org/10.53941/ijamm020100>
- Zong, Z., Wang, X., Tian, C., Chen, Y., Fu, S., Qu, L., Ji, L., Li, J., & Zhang, G. (2018). PMF and PSCF based source apportionment of PM<sub>2.5</sub> at a regional background site in North China. *Atmos. Res.*, 203(December 2017), 207–215. <https://doi.org/10.1016/j.atmosres.2017.12.013>



## Appendices

Table 8.1 Chemical structures of 20 PAHs investigated in this study

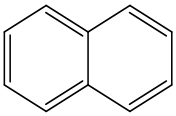
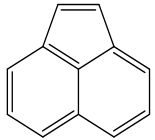
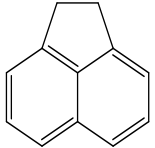
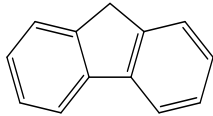
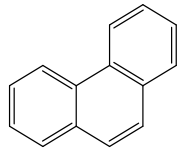
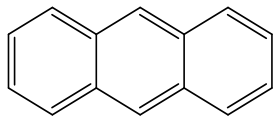
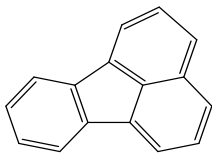
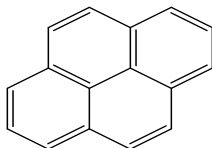
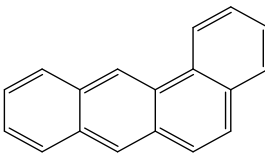
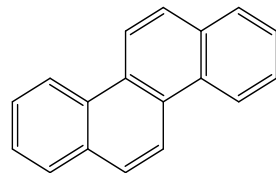
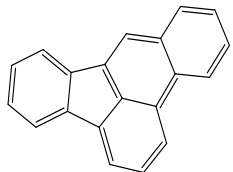
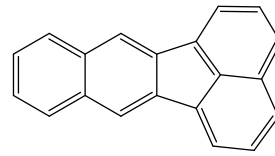
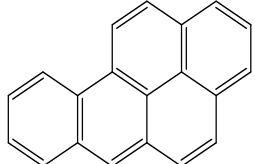
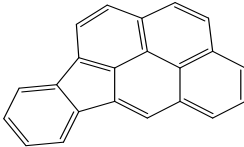
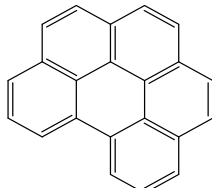
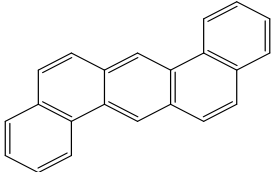
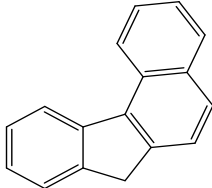
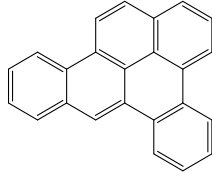
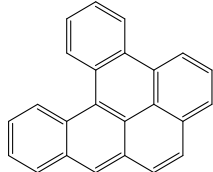
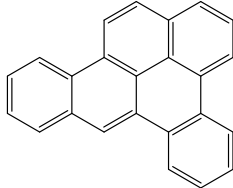
<b>Naphthalene (NaP)</b>	<b>Acenaphthylene (Acy)</b>	<b>Acenaphthene (Ace)</b>	<b>Fluorene (Flu)</b>	<b>Phenanthrene (Phe)</b>
				
<b>Anthracene (Ant)</b>	<b>Fluoranthene (Flt)</b>	<b>Pyrene (Pyr)</b>	<b>Benz[a]anthracene (BaA)</b>	<b>Chrysene (Chr)</b>
				
<b>Benzo[b]fluoranthene (BbF)</b>	<b>Benzo[k]fluoranthene (BkF)</b>	<b>Benzo[a]pyrene (BaP)</b>	<b>Indeno[1,2,3-c,d]pyrene (IPyr)</b>	<b>Benzo[g,h,i]perylene (BghiP)</b>
				
<b>Dibenz[a,h]anthracene (DahA)</b>	<b>7H-benzo[c]fluorene (7H-BcF)</b>	<b>Dibenzo[a,h]pyrene (DBahPyr)</b>	<b>Dibenzo[a,l]pyrene (DBalPyr)</b>	<b>Dibenzo[a,e]pyrene (DBaePyr)</b>
				

Table 8.2 BS Mapping of five factors for source apportionment of PAHs

	NGC	CC	VE	BB	VUP	Unmapped
Boot Factor 1	97	1	1	0	1	0
Boot Factor 2	0	98	1	1	0	0
Boot Factor 3	1	2	95	1	1	0
Boot Factor 4	1	0	3	99	0	0
Boot Factor 5	0	2	0	1	97	0

Table 8.3 Summary of MLR model for source apportionment to PAH mass concentration and LECR

	R <sup>2</sup>	Adjusted R <sup>2</sup>	Standard Error
C-16	0.964	0.930	1.389
C-20	0.963	0.927	1.481
LECR-16	0.804	0.796	0.213
LECR-20	0.884	0.782	1.055

C-16: mass concentration of 16 PAHs, C-20: mass concentration of 20 PAHs,

LECR-16: Lifetime excess cancer risk of 16 PAHs, LECR-20: Lifetime excess cancer risk of 20 PAHs

Table 8.4 Summary of regression coefficients of sources contribution to PAH mass concentration and LECR

	NGC	CC	VE	BB	VUP
C-16	0.85	0.66	0.61	0.56	0.31
C-20	0.86	0.66	0.63	0.57	0.35
LECR-16	0.80	0.48	0.66	0.40	0.27
LECR-20	0.81	0.54	0.55	0.56	0.26

C-16: mass concentration of 16 PAHs, C-20: mass concentration of 20 PAHs,

LECR-16: Lifetime excess cancer risk of 16 PAHs, LECR-20: Lifetime excess cancer risk of 20 PAHs, p-value ≤0.05 indicates that all sources contribute to LECR and were considered in MLR

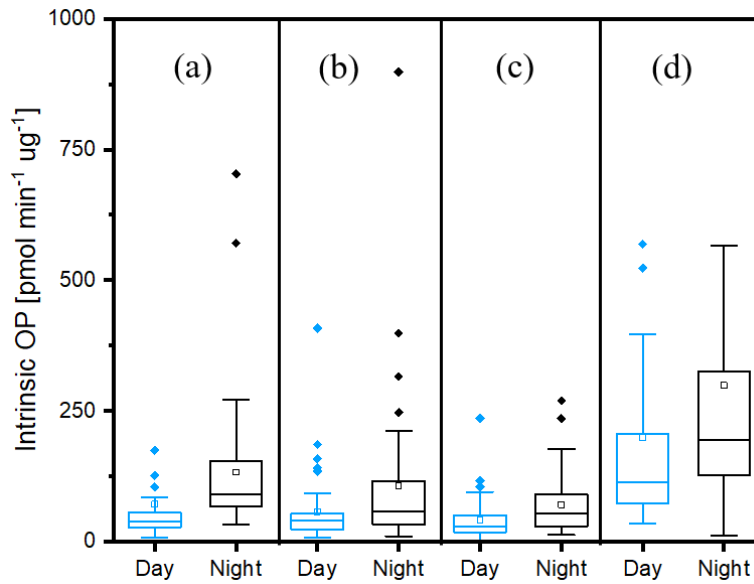


Figure 8-1 Day and night intrinsic OP of water (a, b) and methanol (c, d)-soluble fraction of PM<sub>2.5</sub> measured in DTT (a, c) and AA (b, d) assays. Median (line across the box), mean (square within the box), first quartile (Q1) (bottom of the box), third quartile (Q3) (top of the box), outlier (square shown outside the box), whiskers shows minimum and maximum values















Table 8.11 Summary of correlation coefficients of source contribution DTTv (nmol min<sup>-1</sup>m<sup>-3</sup>) induced by water-soluble fraction of PM<sub>2.5</sub>

Sources	Unstandardized		Standardized		Source contribution (nmol min <sup>-1</sup> m <sup>-3</sup> )	
	Day	Night	Day	Night	Day	Night
IE	0.05	-0.02	0.37	-0.20	0.066	0.057
BB	0.03	0.01	0.19	0.09	0.033	0.026
SA	0.01	-0.02	0.17	-0.33	0.029	0.093
ME	0.05	-0.04	0.39	-0.44	0.069	0.124
VE	0.01	0.01	0.08	0.04	0.014	0.012
RD	0.03	-0.03	0.22	-0.27	0.039	0.079

Daytime:  $r^2 = 0.82$ , adjusted  $r^2 = 0.79$ ,  $p \leq 0.05$ , Nighttime:  $r^2 = 0.75$ , adjusted ( $r^2$ ) = 0.71,  $p \leq 0.05$

Table 8.12 BS Mapping of six factors for source apportionment of PM<sub>2.5</sub>

	IE	BB	SA	ME	VE	RD	Unmapped
Boot Factor 1	145	2	1	2	0	0	0
Boot Factor 2	0	148	1	0	0	1	0
Boot Factor 3	1	0	148	0	0	0	0
Boot Factor 4	0	0	0	149	1	0	0
Boot Factor 5	1	0	0	0	146	0	0
Boot Factor 6	0	1	0	0	1	148	0

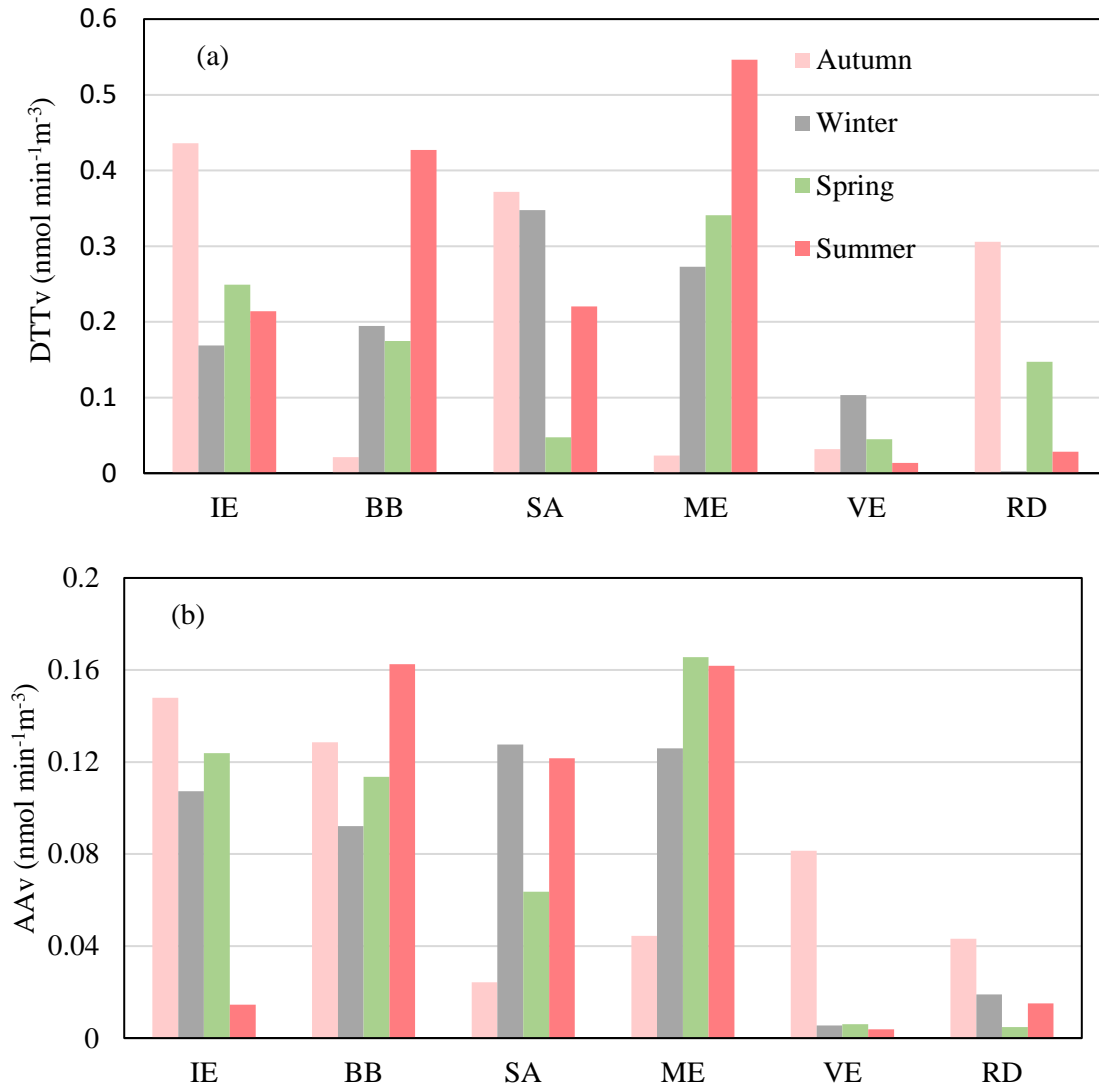


Figure 8:2 Seasonal source contributions to the extrinsic OP of PM<sub>2.5</sub> induced by water-soluble fractions : (a) DTTv, (b) AAv

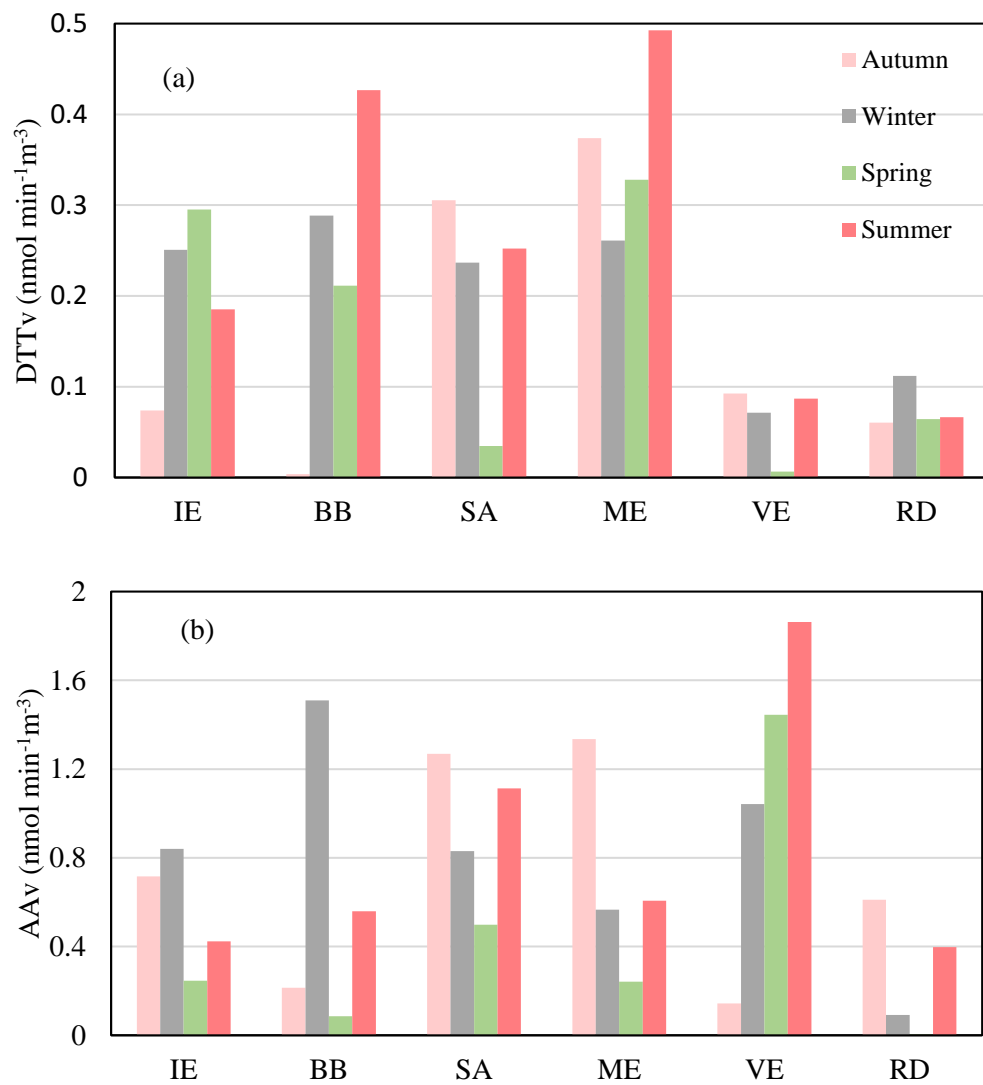


Figure 8:3 Seasonal source contributions to the extrinsic OP of PM<sub>2.5</sub> induced by methanol-soluble fractions : (a) DTT<sub>v</sub>, (b) AA<sub>v</sub>

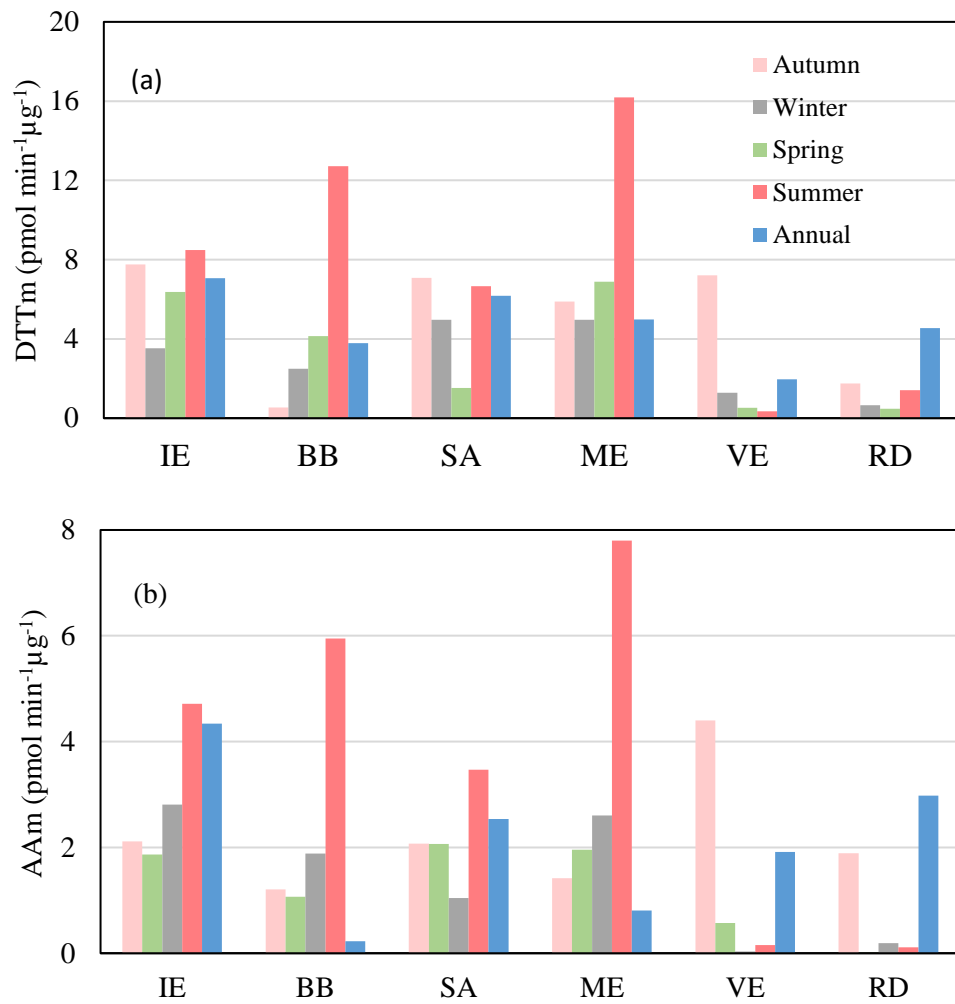


Figure 8-4 Seasonal source contributions to the intrinsic OP induced water-soluble fractions of PM<sub>2.5</sub>: (a) DTTm, (b) AAm

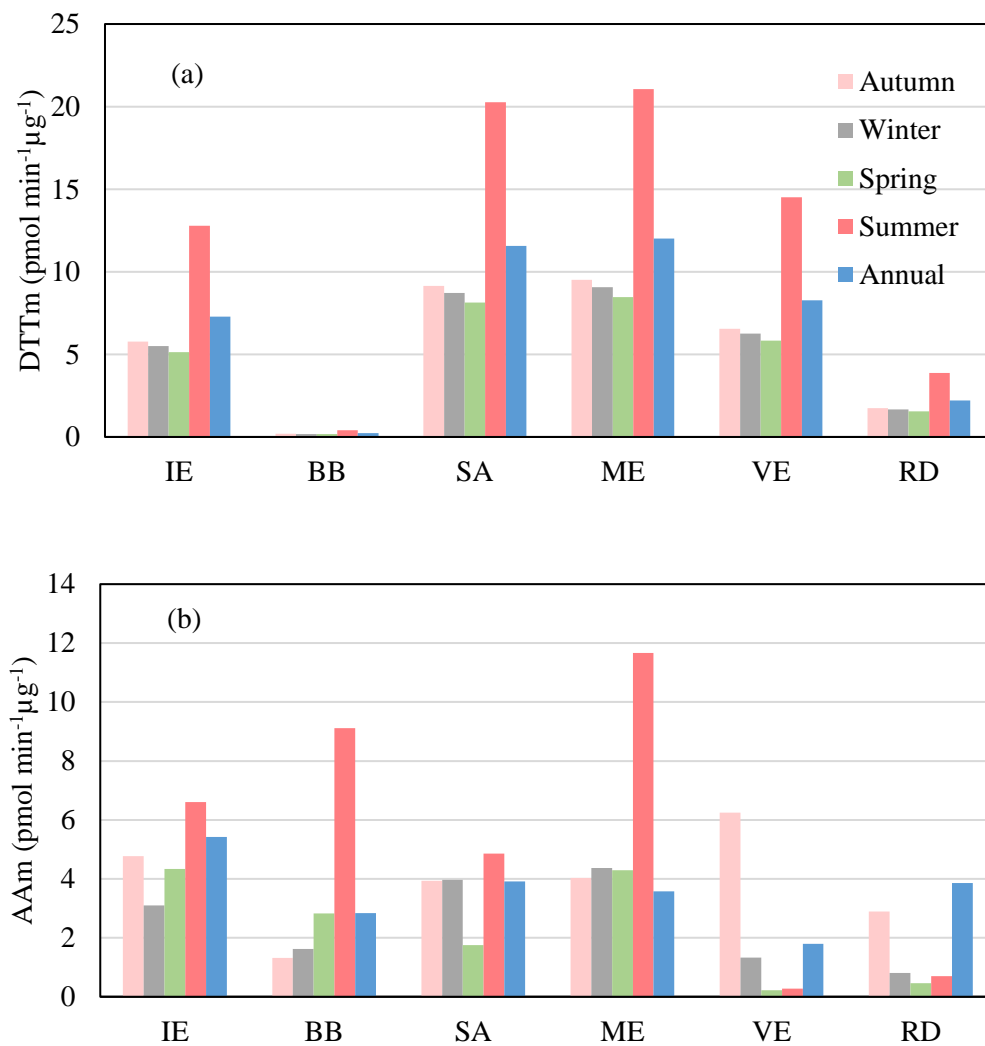


Figure 8-5 Seasonal source contributions to the intrinsic OP induced by methanol-soluble fractions of PM<sub>2.5</sub>: (a) DTTm, (b) AAm

Table 8.13 Intrinsic OP induced by water-soluble PM size fractions in DTT and AA assays

Dp ( $\mu\text{m}$ )	DTTm			AAm		
	Winter	Summer	Average	Winter	Summer	Average
$\leq 0.49$	14.9	$\pm 79.0$	$\pm 46.9$	4.27	$\pm 29.9$	$\pm 17.1$
	5.58	46.3	45.9	3.02	23.2	20.9
0.49–0.95	9.61	$\pm 18.9$	$\pm 14.3$	1.80	$\pm 11.1$	$\pm 6.45$
	6.81	9.79	9.56	0.97	9.12	7.93
0.95–1.5	11.7	$\pm 34.4$	$\pm 23.0$	0.96	$\pm 12.5$	$\pm 6.72$
	7.19	22.3	19.9	0.61	9.56	8.87
1.5–3	13.5	$\pm 27.2$	$\pm 20.4$	1.06	$\pm 10.5$	$\pm 5.75$
	8.80	20.9	17.1	0.64	6.74	6.71
3–7.2	7.85	$\pm 18.9$	$\pm 13.4$	1.15	$\pm 18.9$	$\pm 14.1$
	3.54	16.5	10.0	0.71	13.3	12.9
$\geq 7.2$	36.7	$\pm 42.3$	$\pm 39.5$	8.99	$\pm 28.7$	$\pm 18.9$
	19.9	22.0	20.8	5.78	23.1	19.3

DTTm, AAm:  $\text{pmol min}^{-1}\mu\text{g}^{-1}$

Table 8.14 Intrinsic OP induced by methanol-soluble PM size fractions in DTT and AA assays

Dp (μm)	DTTm			AAm		
	Winter	Summer	Average	Winter	Summer	Average
≤ 0.49	14.3 ±	57.8 ±	36.0 ±	27.2 ±	176.6 ±	101.9 ±
	9.45	49.2	41.2	14.9	122.5	114.6
0.49–0.95	12.4 ±	38.9 ±	25.7 ±	17.1 ±	37.6 ±	27.4 ±
	9.16	70.0	50.9	17.5	22.6	22.4
0.95–1.5	11.9 ±	29.4 ±	20.7 ±	12.9 ±	54.2 ±	33.6 ±
	7.81	21.1	17.9	10.9	37.5	34.3
1.5–3	15.0 ±	24.1 ±	19.5 ±	21.3 ±	39.1 ±	30.2 ±
	10.9	24.7	19.3	16.3	24.8	22.5
3–7.2	8.86 ±	50.3 ±	29.6 ±	27.1 ±	24.5 ±	25.8 ±
	7.62	63.4	43.9	21.8	15.5	18.6
≥7.2	32.2 ±	42.9 ±	37.5 ±	98.7 ±	145.7 ±	117.7 ±
	18.6	27.2	23.5	53.9	82.6	74.2

DTTm, AAm: pmol min<sup>-1</sup>μg<sup>-1</sup>



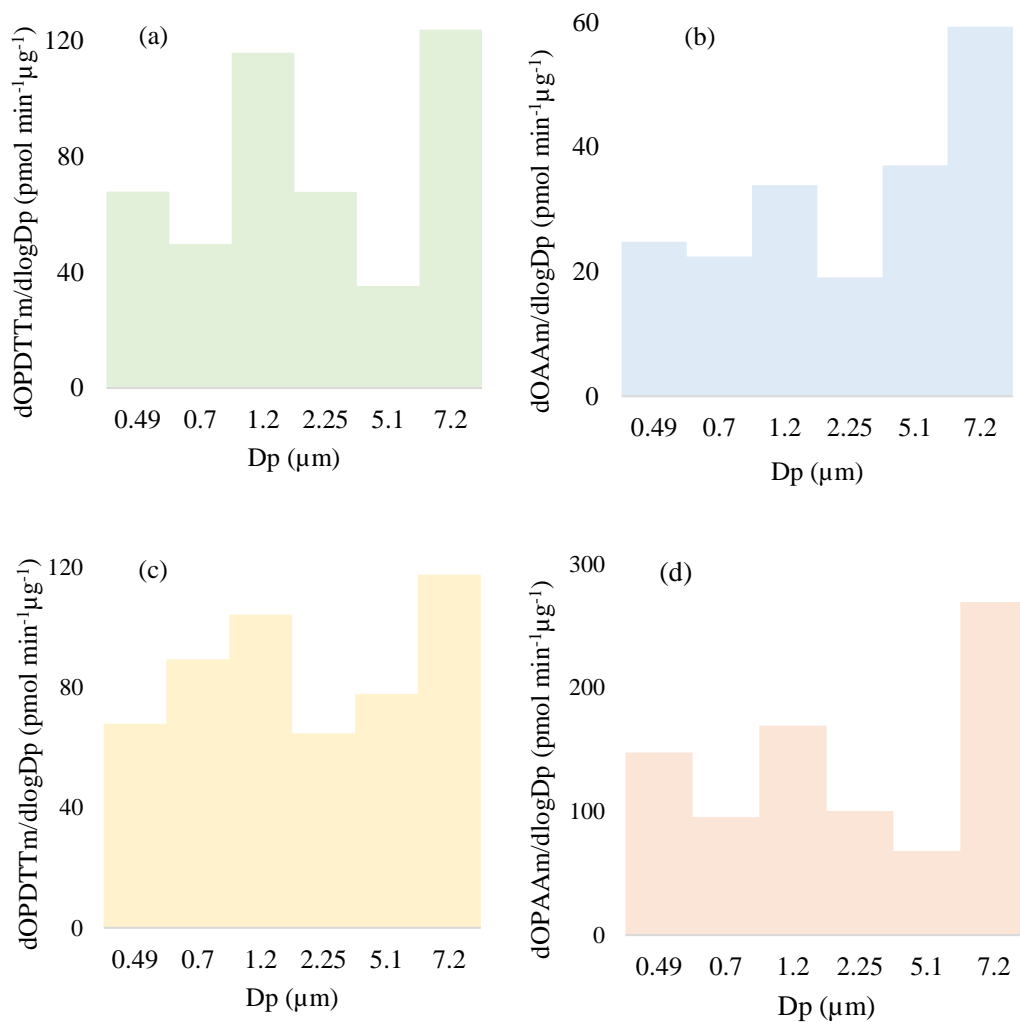


Figure 8-6 Size distribution of intrinsic OP ( $d\text{OP} = \text{mean extrinsic OP (pmol min}^{-1} \mu\text{g}^{-1})$ ,  $d\log D_p = \text{logarithmic difference of aerodynamic diameter, } D_p, \mu\text{m}$ ) of water (a, b) and methanol (c, d): DTT (a, c), AA (b, d) assays



Table 8.16 Pearson's correlation (r) between OP induced by methanol-soluble fraction of 0.49–0.95 μm particles and chemical compositions

	DTTv	DTTm	AAv	AAm	PM <sub>0.49-0.95</sub>	Cu	Pb	Fe	Mn	V	Cr	Zn	Co	Ni	As	NaP	Acy	Ace	Flu	Phe	Ant	Flt	Pyr	7H-BcF	BaA	Chr	BbF	BkF	BaP	InPyr	DBahA	BghIP	DBahPyr	DBalPyr	DBaePyr	1,4-NQ	1,2-NQ	1,4-AQ	O3	Temp	RH									
DTTv	1																																																	
DTTm	-0.22	1																																																
AAv	0.14	0.43	1																																															
AAm	-0.29	0.92**	0.68*	1																																														
PM <sub>0.49-0.95</sub>	0.34	-0.86	-0.03	-0.67	1																																													
Cu	-0.13	-0.64	-0.06	-0.51	0.65*	1																																												
Pb	0.13	-0.6	0.28	-0.38	0.72**	0.8**	1																																											
Fe	0.27	-0.43	0.38	-0.26	0.53*	0.77**	0.82**	1																																										
Mn	0.11	-0.46	0	-0.38	0.28	0.45	0.7**	0.59*	1																																									
V	-0.02	-0.72	-0.03	-0.5	0.84**	0.71**	0.58*	0.5*	0.17	1																																								
Cr	0.11	-0.66	0.16	-0.48	0.69*	0.83**	0.98**	0.82**	0.77**	0.6*	1																																							
Zn	-0.15	-0.47	-0.17	-0.4	0.2	0.54*	0.61*	0.52*	0.93**	0.2	0.69*	1																																						
Co	0.16	-0.69	0.12	-0.51	0.84**	0.8**	0.91**	0.73**	0.51*	0.68*	0.89**	0.41	1																																					
Ni	0.06	-0.34	-0.08	-0.3	0.59*	0.45	0.18	0.17	-0.46	0.61*	0.13	-0.46	0.48	1																																				
As	0.19	-0.58	0.23	-0.4	0.74**	0.83**	0.96**	0.78**	0.59*	0.6*	0.93**	0.5*	0.91**	0.32	1																																			
NaP	0.78**	-0.16	0.03	-0.23	0.12	-0.28	-0.04	0.04	0.08	-0.28	-0.06	-0.06	-0.15	-0.26	-0.03	1																																		
Acy	0.27	-0.63	0.07	-0.5	0.77**	0.82**	0.67*	0.79**	0.19	0.7**	0.65*	0.17	0.8**	0.69*	0.73**	-0.03	1																																	
Ace	0.09	-0.42	-0.26	-0.43	0.32	0.38	0.54*	0.25	0.6*	-0.03	0.53*	0.55*	0.57*	-0.05	0.57*	0.06	0.24	1																																
Flu	0.36	-0.55	0.22	-0.4	0.65*	0.53*	0.86**	0.61*	0.62*	0.26	0.8**	0.47	0.78**	0.07	0.84**	0.34	0.52*	0.72**	1																															
Phe	0.34	-0.26	-0.29	-0.35	0.05	-0.05	0.17	0	0.47	-0.4	0.16	0.42	0.1	-0.41	0.16	0.58*	-0.08	0.77**	0.56*	1																														
Ant	0.51*	-0.27	0.12	-0.2	0.37	-0.02	0.09	0.06	-0.21	0.05	-0.01	-0.24	0.02	0.16	0.14	0.79**	0.22	-0.02	0.39	0.34	1																													
Flt	0.23	0.4	0.81**	0.54*	-0.17	0.02	0.24	0.54*	0.27	-0.04	0.21	0.12	0.02	-0.31	0.19	0.04	0.07	-0.29	0.06	-0.28	-0.13	1																												
Pyr	0.15	-0.31	-0.29	-0.35	0.07	0.01	0.26	-0.03	0.56*	-0.32	0.25	0.54*	0.13	-0.48	0.22	0.47	-0.16	0.78**	0.59*	0.96**	0.29	-0.32	1																											
7H-BcF	0.13	-0.35	-0.26	-0.37	0.13	0.05	0.31	-0.01	0.56*	-0.26	0.3	0.54*	0.17	-0.46	0.25	0.48	-0.14	0.75**	0.63*	0.93**	0.34	-0.33	0.99**	1																										
BaA	0.09	-0.38	-0.24	-0.38	0.16	0.13	0.39	0.06	0.65*	-0.19	0.39	0.64*	0.22	-0.48	0.33	0.42	-0.11	0.77**	0.66*	0.89**	0.27	-0.27	0.98**	0.99**	1																									
Chr	-0.06	-0.32	-0.16	-0.3	0.13	0.32	0.55*	0.27	0.83**	-0.09	0.57*	0.8**	0.44	-0.42	0.49	0.01	0.02	0.89**	0.64*	0.73**	-0.19	-0.07	0.81**	0.79**	0.85**	1																								
BbF	0.38	-0.23	-0.31	-0.36	-0.02	0.11	-0.08	0.27	0.17	-0.18	-0.04	0.26	-0.1	-0.16	-0.06	0.56*	0.28	0.18	0.1	0.52*	0.38	-0.04	0.36	0.31	0.28	0.12	1																							
BkF	0.1	-0.47	-0.24	-0.45	0.21	0.27	0.46	0.24	0.72**	-0.1	0.48	0.75**	0.28	-0.46	0.39	0.43	0.04	0.74**	0.68*	0.86**	0.29	-0.19	0.94**	0.95**	0.97**	0.83**	0.43	1																						
BaP	0.03	-0.46	-0.26	-0.43	0.18	0.26	0.46	0.21	0.75**	-0.09	0.48	0.78**	0.27	-0.51	0.37	0.35	-0.02	0.73**	0.64*	0.83**	0.21	-0.2	0.93**	0.94**	0.97**	0.86**	0.36	0.99**	1																					
InPyr	0.02	-0.51	-0.24	-0.47	0.25	0.37	0.54*	0.31	0.79**	0	0.56*	0.83**	0.34	-0.45	0.46	0.32	0.08	0.73**	0.68*	0.79**	0.2	-0.16	0.89**	0.9**	0.94**	0.86**	0.38	0.99**	0.99**	1																				
DBahA	0.31	-0.32	-0.31	-0.39	0.01	-0.01	0.11	0.11	0.5*	-0.31	0.13	0.54*	-0.05	-0.54	0.05	0.68*	-0.06	0.49	0.41	0.88**	0.42	-0.15	0.85**	0.83**	0.81**	0.56*	0.75**	0.87**	0.84**	0.81**	1																			
BghIP	0.01	-0.51	-0.23	-0.46	0.25	0.37	0.55*	0.31	0.8**	0.01	0.57*	0.84**	0.35	-0.46	0.46	0.3	0.07	0.72**	0.67*	0.77**	0.18	-0.14	0.88**	0.89**	0.94**	0.86**	0.36	0.98**	0.99**	0.89**	0.8**	1																		
DBahPyr	-0.25	-0.33	-0.41	-0.34	0.02	0.18	0.27	-0.07	0.57*	-0.17	0.29	0.68*	0.1	-0.48	0.21	0.16	-0.21	0.69*	0.44	0.75**	0.1	-0.4	0.9**	0.9**	0.93**	0.81**	0.22	0.91**	0.93**	0.91**	0.72**	0.91**	1																	
DBalPyr	0.4	-0.29	-0.28	-0.39	0.23	0.13	0.05	0.07	-0.09	-0.19	-0.01	-0.07	0.14	0.23	0.15	0.58*	0.35	0.48	0.43	0.68*	0.66	-0.42	0.53*	0.52*	0.43	0.18	0.68**	0.46	0.37	0.36	0.6*	0.33	0.31	1																
DBaePyr	-0.24	-0.51	-0.19	-0.42	0.36	0.62*	0.73	0.38	0.77**	0.23	0.74**	0.81**	0.62*	-0.15	0.69*	-0.16	0.24	0.83**	0.69*	0.52*	-0.13	-0.17	0.67**	0.68*	0.76**	0.91**	0	0.77**	0.8**	0.84**	0.39	0.84**	0.79**	0.14	1															
1,4-NQ	-0.33	0.44	0.07	0.33	-0.52	-0.21	-0.02	-0.16	0.29	-0.51	0.02	0.21	-0.09	-0.45	-0.11	-0.4	-0.47	0.26	-0.04	0.07	-0.71	0.13	0.14	0.11	0.14	0.43	-0.41	0.04	0.1	0.06	-0.14	0.07	0.18	-0.4	0.26	1														
1,2-NQ	-0.11	-0.14	-0.35	-0.18	0.02	-0.34	-0.23	-0.47	0.07	0.17	-0.14	0.02	-0.16	-0.16	-0.3	-0.23	-0.45	-0.18	-0.35	-0.21	-0.43	-0.25	-0.11	-0.11	-0.08	-0.04	-0.5	-0.18	-0.1	-0.14	-0.25	-0.12	-0.01	-0.62	-0.07	0.22	1													
1,4-AQ	0.33	0.06	-0.45	-0.19	-0.15	-0.13	-0.38	-0.19	-0.28	-0.33	-0.39	-0.25	-0.19	0.2	-0.21	0.28	0.12	0.27	-0.14	0.42	0.18	-0.33	0.19	0.1	0.03	-0.02	0.63*	0.04	-0.03	-0.05	0.31	-0.08	0	0.71	-0.17	-0.24	-0.35	1												
O <sub>3</sub>	0.04	-0.26	0.3	0.01	0.43	0.32	0.44	0.41	0.37	0.6*	0.39	0.33	0.41	0.06	0.45	-0.2	0.3	0.08	0.19	-0.15	-0.11	0.4	-0.12	-0.11	-0.02	0.17	-0.13	0.02	0.05	0.1	-0.12	0.12																		









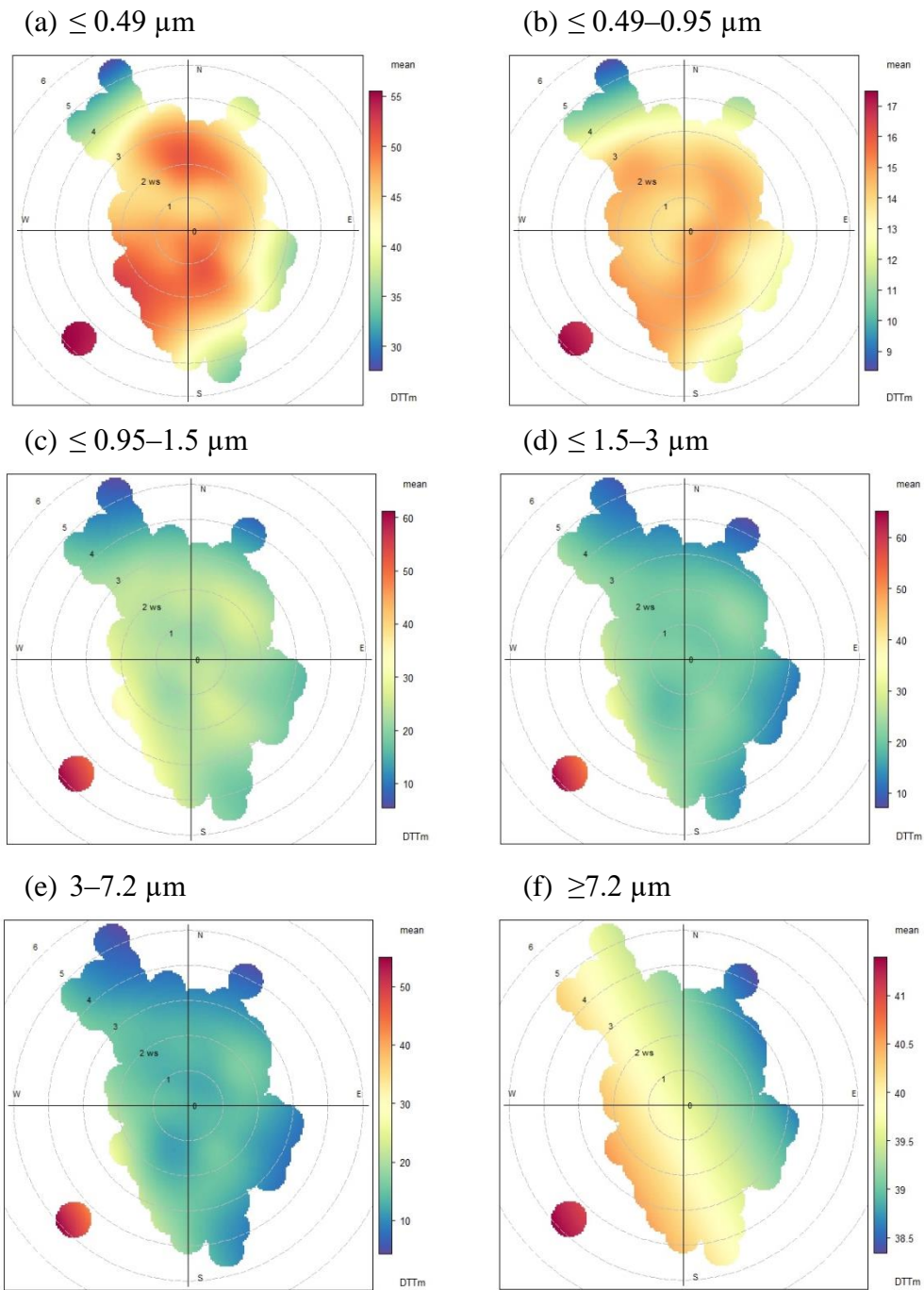
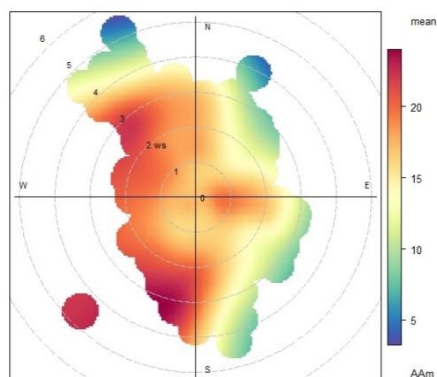


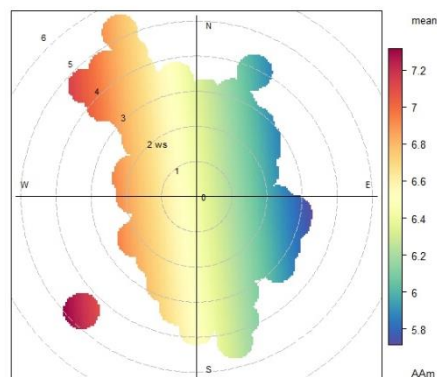
Figure 8-7 Bivariate polar plots of size-resolved concentration of DTTm ( $\text{nmol min}^{-1}\mu\text{g}^{-1}$ ) induced by water-soluble fractions: ultrafine (a, b), accumulation (c, d), coarse (e, f) particles



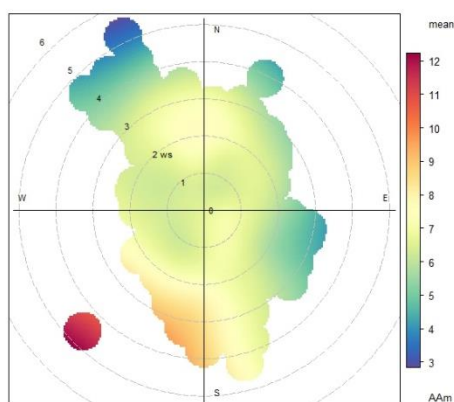
(a)  $\leq 0.49 \mu\text{m}$



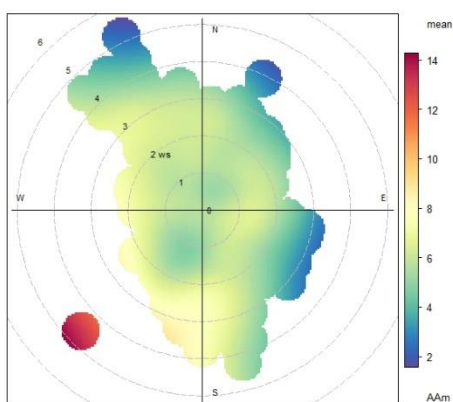
(b)  $\leq 0.49\text{--}0.95 \mu\text{m}$



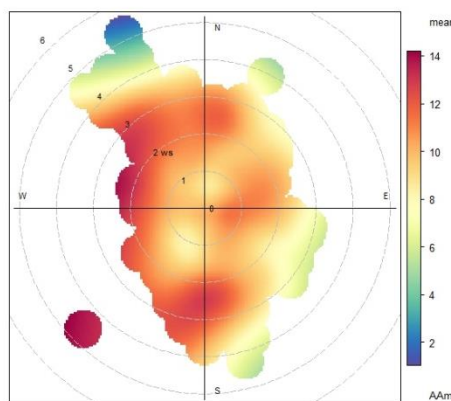
(c)  $\leq 0.95\text{--}1.5 \mu\text{m}$



(d)  $\leq 1.5\text{--}3 \mu\text{m}$



(e)  $3\text{--}7.2 \mu\text{m}$



(f)  $\geq 7.2 \mu\text{m}$

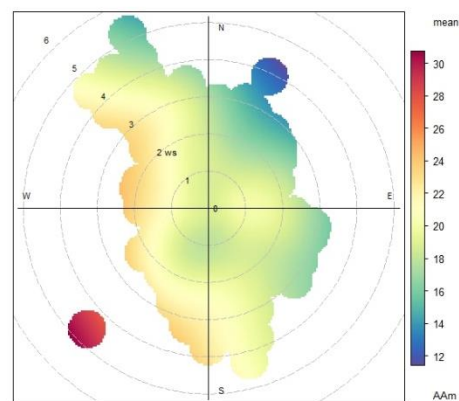


Figure 8-8 Bivariate polar plots of size-resolved concentration of AAm ( $\text{nmol min}^{-1} \mu\text{g}^{-1}$ ) induced by water-soluble fractions: ultrafine (a, b), accumulation (c, d), coarse (e, f) particles

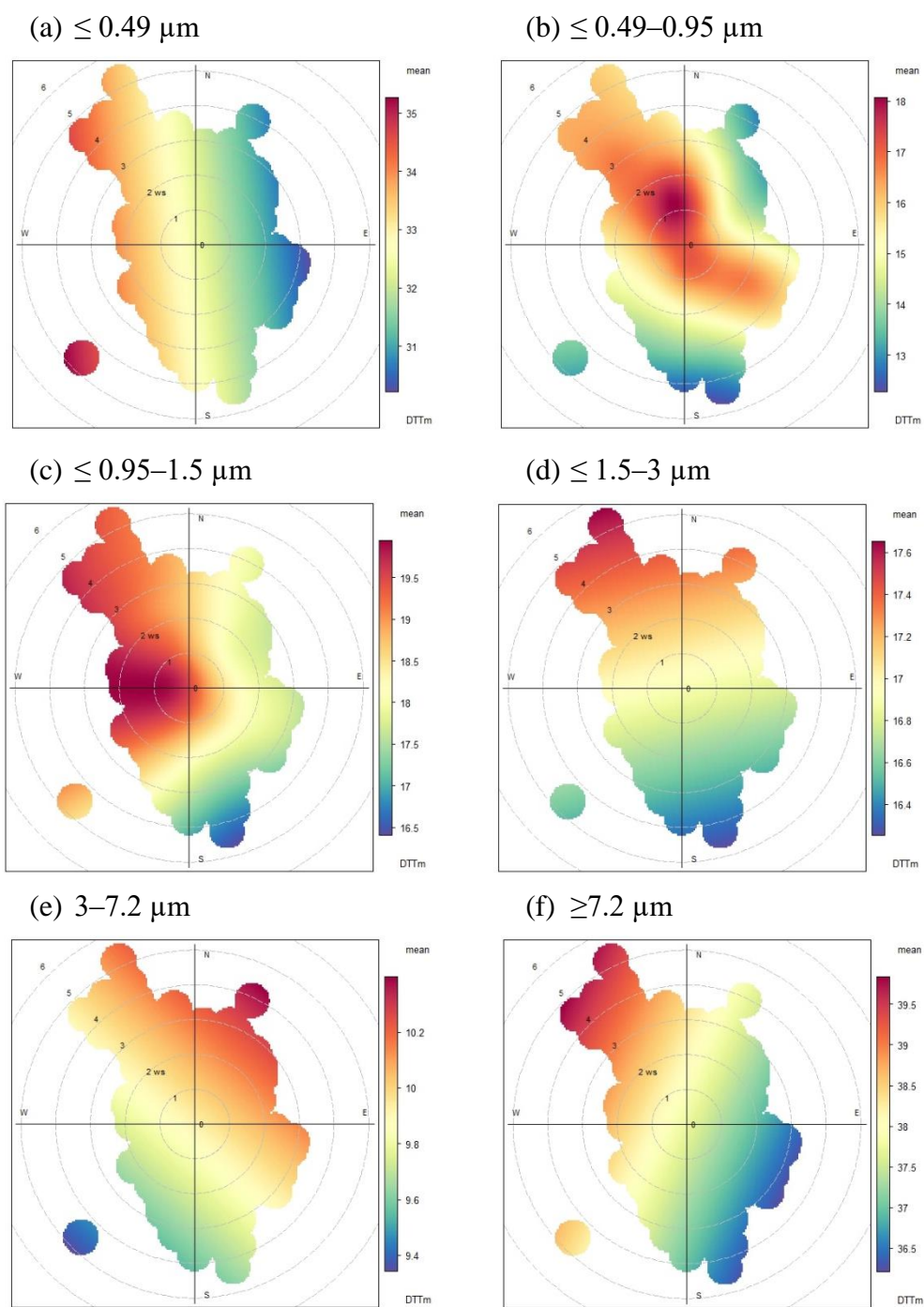
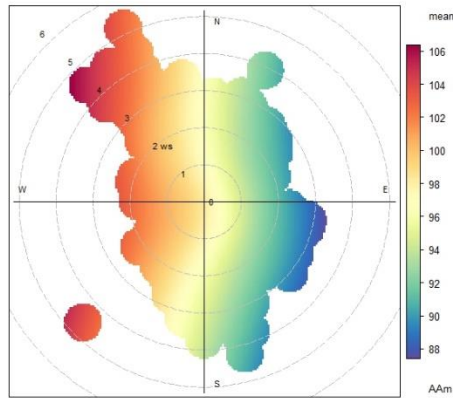
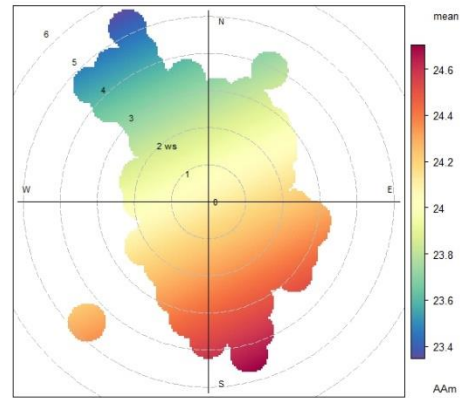


Figure 8-9 Bivariate polar plots of size-resolved concentration of DTTm ( $\text{nmol min}^{-1} \mu\text{g}^{-1}$ ) induced by methanol-soluble fractions: ultrafine (a, b), accumulation (c, d), coarse (e, f) particles

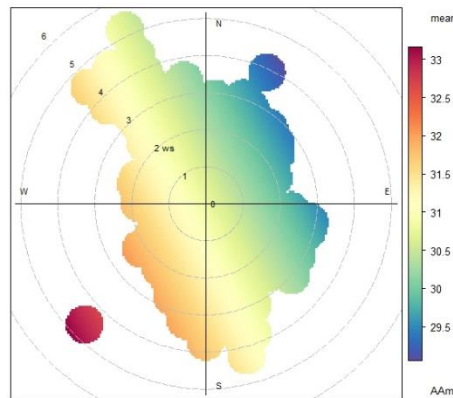
(a)  $\leq 0.49 \mu\text{m}$



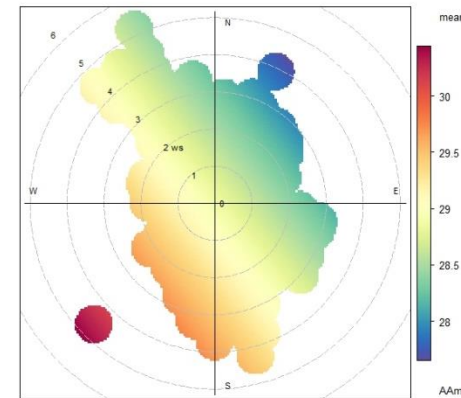
(b)  $\leq 0.49\text{--}0.95 \mu\text{m}$



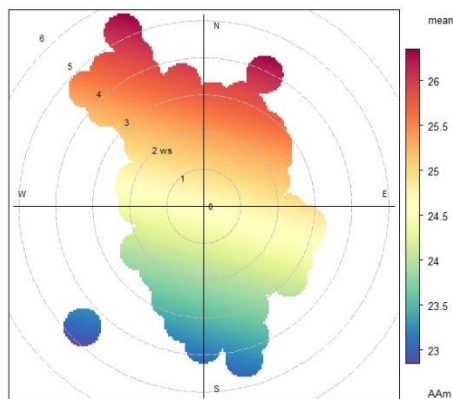
(c)  $\leq 0.95\text{--}1.5 \mu\text{m}$



(d)  $\leq 1.5\text{--}3 \mu\text{m}$



(e)  $3\text{--}7.2 \mu\text{m}$



(f)  $\geq 7.2 \mu\text{m}$

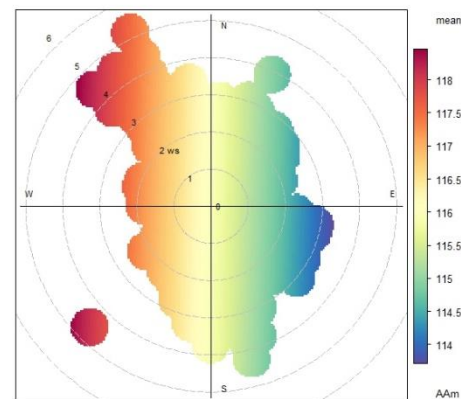


Figure 8-10 Bivariate polar plots of size-resolved concentration of AAm ( $\text{nmol min}^{-1}\mu\text{g}^{-1}$ ) induced by methanol-soluble fractions: ultrafine (a, b), accumulation (c, d), coarse (e, f) particles

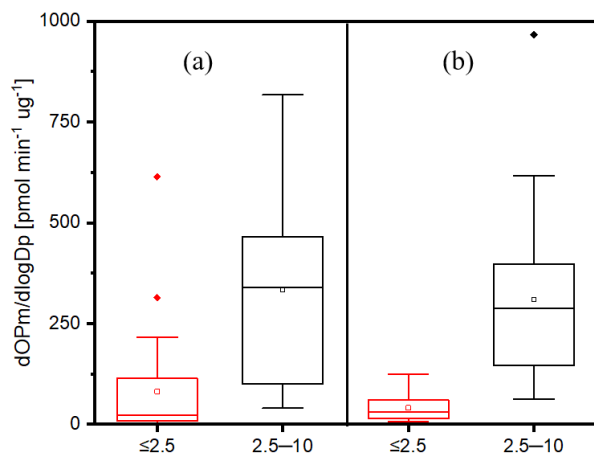


Figure 8-11 Size distribution of intrinsic OP ( $dOP_v = \text{mean extrinsic OP (nmol min}^{-1} \text{ m}^{-3})$ ,  $d\log D_p = \text{logarithmic difference of aerodynamic diameter}$ ) of water-soluble fractions of fine ( $\leq 2.5 \mu\text{m}$ ) and coarse particles ( $2.5\text{--}10 \mu\text{m}$ ) in DTT (a) and AA (b) assays. Median (line across the box), mean (square within the box), first quartile (Q1) (bottom of the box), third quartile (Q3) (top of the box), outlier (square shown outside the box), whiskers shows minimum and maximum values

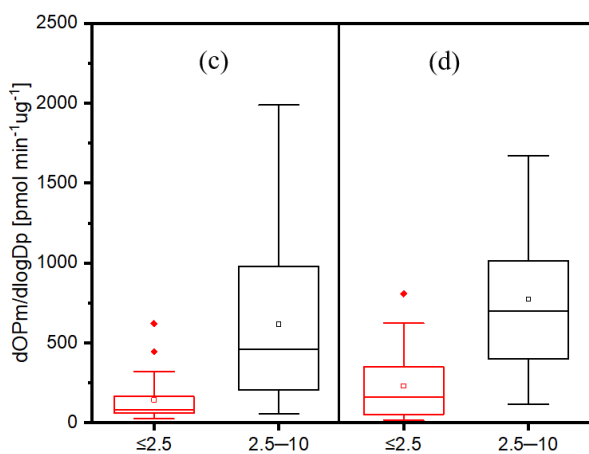


Figure 8-12 Size distribution of intrinsic OP ( $dOP_v = \text{mean extrinsic OP (nmol min}^{-1} \text{ m}^{-3})$ ,  $d\log D_p = \text{logarithmic difference of aerodynamic diameter}$ ) of methanol-soluble fractions of fine ( $\leq 2.5 \mu\text{m}$ ) and coarse particles ( $2.5\text{--}10 \mu\text{m}$ ) in DTT (a) and AA (b) assays. Median (line across the box), mean (square within the box), first quartile (Q1) (bottom of the box), third quartile (Q3) (top of the box), outlier (square shown outside the box), whiskers shows minimum and maximum values

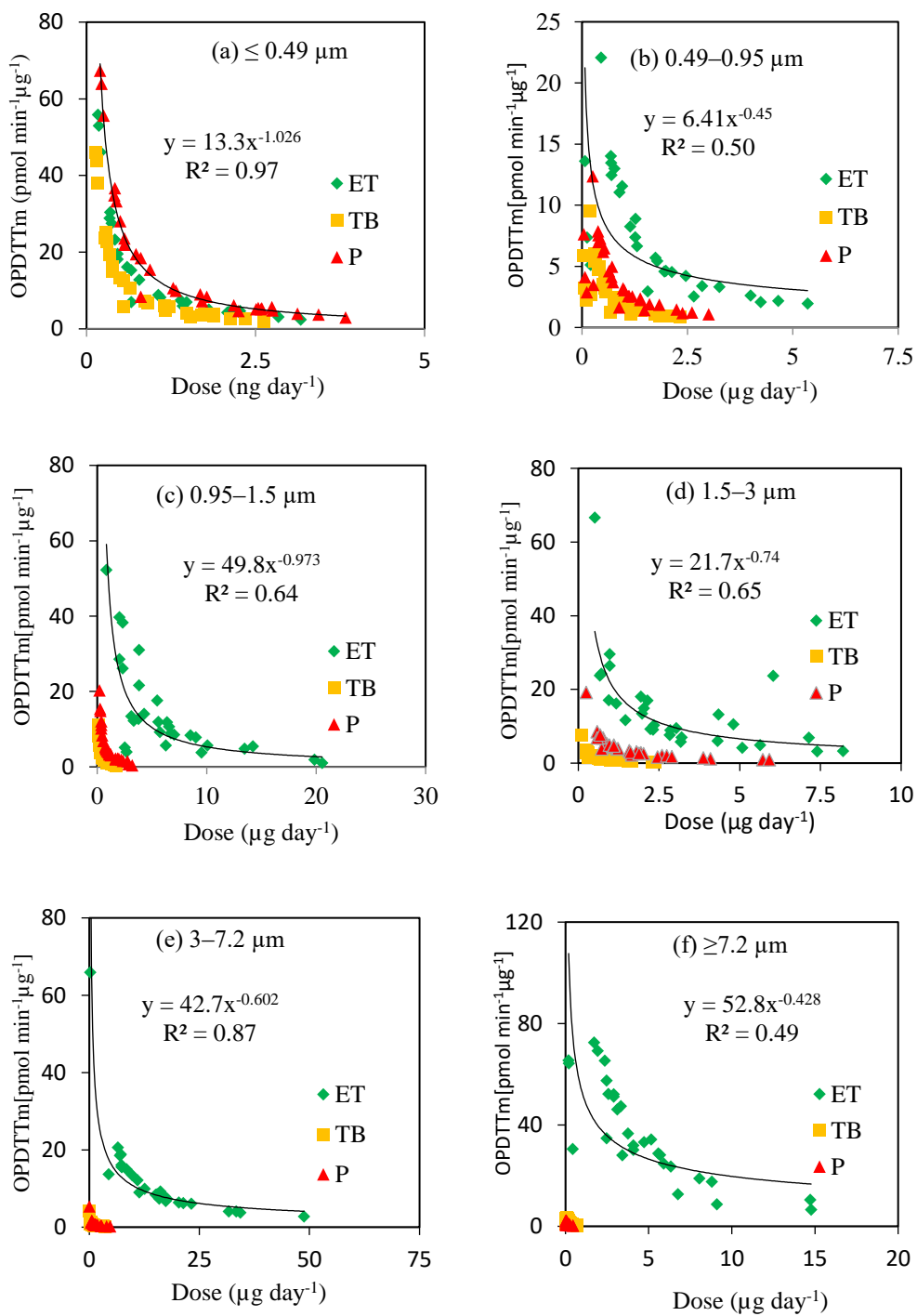


Figure 8-13 Association of lung-deposited dose and intrinsic OP of PM size fractions in DTT assay: (a)  $\leq 0.49\mu\text{m}$ , (b)  $0.49-0.95 \mu\text{m}$ , (c)  $0.95-1.5 \mu\text{m}$ , (d)  $1.5-3 \mu\text{m}$ , (e)  $3-7.2 \mu\text{m}$ , and (f)  $\geq 7.2 \mu\text{m}$

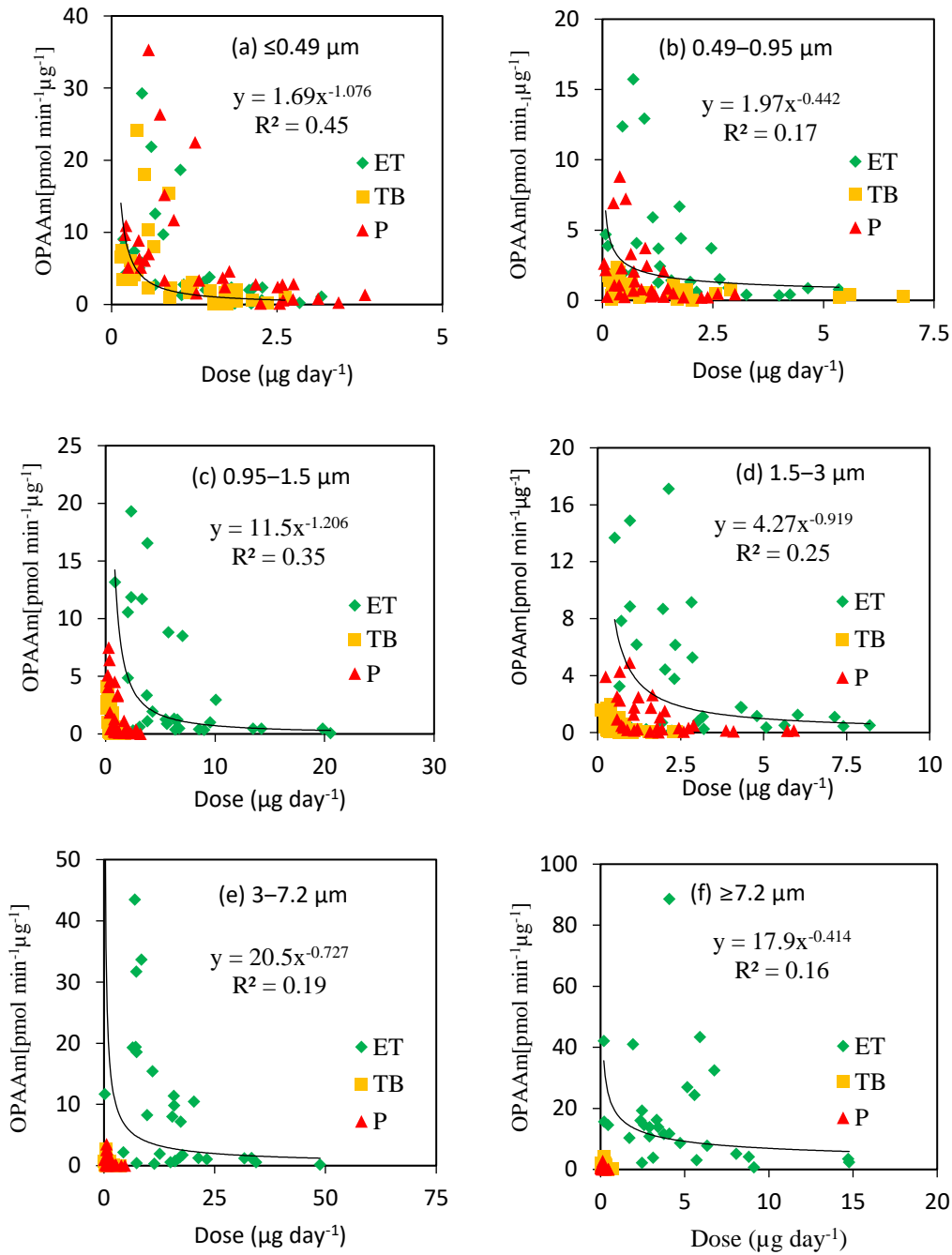


Figure 8-14 Association of lung-deposited dose and intrinsic OP of PM size fractions in AA assay: (a)  $\leq 0.49 \mu\text{m}$ , (b)  $0.49-0.95 \mu\text{m}$ , (c)  $0.95-1.5 \mu\text{m}$ , (d)  $1.5-3 \mu\text{m}$ , (e)  $3-7.2 \mu\text{m}$ , and (f)  $\geq 7.2 \mu\text{m}$